

INFORMATION TO USERS

This manuscript has been reproduced from the microfilm master. UMI films the text directly from the original or copy submitted. Thus, some thesis and dissertation copies are in typewriter face, while others may be from any type of computer printer.

The quality of this reproduction is dependent upon the quality of the copy submitted. Broken or indistinct print, colored or poor quality illustrations and photographs, print bleedthrough, substandard margins, and improper alignment can adversely affect reproduction.

In the unlikely event that the author did not send UMI a complete manuscript and there are missing pages, these will be noted. Also, if unauthorized copyright material had to be removed, a note will indicate the deletion.

Oversize materials (e.g., maps, drawings, charts) are reproduced by sectioning the original, beginning at the upper left-hand corner and continuing from left to right in equal sections with small overlaps.

Photographs included in the original manuscript have been reproduced xerographically in this copy. Higher quality 6" x 9" black and white photographic prints are available for any photographs or illustrations appearing in this copy for an additional charge. Contact UMI directly to order.

ProQuest Information and Learning
300 North Zeeb Road, Ann Arbor, MI 48106-1346 USA
800-521-0600

UMI[®]

**Nanosecond Time-Resolved Diffuse Reflectance Studies of Reactive Carbocations
and Charge Migration in Non-Acidic Zeolites**

by

Melanie A. O'Neill

Submitted in partial fulfillment of the requirements
for the Degree of Doctor of Philosophy

at

Dalhousie University
Halifax, Nova Scotia
January 2001

© Copyright by Melanie A. O'Neill, 2001



National Library
of Canada

Acquisitions and
Bibliographic Services

395 Wellington Street
Ottawa ON K1A 0N4
Canada

Bibliothèque nationale
du Canada

Acquisitions et
services bibliographiques

395, rue Wellington
Ottawa ON K1A 0N4
Canada

Your file *Votre référence*

Our file *Notre référence*

The author has granted a non-exclusive licence allowing the National Library of Canada to reproduce, loan, distribute or sell copies of this thesis in microform, paper or electronic formats.

The author retains ownership of the copyright in this thesis. Neither the thesis nor substantial extracts from it may be printed or otherwise reproduced without the author's permission.

L'auteur a accordé une licence non exclusive permettant à la Bibliothèque nationale du Canada de reproduire, prêter, distribuer ou vendre des copies de cette thèse sous la forme de microfiche/film, de reproduction sur papier ou sur format électronique.

L'auteur conserve la propriété du droit d'auteur qui protège cette thèse. Ni la thèse ni des extraits substantiels de celle-ci ne doivent être imprimés ou autrement reproduits sans son autorisation.

0-612-66641-7

Canada

DALHOUSIE UNIVERSITY

FACULTY OF GRADUATE STUDIES

The undersigned hereby certify that they have read and recommend to the Faculty of Graduate Studies for acceptance a thesis entitled "Nanosecond Time-Resolved Diffuse Reflectance Studies of Reactive Carbocations and Charge Migration in Non-Acidic Zeolites"

by Melanie A. O'Neill

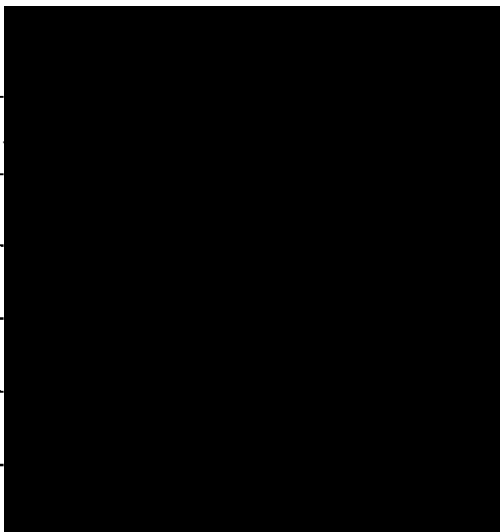
in partial fulfillment of the requirements for the degree of Doctor of Philosophy.

Dated: January 5, 2001

External Examiner _____

Research Supervisor _____

Examining Committee _____



DALHOUSIE UNIVERSITY

DATE: January 12, 2001

AUTHOR: Melanie A. O'Neill

TITLE: Nanosecond Time-Resolved Diffuse Reflectance Studies of Reactive
Carbocations and Charge Migration in Non-Acidic Zeolites

DEPARTMENT OR SCHOOL: Chemistry

DEGREE: Ph. D.

CONVOCATION: May

YEAR: 2001

Permission is herewith granted to Dalhousie University to circulate and to have copied for non-commercial purposes, at its discretion, the above title upon the request of individuals or institutions.


Signature of Author

The author reserves other publication rights, and neither the thesis nor extensive extracts from it may be printed or otherwise reproduced without the author's written permission.

The author attests that permission has been obtained for the use of any copyrighted material appearing in this thesis (other than brief excerpts requiring only proper acknowledgement in scholarly writing), and that all such use is clearly acknowledged.

The fireflies, twinkling among the leaves, make the stars wonder.

- Rabindranath Tagore (1861 – 1941)

Table of Contents

Table of Contents	v
List of Figures	ix
List of Tables	xxviii
Abstract	xxxii
List of Abbreviations	xxxiii
Acknowledgements	xxxv
Chapter 1. Introduction to the Study of Reaction Dynamics in Zeolites	1
1.1 Zeolites	1
1.1.1 Structural Features of Zeolites: Topology and Composition	1
1.1.2 Inside the Zeolite Cavities	7
1.1.3 Molecular Guests in Zeolites	14
1.2 Using Zeolites to Control Reaction Dynamics: Experimental Examples	23
1.2.1 Influence of Zeolites on the Lifetimes of Reactive Intermediates	23
1.2.2 Influence of Zeolites on Reaction Pathways	27
1.3 Scope and Significance of Thesis	31
Chapter 2. General Background and Concepts	33
2.1 Laser Flash Photolysis	33
2.2 Nanosecond Time-Resolved Diffuse Reflectance	34
2.3 Transient Kinetics in Heterogeneous Media	36
2.4 Defining the Quantity of Adsorbates within Zeolites	38
Chapter 3. Generation and Reactivity of Carbocations in Non-Acidic Zeolites	40
3-1 Introduction	40
3.1.1 Studies of Reactive Carbocations in Solution	40
3.1.2 Carbocations in Zeolites	44
3.2 Generation and Reactivity of Cumyl Cations in Non-Acidic Zeolites	46
3.2.1 Results	49

3.2.1.1	<i>Generation of the 4-Methoxycumyl Cation in Dry Alkali Metal Cation Zeolites</i>	50
3.2.1.2	<i>Absolute Reactivity of the 4-Methoxycumyl Cation in Alkali Metal Cation Zeolites</i>	54
3.2.1.3	<i>Kinetic Isotope Effects on the Absolute Reactivity of the 4-Methoxycumyl Cation in Alkali Metal Cation Zeolites</i>	56
3.2.1.4	<i>Products Derived from Irradiation of 4,4-Dimethoxybicumene in NaY</i>	58
3.2.1.5	<i>Bimolecular Reactions of the 4-Methoxycumyl Cation with Coadsorbed Quenchers in Alkali Metal Cation Zeolites</i>	62
3.2.1.6	<i>Generation and Reactivity of other Cumyl Cations in Alkali Metal Cation Zeolites</i>	73
3.2.1.7	<i>Preliminary Experiments with 4,4'-(N-N-Dimethylamino)bicumene in Alkali Metal Cation Zeolites</i>	82
3.2.2	Discussion	111
3.2.2.1	<i>Mechanism for Formation of Cumyl Cations in Non-Acidic Zeolites</i>	111
3.2.2.2	<i>Mechanism for Intrazeolite Decay of Cumyl Cations</i>	112
3.2.2.3	<i>Reactivity of Cumyl Cations in Dry Alkali Metal Cation Zeolites: Zeolite Nucleophilicity</i>	117
3.2.2.4	<i>Substituent Effects on the Reactivity of Cumyl Cations in AlkaliMetalCation Zeolites</i>	126
3.2.2.5	<i>Bimolecular Addition Reactions of Cumyl Cations in Alkali Metal Cation Zeolites</i>	129
3.2.2.6	<i>Preliminary Ideas Concerning the Formation of the 4-Dimethylaminocumyl Cation in Alkali MetalCation Zeolites</i>	140
3.3	Generation and Reactivity of 9-Fluorenyl Cations in Non-Acidic Zeolites	142
3.3.1	Results	149
3.3.1.1	<i>Laser Photolysis of 9-Alkyl- and 9-Vinyl-9-Fluorenols in Alkali Metal Cation Zeolites</i>	149
3.3.1.2	<i>Laser Photolysis of 9-Fluorenol in Alkali Metal Cation Zeolites</i>	158
3.3.1.3	<i>Diphenylmethyl Cations in Alkali Metal Cation Zeolites</i>	161
3.3.1.4	<i>Laser Photolysis of 9-Cyclopropyl-9-Fluorenol in Alkali Metal Cation Zeolites</i>	162
3.3.1.5	<i>Influence of Coadsorbed Protic Reagents on the Generation and Reactivity of 9-Fluorenyl Cations in Alkali Metal Cation Zeolites</i>	167
3.3.1.6	<i>Other 9-Fluorenyl Precursors in Alkali Metal Cation Zeolites</i>	176
3.3.1.7	<i>Triene Isomers of 9-Fluorenols</i>	177

3.3.2 Discussion	215
3.3.2.1 <i>Generation of 9-Fluorenyl Cations from Photoexcited 9-Fluorenols in Alkali Metal Cation Zeolites</i>	215
3.3.2.2 <i>Absolute Reactivity of 9-Fluorenyl Cations in Alkali Metal Cation Zeolites</i>	220
3.3.2.3 <i>Substituent Effects on the Intrazeolite Reactivity of 9-Fluorenyl Cations</i>	224
3.3.2.4 <i>Influence of Coadsorbed Protic Reagents on the Intrazeolite Reactivity of 9-Fluorenyl Cations</i>	226
3.4 Synopsis of Current Views of Carbocation Chemistry in Non-Acidic Zeolites and Direction of Future Studies	228
Chapter 4. Photogeneration and Migration of Electrons and Holes in NaY	232
4.1 Introduction	232
4.1.1 A Brief Introduction to Electron Transfer	232
4.1.2 Studies of Electron Transfer and Redox Processes in Zeolites	242
4.1.3 Scope of Chapter Four	248
4.2 Results	249
4.2.1 Nanosecond Laser Flash Photolysis of Chloranil in NaY	250
4.2.2 Photoexcitation of Chloranil in NaY containing a Secondary Electron Donor	253
4.2.3 Photoexcitation of t-Anethole in NaY containing a Secondary Electron Acceptor	259
4.2.4 Steady-State Fluorescence Measurements	266
4.3 Discussion	288
4.3.1 Generation of Holes in Zeolites: NaY as a Single Electron Donor	288
4.3.2 Mechanism(s) for Intrazeolite Electron Transfer Following Selective Excitation of an Electron Acceptor in NaY	293
4.3.3 Mechanism(s) for Intrazeolite Electron Transfer Following Selective Excitation of an Electron Donor in NaY	297
4.3.4 Estimating the Distance of Electron and Hole Migration in Zeolite NaY	300
4.3.5 Direction for Ongoing Studies of Charge Migration in Zeolites	317
Chapter 5. Experimental	320
5.1 General	320
5.2 Materials	320
5.2.1 Bicumenes	320
5.2.2 9-Fluorenols and 9-Substituted Fluorenes	324

5.2.3 Other Materials	325
5.2.4 Zeolites	326
5.3 Transient Generation	326
5.4 Experimental Procedures	328
5.4.1 Preparation of Zeolite Samples	328
5.4.2 Inclusion of Alcohols, Alkyl Enol Ethers, and Water into Zeolite-Adsorbate Composites	331
5.4.3 Steady-State Photolysis	332
Appendix 1. Examination of the Water and Residual Organic Solvent Content in Zeolite Samples	333
References	342

List of Figures

1-1	Framework topology of faujasite.....	2
1-2	Schematic representation of tetrahedral zeolite building blocks and their linkage to form a microporous network.....	3
1-3	Generation of various zeolite topologies through spatial arrangement of sodalite and pentasil substructures.....	4
1-4	Three occupancy sites of counterbalancing cations in faujasite zeolites (zeolites X and Y).....	6
1-5	The current experimental approach to studying reaction dynamics in zeolites involving direct examination of reactive intermediates.....	23
3-1	Transient diffuse reflectance spectrum generated upon 266 nm laser irradiation of 4,4'-dimethoxybicumene in evacuated (10^{-4} Torr) NaY. Inset shows the decay monitored at 360 nm under vacuum and oxygen conditions.....	86
3-2	Decay traces monitored at 360 nm following 266 nm laser irradiation of 4,4'-dimethoxybicumene in NaY containing various concentrations methanol. Inset shows the observed decay rate constant measured at 360 nm as a function of methanol concentration in NaY.....	86
3-3	Transient diffuse reflectance spectrum observed upon 266 nm laser irradiation of 4-methylanisole in evacuated NaY. Inset shows the observed decay rate constant and change in diffuse reflectance monitored at 440 nm as a function of methanol concentration in NaY.....	87
3-4	Transient diffuse reflectance spectrum generated upon 308 nm laser photolysis of chloranil in evacuated NaY with coadsorbed 4,4'-dimethoxybicumene. Inset shows the decay traces monitored at 360 nm following direct excitation of 4,4'-dimethoxybicumene with 266 nm laser light and 308 nm excitation of chloranil in the presence of 4,4'-dimethoxybicumene	87

3-5	Transient diffuse reflectance spectra obtained after 266 nm laser photolysis of 4,4'-dimethoxybicumene in LiY, RbY, NaX and Na β	88
3-6	Stretched kinetic decay traces of the 4-methoxycumyl cation monitored at 360 nm in evacuated alkali metal cation Y zeolites.....	89
3-7	Stretched kinetic decay traces of the 4-methoxycumyl cation monitored at 360 nm in evacuated Na ⁺ zeolites.....	89
3-8	Distribution of lifetimes of the 4-methoxycumyl cation in evacuated LiY, NaY, KY, RbY and CsY obtained by fitting the stretched decay traces observed at 360 nm according to the ESM method.....	90
3-9	Transient diffuse reflectance spectrum observed upon 266 nm laser irradiation of 4,4'-dimethoxybicumene- <i>d</i> ₁₂ in evacuated NaY and oxygen-saturated LiY. Inset compares the transient spectrum obtained after photolysis in evacuated and oxygen-saturated NaY.....	91
3-10	Decay traces monitored at 360 nm following 266 nm laser photolysis of 4,4'-dimethoxybicumene and 4,4'-dimethoxybicumene- <i>d</i> ₁₂ in oxygen-saturated LiY, NaY, KY, RbY and CsY.....	92
3-11.	Decay traces observed at 360 nm following 266 nm laser irradiation of 4,4'-dimethoxybicumene in dry and hydrated LiY, NaY, KY, RbY and CsY. The water content is 12.5 %, 10 %, 6 %, 3 % and 2 % by weight in LiY through CsY, respectively.....	93
3-12	Decay traces observed at 360 nm following 266 nm laser irradiation of 4,4'-dimethoxybicumene in dry and hydrated Na β , NaMor and NaX. The samples contain 3 %, 4 %, and 5 %, water by weight in Na β , NaMor and NaX, respectively.....	94
3-13	Decay rate constant of the 4-methoxycumyl cation in LiY, NaY, KY and RbY as a function of methanol concentration.....	95

3-14	Normalized initial change in diffuse reflectance due to the 4-methoxycumyl cation at 360 nm observed in LiY, NaY, KY, RbY and CsY as a function of methanol concentration.....	95
3-15	Decay rate constant of the 4-methoxycumyl cation in NaY as a function of methanol, ethanol, <i>isopropanol</i> and <i>tert</i> -butanol concentration.....	96
3-16	Initial change in diffuse reflectance due to the 4-methoxycumyl cation observed at 360 nm in NaY as a function of methanol, ethanol, <i>isopropanol</i> , <i>isobutanol</i> , <i>tert</i> -butanol and TFE concentration.....	96
3-17	Initial change in diffuse reflectance due to the 4-methoxycumyl cation observed at 360 nm in NaY as a function of ethyl vinyl ether, propyl vinyl ether, butyl vinyl ether, <i>tert</i> -butyl vinyl ether, <i>isopropenyl</i> methyl ether and ethyl propenyl ether concentration.....	97
3-18	Decay rate constant of the 4-methoxycumyl cation in NaY as a function of ethyl vinyl ether, propyl vinyl ether and <i>tert</i> -butyl vinyl ether concentration.....	97
3-19	Decay rate constant of the 4-methoxycumyl cation in NaY as a function of ethyl vinyl ether, <i>isopropenyl</i> methyl ether and ethyl propenyl ether concentration.....	98
3-20	Transient absorption spectrum generated after 308 nm laser irradiation of chloranil in nitrogen-saturated HFIP containing 0.16 mM 4,4'-dimethylbicumene. Inset shows growth traces observed at 330 nm for 4,4'-dimethylbicumene. concentration of 0.16 mM and 0.47 mM.....	98
3-21	Transient absorption spectrum generated after 308 nm laser irradiation of chloranil in nitrogen-saturated HFIP containing 0.16 mM 4,4'-dimethylbicumene. Inset shows decay traces monitored at 330 nm in the presence of 0 mM, 0.10 mM and 0.40 mM <i>tert</i> -butyl ammonium bromide.....	99
3-22	Growth rate constant measured at 335 nm following 308 nm laser photolysis of chloranil in oxygen-saturated HFIP as a function of 4,4'-dimethylbicumene. concentration.....	99

3-23	Transient absorption spectrum generated after 308 nm laser irradiation of chloranil in nitrogen-saturated HFIP containing 0.16 mM 4,4'-difluorobicumene.....	100
3-24	Transient absorption spectrum generated after 308 nm laser irradiation of chloranil in nitrogen-saturated HFIP containing 0.16 mM bicumene.....	100
3-25	Transient absorption spectrum observed upon 308 nm laser irradiation of chloranil in nitrogen-saturated HFIP containing 7.6 mM 3,3'-dimethoxybicumene.....	101
3-26	Transient diffuse reflectance spectrum generated after 266 nm laser irradiation of 4,4'-dimethylbicumene in evacuated LiY.....	101
3-27	Transient diffuse reflectance spectrum generated after 266 nm laser irradiation of 4,4'-dimethylbicumene in oxygen-saturated LiY. The inset compares the transient diffuse reflectance spectra observed following laser irradiation of 4,4'-dimethylbicumene in LiY under vacuum and oxygen conditions.....	102
3-28	Transient diffuse reflectance spectrum generated after 266 nm laser irradiation of 4,4'-dimethylbicumene in oxygen-saturated NaY. The inset compares the transient diffuse reflectance spectra observed following laser irradiation of 4,4'-dimethylbicumene in NaY under vacuum and oxygen conditions.....	102
3-29	Transient diffuse reflectance spectrum generated after 266 nm laser irradiation of 4,4'-dimethylbicumene in oxygen-saturated KY. The inset compares the transient diffuse reflectance spectra observed following laser irradiation of 4,4'-dimethylbicumene in KY under vacuum and oxygen conditions.....	103
3-30	Transient diffuse reflectance spectra observed immediately after 266 nm laser photolysis of 4,4'-dimethylbicumene in dry and hydrated NaY. The influence of methanol on the change in diffuse reflectance observed at 335 nm immediately following laser photolysis of 4,4'-dimethylbicumene in dry NaY is shown in the inset.....	103
3-31	Decay traces of the 4-methylcumyl cation observed at 335 nm in oxygen-saturated LiY, NaY and KY.....	104

3-32	Observed decay rate constant for the 4-methylcumyl cation in NaY as a function of HFIP concentration. Inset shows the decay kinetics of the 4-methylcumyl cation observed at 335 nm in NaY and NaY containing 1.9 M HFIP.....	104
3-33	Decay traces of the 4-fluorocumyl cation observed at 330 nm in oxygen-saturated LiY, and oxygen-saturated LiY containing 0.3 M HFIP. The variation in decay rate constant of the 4-fluorocumyl cation in LiY with HFIP concentration is shown in the inset.....	105
3-34	Transient diffuse reflectance spectrum generated after 266 nm laser photolysis of 4,4'-difluorobicumene in LiY containing 0.8 M HFIP.....	105
3-35	Transient diffuse reflectance spectrum observed upon 266 nm laser irradiation of 3,3'-dimethoxybicumene in evacuated and oxygen-saturated LiY.....	106
3-36	Transient diffuse reflectance spectrum generated after 266 nm laser photolysis of bicumene in LiY containing 1 M HFIP. Inset shows the initial change in diffuse reflectance monitored at 320 nm as a function of HFIP concentration.....	106
3-37	Transient diffuse reflectance spectrum generated after 266 nm laser photolysis of 4,4'-dimethylbicumene in oxygen-saturated Na β . The decay traces of the 4-methylcumyl cation monitored at 340 nm under vacuum and oxygen conditions are shown in the inset.....	107
3-38	Transient diffuse reflectance spectrum generated after 266 nm laser photolysis of 4,4'-difluorobicumene in oxygen-saturated Na β	107
3-39	Transient diffuse reflectance spectrum generated after 266 nm laser photolysis of bicumene in oxygen-saturated Na β	108
3-40	Transient diffuse reflectance spectrum generated after 266 nm laser photolysis of 4,4'-difluorobicumene in evacuated Na β	108

3-41	Transient diffuse reflectance spectrum observed upon 308 nm laser photolysis of 4,4'-(<i>N,N</i> -dimethylamino)bicumene in evacuated NaY. Inset shows the growth and decay traces monitored at 380 nm and 485 nm, respectively.....	109
3-42	Transient diffuse reflectance spectrum generated after 308 nm laser photolysis of 4,4'-(<i>N,N</i> -dimethylamino)bicumene in evacuated KY. Inset shows the decay and growth traces monitored at 380 nm and 485 nm, respectively.....	109
3-43	Plot of the fraction of prompt formation of the 4-dimethylaminocumyl cation in alkali metal cation Y zeolites versus metal cation radius.....	110
3-44	Plot of the growth rate constant of the 4-dimethylaminocumyl cation in alkali metal cation Y zeolites versus metal cation radius.....	110
3-45	Relationship between the lifetime of the 4-methoxycumyl cation in alkali metal cation zeolites and the charge on the zeolite framework oxygen as calculated from Sanderson electronegativity principles.....	121
3-46	Relationship between the lifetime of the 4-methylcumyl cation in alkali metal cation zeolites and the charge on the zeolite framework oxygen as calculated from Sanderson electronegativity principles.....	123
3-47	Relationship between the observed rate constant for decay of substituted cumyl cations in LiY , Na β and HFIP. and the substituent constant σ^{c+}	127
3-48	Transient diffuse reflectance spectrum generated after 308 nm laser irradiation of 9-methyl-9-fluorenol in oxygen-saturated NaY. Inset shows the decay trace monitored at 485 nm.....	179
3-49	Transient diffuse reflectance spectrum generated after 308 nm laser irradiation of 9-methyl-9-fluorenol in evacuated NaY. Inset shows the decay trace monitored at 485 nm under vacuum and oxygen conditions.....	179
3-50	Transient diffuse reflectance spectrum generated after 308 nm laser irradiation of 9-methyl-9-fluorenol in oxygen-saturated NaY. Inset shows the decay trace monitored at 370 nm.....	180

3-51	Transient diffuse reflectance spectrum generated after 308 nm laser irradiation of fluorene in oxygen-saturated NaY.....	180
3-52	Transient diffuse reflectance spectrum generated after 308 nm laser irradiation of 9-methyl-9-fluorene in oxygen-saturated LiY. Inset shows the decay trace monitored at 485 nm under vacuum and oxygen conditions.....	181
3-53	Transient diffuse reflectance spectrum generated immediately after 308 nm laser irradiation of 9-methyl-9-fluorene in evacuated and oxygen-saturated KY. Inset shows the transient spectrum generated in KY under vacuum conditions.....	181
3-54	Transient diffuse reflectance spectrum generated immediately after 308 nm laser irradiation of 9-methyl-9-fluorene in evacuated and oxygen-saturated RbY. Inset shows the transient spectrum generated in RbY under vacuum conditions.....	182
3-55	Transient diffuse reflectance spectrum generated immediately after 308 nm laser irradiation of 9-methyl-9-fluorene in evacuated and oxygen-saturated CsY. Inset shows the transient spectrum generated in CsY under vacuum conditions.....	182
3-56	Yield of triplet 9-methyl-9-fluorene as a function of alkali metal cation radius observed following laser photolysis of 9-methyl-9-fluorene in evacuated alkali metal cation Y zeolites.....	183
3-57	Yield of the radical cation and the triene isomer of 9-methyl-9-fluorene as a function of alkali metal cation radius observed following laser photolysis of 9-methyl-9-fluorene in evacuated alkali metal cation Y zeolites.....	183
3-58	Transient diffuse reflectance spectrum generated after 308 nm laser irradiation of 9-methyl-9-fluorene in evacuated NaX. Inset compares the decay traces monitored at 485 nm following photolysis of 9-methyl-9-fluorene in NaY and NaX.....	184
3-59	Transient diffuse reflectance spectrum generated after 308 nm laser irradiation of 9-methyl-9-fluorene in oxygen-saturated Na β . The decay trace monitored at 485 nm is shown in the inset.....	184

- 3-60** Transient diffuse reflectance spectrum generated after 308 nm laser irradiation of 9-ethyl-9-fluorenol in oxygen-saturated LiY. Inset compares the decay traces monitored at 485 nm under vacuum and oxygen conditions.....185
- 3-61** Transient diffuse reflectance spectrum generated after 308 nm laser irradiation of 9-isopropyl-9-fluorenol in oxygen-saturated NaY. The decay trace monitored at 485 nm is shown in the inset.....185
- 3-62** Transient diffuse reflectance spectrum generated after 308 nm laser photolysis of 9-ethyl-9-fluorenol in oxygen-saturated Na β . Inset compares the decay traces at 485 nm in evacuated and oxygen-saturated Na β186
- 3-63** Transient diffuse reflectance spectrum generated after 308 nm laser photolysis of 9-isopropyl-9-fluorenol in oxygen-saturated Na β . Inset compares the decay traces at 485 nm under vacuum and oxygen conditions.....186
- 3-64** Transient diffuse reflectance spectrum generated after 308 nm laser irradiation of 9-vinyl-9-fluorenol in oxygen-saturated NaY. Inset compares the decay traces monitored at 485 nm under vacuum and oxygen conditions.....187
- 3-65** Transient diffuse reflectance spectrum generated after 308 nm laser photolysis of 9-fluorenol in oxygen-saturated LiY. Inset shows the transient absorption spectrum generated after 308 nm laser photolysis of 9-fluorenol in HFIP.....187
- 3-66** Transient diffuse reflectance spectrum generated after 308 nm laser photolysis of 9-fluorenol in oxygen-saturated LiY. The decay traces monitored at 370 nm under vacuum and oxygen conditions are shown in the inset.....188
- 3-67** Transient diffuse reflectance spectrum generated after 308 nm laser photolysis of 9-fluorenol in evacuated LiY. Inset compares the transient spectra observed under vacuum and oxygen conditions.....188
- 3-68** Transient diffuse reflectance spectrum generated after 308 nm laser photolysis of 9-fluorenol in oxygen-saturated NaY. Inset shows the same transient spectrum observed at longer delay times following the laser pulse.....189

3-69	Transient diffuse reflectance spectrum generated after 308 nm laser irradiation of 9-fluorenonol in evacuated KY. Inset compares the transient spectra generated after laser photolysis of 9-fluorenonol in KY under vacuum and oxygen conditions....	189
3-70	Transient diffuse reflectance spectrum generated after 308 nm laser irradiation of 9-fluorenonol in evacuated RbY. Inset compares the transient spectra generated after laser photolysis of 9-fluorenonol in RbY under vacuum and oxygen conditions.....	190
3-71	Transient diffuse reflectance spectrum generated after 308 nm laser irradiation of 9-fluorenonol in evacuated CsY. Inset compares the transient spectra generated after laser photolysis of 9-fluorenonol in CsY under vacuum and oxygen conditions.....	190
3-72	Yield of triplet 9-fluorenonol as a function of cation radius observed following laser photolysis of 9-fluorenonol in evacuated alkali metal cation Y zeolites.....	191
3-73	Yield of the radical cation and the triene isomer of 9-fluorenonol as a function of alkali metal cation radius observed following laser photolysis of 9-fluorenonol in evacuated alkali metal cation Y zeolites.....	191
3-74	Transient diffuse reflectance spectrum generated after 308 nm laser irradiation of 9-fluorenonol in evacuated NaX.....	192
3-75	Transient diffuse reflectance spectrum generated after 308 nm laser irradiation of 9-fluorenonol in evacuated Na β . The transient diffuse reflectance spectrum in oxygen-saturated Na β is given in the inset.....	192
3-76	Transient diffuse reflectance spectrum generated after 308 nm laser irradiation of 9-fluorenonol in evacuated NaMor. Inset shows the decay traces observed at 515 nm under vacuum and oxygen conditions.....	193
3-77	Transient diffuse reflectance spectrum generated by two laser (266 and 308 nm) excitation of diphenylacetic acid in evacuated NaY.....	193

3-78	Transient diffuse reflectance spectrum generated by two laser (266 and 308 nm) excitation of diphenylacetic acid in evacuated LiY, NaY, KY, RbY and CsY...194
3-79	Decay traces monitored at 440 nm following two laser excitation of diphenylacetic acid in evacuated LiY and RbY.....195
3-80	Transient diffuse reflectance spectrum generated after 308 nm laser irradiation of 9-cyclopropyl-9-fluorenol in evacuated NaY. Inset shows the transient absorption spectrum generated after 308 nm laser photolysis of 9-cyclopropyl-9-fluorenol in TFE.....195
3-81	Decay traces monitored at 445 nm following 308 nm laser photolysis of 9-cyclopropyl-9-fluorenol in evacuated and oxygen-saturated NaY.....196
3-82	Normalized decay traces monitored at 445 nm following 308 nm laser photolysis of 9-cyclopropyl-9-fluorenol in dry NaY, and in NaY containing 6 weight % water or methanol.....196
3-83	Transient diffuse reflectance spectrum generated after 308 nm laser irradiation of 9-cyclopropyl-9-fluorenol in evacuated NaY. Inset shows the decay trace monitored at 370 nm.....197
3-84	Transient diffuse reflectance spectrum generated after 308 nm laser photolysis of 9-cyclopropyl-9-fluorenol in LiY, NaY, KY, RbY and CsY. Insets show decay traces monitored at 445 nm in each zeolite.....198
3-85	Yield of the 9-cyclopropyl-9-fluorenyl cation as a function of alkali metal cation radius observed following laser photolysis of 9-cyclopropyl-9-fluorenol in evacuated alkali metal cation Y zeolites.....199
3-86	Yield of the radical cation and the triene isomer of 9-cyclopropyl-9-fluorenol as a function of alkali metal cation radius observed following laser photolysis of 9-cyclopropyl-9-fluorenol in evacuated alkali metal cation Y zeolites.....199

3-87	Yield of the 9-cyclopropyl-9-fluorenyl cation, relative to the 9-cyclopropyl-9-fluorenyl radical cation and triene isomer, as a function of alkali metal cation radius observed following laser photolysis of 9-cyclopropyl-9-fluorenyl in evacuated alkali metal cation Y zeolites.....	200
3-88	Variation in the first-order decay rate constant and yield of the 9-cyclopropyl-9-fluorenyl cation as a function of alkali metal cation radius.....	200
3-89	Transient diffuse reflectance spectrum generated after 308 nm laser irradiation of 9-cyclopropyl-9-fluorenyl in evacuated NaX. The inset compares the decay kinetics monitored at 445 nm following laser photolysis of 9-cyclopropyl-9-fluorenyl in evacuated NaY and NaX.....	201
3-90	Transient diffuse reflectance spectrum generated after 308 nm laser irradiation of 9-cyclopropyl-9-fluorenyl in evacuated NaX. The decay trace monitored at 370 nm is shown in the inset.....	201
3-91	Decay traces observed at 445 nm following 308 nm laser photolysis of 9-cyclopropyl-9-fluorenyl in dry NaY, and NaY containing 6 weight % water or methanol.....	202
3-92	Normalized variation in the change in diffuse reflectance observed at 445 nm immediately following 308 nm laser photolysis of 9-cyclopropyl-9-fluorenyl in NaY as a function of the concentration of water or methanol.....	202
3-93	Transient diffuse reflectance spectrum generated after 308 nm laser irradiation of 9-cyclopropyl-9-fluorenyl in NaY containing 6 weight % coadsorbed water....	203
3-94	Decay traces monitored at 370 nm following laser photolysis of 9-cyclopropyl-9-fluorenyl in dry NaY and NaY containing 6 weight % methanol or water.....	203
3-95	Transient diffuse reflectance spectrum generated after 308 nm laser irradiation of 9-cyclopropyl-9-fluorenyl in NaY containing 6 weight % coadsorbed methanol.....	204

3-96	Variation in the first-order decay rate constant of the 9-cyclopropyl-9-fluorenyl cation monitored at 445 nm in NaY as a function of the concentration of methanol.....	204
3-97	Variation in the first-order decay rate constant of the 9-cyclopropyl-9-fluorenyl cation monitored at 445 nm in NaY as a function of the concentration of water.....	205
3-98	Variation in the change in diffuse reflectance due to the 9-cyclopropyl-9-fluorenyl cation in NaY as a function of the concentration of methanol.....	205
3-99	Transient diffuse reflectance spectrum generated after 308 nm laser irradiation of 9-cyclopropyl-9-fluorenyl in hydrated LiY. The inset compares the decay traces monitored at 445 nm under dry and hydrated conditions.....	206
3-100	Transient diffuse reflectance spectrum generated after 308 nm laser irradiation of 9-cyclopropyl-9-fluorenyl in hydrated KY. The inset compares the decay traces monitored at 445 nm in dry and hydrated KY.....	206
3-101	Transient diffuse reflectance spectrum generated after 308 nm laser irradiation of 9-cyclopropyl-9-fluorenyl in hydrated RbY. The inset compares the decay traces monitored at 445 nm in dry and hydrated RbY.....	207
3-102	Transient diffuse reflectance spectrum generated after 308 nm laser irradiation of 9-cyclopropyl-9-fluorenyl in hydrated CsY. The inset compares the decay traces monitored at 445 nm in dry and hydrated CsY.....	207
3-103	Transient diffuse reflectance spectrum generated after 308 nm laser photolysis of 9-methyl-9-fluorenyl in dry NaY, and NaY containing 3 weight % coadsorbed water. The inset compares the decay kinetics monitored at 445 nm in dry NaY and NaY containing approximately 1 weight % and 3 weight % coadsorbed water.....	208
3-104	Decay traces monitored at 445 nm following 308 nm laser photolysis of 9-fluorenyl in dry NaY and NaY containing coadsorbed water.....	208

3-105	Decay traces monitored at 370 nm following 308 nm laser photolysis of 9-methyl-9-fluorenol in dry NaY and NaY containing 1 weight % and 3 weight % coadsorbed water.....	209
3-106	Transient diffuse reflectance spectrum generated after 308 nm laser photolysis of 9-methyl-9-fluorenol in dry Na β , and in Na β containing 3 weight % coadsorbed water. The inset compares the decay kinetics monitored at 370 nm in Na β under dry and hydrated conditions.....	209
3-107	Variation in the change in diffuse reflectance at 445 nm due to the 9-cyclopropyl-9-fluorenyl cation following laser photolysis of 9-cyclopropyl-9-fluorenol in NaY as a function the concentration of coadsorbed HFIP.....	210
3-108	Variation in the first-order decay rate constant of the 9-cyclopropyl-9-fluorenyl cation monitored at 445 nm following laser photolysis of 9-cyclopropyl-9-fluorenol in NaY as a function the concentration of coadsorbed HFIP.....	210
3-109	Variation in the change in diffuse reflectance at 485 nm due to the 9-methyl-9-fluorenyl cation and at 515 nm due to the 9-fluorenyl cation following laser photolysis of 9-methyl-9-fluorenol and 9-fluorenol, respectively, in NaY as a function the concentration of coadsorbed HFIP.....	211
3-110	Variation in the first-order decay rate constant of the 9-methyl-9-fluorenyl cation monitored at 485 nm and the 9-fluorenyl cation monitored at 515 nm following laser photolysis of 9-methyl-9-fluorenol and 9-fluorenol, respectively, in NaY as a function the concentration of coadsorbed HFIP.....	211
3-111	Normalized variation in the change in diffuse reflectance at 485 nm due to the 9-methyl-9-fluorenyl cation following laser photolysis of 9-methyl-9-fluorenol in NaY as a function the concentration of coadsorbed HFIP and HFIP-OD.....	212
3-112	Normalized variation in the change in diffuse reflectance at 485 nm due to the 9-methyl-9-fluorenyl cation following laser photolysis of 9-methyl-9-fluorenol in Na β as a function the content of coadsorbed HFIP content HFIP-OD. Inset shows the same variation in the change in diffuse reflectance plotted against the HFIP content squared.....	212

3-113	Transient diffuse reflectance spectrum generated after 308 nm laser irradiation of 9-methoxyfluorene in evacuated NaY. The inset shows the decay trace monitored at 370 nm.....	213
3-114	Transient diffuse reflectance spectrum generated after 308 nm laser irradiation of 9-acetoxyfluorene in evacuated NaY. The inset shows the decay trace monitored at 370 nm.....	213
3-115	Decay traces of the triene isomers of 9-methyl-9-fluorene and 9-fluorene in methanol.....	214
3-116	Decay traces of the triene isomers of 9-methyl-9-fluorene and 9-methyl-9-fluorene in NaY.....	214
3-117	Variation in the log of the lifetime of the 9-cyclopropyl-9-fluorene cation and the 4-methoxycumyl cation as a function of charge on the framework oxygen.....	223
4-1	Transient diffuse reflectance spectrum obtained after 308 nm laser photolysis of chloranil ($\langle S \rangle = 0.08$) in evacuated NaY.....	268
4-2	Transient diffuse reflectance spectrum obtained after 308 nm laser photolysis of chloranil ($\langle S \rangle = 0.02$) in evacuated NaY. Inset shows the transient diffuse reflectance spectrum observed at longer delay times after laser irradiation.....	268
4-3	Normalized decay traces monitored at 420 nm and 500 nm following 308 nm laser photolysis of chloranil ($\langle S \rangle = 0.08$) in evacuated NaY.....	269
4-4	Normalized decay traces monitored at 500 nm following 308 nm laser photolysis of chloranil ($\langle S \rangle = 0.08$) in evacuated and oxygen-saturated NaY.....	269
4-5	Transient diffuse reflectance spectrum obtained after 308 nm laser photolysis of chloranil ($\langle S \rangle = 0.02$) in oxygen-saturated NaY.....	270
4-6	Transient diffuse reflectance spectrum observed after 308 nm laser photolysis of chloranil ($\langle S \rangle = 0.02$) in evacuated and oxygen-saturated NaY.....	270

- 4-7** Transient diffuse reflectance spectrum observed after 308 nm laser photolysis of chloranil ($\langle S \rangle = 0.02$) in evacuated and oxygen-saturated NaY. The inset shows the decay traces monitored at 420 nm following 308 nm laser photolysis of chloranil in evacuated and oxygen-saturated NaY.....271
- 4-8** Transient diffuse reflectance spectrum obtained after 308 nm laser photolysis of chloranil ($\langle S \rangle = 0.04$) in evacuated NaY containing coadsorbed 4,4'-dimethoxybicumene ($\langle S \rangle = 0.1$).....271
- 4-9** Transient diffuse reflectance spectra obtained after 308 nm laser photolysis of chloranil ($\langle S \rangle = 0.04$) in evacuated NaY containing coadsorbed 4,4'-dimethoxybicumene ($\langle S \rangle = 0.1$), and after 266 nm laser photolysis of 4,4'-dimethoxybicumene ($\langle S \rangle = 0.1$) in evacuated NaY. The decay traces monitored at 360 nm are shown in the inset.....272
- 4-10** Transient diffuse reflectance spectrum obtained after 308 nm laser photolysis of chloranil ($\langle S \rangle = 0.04$) in oxygen-saturated NaY containing coadsorbed 4,4'-dimethoxybicumene ($\langle S \rangle = 0.1$).....272
- 4-11** Transient diffuse reflectance spectrum generated after 308 nm laser photolysis of chloranil ($\langle S \rangle = 0.08$) in NaY containing 4,4'-dimethoxybicumene ($\langle S \rangle = 0.04$) under vacuum, nitrous oxide and oxygen conditions.....273
- 4-12** Transient diffuse reflectance spectrum obtained after 308 nm laser photolysis of a 25 day old sample containing chloranil ($\langle S \rangle = 0.04$) and 4,4'-dimethoxybicumene ($\langle S \rangle = 0.07$) in evacuated NaY. The inset compares the decay trace monitored at 360 nm in the fresh sample and the 25 day old sample.....273
- 4-13** Transient diffuse reflectance spectrum observed immediately following 308 nm and 532 nm laser photolysis of chloranil ($\langle S \rangle = 0.02$) in evacuated NaY containing coadsorbed 4,4'-dimethoxybicumene ($\langle S \rangle = 0.1$).....274

4-14	Transient diffuse reflectance spectrum obtained after 308 nm laser photolysis of chloranil ($\langle S \rangle = 0.02$) and 4,4'-dimethoxybicumene ($\langle S \rangle = 0.01$) in oxygen-saturated NaY.....	274
4-15	Transient diffuse reflectance spectrum obtained after 308 nm laser photolysis of chloranil ($\langle S \rangle = 0.02$) in oxygen-saturated NaY and chloranil ($\langle S \rangle = 0.02$) and 4,4'-dimethoxybicumene ($\langle S \rangle = 0.01$) in oxygen-saturated NaY.....	275
4-16	Transient diffuse reflectance spectrum obtained after 308 nm laser photolysis of chloranil ($\langle S \rangle = 0.02$) in oxygen-saturated NaY containing various concentrations of DMB: $\langle S \rangle = 0$, $\langle S \rangle = 0.002$, $\langle S \rangle = 0.01$, $\langle S \rangle = 0.02$, $\langle S \rangle = 0.04$, and $\langle S \rangle = 0.1$	276
4-17	Yield of the 4-methoxycumyl cation generated by 308 nm laser photolysis of chloranil in evacuated NaY as a function of concentration of coadsorbed 4,4'-dimethoxybicumene.....	277
4-18	Yield of chloranil triplet and chloranil radical anion generated by 308 nm laser photolysis of chloranil in evacuated NaY as a function of the concentration of coadsorbed 4,4'-dimethoxybicumene.	277
4-19	Transient diffuse reflectance spectrum obtained after 308 nm laser photolysis of <i>t</i> -anethole ($\langle S \rangle = 0.1$) in evacuated NaY.....	278
4-20	Normalized decay traces monitored at 380 nm and 600 nm following 308 nm of <i>t</i> -anethole ($\langle S \rangle = 0.1$) in evacuated NaY (total time = 500 μ s).....	278
4-21	Normalized decay traces monitored at 380 nm and 600 nm following 308 nm of <i>t</i> -anethole ($\langle S \rangle = 0.1$) in evacuated NaY (total time = 20 μ s).....	279
4-22	Decay traces monitored at 700 nm following 308 nm of <i>t</i> -anethole ($\langle S \rangle = 0.1$) in evacuated NaY and nitrous oxide-saturated NaY.....	279
4-23	Transient diffuse reflectance spectrum obtained after 308 nm laser photolysis of <i>t</i> -anethole ($\langle S \rangle = 0.1$) in evacuated and nitrous oxide-saturated NaY.....	280

4-24	Transient diffuse reflectance spectrum obtained after 308 nm laser photolysis of <i>t</i> -anethole ($\langle S \rangle = 0.1$) in evacuated NaY containing coadsorbed 1,4-dicyanobenzene ($\langle S \rangle = 0.2$).....	280
4-25	Decay traces monitored at 340 nm following 308 nm laser photolysis of <i>t</i> -anethole ($\langle S \rangle = 0.1$) in evacuated NaY and An ($\langle S \rangle = 0.1$) in NaY containing coadsorbed 1,4-dicyanobenzene ($\langle S \rangle = 0.2$).....	281
4-26	Transient diffuse reflectance spectrum obtained after 308 nm laser photolysis of <i>t</i> -anethole ($\langle S \rangle = 0.1$) in nitrous oxide-saturated NaY containing coadsorbed 1,4-dicyanobenzene ($\langle S \rangle = 0.2$). Inset compares the transient spectra observed after photolysis under vacuum and nitrous oxide conditions.....	281
4-27	Transient diffuse reflectance spectrum obtained after 308 nm laser photolysis of <i>t</i> -anethole ($\langle S \rangle = 0.1$) in nitrogen-saturated NaY containing various concentrations of coadsorbed 1,4-dicyanobenzene: $\langle S \rangle = 0$, $\langle S \rangle = 0.05$, $\langle S \rangle = 0.1$, $\langle S \rangle = 0.2$, and $\langle S \rangle = 1$	282
4-28	Decay traces monitored at 700 nm following 308 nm laser photolysis of <i>t</i> -anethole ($\langle S \rangle = 0.1$) in nitrogen-saturated NaY containing various concentrations of coadsorbed 1,4-dicyanobenzene: $\langle S \rangle = 0$, $\langle S \rangle = 0.05$, $\langle S \rangle = 0.1$, and $\langle S \rangle = 0.2$	283
4-29	Yield of 1,4-dicyanobenzene radical anion and sodium-cluster trapped electrons observed upon 308 nm laser photolysis of <i>t</i> -anethole ($\langle S \rangle = 0.1$) in nitrogen-saturated NaY as a function of 1,4-dicyanobenzene concentration.....	283
4-30	Decay traces monitored at 380 nm and 340 nm following 308 nm laser photolysis of <i>t</i> -anethole ($\langle S \rangle = 0.1$) in evacuated NaY containing coadsorbed 1,4-dicyanobenzene ($\langle S \rangle = 1$).....	284
4-31	Decay traces monitored at 380 nm and 340 nm following 308 nm laser photolysis of <i>t</i> -anethole ($\langle S \rangle = 0.1$) in evacuated NaY containing coadsorbed 1,4-dicyanobenzene ($\langle S \rangle = 0.05$).....	284

4-32	Transient diffuse reflectance spectrum obtained after 308 nm laser photolysis of <i>t</i> -anethole ($\langle S \rangle = 0.1$) in nitrogen-saturated, and nitrous oxide-saturated NaY containing various concentrations of coadsorbed of 1,4-dicyanobenzene: $\langle S \rangle = 0.05$, $\langle S \rangle = 0.1$, $\langle S \rangle = 0.2$, and $\langle S \rangle = 1$	285
4-33	Steady-state fluorescence spectra observed following 308 nm excitation of <i>t</i> -anethole in NaY ($\langle S \rangle = 0.10$) and hexane (ca. 10^{-4} M).....	286
4-34	Steady-state fluorescence spectra observed following 308 nm excitation of <i>t</i> -anethole in NaY ($\langle S \rangle = 0.10$) containing various concentrations of coadsorbed 1,4-dicyanobenzene: $\langle S \rangle = 0$, $\langle S \rangle = 0.02$, $\langle S \rangle = 0.04$, $\langle S \rangle = 0.2$, $\langle S \rangle = 0.3$, and $\langle S \rangle = 1$	286
4-35	Variation in <i>t</i> -anethole steady-state fluorescence monitored at 338 nm following 308 nm excitation of <i>t</i> -anethole ($\langle S \rangle = 0.10$) in NaY as a function of 1,4-dicyanobenzene concentration.....	287
4-36	Perrin plot of $-\ln(1-Y/Y_{\text{infinity}})$ against 4,4'-dimethoxybicumene concentration, where Y represents the yield of the 4-methoxycumyl cation in NaY. The shaded region indicates the behaviour expected for 4,4'-dimethoxybicumene and chloranil molecules in direct contact.....	305
4-37	Perrin plot of $-\ln(1-Y/Y_{\text{infinity}})$ or $\ln(Y_0/Y)$ against 1,4-dicyanobenzene concentration, where Y represents the yield of the 1,4-dicyanobenzene radical anion and trapped electron, respectively in NaY. The shaded region indicates the behaviour expected for 1,4-dicyanobenzene and <i>t</i> -anethole molecules in direct contact.....	305
4-38	Calculated occupancy probabilities for molecules in shells b , c , d , e , and f surrounding a central shell, a , as a function of the fractional occupancy of 4,4'-dimethoxybicumene in NaY.....	309
4-39	Calculated sum of occupancy probabilities for molecules in shells b , b + c , b + c + d , b + c + d + e , and b + c + d + e + f as a function of 4,4'-dimethoxybicumene fractional occupancy in NaY.....	310

4-40	Experimental variation in the yield of the 4-methoxycumyl cation as a function of the fractional occupancy of 4,4'-dimethoxybicumene in NaY compared to the variation predicted by the shells model (dotted lines) incorporating shells b , b + c , b + c + d , b + c + d + e , and b + c + d + e + f	312
4-41	Experimental variation in the yield of the 1,4-dicyanobenzene radical anion as a function of the fractional occupancy of 1,4-dicyanobenzene in NaY compared to the variation predicted by the shells model.....	313
5-1	Schematic representation of the laser system used in nanosecond diffuse reflectance studies.....	327
A-1	Amount of water adsorbed (mass %) as a function of time by a dehydrated sample of NaX.....	339
A-2	Decay traces monitored at 360 nm following 266 nm laser photolysis of 4,4'-dimethoxybicumene in NaY containing 11 % and 2 % residual hexane by mass.....	339
A-3	Transient diffuse reflectance spectrum obtained after 266 nm laser photolysis of 4,4'-dimethoxybicumene in NaY containing 11 % residual hexane by mass.....	340
A-4	Transient diffuse reflectance spectrum obtained after 266 nm laser photolysis of 4,4'-dimethoxybicumene in NaY containing 2 % residual hexane by mass.....	340

List of Tables

1-1	Pore sizes and topological dimensions for selected zeolites.....	4
1-2	Influence of alkali metal cation on some physical parameters within MY zeolites.....	8
2-1	Typical unit cell formula and molecular mass of alkali metal cation faujasites...39	
3-1	Solvent reactivities of selected carbocations at 20 °C.....	43
3-2	Rate constants (k_m) for fragmentation of radical cations.....	49
3-3	Description of zeolites used in study of the 4-methoxycumyl cation.....	54
3-4	Lifetime(s) of the 4-methoxycumyl cation in alkali metal cation zeolites.....	56
3-5	Kinetic isotope effects on the decay of the 4-methoxycumyl cation in alkali metal cation zeolites.....	57
3-6	Relative product yields from steady-state irradiation of 4,4'-dimethoxybicumene in NaY following post-photolysis addition of methanol and dichloromethane extraction.....	58
3-7	Second-order rate constants and slopes of static quenching plots for addition of methanol to the 4-methoxycumyl cation in alkali metal cation Y zeolites.....	67
3-8	Absolute and relative second-order rate constants and slopes of static quenching plots for addition of simple alcohols to the 4-methoxycumyl cation in NaY.....	68
3-9	Second-order rate constants for reaction of 4,4'-dichlorodiphenylmethyl and 4,4'-dimethylphenylmethyl cation with vinyl ethers in acetonitrile at 20 °C.....	70
3-10	Second-order rate constants and slopes of static quenching plots for reaction of 4-methoxycumyl cation with simple vinyl ethers in NaY.....	71

3-11	Second-order rate constants for electron transfer quenching of photoexcited chloranil by bicumene donors in HFIP.....	76
3-12	λ_{\max} and decay rate constants for various cumyl cations in HFIP.....	76
3-13	Decay rate constants of the 4-methylcumyl cation in alkali metal cation zeolites.....	79
3-14	First order decay rate constants and lifetimes of cumyl cations in dry Na β	82
3-15	Yield of the 4-dimethylaminocumyl cation relative to the 4,4'-(<i>N,N</i> -dimethylamino)bicumene radical cation, fraction of prompt formation and growth rate constant of the 4-dimethylaminocumyl cation observed following laser photolysis of 4,4'-(<i>N,N</i> -dimethylamino)bicumene in alkali metal cation Y zeolites.....	85
3-16	Sanderson electronegativities of atomic constituents of alkali metal cation zeolites.....	120
3-17	Unit cell composition, equalized electronegativity and partial charge on the framework oxygen atoms for zeolites examined.....	121
3-18	Correlation of the substituent parameter, σ^{c+} , with the decay of substituted cumyl cations in various environments.....	129
3-19	Diffusion coefficients of various alcohols in alkali metal cation Y zeolites derived from second-order rate constants for addition to the 4-methoxycumyl cation...	134
3-20	Diffusion coefficients of various alkyl enol ethers in NaY derived from second-order rate constants for addition to the 4-methoxycumyl cation.....	138
3-21	First-order rate constants for reactions of 9-fluorenyl, diphenylmethyl and triphenylmethyl cations with solvent.....	147

3-22	First-order decay rate constants for 9-fluorenyl cations and the diphenylmethyl cation in alkali metal cation zeolites LiY, NaY and Na β	151
3-23	First-order rate constants for decay of the 9-R-9-fluorenol radical cations and the fluorene radical cation observed at 640 nm in alkali metal cation zeolites.....	153
3-24	Decay rate constants of the 9-cyclopropyl-9-fluorenyl cation in dry and hydrated alkali metal cation Y zeolites, ratio of decay rate constant under hydrated and dry conditions, and increase in carbocation yield upon hydration.....	164
3-25	Variation in the decay rate constant and initial change in diffuse reflectance for 9-R-9-fluorenyl cations versus weight fraction of HFIP.....	174
3-26	Variation in the initial change in diffuse reflectance for the 9-methyl-9-fluorenyl cation versus weight fraction (NaY) or weight fraction squared (Na β) of HFIP and HFIP-OD.....	176
3-27	First-order rate constants for decay of the triene isomers of 9-R-9-fluorenols in methanol and NaY.....	178
3-28	Lifetimes of 9-R-9-fluorenyl cations in LiY, NaY, TFE, and water, and reactivity range exhibited by these carbocations in each environment.....	227
3-29	First-order rate constants for decay of carbocations in alkali metal cation zeolites and solution.....	229
4-1	Extinction coefficients of the chloranil triplet, chloranil radical anion and 4-methoxycumyl cation.....	258
4-2	First-order decay rate constants of the <i>t</i> -anethole radical cation ($\langle An \rangle = 0.1$) and 1,4-dicyanobenzene radical anion monitored at 380 nm and 340 nm, respectively, in evacuated NaY.....	265
4-3	Intracavity distances in NaY obtained from the shell model, and intermolecular distances between chloranil and 4,4'-dimethoxybicumene, and <i>t</i> -anethole and 1,4-dicyanobenzene within the cavities.....	307

4-4	Distribution of 4,4'-dimethoxybicumene in various shells surrounding a central NaY cavity as a function of 4,4'-dimethoxybicumene occupancy level.....	308
4-5	Distribution of 1,4-dicyanobenzene in various shells surrounding a central NaY cavity as a function of 1,4-dicyanobenzene occupancy level.....	309
A-1	Observed mass loss due to volatile adsorbates present in zeolite samples prepared under several different conditions.....	334
A-2	Observed mass loss due to volatile adsorbates, and mass due to residual solvent in zeolite samples prepared under several different conditions.....	336
A-3	Observed mass loss due to volatile adsorbates, and mass due to residual hexane in zeolite samples prepared under various conditions.....	337
A-4	Observed mass loss due to volatile adsorbates, and mass due to residual hexane in zeolite samples prepared by heating under reduced pressure.....	338

Abstract

Considerable current research is directed towards understanding host-guest interactions and chemical transformations within zeolites. Despite this effort, and the ubiquity of zeolitic materials in research and industry, much remains to be discovered about the specific mechanisms of intrazeolite reactions. This thesis describes investigations aimed at probing the internal environments within non-acidic zeolites, and evaluating the roles zeolites play in reaction dynamics of encapsulated guest molecules. Two fundamental reaction types provide the specific focus: (i) reactions mediated by carbocation intermediates; and (ii) reactions proceeding *via* charge migration. Nanosecond time-resolved diffusion reflectance spectroscopy is used to directly observe reactive intermediates and to establish mechanistic descriptions of intrazeolite reactions.

Alkali metal cation zeolites are employed in order to elucidate the role of zeolitic parameters other than acidity on the generation, absolute and bimolecular reactivity of carbocations. Two photochemical methods are used to create reactive carbocations in non-acidic zeolites: (i) rapid fragmentation of photogenerated bicumene radical cations; and (ii) photoheterolysis of 9-fluorenols. Studies of cumyl and 9-fluorenyl cations in dry zeolites (MY, M= Li⁺, Na⁺, K⁺, Rb⁺ and Cs⁺, NaX, NaMor and Naβ) indicate that the absolute reactivity of carbocations is strongly dependent on the alkali cation, the Si/Al ratio and the framework morphology. Investigations of the 4-methoxycumyl cation, including kinetic isotope effects and product studies, suggest that the mechanism for intrazeolite decay involves direct attack of the zeolite lattice on the carbocation leading to a framework-bound alkoxy species. The carbocation lifetime is thus correlated to zeolite nucleophilicity and can be modulated over several orders of magnitude with changes in the zeolite environment. The results establish that non-acidic zeolites support the generation of reactive carbocations, including the 9-fluorenyl cation, as transient intermediates which receive stabilization from the zeolite matrix, but are reactive towards attack by nucleophilic framework sites. Consequently, the range of reactivities for carbocations within non-acidic zeolites is reduced relative to solution. Intrazeolite addition reactions of small alcohols, alkyl enol ethers, and water to carbocations are described in terms of both static and dynamic quenching involving molecular diffusion through the heterogeneous topology and rapid intracavity coupling between the nucleophile and the carbocation. Thus, the zeolite *reduces* the efficiency of dynamic quenching but *enhances* the reactivity of the nucleophile towards intracavity addition to the carbocation. Furthermore, alkali metal cation zeolites are shown to influence carbocation formation by assisting photoheterolysis of 9-fluorenols in the absence and presence of coadsorbed protic reagents. These studies also afford insight into the dynamics of carbocation generation within non-acidic zeolites in competition with alternative reaction pathways available to photoexcited 9-fluorenols.

Reactions proceeding *via* charge migration between NaY encapsulated electron donors and acceptors are explored in order to probe the role of the zeolite in these redox processes, and to characterize the mobility of electrons and holes within the zeolite. Electron migration is initiated by photoexciting *t*-anethole in NaY containing coadsorbed 1,4-dicyanobenzene as an electron acceptor, while hole migration is initiated by photoexciting chloranil in NaY containing coadsorbed 4,4'-dimethoxybicumene as an electron donor. Results demonstrate ultrafast redox reactions leading to long-lived charge separated states within the zeolite cavities. The efficiencies of the redox process are examined as a function of donor-acceptor concentration and the inclusion of nitrous oxide as an electron trap. Interpreting the experimental data with two independent models provides clear evidence that the redox chemistry occurring within NaY cannot be completely accounted for by contact interactions between the incorporated molecules. From these models, it is estimated that the zeolite can mediate electron and hole migration over distances of 11 Å and 18 Å, respectively.

List of Abbreviations

AcN	acetonitrile
An	<i>trans</i> -anethole
BET	back electron transfer
BVE	butyl vinyl ether
CT	charge transfer
Chl	chloranil
cPrFOH	9-cyclopropyl-9-fluorenol
DCB	1,4-dicyanobenzene
DFB	4,4'-difluorobicumene
DMB	4,4'-dimethoxybicumene
3-DMB	3,3'-dimethoxybicumene
DMeB	4,4'-dimethylbicumene
DMeAB	4,4'-(<i>N,N</i> -dimethylamino)bicumene
EPE	ethyl propenyl ether
ESM	exponential series method
ET	electron transfer
EtFOH	9-ethyl-9-fluorenol
EVE	ethyl vinyl ether
HFIP	1,1,1,3,3,3-hexafluoro <i>isopropanol</i>
IME	isopropenyl methyl ether
ISC	intersystem crossing
iPrFOH	9- <i>isopropyl</i> -9-fluorenol
MeOH	methanol
MeFOH	9-methyl-9-fluorenol
Mor	Mordenite
MV ²⁺	methyl viologen
PET	photoinduced electron transfer
PVE	propyl vinyl ether
tBVE	<i>tert</i> -butyl vinyl ether
TFE	2,2,2-trifluoroethanol
TPP ⁺	triphenylpyrylium ion
vFOH	9-vinyl-9-fluorenol

λ	wavelength
ϵ	extinction coefficient
Δr	change in diffuse reflectance
$\Delta J/J_0$	change in diffuse reflectance
$\Delta \text{O.D.}$	change in optical density
k	rate constant
τ	lifetime
K	equilibrium constant
ΔG^0	free energy change
E_{ox}^0	standard oxidation potential
E_{red}^0	standard reduction potential
$\langle S \rangle$	fractional occupancy

Acknowledgements

I would like to express my deepest appreciation to my supervisor, Professor Frances Cozens. Professor Cozens has been a constant source of knowledge and insight, motivation and support, throughout my studies, and has contributed so much to what I have learned and the way that I have come to think.

In addition, I wish to convey my most sincere gratitude to Professor Norm Schepp. Professor Schepp's interest and enthusiasm for this research, as well as his seemingly endless ideas and patience, have been invaluable.

I would also like to thank my colleague and friend, Wendy, who I have relied on daily for companionship and advice, and who has always provided this selflessly. I very much appreciate her sincere friendship and support, and wish her all possible happiness in this life.

I have been very fortunate to have had the opportunity to meet, interact and become close friends with many labmates over these past few years. To those people who have made me smile, and have endured my unusual ways with a smile in return, Roumiana, Mariluz, Elaine, Suzanne, Sandy, Aviva, Karen and Elizabeth, I say thank-you.

I would also like to express my appreciation to Professor Pincock and Professor Arnold for their interest, patience, and consistently wise advice, throughout my studies at Dalhousie.

Finally, I thank my Friend, Davy, for showing me the beauty that can be within one person.

Chapter 1. Introduction to the Study of Reaction Dynamics in Zeolites

1.1 Zeolites

Zeolites are inorganic solids, naturally occurring minerals closely related to sand and clay.¹⁻⁶ Zeolites are also supramolecular hosts and heterogeneous catalysts.^{7,8} The ability of zeolites to host molecular guests in supramolecular assemblies and to catalyze chemical transformations is a consequence of the unique structural and physicochemical features of these materials. Zeolites are crystalline aluminosilicates possessing an open framework structure of molecular-sized pores, channels and cavities, Figure 1-1. As a result, molecules can be adsorbed within the microporous network, and physical and chemical transformations can take place on the large internal surfaces. The regular periodic molecular-sized void spaces throughout the zeolite particle, typically 0.1 to 10 μm , facilitates the novel spatial arrangement of thousands of molecules with significant long-range ordering. In addition, the internal zeolite environment is characterized by a negatively charged lattice with interstitial charge-balancing cations residing within the micropores. The combined structural and chemical features generate a strongly polar anionic network of well-defined void spaces with localized electrostatic fields and active acidic and basic sites. Consequently, zeolites are unique organized media for confining molecular guests and manipulating their reactivity. As a result, zeolites have been heavily exploited commercially in a vast array of diverse applications,^{9,10} most notably as heterogeneous catalysts for reactions in the petrochemical industry and the synthesis of fine chemicals,¹¹ as well as adsorbants and separating reagents in a myriad of processes. The attractive and versatile properties of zeolites have also rendered these materials a favorite in academic research. A common thread in much of the current research is based on the concept that the local environment within zeolites can control or manipulate reaction dynamics. The notion of supramolecular chemistry in zeolites, wherein the zeolite acts as a scaffold for molecular organization and participates directly in the chemical transformations, is an ongoing pursuit in the understanding of these processes and the design of new materials.

1.1.1 Structural Features of Zeolites: Topology and Composition

Knowledge of zeolite structure is essential to the elucidation and rationalization of physical and chemical properties of zeolitic materials. Structural elucidation of zeolites

often relies on powder X-ray diffraction data,¹²⁻¹⁶ but includes other techniques such as solid-state NMR,¹⁷⁻¹⁹ as well as neutron diffraction.¹⁸⁻²⁰ In order to describe the structure of a zeolite, a consideration of the framework topology, the connectivity between the tetrahedral building blocks in three-dimensional space, and the composition including the atomic constituents of the framework, as well as the counterbalancing cations and any additional non-framework species which might be present is required.

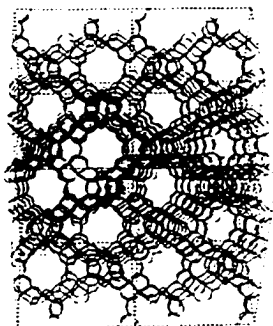


Figure 1-1. Framework topology of Faujasite.

The common feature of all zeolite topologies is linkage of the primary building blocks, SiO_4^{4-} and AlO_4^{5-} tetrahedra, *via* shared oxygen atoms to create substructures of characteristic size and shape, Figure 1-2. Each substructure can be arranged in numerous ways resulting in a myriad of unique, well-defined zeolite topologies with considerable variation in internal geometry and dimensions, Figure 1-3. For instance, the assemblage of sodalite cages generates three-dimensional networks of cavities and pores of various sizes and connectivities. In the synthetic faujasites, zeolites X and Y, the cavities, or supercages, are approximately 13 Å in diameter. Each is tetrahedrally linked to four others through 7.4 Å diameter pores containing twelve oxygen atoms, whereas zeolites constructed of pentasil units consist of uniform tubular channels rather than cavities. These channels vary in diameter and length and may be interconnected as in ZSM-5 and Mordenite, or isolated as in Linde Type L. A testament to the variability of zeolite topology is the existence of approximately 40 different types of natural zeolites and currently greater than 100 synthetic forms.

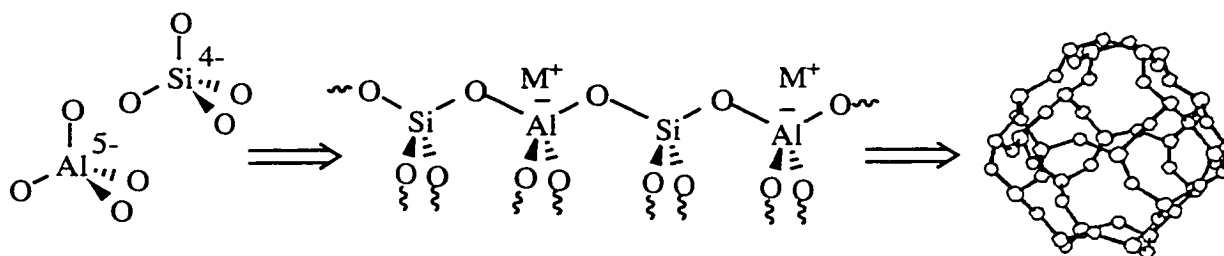


Figure 1-2. Schematic representation of tetrahedral zeolite building blocks and their linkage to form a microporous network.

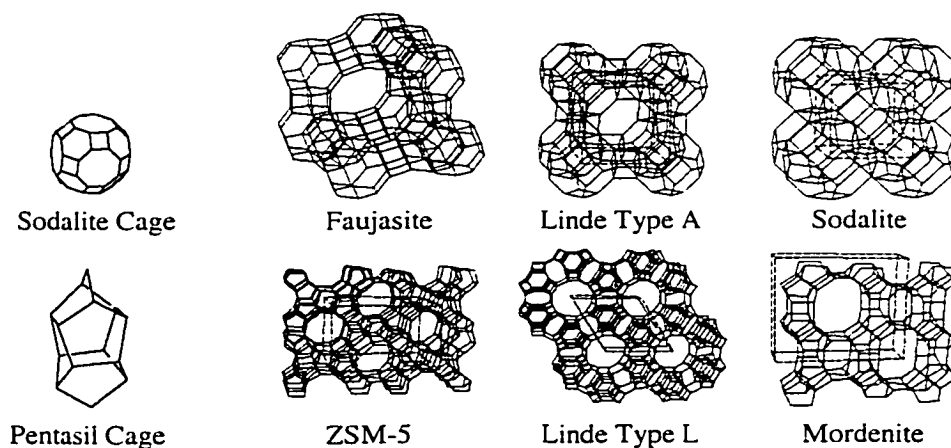


Figure 1-3. Generation of various zeolite topologies through spatial arrangement of sodalite and pentasil substructures.

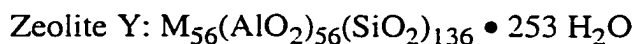
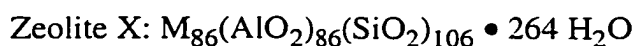
Although the specific arrangements of the tetrahedral building blocks generate a vast array of zeolite architectures, several parameters useful in describing zeolite topologies can be applied to all materials. The most common parameters are the pore size, the channel system and dimensionality, and the type of secondary building units. The pore size is usually defined as the number of tetrahedral (T) atoms, or oxygen atoms found in the rings of atoms forming the pores. Zeolites are classified as small, medium or large pore depending on whether they possess 8, 10 or 12 oxygen atoms in the pore opening, respectively. The size of these rings, as calculated using 1.35 Å for the covalent diameter of oxygen, are approximately 4.1 Å, 5.5 Å and 7.4 Å, respectively. However, it is important to remember that the rings can be distorted easily by, for instance, thermal motion or cation binding, so the effective, or kinetic, pore diameter may be up to a few Å larger than the crystallographic one. The size of these pores, or oxygen windows, is very

significant since it determines which molecular guests will have access to the supercages and how readily guests will diffuse from one supercage to another. The microporous network may consist of pores, channels, cavities or cages, windows, pockets and their various combinations. This system is one-dimensional, for zeolites consisting of a series of isolated tubes, two-dimensional when channels intersect to form isolated layers, or three-dimensional for zeolites with channels intersecting in three unique directions. The secondary building units are finite subunits of T-atoms which can be observed in many zeolite topologies in a variety of patterns. Often the zeolite architecture can be derived from the repetition of this finite unit throughout the structure. Table 1-1 presents the pore diameters and channel systems for some commonly encountered zeolite types.

Table 1-1. Pore sizes and topological dimensions for selected zeolites.²

Zeolite Name	Pore Diameter / Å	Channel System/Cage Diameter
Faujasite (Zeolite X and Y)	7.4	3-D channel with cage / 13 Å
Linde Type A	4.2	3-D channel with cage / 11.4 Å
Sodalite	2.3	3-D channel with cage / 6.6 Å
ZSM-5	5.2x5.6; 5.1x5.5	two interconnected channels
Linde Type L	7.1	single channel with lobe / 7.5 Å
Mordenite	6.5x7.0; 2.6x5.7	two interconnected channels

Zeolites are composed of a framework of silicon, aluminum and oxygen as well as non-framework bound cations and adsorbed water. For instance, the typical unit cell composition of zeolites X and Y, the synthetic analogues of the naturally occurring faujasite zeolite, are^{2,5}:



where M is a monovalent cation. Zeolites X and Y are topologically identical, but can be distinguished by compositional differences in the number of framework aluminum atoms and counterbalancing cations. In order to gain some perspective on the unit cell size, consider that one unit cell contains eight supercages and that each of these large cavities can house 28 water molecules.

One of the most significant parameters in the structure of any zeolite is the ratio

of silicon to aluminum (Si/Al ratio) in the framework. Natural and synthetic zeolites exhibit a wide range of Si/Al ratios varying from about one to infinity. The lower limit of one arises from the fact that no two aluminum atoms can share the same oxygen, as described by Loewenstein's rule,²¹ due to the energetically unfavorable situation of having two adjacent negative charges. Zeolite X, with a Si/Al ratio of approximately 1.5, therefore has one of the highest concentrations of framework aluminum. Its structural analogue, zeolite Y, has a Si/Al ratio of about 2.5. Conversely, zeolites can also be highly dealuminated resulting in very large Si/Al, or contain no framework aluminum at all, such as silicalite which has a Si/Al of infinity.

To compensate for the charge imbalance caused by each AlO_4^{5-} unit, extra-lattice cations such as protons, alkali or alkaline earth metals are found within the cages, channels and cavities of zeolites. These cations are mobile and readily exchanged since they are not covalently bound to the framework. This characteristic has led to the widespread use of zeolites in detergents, waste-water treatment and many other processes involving selective ion-exchange. As a general rule, zeolite cations will tend to occupy intrazeolite sites that provide the best coordination polyhedra with the framework oxygen atoms. However, cation-cation, cation-framework and cation-ligand interactions will play a role, as will the size, charge, degree of hydration and mobility of the cation. It is possible, however, to specify sites within zeolite frameworks where the cations tend to localize. There are generally more sites than cations and thus motion between the sites is anticipated, consistent with the notion that the intrazeolite cations are not static entities.

The positions of the cations have been studied quite extensively in the faujasite-type zeolites X and Y by X-ray powder diffraction,¹³ and more recently by solid-state NMR spectroscopy.²² In faujasites several distinct sites have been distinguished, three of which are represented in Figure 1-4. Site I cations, of which there are 16 per unit cell in both zeolite X and Y, lie on the hexagonal prism faces connecting the sodalite cages. Site II cations sit on the open hexagonal faces, with 32 cations per unit cell in both zeolites. Site III cations, with 38 per unit cell of zeolite X, but only 8 per unit cell of zeolite Y, are found on the walls of the large supercage cavity. Notably, only those cations at sites II and III will be accessible to incorporated guests.²³

Zeolites are notorious for their ability to absorb water, and in fact derive their name from this characteristic. In 1756 when the Swedish mineralogist Cronstedt discovered minerals that appeared to boil when heated, he named these minerals zeolites from the Greek words *zein*, to boil, and *lithos*, stone.²⁴ The boiling phenomenon observed by Cronstedt was due to the expulsion of water from the microporous internal surface of the zeolite. The extent and location of water molecules within zeolites will

depend on a number of factors including the size and shape of the interior voids as well as the Si/Al ratio and the number and charge of the counterbalancing cations. The binding of water within the zeolite is chiefly through a direct coordination to the framework cations, as well as hydrogen bonding with a framework oxygen. In the hydrated state, the framework anionic charge may be balanced directly by the cations, or indirectly by water molecules forming hydration complexes with the cations. The water molecules near the periphery are more tightly bound than those in the center, and the water frequently moves from site to site. However, the confined nature and the existence of particular binding sites and positions, give the framework control over the water distribution and thus distinguish zeolitic water from the amorphous, homogeneous liquid. For instance, although the water in zeolites is quite mobile, it diffuses about one to two orders of magnitude slower than in pure liquid water.²⁵

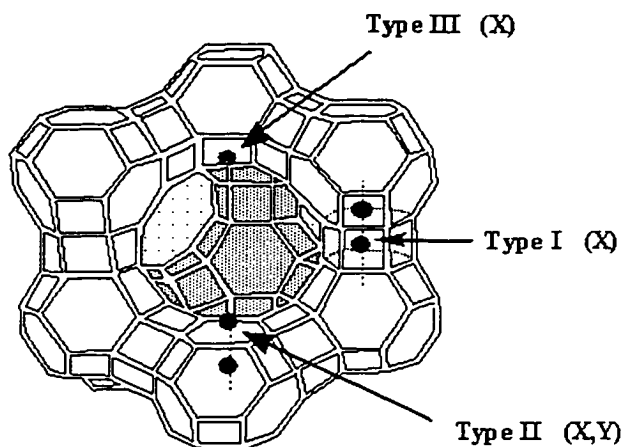


Figure 1-4. Three occupancy sites of counterbalancing cations in faujasite zeolites (zeolites X and Y). Reproduced from reference 23.

Removal of the intrazeolite water can be accomplished by heating, or activating, the zeolite. In faujasites, most of the zeolitic water is lost by 400 °C, although the strongly polarizing cations, particularly divalent cations, can hold the last water molecules quite tenaciously.³ For the relatively weakly polarizing alkali metal cations, activation temperatures between 400 to 500 °C lead to the escape of water with minimal structural changes. The initially hydrated cations may migrate towards the framework oxygen atoms in order to adopt the final anhydrous configuration, and local movement of the framework atoms to achieve cation coordination might occur. However, the

framework structure and crystallinity will remain intact and largely unchanged.³ As an example, consider the results of an investigation of the thermal properties of Y zeolites.²⁶ From thermogravimetric analysis, the water content in a NaY sample was found to be 26 % by weight. Differential thermal analysis conducted on this sample yielded an endothermic peak at 230 °C with a width of approximately 70 °C which was attributed to loss of this water from the NaY cavities. In addition, an exothermic peak was observed at 930 °C which was associated with the collapse of the framework and therefore related to the thermal stability of the zeolite. However, a more realistic measure of the thermal stability of the zeolite is obtained by monitoring the X-ray powder patterns as a function of temperature. This directly reveals changes in crystallinity, and therefore gradual framework breakdown. The temperature at which the lattice begins to collapse, T_{amf} , is generally lower than the exothermic peak observed in DTA curves. For the NaY sample under study, the T_{amf} value was found to be 820 °C.

Two recent investigations by Hunger and coworkers have considered the interaction of water with alkali metal cation zeolites.^{27,28} Temperature-programmed-desorption studies of water in alkali metal cation X zeolites found that the energy of water desorption from these zeolites exhibited a wide distribution with two characteristic ranges, one between 55 and 65 kJ/mol and a second between 65 and 95 kJ/mol. The higher energy desorption peak exhibited a systematic decrease with increasing size of the alkali cation, indicating an overall decrease in the desorption energy for removal of water as the size of the counterion becomes larger. Furthermore, X-ray powder diffraction studies were employed to reveal the arrangement of water molecules at low loadings in MNaX and MNaY (M = K, Rb, Cs). Within these zeolites, only sodium directly interacts with water to form clusters while the heavier cations indirectly influence the formation of specific sodium-water distributions.

1.1.2 Inside the Zeolite Cavities

Intrazeolite Space. Due to the open framework structure of zeolite, a large fraction of the internal environment is empty space. For instance, the supercages of Y zeolites possess approximately 800 Å³ of vacant space.²⁹ These large internal void volumes facilitate the adsorption of a wide variety of molecules thereby making chemistry within these materials possible. The enormous internal surface area (up to 1000 m²/g) is capable of absorbing large quantities of guest molecules, inducing adsorbates to pass through the outer shell of the particle. Molecules will be admitted within the zeolite host according to the size and shape restrictions of the zeolite

framework, as well as the size of the associated cations and the degree of hydration. Charge balancing cations directly influence the free volume within zeolite micropores, Table 1-2, and therefore the adsorption, mobility and reactivity of included guests.

Table 1-2. Influence of alkali metal cation on some physical parameters within MY zeolites.

Cation (M ⁺)	Cation Ionic Radius ^a / Å	Electrostatic Field in Cage ^a / V/Å	Cation Electrostatic Potential ^a (e/r) / V	Vacant Space in Supercage ^b / Å ³	
				Y zeolite	X Zeolite
Li	0.76	2.1	1.67	834	873
Na	1.02	1.3	1.05	827	852
K	1.38	1.0	0.75	807	800
Rb	1.52	0.8	0.67	796	770
Cs	1.67	0.6	0.59	781	732

^aRef. 30; ^bRef. 29

Intrazeolite Microenvironment. The zeolite interior should not, however, be viewed as mere empty space. In contrast to many other hosts such as cyclodextrins, micelles and vesicles, which chiefly provide molecular encapsulation and organization, the zeolite is an active host influencing the conformation and reactivity of guests, and participating directly in chemical transformations. This is a consequence of the unique microenvironment within zeolites, as well as the existence of specific reaction sites. Zeolites are constructed from an anionic backbone and house counterbalancing cations dispersed through a network of internal void spaces. The open structure consisting of well-defined anionic sites, [Si-O-Al]⁻, with spatially separated cationic sites, generates strong electrostatic fields within the cavities of zeolites. These electrostatic fields are fundamental to defining the zeolite microenvironment and its catalytic properties. Research carried out some thirty years by zeolite scientists such as Rabo and Ward, who examined the catalytic activity of zeolites, established that the zeolite cavities possess powerful electrostatic fields.^{30,31} In anhydrous zeolites, the cations at sites II and III are incompletely coordinated to the lattice oxygen atoms, Figure 1-4, and consequently the cationic charge is only partially shielded. The faces of the cations exposed to the center of the cavity are unshielded and correspondingly, the anionic zeolite framework is also only partially shielded. These partially shielded charged centers contribute significantly to the strong electrostatic fields that extend into the supercage.³² Electrostatic fields in zeolite cavities are determined from both theoretical calculations and experimental

measurements using techniques such as IR and NMR spectroscopy.¹³ Most calculations of electrostatic fields and electric field gradients, such as those presented in Table 1-2,^{29,30} have been made using the ionic lattice approximation, although these have been extended to a three-dimensional description of the field and potential within the supercavities of faujasites.³³

In describing the zeolite interior, the term electrostatic field is used somewhat interchangeably with polarity or micropolarity. Generally speaking the term polarity is used to describe the ability of a solvent to polarize a solute. However, in zeolites the electrostatic fields are responsible for molecular polarization. Molecules adsorbed within zeolites are therefore constantly subjected to the influence of these electrostatic fields. As a result, the guest molecule will tend to polarize itself such that the negative end of the molecule is stabilized by the zeolitic cations, while the positive end of the molecule is stabilized by the anionic framework. Thus, the electrostatic fields and polarity within zeolites are a consequence of the same phenomenon, namely, the existence of incompletely shielded counterbalancing cations. Consequently, the electrostatic fields and the polarity within zeolite cavities is highly counterion dependent, Table 1-2.

Many studies have addressed the notion of micropolarity in zeolites.^{29,34-38} The observed stabilization of ground state charge-transfer complexes between electrophilic organic cations and arene donors,³⁹⁻⁴¹ oxygen and hydrocarbons,⁴²⁻⁴⁵ and aromatics and tetracyanobenzene⁴⁶ has suggested that the environment within zeolites must be very polar and possesses properties analogous to highly ionizing solvents. However, few quantitative measurements of intrazeolite polarity have been made, and direct comparisons are complicated due to different methods of sample preparation and correspondingly potentially different concentrations of coadsorbed water. Two independent studies quantifying the micropolarity of the alkali metal cation faujasites were recently reported.^{37,38} Examining the S_N1-type heterolysis reactions of β-substituted radicals in alkali metal cation Y zeolites, Ortiz *et al.* quantitatively established that these zeolites possess strong ionizing abilities comparable to solvents such as 2,2,2-trifluoroethanol (TFE) and aqueous methanol.³⁷ The ionizing power of LiY was found to exceed that of highly ionizing solvents such as 1,1,1,3,3,3-hexafluoroisopropanol (HFIP) and water. NaY was found to be slightly less ionizing, similar to 70 % aqueous methanol, and the ionizing power decreased progressively with increasing cation size. Analogous findings were also recently reported by Uppili *et al.* using the polarity-dependent absorption, emission, and excited state lifetimes of three organic probes.³⁸ The interior cavities of Li⁺- and Na⁺-exchanged X and Y zeolites were found to be more polar than all other organic solvents and water, and therefore denoted as “superpolar”.

Larger alkali cation zeolites are still highly polar, but somewhat less polar than water. In addition, the polarity of alkali cation X zeolites was found to be lower than Y zeolites, consistent with calculations suggesting that the electrostatic field within Y zeolites is larger than within X zeolites.³² Significantly, both studies found that inclusion of water, actually *decreases* the polarity and ionizing ability of alkali metal zeolites, as a result of shielding or attenuation of the powerful electrostatic fields of the counterbalancing cations due to hydration.

Intrazeolite “Active Sites”. In addition to a microenvironment characterized by strong electrostatic fields and high polarity within a confined environment, zeolites possess numerous sites which have the potential to interact and/or react directly with included molecules. The notion of so-called “active-sites” is derived from zeolite catalysis and the identification of specific sites or functionalities that are associated with catalytic activity. The isomorphous insertion of the trivalent aluminum atoms into the tetrahedral zeolite matrix is invariably responsible, either directly or indirectly, for the existence of zeolite active sites.

Certainly the most well studied “active-sites” in zeolites are the Brønsted acid sites within proton-exchanged zeolites. Protonation of the oxygen atom within the [Si-O-Al]⁻ site generates a bridged hydroxyl group which is responsible for the Brønsted acidity in protic zeolites. Experimental investigations of Brønsted acidic zeolites are not the subject of this thesis and no discussion of Brønsted acidic zeolites will be provided herein. The nature and characterization of Brønsted acid sites within protic zeolites, as well as heterogeneous catalysis by these materials is extensively reviewed in the literature.⁴⁷⁻⁴⁹

As suggested by the molecular formulae of alkali metal zeolites, these materials possess no protons and therefore no Brønsted acid sites. However, it is possible that a low concentration of Brønsted acid sites could exist within cation-exchanged zeolite as a consequence of cation deficiencies, such as replacement of M⁺ by H₃O⁺ during ion exchange or synthesis.^{2,30} The level of Brønsted acidic sites lies below the detection limit of most standard techniques, including the most reliable, magic-angle spinning (MAS) NMR,⁵⁰ but recent studies using sensitive molecular indicators have provided evidence for very low levels of Brønsted acid sites in alkali metal Y zeolites.^{50,51} From the experimental results in these studies, estimates were made that alkali metal cation Y zeolites possess approximately one proton in every 16 supercages. This corresponds to one acidic site per 110 aluminum atoms, so that less than 1 % of the cations in these zeolites are protons. No Brønsted acid sites were detected in alkali metal X zeolites using this technique. Although such Brønsted acid sites are rarely thought to play a role in the

chemistry within alkali metal cation zeolites, a few recent experimental studies have reported that Brønsted acid sites can exert measurable effects.⁵²⁻⁵⁴ In general, however, the molecular formulae of zeolites is not always an accurate representation of the chemical constituents within. For instance, alkaline earth metal cation zeolites which are likewise non-protic according to their molecular formula usually act as strong Brønsted acids. In this case, the acid sites are generated by the dissociation of water into H^+ and OH^- ions induced by the strongly polarizing divalent cations upon dehydration.^{3,30}

The intrazeolite environment of all zeolites, both proton and metal cation exchanged zeolites, is characterized by strong Lewis acid sites. As a result, potent electron accepting sites exist within the zeolite void spaces and zeolitic materials are powerful oxidants. This is particularly true for acid zeolites where the strongly oxidizing environment often results in spontaneous oxidation of guest molecules. Since the first report of thermal generation of organic radical cations within NH_4^+ Y zeolites by Stamires and Turkevich in 1964,⁵⁵ the generality of this phenomenon has been unambiguously established through the investigations of several groups including Hall,⁵⁶ Rhodes,^{57,58} Fripiat,⁵⁹ Roduner,^{60,61} Thomas,⁶² Corma and García,⁶³⁻⁶⁶ and Gener.⁶⁷ In contrast to the ease of thermal ionization of included substrates in Brønsted acid zeolites, spontaneous generation of radical cations at room temperature in non-acidic zeolites does not typically occur. One rare example is the rapid formation of the radical cations of α,ω -diphenyl polyenes upon contact with Na-ZSM-5 zeolite. In this case the radical cations are sufficiently stabilized within the zeolite host to be studied by conventional spectroscopic techniques.⁶⁸ However, the ionization was specific to the ZSM-5 zeolite and the chosen substrate, and is therefore the exception, rather than the rule. Most reagents included within non-acidic zeolites, particularly faujasite zeolites are resistive to thermal oxidation by the framework. Instead, the oxidative capabilities of non-acidic zeolites have been well documented through studies of photoexcited guests. Thus, although thermal oxidation is generally not observed, photoionization of many types of included guests is a facile reaction in alkali metal cation exchanged zeolites.^{66,69-75}

Several types of Lewis acid, or electron accepting sites have been proposed to account for both thermal and photochemically induced oxidation reactions. In general, however, the Lewis acid sites will be cations, such as aluminum ions, or counterbalancing cations.¹³ It is commonly accepted that aluminum Lewis acid sites are necessary for the thermal oxidations observed in Brønsted acidic zeolites.^{62,76} However, the exact nature of the accepting species, for instance framework or extraframework aluminum, as well as the possible role of oxygen in the reactions, are not completely understood. On the other hand, considerable evidence now indicates that cation clusters act as electron accepting

sites in metal cation exchanged zeolites. The existence of cation-cluster trapped electrons was first proposed by Kasai and coworkers in the late 1960s and early 1970s, wherein the exposure of Y zeolites to Na vapour resulted in the generation of Na_4^{3+} due to ionization of the Na atoms induced by the electrolytic properties of the zeolites.^{31,77} The bright pink Na_4^{3+} clusters were identified by ESR measurements and found to be replaced by signals due to superoxide when the samples were exposed to oxygen. The existence of different cluster species such as Na_3^{2+} and K_4^{3+} has since been established, but clusters of larger cations such as Rb^+ have not been observed.^{78,79}

Cation-cluster trapped electrons have now been extensively characterized and studied chiefly through the combination of ESR and UV-vis spectroscopy. Thomas and coworkers have conducted detailed investigations of the nature and reactivity of electrons generated by high energy irradiation of zeolites.⁸⁰⁻⁸⁵ Using time-resolved diffuse reflectance coupled with ESR spectroscopy, Thomas *et al.* have definitively proven that cation clusters, M_n^{n+} ($\text{M} = \text{Na}, \text{K}, \text{Ag}, n = 2-6$), act as Lewis acid electron accepting sites within a variety of metal cation-exchanged zeolites (e.g. X, Y, A, sodalite). The cation-cluster trapped electrons are directly observed as transient species in anhydrous zeolites, with lifetimes in the low nanosecond (ns) to millisecond (ms) range, depending on the cation, the size of the cluster, the framework topology, the Al content in the zeolite, and the temperature. Decay of the trapped electrons is presumed to be a consequence of recombination of the trapped electron with the hole generated in the zeolite framework upon ionization. Observation of cation trapped electrons is influenced by the presence of other electron traps such as oxygen. In hydrated zeolites, water acts as an electron trap instead of, or in addition to, the metal cation. Similar results concerning the spectral properties and reactivity of trapped electron clusters were recently reported by Hashimoto *et al.* in a nanosecond diffuse reflectance study of Na_4^{3+} , Na_3^{2+} , and Na_2^+ generated by 248 nm laser photolysis of zeolites NaX and NaA.⁸⁶ In addition, identical trapped electron species have been detected upon photoionization of organic molecules with zeolites by Thomas⁶⁹⁻⁷¹ and others.^{66,72,73,87} The ability of the zeolite to stabilize an electron decreases in the sequence of $\text{Li} > \text{Na} > \text{K} > \text{Rb} > \text{Cs}$, and for the same counterion decreases in the order of $\text{Y} > \text{X} > \text{A} \approx \text{sodalite}$. These trends correlate with the electronegativity of the framework. Within the alkali metal cation series, then, the Lewis acidity of the framework decreases as the counterion size increases.^{30,88,89}

In addition to being Lewis acids, zeolites also possess Lewis basic, or electron donating sites. It is generally accepted that the electron rich framework oxygen atoms are largely responsible for Lewis basicity in zeolites.^{90,91} These oxygen sites may act as formal Lewis bases, thereby donating an electron pair to form a coordinative interaction

with another reagent, or as reductants, thereby donating a single electron to reduce another reagent. Electron donation by zeolites has been the subject of surprisingly few investigations, as compared to the extensive studies concerning the electron accepting properties of zeolites. However, the amphoteric nature of zeolites as both electron acceptors and electron donors is recognized, and several examples demonstrating the electron donating ability of zeolites and Lewis base catalysis exist. For example, thermal donation of a single electron to powerful electron acceptors such as trinitrobenzene^{92,93} and tetracyanoethylene⁹³ was observed 30 years ago upon simply immersing the zeolites in solutions of the compounds at room temperature. More recent reports include the reduction of tetrachloro-1,2-benzoquinone (*o*-chloranil) in CsY modified with cesium acetate to enhance the Lewis basicity.⁹⁴

Studies of Lewis basicity in zeolites have been the subject of increasing interest over the last few years.^{90,91} Numerous methods exist for the characterization of basic sites in zeolites, including the study of adsorbed probe molecules, for instance as colored indicators, temperature-programmed desorption studies, IR spectroscopic investigations, ESR techniques, the determination of binding energies using X-ray photoelectron spectroscopy, and theoretical estimations. A common conclusion arising from such investigations is that the basicity of the zeolites is correlated to chemical composition, and increases with increasing aluminum content and increasing alkali counterion size. For example, IR spectroscopic studies of molecular probes such as pyrrole⁸⁸ and butyne⁹⁵ adsorbed on basic sites established that the base strength of the oxygen atoms increases with decreasing Si/Al ratio and decreasing electronegativity of the cation, and also indicate the heterogeneity of basic sites within a single zeolite type. Similar conclusions have been made from studies employing X-ray photoelectron spectroscopy to characterize the electronic structure and basicity within alkali metal zeolites.^{96,97} Calculations aimed at estimating the charge on the framework oxygen atom and zeolite cations also support the experimentally observed trends in Lewis basicity.⁹⁰

While the sites of electron pair and single electron donation have consistently been proposed to be the zeolite lattice oxygen atoms, particularly those within a [Si-O-Al]⁻ bridge, much is still unknown about the precise location, structure and reactivity of the donating site, and the hole that is generated in the zeolite matrix in the case of single electron donation. The aforementioned studies of Thomas *et al.* concerning electron generation within zeolite matrices *via* high energy irradiation discuss the corresponding hole produced in the framework, albeit in somewhat less detail.⁸⁰⁻⁸⁵ The hole is assumed to be trapped by Lewis basic sites within the framework, presumably the lattice oxygen atoms. The suggestion that holes reside on zeolite lattice oxygen atoms, particularly

those bridging the Si and Al, was made as early as 1973 based on ESR studies following γ -irradiation of NaX and NaY.^{93,98-100} More recent ESR characterizations of the zeolite hole by Thomas *et al.*⁸⁵ and by Samoilova *et al.*⁹⁴ provide further support that the zeolite hole is localized on the oxygen atom. However, the exact nature of this species as well as the existence and extent of delocalization of positive charge to the neighbouring aluminum atoms remains unclear.

Few studies have addressed the role of zeolites as electron donors in reactions with photoexcited guests. In 1994, Cozens *et al.* observed that photoexcitation of the xanthylum cation in acid zeolites generated a transient characteristic of the xanthyl radical and tentatively suggested that the electron may have been donated from the zeolite framework.¹⁰¹ In 1997 Alvaro *et al.*¹⁰² reported the photoreduction of methyl viologen, and Hashimoto¹⁰³ reported the photoreduction of 1,2,4,5-tetracyanobenzene and a series of slightly weaker electron acceptors, within the cavities of alkali metal cation Y zeolites. These studies represent the first definitive examples showing that zeolites can act as single electron donors in photoinduced electron transfer reactions with included guests. In each case a relatively powerful photoreductant, E_{red}° of 3.1 V and 3.16 V for the singlet excited state of methyl viologen and tetracyanobenzene, respectively, were employed. Both studies found that the electron donating ability of the zeolite increases with increasing alkali counterion size, as anticipated from the corresponding trends in Lewis acidity.^{30,88,89}

1.1.3 Molecular Guests in Zeolites

Inclusion of Molecular Guests within Zeolites. Descriptions of the intrazeolite environment as a network of molecular-sized void spaces characterized by strong electrostatic fields and active acidic, basic, oxidizing and reducing sites provide clues to the utility of these materials as media for conducting a variety of interesting and useful chemical reactions. In order to use zeolites to carry out such chemical transformations, the reagent(s) of interest must be first included within the zeolite interior. Furthermore, in order to rationally study the chemistry of guest species within zeolite hosts, a protocol for guest inclusion which is reproducible and minimizes the introduction of unwanted materials or variables must be employed.

In their pioneering studies of thermal ionization of organic substrates within NH_4^+ Y zeolites, Stamires and Turkevich included the guest molecules within the zeolite host using a carrier solvent, *n*-hexane or chloroform.⁵⁵ This procedure remains as one of the most common ones for inclusion of molecules within zeolites today. Following

activation of the zeolite to remove the coadsorbed water, reagent molecules are incorporated by stirring the activated zeolite in solutions of inert and typically volatile solvents such as hexane or dichloromethane which should have a relatively low affinity for the zeolite. Provided that the molecules of interest are smaller than the dimensions defining the zeolite apertures, adsorption is generally assumed to result in inclusion of the guest molecules within the interior zeolite structure. This assumption is supported by the fact that the external surface area is dramatically smaller (< 1 %) than the internal surface area. Notably, however, a large number of variables exist even within this single technique: (i) the time allowed for the adsorption process to occur; (ii) the temperature at which the adsorption process is carried out; (iii) whether or not the carrier solvent is removed, how the carrier solvent is removed, and the amount of residual solvent remaining in the composite; and (iv) the amount of water introduced during the entire procedure and during subsequent experimentation. Furthermore, other methods of guest incorporation such as vapour phase adsorption introduce a new set of variables. Achieving reproducible methods for preparing zeolite/guest composites is an important aspect of all studies of intrazeolite reactions, and the potential differences induced by sample handling must be recognized when comparing results obtained from different laboratories.

Location, Distribution and Diffusion of Molecular Guests within Zeolites.

Generally speaking, adsorbed guests do not form an intercrystalline fluid, but rather occupy crystallographically controlled sites and can be considered part of the crystalline solid.³ Due to thermal motions, however, the picture of adsorbed species is necessarily a much more disordered one. Thus, one can imagine a statistical assemblage of similar, but not identical, sites where the occupancy is mostly governed by relatively weak chemical forces. Obviously the greater the interactions between the guest molecules and the framework and/or cations, the better defined the molecular positions will be.

In order to understand the reaction dynamics of molecules in zeolites, some knowledge concerning the location of guest molecules is necessary. Determination of guest location is often accomplished using molecular modeling,^{64,74,104-107} diffraction techniques (X-ray or neutron),^{40,108} or a combination of these methods.¹⁰⁹⁻¹¹¹ For example, high resolution X-ray diffraction and X-ray photoelectron spectroscopy coupled with molecular modeling provided direct evidence for the location of the *tris para*-methoxy substituted trityl cation encapsulated within the supercages of HY zeolite.¹¹⁰ Similarly, molecular mechanics have been combined with X-ray diffraction data in a comprehensive investigation of the adsorption and diffusion of several aromatic hydrocarbons in zeolite Y.¹⁰⁹ X-ray crystallography has also been employed to examine

the location and interactions of two guest species within a zeolite host as in the intermolecular charge transfer complexes between pyridinium acceptor and arene donors.⁴⁰

Spectroscopic techniques including UV-vis,^{112,113} IR^{30,76,105,112,114-117} and NMR spectroscopy^{22,116,118-120} are also essential tools defining molecular locations and adsorbate interactions within zeolites. For example, IR spectroscopy has been used to confirm that the triphenylpyrylium cation was synthesized inside the supercages of HY¹⁰⁵ and to investigate the location of benzene in Na β in the presence of coadsorbates.¹¹⁷ From ²H NMR studies of phenanthrene-*d*₁₀, Hepp *et al.* established that the aromatic guests exist within faujasite zeolites, as a complex with the zeolite cation, or as a mobile molecule within the pores.¹¹⁸ In addition, the study found that the heat of dissociation of the complexed state was proportional to the ionic radius of the alkali metal counterion, as predicted for an electrostatic binding interaction between the aromatic moiety and the cation. Two recent studies have combined MAS NMR (²³Na and ¹³³Cs) with synchrotron X-ray powder diffraction to determine the location and binding of CF₂HCF₂H in zeolite Y and the migration of cations upon adsorption of guests and during dehydration.^{22,120}

Due to the heterogeneous nature of the zeolite interior, a single type of guest molecule will most likely be located at more than one type of intrazeolite site. Studies of the intrazeolite reactivity of guest molecules are consistent with this notion, and the existence of several adsorption sites is often invoked to explain the range of reactivity. Early investigations by Casal and Scaiano established the intermediates in zeolites may display a range of lifetimes and/or reactivities as a result of the inhomogeneity of adsorption sites.¹²¹ They noted that ketone triplets in silicalite exhibit two distinct lifetimes under vacuum conditions, and two different rate constants for reaction with oxygen. Similarly, investigations by Johnston *et al.*^{122,123} found that zeolite-encapsulated diphenylmethyl radicals decay over a remarkable range of 9 orders of magnitude due to the influence of the heterogeneous zeolite topology on molecular diffusion. Garcia-Garibay and coworkers observed that photolysis of dibenzylketone in NaX involves three stages resulting in the generation of three types of radicals, each of which could be selectively quenched by varying the pressure of oxygen.¹²⁴ The existence of at least two distinct adsorption sites was proposed to rationalize the biexponential fluorescence lifetimes of phenanthrene, naphthalene and pyrene NaY.¹²⁵ Inclusion of xenon was found to selectively quench only the short-lived fluorescence, presumed to be due to species adsorbed at cation sites. The reactivity of pyrene and anthracene towards photoionization in alkali metal cation zeolites also suggests that these molecules may be

adsorbed in at least two different sites, active and non-active in terms of ionization. Thus, those species adsorbed at active sites undergo single photon ionization, while those species at non-active sites yield singlet states which can either ionize by absorbing a second photon, emit to the ground state, or intersystem cross to the triplet state.^{69,70}

Due to the existence of numerous occupancy sites with distinct characteristics, an adsorbed molecule does not necessarily experience the same environment as a neighbouring adsorbate and therefore may not behave in precisely the same manner. In addition, for any particular family¹²⁶ of sites, such as sites near or at a cation, there may exist a variety of adsorbate arrangements which are closely related but unique. Thus, while the characteristics of all sites within a family are the same, individual sites show slightly different properties resulting in a distribution of adsorbed molecules with, potentially, a distribution of properties. Such a description is completely logical considering the heterogeneous environment within the zeolite.

Although the interior of a zeolite is heterogeneous, the crystallinity of zeolitic materials ensures the periodic repetition of identical structural units. Thus, these materials are heterogeneous on a molecular scale, but on a micrometer scale the interior of the zeolite particle is quite homogeneous. Therefore, the fact that the distribution of guest molecules within the cavity is heterogeneous does not preclude homogeneous, randomized distribution throughout the thousands of cavities within a zeolite particle. This is, in fact, the situation for many adsorbate-zeolite composites, wherein the distribution of the adsorbates can be described by a statistical randomization of molecules throughout the zeolite particle.

There are, however, circumstances in which the confined reaction cavities of zeolites can promote the aggregation of guests. The classic, well-studied example is pyrene, although similar behaviour is also observed for other aromatics such as anthracene and naphthalene. Studies of the distribution of pyrene by Ramamurthy *et al.* found that pyrene forms dimers in the ground state upon inclusion within NaY.¹²⁶ Excitation of the pyrene-zeolite composites resulted in emission from monomer and excimer forms, and a broad distribution of monomer fluorescence decay lifetimes. Inclusion of water caused a reduction in the excimer emission and a narrowing in the distribution of decay lifetimes to one or two sharp maxima. It was suggested that water interfered with absorption sites thereby rendering the distribution more homogeneous. Cozens *et al.* conducted a detailed study of the intrazeolite distribution and mobility of pyrene.¹²⁷ In this case, the dimer aggregates formed upon inclusion of pyrene within NaY were observed to separate and form a monomeric dispersion. Remarkably, the equilibration of the pyrene molecules through the zeolite matrix took place over periods

of several days to several weeks, with the precise time being a sensitive function of pyrene concentration and sample conditions, such as the presence of water or inert gases. These investigations helped establish that the pyrene molecules do eventually attain a homogeneous distribution throughout the framework. For pyrene this process is dramatically slower than for many other adsorbates. This has been attributed to interactions between the zeolite cations and pyrene's π -cloud resulting in polarization of the ground state molecule and consequently enhanced dimer-type interactions with a second ground state species. As well, the similarity in molecular dimensions of pyrene and the zeolite pores are thought to play a role. This hinders the ability of pyrene to migrate into the matrix and promotes the initial clustering of molecules in the exterior cages along the peripheries of the zeolite particle.

Several other examples of molecular aggregation facilitated by the confined intrazeolite environment have been noted. For instance, two independent studies have recently shown that ground state aggregation of anthracene¹²⁸ and naphthalene¹²⁹ in cation-exchanged Y zeolites is promoted by a cation- π interaction between the zeolite cations and the aromatic guest, in a fashion analogous to that observed for pyrene. The presence of coincluded solvents, notably water, can hinder this interaction and thereby promote a monomeric distribution. Pines *et al.* employed multiple quantum NMR methods to investigate the distribution of benzene in NaY as a function of concentration.¹³⁰ Using this technique, the average number of dipole-dipole coupled protons in each zeolite supercage, as well as the magnitude of the dipole-dipole coupling can be determined, providing a measure of the average number of molecules within each cavity and the relative distances between groups of protons, respectively. These studies revealed isolated clusters of benzene molecules in the supercages at low loadings (less than 3 molecules per supercage) and weakly coupled clusters of benzene molecules in the supercages at high loadings. In all cases a uniform, statistical distribution was observed between supercages (*i.e.* an equal numbers of benzene molecules in each supercage). Similarly, Davis and coworkers applied thermogravimetric analysis, Raman, and NMR spectroscopy to examine the distribution and motion of hexamethylbenzene, adamantane and naphthalene in NaY.¹³¹ The experiments confirmed that the organic species reside in the supercages, but suggested that hexamethylbenzene molecules associate in pairs such that some cages were doubly-occupied while others were empty.

In contrast to the behaviour of the aromatic hydrocarbons, the cationic dye, thionin, has been reported to exist as a monomer within the large pores of dry Y zeolites, but to generate dimers upon hydration.¹³² This is analogous to the behaviour of thionin in homogeneous solution where dimer formation requires aqueous conditions. In this

case, the sufficient free volume to accommodate the dimer, the high loading level of the dye, and the tendency for dimerization in aqueous media, contribute to intrazeolite dimerization. A similar enhancement of intrazeolite dimerization in the presence of water was recently reported for another organic cation, methyl viologen, in zeolite Y, L and Mordenite.¹³³

Strong intermolecular interactions facilitate the aggregation of molecular species within zeolites, as has been demonstrated by pioneering studies of Yoon and Kochi concerning the assemblage of charge transfer complexes between methyl viologen and other pyridinium ion acceptors with arene donors in zeolites.^{39-41,134} In these studies, X-ray crystallography was employed to definitively establish the necessary cofacial arrangement of the donor and acceptor within the zeolite cavity. In addition to the strong intermolecular interactions between the reagents, both size and shape restrictions imposed by the zeolite were found to influence complex formation. High intrazeolite concentrations and strong donor-acceptor interactions render aggregation more favorable than dispersion through the framework for these adsorbates. Recently, the formation of charge-transfer complexes between two uncharged reagents within alkali metal zeolites has also been reported.⁴⁶

The limited free volume of zeolite cavities has been shown to influence intermolecular aggregation and formation of charge-transfer complexes between methyl viologen and aromatic donors.¹⁰⁷ The complexation was enhanced as the size of the alkali metal cation increased due to the tighter fit and closer intermolecular contact enforced in the larger alkali counterion zeolites. In another example, dimerization of an amine radical cation with a neutral amine was observed within the confines of NaY.¹³⁵ The dimerization reaction does not take place in homogenous solution, except in intramolecular systems where close proximity is ensured.

One final point to be made concerning the aggregation of molecular adsorbates within zeolites relates to the method of composite preparation. The method of guest inclusion can play a distinct role in the resulting distribution of guests within zeolites. For instance, Corma *et al.* found that inclusion of thianthrene in large pore zeolites HY and H β using organic solutions results in dimer aggregates, while vapour phase adsorption leads to more facile intracrystalline diffusion and therefore a dispersion of monomers with the zeolite.⁶⁴

Intrazeolite diffusion^{25,47,136-138} is highly significant to zeolite-mediated separations, reactions and heterogeneous catalysis, and plays a vital role in governing reaction rates and product selectivity. Consequently, diffusion in zeolites is a vast and intricate field of study. Two factors which must be recognized when considering

intrazeolite diffusion are: (i) the size of the molecules in relation to the zeolitic pore sizes; and (ii) due to the large internal surface, the ratio of the number of adsorbed molecules to the number of gas molecules will be very high; therefore, diffusion will involve surface diffusion in addition to gaseous diffusion. Intracrystalline diffusion in zeolites is dominated by the continuous interaction of the adsorbate molecules with the walls of the framework, as dictated by the porous network of molecular sized pores and channels of the zeolite. Ultimately, the adsorbate never escapes the force field of the zeolite, and intracrystalline diffusion has also been termed *configurational diffusion* due to the strong interaction of the molecules with the surrounding media. As a result of these considerations, diffusion of molecules in zeolites represents a complex problem and investigations of this diffusion are often difficult to conduct as well as interpret. Macroscopic measurements of diffusion coefficients, for instance, by direct measurement of diffusion rates through a sample, or by concentration measurements as a function of time, generally yield apparent, rather than true, diffusion coefficients. Since concentration gradients necessarily exist, these measurements are thought to occur under non-equilibrium conditions. Conversely, measurements of diffusion coefficients for an equilibrium state represent microscopic measurements where the molecular motions responsible for diffusion are directly examined. NMR techniques are most commonly employed in these experiments.^{136,139} Not surprisingly, large discrepancies have been reported for diffusion coefficients derived from various experimental techniques; although, good agreement may be obtained depending on the factors governing diffusion within a particular system.¹⁴⁰

Many variables affect the rates of intrazeolite diffusion. These include the channel geometry and dimensions, the size, shape, planarity and polarity of the diffusing species, cation distribution, size, charge and number, the concentration of adsorbates and the temperature. These parameters may work by altering the space available for motion, the nature and strength of the adsorbate interactions with the host, or a combination of the two. Ultimately, the combined factors determine the energetics of interaction of the guest with the zeolite host surface and hence the activation energies for intrazeolite diffusion. Generally, activation energies are quite high, a fact which is manifested by the rather strong dependence of intrazeolite diffusivities on temperature. For instance, activation energies of 0 to 50 kJ/mol for pore sizes between 10 to 5 Å are typical, and the activation energies rise dramatically as the dimensions of the diffusing molecules approach the pore sizes. A recent study of benzene diffusion in the medium pore zeolite ZSM-5 (free aperture of channels approximately 5.5 Å) reported an activation energy for diffusion of 30 kJ/mol.¹⁴⁰ Diffusion limited processes are not uncommon for diffusional activation

energies in excess 15 kcal/mol. The activated diffusion in zeolites is thought to proceed *via* a sequence of thermally activated jumps between regions of relatively low potential energy. The jump time can be quite rapid, however, and adsorbed molecules may jump rapidly from site to site with occasional escape from the zeolite cavity. The probability for cage escape resulting in diffusional motion will depend on the zeolite architecture which influences the length of the jumps, and the strength of the molecular interactions which influence the residence time at a particular site.

A number of techniques have been employed to measure diffusion coefficients for a number of molecules in zeolites, in particular X and Y zeolites, although agreement between various techniques is rarely achieved. Due to the extensive combination of variables affecting molecular motion in zeolites, intrazeolite diffusion coefficients ranging from 10^{-4} to 10^{-16} $\text{cm}^2 \text{s}^{-1}$, have been reported.²⁵ The diffusion coefficients and factors influencing diffusion vary dramatically with molecular size and functionality. For saturated hydrocarbons, which exhibit relatively small adsorbate interactions with zeolite walls, diffusion is largely governed by geometric constraints of the pore structure and can be understood in terms of mainly steric effects. At low loadings the diffusivity is about one order of magnitude less than in the free liquid, while at high loadings it drops off dramatically due to intermolecular collisions. The interaction between the cations and double bonds plays a decisive role in the diffusion of unsaturated hydrocarbons. Diffusion coefficients obtained through pulsed field gradient NMR for benzene and xylene of 2×10^{-7} and 5×10^{-11} $\text{cm}^2 \text{s}^{-1}$, respectively, have been reported, while the considerably more bulky dimethylnaphthalene was found to have a diffusion coefficient of ca. 10^{-12} $\text{cm}^2 \text{s}^{-1}$ from gravimetric techniques.²⁵ The diffusion of polar molecules such as water, ammonia or methanol is strongly influenced by the tight interactions between these molecules and the ionic zeolite network.²⁵ This is particularly true for water which is tightly coordinated to the zeolite cation and acts as a H-donor in a H-bonding interaction with the framework oxygen.

Interaction Between Molecular Guests and Zeolite Hosts. Zeolites have often been described as nanoscopic, or microscopic reaction vessels in which chemical reactions can be carried out and manipulated on a molecular level.¹⁴¹ As molecular-sized enclosures, zeolite micropores can alter the energy surfaces that determine guest reactivity. Guest molecules will be strongly influenced by non-bonding interactions, electrostatic forces, and size and shape considerations. In a broad sense, the influence of zeolite encapsulation on guest reactivity is considered to be derived from three types of effects: (i) passive influences whereby the zeolite defines structural possibilities available to a guest molecule and provides entropic perturbations due to its confined

environment; (ii) active influences whereby the zeolite alters the electronic structure of the reactant and therefore its reactivity; and (iii) statistical influences whereby occupational and topological factors alter reactivity. Ultimately these influences will manifest themselves in the sequence of events necessary for chemical transformation within zeolites, namely reactant diffusion through the zeolite micropores to reach an active site, adsorption on the active site, chemical reaction to generate adsorbed products, desorption, and intrazeolite diffusion of the products.

In a passive sense, the zeolite can influence reactivity by acting as a medium for molecular organization and confinement. Although there may be no significant host-guest interactions, the zeolite controls the free volume for reaction and manipulates molecular conformation and diffusion. Thus, reactivity can be understood in terms of cavity size, shape, and flexibility.

When interactions between the guest and the framework or included cations become significant, the zeolite is considered to play an active role in the reaction dynamics, and additional factors need to be considered. Such interactions may vary from weaker van der Waals forces to stronger hydrogen bonding or electrostatic interactions. Molecular polarization by weak van der Waals forces can influence the behaviour of adsorbed species by, for instance, leading to the positioning of a molecule within a zeolite cavity near a specific site. Electrostatic interactions between the zeolite host and molecular guest can induce a significant polarization of adjacent molecules and displacement of the electronic distribution of confined guests, thereby altering reactivity. In addition, zeolite active sites can participate directly by reaction with a guest molecule.

Inclusion of guest molecules within zeolites often produces dramatic changes in the molecular properties of the guest. Rationale for these changes is typically provided by the influences of the physical confinement, the electrostatic properties and intermolecular interactions within the zeolite. More recently, these rationales have been extended by the notion that *electronic confinement* may contribute to the activation of guest molecules towards physical and chemical changes within the confined space of the zeolite.^{142,143} The underlying concept of electronic confinement is that molecular orbitals of the guest molecules are not extended as in the gas phase, but are limited to the zeolite walls. The effect becomes progressively more significant as the molecular size of the adsorbate approaches the dimensions of the cavities. The electronic confinement can thereby alter the molecular orbital energies, as has been demonstrated by Hückel Molecular Orbital Theory,¹⁴² and *ab initio* calculations.¹⁴³ Recently, experimental evidence supporting the concept of electronic confinement of zeolite encapsulated anthracene was reported, wherein a bathochromic shift in the 0-0 transition and a

shortening of the fluorescence lifetime of anthracene was attributed to increased energy of the HOMO and reduction of the band gap.¹⁴⁴

1.2 Using Zeolites to Control Reaction Dynamics: Experimental Examples

The discussion thus far has introduced the fundamental structural features and microenvironment which are the essence of zeolitic materials. As well, the behaviour of included molecules has been described in order to visualize how such guests may localize within, diffuse through, and interact with the zeolite host. A question which has yet to be addressed is: how does the zeolite control or modify the reactivity or reaction selectivity of guest molecules. The approach used in the present work addresses this question by examining the behaviour of reactive intermediates including their formation, their reactivity and reaction pathways, Figure 1-5. This approach has been used by other researchers interested in the same question, and a brief survey of some results from their work is presented herein.

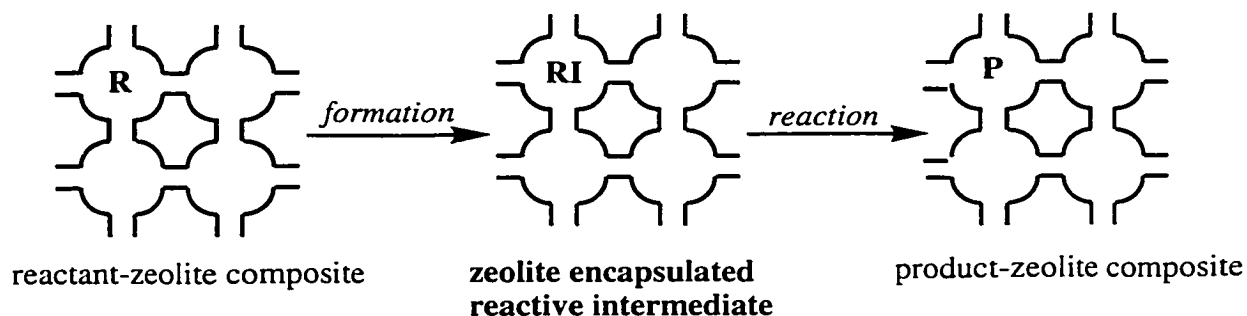


Figure 1-5. The current experimental approach to studying reaction dynamics in zeolites involves direct examination of reactive intermediates.

1.2.1 Influence of Zeolites on the Lifetimes of Reactive Intermediates

As outlined below, the degree and consistency with which zeolites have been shown to influence the lifetime of chemically relevant intermediates is quite remarkable.

Triplet Excited States. One of the earliest investigations of a reactive intermediate in a zeolite was the β -phenylpropiophenone triplet in the non-aluminum zeolite, silicalite. In 1985, Scaiano and Casal reported the triplet lifetime of β -phenylpropiophenone to be ca. 10^5 times longer in silicalite than in homogeneous solution. This observation was attributed to inhibited deactivation as a result of

conformational restrictions induced by zeolite encapsulation.¹²¹ Subsequently, several examples demonstrating the enhanced lifetime of triplets within zeolite hosts (typical lifetimes in the μs time regime) have appeared.^{52,54,135,145} Most recently, flexible molecules adopting a frozen conformation within the zeolite matrix have been shown to have their deactivation pathways reduced.¹⁴⁶

Carbon-Centered Radicals. Supramolecular control of radical-radical reactions in zeolites has been extensively studied by Turro and coworkers for nearly 15 years.²⁴ This research examines the influence of zeolite size, shape and diffusional parameters on the reactivity of a geminate pair of carbon-centered radicals generated photochemically within non-acidic zeolites. The investigations were initiated by pioneering studies of the photolysis of dibenzylketones which established that the radical coupling derived products varied dramatically as a function of the internal architecture of the zeolite¹⁴⁷ as well as the framework composition and charge-balancing cation.¹⁴⁸ Subsequent studies have examined, for instance, the influence of substrate loading,¹⁴⁹ and surface coverage^{150,151} on the observed photochemistry and reaction selectivity. Overall, these studies have demonstrated and rationalized the notion that zeolites can induce selectivity in radical-radical reactions which are completely nonselective in solution, and introduce new radical reactions which do not occur in solution.

The most recent experiments of the Turro group in this area have focused on diphenylmethyl radicals and the ability of zeolite encapsulation to render these species "supramolecularly persistent".¹⁵²⁻¹⁵⁴ For instance, within the restricted spaces of the MFI zeolite LZ-105 (e.g. topology of ZSM-5), diphenylmethyl radicals with half-lives of several weeks have been reported. The remarkable ability of zeolites to enhance the lifetimes of carbon-centered radicals, in particular the relatively stabilized diphenylmethyl radical was initially demonstrated with a nanosecond diffuse reflectance study of diphenylmethyl radicals in 1990, wherein the radicals were found to decay over the incredibly wide range of hundreds of nanosecond to minutes, and perhaps longer.¹²² Only recently has the more reactive benzyl radical been observed in alkali metal cation zeolites using transient spectroscopy.¹⁵⁵ The detection of this radical had previously been unsuccessful, presumably due to rapid in-cage coupling of the geminate radical pair when the radicals were generated by traditional precursors such as dibenzylketone. The approach adopted by Cozens *et al.*¹⁵⁵ employed a photochemical precursor which generated a single benzyl radical within any supercage upon photochemical formation. The resultant benzyl radicals were also found to be relatively long-lived within the confines of the zeolite environments, with decay over tens to hundreds of μs *via* slow intrazeolite diffusion followed by radical-radical coupling.

Radical Cations. The ability of zeolite environments to stabilize radical cations is well-known from the spontaneous formation and persistence of these species in acidic zeolites.^{56-62,64-66} Favorable radical cation generation in non-acidic zeolites is also evident, in this case from studies of photoexcited guests where ionization is facilitated within the zeolite. Unlike in solution where photochemical ionizations typically require the absorption of two photons, photoionization has been found in some cases to be monophotonic in zeolites. The monophotonic generation of radical cations upon photoionization in zeolite cavities was first demonstrated by Thomas *et al* for pyrene and anthracene in alkali metal cation Y and X zeolites.⁶⁹ Photoexcitation of pyrene^{70,89,156} as well as anthracene, naphthalene and stilbene⁷¹ has been the subject of several additional reports of the Thomas group. In each case, single photon ionization is proposed to be associated with the adsorption of guests at specific framework sites which promote ionization. The resultant radical cations are significantly longer lived than in solution. Photoionization of organic substrates in alkali metal cation zeolites leading to relatively stabilized radical cations has been investigated by several other research groups. For instance, along with the investigations of Thomas, photoionization of *trans*-stilbene in Na⁺-exchanged zeolites has been studied by the groups of Scaiano,⁷⁵ Johnston⁷² and Hashimoto.⁷³ Photoionization of styrenes within NaY leading to the corresponding radical cations has also been investigated.^{66,87} Interestingly, although the styrene radical cations were observed to be significantly less reactive than in typical organic solvents, the stabilizing influence of the zeolite was most dramatic for the parent styrene radical cation, and played less of a role in stabilizing the 4-methoxysubstituted radical cation. Photoionization of 1,1-diarylethylenes in NaY and NaX has also recently been reported.¹⁵⁷

Radical Ion Pairs. Perhaps the most cited examples of the ability of zeolites to modify reaction dynamics by influencing the lifetime of reactive intermediates is the stabilization of radical ion pairs generated *via* photoinduced electron transfer (PET). The classical example of the intrazeolite stabilization of radical ions comes from the seminal studies of Yoon and Kochi.^{158,159} These investigations demonstrated that back electron transfer (BET) between radical ions generated upon excitation of charge-transfer complexes between pyridinium ion acceptors and arene donors within NaY could be five to six orders of magnitude slower than in homogeneous solution. Correspondingly, it was estimated that the charge transfer ion pair was stabilized within the zeolite supercage by approximately 8 kcal/mol over solution. The dramatic stabilization of the radical ion pairs and significant reduction in rate constants for energy wasting BET was attributed to adsorption effects of the ionic species at the polar aluminosilicate surface and strong

electrostatic fields within the zeolite cage. Notably, PET between intrazeolite charge transfer complexes was recently extended by Hashimoto and coworkers to include neutral charge-complexes.⁴⁶ In these studies, the neutral species 1,2,4,5-tetracyanobenzene was employed as the acceptor, in contrast to the cationic organic acceptors used by Kochi and Yoon. Photoexcitation of the neutral charge transfer complexes between 1,2,4,5-tetracyanobenzene and arene donors was observed to generate radical ions which decayed *via* charge recombination with rate constants ranging from 10^8 to 10^9 s⁻¹. The lifetimes of the radical ions are therefore significantly longer, by at least one order of magnitude, than observed in solution, consistent with the notion that decreased rates of BET and stabilization of radical ion pairs is an inherent property of the intrazeolite environment. However, the magnitude of radical ion stabilization is substantially less when the radical ion is generated from the neutral charge-transfer complex as compared to the cationic charge-transfer complex of Kochi and Yoon.

Dutta and coworkers have been investigating intermolecular electron transfer between tris(bipyridine)ruthenium(II) ($\text{Ru}(\text{bpy})_3^{2+}$) imprisoned within NaY cavities and bipyridinium ions incorporated in adjacent cavities.¹⁶⁰⁻¹⁶² They have observed ET quenching of the excited state $\text{Ru}(\text{bpy})_3^{2+}$, with ET occurring *via* contact interactions through the zeolite pores. The resulting ion pair (both ions positively charged) was again observed to have a lifetime significantly longer than in homogeneous solution. In this case, decay proceeds *via* charge recombination with rate constants between 10^4 to 10^5 s⁻¹ depending on the oxidation potential and concentration of the bipyridinium ion donor. Interestingly, at high bipyridinium ion loadings, substantially longer-lived charge separation could be achieved (e.g. lifetimes of hours). This has been attributed to charge propagation *via* electron hopping along the densely populated donor molecules aligned within the zeolite voids. Extensions of this research, by the groups of Dutta,¹⁶³⁻¹⁶⁵ Mallouk,¹⁶⁶⁻¹⁷⁰ and Kincaid,^{171,172} have involved the design and construction of more elaborate assemblies of redox reagents directed towards artificial photosynthetic mimics and energy storage applications. The underlying theme in each case is to generate long-lived charge separated states by employing the spatial organization and stabilization uniquely provided by zeolitic systems.

Carbocations. Unlike the other reactive intermediates discussed thus far, studies of carbocations in zeolites have essentially been restricted to acidic zeolites. This has largely been due to the ease of generation and the persistence of many carbocations in the strongly acidic environment, as well as the significant role carbocations play in commercially valuable reactions catalyzed by acid zeolites. The observed stabilization, and in some cases persistence, of carbocations within these zeolites is largely associated

with the strongly acidic conditions of the media, however, the high polarity of the zeolite interior, the low nucleophilicity of the framework oxygen atoms in acidic zeolites, and the protection from nucleophilic attack also play a role. For instance, the recently reported synthesis of reactive squaraine dyes within acidic zeolites, which has previously been unsuccessful in solution due to rapid nucleophilic attack of water and methanol, has been attributed to the prevention of nucleophilic attack by the tight confinement within the zeolite cavities.¹⁷³ Certainly more than mere acidity is responsible for the influence of these zeolites on the lifetimes of carbocation intermediates. Furthermore, in these extreme cases where the stability imparted by the zeolite renders the intermediate very long-lived, new investigations of the intermediates not readily available in solution are made possible.

Persistent carbocations in acid zeolites have been studied extensively by the groups of Corma and García.⁶⁵ Carbocations such as xanthylium,^{63,101} dibenzotropylium,⁶³ α,ω -diphenylallyl,^{174,175} and 1,5-diphenylpentadienyl cations¹⁷⁶ have been generated by functional group transformation of an incorporated neutral precursor, while other carbocations, such as the trityl,¹⁷⁷ pyrylium,^{105,177} and 9-aryl xanthylium cation,¹⁰⁶ which are too large to fit through zeolite pores, have been synthesized by a ship-in-a-bottle methodology which relies on C-C bond formation within the zeolite host.

1.2.2 Influence of Zeolites on Reaction Pathways

Other remarkable examples of the influence of zeolites on reaction dynamics are obtained from studies of specific chemical transformations of guest molecules in zeolites. In such cases, the zeolite can truly be viewed as a *microscopic reaction vessel* which facilitates the desired chemical transformation while minimizing undesired side products.

Over the last decade or so, the research group of Ramamurthy *et al.* has focused on the study of photochemistry in the organized and confined environments of zeolites.^{23,141,178-182} These studies have been directed both towards using the photophysical and photochemical reactions as probes of the zeolite environment, and applying the zeolite as a medium to control the photoprocesses of organic molecules. From these investigations, a large number of diverse examples have emerged, which unambiguously demonstrate the influence of zeolites on the reaction dynamics of organic guests within zeolites, in this case, reactions dynamics initiated photochemically. For instance, photophysical processes such as absorption,¹²⁶ emission¹⁸³⁻¹⁸⁵ and energy transfer,¹⁸⁶ can be dramatically influenced by zeolite encapsulation, and by the specific

nature of the zeolite environment. In addition, photochemical reactions such as photoinduced electron transfer,^{87,187} Norrish type I and II reactions of excited ketones,^{185,188,189} photoisomerizations,¹⁹⁰ photodimerizations,^{191,192} photo-Fries^{193,194} and photo-Claisen¹⁹⁵ rearrangements, singlet oxygen mediated oxidation of olefins,^{196,197} and photoreduction of steroidal enones¹⁹⁸ exhibit selectivity unique to the zeolite environment. While the precise explanation for each specific effect varies, the underlying theme is that the size, shape and chemical environment within the zeolite cavity is responsible for the observed effects. In some cases this is attributed to passive effects, such as, restriction of the rotational and translational motion of reactants, transition states or products, or active effects such as electrostatic interactions or interactions with light or heavy zeolite cations. Cation-guest interactions have been found to be particularly influential, and often play a direct role in the observed reaction pathways. Cation binding can stabilize an adsorbed molecule near a cation site, introduce steric hindrance to certain reaction pathways, or induce changes in preferred molecular conformations. Effects involving cation-guest interactions depend largely on the binding strength and therefore on the charge density, or electrostatic potential of the cation, as well as the number of accessible cations. For example, strong binding interactions with charge dense cations such as Li⁺ or Na⁺ may alter the absorption spectra of included aromatic species and decrease the lifetime of excited states by enhancing radiationless relaxation processes. Conversely, charge diffuse atoms such as Rb⁺ and Cs⁺ tend to bind organic guests more weakly and exert different influences such as enhanced singlet to triplet intersystem crossing and phosphorescence.

Oxidation of hydrocarbons is an industrially significant reaction and one of the most important applications of catalysis. Recent investigations have demonstrated that zeolites effectively promote selective photooxidation of hydrocarbons, and could thus play a role as benign, environmentally-friendly catalysts of these reactions. Photooxidation reactions in zeolites are thought to proceed *via* a charge-transfer complex between the hydrocarbon and molecular oxygen. The remarkable ability of zeolites to modulate the photooxidation has been attributed to the stabilization of these complexes imparted by the large electrostatic fields within the zeolite cavities.

Frei and coworkers reported the unprecedented stabilization of charge-transfer complexes between oxygen and alkenes such as 2,3-dimethylbutene, *cis*- or *trans*-2-butene in NaY by more than 10 000 cm⁻¹ (300 nm).^{42,43} Similarly, absorption of the cyclohexane-O₂ charge-transfer complex in NaY was observed to shift from the UV into the visible.⁴⁴ Furthermore, long wavelength (500 – 700 nm) excitation of these charge-transfer complexes resulted in highly controlled, highly selective photochemical

reactions. For instance, red-light induced reaction of O₂ with *cis*- or *trans*-2-butene gives allylic hydroperoxides as the only products. Likewise, visible irradiation induced oxidation of cyclohexane to cyclohexyl hydroperoxide and cyclohexanone, and thermal rearrangement of the resultant hydroperoxide yields cyclohexanone as the sole product. These represent the first examples of such selective oxidations of alkenes and cyclohexane by O₂. The remarkable reaction control was attributed to the strong stabilization of the excited charge-transfer complexes within the NaY matrix, presumably due to very strong electrostatic interactions within the cavities. As a consequence, low-energy visible light, rather than UV irradiation, can be used to excite the complexes, thereby accessing low energy photooxygenation pathways not available in homogeneous solution, and minimizing excess energy in the primary products. This may prevent additional reactions such as fragmentation, or diffusion out of the cage and resulting random couplings. Furthermore, the use of visible photons prevents secondary photochemical reactions.

Similarly, the photooxidation of toluene and *p*-xylene in a series of Na⁺, Ca²⁺ and Ba²⁺-exchanged zeolites has recently been investigated by Larson and Grassian.^{199,200} Photoexcitation of the oxygen charge-transfer complexes with visible light leads selectively to the aldehyde oxidation products, and the efficiency and selectivity of photooxidation correlated nicely with the measured electrostatic fields within the zeolite cavities. Thus, zeolites possessing larger electrostatic fields promoted photooxidation more efficiently presumably due to greater stabilization of the intermolecular charge-transfer state formed upon excitation. The electrostatic fields were determined to be larger for divalent cations and for zeolites with higher Si/Al ratios, consistent with previously reported measurements and calculations.^{4,31} In addition, the selectivity was found to vary with zeolite topology, and selectivity was reduced when UV light was employed as an excitation source due to the introduction of additional reaction pathways not accessible *via* visible excitation.

Charge-transfer complexes between *trans*-stilbene and molecular oxygen have also been found to exhibit enhanced stability in alkali metal cation zeolites as compared to solution.⁴⁵ Both the strong electrostatic fields, and the condensation effect exerted by the zeolite environment were proposed to rationalize the enhanced stability. Product variability could be achieved by exciting the charge-transfer complex at different wavelengths. Thus excitation with 313 nm light yielded the benzaldehydes *via* the stilbene radical cation derived from ET, while 254 nm excitation induced isomerization and formation of phenanthrenes without the generation of oxygenation products.

The restricted space and high internal electrostatic fields within zeolites have also been exploited to manipulate oxygenation reactions involving singlet oxygen.^{196,197,201-203} Zhou and Clennan have recently reported on the photooxidation of sulfides in methylene blue doped NaY. The methylene blue serves as an energy transfer photosensitizer to generate the singlet oxygen and initiate the reaction. These studies have revealed the zeolite encapsulation modifies the selectivity of sulfide oxidation and introduces reactions not observed in homogenous solution.²⁰¹ As well, an investigation of the competitive reactions of singlet oxygen with sulfide and olefinic moieties within the same molecules found a dramatic increase in sulfoxide formation in the zeolite as compared to solution.²⁰² This was attributed to stabilization of the persulfoxide intermediate by the zeolite host and the concomitant inhibition of singlet oxygen quenching. Similarly, Stratakis and Froudakis²⁰³ employed thionin-doped NaY as a photosensitizer to generate singlet oxygen and initiated photooxygenation of geminal dimethyl trisubstituted alkenes. In NaY, the less substituted side of the olefin was observed to be dramatically more reactive towards photooxygenation than in solution. On the basis of theoretical calculations, this enhanced reactivity was attributed to an interaction between the alkali cation, the olefin and the oxygen molecule in the transition state for the reaction.

The reactivity of energy and electron transfer photosensitizers encapsulated within zeolites is often distinct from the reactivity observed in homogeneous solution. Modification of the properties of 4-aminobenzophenone, an energy transfer photosensitizer, was accomplished by zeolite inclusion.²⁰⁴ The confined spaces and electrostatic fields within the zeolite cavities induced variations in the properties of the excited state and the ability of the 4-aminobenzophenone to act as a photosensitizer. In addition, mechanistic variations from energy transfer to electron transfer were observed to be dependent on nature of zeolite environment.

A zeolite-encapsulated ET photosensitizer that has been extensively studied by the groups of Corma, García, and Scaiano is the triphenylpyrylium ion (TPP⁺).^{105,205,206} This ion is synthesized and imprisoned within the cavities of Y zeolites and displays significantly modified photosensitization properties when incarcerated within the zeolite. For example, TPP⁺-zeolites composites act as heterogeneous photocatalysts for the generation of the hydroxyl radical from water, despite the fact that this reactions does not take place in aqueous solution.²⁰⁶ Although the reaction is exothermic in solution, nucleophilic attack of water on the cationic sensitizer prevents the ET reaction. Inhibition of this nucleophilic attack by confinement within the zeolite cavities allows the ET to proceed. Conversely, PET sensitized cyclodimerization of 1,3-cyclohexadiene

using TPP⁺ or dibenzotropylium ion sensitizers was found to be less efficient in zeolites than in homogeneous solution.²⁰⁵ This was attributed to light scattering as well as mobility restrictions and diffusional difficulties within the solid-state host. A third example comes from the use of TPP⁺ in the photosensitized isomerization of *cis*-stilbene within cavities of zeolite Y and the extra large pore zeolite MCM-41.¹⁰⁵ Within zeolite Y, the reaction was not perturbed by oxygen as it is in homogeneous solution where byproducts due to oxidative cleavage are observed. This was attributed to enhanced in-cage isomerization made possible by a reduction in the rate of back electron transfer. However, although a higher yield of in-cage isomerization was observed within zeolite Y, the overall isomerization efficiency was relatively low due to diffusional restrictions of the zeolite framework. By employing the extra large pore MCM-41, an optimized balance between the cage effect and diffusional motion was achieved.

1.3 Scope and Significance of Thesis

Zeolites are at the forefront of the current thrust towards molecular scale control and catalysis of specific chemical reactions using host-guest interactions and supramolecular chemistry. In this regard, studies of zeolites extend from the most fundamental research, to a wide range of practical applications. Although considerable effort has been directed towards understanding both thermal and photochemical transformations within these unique microheterogeneous systems, the systematic design and application of zeolites for both routine and novel chemistry remains significantly beneath its potential. This fact is ultimately rooted in an incomplete understanding of reaction dynamics in these complex systems. The general theme of this doctoral thesis is the application of time resolved (ns) studies of reactive intermediates to the investigation of reaction dynamics within zeolites. Studies of reactive intermediates within zeolites provide a powerful tool for elucidating the mechanisms by which zeolites influence fundamental chemical reactions.

The experimental approach uses reactive intermediates to probe zeolite-guest interactions and to establish quantitative kinetic descriptions of reaction dynamics within zeolites. A major focus in this effort is directed towards expanding the understanding of specific reactions. Two types of reactions are addressed in the current work: (i) intrazeolite reactions of reactive carbocation intermediates and (ii) reactions mediated by intrazeolite charge migration (movement of electrons and holes). By extending investigations of these reactions from homogeneous solution to the heterogeneous environment within zeolites, a better understanding of these types of reactions may be

obtained. A second major focus is to employ the reaction and, particularly, the reactive intermediate as a probe of the zeolite environment. Applying knowledge obtained from studies of these types of reactions in solution, with experimental observations concerning how these reaction dynamics are modulated inside zeolite cavities, provides insight into the nature of the zeolite environment. In addition, an underlying objective of the research described herein is the exploration of intrazeolite reaction mechanisms in order to enhance the understanding needed for further development of these materials as solid-state molecular hosts and catalysts. In this regard, the reactivity of the intermediates examined is directed towards understanding how the zeolite environments modulate reactions proceeding through these intermediates.

Chapter 2. General Background and Concepts

2.1 Laser Flash Photolysis

Laser flash photolysis^{207,208} is a technique developed in the late 1960s which enables the generation, direct observation, and study of transient species using a short, intense laser pulse. This technique is a very powerful tool for direct measurement of reaction kinetics and investigation of reaction mechanisms. Three fundamental requirements exist for the application of laser flash photolysis to the successful study of a reactive intermediate: (i) As the technique relies on light to generate the transient of interest, a photochemical reaction which converts a precursor molecule into the reactive intermediate must be available. (ii) The reactive intermediate must be observable with the detection method employed. Since the most common method for transient detection, and the method employed herein, is optical spectroscopy, the transient species must absorb in the UV-visible region of the spectrum. (iii) The reactive intermediate must also have a sufficient lifetime to be detected. In simplest terms this means that the lifetime of the transient, defined as $1/k$, where k is the observed rate constant for transient decay, must exceed the width of the laser pulse used for transient generation. In other words, the time required for transient disappearance must be greater than the time required for transient formation, which for nanosecond (ns) laser flash photolysis is the duration of the laser pulse. This is the basis of the fundamental requirement of a brief laser pulse and the impetus for employing ever faster lasers in the study of the more reactive transient species.

The nanosecond laser flash photolysis apparatus is constructed from four fundamental components: the excitation source, the monitoring beam, the detection system, and the data acquisition and processing system. The excitation source is invariably a pulsed laser, but considerable variability exists in laser specifications including the energy per pulse, repetition rate, pulse duration and output wavelength. In nanosecond laser flash photolysis applications, energies between 4 and 100 mJ per pulse are typically employed, and pulse widths in the 2 to 20 ns range are common. Most commercial lasers have repetition rates considerably higher than required for the nanosecond laser photolysis experiment where the laser is often pulsed at 1 Hz or slower during data acquisition. The monitoring beam is typically a xenon arc lamp with output in the 75 to 250 W range. The low output lamps are frequently operated in a pulsed mode such that the lamp intensity is increased by a factor of 2 to 20 for a few

milliseconds during data acquisition. The detection system commonly employed in nanosecond flash photolysis is based on the combination of a monochromator with a fast photomultiplier. This allows time-resolved monitoring of transient absorption at a single wavelength with access to spectral information *via* point-by-point acquisition at individual wavelengths. Data acquisition in nanosecond flash photolysis involves capturing the transient signal by a digital oscilloscope, referred to as a transient digitizer, which converts the PMT output into digital form and transfers the data to a computer for further processing.

The essential data obtained from the laser photolysis experiment is the transient *decay trace*, or *kinetic trace*, which is the variation in the transient signal as a function of time. In transmission experiments the fraction of transmitted light absorbed by the transient, expressed as change in optical density, ΔOD , is measured. The ΔOD is derived from the collected data consisting of the transmission intensity of the monitoring beam prior to photolysis, I_0 , and an array of data points describing the signal voltage of the PMT as a function of time I_t , according to eq. 2-1, where the signal represents the fraction of light absorbed by the transient species.

$$\Delta OD = -\log(1 - \text{signal}/I_0) = -\log(I_t/I_0) = A_t \quad 2-1$$

Since ΔOD is a logarithmic function of the intensity of transmitted light, it is equal to the variation in transient absorbance as a function of time, A_t , and proportional to the concentration of the transient according to the Beer-Lambert law. As a result the decay trace represents the time variation in transient concentration from which kinetic information can be obtained directly. The optical densities measured in the laser flash experiments are not absolute optical densities but rather changes in optical density relative to the optical density of the precursor prior to photolysis. Thus the I_0 defined in eq. 2-1 represents the prepulse intensity which will be determined by the monitoring beam intensity as well as the absorption of the starting solution. As a result, a negative signal is possible and corresponds to a bleaching situation where absorption due to the products or transients produced by photolysis is less than the starting solution.

2.2 Nanosecond Time-Resolved Diffuse Reflectance

Much of the previous discussion of laser flash photolysis studies of transmissive samples also applies to opaque samples. The significant difference is that studies of opaque samples cannot use transmitted light to observe transient intermediates. In laser

photolysis experiments on non-transmissive samples it is thus necessary to excite the sample from the front face and use diffuse reflected light rather than transmitted light to monitor transient absorption (see experimental section for schematic). The use of diffuse reflected light to monitor transients species, a technique largely developed by Wilkinson and coworkers^{209,210} beginning in the early 1980s, has extended the utility of laser flash photolysis to include opaque, heterogeneous and highly scattering samples. This advancement has facilitated studies of fast reaction dynamics of molecules adsorbed on surfaces such as catalytic oxides, within microporous solid-state hosts such as zeolites, on semiconductor powders, organic microcrystals and polymers, and within many biologically relevant media.

Reflectance from scattering surfaces or fine particles consists of two components, specular reflectance and diffuse reflectance. Specular, or regular reflectance, is reflected in planes parallel and perpendicular to the incident light, at angles equal to the angle of incidence. Conversely, the diffuse reflected light is unpolarized and distributed symmetrically with respect to the surface regardless of the angle of incidence or polarization of the incident light. The source of diffuse reflectance is light that has penetrated below the surface and into the individual particles which comprise the sample. For typical diffuse reflecting samples, the penetration depth is of the order of several hundreds of μm to a few mm, with the exact value depending on the absorption and scattering coefficients of the sample as well as the laser flux. The light returns to the surface due to multiple scattering at the particle interfaces and is attenuated by absorption within the particles. Analysis of the diffuse reflected light is often based on the Kubelka-Munk treatment for strongly scattering samples. In this treatment the interaction of light absorbers randomly distributed in diffuse media is described according to eq. 2-2

$$F(R) = K / S = (1-R)^2 / 2R \quad 2-2$$

where $K = 2\varepsilon C$, ε is the extinction coefficient and C is the concentration, S is the scattering coefficient and R is the diffuse reflectance. The expression on the right side of eq. 2-2 is the remission function and is linearly related to the concentration of homogenous absorbers. For small changes in reflectance, as observed during transient generation, the relative change in the reflected light, Δr , is found to be a useful parameter which can be considered proportional to transient concentration. The relative change in reflected light is given by eq. 2-3 where J_0 is the intensity of the diffuse reflected light before transient production and ΔJ is the change in diffuse reflected intensity upon laser excitation.

$$\Delta r = \Delta J/J_0 \quad 2-3$$

Therefore, in diffuse reflectance experiments the kinetic trace is recorded as the fraction of diffuse reflected light absorbed by the intermediate, $\Delta J/J_0$, as a function of time, and is a measure of the time dependent variation in transient concentration.

Several other practical considerations also render laser flash photolysis studies of transients in opaque media different from transparent solution. The higher sensitivity of the technique to emission from the sample, particularly fluorescence, makes measurements at short times less reliable than in solution and often results in reduced time resolution for diffuse reflectance detection. Also, scattering of the laser pulse generally means a wider separation between the excitation and monitoring wavelengths (typically at least 20 nm) is necessary in the solid samples as compared to solution. A third unique feature of transient studies in the solid state is that the simple kinetic treatments often encountered in homogeneous solution are rarely observed in heterogeneous media. Kinetic analysis in heterogeneous environments is discussed in the following section.

2.3 Transient Kinetics in Heterogeneous Media

As discussed in the preceding section, the absolute reactivity of a transient species in solid supports such as zeolites can be measured by monitoring the intensity of the transient signal at a specific wavelength as a function of time using nanosecond laser photolysis. The simplest possible scenario would involve transient decay *via* a single reaction pathway characterized by first-order or pseudo first-order kinetics. In this case, the time dependence of the change in diffuse reflectance, $(\Delta J/J_0)_t$, can be modeled as a single exponential decrease from the initial change in diffuse reflectance, $(\Delta J/J_0)_i$, characterized by the rate constant, k , eq 2-4.

$$(\Delta J/J_0)_t = (\Delta J/J_0)_i \exp(-kt) \quad 2-4$$

This is equivalent to the time dependent variation in transient (T) concentration, $[T]_t$, and fitting the kinetic trace to the exponential equation given in eq. 2-5 would yield k , the first-order rate constant for transient decay.

$$[T]_t = [T]_i \exp(-kt) \quad 2-5$$

The simplest scenario of first-order kinetics characterized by a single, distinct rate constant is not often encountered for transient decay within a zeolite matrix. Due to the heterogeneous nature of the intrazeolite environment, encapsulated reagents may reside at a variety of unique sites thereby decaying with a distribution of decay rate constants, and/or *via* mechanistically different reaction pathways.^{122,123,126,211} As a result, transient decay kinetics exhibiting a wide range of lifetimes are commonly observed in zeolite environments. This often means that transient decay can be followed over several orders of magnitude. The intrazeolite decay of diphenylmethyl radicals presents an extreme example where the disappearance of the transient is observed over 9 orders of magnitude from hundreds of nanoseconds to hours.¹²² Decay over such a broad time range is typically non-exponential and often characterized by a gradual decrease in decay rate constant over time. This behaviour, which has been observed in a variety of heterogeneous processes, is described as a *stretched exponential decay*.^{211,212}

In such cases, simple first or second-order kinetic analyses, or combinations of these, often fail to accurately describe the decay profiles of transient species within heterogeneous systems, and to realistically rationalize decay kinetics that occur over a wide range of time scales. This is true in spite of the fact that reasonable and even excellent fits to experimental decay profiles can be obtained using multiple exponentials. For instance, the summations of three or four exponentials are powerful functions which will fit virtually any decay with random residuals.²¹¹ However, attaching physical meaning to the resultant rate constants is not always reasonable. For instance, two, three and four exponential models have been shown to fit data having their origins in distributions of lifetimes. Thus, a wide variety of distributions such as Gaussian, triangle, and rectangle can be fit with a double exponential, while three exponentials will fit even more distributions, and four exponentials will fit almost any distribution. This does not suggest that fitting a decay profile to a multiple exponential function is necessarily incorrect, but indicates that a decay profile which fits nicely to a few exponentials does not preclude the existence of a distribution of lifetimes. Thus, in heterogeneous systems with different local environments, the safest approach initially describes the transient decay as a distribution of rate constants, until evidence to the contrary is presented.

Studies of transient kinetics in heterogeneous systems must distinguish between discrete lifetimes and lifetime distributions and determine if a multiple exponential fit is a realistic representation of the decay profile is significant. One way this problem can be addressed is to analyze the data for a given system with no initial assumption of discrete lifetimes. As a result, dispersive kinetic analysis is being increasingly applied to

understanding transient kinetics in solid-state systems. This analysis assumes a distribution of decay rate constants, with the most probable rate constant(s) being the maxima of the distribution. The rationale for selecting a most probable value is related to the width of the distribution about this value.

The simplest proposed model to explain the stretched exponential decays often observed in heterogeneous reactions is based on a distribution of first-order processes that can be described mathematically by a series of rate constants rationalized due to the heterogeneous nature of the media. In such cases the *exponential series method* (ESM) can be used to recover the lifetime distribution from the experimental data. ESM is based on a trial function consisting of a sum of exponentials with 50 to 200 terms, eq. 2-6

$$f(t) = \sum a_k \exp(-t / \tau_k) \quad 2-6$$

where t is time, and τ_k are fitted lifetimes each associated with a pre-exponential factor, a_k . In the application of ESM, the lifetimes are fixed values (in contrast to multiple exponential fits which allow lifetimes to be free parameters) equally separated in $\log \tau$ space. The iteration begins with equal pre-exponential coefficients for each lifetime and proceeds to vary the coefficients until the best fit is obtained. The best fit criterion minimizes the parameter χ^2 which is based on minimizing the differences between the fitting function and the actual decay curve. The resulting solution is thus expressed as a set of amplitudes associated with a large series of fixed lifetime exponentials over the complete range of time of transient decay.

ESM and similar dispersive analyses recover the distribution associated with a decay curve with no assumption as to the nature of the decay. Such analyses are therefore useful to account for the possibility that the transient decay might involve a broad distribution. Distribution recovery is likewise useful to establish that analysis based on a few exponentials can indeed be valid for a specific system. Thus where distribution analysis recovers a narrow ranges of lifetimes characterized by a few distinct lifetimes, greater confidence in an interpretation based on transient decay *via* a few discrete first-order processes is obtained.

2.4 Defining the Quantity of Adsorbates within Zeolites

In the upcoming chapters examining the reactions of guest molecules in zeolites, the amount of the adsorbate within the zeolite framework will be discussed. The amount

of adsorbate within the zeolite is expressed in terms of occupancy number, loading level, or molarity, as described below.

A useful parameter to describe the concentration of adsorbates in X and Y-type zeolites is the *occupancy number*, $\langle S \rangle$, which is simply the average number of adsorbate molecules per zeolite cavity. As shown in eq. 2-7, the occupancy number may be determined from the amount of adsorbate included into a known zeolite mass given the molecular mass of the zeolite unit cell and the fact that the unit cells of faujasite zeolites contain 8 cavities.²

$$\begin{aligned} \langle S \rangle &= \text{moles of adsorbate/moles of zeolite cavities} && \text{2-7} \\ &= \text{moles of adsorbate}/(8 * \text{mass zeolite/unit cell mass}) \end{aligned}$$

The unit cell formulae and molecular masses of the alkali metal cation zeolites used in this study are given in Table 2-1. The amount of adsorbate within the zeolite is also expressed in terms of the *loading level*, or *loading*, which is simply the number of cavities per molecule and is thus the reciprocal of $\langle S \rangle$.

Table 2-1. Typical unit cell formula and molecular mass of alkali metal cation faujasites.

Zeolite	Typical Unit Cell Formula	Molecular Mass (g/unit cell)
LiY	$\text{Li}_{26}\text{Na}_{30}\text{Al}_{56}\text{Si}_{136}\text{O}_{384}$	12344
NaY	$\text{Na}_{56}\text{Al}_{56}\text{Si}_{136}\text{O}_{384}$	12762
KY	$\text{K}_{54}\text{Na}_2\text{Al}_{56}\text{Si}_{136}\text{O}_{384}$	13362
RbY	$\text{Rb}_{25}\text{Na}_{31}\text{Al}_{56}\text{Si}_{136}\text{O}_{384}$	14324
CsY	$\text{Cs}_{26}\text{Na}_{30}\text{Al}_{56}\text{Si}_{136}\text{O}_{384}$	15620
NaX	$\text{Na}_{86}\text{Al}_{86}\text{Si}_{106}\text{O}_{384}$	13418

The concentration of adsorbate within the zeolite refers to the number of moles of substrate per liter of zeolite, and is hence denoted as the molarity, M. Given that the faujasite unit cell² (uc) contains 8 cavities and has a volume of $1.5 \times 10^4 \text{ \AA}^3$, the molarity of the adsorbate can be determined from the number of molecules per cavity, $\langle S \rangle$ according to eq. 2-8, where N_{AV} is Avagadro's number.

$$\begin{aligned} [S] \text{ (moles/L)} &= \langle S \rangle * (8 \text{ cavities/uc}) * (\text{uc}/1.5 \times 10^4 \text{ \AA}^3) * (10^{-27} \text{ \AA}^3/\text{L}) * (\text{moles}/N_{AV}) && \text{2-8} \\ &= \langle S \rangle * (5.33/6.022) \end{aligned}$$

Chapter 3. Generation and Reactivity of Carbocations in Non-Acidic Zeolites

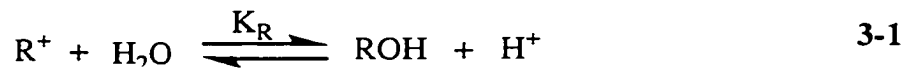
3-1 Introduction

Carbocations are organic ions possessing positively charged carbon atoms that have been implicated as intermediates in many chemical and biochemical reactions.^{213,214} Chemists first took an interest in carbocations in the 1920s, and in the ensuing 50 years or so, carbocation chemistry became one of the most actively pursued areas of organic chemistry. Of particular significance has been the extensive work, primarily from the laboratories of Olah, on the generation of a diverse array of carbocation intermediates in superacid media where these species are sufficiently long-lived to be directly observable by standard spectroscopic methods, most notably NMR.^{215,216} Today, carbocations are familiar entities, and the chemistry of carbocations, their generation, properties and reactivity, are in many regards a mature field. The existence of carbocations as intermediates has been established by examining the kinetics, products, stereochemistry, and substituent effects of carbocation-mediated reactions, and more recently, by direct observation of transient carbocations using laser flash photolysis. From such studies it is recognized that carbocations react readily *via* nucleophilic addition, elimination of a proton from a carbon adjacent to the cationic center, and skeletal rearrangement to other more stable carbocations.

3.1.1 Studies of Reactive Carbocations in Solution

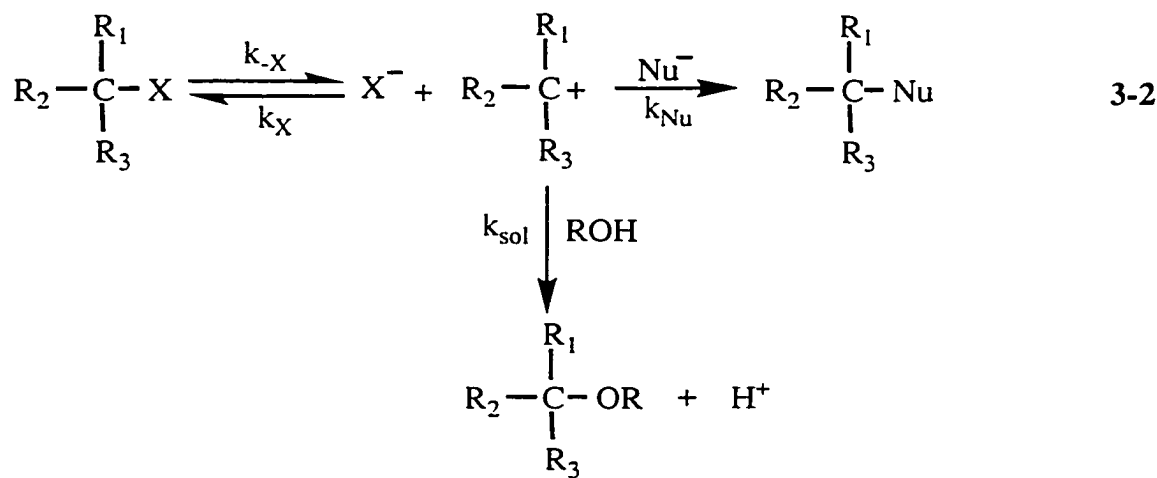
Although a carbocation intermediate can be identified and studied without actually observing it, the most informative means of investigating the structure, stability and reactivity of carbocations is through direct observation. Strongly resonance-stabilized carbocations such as the *tris*-(4-*N,N*-dimethylaminophenyl)-methyl cation can be generated and observed by adding the alcohol to a sufficiently acidic aqueous solution. Generally, however, less stabilized carbocations are difficult to generate in detectable quantities, and for many years investigations of these cations relied on the use of strongly ionizing, non-nucleophilic media such as liquid SO₂ or concentrated sulfuric acid.²¹³ In such environments many carbocations such as the triphenylmethyl cation are sufficiently long-lived to be studied and characterized spectroscopically.^{217,218} In addition, studies of the ionization of aryl carbinols in sulfuric acid afforded values for the carbocation-

carbinol equilibrium constant, pK_R , eq. 3-1, which serve as a quantitative measure of the relative carbocation stability.



As interest in the direct observation of carbocations increased, the use of NMR spectroscopy emerged as a valuable tool for detailed structural studies of carbocations in strong acid solutions.²¹⁹ The advancement of superacid solvents and cryogenic methods made it possible to generate and study the structures of increasingly more unstable carbocations such as the *tert*-butyl cation and the phenethyl cation.^{220,221}

The use of strongly acidic media to generate and characterize the spectral and structural features of carbocations represents a significant achievement in the study of these intermediates. However, studies of carbocations in strongly acidic media cannot address questions concerning the reactivity of carbocations towards solvent or other nucleophiles. The environment experienced by a carbocation in superacid solution is not representative of the environment in which many organic reactions involving carbocation intermediates occur. Thus, in order to understand carbocation reactivity, it is necessary to study the carbocation under more typical solvolytic conditions. Generally, however, carbocations are too short-lived under solvolytic conditions to be observed with standard static techniques. While the reactivities of relatively stabilized triarylmethyl cations have been measured directly by employing rapid mixing techniques,^{222,223} an approach based on competitive reactions was originally used for most other carbocations. In these studies, the carbocation is an undetected intermediate, generated by the solvolytic dissociation of a good leaving group, eq. 3-2.



Partitioning of the carbocation between the solvent and a second nucleophile generates two different products. A ratio of the rate constants can be obtained from the product ratio, and in some cases estimates of absolute rate constants can be obtained if one of the nucleophiles reacts at the diffusion-controlled limit.^{224,225}

Studies of the absolute reactivity of carbocations are readily accomplished using laser flash photolysis.^{226,227} With laser flash photolysis, reactive carbocations can be directly observed and the reaction kinetics of these intermediates can be quantitatively examined in various media. In order to successfully apply the technique, a photochemical reaction must be available to generate the carbocation, and the carbocation must have a sufficient lifetime to be observed. In other words, the lifetime of the carbocation must be at least as long as the length of the light pulse used to make it. An additional requirement is an appropriate means of detection. By far the most common detection method employed in laser flash photolysis is UV-Vis spectroscopy, which means that only transients with suitable chromophores can be observed. Consequently, most of the carbocations studied by laser flash photolysis have conjugated π -systems, usually aryl groups attached to the cationic center. These carbocations generally absorb strongly in the UV-visible region, and absorption spectral data of many carbocations are available from earlier studies in strong acid media and from more recent investigations employing laser flash photolysis. The carbocation can then be identified by the transient absorption spectrum and the kinetic behaviour, particularly in the presence of nucleophilic quenchers. The transient assignment can be verified by product studies using steady-state photolysis which yield products originating from a carbocation intermediate.

Over the past 10 to 15 years, nanosecond laser flash photolysis has been employed to directly measure rates constant for addition of solvent and nucleophiles to a number of carbocations including triarylmethyl,²²⁸⁻²³¹ and diarylmethyl²³⁰⁻²³³ cations, cumyl, phenethyl and benzyl cations,^{234,235} cyclohexadienyl cations,²³⁶⁻²⁴⁰ and 9-fluorenyl cations.^{237,239,241,242} These comprehensive studies have provided significant insight into carbocation chemistry, especially with regard to the dramatic influences of the nature of the solvent and the structure of the carbocation on the observed reactivity.²²⁶

In addition to the distinct absorption characteristics, transient carbocations can often be identified by characteristic reactivity in solution. Carbocations typically decay *via* addition of nucleophiles, often the solvent, or by deprotonation. In most solvents carbocations decay in a single exponential fashion, as predicted by pseudo first-order kinetics. In such cases, the reactivity of carbocations can therefore be described by a

unimolecular decay rate constant characteristic of the solvent, k_s , with the lifetime of the carbocation corresponding to $1/k_s$. Table 3-1 presents some selected examples of carbocations which have been studied by nanosecond laser flash photolysis in solution, along with their respective k_s values. The dramatic effect of the nature of surrounding solvent on the lifetime of the carbocations is immediately obvious from a perusal of these data. Notably, TFE and particularly HFIP display very low reactivity towards carbocations. The unusually low nucleophilicity of these solvents has been exploited by carbocation chemists to enhance the lifetime of reactive carbocations such that they can be directly studied using nanosecond laser flash photolysis.

Table 3-1. Solvent reactivities of selected carbocations at 20 °C^a

Carbocation	k_w^b / s^{-1}	k_{TFE} / s^{-1}	k_{HFIP} / s^{-1}
(4-MeOC ₆ H ₄) ₃ C ⁺	1.0×10^1	-	-
(C ₆ H ₅) ₃ C ⁺	1.5×10^5	-	-
(4-CF ₃ C ₆ H ₄) ₂ (C ₆ H ₅)C ⁺	8.8×10^6	-	-
(4-MeOC ₆ H ₄) ₂ CH ⁺	1.0×10^5	1.4×10^1	-
(C ₆ H ₅) ₂ CH ⁺	1.3×10^9	3.2×10^6	$\sim 1.0 \times 10^1$
9-Xanthylum	2.3×10^4	-	-
9-Phenyl-9-Xanthylum	2.3×10^1	-	-
9-Phenyl-9-Fluorenyl	1.5×10^7	1.5×10^4	-
9-Methyl-9-Fluorenyl	-	8.5×10^6	-
9-Fluorenyl	$> 4 \times 10^{10}$	8×10^8	2×10^4
4-MeOC ₆ H ₄ C ⁺ (CH ₃) ₂	$\sim 4 \times 10^7$	1.6×10^4	-
C ₆ H ₅ C ⁺ (CH ₃) ₂	-	-	9×10^3

^aAdapted from Ref. 226; ^busually 4:1 or 3:1 acetonitrile:water.

The data in Table 3-1 also demonstrate the importance of substituent effects in carbocation reactivity. For instance, the dramatic influence of *p*-methoxy groups is revealed in the reactivity of the triarylmethyl and diarylmethyl cations. The diphenylmethyl cation is four orders of magnitude more reactive in water than the dianisylmethyl cation which is stabilized by electron donating methoxy substituents. On the other hand, introduction of electron withdrawing substituents to the aromatic ring such as trifluoromethyl groups can lead to substantially enhanced reactivity. Alkyl substituents can also play a significant role in carbocation behaviour. Thus replacing

hydrogen atoms at the carbocation center with methyl groups leads to kinetic and thermodynamic stabilization and a decrease in reaction rate constants. The overall effect depends on the structure of the carbocation such that the influence tends to be less significant when other stabilizing substituents are already present. Steric factors could also play a role in the enhanced lifetimes observed upon alkyl substitution at the carbocation center.

3.1.2 Carbocations in Zeolites

Acid Zeolites and Carbocations. By far the most important application of zeolite catalysts is in the petroleum industry where acidic zeolites are now indispensable.^{10,243} Carbocations are believed to be key intermediates in the hydrocarbon transformations and other industrially significant reactions catalyzed by acidic zeolites.⁴⁷ This belief originated not from the direct observation of carbocation intermediates in the reactions, but by analogy with similar transformations in liquid superacid media where the role of the carbocation has been firmly established.³ Correspondingly, this has led to the view of zeolites as solid superacids and the notion that the catalytic activity of these materials is a consequence of this acidity.

The efficient catalytic activity of zeolites and the important role of carbocations in these catalytic reactions has been the impetus for much research aimed at understanding the chemistry of carbocations generated within the channels and cavities of zeolites.^{8,47,49,62,63,65,66,101,106,110,113,146,174-177,244-263} These studies have been restricted to carbocations produced in proton-exchanged Brønsted zeolites, or zeolites with divalent metal ions such as Ca^{2+} , which possess acidic properties upon thermal activation.²⁶⁴⁻²⁶⁸ This is primarily due to the fact that in the highly acidic environment carbocations are easily generated and, more importantly, are thermodynamically and kinetically stabilized to the extent that they can be readily examined by steady-state techniques such as solid-state NMR,^{62,246,248-259} UV-Vis diffuse reflectance^{8,47,62,63,65,66,101,106,110,146,174-177,244,245} and UV-Vis absorption spectroscopy.^{113,260,261}

The results from these studies of carbocations in acidic zeolites have led to tremendous advances in our understanding of the nature of carbocations within acidic zeolites and the reactivity of carbocation intermediates in zeolite catalysis.^{47,49,249,263} Most significantly, this research has contributed immensely to the emerging picture of Brønsted zeolites not as superacid solid materials as once envisioned, but as strong acids whose ability to stabilize electrophilic species and influence their reactivity is inexorably tied to the dynamic role of the zeolite framework in carbocation chemistry.²⁴⁹ Thus,

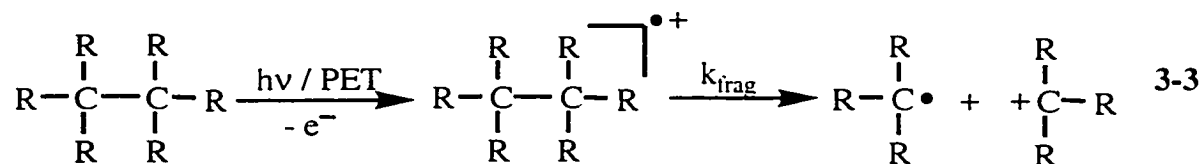
although several types of relatively stabilized carbocations such as triarylmethyl,^{110,257,258} xanthylium,^{63,101,106} dibenzotropylium,⁶³ indanyl,²⁵¹ and cyclopentenyl^{246,252} cations can be detected as stable ions in acidic zeolites, more reactive species such as phenethyl^{66,251} cations do not persist within these environments. The reactivity of such species is consistent with current predictions regarding the stability of reactive carbocations within these acidic environments.^{247,249} This does not preclude these carbocations as *transient* intermediates in zeolite catalysis, but it does suggest that the catalytic role of zeolite properties other than acidity warrants further investigation. Thus, future advances in carbocation-mediated chemistry within zeolite hosts rely on elucidating the role of carbocations as *intermediates*, rather than persistent species, in zeolite catalyzed processes, and the influence of the zeolite environment on the lifetimes and reaction mechanisms of carbocations.

Studies of Carbocations in Non-Acidic Zeolites. Further insights into carbocation-mediated reactions can be obtained from studies of carbocation intermediates in non-protic, alkali metal cation-exchanged zeolites. In particular, the interactions between the zeolite framework structure and incorporated carbocations can be directly probed in the absence of the strongly acidic environment. For example, the effect of changing the counterion on the kinetic stability of carbocations within zeolite cavities can be readily explored with alkali metal cation zeolites, but not with Brønsted zeolites. As a result, with non-protic zeolites it is possible to examine the effect of properties such as electrostatic field strength and exchangeable-cation size on the chemistry of carbocations located within the zeolite cavities. Furthermore, while the negatively charged framework in proton-exchanged zeolites is generally presumed to act as a large, relatively non-nucleophilic counterion, the possibility that localized sites of electron density in these zeolite frameworks, namely the $[\text{Si-O-Al}]^-$ bridges, may be reactive towards carbocation intermediates can be directly explored. In addition, non-protic cation exchanged zeolites are suitable media for determining the dynamics of second-order reactions of coinorporated nucleophiles with carbocations. These reactions are difficult to study in Brønsted zeolites due to the reversible addition of nucleophiles like water or alcohols in the highly acidic environment, as well as the probability that the nucleophilicity of many common nucleophiles will be considerably reduced by protonation. As well, the stability of some nucleophiles such as alkenes will be low within the strongly acidic environment of the proton-exchanged zeolites. Furthermore, the role that non-protic zeolites may play in carbocation formation in the absence of the strongly acidic environment can be addressed.

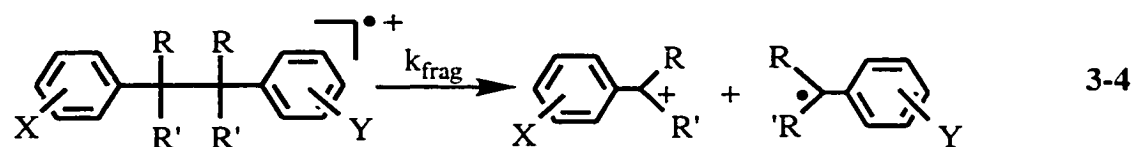
In order to study carbocation intermediates in non-acidic zeolite environments, suitable techniques for the generation of these reactive species must be employed. Although many organic substrates spontaneously generate carbocations upon inclusion within acidic zeolites, these substrates are generally thermally stable within alkali metal cation zeolites. Photochemistry provides the necessary tool to generate reactive carbocations in non-acidic zeolites. In the present work two photochemical reactions have been applied to the generation of carbocations in alkali metal cation zeolites: (i) rapid carbon-carbon bond cleavage of photogenerated bicumene radical cations; (ii) photoheterolysis of 9-fluorenyls. Chapter 3 of this thesis discusses the photochemical generation and reactivity of the corresponding cumyl and 9-fluorenyl cations within alkali metal cation zeolites. To the best of my knowledge, these results represent the first generation and direct observation of reactive carbocations in non-acidic zeolites and include a detailed study of the unimolecular and bimolecular reactions of these intermediates.

3.2 Generation and Reactivity of Cumyl Cations in Non-Acidic Zeolites

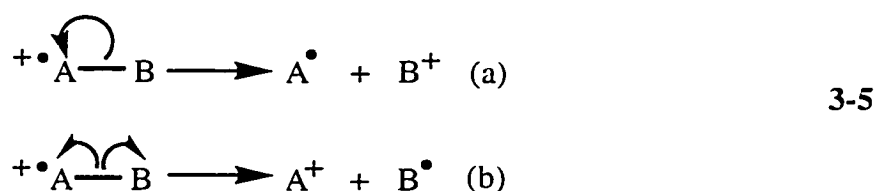
Addition or removal of an electron from a molecule can activate the molecule towards bond fragmentation, thereby inducing the cleavage of bonds which are typically very strong in the neutral molecules.²⁶⁹ Unimolecular fragmentation of radical ions is a significant, general reaction which constitutes the elementary step of many electron-transfer-initiated processes. Consequently, carbon-carbon bond cleavage of photochemically generated radical cations to the corresponding carbocation and radical fragments, eq. 3-3, has attracted considerable attention from several research groups including those of Arnold,²⁷⁰⁻²⁷³ Das^{274,275} and Albini.^{276,277}



Maslak *et al.* have conducted extensive investigations concerning the fragmentation of bibenzylic radical cations²⁷⁸⁻²⁸³ and radical anions²⁸⁴⁻²⁸⁸ possessing a variety of different aromatic and benzylic substituents, eq. 3-4.

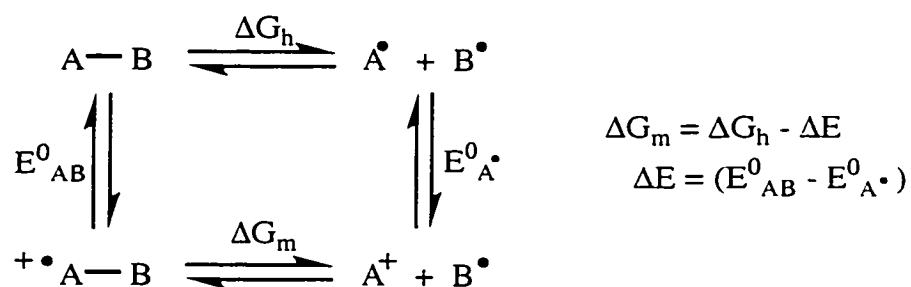


The general factors governing the rate constants for carbon-carbon bond cleavage in radical ions, k_m , have been described by Maslak.^{269,289,290} In a general sense it is possible to consider radical ions as either σ -type radical ions, in which the unpaired electron is formally located in a σ -orbital, or π -type radical ions, in which the unpaired electron is delocalized over a π system. For π -type radical cations, which are more commonly encountered in photoinduced electron transfer reactions, the unpaired electron is necessarily localized on one side of the scissile bond. In order to activate the scissile bond towards cleavage, the unpaired electron must be transferred across this bond. The electron apportionment can formally be considered to occur *via* two modes, eq. 3-5: a heterolytic mode where the charge is transferred (a), and a homolytic mode where the spin is transferred (b).



Maslak has coined the term *mesolysis* as a description for unimolecular fragmentations of radical ions which represents this dual possibility.

Scheme 3-1

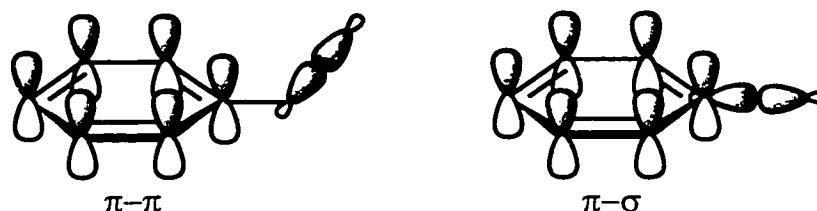


The thermodynamics governing radical ion fragmentation, ΔG_m , can be described by a simple thermodynamic cycle, Scheme 3-1, which depends on the free energy change of bond homolysis of the neutral precursor, ΔG_h , and the difference in redox potentials of the precursor and the ionic fragment, ΔE . Since the electron is added to or removed from a formally nonbonding orbital, the radicals are easier to reduce or oxidize than the corresponding neutral species. As a result, ΔE is always positive and a weakening of the scissile bond is observed upon oxidation or reduction of the precursor. This is the source

of the redox activation. For the bibenzylic substrates investigated by Maslak *et al.*, the mesolysis reactions have been essentially thermoneutral, with ΔG_m varying from approximately -2 to 3 kcal/mol.²⁸⁹ In general, it is possible to design reactions with high driving forces by employing structural variations which alter the homolytic bond energy and redox potentials of the substrate.

In addition to thermodynamics, stereoelectronic factors influence the efficiency of mesolysis, since cleavage requires removal of electron density from the scissile bond (for radical cations). For π -type radical cations the unpaired electron must be transferred from the π -system to the scissile bond. Scheme 3-2 presents two extreme situations. In the first situation, denoted π - π fragmentation, the scissile bond overlaps with the π -system. This type of scenario is observed for benzylic substrates. In this case the most effective dihedral angle between the π -system and the plane defined by the scissile bond is 90° . This arrangement permits the charge and spin of the radical cation to delocalize throughout the molecule as the bond elongates. For dihedral angles of less than 90° the cleavage is expected to be less efficient.

Scheme 3-2



The other extreme, a π - σ fragmentation, corresponds to a situation in which there is no overlap between the scissile bond and the unpaired electron. In this case, the dihedral angle is zero as would be observed in aromatic or vinyl substrates, for instance. Here the bond must first elongate until the energy in the bond is close to the energy of the orbital containing the unpaired electron. At this point the interaction leading to bond cleavage can be considered analogous to a dissociative intramolecular electron transfer. The π - σ fragmentation is limited to polar bonds such as carbon-halogen, carbon-oxygen or carbon-sulfur.

The kinetics of radical ion fragmentation will be a result of the combination of thermodynamics and stereoelectronic factors. Although no quantitative theory of radical ion fragmentation that accounts for all variables currently exists, the data suggest that the kinetic barriers to bond fragmentation within the radical ions will be low. In particular,

exergonic processes will have very large cleavage rates (i.e. $> 10^9 \text{ s}^{-1}$) which are difficult to measure directly. Table 3-2 presents selected examples of mesolysis rates constants for some bibenzylic precursors studied by Maslak and co-workers. These fragmentation rate constants reveal the dramatic influence of radical cation structure on the fragmentation reaction. For instance, aromatic substituents which increase the extent of charge delocalization, and steric crowding of bulkier groups attached to the scissile bond both increase the rate constant for bond cleavage.

Table 3-2. Rate constants (k_m) for fragmentation of radical cations.^{a,b}

Radical Cation Precursors	k_m / s^{-1}
<i>p</i> -Me ₂ N-C ₆ H ₄ C(Et) ₂ -C(Et) ₂ Ph	1.58×10^5
<i>p</i> -Me ₂ N-C ₆ H ₄ C(Pr) ₂ -C(Pr) ₂ Ph	4.36×10^5
<i>p</i> -Me ₂ N-C ₆ H ₄ C(Bu) ₂ -C(Bu) ₂ Ph	5.37×10^5
<i>p</i> -MeO-C ₆ H ₄ C(Me) ₂ -C(Me) ₂ C ₆ H ₄ - <i>p</i> -CN	2.63×10^6
<i>p</i> -MeO-C ₆ H ₄ C(Me) ₂ -C(Me) ₂ C ₆ H ₄ - <i>p</i> -CF ₃	1.58×10^6
<i>p</i> -MeO-C ₆ H ₄ C(Me) ₂ -C(Me) ₂ Ph	2.45×10^7
<i>p</i> -MeO-C ₆ H ₄ C(Me) ₂ -C(Me) ₂ C ₆ H ₄ - <i>p</i> -Me	1.10×10^8
<i>p</i> -MeO-C ₆ H ₄ C(Me) ₂ -C(Me) ₂ C ₆ H ₄ - <i>p</i> -MeO	6.02×10^8
<i>p</i> -MeO-C ₆ H ₄ C(Et) ₂ -C(Et) ₂ C ₆ H ₄ - <i>p</i> -MeO	4.63×10^9

^aAdapted from Ref. 269; ^bdichloromethane/methanol.

3.2.1 Results

The following sections present results concerning the generation and reactivity of cumyl cations in alkali metal cation zeolites. In each case the carbocations were generated photochemically, either *via* nanosecond laser flash techniques or steady-state irradiation, from the appropriate bicumene precursors. Dark experiments in which the bicumene precursors were incorporated into the zeolite and subsequently removed by continuous extraction establish that these molecules are thermally stable within alkali metal cation zeolites. The nanosecond laser flash photolysis apparatus employed in the time resolved diffuse reflectance experiments is described in detail in the experimental section. Excitation of the bicumene precursors was accomplished with the fourth harmonic from a Nd:Yag laser (266 nm, $< 10 \text{ mJ}$, $< 10 \text{ ns}$). This means that a photogenerated transient with a lifetime shorter than 10 ns is not observable, and sets an upper limit on measurable rate constants for transient decay of ca. $1 \times 10^8 \text{ s}^{-1}$. In practice

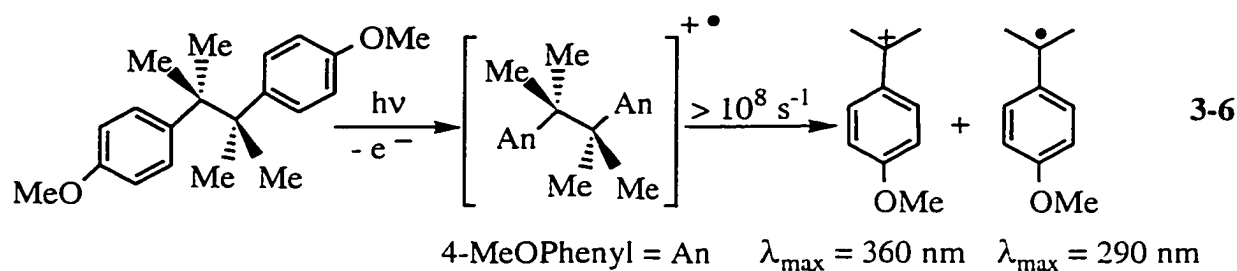
the rate constants measurable for transient decay in solid-state samples such as zeolites are reduced somewhat, particularly due to luminescence and light scattering from the solid particles.

Inclusion of the bicumene precursors in dehydrated alkali metal cation zeolites was accomplished using hexane as a carrier solvent. The external surface of the zeolite was subsequently washed with hexane to remove bicumene molecules which may have been adsorbed on the external surface (see experimental section for details). During sample preparation the utmost care was taken to avoid rehydration of the zeolite. Detailed analysis of the zeolite composites after preparation determined that little, if any, water (*i.e.* < 1 wt %) is adsorbed during sample inclusion (see appendix). The hexane was removed by vacuum pumping (ca. 10^{-3} Torr) at room temperature for a period of 5-12 hours. Dried zeolite composites were then transferred to quartz laser cells or steady-state irradiation vessels under an atmosphere of dry nitrogen. Samples for nanosecond laser photolysis were re-evacuated at 10^{-4} Torr for at least 12 hours and sealed prior to the experiments. Samples for steady-state irradiation were purged with dry nitrogen or argon for at least 30 minutes prior to irradiation and a continuous gas flow was maintained throughout the photolysis. Coinclusion of secondary adsorbates was accomplished by vapour phase adsorption for the small volatile alcohols and alkyl enol ethers. Inclusion of water involved exposure of the zeolite sample to the ambient atmosphere.

Zeolite/bicumene composites used in nanosecond laser experiments have an occupancy number, $\langle S \rangle$, of 0.10. In other words, the average loading level is one bicumene molecule in every 10 zeolite supercages and corresponds to approximately 20 mg bicumene/g zeolite. A slightly higher bicumene concentration of between 60 – 90 mg/g NaY, or one molecule in every 2 - 3 supercages, was used for steady-state irradiations. Laser experiments in NaMor and Na β were also carried out at a concentration of ca. 20 mg bicumene/g zeolite.

3.2.1.1 Generation of the 4-Methoxycumyl Cation in Dry Alkali Metal Cation Zeolites

Laser irradiation (266 nm, < 10 mJ, <10 ns) of 4,4'-dimethoxybicumene (DMB) incorporated within the cavities of dry NaY under vacuum (10^{-4} Torr) conditions yields a transient diffuse reflectance spectrum with an intense absorption centered at 360 nm, Figure 3-1 (The figures described in section 3.2.1.1 to 3.2.1.7 are found on pages 86 to 110). This transient absorption is assigned to the 4-methoxycumyl cation formed *via* rapid fragmentation of the DMB radical cation generated by laser induced photoionization, eq. 3-6.^{269,279,280,283}



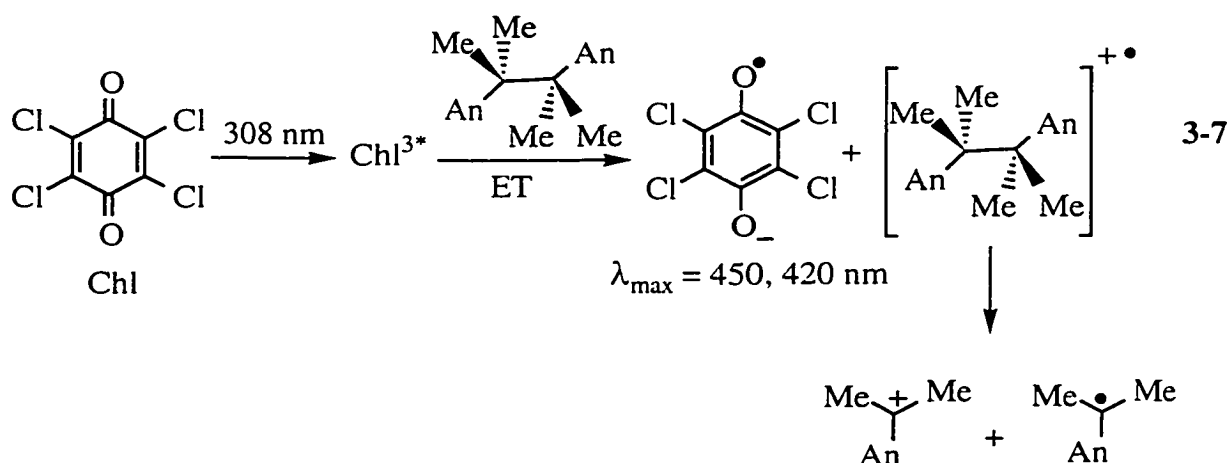
This assignment is based on several observations. The location of the absorption maximum and the symmetrical shape of the absorption band are identical to that of the 4-methoxycumyl cation previously reported in solution.²³⁴ The reactivity of the transient species is also characteristic of a carbocation species.²²⁶ The introduction of oxygen has no influence on the decay rate constant or absorption of the transient, Figure 3-1 inset, while the inclusion of nucleophiles such as methanol accelerates the decay rate constant of the transient observed at 360 nm, Figure 3-2. Furthermore, the possibility that the transient is actually the precursor radical cation can be ruled out as substituted anisole radical cations have absorption maxima near 420 nm in solution^{291,292} and in zeolites, and are unreactive toward nucleophiles such as methanol in NaY, Figure 3-3. In fact, reaction of the DMB radical cation within the laser pulse is consistent with cleavage rate constants of approximately 10^8 s^{-1} in solution,^{269,283} Table 3-2, and indicates fragmentation in NaY is also rapid ($> 10^8 \text{ s}^{-1}$).

In addition to the intense absorption at 360 nm due to the carbocation, a weaker, sharp band at 290 nm is also visible in the time-resolved diffuse reflectance spectrum, Figure 3-1. The decay of this band is significantly slower than the decay of the carbocation at 360 nm indicating that a second transient is produced upon laser irradiation of DMB in NaY. In contrast to the carbocation band at 360 nm, the transient at 290 nm is quenched by the inclusion of oxygen within the zeolite framework. This band can be assigned confidently to the 4-methoxycumyl radical produced as the second fragmentation product upon cleavage of the DMB radical cation, eq. 3-6. The location of the absorption maxima at 290 nm²⁹³ and the quenching of the transient by oxygen support this assignment. In addition, the relatively long lifetime of this transient species is consistent with that demonstrated for similar zeolite encapsulated benzylic radicals.¹⁵⁵

Further evidence that the 4-methoxycumyl cation originates from fragmentation of the DMB radical cation within the laser pulse can be obtained by generating this radical cation *via* an alternate route. In addition to direct photoionization, it should also be possible to create the DMB radical cation by photoinduced electron transfer (PET).

An appropriate electron acceptor for the PET experiment is 2,3,5,6-tetrachloro-1,4-benzoquinone (chloranil). Photoexcited chloranil is a powerful one electron oxidant ($E_{\text{red}}^{\circ} = 0.02 \text{ V}^{294}$, $E_{\text{red}}^{3*} = 2.15 \text{ V}^{295}$) and can be selectively excited in the presence of DMB using 308 nm laser irradiation where the DMB chromophore has no absorption. In addition, PET between chloranil and DMB is diffusion controlled in solution.²⁸³ Furthermore, the radical anion produced by reduction of chloranil has a very characteristic absorption spectrum and is thus readily and confidently identified.²⁹⁶⁻²⁹⁸ Therefore, direct evidence for PET following excitation of chloranil coadsorbed in the DMB/NaY composites can be obtained by detection of the chloranil radical anion and the 4-methoxycumyl cation. This would provide compelling evidence that the initial product of PET, the DMB radical cation, undergoes rapid fragmentation to the carbocation within the zeolite host.

Figure 3-4 shows the transient diffuse reflectance spectrum obtained upon 308 nm laser irradiation ($< 20 \text{ ns}$, $< 100 \text{ mJ}$) of chloranil in evacuated NaY ($\langle S \rangle = 0.04$) containing coadsorbed DMB ($\langle S \rangle = 0.10$). The spectrum clearly shows the distinct absorption of the 4-methoxycumyl cation at 360 nm, as well as characteristic bands of the chloranil radical anion at 420 nm and 450 nm.²⁹⁶⁻²⁹⁸ A short-lived broad absorption near 500 nm due to the chloranil triplet²⁹⁷⁻²⁹⁹ is also observed under vacuum conditions. No transients are detected when DMB is excited with 308 nm laser light in NaY in the absence of chloranil. These results indicate that fast ($> 10^8 \text{ s}^{-1}$) intrazeolite electron transfer (ET) takes place between chloranil and DMB leading to the chloranil radical anion and the DMB radical cation which rapidly cleaves to the carbocation and radical fragments, eq. 3-7.



Rapid PET within the NaY matrix is consistent with the diffusion controlled PET between chloranil and DMB observed in solution. Observing the 4-methoxycumyl cation under these photoinduced electron transfer conditions directly supports the conclusion that the carbocation is derived by rapid fragmentation of the DMB radical cation formed by photoionization in the absence of sensitizer, eq. 3-6.

Direct laser irradiation of DMB included in alkali metal cation zeolites other than NaY ($\langle S \rangle = 0.10$; 20 mg DMB/g zeolite) consistently generates transient diffuse reflectance spectra dominated by an intense absorption at 360 nm and a weaker absorption band at 290 nm. Representative transient spectra are shown in Figure 3-5. In all alkali metal cation zeolites, the transient spectra closely resemble that observed upon photolysis of DMB in NaY, where the transient absorption bands at 360 nm and 290 nm were assigned to the 4-methoxycumyl cation and the 4-methoxycumyl radical, respectively. Several features of the transient kinetics observed in these alkali metal cation zeolites are also comparable to the results obtained in NaY. In each case the decay kinetics at 360 nm are different from the decay kinetics at 290 nm indicating the presence of two distinct transient species. Inclusion of oxygen into the zeolite samples has no influence on the decay kinetics or absorption of the transient at 360 nm, but results in essentially complete quenching of the transient at 290 nm. Conversely, the addition of nucleophiles to the zeolite composites accelerates the transient decay at 360 nm but has no influence on the decay kinetics at 290 nm. The combined spectral appearance and transient reactivity unambiguously demonstrate that the transients observed following laser photolysis of DMB in other alkali metal cation zeolites are the 4-methoxycumyl cation and the 4-methoxycumyl radical. Therefore, these results establish that rapid cleavage of photogenerated DMB radical cations can also be used to generate the 4-methoxycumyl cation within other alkali metal cation-exchanged Y zeolites (LiY, KY, RbY and CsY), and in zeolites with different Si/Al ratios and framework morphologies (NaX, Si/Al = 1.2, NaMordenite, Si/Al = 6.5, and Na β , Si/Al = 18), Table 3-3.

Table 3-3. Description of zeolites used in study of the 4-methoxycumyl cation.¹²

Zeolite	Si/Al	Counterion ^a	Pore Diameter / Å	Channel System/Cage Diameter
Faujasite Y	2.4	Alkali M ⁺	7.4	3-D channel with cage / 13 Å
Faujasite X	1.2	Na ⁺	7.4	3-D channel with cage / 13 Å
β	18	Na ⁺	7.6x6.4; 5.5x5.5	Tridirectional channels
Mordenite	6.5	Na ⁺	6.5x7.0; 2.6x5.7	Unidirectional channels

^aM⁺ = Li⁺, Na⁺, K⁺, Rb⁺, Cs⁺.

3.2.1.2 Absolute Reactivity of the 4-Methoxycumyl Cation in Alkali Metal Cation Zeolites

The absolute reactivity of the 4-methoxycumyl cation in dry alkali metal cation zeolites can be measured by monitoring the intensity of the transient signal at 360 nm as a function of time using nanosecond laser photolysis. As described in section 2.3, the heterogeneous nature of the intrazeolite environment raises the possibility that encapsulated transients may decay with a distribution of decay rate constants, or that more than one mechanistically distinct reaction pathway might exist for a reactive intermediate such as a carbocation. Transient decay kinetics over several orders of magnitude consisting of several distinct rate constants and distributions of rate constants are well known in zeolites.^{52,54,66,75,121-123,126,159} Thus, in order to obtain an accurate representation of the reactivity of the 4-methoxycumyl cation in alkali metal cation zeolites it is necessary to examine the decay profile over several different time scales and to consider the possibility that many individual decay rate constants may contribute to the decay. By combining the kinetic traces observed at several different time scales, stretched exponential traces representing the disappearance of the carbocation over several decades are obtained. Stretched decay traces of the 4-methoxycumyl cation in zeolites with various alkali metal counterions, Si/Al ratios, and framework topologies are shown in Figures 3-6 and 3-7. Qualitatively, the decay profiles clearly show that the rate constant for the decay of the 4-methoxycumyl cation depends strongly on the framework composition and morphology. In particular, the rate of decay increases significantly as the size of the alkali metal cation increases from Li⁺ to Cs⁺. Furthermore, the carbocation decays significantly more slowly in Naβ and NaMor which have high Si/Al ratios, than in a zeolite such as NaX which has a low Si/Al ratio.

In order to derive quantitative information about the absolute reactivity of these carbocations, and to account for the possibility that the carbocation decays with a broad distribution of lifetimes, the decay traces were analyzed with the ESM described in section 2.3.^{211,212} Interestingly, the results of such analyses revealed a narrow range of lifetimes evenly distributed about one or two central values, Figure 3-8. This suggests that the decay of the 4-methoxycumyl cation in alkali metal cation zeolites is the result of one or two first-order processes. Consistent with this suggestion is the fact that fitting the decay kinetics to a single or biexponential expression, eq. 3-8 and 3-9 respectively, yields rate constants very similar to those obtained from the distribution analysis.

$$(\Delta J/J_o)_t = (\Delta J/J_o)_i \exp(-kt) \quad 3-8$$

$$(\Delta J/J_o)_t = (\Delta J/J_o)_1 \exp(-k_1 t) + (\Delta J/J_o)_2 \exp(-k_2 t) \quad 3-9$$

In equation 3-8, k is the rate constant for carbocation decay *via* a single exponential process and $(\Delta J/J_o)_i$ is the total change in diffuse reflectance due to carbocation decay. In the biexponential equation 3-9, k_1 and k_2 are the two distinct decay rate constants while $(\Delta J/J_o)_1$ and $(\Delta J/J_o)_2$ correspond to the change in diffuse reflectance due to carbocation decay *via* process 1 and 2, respectively. In other words, the relative magnitude of each decay pathway is represented by the values $(\Delta J/J_o)_1$ and $(\Delta J/J_o)_2$. The relative magnitudes of each decay pathway can likewise be obtained from the amplitude ratio of the peaks observed in the lifetime distribution plots. For all biexponential decays, similar contributions for the two decay components were obtained from either the distribution analysis or from the biexponential fits.

The lifetimes and their relative contribution to the total decay as determined from the ESM or by fitting the data to a single or double first-order rate equations are presented in Table 3-4. In LiY the decay of the 4-methoxycumyl cation fit best to a biexponential expression yielding lifetimes of 26 μ s and 5 μ s. The longer lifetime of 26 μ s represents the dominant pathway contributing 81 % of the total decay, while the shorter lifetime of 5 μ s contributed 19 %. The decay in NaY is single exponential with a lifetime of 4.6 μ s, which is significantly shorter than observed in LiY. In KY and RbY the decay kinetics were best fit to a model consisting of two consecutive first-order processes. In KY the shorter lifetime component of 1 μ s accounted for 74 % of the total decay, while in RbY two relatively short lifetimes of 0.3 μ s and 0.9 μ s contributed 42 % and 58 % to the observed decay respectively. The relatively weak transient signal of the 4-methoxycumyl cation in CsY was fit to a first-order decay yielding a single short lifetime of 0.4 μ s. Overall these quantitative results demonstrate that the lifetime of the

4-methoxycumyl cation in Y zeolites decreases dramatically upon varying the alkali metal counterion from Li^+ to Cs^+ , Table 3-4.

The rate constants for the decay of the 4-methoxycumyl cation in other alkali metal cation zeolites have also been determined by ESM. In NaX, the carbocation was found to decay very rapidly with a single lifetime of 0.5 μs . Conversely, in the other alkali metal cation zeolites studied, NaMor and Na β , the carbocation exhibited very little decay on times scales as long as 1 ms, the longest time accessible with the nanosecond laser system, indicating that the carbocation is very long-lived within these two zeolites, Figure 3-7. The decay kinetics of the carbocation in NaMor and Na β were modeled by fitting the small observed decay to a first order expression with the assumption that the carbocation decays completely to the baseline. This yielded lifetimes of ca. 1000 μs and ca. 3000 μs for the 4-methoxycumyl cation in NaMor and Na β respectively. The lifetimes of the 4-methoxycumyl cation in various alkali metal cation zeolites are summarized in Table 3-4.

Table 3-4. Lifetime(s) of the 4-methoxycumyl cation in various alkali metal cation zeolites.

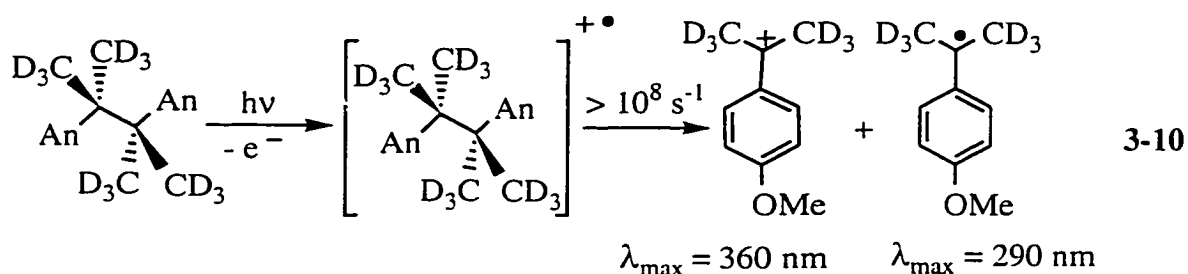
Zeolite	Si/Al Ratio	Lifetime ^a / μs	
		1st component	2nd component
LiY	2.4	26 (81 %)	5.0 (19 %)
NaY	2.4	4.6 (100 %)	---
KY	2.4	1.0 (74 %)	4.5 (26 %)
RbY	2.4	0.3 (42 %)	0.9 (58 %)
CsY	2.4	0.4 (100 %)	---
NaX	1.2	0.5 (100 %)	---
NaMor	6.5	~ 1000	---
Na β	18	~ 3000	---

^aLifetimes calculated using the ESM or by fitting the data to a single or double first-order rate equations. The value in brackets refers to the percent of transient which decays with the corresponding lifetime.

3.2.1.3 Kinetic Isotope Effects on the Absolute Reactivity of the 4-Methoxycumyl Cation in Alkali Metal Cation Zeolites

Laser photolysis of 4,4'-dimethoxybicumene- d_{12} (DMB- d_{12}) in dry alkali metal cation Y zeolites generates transient diffuse reflectance spectra with an intense,

symmetrical absorption band at 360 nm characteristic of the 4-methoxycumyl cation. The transient spectra obtained in each alkali metal cation zeolite are identical to those observed for the non-deuterated analog under both vacuum and oxygen conditions, Figure 3-9. As a result, the transients observed following laser irradiation of DMB- d_{12} in alkali metal cation Y zeolites are readily assigned to the 4-methoxycumyl- d_6 cation and 4-methoxycumyl- d_6 radical, eq. 3-10.



The decay traces of the deuterated and non-deuterated 4-methoxycumyl cations in dry oxygen-saturated alkali metal cation zeolites are shown in Figure 3-10. As can be seen from these plots, the rate constant for decay of the 4-methoxycumyl cation in Y zeolites is influenced little by isotopic substitution. The rate constants for decay of the deuterated 4-methoxycumyl cation are obtained from ESM analysis and by fitting the decay traces to a single or double exponential as required. In each alkali metal cation Y zeolite the decay of the deuterated carbocation is slightly slower than the corresponding non-deuterated cation, yielding kinetic isotope effects which are close to unity, $k_{\text{H}}/k_{\text{D}} \sim 1.4$, Table 3-5.

Table 3-5. Kinetic isotope effects for the decay of the 4-methoxycumyl cation in alkali metal cation zeolites.

Zeolite	$k_{\text{H}} / k_{\text{D}}$
LiY	1.46 ± 0.20
NaY	1.30 ± 0.18
KY	1.40 ± 0.20
RbY	1.43 ± 0.20
CsY	1.39 ± 0.20

3.2.1.4 Products Derived from Irradiation of 4,4-Dimethoxybicumene in NaY

Steady-state irradiations of DMB in NaY ($\langle S \rangle \sim 0.3 - 0.5$) were conducted using a medium pressure 450 W mercury lamp passed through a quartz filter. After photolysis for approximately 80 hours under a continuous flow of dry nitrogen or argon, small amounts of methanol (typically 50 to 100 $\mu\text{L} / \text{g}$) were injected into the sealed cell and vaporized. The resultant products were then separated from the zeolite by continuous extraction with dichloromethane in an ambient atmosphere for 24 to 48 hours. The photochemical conversion was consistently about 10 %, while the mass balance varied between 40 to 60 % for different trials. The extracts were analyzed by a combination of GC, GC/MS and HPLC and products were identified by comparison to authentic samples. The steady-state photolysis products and relative yields are provided in Table 3-6.

Table 3.6. Relative product yields from steady-state irradiation of DMB in NaY following post-photolysis addition of methanol and dichloromethane extraction.

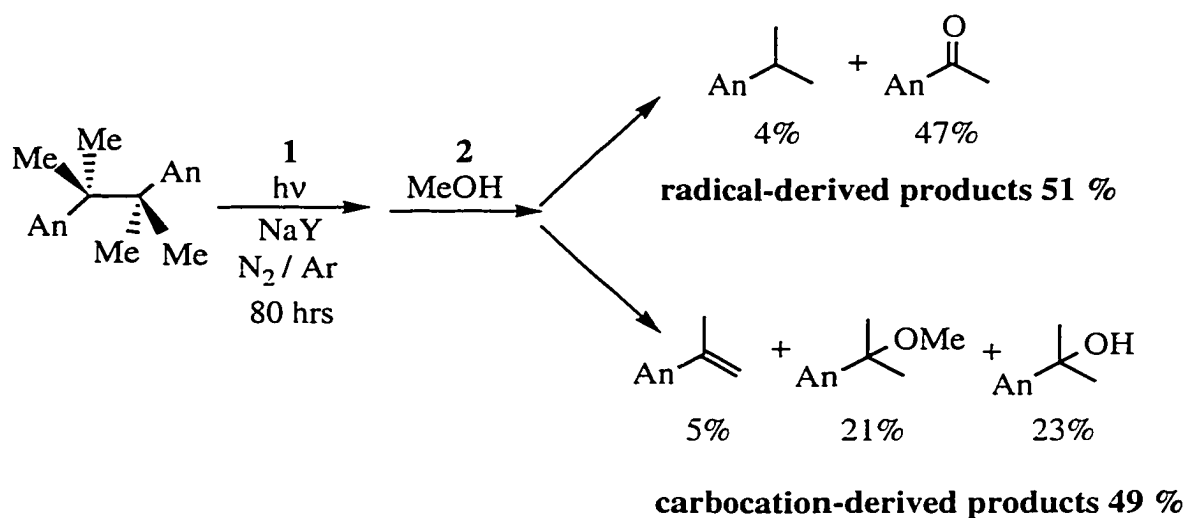
Radical Derived Products (51 %)		Carbocation Derived Products (49 %)	
4-methoxyacetophenone	92 %	4-methoxycumyl alcohol	47 %
4-methoxycumene	8 %	4-methoxycumyl methyl ether	43 %
		α -methyl-4-methoxystyrene	10 %

The steady-state photolysis conditions leading to the observed products are represented in Scheme 3-3. As shown in this scheme, the products are derived from the 4-methoxycumyl cation and the 4-methoxycumyl radical in a 1:1 ratio. This is completely consistent with rapid fragmentation of the photogenerated DMB radical cation to form the carbocation and radical intermediates in alkali metal cation zeolites as observed in the nanosecond laser studies. A significant observation to be made from these data is that α -methyl-4-methoxystyrene comprises only 10 % of the carbocation derived products. The low yield of styrene indicates that deprotonation of the 4-methoxycumyl cation is not a significant decay pathway of this carbocation leading to products.

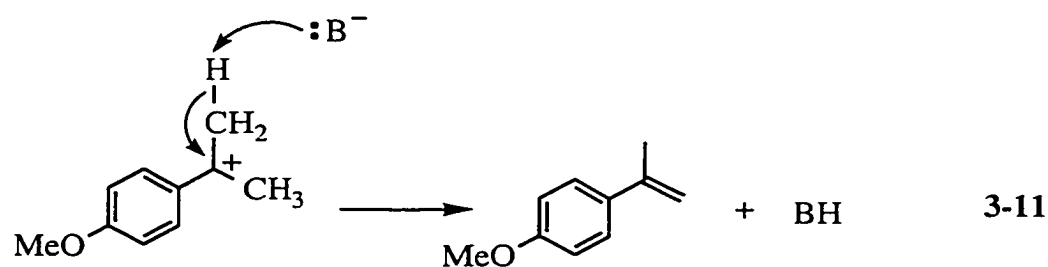
Two photoproducts, 4-methoxycumyl alcohol and 4-methoxycumyl methyl ether, account for 90 % of carbocation derived products, Table 3-6. Although these products are characteristic of direct nucleophilic addition to the free carbocation center, such a mechanism cannot account for the observation of these adducts, particularly the methyl ether, under the experimental conditions. Since methanol is added to the zeolite composite only *after* the lengthy irradiation is complete, a direct reaction with the

carbocation which has a lifetime of a few microseconds within NaY is impossible. Instead, the reactive carbocation must rapidly form a second, longer-lived intermediate, which subsequently reacts with the methanol to yield the solvolysis-type product. A similar mechanism can be used to account for alcohol formation since water is also adsorbed by the zeolite composite during the post-photolysis extraction. Alternatively, the alcohol could be formed by slow diffusion of trace amounts of water present within the zeolite, although great care was taken to exclude water from the zeolite during sample preparation and photolysis.

Scheme 3-3

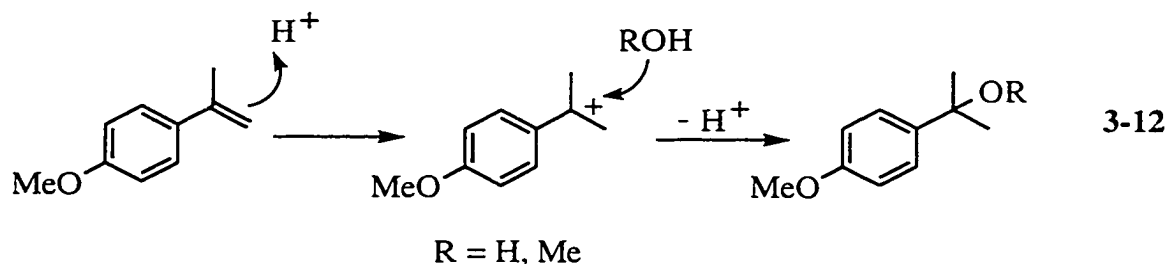


The high yields of the alcohol and ether products, accompanied by the low yield of styrene suggest, as mentioned above, that deprotonation of the 4-methoxycumyl cation, eq. 3-11, is a minor reaction pathway of this carbocation in NaY.



In order to be confident that this interpretation is valid, additional experimentals are necessary to establish that the alcohol, ether and styrene are the primary products of

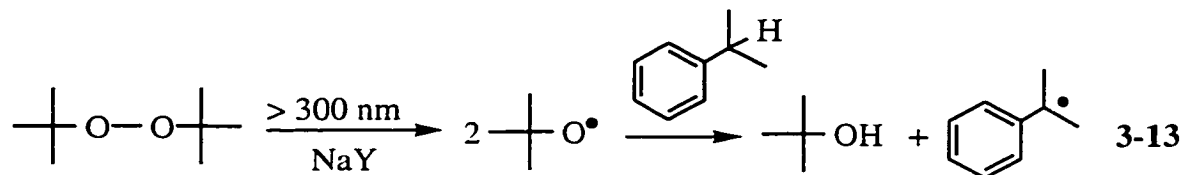
carbocation decay and that no interconversion of any of these materials takes place. In particular, the possibility that the alcohol and the ether are derived from α -methyl-4-methoxystyrene during work-up, eq. 3-12, especially considering that a small concentration of protons would be generated upon styrene formation, eq. 3-11, must be eliminated.



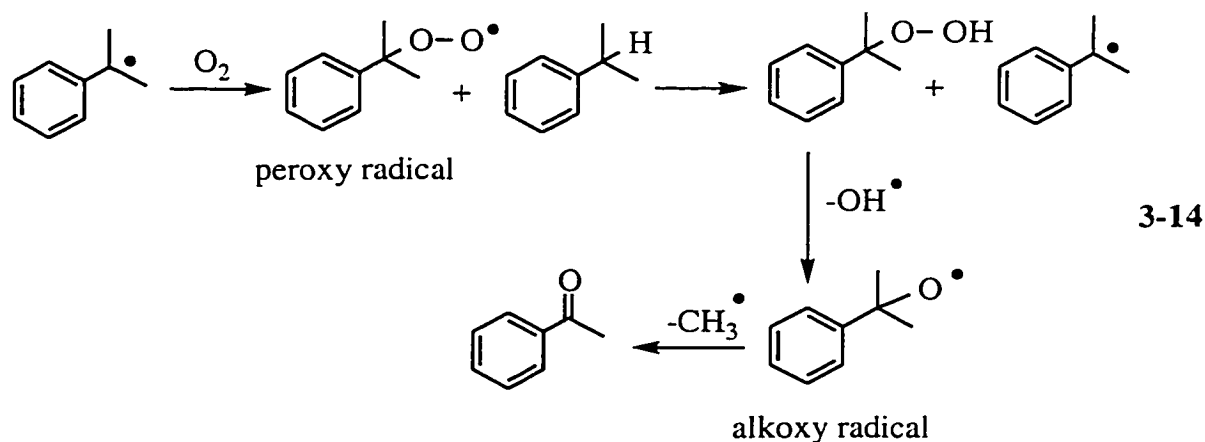
To test for this possibility, the styrene was incorporated into NaY containing perchloric acid in a concentration of approximately 1 proton in every 2 cavities. This concentration of protons is 25 times greater than the maximum concentration of protons that would be formed during the steady-state photolytic studies, if all 4-methoxycumyl cations generated undergo deprotonation (ca. 1 proton in 50 cavities). After approximately 20 hours, methanol was added to the acidified zeolite composite containing the styrene, and the material was extracted in the same manner as described for the product studies. No methyl ether and only an extremely small amount (< 0.01 %) of the alcohol were obtained from this procedure. These results therefore indicate that the styrene, once formed, is not converted to the carbocation derived products under our reaction conditions. Consistent with these results is the fact that anethole and 4-methoxystyrene have been shown to be thermally stable over these time periods in NaY⁶⁶ although the estimated concentration of Brønsted acid sites in these zeolites could be as high as ca. 1 site per 16 cavities.⁵¹

Hydrogen abstraction by the 4-methoxycumyl radical to generate the hydrocarbon is a minor reaction of the 4-methoxycumyl radical within NaY (8 %). Whereas the most abundant photoproduct observed upon irradiation of DMB in NaY is 4-methoxyacetophenone (47 %). Two additional experiments were conducted to establish that this product originates from oxygen trapping of the 4-methoxycumyl radical. In the first experiment the cumyl radical was generated independently in NaY under a continuous stream of nitrogen. This was accomplished by selective irradiation of di-*tert*-butyl peroxide in NaY containing coadsorbed cumene. Photocleavage of the peroxide

generates the *tert*-butoxy radical which subsequently abstracts a hydrogen from cumene to yield the cumyl radical, eq. 3-13.



After photolysis the products were extracted from the zeolite and analyzed by GC and GC/MS. This analysis revealed that acetophenone is the major photoproduct (ca. 50 %) generated in this experiment. Observing significant ketone formation under these conditions indicates that there is a sufficient concentration of oxygen within the zeolite framework to trap these radicals, even under a continuous flow of nitrogen. This is consistent with reports in the literature which discuss tightly framework bound oxygen.^{56,59} The initial product obtained from oxygen trapping of the cumyl radical is a peroxy radical. A likely mechanism for the conversion of this peroxy radical to acetophenone is presented in eq. 3-14. The peroxy radical can abstract a hydrogen atom from the precursor cumene thereby propagating the radical chain. The hydrogen atom abstraction product can subsequently lose hydroxyl radical to generate the alkoxy radical shown. Other reactions of the initial peroxy radical such as radical-radical coupling reactions will also lead to this alkoxy radical intermediate. This intermediate is known to lose a methyl radical to yield acetophenone.³⁰⁰



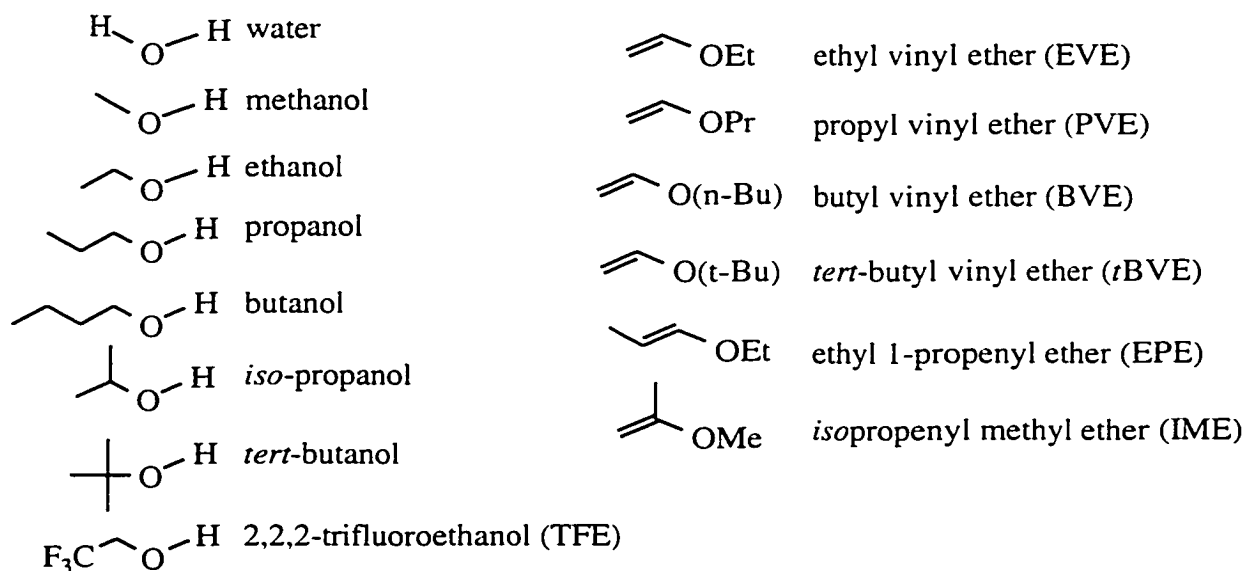
In the second experiment, α -methyl-4-methoxystyrene was irradiated in NaY under a continuous flow of dry nitrogen in order to eliminate the possibility that the ketone is produced by secondary photolysis of the styrene. In this case, no detectable amounts of

4-methoxyacetophenone were observed for conversions as high as 35 % suggesting that the concentration of oxygen in NaY is insufficient to lead to competitive olefin oxidation.

3.2.1.5 Bimolecular Reactions of the 4-Methoxycumyl Cation with Coadsorbed Quenchers in Alkali Metal Cation Zeolites

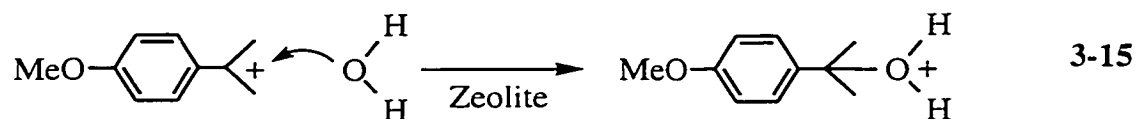
The results described in the previous sections concern the absolute reactivity of the 4-methoxycumyl cation in dry alkali metal cation zeolites. These results demonstrate that the 4-methoxycumyl cation exists as a reactive intermediate within non-protic zeolites, having lifetimes in the μs range which are highly dependent on the nature of the zeolite environment. These relatively short lifetimes are observed in the absence of any coadsorbed nucleophiles, indicating that the zeolite host is directly involved in the absolute reactivity of the encapsulated carbocation. Additional information concerning the role of zeolites in carbocation chemistry can be derived from studying nucleophilic addition reactions to encapsulated carbocations. This section presents results regarding bimolecular reactions of the 4-methoxycumyl cation with water, small alcohols and alkyl enol ethers in alkali metal cation zeolites, Scheme 3-4.

Scheme 3-4



Intrazeolite Addition of Water to the 4-Methoxycumyl Cation. Laser irradiation of DMB in hydrated (2–12 wt % depending on the zeolite) alkali metal cation Y zeolites leads to only weak absorption at 360 nm, Figure 3-11. This indicates that little

or no 4-methoxycumyl cation is observed following the 10 ns laser pulse in Y zeolites containing coadsorbed water. In LiY and NaY the initial intensity observed at 360 nm is reduced by at least 80 % and 90 %, respectively relative to dry conditions. In hydrated KY, RbY, and CsY, essentially no signal due to the 4-methoxycumyl cation can be detected at 360 nm upon laser irradiation. One possible explanation for the reduced yield of carbocation is that coadsorbed water is interfering with carbocation formation. If water reacts with the precursor DMB radical cation, or inhibits photoionization to form the radical cation, the yield of the 4-methoxycumyl cation would decrease upon hydration. However, the behaviour of 4-methylanisole in Y zeolites is inconsistent with this explanation. Neither the yield of radical cation formation nor the lifetime of the 4-methylanisole radical cation generated upon laser photolysis of 4-methylanisole is influenced by the inclusion the water in NaY. Photoionization of 4-methylanisole and DMB will be very similar as will the reactivity of the resultant radical cations towards nucleophiles. Reduced photoionization or rapid trapping of the DMB radical cation by water does not appear to be a viable explanation for the low yield of the 4-methoxycumyl cation under hydrated conditions. A more likely rationale for the substantially reduced yield of carbocation upon hydration is nucleophilic addition of the coadsorbed water to the carbocation, eq. 3-15.



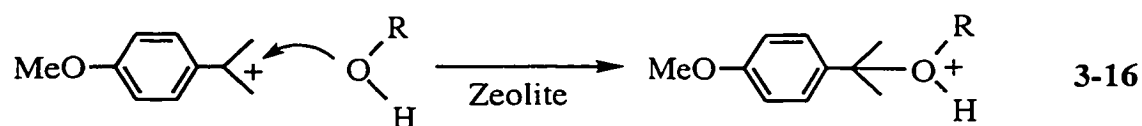
The addition reaction accelerates the decay of the carbocation such that it is essentially complete within the ca. 10 ns laser pulse, resulting in a significant reduction in the *observed* carbocation yield. Since the addition reaction is taking place within the laser pulse, the reaction dynamics cannot be observed directly. As such, the addition reaction in this case is designated as a *static quenching* process since it involves addition of water which is too rapid to be time-resolved with the nanosecond system.

Notably in hydrated LiY and NaY, where a low yield of carbocation can be detected following the 10 ns laser pulse, the decay of this carbocation is significantly faster than observed under dry conditions. In LiY, the lifetime of the residual carbocation observed in the presence of coadsorbed water is about 25 times shorter than the same carbocation under dry conditions. In hydrated NaY, the yield of carbocation is even smaller and the decay of this carbocation is approximately 5 times faster than observed in dry NaY. Thus while the vast majority of nucleophilic addition of water to the 4-

methoxycumyl cation in alkali metal cation zeolites involves a static process which takes place in less than 10 ns, a small fraction of the carbocations generated in hydrated LiY and NaY react with water over time scales available to the nanosecond system. This reaction can be designated as a *dynamic quenching* process since it involves the time-resolved addition of water to the carbocation and is therefore accompanied by a measured increase in rate constant for carbocation decay.

Bimolecular addition of water to the 4-methoxycumyl cation is also observed in other Na⁺ zeolites, Figure 3-12. Essentially no 4-methoxycumyl cation is detected in post-hydrated NaMor (4 wt %), indicating efficient static quenching of the carbocation in this zeolite as described for the alkali metal cation Y zeolites. However, in hydrated Naβ (3 wt %) the initial intensity of the 4-methoxycumyl cation at 360 nm is the same as observed under dry conditions suggesting that no static quenching is taking place within this zeolite. However, the rate constant for decay of the 4-methoxycumyl cation in Naβ is dramatically increased from $3.3 \times 10^2 \text{ s}^{-1}$ to $4 \times 10^4 \text{ s}^{-1}$ by the inclusion of water. This exemplifies a dynamic quenching process where the coadsorbed water is reacting with the carbocation over observable time scales following the laser pulse. In NaX coadsorbed water (5 wt %) has little effect on the intensity of the carbocation immediately following the laser pulse. Likewise, the decay rate constant of the carbocation in NaX is essentially uninfluenced by water, increasing just slightly from $2.0 \times 10^6 \text{ s}^{-1}$ to $2.7 \times 10^6 \text{ s}^{-1}$ upon hydration. Thus neither dynamic nor static quenching of the 4-methoxycumyl cation by water appear to be significant within this zeolite.

Intrazeolite Addition of Alcohols to the 4-Methoxycumyl Cation. The decay traces of the 4-methoxycumyl cation in NaY containing increasing amounts of coadsorbed methanol are shown in Figure 3-2. As can be seen in this figure, the inclusion of small amounts of methanol within the zeolite network has two distinct effects on the carbocation signal at 360 nm. First, the intensity of the signal due to the 4-methoxycumyl cation immediately following the laser pulse decreases with increasing methanol content. Second, the observed rate constant for the decay of the 4-methoxycumyl cation increases with increasing methanol content. These effects on the carbocation signal are analogous to those observed upon the inclusion of water in the alkali metal cation zeolites and can be attributed to nucleophilic addition of methanol to the 4-methoxycumyl cation, eq 3-16.



As previously described, the addition reaction increases the rate constant for carbocation decay. In some cases the increased decay rate constant causes the carbocation to be too short-lived to be observed immediately following the laser pulse. This results in static quenching as observed by a decrease in carbocation signal immediately following the laser pulse. In other cases the increase in the decay rate constant is not sufficient to cause the carbocation to disappear completely within the laser pulse. This results in dynamic quenching as observed by an increase in the rate constant for carbocation decay as a function of the methanol concentration.

Control experiments were again performed in order to ensure that the added alcohol was not interfering with radical cation formation. Therefore, 4-methylanisole was irradiated in NaY containing small concentrations of coadsorbed alcohols. As shown in Figure 3-3, the inclusion of methanol has no influence on the yield of radical cation generated by photoionization of 4-methylanisole, or the rate constant for decay of the 4-methylanisole radical cation. Thus it is likely that formation of the DMB radical cation *via* photoionization and cleavage of the resultant radical cation to generate the carbocation is uninfluenced by the addition of alcohol to the zeolite. Therefore, the decrease in carbocation yield observed following laser photolysis of DMB in NaY containing coadsorbed methanol must represent a static quenching process whereby some carbocations react with methanol within the laser pulse such that they are no longer detected with the nanosecond system.

The addition of methanol to the 4-methoxycumyl cation, eq 3-16, is a bimolecular reaction which can be described by a second order-rate expression, eq. 3-17,

$$\text{Rate} = d[\text{C}^+]/dt = k_{\text{MeOH}}[\text{C}^+][\text{MeOH}] \quad 3-17$$

where $d[\text{C}^+]/dt$ represents the time-dependent change in the concentration of the carbocation, and k_{MeOH} is the second-order rate constant for methanol addition. In the static quenching process, the addition reaction cannot be observed directly and no information concerning the second order rate constant for this rapid reaction can be obtained. However, for the dynamic quenching process, methanol addition to the carbocation can be monitored over a period of several μs allowing measurement of the observed rate constant for carbocation decay in the presence of methanol. Under the experimental conditions employed, the concentration of methanol ($\langle S \rangle \sim 0.4 - 3$) is significantly greater than the concentration of carbocation generated *via* photolysis of the DMB precursor. As a result, the concentration of methanol is essentially constant, and pseudo first-order kinetics can be assumed, eq 3-18.

$$[\text{MeOH}] \gg [\text{C}^+]: \text{Rate} = d[\text{C}^+]/dt = k_{\text{obs}}[\text{C}^+] \quad \text{3-18}$$

$$k_{\text{obs}} = k_{\text{MeOH}}[\text{MeOH}]$$

In this situation the observed rate constant for carbocation decay is a linear function of methanol concentration with a slope equal to the second-order rate constant for intrazeolite addition of methanol to the carbocation. A plot of the observed rate constant for carbocation decay versus the concentration of methanol, shown in Figure 3-13, is indeed linear, and yields a second-order rate constant of $2.6 \times 10^5 \text{ M}^{-1} \text{ s}^{-1}$ for addition of methanol to the 4-methoxycumyl cation in NaY.

Bimolecular addition of methanol to the 4-methoxycumyl cation is also observed in other alkali metal cation Y zeolites. Dynamic quenching of the 4-methoxycumyl cation by methanol is observed in LiY, KY and RbY. The decay of the carbocation also increases linearly with methanol concentration in these zeolites, Figure 3-13. The slopes of these plots, which represent the second-order rate constants for methanol addition to the carbocation, vary slightly but systematically with the nature of the alkali metal cation. The quenching rate constant is smallest in LiY and increases with counterion size to a maximum in RbY where the second-order rate constant is 2 times larger than for the same reaction in NaY, Table 3-7. No dynamic quenching of the 4-methoxycumyl cation by methanol is observed in CsY, where the rate constant for decay of the 4-methoxycumyl cation remains essentially invariant up to loadings of four molecules of methanol per cavity. Static quenching of the 4-methoxycumyl cation by methanol is observed in all alkali metal cation Y zeolites. In each zeolite, a plot of the change in diffuse reflectance at 360 nm immediately following the laser pulse versus methanol concentration is linear, Figure 3-14. The slopes of these plots vary slightly depending on the alkali counterion, reflecting subtle differences in the sensitivity of the carbocation to static quenching in each zeolite.

The behaviour of the 4-methoxycumyl cation in other alkali metal cation zeolites containing coadsorbed methanol parallels that observed under hydrated conditions. In Na β the inclusion of methanol leads to a dramatic increase in the decay rate constant of the 4-methoxycumyl cation indicating dynamic quenching. However, there is no static quenching by methanol in this zeolite as the initial intensity of the carbocation signal is unaffected by methanol. Likewise in NaMor, static quenching is observed but dynamic quenching is not. Finally, in NaX neither static nor dynamic quenching of the 4-methoxycumyl cation by methanol is detected.

Table 3-7. Second-order rate constants and slopes of static quenching plots for addition of methanol to the 4-methoxycumyl cation in alkali metal cation Y zeolites.

Zeolite	$k_{\text{MeOH}} / 10^5 \text{ M}^{-1} \text{ s}^{-1}$	Relative Quenching Constant	Static Quenching Slope $(\Delta J/J_0) / \text{M}^{-1}$
LiY	(1.5 ± 0.1)	0.58	(0.032 ± 0.002)
NaY	(2.6 ± 0.2)	1	(0.045 ± 0.002)
KY	(3.5 ± 0.3)	1.4	(0.025 ± 0.002)
RbY	(5.4 ± 0.5)	2.1	(0.032 ± 0.002)
CsY	no quenching	-	(0.018 ± 0.002)

The reactivity of the 4-methoxycumyl cation in NaY containing other small alcohols of comparable nucleophilicity was also investigated. Results similar to those described for quenching of the 4-methoxycumyl cation by methanol in NaY are also observed upon addition of ethanol to the zeolite composite. However, the magnitude of dynamic quenching by ethanol is significantly reduced relative to methanol, Figure 3-15. The second-order rate constant for addition of ethanol to the 4-methoxycumyl cation in NaY is approximately half that for addition of methanol, Table 3-8. A more dramatic decrease in the efficiency of dynamic quenching is observed for the bulkier alcohols, *isopropanol*, *butanol* and *isobutanol*, where the second-order rate constants are reduced by 70 to 80 % relative to methanol. With *tert*-butanol, essentially no dynamic quenching is observed and the lifetime of the 4-methoxycumyl cation is independent of alcohol concentration. Overall these results suggest that the efficiency of intrazeolite dynamic quenching decreases with quencher size both in terms of chain length and chain branching.

Although the size of the alcohol quencher exerts a significant influence on the efficiency of dynamic quenching, the magnitude of static quenching was essentially independent of alcohol structure within this series. Although there is some scatter in the static quenching data presented in Figure 3-16, it is clear that the decrease in intensity of the carbocation at 360 nm in the presence of larger alcohols such as *tert*-butanol is similar to that observed for smaller alcohols such as methanol and ethanol.

Table 3-8. Absolute and relative second-order rate constants and slopes of static quenching plots for addition of simple alcohols to the 4-methoxycumyl cation in NaY.

Alcohol	$k_{\text{ROH}} / 10^5 \text{ M}^{-1} \text{ s}^{-1}$	Relative Quenching Constant	Static Quenching Slope ($\Delta J/J_0$) / M^{-1}
methanol	2.6 ± 0.2	1	0.045 ± 0.003
ethanol	1.5 ± 0.2	0.58	0.033 ± 0.003
<i>isopropanol</i>	1.1 ± 0.2	0.42	0.022 ± 0.003
butanol	0.9 ± 0.2	0.35	0.03 ± 0.01
<i>isobutanol</i>	0.6 ± 0.2	0.23	0.045 ± 0.009
<i>tert</i> -butanol	No quenching	-	0.058 ± 0.009
trifluoroethanol	0.7 ± 0.2	0.27	0.045 ± 0.003

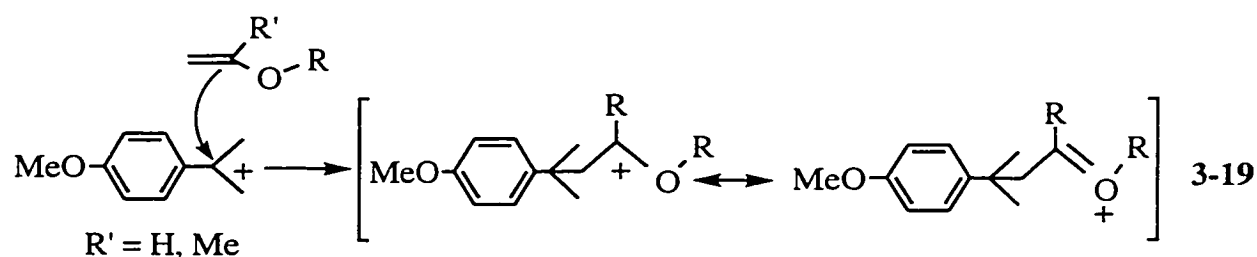
Inclusion of TFE, an alcohol structurally similar to ethanol but with significantly reduced nucleophilicity, also leads to quenching of the 4-methoxycumyl cation in NaY. The influence of TFE on the decay rate constant of the carbocation is substantially smaller than methanol or ethanol. The second-order rate constant for quenching by TFE is 2-fold and 4-fold smaller than observed for ethanol and methanol respectively, Table 3-8. This reduction in efficiency of dynamic quenching is consistent with the trends based on alcohol size observed using non-fluorinated alcohols. Interestingly, the magnitude of static quenching by TFE is found to be comparable to those of the non-fluorinated alcohols, Figure 3-16. The observation of static quenching indicates that a rapid addition reaction occurs when the TFE and the carbocation are encapsulated within the same zeolite cavity. This is significant considering the relatively low nucleophilicity of TFE and the fact that the rate constant of $1.6 \times 10^4 \text{ s}^{-1}$ for decay of 4-methoxycumyl cation in neat TFE is significantly smaller, by an order of magnitude, than the rate constant of $2.2 \times 10^5 \text{ s}^{-1}$ for decay of the 4-methoxycumyl cation in dry NaY.

Addition of Alkyl Enol Ethers to the 4-Methoxycumyl Cation in NaY.

Nucleophilic addition of olefins to carbocations is an important reaction of these intermediates leading to carbon-carbon bond formation.^{301,302} The addition of π nucleophiles such as alkenes and dienes to most carbocation centers is relatively slow and thus not readily probed with nanosecond laser photolysis techniques.³⁰² However, replacing the alkyl group on the olefinic carbon by an alkoxy is known to increase the reactivity of these nucleophiles by several orders of magnitude.³⁰² For instance, the reactivity of alkyl enol ethers towards nucleophilic addition of benzylic-type carbocations is similar to small organic alcohols and water.^{233,302,303} As a result, alkyl enol ethers are

ideal candidates to study intrazeolite addition of π -nucleophiles to carbocations and to compare the observed reaction dynamics with results obtained using alcohols and water. Bimolecular reactions between the 4-methoxycumyl cation and alkyl enol ethers were therefore investigated in order to probe the influence of zeolite encapsulation on addition reactions of olefinic nucleophiles and on the mobility of alkyl enol ethers.

Addition of an alkyl enol ether to the 4-methoxycumyl cation yields a second positively charged intermediate which can be considered as a resonance combination of a carbocation and oxonium ion, eq. 3-19.


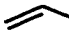

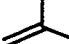




The positively charged carbon center formally will be a secondary or tertiary carbocation depending on the nature of the alkyl enol ether precursor. As shown in Scheme 3-4, a series of alkyl enol ethers of varied size and nucleophilicity was chosen to explore the intrazeolite addition reactions. Studies of the reactivity of alkyl enol ethers containing unsubstituted olefin moieties (vinyl ethers) towards diarylmethyl cations in solution have shown that rate constants for nucleophilic addition vary little with the length of the alkyl chain.²³³ For instance, as shown in Table 3-9, the second-order rate constants for addition of ethyl vinyl ether and butyl vinyl ether to the 4,4'-dichlorodiphenylmethyl cation in acetonitrile solution are essentially identical. Thus, vinyl ethers with similar nucleophilicity but varied alkyl chain length, ethyl vinyl ether (EVE), propyl vinyl ether (PVE), and butyl vinyl ether (BVE) can be used to probe the influence of the intrazeolite mobility of vinyl ethers on these quenching reactions. The bulkier substrate, *tert*-butyl vinyl ether (tBVE), shows a slight increase in quenching efficiency in solution, but will still provide an additional probe of vinyl ether mobility. Two alkyl enol ethers with methyl substituted olefins (IME and EPE) are also considered in the current study, in order to examine the influence of varied nucleophilicity on the quenching reactions. Each of these olefins should exhibit enhanced nucleophilicity due to the electron donating methyl substituents. Consistent with this notion are the data presented in Table 3-9 which demonstrate the enhanced reactivity of both *isopropenyl* methyl ether (IME) and

ethyl 1-propenyl ether (EPE) in nucleophilic addition reactions with the 4,4'-dichlorodiphenylmethyl cation.

The rate constants reported in Table 3-9 are for nucleophilic addition of several alkyl enol ethers to diphenylmethyl cations. The variation in relative reactivity with alkyl enol ether structure is maintained even though the inherent reactivity of the 4,4'-dichlorodiphenylmethyl cation and the 4,4'-dimethyldiphenylmethyl cation are somewhat different, k_{AcN} of $2.8 \times 10^6 \text{ s}^{-1}$ and $3.5 \times 10^5 \text{ s}^{-1}$, respectively.²³² Furthermore, based on the similar inherent reactivities of the 4,4'-dimethylphenylmethyl cation and the 4-methoxycumyl cation, k_{TFE} of $2.4 \times 10^4 \text{ s}^{-1}$ ²²⁹ and $1.6 \times 10^4 \text{ s}^{-1}$,²³⁴ respectively, similar absolute rate constants and relative nucleophilicity trends are anticipated for addition reactions of alkyl enol ethers to the 4-methoxycumyl cation. As a result, addition of these alkyl enol ethers to the 4-methoxycumyl cation in solution is predicted to be well below the diffusion-controlled limit (ca. 10^6 – $10^7 \text{ M}^{-1} \text{ s}^{-1}$) and to show significant variation in rate constant as a function of the alkyl enol ether structure.

Table 3-9. Second-order rate constants for reaction of 4,4'-dichlorodiphenylmethyl and 4,4'-dimethylphenylmethyl cation with vinyl ethers in acetonitrile at 20 °C.^a

Nucleophile		$k / \text{M}^{-1} \text{s}^{-1}$	
		(4-ClC ₆ H ₄)CH ⁺	(4-MeC ₆ H ₄)CH ⁺
 OEt	EVE	1.7×10^8	6.3×10^6
 O(n-Bu)	BVE	2.0×10^8	
 O(t-Bu)	tBVE	4.2×10^8	
 OMe	IME	7.4×10^8	3.7×10^7
 OEt	EPE	1.3×10^9	
 OEt		2.2×10^9	2.2×10^8

^aAdapted from ref. 300.

Both static and dynamic quenching of the 4-methoxycumyl cation are observed upon inclusion of various alkyl enol ethers within NaY. Static quenching, as previously described using water and small alcohols as quenchers, is manifested as a decrease in the intensity of the carbocation signal immediately following the laser pulse. As shown in

Figure 3-17, static quenching of the 4-methoxycumyl cation by each alkyl enol ether is observed in NaY. The magnitude of static quenching is largely independent of the alkyl enol ether itself, Table 3-10, consistent with a rapid reaction in all cases. Dynamic quenching of the 4-methoxycumyl cation by alkyl enol ethers is also observed as an increase in the rate constant for carbocation decay with increasing concentration of alkyl enol ether within the zeolite composite. In all cases the relationship between the rate constant for carbocation decay and alkyl enol ether concentration is linear, Figure 3-18, and the second-order rate constants for the addition of each alkyl enol ether to the 4-methoxycumyl cation are obtained from the slopes of the plots, Table 3-10. Notably the magnitude of dynamic quenching decreases with alkyl chain size along the series of vinyl ethers, Figure 3-18, such that EVE is the most efficient dynamic quencher and tBVE is the least efficient. This trend is consistent with similar effects exerted by alkyl chain length and size on the efficiency of dynamic quenching by alcohols previously described. On the other hand, dynamic quenching by alkyl enol ethers seems to be largely uninfluenced by the slight differences in the size and shape induced of an α - or β -methyl group on the olefinic moiety, Figure 3-19.

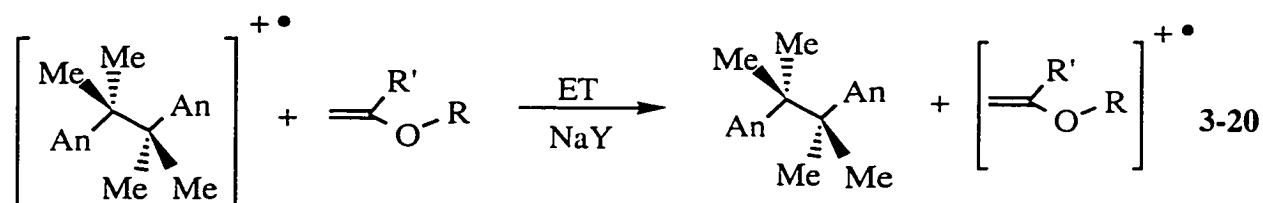
Table 3-10. Second-order rate constants and slopes of static quenching plots for reaction of 4-methoxycumyl cation with simple alkyl enol ethers in NaY.

Quencher	$k_q / 10^5 \text{ M}^{-1} \text{ s}^{-1}$	Static Quenching $(\Delta J/J_0) / \text{M}^{-1}$
EVE	(1.93 ± 0.09)	(0.083 ± 0.005)
PVE	(1.61 ± 0.06)	(0.072 ± 0.004)
BVE	(1.57 ± 0.09)	(0.063 ± 0.004)
tBVE	(0.75 ± 0.08)	(0.072 ± 0.005)
IME	(1.95 ± 0.05)	(0.077 ± 0.004)
EPE	(1.95 ± 0.09)	(0.069 ± 0.003)

It must be recognized that the observed quenching of the 4-methoxycumyl cation by alkyl enol ethers included within NaY may involve processes other than olefin addition. One alternative pathway arises from fact that alkyl enol ethers possess two potentially nucleophilic sites, the π electrons of the olefin moiety and the non-bonding electrons of the ether oxygen, which may interact with the 4-methoxycumyl cation. In solution, the addition of alkyl enol ethers to carbocations proceeds exclusively *via* olefin attack.^{233,302,303} To verify that intrazeolite reactions likewise involve carbon-carbon

rather than carbon-oxygen bond formation, the reactivity of the 4-methoxycumyl cation in NaY containing coadsorbed ethers was also considered. Such studies found that the inclusion of diethyl ether has no influence on either the initial yield or the decay rate constant of the 4-methoxycumyl cation in NaY. This is consistent with the expected low reactivity of the ether towards carbocation addition and suggests that the nucleophilic addition of alkyl enol ethers proceeds *via* olefinic addition to the carbocation center as proposed in eq. 3-19 and as observed for these nucleophiles in homogeneous solution. Furthermore, neither the decay rate constant or the yield of the 4-methoxycumyl cation is influenced when the carbocation is generated in NaY containing 2-methylbutene, even at concentrations in excess of several olefin molecules per cavity. This indicates that nucleophilic attack of alkenes on carbocations is relatively slow in zeolites, as it is in solution. These observations demonstrate that neither isolated olefinic or isolated ether moieties are sufficiently nucleophilic to undergo addition reactions with the reactive 4-methoxycumyl cation in NaY. The enhanced nucleophilicity associated with the enol functionality is required in order to accelerate the nucleophilic attack such that it can take place in competition with other pathways for carbocation decay.

A second possible reaction pathway exists as a consequence of the relatively low oxidation potentials of alkyl enol ethers. Thus it is possible that the initially formed DMB radical cation reacts with the coincluded alkyl enol ethers *via* electron transfer. The electron transfer would generate the radical cation of the alkyl enol ether and reform the neutral bicumene precursor, eq. 3-20, thereby decreasing the yield of the 4-methoxycumyl cation observed immediately following the laser pulse.

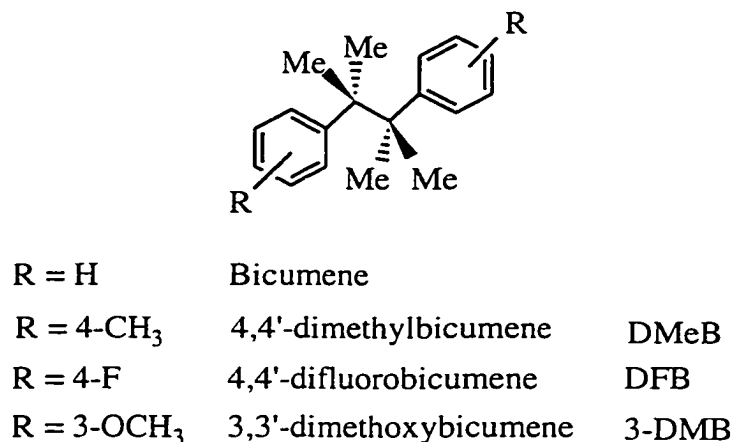


In order for this mechanism to explain the observed static quenching, rapid electron transfer between the alkyl enol ether and the DMB radical cation prior to carbon-carbon bond cleavage is necessary. However, the oxidation potentials of all alkyl enol ethers used in this study ($E_{\text{ox}}^{\circ} = 1.99\text{--}1.61 \text{ V}$)³⁰⁴ are equal or higher than the oxidation potential of DMB ($E_{\text{ox}}^{\circ} \sim 1.6 \text{ V}$).²⁸³ As a result, the thermodynamically uphill electron transfer is not expected to compete with rapid cleavage of the DMB radical cation and is therefore not the origin of the observed static quenching.

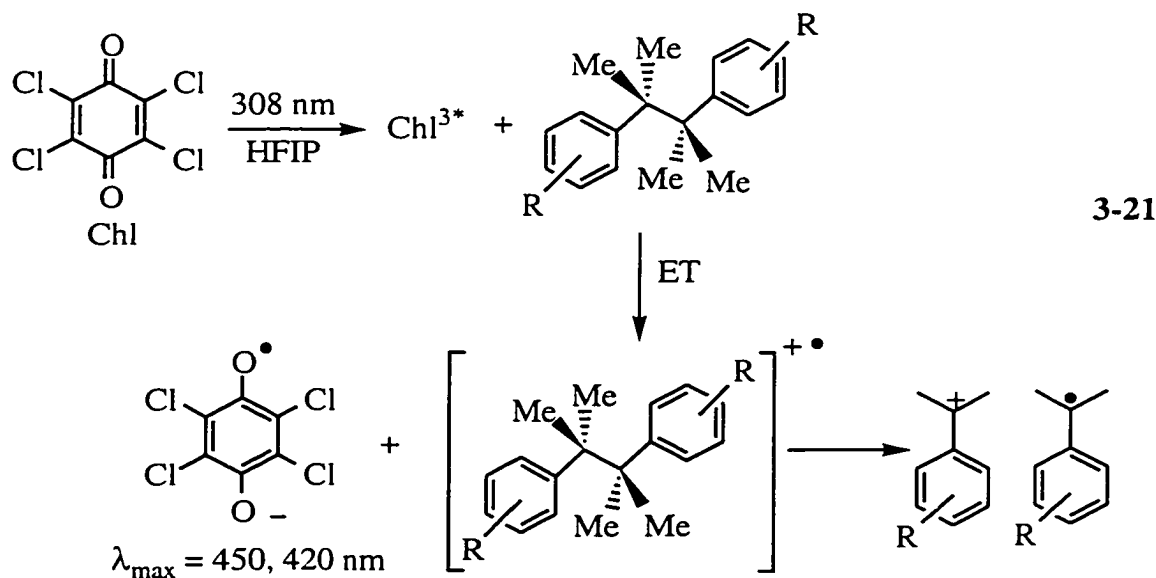
3.2.1.6 Generation and Reactivity of other Cumyl Cations in Alkali Metal Cation Zeolites

Rapid fragmentation of photogenerated DMB radical cations is a convenient, efficient tool for the generation and study of reactive 4-methoxycumyl cations in non-protic zeolites. In order to examine the applicability of this methodology to other substrates and to probe the influence of aryl substituents on the intrazeolite reactivity of carbocations, several additional bicumenes were considered as shown in Scheme 3-5.

Scheme 3-5



The radical cations of the substituted bicumenes were first generated in HFIP in order to verify that each photogenerated radical cation efficiently undergoes cleavage on the nanosecond to sub-ns time scale, as observed for the DMB radical cation, and to characterize the carbocation and radical fragments in solution. Direct 266 nm laser irradiation (< ca. 10 mJ per pulse) of the bicumene precursors in solution results in a relatively low yield of transients. Thus the bicumene radical cations were generated *via* PET with chloranil as a sensitizer, eq. 3-21.



The transient absorption spectrum obtained immediately following 308 nm laser photolysis of chloranil in HFIP containing 4,4'-dimethylbicumene (DMeB) is shown in Figure 3-20. In this time regime, the chloranil triplet, with a broad absorption in the 500 nm region,²⁹⁷⁻²⁹⁹ is observed to decay while the chloranil radical anion with absorption maxima at 420 nm and 450 nm²⁹⁶⁻²⁹⁸ grows in. In addition, an intense, symmetrical absorption band at 335 nm is also observed to form with a rate constant that is identical to the decay of the chloranil triplet. This observation suggests that the decay of the chloranil triplet and the growth observed at 335 nm are due to the same process. The explanation for triplet quenching leading to the observed growths is ET from DMeB to triplet chloranil resulting in the formation of corresponding radical ions, eq. 3-21. Consistent with this explanation is the previously reported observation of rapid PET between several other similar bicumene precursors and chloranil.²⁸³ The feasibility of PET between DMeB and chloranil can be accessed from the free energy, ΔG_{PET} , calculated according to the Rehm-Weller equation,³⁰⁵ eq. 3-22,

$$\Delta G_{\text{PET}} = 23.06 \left[E_{\text{ox}} (\text{D} / \text{D}^{\bullet+}) - E_{\text{red}} (\text{A} / \text{A}^{\bullet-}) - e^2 / \alpha \epsilon \right] - E_{00} \quad 3-22$$

where E_{ox} and E_{red} are the oxidation and reduction potentials, in volts, of the donor and acceptor, respectively, and E_{00} is the excited-state energy of the excited reactant in kcal/mol. The term, $e^2/\alpha\epsilon$, is a Coulombic attraction term describing the energy gained by bringing the two radical ions to an encounter distance, α , in a medium of dielectric constant ϵ . This Coulombic term can often be neglected, particularly for solvent-separated ions that dissociate beyond their respective Coulombic fields, or for solvents with large dielectric constants. For instance, in acetonitrile the Coulombic energy is less than ca. 1.3 kcal/mol at separation distances greater than ca. 7 Å.³⁰⁶ Assuming that the oxidation potential of DMeB can be approximated by the oxidation potential of *p*-xylene²⁶⁹ ($E_{\text{ox}}^{\circ} = 2.06 \text{ V}$ ³⁰⁷), the free energy for electron transfer between DMeB and photoexcited chloranil ($E_{\text{red}} = 0.02$, $E_{00} = 55 \text{ kcal/mol}$) is estimated to be approximately -8 kcal/mol. Based on this exergonicity, diffusion controlled ET is anticipated between DMeB and photoexcited chloranil and is therefore the probable explanation for the observed triplet quenching.

The transient species growing in at 335 nm cannot be the radical cation of DMeB, which should have an absorption band near 450 nm similar to toluene.³⁰⁸ However, the absorption band at 335 nm is identical to the known absorption spectrum of the 4-methylcumyl cation.²³⁴ The transient absorbing at 335 nm is readily identified as the 4-methylcumyl cation derived from rapid fragmentation of the initial PET generated DMeB

radical cation, eq. 3-21. Consistent with this assignment is the fact that the transient at 335 nm is unreactive towards oxygen, Figure 3-21, but is quenched by nucleophiles such as bromide ion, Figure 3-21, inset. These results indicate that the DMeB radical cation undergoes rapid fragmentation ($> 10^8 \text{ s}^{-1}$) to the 4-methylcumyl cation and the 4-methylcumyl radical and is thus not an observable intermediate using nanosecond laser photolysis. The 4-methylcumyl radical is known to absorb near 320 nm²⁹³ and is thus outside the monitoring range accessible using 308 nm laser excitation in the presence of chloranil.

In the experiments described, direct observation of chloranil triplet quenching by ET from DMeB is possible, leading to the observed triplet decay and corresponding growth of the chloranil radical anion and the 4-methylcumyl cation. The second-order rate constant describing the ET reaction is given by eq. 3-23.

$$\begin{aligned} \text{Rate} &= k_{\text{ET}}[\text{Chl}^{3*}][\text{Bicumene}] \\ [\text{Bicumene}] \gg [\text{Chl}^{3*}]: \text{Rate} &= k_{\text{obs}}[\text{Chl}^{3*}] & \mathbf{3-23} \\ k_{\text{obs}} &= k_{\text{ET}}[\text{Bicumene}] \end{aligned}$$

As previously discussed (section 3.2.1.5), under conditions where the concentration of one reagent is in large excess, pseudo-first order kinetics can be assumed. In this case the concentration of the bicumene is significantly larger than the concentration of photoexcited chloranil. Thus it is possible to obtain the second-order rate constant, k_{ET} , by measuring the observed rate constant, k_{obs} , either for decay of the chloranil triplet, growth of the chloranil radical anion or growth of 4-methylcumyl cation, as a function of DMeB concentration, eq. 3-23. For instance, a plot of the rate constant for the growth of the 4-methylcumyl cation versus DMeB concentration is linear, Figure 3-22, and a second-order ET rate constant of $2.3 \times 10^9 \text{ M}^{-1} \text{ s}^{-1}$ is obtained from the slope.

The radical cations of the other bicumenes presented in Scheme 3-5 can also be generated by ET quenching of the chloranil triplet, Figures 3-23 to 3-25. Analogous results are observed in each case and it is possible to directly monitor the ET reactions in HFIP and thereby measure the rate constants for ET between the bicumenes and photoexcited chloranil. As can be seen in Table 3-11, in each case the measured rate constants for ET are all very close to the diffusion controlled limit.

Table 3-11. Second-order rate constants obtained for ET quenching of photoexcited Chl by bicumene donors in HFIP.

Bicumene	$k_{\text{PET}} \text{ Chloranil} / 10^9 \text{ M}^{-1} \text{ s}^{-1}$
4,4'-Dimethyl	2.3 ± 0.2
4,4'-Difluoro	1.4 ± 0.1
Parent	1.9 ± 0.1
3,3'-Dimethoxy	3.9 ± 0.3

As shown in Figures 3-23 to 3-25, the DFB, bicumene and 3-DMB radical cations must undergo rapid cleavage within the laser pulse to generate the corresponding carbocation and radical fragments upon PET generation. In each case, the initially photogenerated bicumene radical cation is not observed. Instead a growth in the 320 to 330 nm region is observed, which can be assigned to the corresponding cumyl cation, and the kinetics for these growths match the decay of the chloranil triplet. These assignments are supported by the known absorption spectrum of the parent cumyl cation,²³⁴ and the absorption spectra of the structurally similar 4-fluoro- and 3-methoxyphenethyl cations,²³⁵ as well as the insensitivity of the transients to oxygen. The experimentally determined absorption maxima for the cumyl cations are given in Table 3-12. The corresponding radical fragment is not observed in any of the transient spectra, which is consistent with the 4-fluorocumyl, cumyl and 3-methoxycumyl radicals having absorption maxima at or below 320 nm.²⁹³ At slightly longer times, after the ET reaction is complete, the decay of the cumyl cations in HFIP can be measured. The rate constants for decay of the cumyl cations in HFIP are presented in Table 3-12.

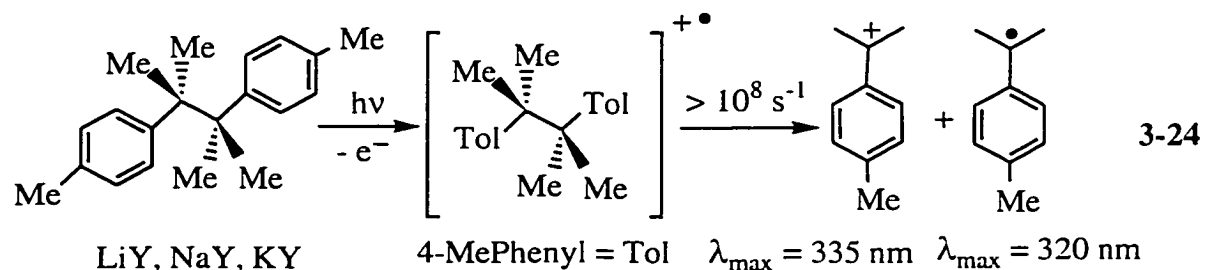
Table 3-12. λ_{max} and decay rate constants for various cumyl cations in HFIP.

Cumyl Cation	$\lambda_{\text{max}} / \text{nm}$	k_{HFIP}
4-Methoxy	360	too slow
4-Methyl	335, 380 (sh)	$(3.5 \pm 0.4) \times 10^3$
4-Fluoro	330	$(8.69 \pm 0.01) \times 10^4$
4-H	325	$(1.24 \pm 0.04) \times 10^5$
3-Methoxy	330	$(2.72 \pm 0.06) \times 10^5$

The results described above demonstrate that the radical cation of each bicumene presented in Scheme 3-5 undergoes rapid cleavage yielding the carbocation and radical

fragments immediately following the 10 ns laser pulse. Thus these bicumenes should be suitable precursors for the photochemical generation of several cumyl cations in alkali metal cation zeolites. Generation and reactivity of the 4-methylcumyl, 4-fluorocumyl, cumyl and 3-methoxycumyl cations in alkali metal cation zeolites is the subject of the following section.

Figure 3-26 shows the transient diffuse reflectance spectrum obtained immediately following 266 nm laser photolysis of DMeB in evacuated (10^{-4} Torr) LiY ($\langle S \rangle = 0.10$). The spectrum consists of a symmetrical absorption band with a maximum at 335 nm along with a distinct shoulder near 320 nm. In addition, broad, ill-defined absorption can be observed in the 500 to 600 nm region. In oxygen-saturated LiY, the transient absorption band at 335 nm remains clearly visible, in contrast to the absorption band at 320 nm, as well as the long wavelength absorption which are both quenched by the inclusion of oxygen within the zeolite composite, Figure 3-27. This indicates that two different transient species are responsible for the absorption bands at 335 nm and 320 nm. The slight decrease in signal intensity at 335 nm under oxygenated conditions, Figure 3-27 inset, can be attributed to quenching of the neighbouring 320 nm absorption band. Similar transient absorption spectra are observed immediately following 266 nm laser photolysis of DMeB in NaY, Figure 3-28, and KY, Figure 3-29. In each case two absorption bands at 335 nm and 320 nm can be observed under vacuum conditions, while only the 335 nm absorption band is detected in oxygen-saturated samples. The transient absorption bands at 335 nm and 320 nm observed following laser photolysis of DMeB in LiY, NaY and KY can be readily assigned to the 4-methylcumyl cation and 4-methylcumyl radical respectively. These transients are formed *via* rapid fragmentation ($> 10^8 \text{ s}^{-1}$) of the DMeB radical cation generated by photoionization of DMeB within the cavities of LiY, NaY and KY, eq. 3-24.



These assignments are supported by the absorption spectra of the 4-methylcumyl cation (*vide supra*) and the 4-methylcumyl radical with characteristic maxima at 335 nm and 320 nm, respectively. In addition, the observed quenching of only the 320 nm transient

absorption by oxygen is consistent with reactivity of oxygen towards carbon-centered radicals but not carbocations. The broad, long wavelength absorption is indicative of electrons trapped by cation clusters within the zeolite.⁸⁰ The trapped electron would be generated along with the DMeB radical cation from the initial photoionization of DMeB bicumene. The long wavelength absorption bands are quenched by the inclusion of oxygen within the zeolite composites, consistent with the reactivity of trapped electrons in these zeolites.⁸⁰

Additional support for the assignment of the 335 nm transient to the 4-methylcumyl cation can be obtained by considering the reactivity of this transient towards coadsorbed nucleophiles. The transient species at 335 nm is found to be reactive towards both water and methanol coadsorbed within the zeolite matrix, consistent with the expected reactivity of a carbocation intermediate. A comparison of the transient diffuse reflectance spectra obtained following laser photolysis of DMeB in dry and hydrated (ca. 10 wt %) NaY is shown in Figure 3-30. Absorption due to the 4-methylcumyl cation is no longer detected immediately following laser photolysis of DMeB in hydrated NaY. This is consistent with rapid addition of coadsorbed water to the carbocation within the laser pulse and is analogous to results previously discussed concerning static quenching of the 4-methoxycumyl cation by water in alkali metal cation Y zeolites. Likewise, the 4-methylcumyl cation is also observed to react with methanol within the NaY matrix. Inclusion of methanol leads to a notable decrease in the yield of the transient at 335 nm, Figure 3-30, inset. The static quenching of the 4-methylcumyl cation by methanol is similar to static quenching of the 4-methoxycumyl cation by methanol as previously described. Due to the significantly enhanced reactivity of the 4-methylcumyl cation as compared to the 4-methoxycumyl cation (*vide supra*), dynamic quenching of the 4-methylcumyl cation in alkali metal cation zeolites is not readily detected.

The lifetime of the 4-methylcumyl cation in dry LiY, NaY, and KY is considerably shorter than lifetime of the 4-methoxycumyl cation in these zeolites. For instance, in dry NaY, the 4-methylcumyl cation decays with a rate constant of $3.2 \times 10^6 \text{ s}^{-1}$, which is approximately 15 times faster than the 4-methoxycumyl cation. This observation is consistent with the relative reactivities of these carbocations observed in solution,²³⁴ and the carbocation stabilizing abilities of the 4-methyl and 4-methoxy phenyl substituents in general.^{226,235} Furthermore, the absolute reactivity of the 4-methylcumyl cation is dependent on counterion, Figure 3-31. The rate constant for carbocation decay increases as the size of the alkali metal counterion increases from Li^+ to K^+ , Table 3-13. This is consistent with the trends observed in the absolute reactivity of

the 4-methoxycumyl cation in alkali metal cation zeolites, although the overall magnitude of the effect is somewhat reduced for the more reactive 4-methylcumyl cation. No absorption due to the 4-methylcumyl cation is observed following laser irradiation of DMeB in either RbY or CsY. Considering the very short lifetime of the 4-methylcumyl cation in LiY, NaY and KY and the progressive decrease in lifetime with alkali cation size it is not surprising that the carbocation is not observed in either RbY and CsY. A likely explanation for the inability to detect the 4-methylcumyl cation in RbY and CsY is that the carbocation decays within the laser pulse in these two zeolites. It is also possible that photoionization to generate the DMeB radical cation does not take place, or is considerably less efficient in these zeolites (*vide infra*).

Table 3-13. Decay rate constants for the 4-methylcumyl cation in alkali metal cation zeolites.

Zeolite	$k_{MY} / 10^6 \text{ s}^{-1}$
LiY	(2.2 ± 0.1)
NaY	(3.2 ± 0.2)
KY	(4.5 ± 0.2)
RbY	not observed
CsY	not observed

As noted above, although static quenching of the 4-methylcumyl cation by nucleophiles is observed in alkali metal cation zeolites, it is difficult to detect dynamic quenching of this carbocation by coadsorbed methanol. This is likely due to the relatively high absolute reactivity of the 4-methylcumyl cation in alkali metal cation zeolites. Dynamic quenching would be manifested as an increase in the decay rate constant of the carbocation with increasing methanol content. However, due to the rapid decay rate constant of the 4-methylcumyl cation in dry zeolites, any increase in rate constant upon coinclusion of nucleophiles would be difficult to detect with the nanosecond system. This is due to the fact that a high concentration of methanol would be necessary in order for bimolecular addition to compete with rapid carbocation decay, and under these conditions the yield of carbocation would be very low as a consequence of static quenching. Interestingly, however, although it is difficult to observe dynamic quenching by added nucleophiles, the opposite effect can be observed. By coinclusion of the relatively non-nucleophilic adsorbate, HFIP, it is possible to *enhance* the lifetime of

the reactive 4-methylcumyl cation in alkali metal cation zeolites. As shown in Figure 3-32, coadsorption of small amounts of HFIP leads to a progressive *decrease* in the rate constant for decay of the 4-methylcumyl cation in NaY.

The reactivity of the 4-methylcumyl cation in alkali metal cation zeolites suggests that direct detection of even more reactive cumyl cations in these zeolites will be limited. In an attempt to observe the 4-fluorocumyl cation, 4,4'-difluorobicumene (DFB) was photolyzed in dry LiY. This yields a very weak, rapidly decaying signal at 330 nm along with a weak, longer lived signal near 300 nm. These transients are tentatively assigned to the 4-fluorocumyl cation and 4-fluorocumyl radical, respectively. Estimation of the decay rate constant for the very weak transient signal observed at 330 nm in oxygen-saturated LiY gives a value of $(5.0 \pm 0.8) \times 10^6 \text{ s}^{-1}$. Further evidence suggesting that this transient signal is due to the 4-fluorocumyl cation is obtained from experiments with coadsorbed HFIP. Inclusion of HFIP in LiY leads to a steady increase in the intensity and lifetime of the transient at 330 nm, Figure 3-33. Thus, the influence of HFIP on this transient is similar to that observed for the 4-methylcumyl cation. The transient spectrum of the 4-fluorocumyl in LiY can be obtained readily in the presence of relatively small amounts of coadsorbed HFIP, Figure 3-34. Attempts to observe the 4-fluorocumyl cation in the other alkali metal cation zeolites were unsuccessful, presumably because the 4-fluorocumyl cation decays too rapidly to be observed under these conditions with the nanosecond laser system.

Fragmentation of the radical cations of bicumene and 3,3'-dimethoxybicumene (3-DMB) yields the cumyl cation and the 3-methoxycumyl cation, respectively. These carbocations are even more reactive than the 4-fluorocumyl cation and direct detection of these cumyl cations is not expected within any of the cation-exchanged Y zeolites. Consistent with these expectations, laser irradiation of bicumene in dry LiY and NaY yields only very weak signals in the transient diffuse reflectance spectrum. A weak, sharp absorption band at 320 nm which is quenched by oxygen suggests the presence of the cumyl radical,²⁹³ while broad, ill-defined absorption at wavelengths greater than ca. 500 nm may be due trapped electrons.⁸⁰ No other transient is observed near 325 nm, the known absorption maximum of the cumyl cation.²³⁴ In combination, these observations suggest that bicumene photoionizes within LiY and NaY to generate the bicumene radical cation which subsequently fragments to the corresponding cumyl cation and cumyl radical. The failure to observe the cumyl cation is therefore most likely due to the fact that the lifetime of the carbocation in these zeolites is too short for detection with the nanosecond system. Notably, however the intensity of both the radical absorption and the electron bands is quite low ($\Delta J/J_0 \leq 0.02$) suggesting that the efficiency of

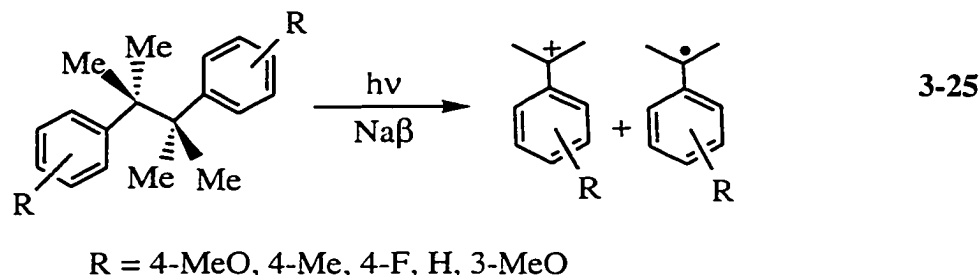
photoionization of the parent bicumene is considerably less than the 4-methoxy substituted derivative. Thus, in addition to the short lifetime of the cumyl cation, the low yield for photochemical formation likely also contributes to the inability to detect this carbocation in alkali metal cation Y zeolites.

Similarly, laser photolysis of 3-DMB in dry LiY or NaY generates no absorption bands which can be assigned to the 3-methoxycumyl cation ($\lambda_{\text{max}} = 330 \text{ nm}$, *vide supra*). Photolysis of this substrate under vacuum conditions does however yield relatively intense broad absorption bands between 400 and 700 nm which are completely quenched by oxygen, Figure 3-35, and are indicative of trapped electrons.⁸⁰ This suggests that photoionization of 3-DMB does indeed take place with reasonable efficiency in these zeolites. The fact that no evidence for the carbocation is obtained is thus again mostly likely due to the short lifetime of this transient within LiY and NaY.

For bicumene, coinclusion of HFIP within the zeolite leads to modest increases in the transient yield observed at 325 nm immediately following laser photolysis, Figure 3-36, inset. Furthermore, the lifetimes of this transient increases upon adsorption of HFIP, consistent with the behaviour of the 4-methylcumyl and 4-fluorocumyl cations reported above. The enhanced yield observed at 325 nm likely is due to detection of the cumyl cation following the laser pulse as a consequence of the increased lifetimes of this carbocations in zeolites containing coadsorbed HFIP. Using this concept it is possible to obtain the transient diffuse reflectance spectrum of the cumyl cation ($\lambda_{\text{max}} = 325 \text{ nm}$) by laser photolysis of bicumene in LiY containing 1 M HFIP (~ 1 molecule HFIP per cavity), Figure 3-36. An attempt was also made to detect the 3-methoxycumyl cation in LiY and NaY containing coadsorbed HFIP. In this case, the intensity of adsorption at 330 nm, the maximum of the 3-methoxycumyl cation, also increases slightly with increasing concentrations of HFIP. However, the signals obtained in the transient diffuse reflectance spectrum are too weak and ill-defined to identify the transient as the 3-methoxycumyl cation.

In order to directly observe each of these reactive cumyl cations within zeolites it is necessary to choose a zeolite environment which is more stabilizing than the alkali metal cation Y zeolites. Based on previous experiments with the 4-methoxycumyl cation, Na β emerges as a good candidate for enhancing the lifetimes of these reactive species. In this zeolite, the 4-methoxycumyl cation has a lifetime of approximately 3000 μs , which is more than 650 times longer than the lifetime of the same carbocation in NaY. As shown in Figure 3-37, laser photolysis of DMeB in Na β under either vacuum or oxygen conditions leads to symmetrical absorption bands with a maximum at 335 nm which is readily assigned to the 4-methylcumyl cation. Similar results are obtained using DFB,

bicumene and 3-DMB, and it is possible to observe the 4-fluorocumyl cation, Figure 3-38, the cumyl cation, Figure 3-39, and the 3-methoxycumyl cation, Figure 3-40, in evacuated and oxygen-saturated Na β . Thus, by employing Na β it is possible to directly observe each of the reactive cumyl cations within a single zeolite environment using nanosecond laser flash photolysis, eq. 3-25.



Although the transient spectra of each cumyl cation exhibits similar features, the lifetimes of the carbocations in Na β depend significantly on substituent in a manner consistent with the known abilities of these groups to influence carbocation reactivity,^{225,226,235} Table 3-14.

Table 3-14. First order decay rate constants and lifetimes of cumyl cations in dry Na β .

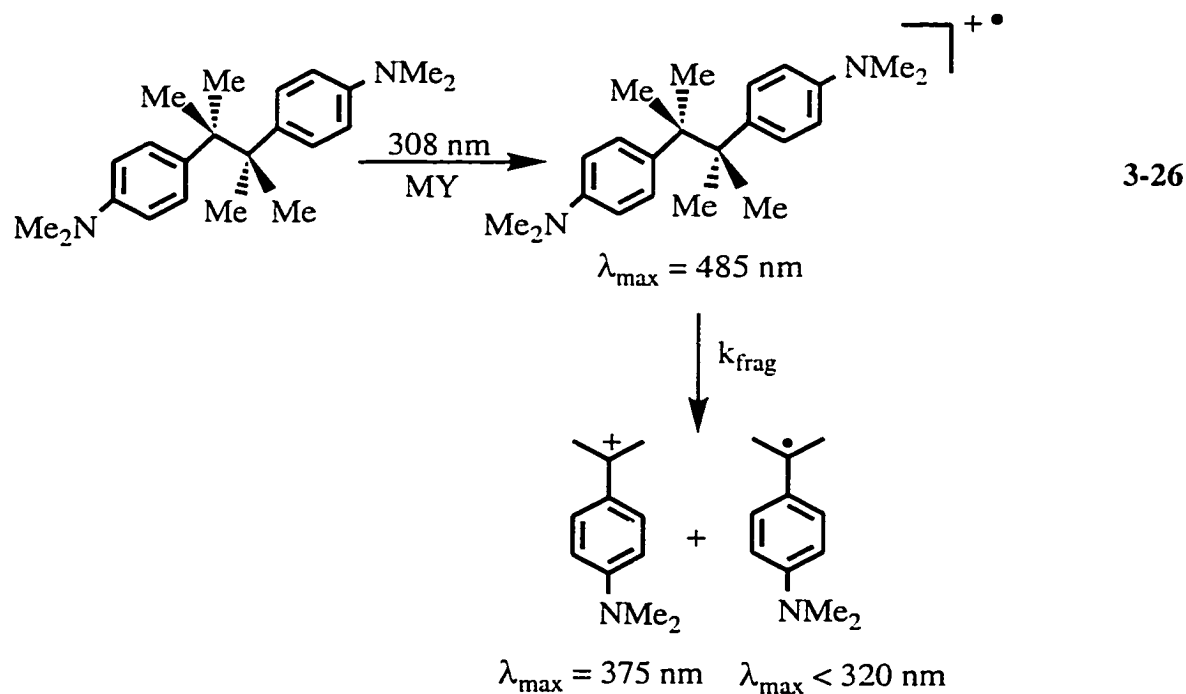
Substituent	$k_{\text{decay}} / \text{s}^{-1}$	$\tau / \mu\text{s}$
4-methoxy	$\sim 3 \times 10^2$	3000
4-methyl	$(3.4 \pm 0.1) \times 10^5$	3
4-fluoro	$(1.0 \pm 0.1) \times 10^6$	1
H	$(1.9 \pm 0.1) \times 10^6$	0.5
3-methoxy	$(2.6 \pm 0.1) \times 10^6$	0.4

3.2.1.7 Preliminary Experiments with 4,4'-(N-N-Dimethylamino)bicumene in Alkali Metal Cation Zeolites

The experimental results described thus far have examined the reactivity of cumyl cations in alkali metal cation zeolites. Although these carbocations arise from photogenerated bicumene radical cations, direct observation of the cleavage reaction leading to carbocation formation has been prohibited by the short lifetime of the radical cation precursors. Thus in each case the bicumene radical cations fragment within the laser pulse such that only the cleavage “products”, the cumyl cations and the cumyl

radicals, can be directly observed. In order to probe the influence of zeolite encapsulation on carbocation formation *via* this cleavage reaction it is necessary to choose a substrate whose radical cation undergoes bond fragmentation in the microsecond time regime. Previously reported studies suggest that 4,4'-(*N,N*-dimethylamino)bicumene (DMAB) may be an appropriate candidate.^{235,282} In 2:1 water:acetonitrile, this radical cation cleaves with a rate constant of ca. $1 \times 10^5 \text{ s}^{-1}$ to yield the 4-dimethylaminocumyl cation.²³⁵ The following section presents results derived from preliminary experimental studies of DMAB in alkali metal cation Y zeolites.

Laser photolysis of DMAB (308 nm, < 20 ns, < 100 mJ) in evacuated NaY leads to the observation of two absorption bands, $\lambda_{\text{max}} = 375 \text{ nm}$ and $\lambda_{\text{max}} = 485 \text{ nm}$, immediately following the laser pulse. At subsequent times, the 485 nm band decays while the transient at 375 nm continues to grow in over times as long as 1 ms, Figure 3-41. In this time regime, the transient diffuse reflectance spectrum looks very similar to the transient absorption spectra recently reported by Cozens *et al.*²³⁵ upon photoexcitation of DMAB in solution where the broad, symmetrical absorption bands with maxima near 500 nm and 380 nm were assigned to the DMAB radical cation and the 4-dimethylaminocumyl cation, respectively. Based on these considerations, the transients observed at 485 nm and 375 nm in NaY are reasonably identified as the DMAB radical cation and the 4-dimethylaminocumyl cation, respectively, eq. 3-26.



The growth traces monitored at 375 nm match well with the decay trace monitored at 485 nm, Figure 3-41 inset, as would be expected for the formation of the carbocation by slow fragmentation of the radical cation, eq. 3-36. Both traces fit nicely to a single first-order kinetic expression, yielding rate constants of $(2.45 \pm 0.08) \times 10^3 \text{ s}^{-1}$ and $(2.62 \pm 0.05) \times 10^3 \text{ s}^{-1}$ at 485 nm and 375 nm, respectively. Interestingly, the rate constant measured for the growth of the 4-dimethylaminocumyl cation observed in NaY is almost 2 orders of magnitude smaller than reported for formation of the 4-dimethylaminocumyl cation *via* cleavage of the DMAB radical cation in solution.²³⁵

It is also clear from Figure 3-41 that not all of the carbocation is formed by this slow fragmentation reaction. Instead, significant absorption at 375 nm is already present immediately after the laser pulse, indicating that some of the carbocation is formed promptly within the laser pulse. This suggests that some rapid process must also be available leading to prompt formation of the carbocation within the laser pulse.

Laser photolysis of DMAB in other alkali metal cation Y zeolites (LiY, KY, RbY and CsY) gives results qualitatively similar to those described for NaY, Figure 3-42. Thus, the DMAB radical cation and the 4-dimethylaminocumyl cation are observed in each zeolite, eq. 3-26. However, the specific features of the transient spectra and kinetics vary as a function of alkali counterion. One trend observed is that the total yield of carbocation relative to the yield of radical cation decreases significantly as the counterion is varied from Li^+ to Cs^+ , Table 3-15. In addition, the proportion of prompt carbocation formation relative to time-resolved carbocation formation significantly increases with alkali counterion size, Table 3-15. Thus, slow carbocation formation becomes a less significant pathway for carbocation generation in the larger cation zeolites. In fact, in CsY almost no time-resolved growth due to carbocation formation is observed. This can be seen in a plot of the relative yield of carbocation from prompt formation as a function of metal cation ionic radius, Figure 3-43. A third trend presented in Table 3-15 concerns the growth rate constant for time-resolved carbocation formation which increases monotonically with counterion size, Figure 3-44.

Table 3-15. Yield of 4-dimethylaminocumyl cation relative to the DMAB radical cation, fraction of prompt formation of the 4-dimethylaminocumyl cation and growth rate constant for the 4-dimethylaminocumyl cation observed following laser photolysis of DMAB in alkali metal cation Y zeolites.

Zeolite	Total Relative Yield Carbocation/Radical Cation	% Prompt Carbocation Formation	$k_{\text{growth } 380} /$ 10^3 s^{-1}
LiY	1.6	50	1.82 ± 0.07
NaY	1.5	54	2.62 ± 0.07
KY	0.47	71	7.1 ± 0.2
RbY	0.43	92	7.2 ± 0.1
CsY	0.45	96	9.7 ± 0.7

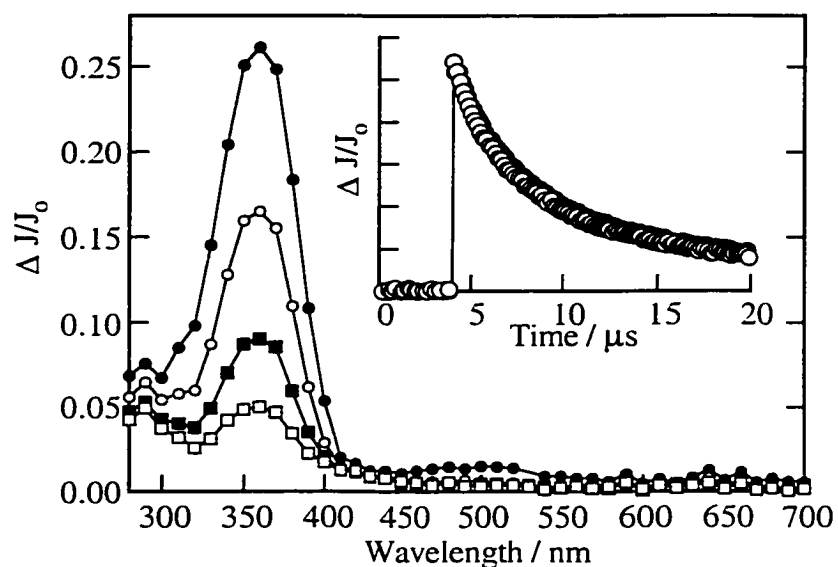


Figure 3-1. Transient diffuse reflectance spectrum generated 400 ns (closed circles), 2.56 μs (open circles), 7.00 μs (closed squares) and 14.0 μs (open squares) after 266 nm laser irradiation of DMB in evacuated (10^{-4} torr) NaY. Inset shows the decay monitored at 360 nm under vacuum (closed circles) and oxygen (open circles) conditions.

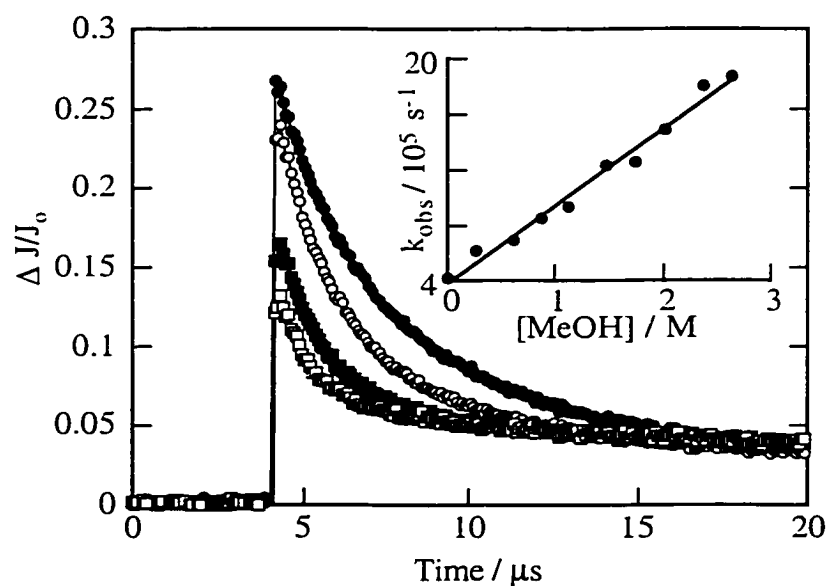


Figure 3-2. Decay traces monitored at 360 nm following 266 nm laser irradiation of DMB in NaY containing 0.03 M (closed circles), 0.10 M (open circles), 0.21 M (closed squares) and 0.31 M (open squares) methanol. Inset shows the observed decay rate constant measured at 360 nm as a function of methanol concentration in NaY.

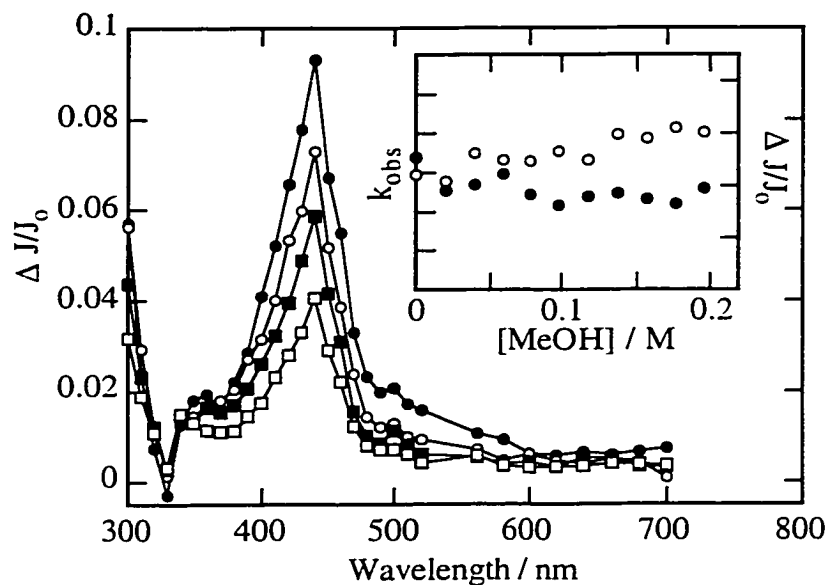


Figure 3-3. Transient diffuse reflectance spectrum generated 480 ns (closed circles), 1.84 μ s (open circles), 4.80 μ s (closed squares) and 14.4 μ s (open squares) after 266 nm laser irradiation of 4-methylanisole in evacuated NaY. Inset shows the observed decay rate constant (closed circles) and change in diffuse reflectance (open circles) monitored at 440 nm as a function of methanol concentration in NaY.

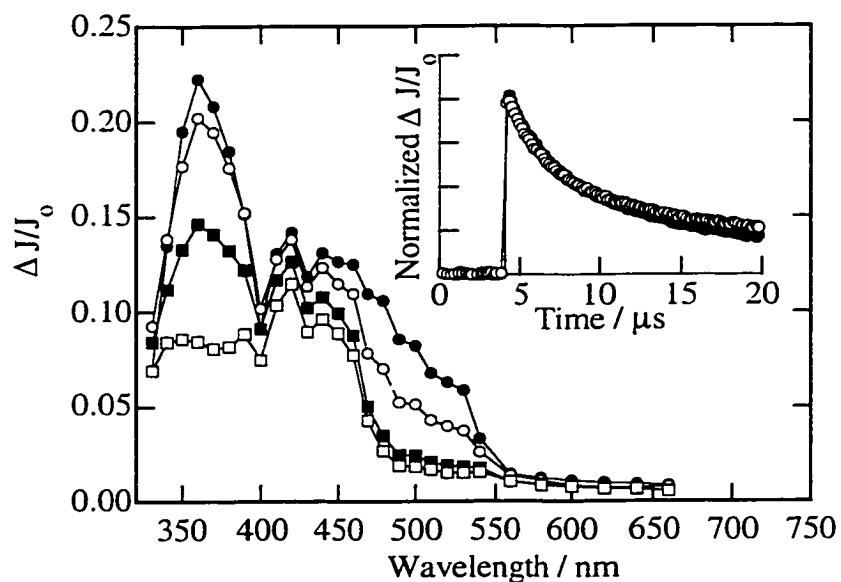


Figure 3-4. Transient diffuse reflectance spectrum generated 400 ns (closed circles), 880 ns (open circles), 3.32 μ s (closed squares) and 13.6 μ s (open squares) after 308 nm laser photolysis of chloranil in evacuated NaY with coadsorbed DMB. Inset shows decay traces monitored at 360 nm following direct excitation of DMB with 266 nm laser light (closed circles) and 308 nm excitation of chloranil in the presence of DMB (open circles).

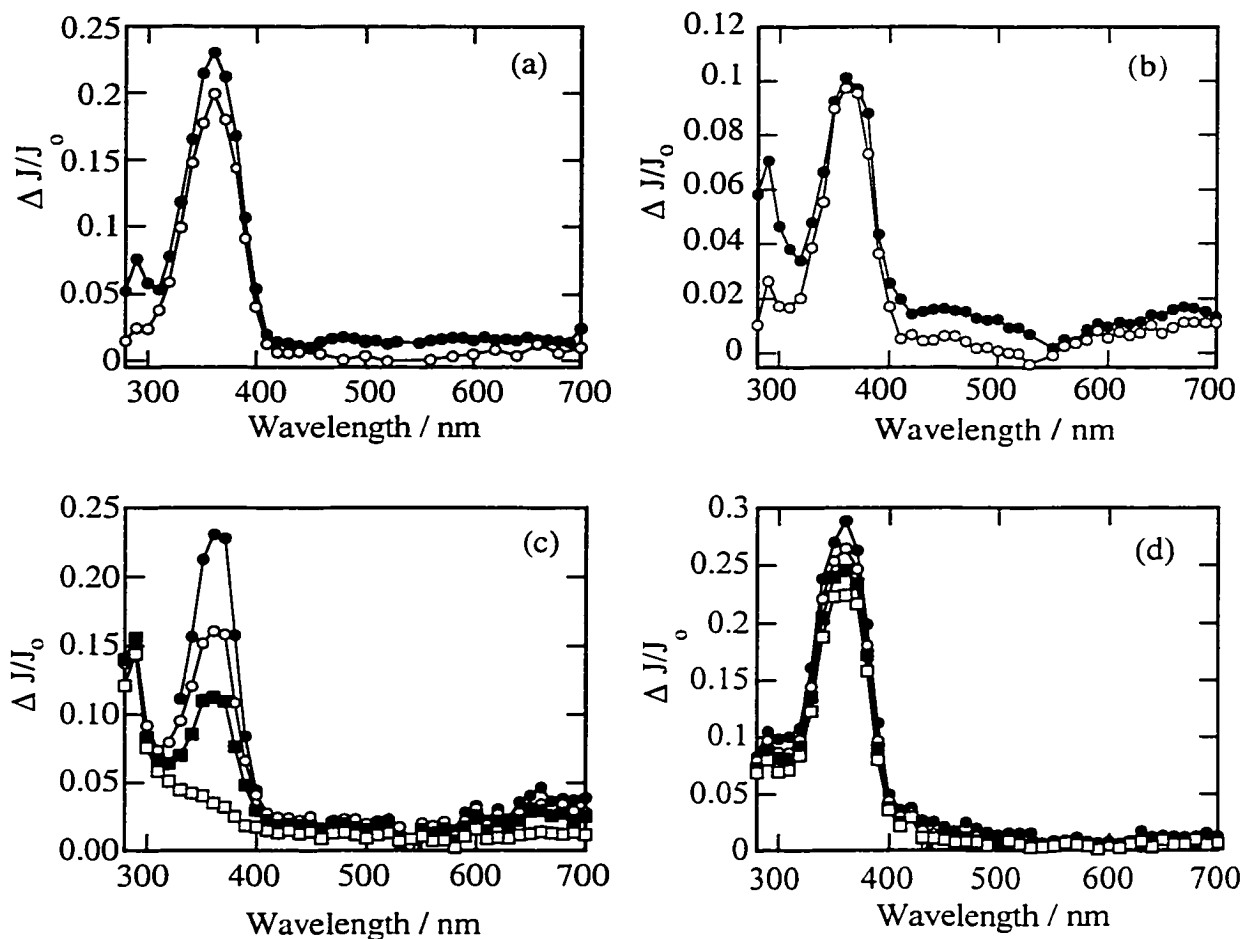


Figure 3-5. Transient diffuse reflectance spectra obtained 320 ns after 266 nm laser photolysis of DMB in evacuated (closed circles) and oxygen-saturated (open circles) LiY (a) and RbY (b). Transient diffuse reflectance spectra obtained 200 ns (closed circles) 800 ns (open circles), 2.16 μs (closed squares) and 14.8 μs (open squares) after 266 nm laser irradiation of DMB in evacuated NaX (c). Transient diffuse reflectance spectrum obtained 14.0 μs (closed circles) 156 μs (open circles), 384 μs (closed squares) and 744 μs (open squares) after 266 nm laser irradiation of DMB in evacuated Na β (d).

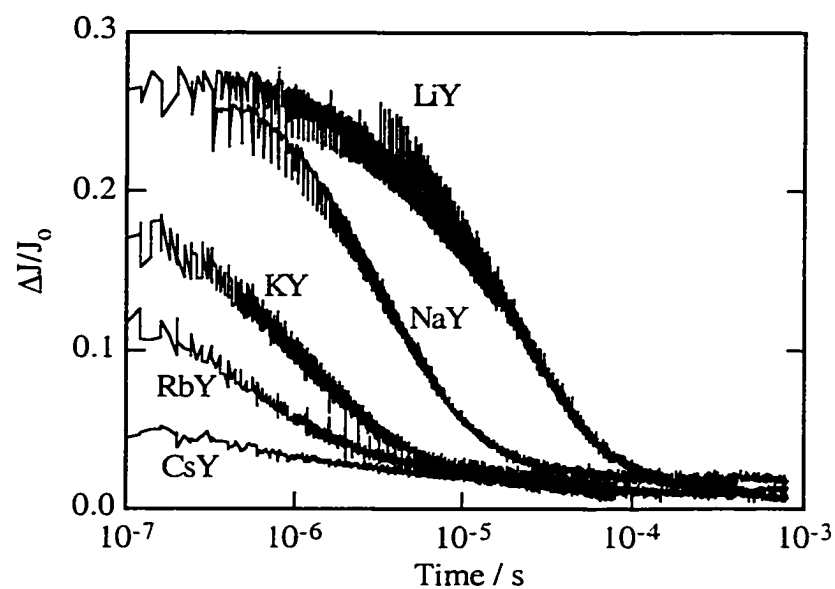


Figure 3-6. Stretched kinetic decay traces of the 4-methoxycumyl cation monitored at 360 nm in evacuated alkali metal cation Y zeolites.

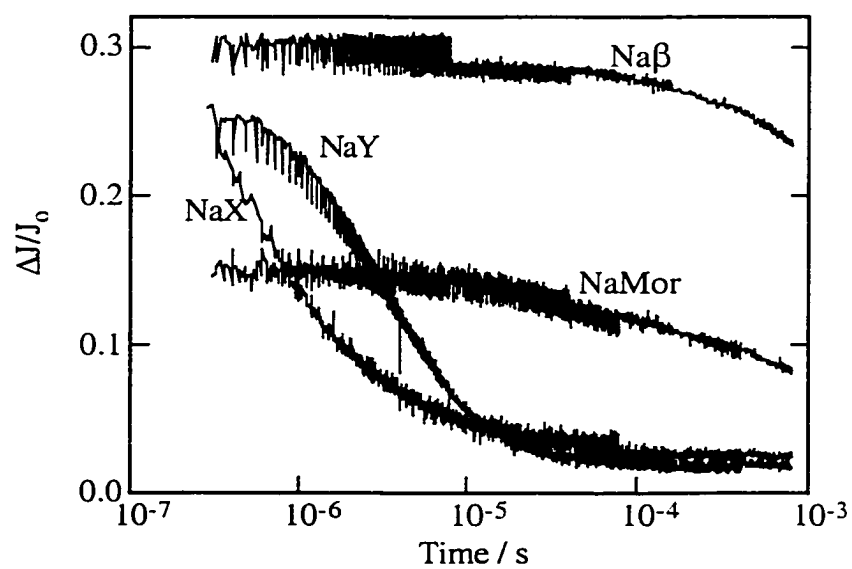


Figure 3-7. Stretched kinetic decay traces of the 4-methoxycumyl cation monitored at 360 nm in evacuated Na^+ zeolites.

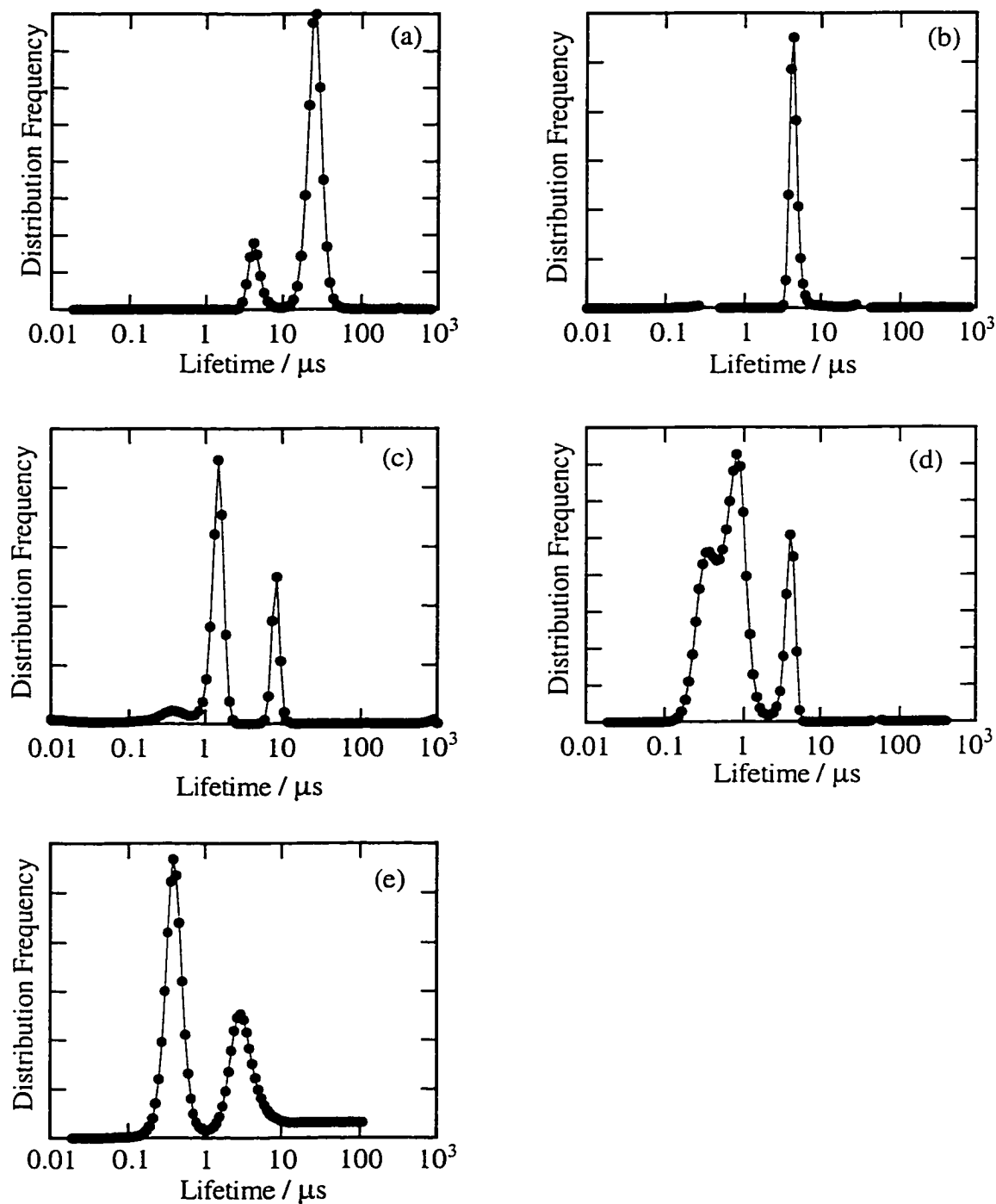


Figure 3-8. Distribution of lifetimes of the 4-methoxycumyl cation in evacuated LiY (a), NaY (b), KY (c), RbY (d), and CsY (e) obtained by fitting the stretched decay traces observed at 360 nm to the function, $f(t) = \sum a_k \exp(-t / \tau_k)$, with 100 terms according to the ESM method (see text, section 2.3).

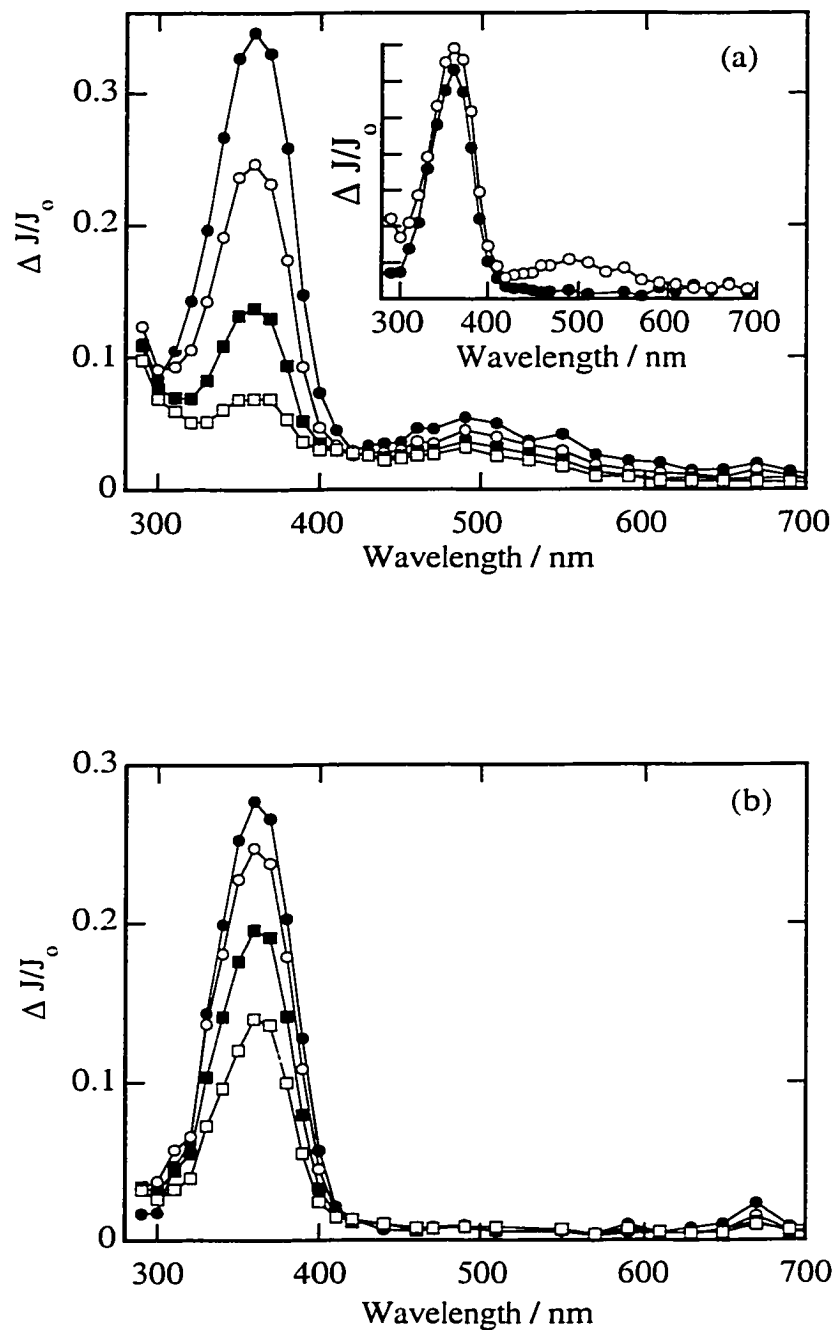


Figure 3-9. Transient diffuse reflectance spectrum observed 400 ns (closed circles), 1.92 μ s (open circles), 6.12 μ s (closed squares) and 14.8 μ s (open squares) after 266 nm laser irradiation of DMB- d_{12} in evacuated NaY (a) and oxygen-saturated LiY (b). Inset compares the transient spectra obtained 400 ns after photolysis in evacuated and oxygen-saturated NaY.

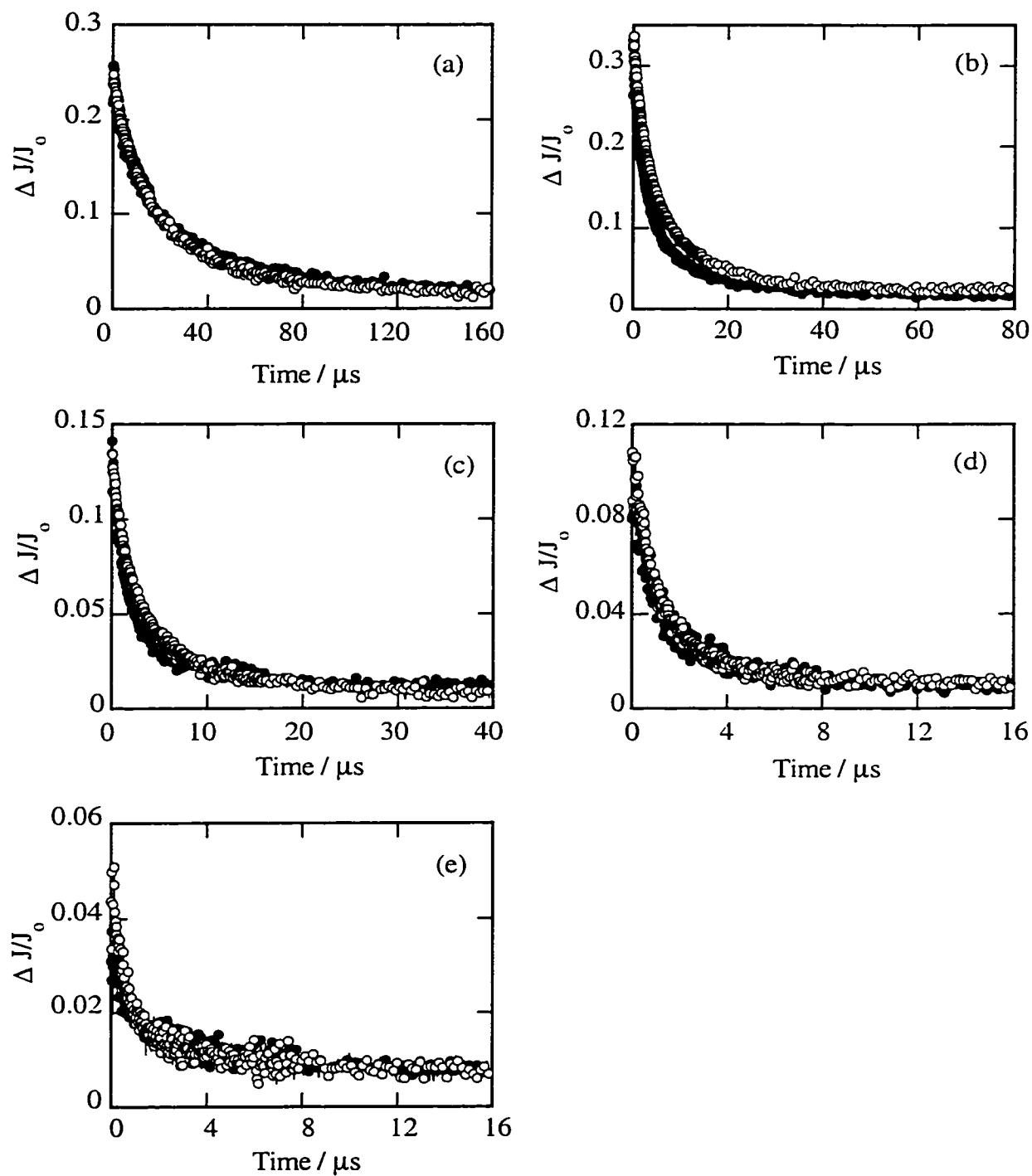


Figure 3-10. Decay traces monitored at 360 nm following 266 nm laser photolysis of DMB (closed circles) and DMB- d_{12} (open circles) in oxygen-saturated LiY (a), NaY (b), KY (c), RbY (d) and CsY (e).

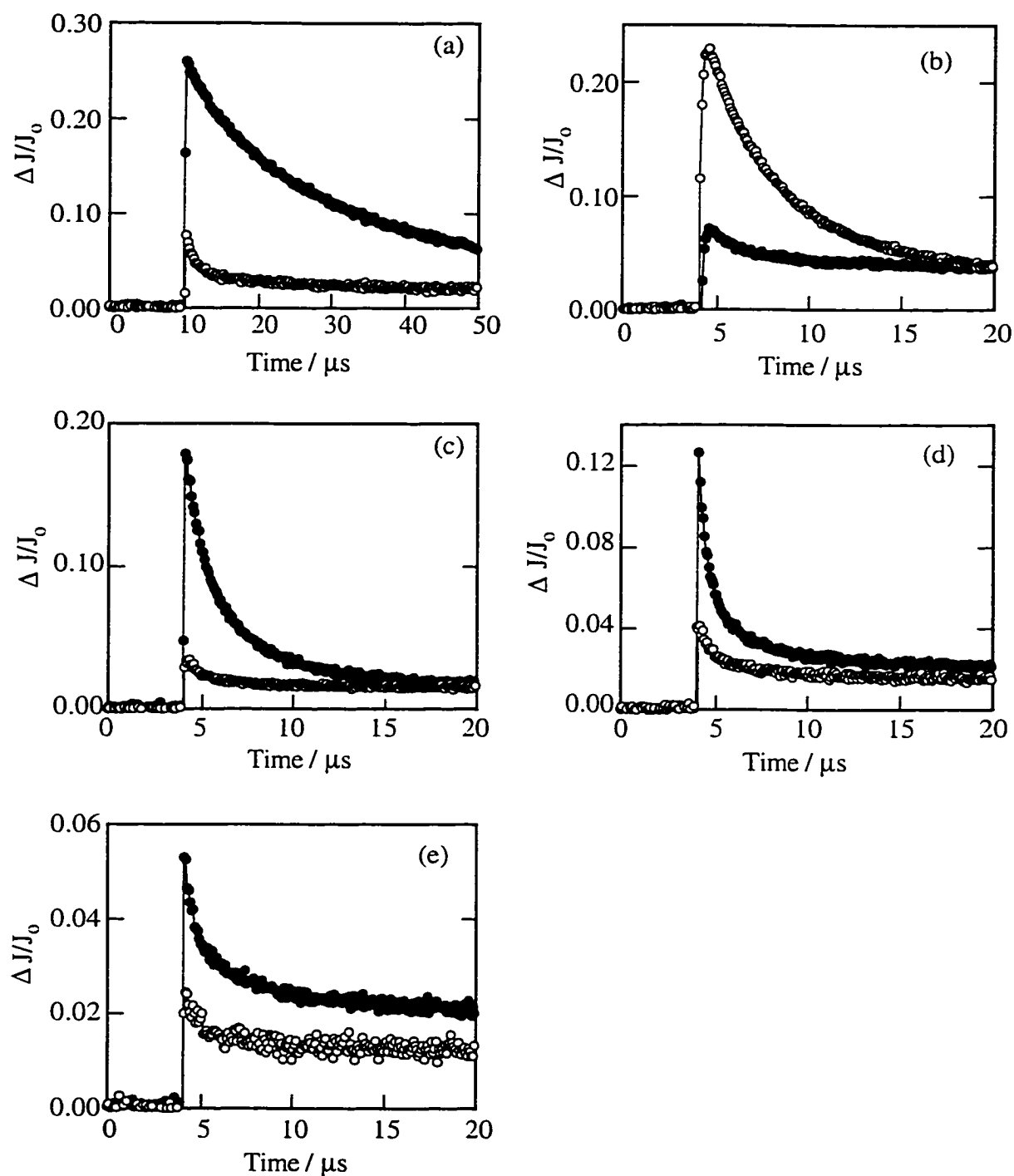


Figure 3-11. Decay traces observed at 360 nm following 266 laser irradiation of DMB in dry (closed circles) and hydrated (open circles) LiY (a), NaY (b), KY (c), RbY (d) and CsY (e). The water content is 12.5 %, 10 %, 6 %, 3 %, and 2 % by weight in LiY through CsY, respectively.

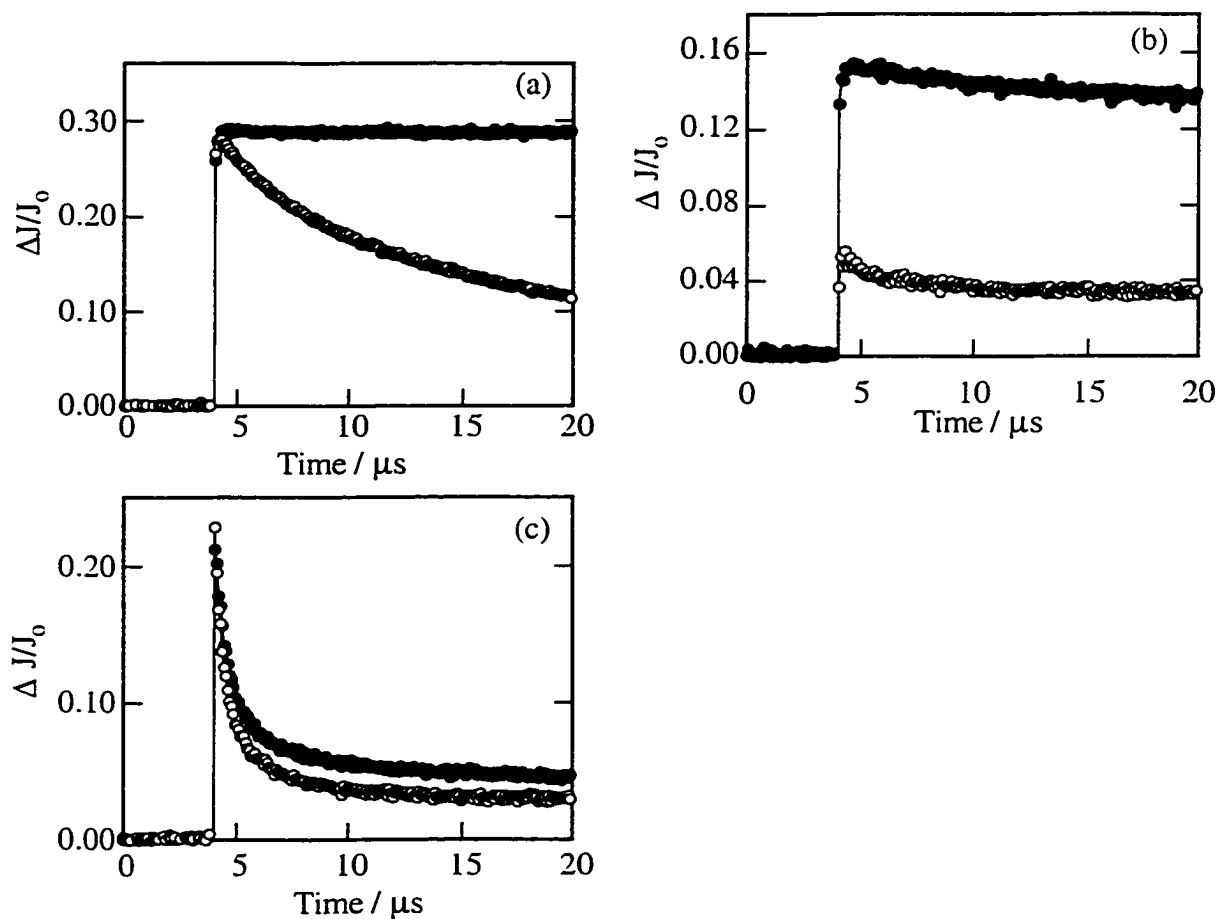


Figure 3-12. Decay traces observed at 360 nm following 266 laser irradiation of DMB in dry (closed circles) and hydrated (open circles) Na β (a), NaMor (b), and NaX (c). The samples contain 3 %, 4 %, and 5 %, water by weight in Na β , NaMor, and NaX, respectively.

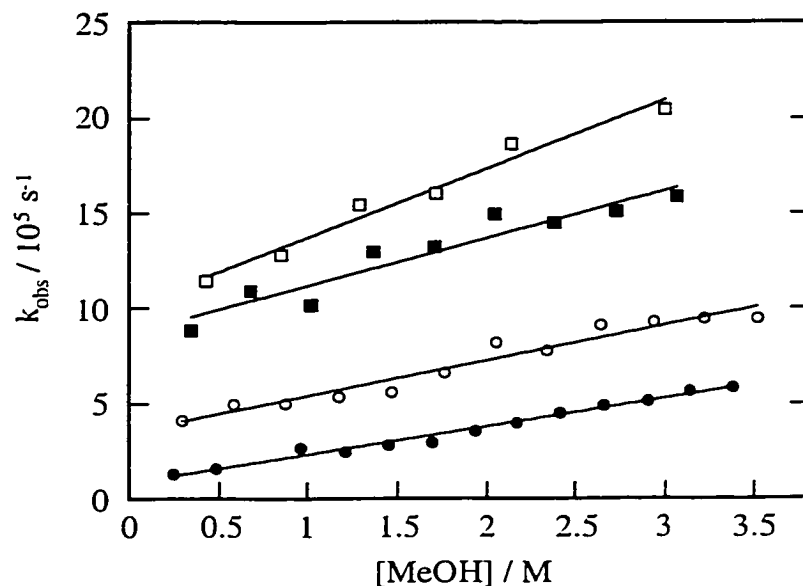


Figure 3-13. Decay rate constant of the 4-methoxycumyl cation in LiY (closed circles), NaY (open circles), KY (closed squares) and RbY (open squares) as a function of methanol concentration.

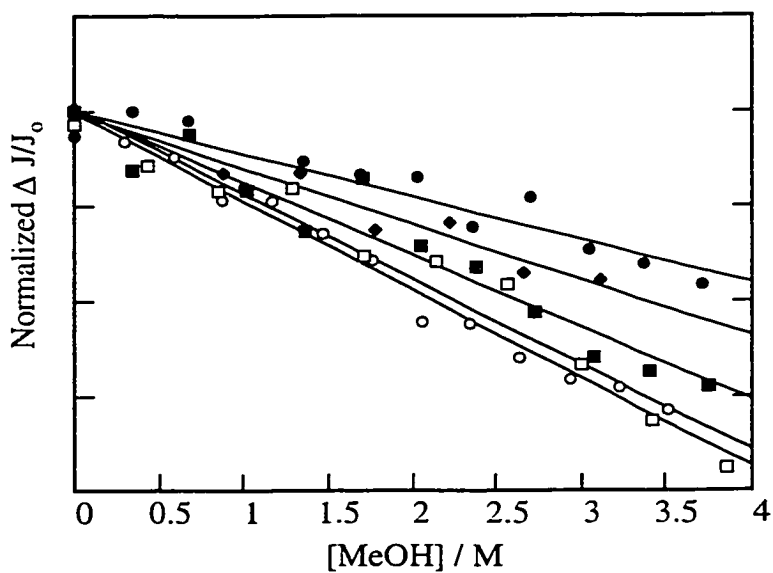


Figure 3-14. Normalized initial reflectance density due to the 4-methoxycumyl cation at 360 nm observed in LiY (closed circles), NaY (open circles), KY (closed squares), RbY (open squares) and CsY (closed diamonds) as a function of methanol concentration.

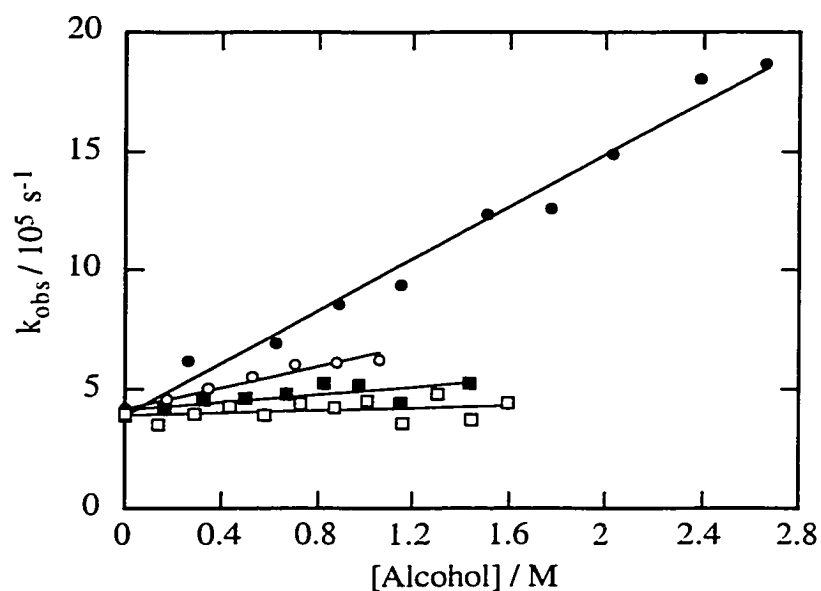


Figure 3-15. Decay rate constant of the 4-methoxycumyl cation in NaY as a function of methanol (closed circles), ethanol (open circles), *isopropanol* (closed squares) and *tert*-butanol (open squares) concentration.

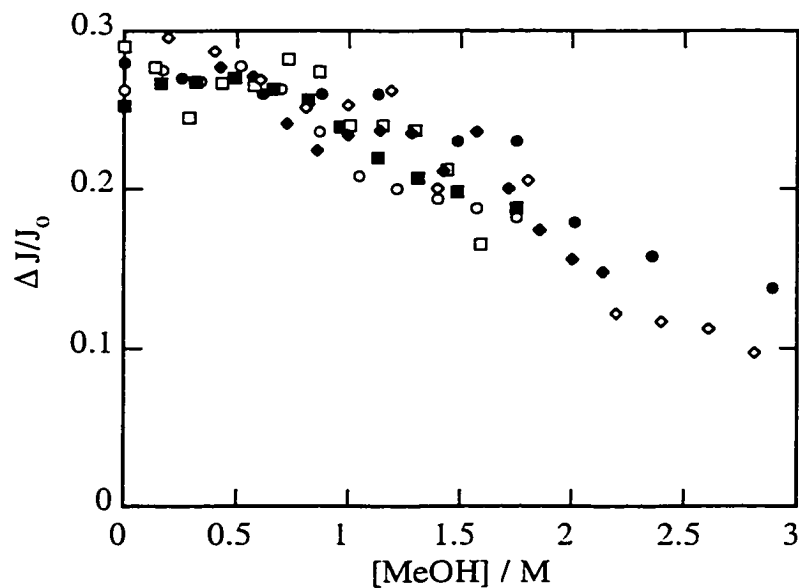


Figure 3-16. Initial reflectance density due to the 4-methoxycumyl cation observed at 360 nm in NaY as a function of methanol (closed circles), ethanol (open circles), *isopropanol* (closed squares), *isobutanol* (open squares), *tert*-butanol (closed diamonds), and 2,2,2-trifluoroethanol (open diamonds) concentration.

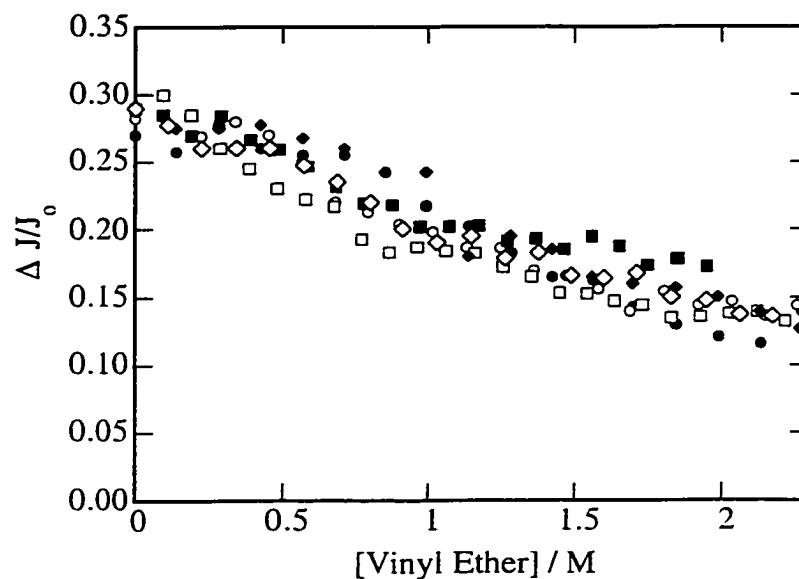


Figure 3-17. Initial reflectance density due to the 4-methoxycumyl cation observed at 360 nm in NaY as a function of ethyl vinyl ether (closed circles), propyl vinyl ether (open circles), butyl vinyl ether (closed squares), *tert*-butyl vinyl ether (open squares), *isopropyl* methyl ether (closed diamonds), and ethyl propyl ether (open diamonds) concentration.

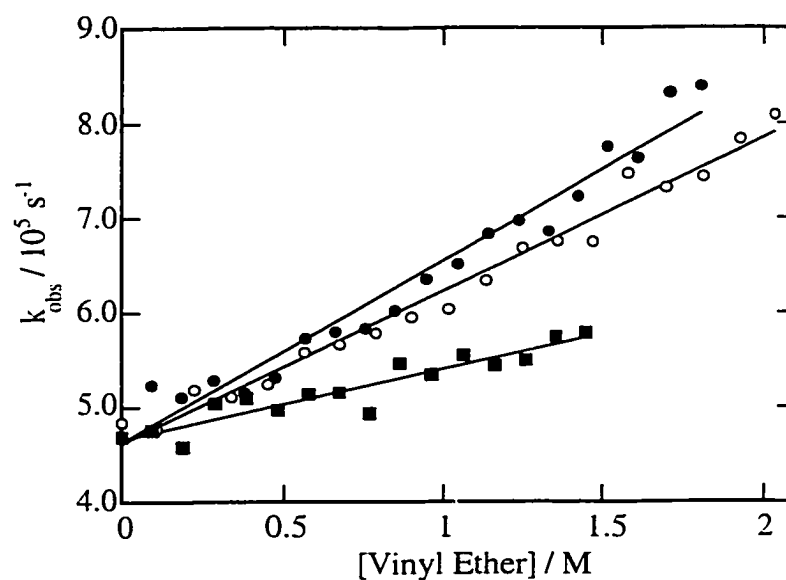


Figure 3-18. Decay rate constant of the 4-methoxycumyl cation in NaY as a function of ethyl vinyl ether (closed circles), propyl vinyl ether (open circles), and *tert*-butyl vinyl ether (closed squares) concentration.

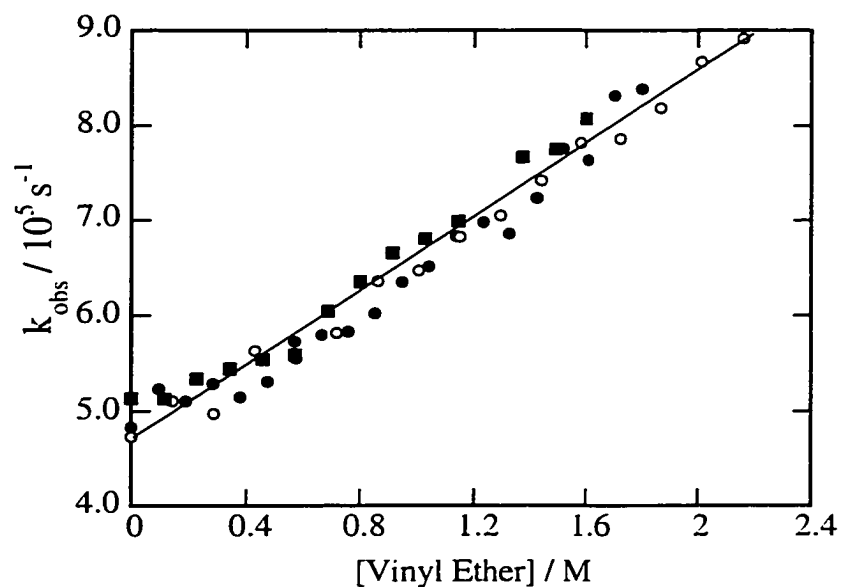


Figure 3-19. Decay rate constant of the 4-methoxycumyl cation in NaY as a function of ethyl vinyl ether (closed circles), *isopropenyl methyl ether* (open circles), and ethyl propenyl ether (closed squares) concentration.

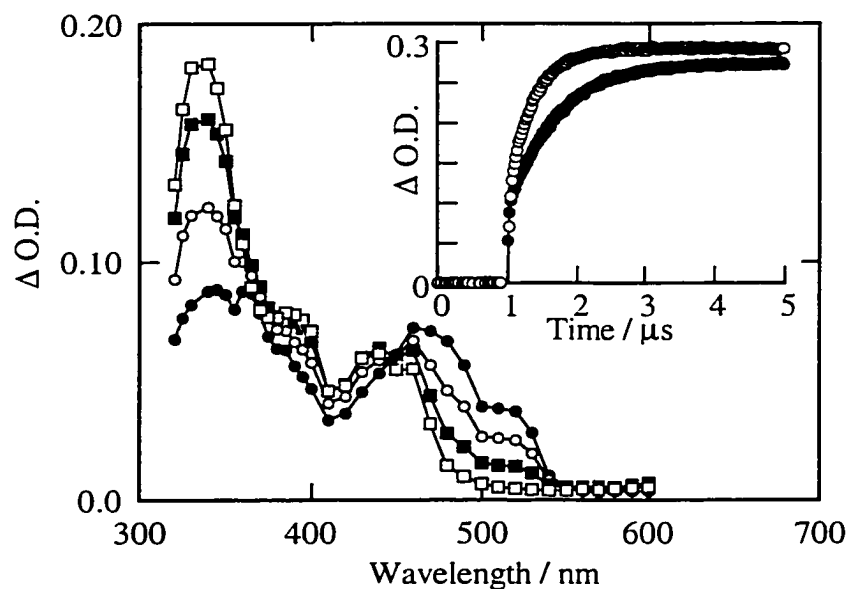


Figure 3-20. Transient absorption spectrum generated 120 ns (closed circles), 370 ns (open circles), 820 ns (closed squares) and 3.72 μ s (open squares) after 308 nm laser irradiation of chloranil in nitrogen-saturated HFIP containing 0.16 mM 4,4'-dimethylbicumene. Inset shows growth traces at 335 nm for DMeB concentrations of 0.16 mM (closed circles) and 0.47 mM (open circles).

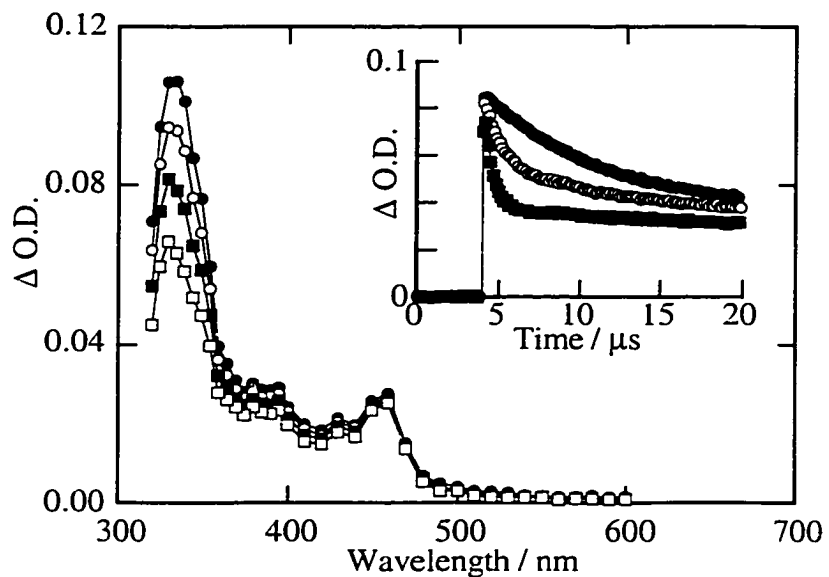


Figure 3-21. Transient absorption spectrum generated 440 ns (closed circles), 2.88 μ s (open circles), 6.80 μ s (closed squares) and 14.8 μ s (open squares) after 308 nm laser irradiation of chloranil in nitrogen-saturated HFIP containing 0.16 mM DMeB. Inset shows decay traces monitored at 330 nm in the presence of 0 mM (closed circles), 0.10 mM (open circles), and 0.40 mM (closed squares) bromide ion.

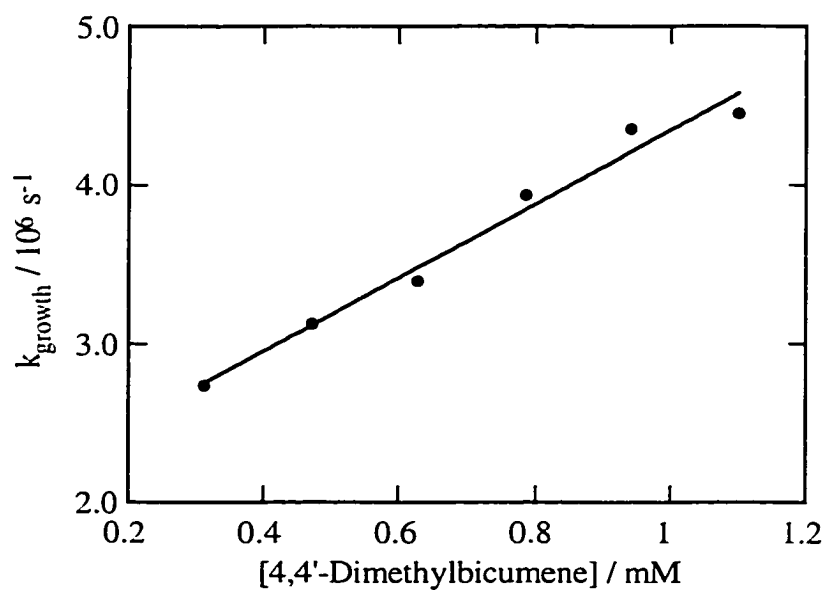


Figure 3-22. Growth rate constant measured at 335 nm following 308 nm laser photolysis of chloranil in oxygen-saturated HFIP as a function of DMeB concentration.

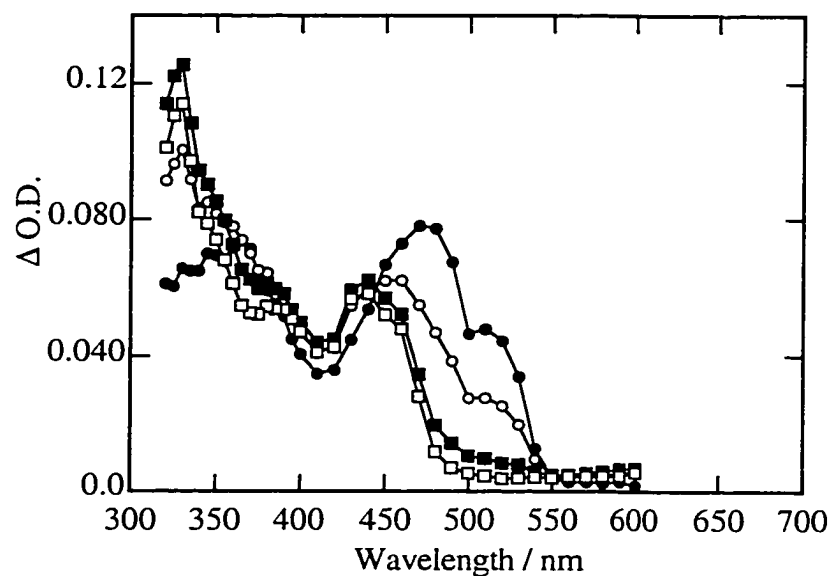


Figure 3-23. Transient absorption spectrum generated 80 ns (closed circles), 530 ns (open circles), 1.60 μ s (closed squares) and 3.70 μ s (open squares) after 308 nm laser irradiation of chloranil in nitrogen-saturated HFIP containing 0.16 mM DFB.

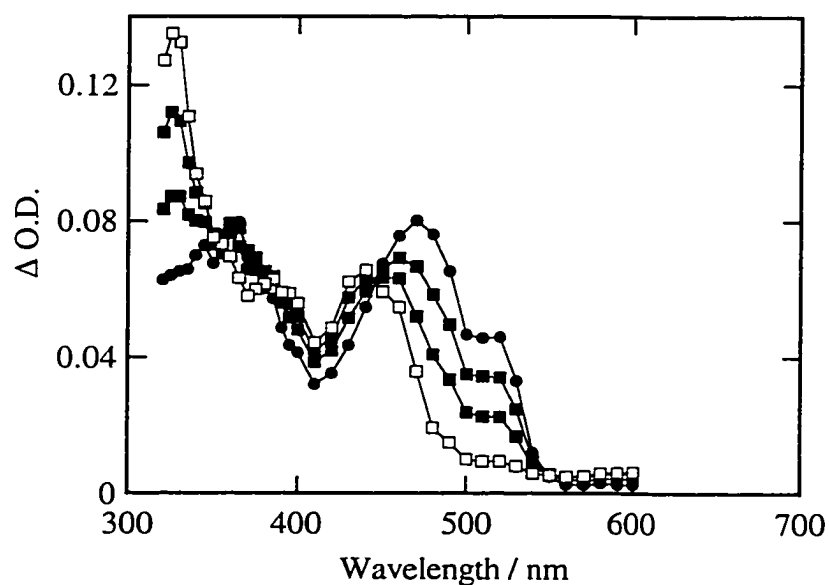


Figure 3-24. Transient absorption spectrum generated 80 ns (closed circles), 360 ns (open circles), 770 ns (closed squares) and 1.85 μ s (open squares) after 308 nm laser irradiation of chloranil in nitrogen-saturated HFIP containing 0.16 mM bicumene.

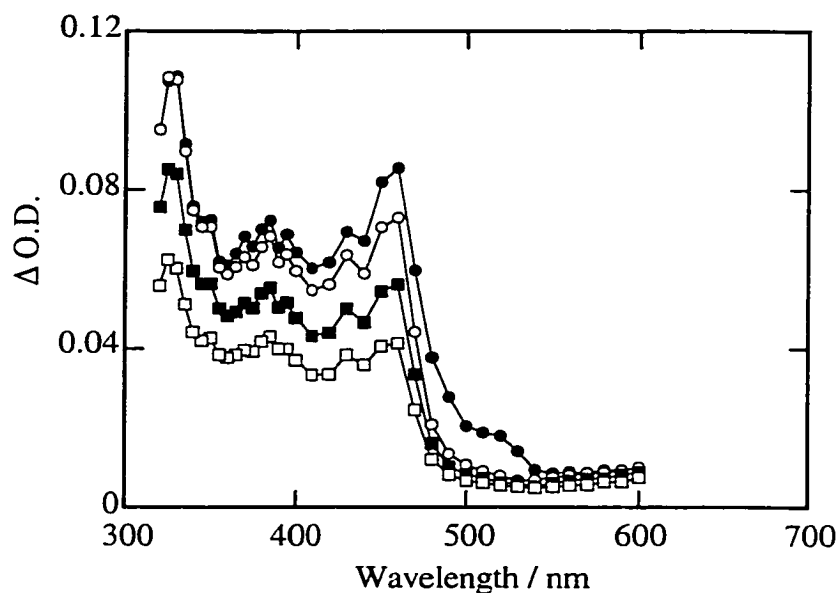


Figure 3-25. Transient absorption spectrum generated 80 ns (closed circles), 430 ns (open circles), 1.57 μ s (closed squares) and 3.70 μ s (open squares) after 308 nm laser irradiation of chloranil in nitrogen-saturated HFIP containing 7.6 mM 3-DMB.

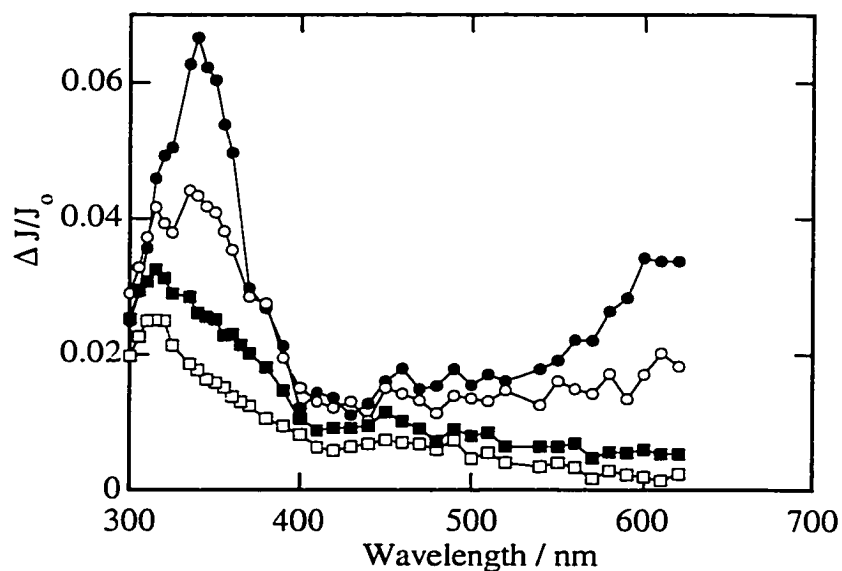


Figure 3-26. Transient diffuse reflectance spectrum generated 200 ns (closed circles), 480 ns (open circles), 1.80 μ s (closed squares) and 7.44 μ s (open squares) after 266 nm laser irradiation of DMeB in evacuated (10^{-4} torr) LiY.

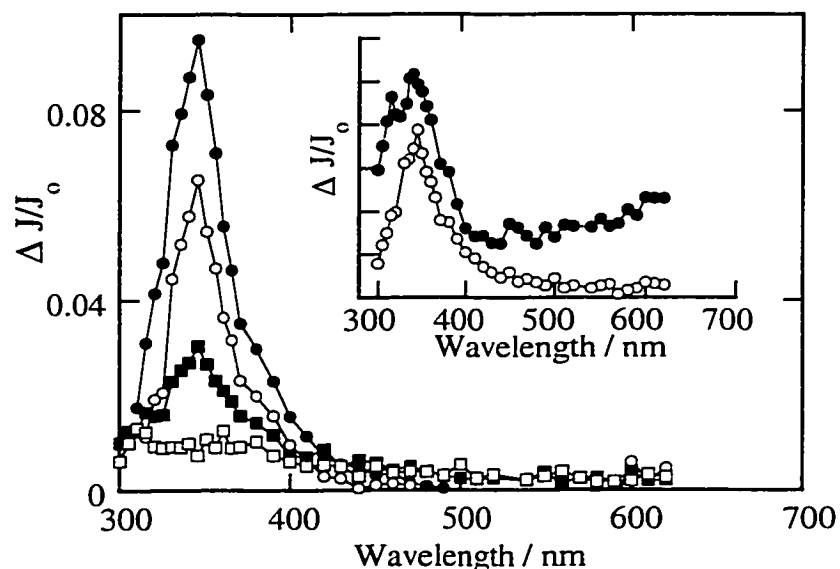


Figure 3-27. Transient diffuse reflectance spectrum generated 80 ns (closed circles), 140 ns (open circles), 480 ns (closed squares) and 3.20 μ s (open squares) after 266 nm laser irradiation of DMeB in oxygen-saturated LiY. The inset compares the transient diffuse reflectance spectra observed 360 ns following laser irradiation of DMeB in LiY under vacuum (closed circles) and oxygen (open circles) conditions.

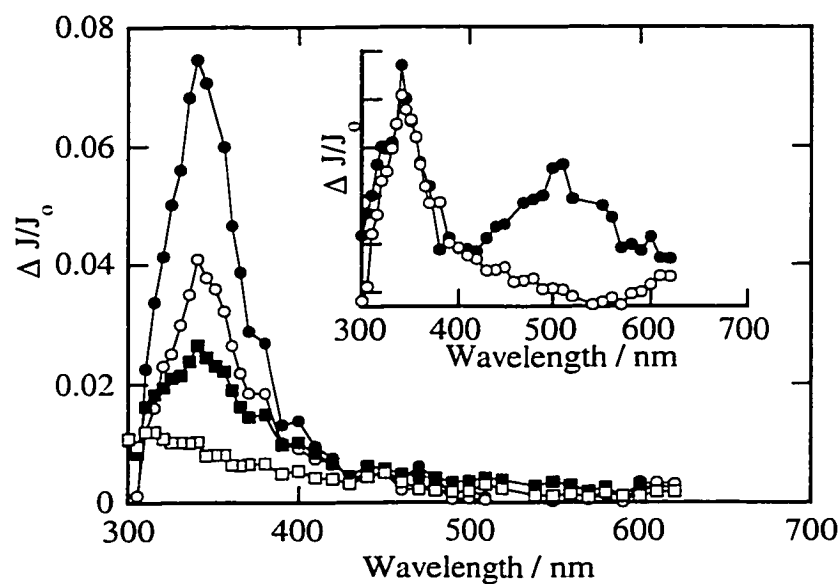


Figure 3-28. Transient diffuse reflectance spectrum generated 80 ns (closed circles), 190 ns (open circles), 360 ns (closed squares) and 3.20 μ s (open squares) after 266 nm laser irradiation of DMeB in oxygen-saturated NaY. The inset compares the transient diffuse reflectance spectra observed 200 ns following laser irradiation of DMeB in NaY under vacuum (closed circles) and oxygen (open circles) conditions.

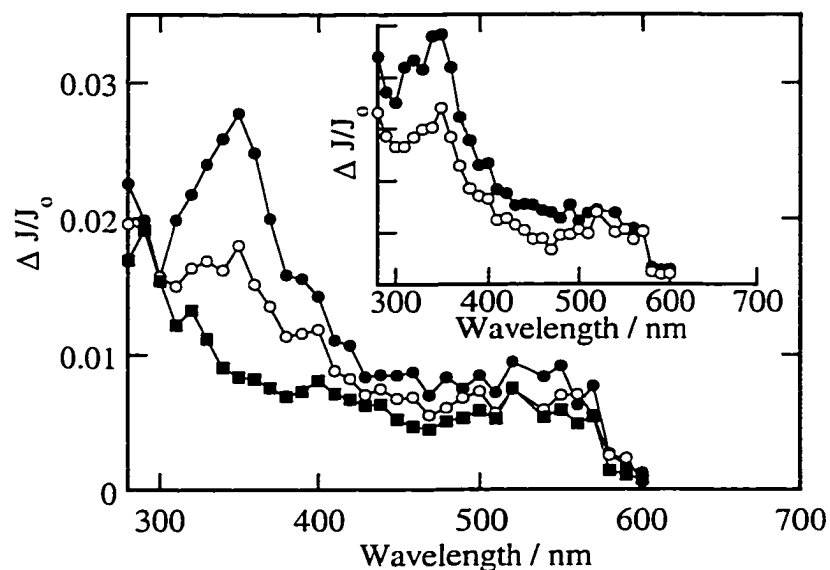


Figure 3-29. Transient diffuse reflectance spectrum generated 80 ns (closed circles), 190 ns (open circles), 360 ns (closed squares) and 3.20 μ s (open squares) after 266 nm laser irradiation of DMeB in oxygen-saturated KY. The inset compares the transient diffuse reflectance spectra observed 200 ns following laser irradiation of DMeB in KY under vacuum (closed circles) and oxygen (open circles) conditions.

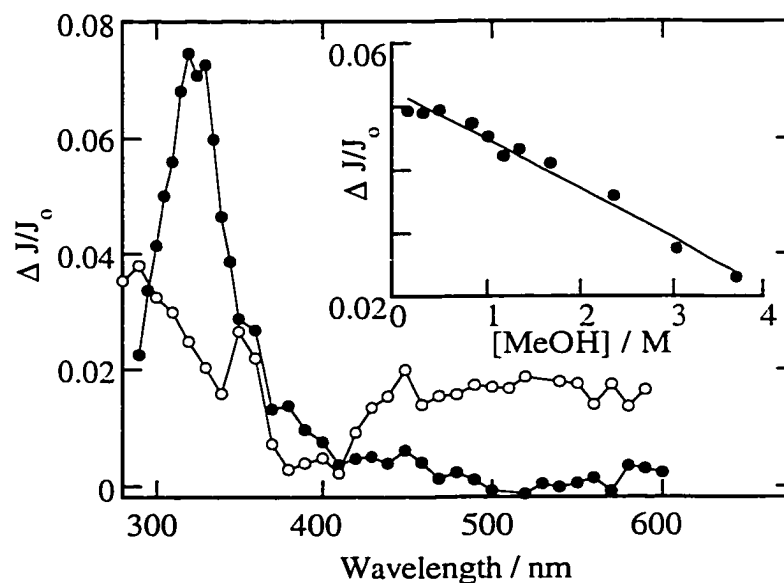


Figure 3-30. Transient diffuse reflectance spectra observed immediately after 266 nm laser photolysis of DMeB in dry (closed circles) and hydrated (open circles) NaY (ca. 10 wt % water). The influence of methanol on the change in diffuse reflectance observed at 335 nm immediately following laser photolysis of DMeB in dry NaY is shown in the inset.

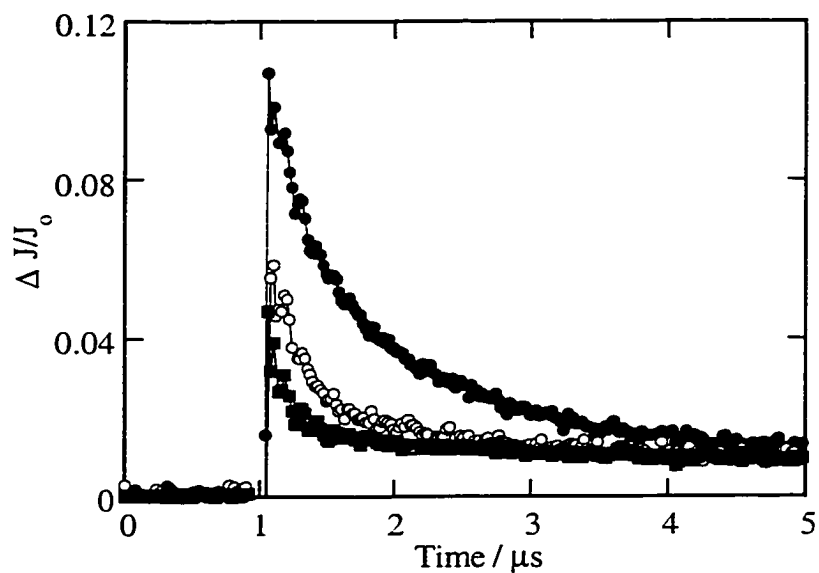


Figure 3-31. Decay traces of the 4-methylcumyl cation observed at 335 nm in oxygen-saturated LiY (closed circles), NaY (open circles) and KY (closed squares).

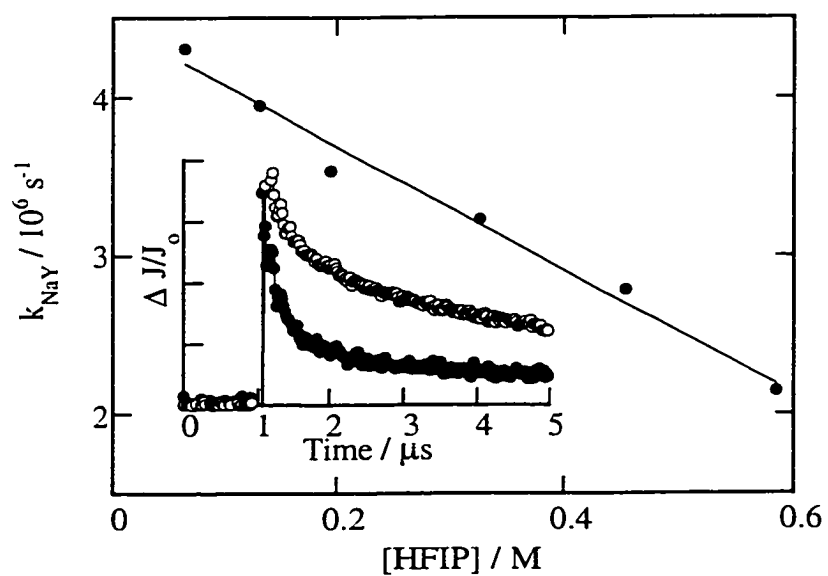


Figure 3-32. Observed decay rate constant for the 4-methylcumyl cation in NaY as a function of HFIP concentration. Inset shows decay kinetics of the 4-methylcumyl cation observed at 335 nm in NaY (closed circles) and NaY containing 1.9 M HFIP (open circles).

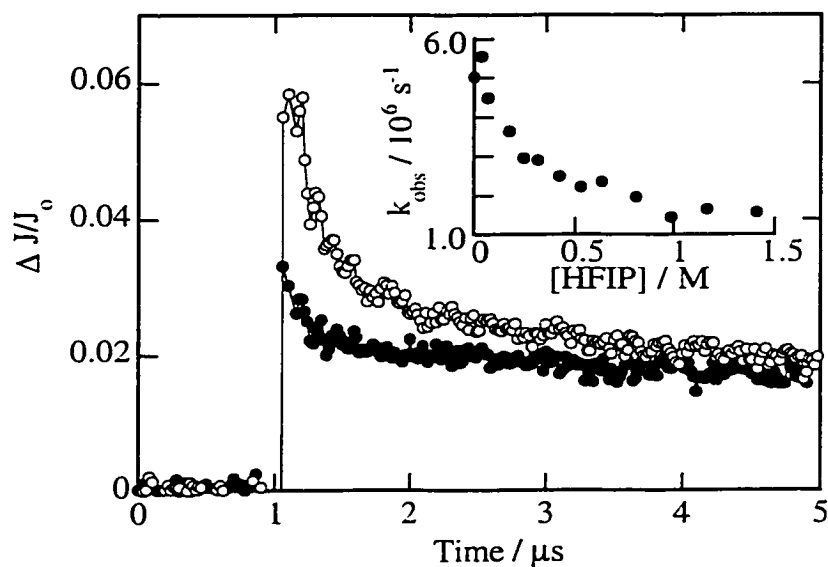


Figure 3-33. Decay traces of the 4-fluorocumyl cation observed at 330 nm in oxygen-saturated LiY (closed circles), and oxygen-saturated LiY containing 0.3 M HFIP (open circles). The variation in decay rate constant of the 4-fluorocumyl cation in LiY with HFIP concentration is shown in the inset.

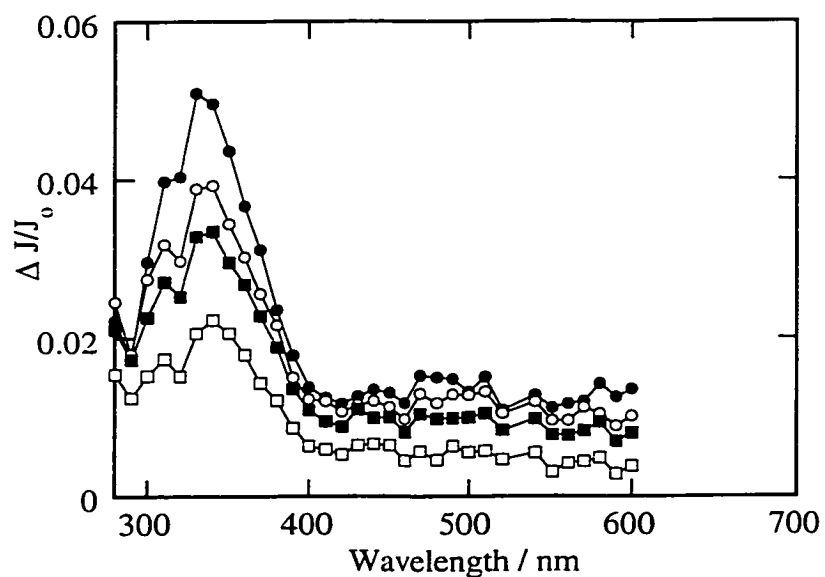


Figure 3-34. Transient diffuse reflectance spectrum generated 2.88 μs (closed circles), 3.48 μs (open circles), 4.72 μs (closed squares) and 15.4 μs (open squares) after 266 nm laser photolysis of DFB in LiY containing 0.8 M HFIP.

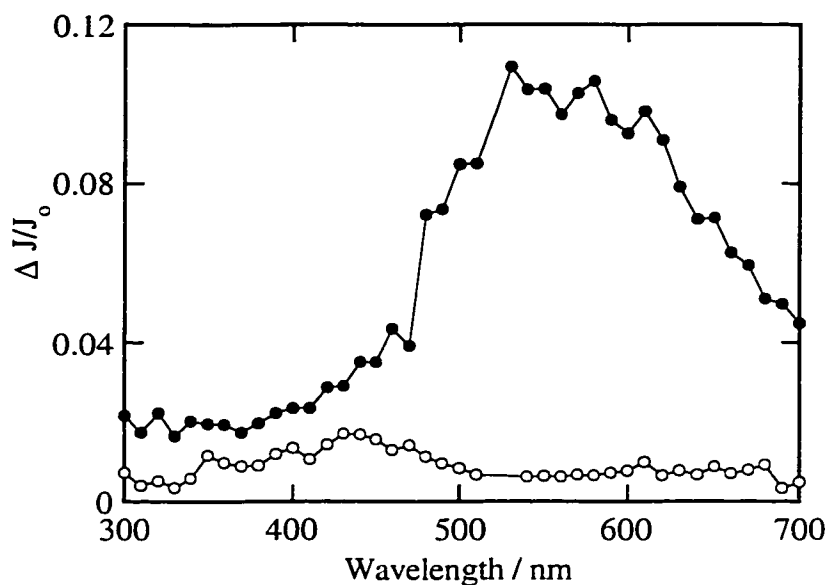


Figure 3-35. Transient diffuse reflectance spectrum observed immediately following 266 nm laser irradiation of 3-DMB in evacuated (closed circles) and oxygen-saturated (open circles) LiY.

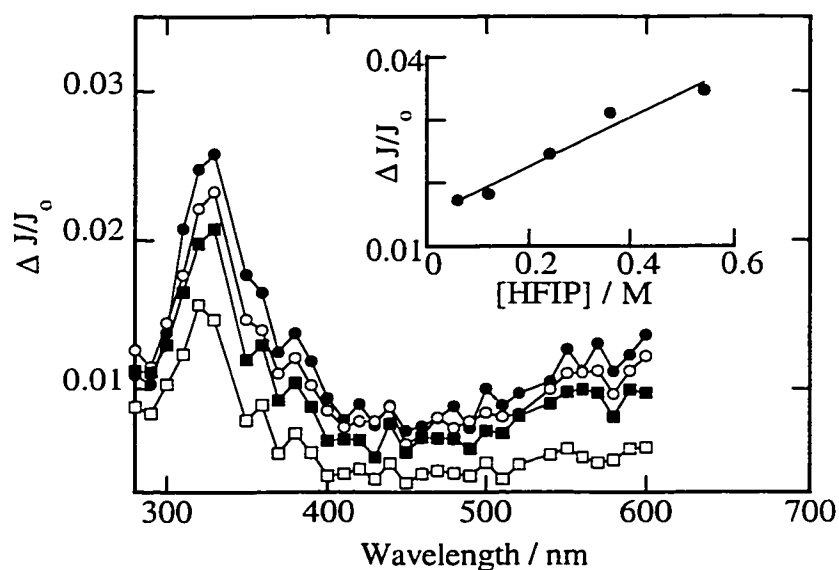


Figure 3-36. Transient diffuse reflectance spectrum generated 3.04 μ s (closed circles), 3.52 μ s (open circles), 4.72 μ s (closed squares) and 15.4 μ s (open squares) after 266 nm laser photolysis of bicumene in LiY containing 1 M HFIP. Inset shows the initial reflectance density monitored at 320 nm as a function of HFIP concentration.

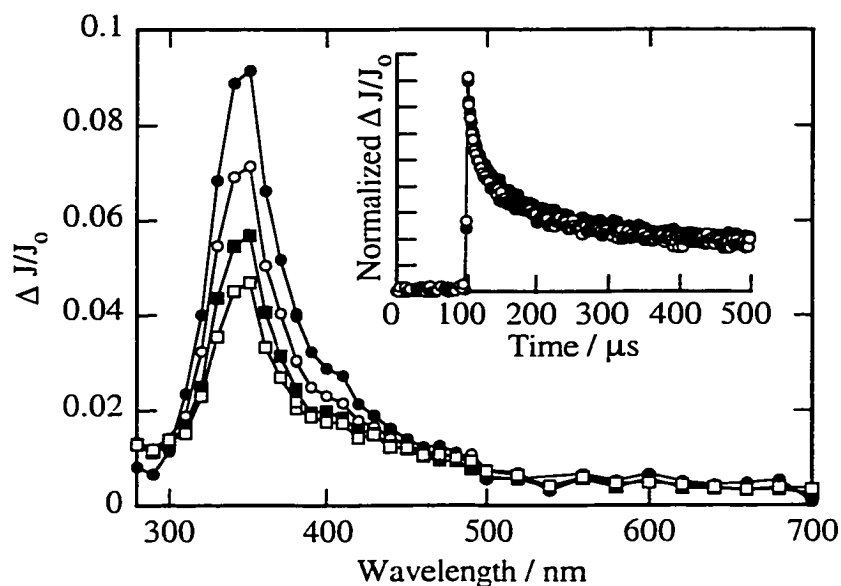


Figure 3-37. Transient diffuse reflectance spectrum generated 160 ns (closed circles), 1.44 μs (open circles), 5.60 μs (closed squares) and 14.8 μs (open squares) after 266 nm laser photolysis of DMeB in oxygen-saturated Na β . The decay traces of the 4-methylcumyl cation monitored at 340 nm under vacuum (closed circles) and oxygen (open circles) conditions are shown in the inset.

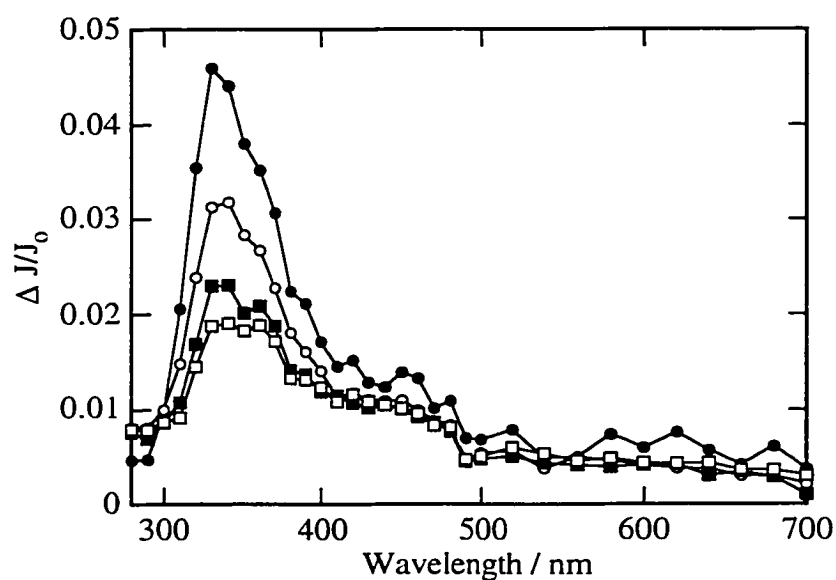


Figure 3-38. Transient diffuse reflectance spectrum generated 160 ns (closed circles), 1.44 μs (open circles), 5.60 μs (closed squares) and 14.8 μs (open squares) after 266 nm laser photolysis of DFB in oxygen-saturated Na β .

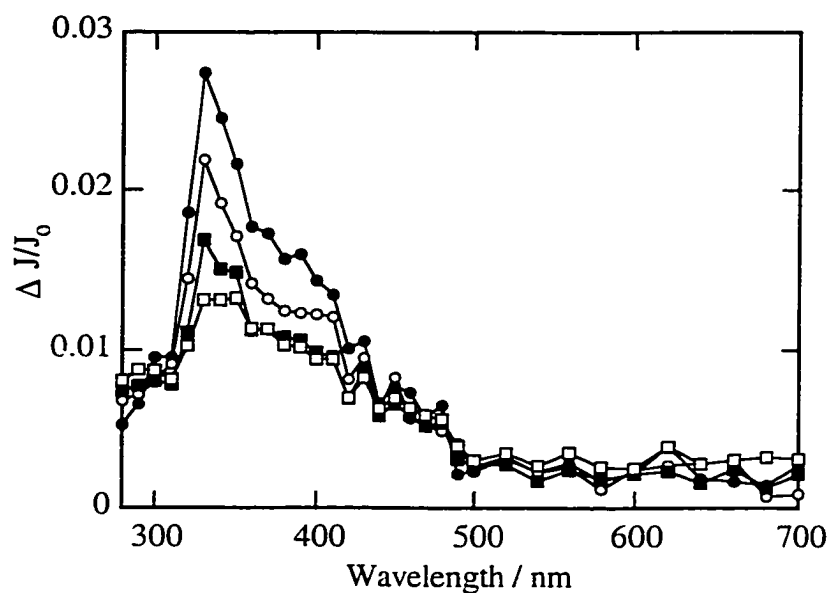


Figure 3-39. Transient diffuse reflectance spectrum generated 400 ns (closed circles), 1.32 μ s (open circles), 4.20 μ s (closed squares) and 14.8 μ s (open squares) after 266 nm laser photolysis of bicumene in oxygen-saturated Na β .

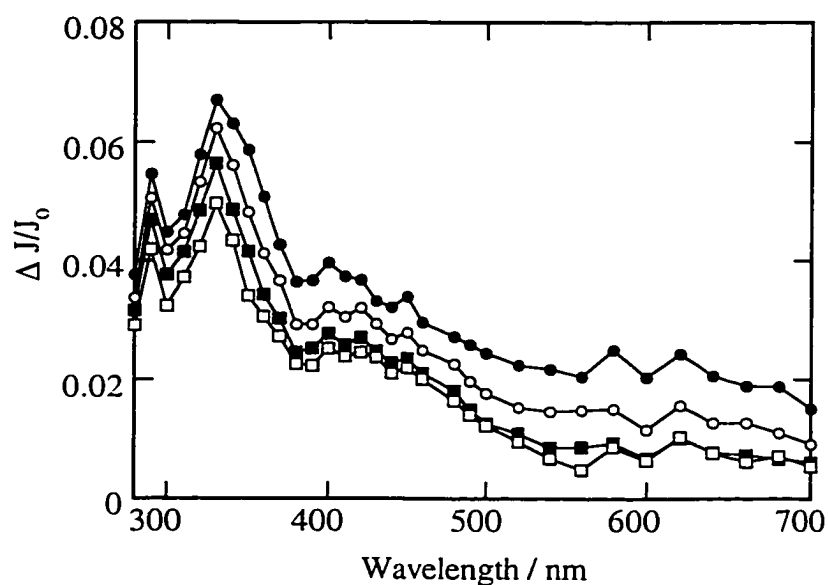


Figure 3-40. Transient diffuse reflectance spectrum generated 400 ns (closed circles), 1.32 μ s (open circles), 4.20 μ s (closed squares) and 14.8 μ s (open squares) after 266 nm laser photolysis of 3-DMB in evacuated (10^{-4} torr) Na β .

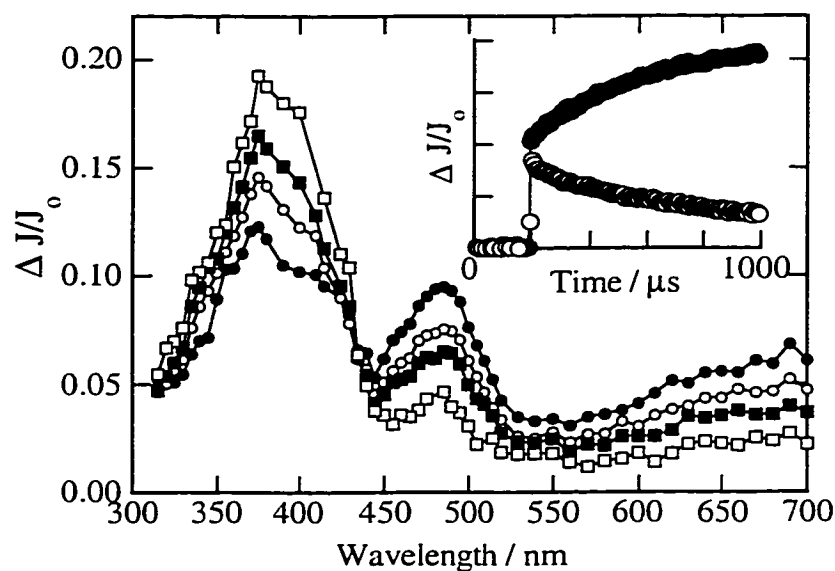


Figure 3-41. Transient diffuse reflectance spectrum generated 4.80 μs (closed circles), 26.0 μs (open circles), 72.8 μs (closed squares) and 149 μs (open squares) after 308 nm laser photolysis of DMAB in evacuated NaY. Inset shows the growth kinetics monitored at 380 nm (closed circles) and the decay kinetics monitored at 485 nm (open circles).

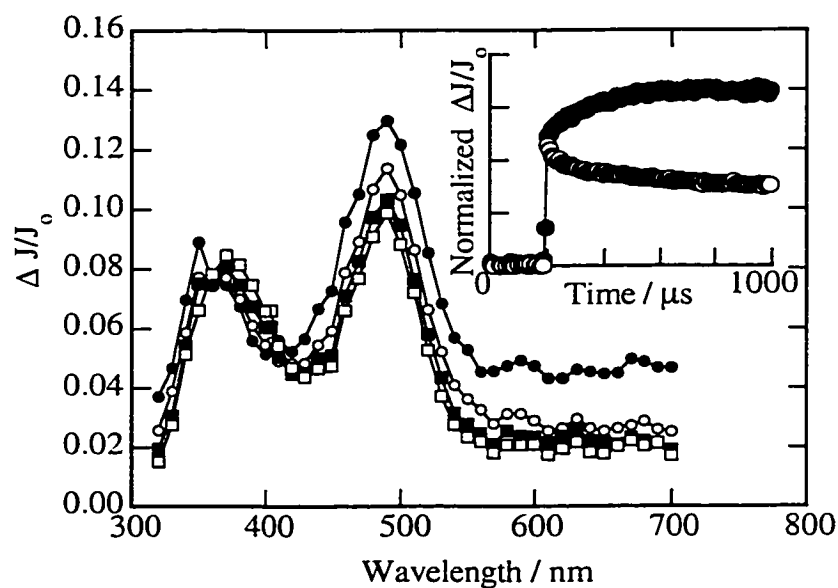


Figure 3-42. Transient diffuse reflectance spectrum generated 8.00 μs (closed circles), 70.0 μs (open circles), 198 μs (closed squares) and 744 μs (open squares) after 308 nm laser photolysis of DMAB in evacuated KY. Inset shows the growth kinetics monitored at 380 nm (closed circles) and the decay kinetics monitored at 485 nm (open circles).

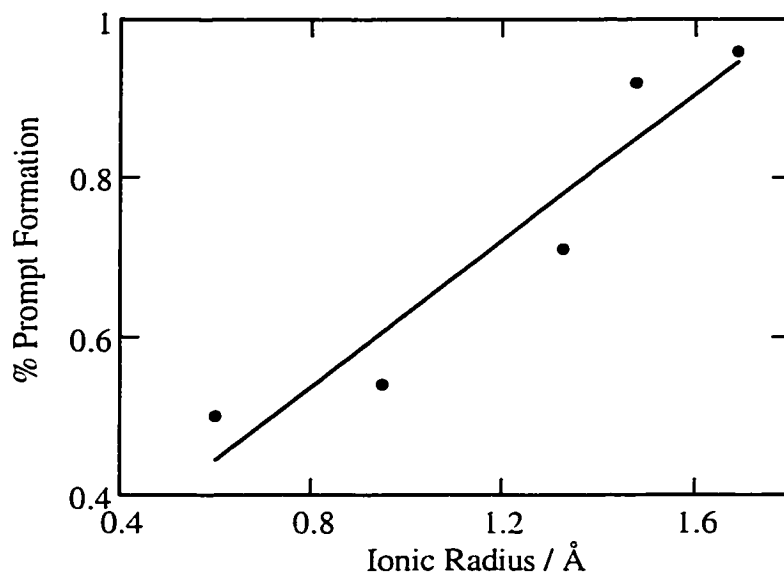


Figure 3-43. Plot of the fraction of prompt formation of the 4-methylaminocumyl cation (*i.e.* within the 10 ns laser pulse) in alkali metal cation Y zeolites versus metal cation radius.

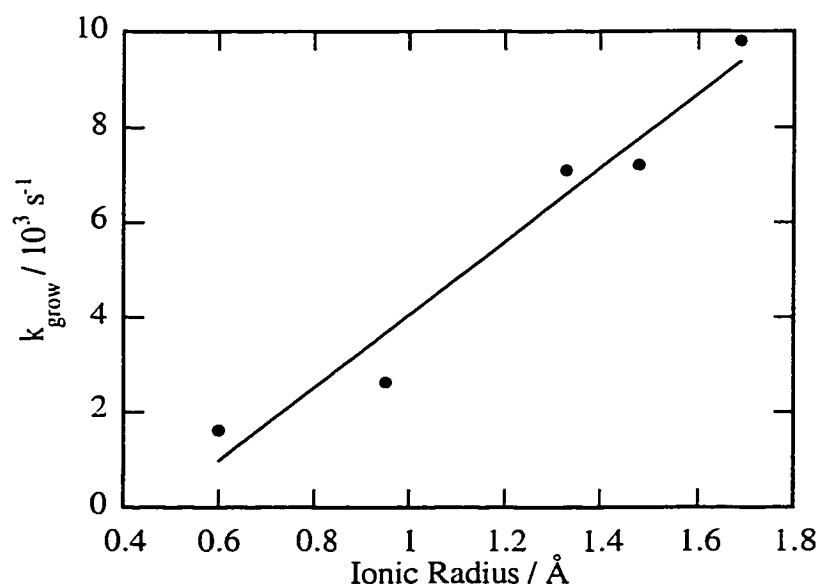


Figure 3-44. Plot of the growth rate constant of the 4-dimethylaminocumyl cation in alkali metal cation Y zeolites versus metal cation radius.

3.2.2 Discussion

3.2.2.1 Mechanism for Formation of Cumyl Cations in Non-Acidic Zeolites

Formation of the reactive 4-methoxycumyl cation upon laser photolysis of DMB within alkali metal cation zeolites is proposed to involve rapid fragmentation of the initially photogenerated DMB radical cation, eq. 3-6. This proposal is completely consistent with the observed reactivity of photoexcited DMB in solution.^{279,280,283} Further support for the proposed mechanism is the formation of 4-methoxycumyl cation following both direct excitation of DMB and ET between DMB and photoexcited chloranil. These observations strongly suggest that the DMB radical cation is the common intermediate and fragmentation of this radical cation is responsible for carbocation formation in each case.

In agreement with the proposed mechanism for carbocation formation is the direct detection of the 4-methoxycumyl radical upon laser irradiation of DMB in alkali metal cation zeolites, and the observation of products derived from this radical following steady-state irradiation of DMB in NaY. Since fragmentation of the DMB radical cation must generate the 4-methoxycumyl radical in addition to the carbocation, the direct observation of the radical and products derived from this intermediate reinforces the proposed mechanism.

According to the proposed mechanism for carbocation formation, every DMB radical cation formed will fragment to yield one 4-methoxycumyl cation and one 4-methoxycumyl radical. If this mechanism is operative in all alkali metal cation zeolites it is expected that the ratio of absorption bands corresponding to each transient species should be independent of the zeolite environment. However, in alkali metal cation Y zeolites the ratio of the intensity of the radical band at 290 nm to the intensity of the carbocation band at 360 nm does not remain constant but increases significantly as the alkali metal cation size increases. An examination of the transient spectra indicates that the overall intensity of the 4-methoxycumyl radical remains fairly constant throughout the alkali metal cation series, and it is a decrease in the intensity of the 4-methoxycumyl cation with counterion size that leads to the observed variation in band ratio. Thus, the yield of the 4-methoxycumyl cation as represented by the intensity of absorption at 360 nm immediately following the laser pulse is significantly lower in zeolites containing larger alkali metal cations such as Rb^+ and Cs^+ compared to Y zeolites containing smaller cations such as Li^+ and Na^+ .

Given the increased reactivity of the carbocation in the larger alkali metal cation zeolites, the reduced carbocation yield in these zeolites is likely a consequence of partial fast quenching of the initially formed carbocation within the laser pulse. As a result, these carbocations would not be detected on the experimental time scale. Such fast quenching of the carbocation is indeed consistent with the dramatic increase in the reactivity of the 4-methoxycumyl cation in CsY compared to LiY. Furthermore, the results obtained in NaX provide additional evidence that fast quenching is responsible for the variation in radical to carbocation absorption ratios. The 4-methoxycumyl cation is significantly more reactive in NaX than in NaY, and has a lifetime similar to that observed in CsY. The ratio of the intensity of the 4-methoxycumyl radical to the 4-methoxycumyl cation in NaX is likewise significantly larger than in NaY and is quite comparable to CsY. Thus, as observed in the alkali metal cation Y zeolites, an increase in carbocation reactivity results in a decrease in the relative intensity of carbocation detected following the 10 ns laser pulse. This is consistent with a partial fast quenching which becomes progressively more important as the reactivity of the carbocation increases and leads to a decrease in the detected yield of the 4-methoxycumyl cation relative to the 4-methoxycumyl radical. In addition, it is expected that the lifetime of the 4-methoxycumyl radical should be relatively long in all alkali metal cation zeolites such that any differences in radical reactivity due to radical mobility will have little impact on the observed intensity ratio of the radical to carbocation bands. The current experimental results are consistent with these expectations as the lifetime of the 4-methoxycumyl radical is several orders of magnitude longer than that of the 4-methoxycumyl cation in alkali metal cation Y zeolites.

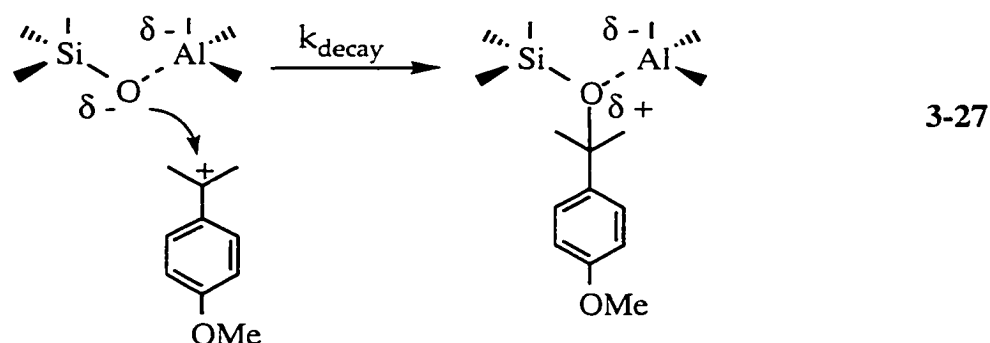
Similarly, the generation of the 4-methyl, 4-fluoro, 3-methoxy, and unsubstituted cumyl cations, involves rapid fragmentation of the initially photogenerated bicumene radical cations within alkali metal cation zeolites. In each case this mechanism is consistent with the experiments carried out in solution where the corresponding radical cation is found to cleave with rate constants greater than 10^8 s^{-1} .

3.2.2.2 Mechanism for Intrazeolite Decay of Cumyl Cations

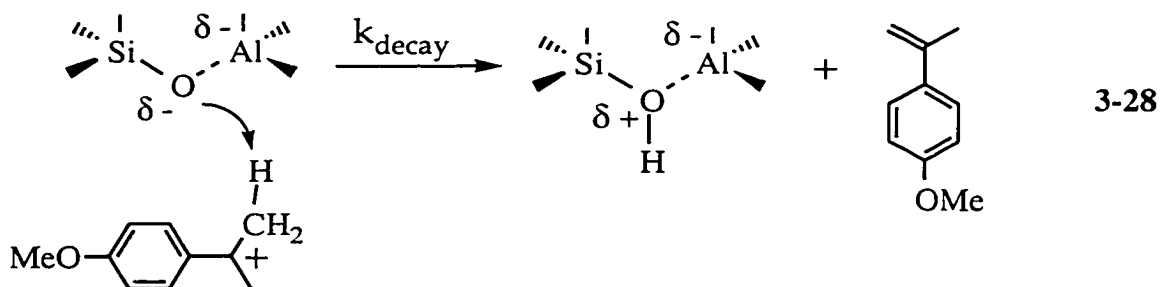
A significant consequence of the current study of zeolite encapsulated 4-methoxycumyl cations is the unambiguous demonstration that this carbocation is a *reactive intermediate* in dry alkali metal cation zeolites. Even under conditions where coadsorbed nucleophiles are rigorously excluded, the lifetimes of the 4-methoxycumyl cation are in the nanosecond to μs time regime. These relatively short lifetimes must

therefore be attributed to a direct interaction between the carbocation and the zeolite host in which it is encapsulated. Furthermore, the reactivity of the 4-methoxycumyl cation is influenced dramatically by the precise nature of the zeolite microenvironment as demonstrated by the variation in lifetime with the alkali metal cation, framework aluminum content and morphology. These observations reinforce the notion that the zeolite framework is a dynamic participant in the mechanism of carbocation decay.

By analogy to the reactivity of carbocations in solution, the mechanism for carbocation decay within zeolites may be envisioned as taking place *via* either addition or deprotonation pathways. For instance, the zeolite could act as a nucleophile, adding to the carbocation to generate a framework-bound adduct, eq. 3-27.



Alternatively, it is possible that the role of the zeolite is as a base, deprotonating the carbocation to yield the corresponding styrene, eq. 3-28.

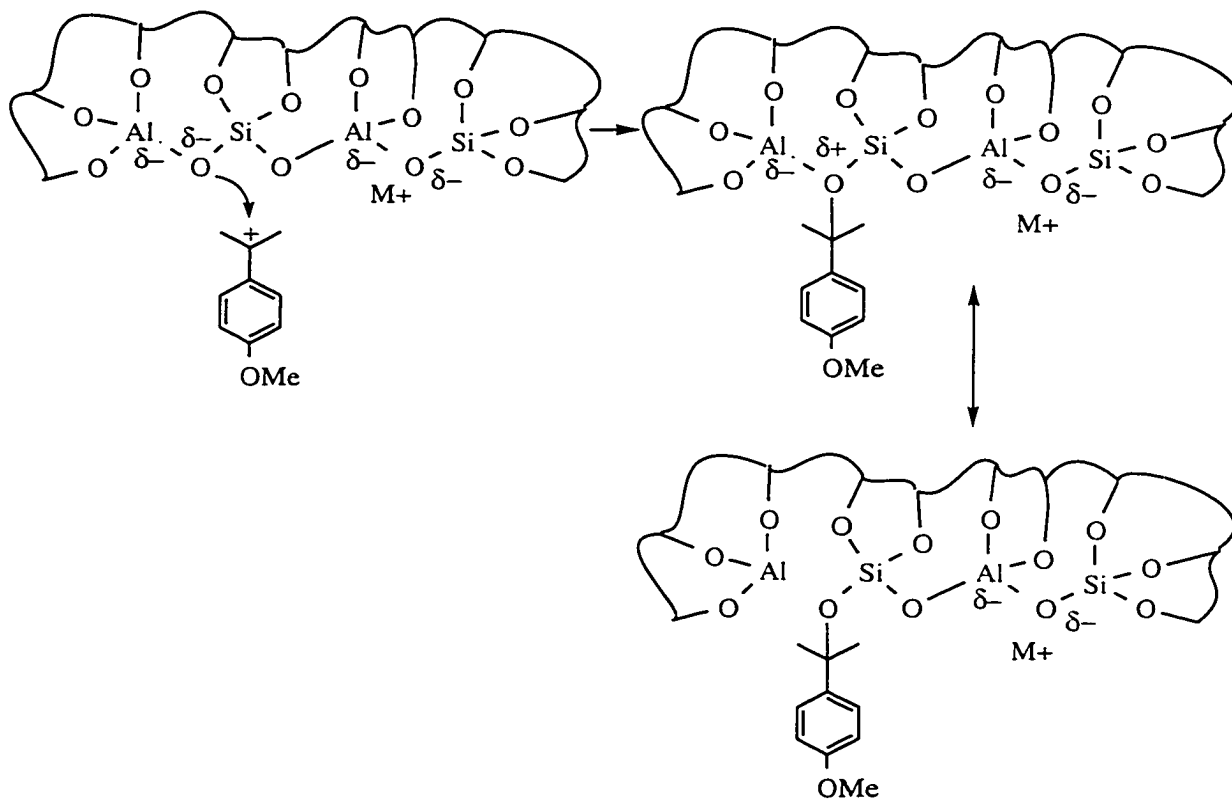


As described below, both the carbocation derived products and the kinetic isotope effects on carbocation decay reveal that the intrazeolite decay of the 4-methoxycumyl cation proceeds *via* nucleophilic addition of the zeolite framework.

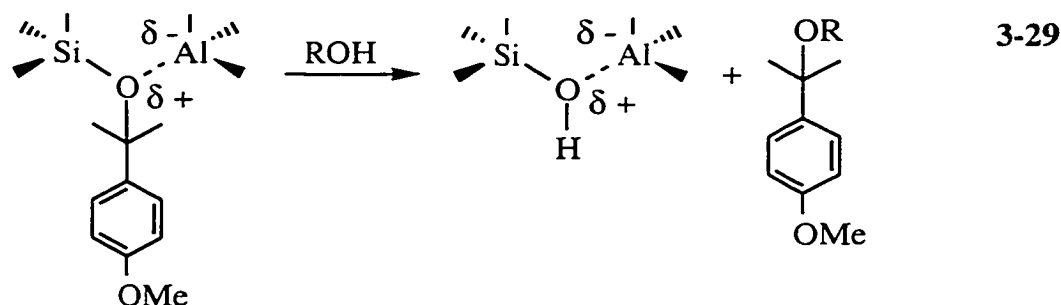
The carbocation derived products observed upon steady-state irradiation studies of DMB within NaY can be rationalized with a mechanism dominated by nucleophilic addition (90 %), rather than deprotonation (10 %). In particular, since the relative yield

of α -methyl-4-methoxystyrene is low, it can be concluded that deprotonation of the 4-methoxycumyl cation by the NaY framework is not a significant mechanistic pathway leading to products. Furthermore, the 4-methoxycumyl methyl ether could only be produced *via* a mechanism that necessarily involves nucleophilic addition of the NaY framework to the carbocation. This mechanism is required since methanol is introduced to the NaY composite only *after* the irradiation period (ca. 80 hours) is complete. Since time-resolved experiments firmly establish that the majority of the carbocations live for only about 5 μ s in NaY, the generation of the 4-methoxycumyl methyl ether cannot be attributed to addition of methanol to the free carbocation. Instead, the initially generated carbocation must first decay to a second, longer-lived intermediate which subsequently reacts with methanol to yield the observed ether product. A reasonable mechanism for carbocation decay involves attack of nucleophilic [Si-O-Al]⁻ framework sites on the free carbocation resulting in the formation of a framework-bound alkoxy species, Scheme 3-6.

Scheme 3-6



Formation of the methyl ether can then be attributed to a solvolysis type reaction of the intermediate alkoxy species in the presence of methanol, eq. 3-29.



A similar mechanistic scheme can also explain the formation of 4-methoxycumyl alcohol, whereby the framework-bound alkoxy intermediate undergoes a solvolysis reaction with water adsorbed by the zeolite framework during the extraction procedure which is conducted in an ambient atmosphere after the photolysis is complete. It is also possible that a small amount of water was present in the zeolite during photolysis to trap a fraction of the framework-bound alkoxy species, or a fraction of the free carbocation. Such water may have been adsorbed by the zeolite during the lengthy photolysis, even under a continuous flow of dry nitrogen or argon. However the precautions taken to avoid hydration during photolysis render it unlikely that enough water was adsorbed to completely account for the relatively high yield of alcohol by direct addition.

The observed kinetic isotope effects are completely consistent with the proposed mechanism for carbocation decay in alkali metal cation zeolites. These isotope effects verify that intrazeolite decay of the 4-methoxycumyl cation does not depend significantly on deprotonation. The measured kinetic isotope effects of $k_H/k_D \sim 1.4$ in all alkali metal cation Y zeolites are very close to unity and thus considerably less than expected for a reaction in which the zeolite acts as a base to remove a proton from the carbon β to the carbocation center, eq. 3-28.³⁰⁹ In fact, studies of deprotonation reactions of cumyl cations by various bases in solution have found kinetic isotope effects in the range of $k_H/k_D \sim 4-5$.^{310,311} The isotope effects measured in Y zeolites closely match values expected for a mechanism that is dominated by nucleophilic addition.^{310,311} Furthermore, the similarity of the measured isotope effects in all alkali metal cation Y zeolites indicates that the mechanism for carbocation decay is consistently nucleophilic addition and that there is not an increasing degree of deprotonation as the counterion size increases. This is significant as it confirms that the variation in carbocation lifetime with alkali metal counterion is not a result of changes in the mechanism for carbocation decay.

The suggested formation of a framework bound alkoxy intermediate within the zeolite is certainly not without literature precedent. Among the numerous studies of

carbocation-mediated reactions and catalysis in acid zeolites, framework-bound alkoxy species have been both proposed and directly observed. For instance, there is considerable evidence from infrared,³¹²⁻³¹⁵ and solid-state NMR studies^{249,253,255,256,259,316-318} of reactive carbocations in Brønsted acid zeolites and even in some uni- and divalent metal exchanged zeolites³¹⁹⁻³²² for the existence of framework-bound alkoxy species. In addition, there have been several theoretical studies which suggest that these intermediates are significant in mechanistic pathways of carbocation-mediated reactions in zeolites.^{263,323,324} Thus, the notion that the μs decay of cumyl cations observed in alkali metal cation zeolites proceeds *via* direct nucleophilic addition of the zeolite to yield framework-bound alkoxy intermediates is consistent with many current views of carbocation behaviour in acid zeolites. In fact, within acidic zeolites, such framework-bound alkoxy species have recently been proposed as mechanistic alternatives to long-lived free carbocations, achieving considerable stabilization through covalent attachment to nucleophilic framework sites. Thus, with the exception of a few highly stabilized carbocations that exist as persistent free species within Brønsted acidic zeolites, carbocations are trapped by the nucleophilic lattice oxygen atoms after some finite time as a transient intermediate (i.e. *via* an $\text{S}_{\text{N}}1$ -like mechanism), or do not actually form, and reaction involves one step addition of the framework oxygen atom to the electrophilic carbon center without proceeding through a carbocation intermediate (i.e. *via* an $\text{S}_{\text{N}}2$ -like mechanism). Similar types of reaction dynamics have been proposed to occur within non-protic zeolites. For instance, the conversion of methyl iodide to ethylene within metal ion zeolites has been described as “acid-base bifunctional catalysis”^{319,320} which can be formally envisioned as an $\text{S}_{\text{N}}2$ -like process whereby the zeolite framework acts as a nucleophile while the metal cation promotes loss of the leaving group.

As a result, the emerging picture of carbocations in acidic zeolite is a continuum of intermediates, from free carbocations stabilized by intermolecular interactions and electrostatic fields within the zeolite, to covalently bound intermediates deriving stabilization from the attachment to electron rich framework sites. Ultimately the transition from one extreme to the other will be a function of the inherent stability of the carbocation within the zeolite microenvironment, and the nature of the zeolite framework. By extending these general concepts to non-acidic zeolites, the results described herein confirm the notion that the role of zeolites in carbocation chemistry far surpasses proton donation and involves dynamic participation of the zeolite framework. Significantly these results, obtained using non-acidic zeolites, provide direct evidence for this continuum of intermediates by detecting the transition from one to another, that is

from free carbocation to framework-bound intermediate, in real time, and provide new insight concerning specific factors about the zeolite microenvironment which regulate the rates of this transition.

3.2.2.3 Reactivity of Cumyl Cations in Dry Alkali Metal Cation Zeolites: Zeolite Nucleophilicity

The experimental results discussed thus far establish that the mechanism for decay of the 4-methoxycumyl cation within alkali metal cation zeolites involves nucleophilic addition of the zeolite framework to the carbocation center. The lifetime of the carbocation varies dramatically with zeolite microenvironment and can be readily modulated by changing the alkali metal counterion, Si/Al ratio and framework morphology. According to the mechanistic proposal for carbocation decay, it should be possible to correlate these parameters and their influence on carbocation reactivity with *zeolite nucleophilicity*.

In the alkali metal cation Y zeolites, the identity of the metal counterion plays a pivotal role in defining the lifetime of encapsulated 4-methoxycumyl cations. For instance, it is possible to observe this carbocation over several hundred μs in LiY, while in CsY it completely disappears in less than 10 μs . As shown in Table 3-4, the lifetime of the 4-methoxycumyl cation decreases dramatically and systematically as the alkali counterion is varied from Li^+ to Cs^+ . Based on the decay mechanism, this 65-fold decrease in the lifetime of the 4-methoxycumyl cation should be associated with an increase in the nucleophilicity of the zeolite framework as the alkali cation size is increased. Several recent studies have emphasized that one effect of cation exchange in Y zeolites is modification of the electron donating ability, or Lewis basicity of the $[\text{Si-O-Al}]^-$ active sites within the framework.^{88,89,95-97,102,103,325} In particular, Cs^+ -exchanged zeolites are considerably stronger Lewis bases than Li^+ -exchanged zeolites. This effect can be rationalized by a progressive decrease in interaction strength between the zeolite counterion and the electron rich framework oxygen sites as the counterion becomes larger and more charge diffuse. Similarly, the tight interaction of a small, charge dense cation such as Li^+ with $[\text{Si-O-Al}]^-$ framework sites will render these sites considerably less nucleophilic than similar framework sites interacting more loosely with a large, charge diffuse cation such as Cs^+ . Variations in cation-framework interactions are thus manifested as significant increases in the framework nucleophilicity, and result in large increases in the rate constant for nucleophilic addition to encapsulated carbocations as the counterion is varied from Li^+ to Cs^+ .

In addition to being affected by the counterion, the kinetic behaviour of the 4-methoxycumyl cation is also strongly influenced by the amount of framework aluminum. For instance, the lifetime of the carbocation in NaX is almost an order of magnitude smaller than in NaY. These zeolites possess identical framework morphologies and counterbalancing cations, but can be distinguished by that fact that NaX has approximately twice the concentration of framework aluminum as NaY. The enhanced reactivity of the carbocation in NaX is consistent with a decay mechanism involving framework addition and can also be correlated to the relative nucleophilicities of NaX and NaY zeolites. Considerable research has shown that the Lewis basicity of zeolites increases as the Si/Al ratio decreases.^{88,90,91,96,97} An increase in Lewis base strength would result in an increase in the nucleophilicity of each site which should enhance the reactivity of these sites towards carbocation addition. The increased reactivity of the 4-methoxycumyl cation in NaX as compared to NaY correlates nicely with this expectation. It must also be recognized that NaX possesses a significantly larger number of [Si-O-Al]⁻ bridges than NaY. NMR investigations^{249,253,255,256,259,316-322} of alkoxy intermediates indicate that framework-bound carbocations covalently attach to [Si-O-Al]⁻ sites and theoretical investigations^{324,326} indicate that the oxygen atoms within [Si-O-Al]⁻ bridges bind carbocations more tightly than oxygen atoms within [Si-O-Si] bridges. Such observations confirm that the [Si-O-Al]⁻ bridges are the dominant nucleophilic sites within the zeolite lattice. As a result, the fact that NaX has a smaller Si/Al ratio than NaY translates into an increase in the number of potential nucleophiles available for attack on encapsulated carbocations in NaX. Thus, in addition to the enhanced nucleophilicity associated with individual sites, the increased concentration of such sites likely also contributes to the higher reactivity of the carbocation in NaX compared to NaY.

The most dramatic variation in carbocation lifetime is observed when the zeolite environment of the Na⁺ faujasites, NaX or NaY, is exchanged for the zeolite environments of NaMor or Naβ. Within these host materials, the 4-methoxycumyl cation is quite unreactive, having estimated lifetimes of ca. 1000 μs and 3000 μs in NaMor and Naβ, respectively. Although these zeolites contain Na⁺ as the counterbalancing cation, they are characterized by particularly high Si/Al ratios (NaMor, Si/Al = 6.5, Naβ, Si/Al = 18). This suggests that the low reactivity of the carbocation within these zeolites is due to a combination of reduced nucleophilicity of active framework sites and a lower concentration of the nucleophilic [Si-O-Al]⁻ bridges relative to the essentially non-nucleophilic [Si-O-Si] bridges. In addition, the framework topology of each of these zeolites is considerably different from the faujasite topology, Table 3-3. Thus, another

important consideration is the more rigorous confinement imposed upon the carbocation by these zeolites. This is particularly important within the one dimensional channel morphology of NaMor. The tighter molecular confinement will inhibit the diffusion of the carbocation towards active nucleophilic sites and may make it more difficult for the carbocation to achieve an orientation which satisfies the electronic and steric requirements associated with formation of the framework bound alkoxy intermediate. Certainly these factors must play a role in defining the observed carbocation lifetime. Notably, however, the 4-methoxycumyl cation is shorter lived in NaMor than Na β , although NaMor is characterized by a significantly more topologically restrictive environment. This suggests that the Si/Al ratio, which is much higher in Na β than in NaMor, continues to play a pivotal role in defining the carbocation lifetime even within zeolites of varied structure.

Since nucleophilicity is an important parameter which defines the lifetime of carbocations within these solid state hosts, a correlation between the observed lifetime trends with a more quantitative measure of zeolite nucleophilicity should exist. According to the proposed mechanism, nucleophilic addition proceeds *via* attack of the framework oxygen within [Si-O-Al]⁻ bridges. Therefore, the nucleophilicity of the zeolite should be proportional to the magnitude of partial negative charge associated with these lattice oxygen atoms. Evaluation of the charge density on individual framework oxygen atoms is certainly not a trivial problem. For instance, not only will the charge density at oxygen atoms of [Si-O-Si] bridges be different from [Si-O-Al]⁻ bridges, but due to the heterogeneous nature of the zeolite environment, the charge density is also expected to vary from one [Si-O-Al]⁻ site to another. As a result of such considerations, a common approach is to assess various physical and chemical properties of zeolites in terms of average values. This approach is not meant to suggest that such homogeneity exists, but is used to envision a global environment within a particular zeolite. Thus, the average charge on the lattice oxygen atoms can provide a picture of the overall nucleophilicity of a zeolite and can be used to compare various zeolite types.

The simplest method for determining the average charge on the oxygen atoms within a zeolite lattice employs Sanderson concepts of electronegativity.³²⁷⁻³³⁰ According to Sanderson's theory of electronegativity equalization, when atoms combine to form a molecule, the individual electronegativities become equal to the geometric mean of the electronegativities of the atomic constituents. Based on this principle, it is possible to determine the equalized electronegativity of a molecule and the partial charge on any atom within the molecule from the electronegativities of the atomic constituents and the molecular formula. As shown in eq. 3-30, the intermediate electronegativity of

any zeolite, S_{zeolite} , can be determined from the unit cell formula where M represents a metal cation and the values of S are the Sanderson electronegativities of the individual atoms given in Table 3-16.

$$\text{For } M_y \text{Na}_{(x-y)} \text{Al}_x \text{Si}_{(192-x)} \text{O}_{384} \quad (x \geq y):$$

$$S_{\text{zeolite}} = (S_{\text{Si}}^{(192-x)} S_{\text{Al}}^x S_{\text{O}}^{384} S_{\text{Na}}^{(x-y)} S_{\text{M}}^y) / (192 + 384 + x) \quad 3-30$$

Table 3-16. Sanderson electronegativities of atomic constituents of alkali metal cation zeolites.

Atom	Sanderson Electronegativity	Atom	Sanderson Electronegativity
Li	0.670	Si	2.138
Na	0.560	Al	1.714
K	0.445	O	3.654
Rb	0.312		
Cs	0.220		

From the intermediate electronegativity of the zeolite and the electronegativities of the constituent elements, the partial charge, δ on any framework atom can be evaluated. The partial charge on an atom within a molecule is defined as the ratio of the change in electronegativity induced upon compound formation to the change in electronegativity induced upon acquiring a full unit charge. For instance, the partial charge on the oxygen atoms within a zeolite framework can be represented by eq. 3-31, where $\Delta S_{\text{O}_{\text{ionic}}}$ is the change in electronegativity associated with an oxygen atom acquiring a full negative charge.

$$\begin{aligned} \delta_{\text{O}} &= (S_{\text{zeolite}} - S_{\text{O}}) / (\Delta S_{\text{O}_{\text{ionic}}}) \\ &= (S_{\text{zeolite}} - S_{\text{O}}) / (1.57 S_{\text{O}}^{1/2}) \end{aligned} \quad 3-31$$

Table 3-17 presents the unit cell composition of each zeolite used in this study of carbocation reactivity, along with the calculated equalized electronegativity and partial charge on the framework oxygen atoms. A plot of the lifetime of the 4-methoxycumyl cation as a function of the charge on the framework oxygen is shown in Figure 3-45. For all the zeolites examined in the present work a clear trend emerges where the lifetime of the encapsulated carbocation increases as the charge on the framework oxygen atom

decreases, which is consistent with the notion of a decrease in the overall nucleophilicity of the zeolite.

Table 3-17. Unit cell composition, equalized electronegativity and partial charge on the framework oxygen atoms for zeolites examined.

Zeolite	Unit Cell Composition	S_{zeolite}	δ_{O}
Zeolite Y	$\text{Li}_{26}\text{Na}_{30}\text{Al}_{56}\text{Si}_{136}\text{O}_{384}$	2.60	-0.350
	$\text{Na}_{56}\text{Al}_{56}\text{Si}_{136}\text{O}_{384}$	2.58	-0.358
	$\text{K}_{54}\text{Na}_2\text{Al}_{56}\text{Si}_{136}\text{O}_{384}$	2.53	-0.375
	$\text{Rb}_{25}\text{Na}_{31}\text{Al}_{56}\text{Si}_{136}\text{O}_{384}$	2.52	-0.378
	$\text{Cs}_{26}\text{Na}_{30}\text{Al}_{56}\text{Si}_{136}\text{O}_{384}$	2.48	-0.391
Zeolite X	$\text{Na}_{86}\text{Al}_{86}\text{Si}_{106}\text{O}_{384}$	2.38	-0.413
Mordenite	$\text{Na}_6\text{Al}_6\text{Si}_{42}\text{O}_{96}$	2.82	-0.278
β	$\text{Na}_4\text{Al}_4\text{Si}_{60}\text{O}_{128}$	2.93	-0.240

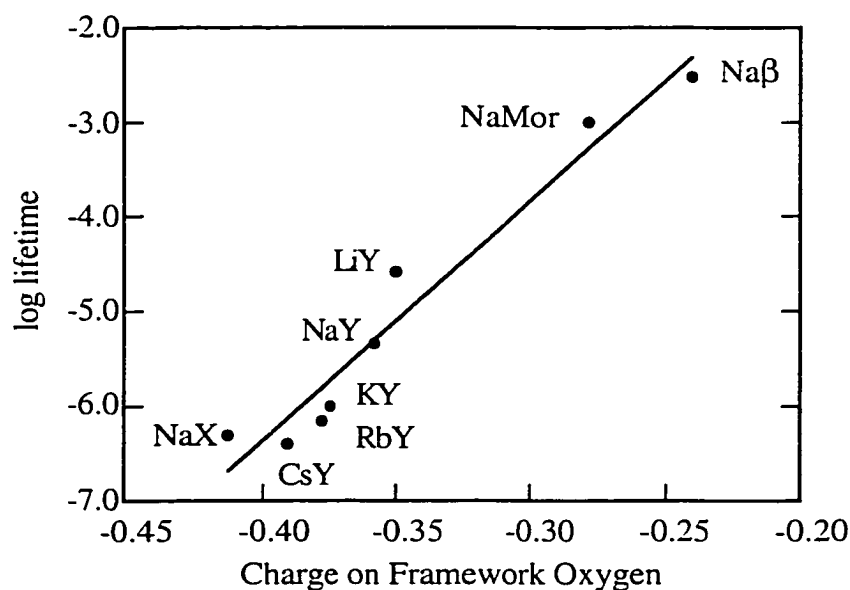


Figure 3-45. Relationship between the lifetime of the 4-methoxycumyl cation in alkali metal cation zeolites and the charge on the zeolite framework oxygen as calculated from Sanderson electronegativity principles.

Interestingly, an analogous trend was recently observed in an NMR study which correlated the isotropic ^{13}C chemical shifts of framework-bound methoxy groups to the partial charges on the framework oxygen atoms determined by Sanderson

electronegativity principles.^{321,322} The observed chemical shift trend was explained in terms of zeolite nucleophilicity and the formation of the framework-bound methoxy groups was attributed to direct nucleophilic attack on the electrophilic guest molecules. In addition, the NMR data also suggested the existence of two distinct framework oxygen atoms, each associated with a unique nucleophilicity. It was proposed that of the four crystallographically non-equivalent oxygen atoms present within the faujasite framework, only the two situated in the α -cage (supercage) would be accessible to guest molecules and thus have an influence on the observed alkoxy formation. While this is likely an oversimplification of the true heterogeneous nature of the zeolite environment and framework nucleophilicity, the current observations of a narrow range of carbocation lifetimes distributed about one or two central values suggests that at least the primary sites involved in forming framework-bound alkoxy species exhibit relatively small variations in nucleophilicity.

Other reactive cumyl cations examined in this study, the 4-methylcumyl, 4-fluorocumyl, cumyl and 3-methoxycumyl cations, exhibit similar intrazeolite reactivity trends as a function of zeolite nucleophilicity. As a result, these cumyl cations are also predicted to decay *via* nucleophilic addition of $[\text{Si-O-Al}]^-$ sites within the zeolite to generate framework bound alkoxy intermediates. Within the alkali metal cation series, the 4-fluorocumyl cation is detected only in LiY. From detailed studies of the 4-methoxycumyl cation, LiY is predicted to be the least nucleophilic alkali metal cation Y zeolite. In fact, based on the current assessment of zeolite nucleophilicity and the short lifetime of the 4-fluorocumyl cation in LiY, expecting to observe this carbocation in the other Y zeolites would be unreasonable. The more reactive carbocations, the unsubstituted cumyl cation and the 3-methoxycumyl cation are not observed in any alkali cation Y zeolites. In order to examine these carbocations within zeolites it is necessary to employ the least nucleophilic zeolite in the series, Na β . Consistent with the significant reduction in nucleophilicity of this zeolite, direct observation of each cumyl cation as a reactive intermediate in Na β is possible.

The slightly less reactive 4-methylcumyl cation is observed in LiY, NaY and KY. In these zeolites the lifetime of the 4-methylcumyl cation becomes progressively shorter as the counterion size is increased, consistent with the proposed decay *via* framework addition and the relative nucleophilicity of these zeolites. Since the 4-methylcumyl cation is observed in three alkali metal cation zeolites, LiY, NaY and KY, it should be possible to correlate the carbocation lifetime with the partial charge on the framework oxygen atoms in these zeolites. As discussed, the existence of such a correlation is consistent with carbocation decay proceeding through nucleophilic addition of the zeolite

framework. Figure 3-46 presents the variation in lifetime of the 4-methylcumyl cation with partial charge on the framework oxygen. As observed for the 4-methoxycumyl cation, a reasonable linear correlation is obtained. Interestingly, the slope of the two Sanderson plots are significantly different. Although the exact value of the slope has no obvious physical meaning, the fact that it is significantly steeper for the 4-methoxycumyl cation than the 4-methylcumyl cation suggests that the overall zeolite nucleophilicity has less influence on the lifetime of the 4-methylcumyl cation than the 4-methoxycumyl cation. Such a suggestion is consistent with the qualitative principles described by the Hammond postulate. Thus, the inherently more reactive intermediate, the 4-methylcumyl cation, is expected to be a less discriminating reactant and exhibit smaller variations in reactivity towards nucleophilic addition as a function of the relative nucleophilic strength.

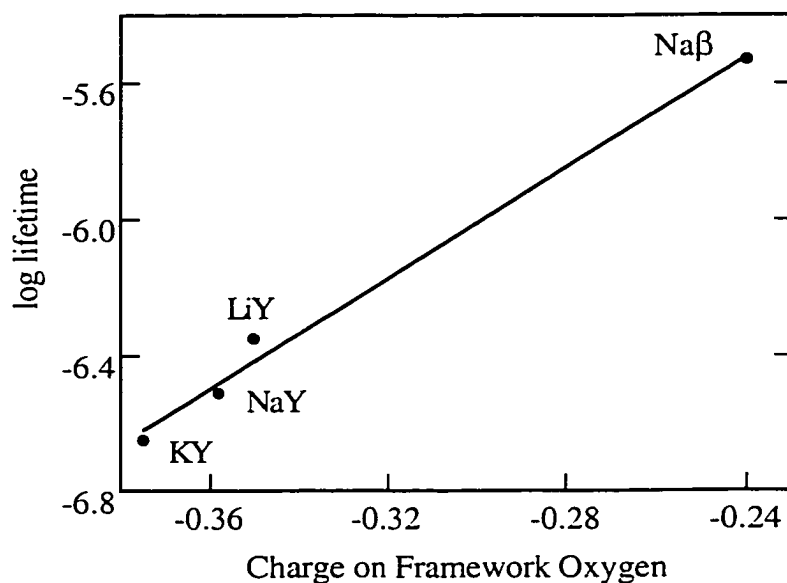


Figure 3-46. Relationship between the lifetime of the 4-methylcumyl cation in alkali metal cation zeolites and the charge on the zeolite framework oxygen as calculated from Sanderson electronegativity principles.

Since the Sanderson plot represents the variation in lifetime of the 4-methylcumyl cation with charge on the framework oxygen, the lifetimes of this carbocation in zeolites where it is not detected can be estimated. Using the measured lifetimes of the 4-methylcumyl cation in LiY, NaY and KY, and the slope of the Sanderson correlation, the lifetime of the 4-methylcumyl cation can be estimated to be 180 ns and 120 ns in RbY and CsY, respectively. These lifetimes correspond to rate constants of $5.5 \times 10^6 \text{ s}^{-1}$ and

$8.3 \times 10^6 \text{ s}^{-1}$. Although rapid, these rate constants are sufficiently small so that the carbocation should be observable with the nanosecond diffuse reflectance apparatus. These results suggest that the failure to detect the 4-methylcumyl cation in RbY and CsY may be due, in part, to inefficient generation of this carbocation in RbY and CsY. A decrease in photoionization efficiency of DMeB in RbY and CsY is consistent with the decrease in Lewis acidity of alkali metal cation zeolites with increasing counterion size.^{30,88,89} Most likely, then, the low yield of 4-methylcumyl cation in combination with the short lifetime of this carbocation renders its detection in RbY and CsY difficult.

The concept of Sanderson electronegativity provides a tool to quantitatively compare a large number of properties relevant to zeolite heterogeneous catalysis. It facilitates an evaluation of the total effect induced by modification of a number of inseparable variables such as the nature and number of counterbalancing cations, and the amount of framework aluminum. As such, limited input, namely chemical composition, is required to describe, rationalize and predict general properties and structure-property relationships. While it is certainly an oversimplification which masks the heterogeneous nature of the zeolite environment, it has proved successful in rationalizing a number of physicochemical characteristics,^{4,331} including Brønsted acidity and catalytic efficiency,³³² Lewis and Brønsted basicity^{88,90,91,325} and redox properties.⁸⁹ For the purpose of the current work Sanderson electronegativity concepts simply provide an additional, more quantitative rationale for the observed variation in zeolite nucleophilicity as a function of counterion and Si/Al ratio. This rationale is consistent with the proposed mechanism of carbocation decay involving nucleophilic addition and predicts the trends observed in carbocation lifetime based on zeolite nucleophilicity.

The absolute nucleophilicity of zeolite active sites is likely not the only factor that defines the intrazeolite lifetime of reactive carbocations. The number of potentially nucleophilic sites available for interaction with the carbocation is also expected to be relevant to the observed reactivity. The number of such sites can be varied by changing the Si/Al ratio. Thus, the increased reactivity of the carbocation in NaX as compared to NaY may also be due to the increased number of nucleophilic $[\text{Si-O-Al}]^-$ bridges with the supercage. Similarly, the decreased reactivity of the carbocation in zeolites NaMor and Na β may be partially attributed to the reduced number of nucleophilic sites accessible to the carbocation in these zeolites. In this regard, the application of Sanderson electronegativity principles are useful as the average framework charges reflect the relative concentration of $[\text{Si-O-Si}]$ sites and $[\text{Si-O-Al}]^-$ sites in the overall zeolite nucleophilicity.

Although zeolite nucleophilicity is certainly pivotal to carbocation reactivity, other factors may play a role in defining the intrazeolite lifetime of encapsulated carbocation intermediates. Of particular relevance in this regard is the ability of zeolites to stabilize positively-charged species. Numerous studies have demonstrated the utility of zeolites as hosts for generating radical cations^{57,58,62,64-66,69,71-73,75,333-335} and carbocations^{62,63,65,66,101,106,110,176} and harnessing the chemistry of these intermediates. In many cases, particularly those involving acidic zeolites, the zeolite host is considered to be a largely non-nucleophilic counterion which can support positively charged species as long-lived entities. The results of the current study clearly show that the framework is much more than a counterion and is in fact an active reagent in the chemistry, in this case participating as a nucleophile. This does not preclude the notion that the unique features of the zeolite environment impart stability to such intermediates. For instance, the mere fact that these reactive carbocations can be generated and observed in the μs time regime indicates that non-acidic zeolites provide an environment that is relatively hospitable to carbocation intermediates.

The electrostatic fields associated with the metal cations within the zeolite cavities are typically assumed to play a significant role in stabilizing charged organic compounds such as carbocations. As shown in Table 1-2, the electrostatic fields within zeolite cavities are strongly dependent on the nature and number of these cations. In alkali metal cation Y zeolites, the electrostatic field in the zeolite cage decreases with increasing alkali metal cation size.³⁰ As a result, the observed decrease in carbocation lifetime with counterion size parallels the decreases in electrostatic stabilization imparted by the zeolite framework and may, in part, reflect a decreased inherent ability of alkali metal cation zeolites to stabilize positively charged intermediates. Notably, however, correlation of carbocation lifetime to electrostatic stabilization alone does not explain the observed lifetime trends. Based solely on electrostatic considerations, the ability of zeolites to stabilize positively charged intermediates should decrease as Si/Al ratio increases. This is contrary to the observed lifetime trends where the carbocation becomes progressively longer-lived as the Si/Al ratio increases. Thus, although the electrostatic stabilization imparted to zeolite encapsulated carbocation intermediates is certainly an important feature in these host-guest systems, the zeolite nucleophilicity must be a dynamic factor governing carbocation reactivity. These concepts are reminiscent of the previous discussion of intrazeolite carbocation chemistry involving a continuum of intermediates and the interconversion of these intermediates. Within this theme, the zeolite host has a continuum of roles, from interacting with a carbocation in a fully ionic sense, providing stabilization by intermolecular interactions and electrostatic fields, to a

fully covalent sense, providing stabilization through binding to electron rich framework sites.

3.2.2.4 Substituent Effects on the Reactivity of Cumyl Cations in Alkali Metal Cation Zeolites

The vast majority of the experimental studies concerning reactive cumyl cations in alkali metal cation zeolites have focused on the 4-methoxycumyl cation. While the specific information derived from studies of this carbocation generates a general picture of intrazeolite reaction dynamics of these intermediates, much can also be learned from studies of other cumyl cations. In particular, the role of substituents in intrazeolite reactivity and the magnitude of substituent effects in different zeolite environments relative to homogeneous solution is not known. In the case of cumyl cations in alkali metal cation zeolites, such studies are hampered by the inherently short lifetimes of derivatives less stable than the 4-methoxycumyl cation and perhaps, in some cases, by less efficient photogeneration from the corresponding bicumene precursors. As a result, an examination of cumyl cations more reactive than the 4-methoxycumyl cation is only possible in zeolite environments with relatively low nucleophilicity. For instance, the 4-methylcumyl cation can be observed directly in LiY, NaY, and KY, but is not detected in larger alkali metal cation Y zeolites. This is due, at least in part, to the enhanced nucleophilicity of these zeolites towards carbocation addition. Consistent with this interpretation is the fact that the lifetime of the 4-methylcumyl cation decreases as the counterion is varied from Li^+ to K^+ . Cumyl cations more reactive than the 4-methyl derivative are only detected in the least nucleophilic zeolites, LiY and Na β . The decay rate constants of the three most stabilized cumyl cations, the 4-methoxy-, 4-methyl- and 4-fluorocumyl cations can be measured in LiY. These carbocations are also observed in Na β along with the parent cumyl cation and the 3-methoxycumyl cation. As a result, the influence of substituent on the reactivity of carbocations in these two zeolites can be evaluated.

The influence of substituents on reactions involving carbocation intermediates is often assessed using linear free energy relationships based on the σ^+ scale. This scale is derived from the $\text{S}_{\text{N}}1$ -solvolysis of cumyl chloride,³³⁶ a reaction in which an initially neutral substrate proceeds through a partial positive transition state to generate a carbocation which then reacts to give the solvent-substituted adducts. Richard *et al.* and McClelland *et al.* have suggested^{225,230} that σ^+ is not the most appropriate parameter for describing reactions initiated by carbocations, particularly since it does not account for

the powerful stabilizing ability of strong π -donating groups on a fully formed carbocation intermediate. Consistent with this suggestion is the observation that strongly electron-donating substituents such as the 4-methoxy or 4-dimethylamino, often fall below the correlation line predicted by the σ^+ scale. As a result an alternative parameter, σ^{c+} , is often applied to reactions of carbocations. The σ^{c+} scale³³⁷ is derived from the ^{13}C NMR chemical shifts of substituted cumyl cations in strongly acidic solutions and therefore more accurately reflects the strong interactions between powerful electron donating groups and a fully formed carbocation intermediate.

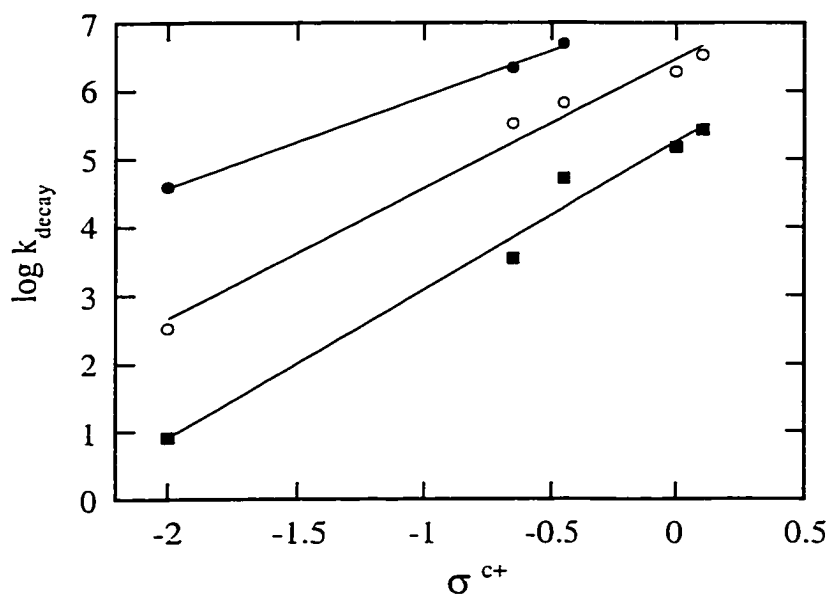


Figure 3-47. Relationship between the observed rate constant for decay of substituted cumyl cations in LiY (closed circles), Na β (open circles) and HFIP (closed squares) and the substituent constant σ^{c+} .

As shown in Figure 3-47, the rate constants for decay of substituted cumyl cations in both LiY and Na β correlate reasonably well with the σ^{c+} parameter. Also included in Figure 3-47 is the correlation between σ^{c+} and the decay rate constants of the cumyl cations measured in HFIP. The slope obtained from each linear free energy relationship, ρ^{c+} , represents the sensitivity of carbocation decay in LiY, Na β and HFIP to substituent effects. The ρ^{c+} values of 1.3, 1.9 and 2.2, respectively, Table 3-18, suggest that the substituents have the greatest influence on carbocation decay in HFIP and the least influence on carbocation decay in LiY. This is in accord with the reactivity-selectivity principle, which simply states that if a reagent is more reactive, it will be less selective as it reacts, and *vice versa*. The reactions currently being considered involve the

transformation of a fully formed carbocation into a carbocation-nucleophile adduct, *via* nucleophile addition. In HFIP, this involves addition of the relatively non-nucleophilic HFIP solvent to the carbocation center generating the nucleophile adduct. In alkali metal cation zeolites, such as LiY, an analogous addition reaction occurs where zeolite framework sites act as the nucleophile and the nucleophile adduct is a framework-bound alkoxy intermediate. The observed substituent effects on cumyl cation reactivity confirm that LiY is a more reactive nucleophile towards carbocation addition than in HFIP. Thus, since HFIP is the least reactive towards carbocation attack, that is, the least nucleophilic, the variation of the cumyl substituents has a greater effect on the rate constants for decay of the carbocation. In contrast, LiY is the most reactive towards carbocation attack, the most nucleophilic, and as a result the ρ^{c^+} value is the smallest. The substituent effects are intermediate in Na β , indicating that the nucleophilicity of this zeolite is less than LiY, but somewhat greater than HFIP.

The linear free energy relationships can also be used to predict the reactivity of other cumyl cations in these zeolite environments. For instance, using the σ^{c^+} correlation observed in LiY, the decay rate constants of the cumyl cation and the 3-methoxycumyl cation in this zeolite are estimated to be $1.8 \times 10^7 \text{ s}^{-1}$ and $2.3 \times 10^7 \text{ s}^{-1}$, respectively. These values are smaller than the detection limit of our nanosecond laser photolysis system to probe intermediates in the solid-state. Based on these extrapolations, the inability to observe these carbocations within alkali metal cation Y zeolites is likely a combination of the large decay rate constants and a relatively low yield from the less easily photoionized bicumene precursor. For instance, the decay rate of $1.8 \times 10^7 \text{ s}^{-1}$ estimated for the cumyl cation in LiY corresponds to a lifetime of 56 ns. This means that 68 % of all cumyl cations generated will have disappeared in 56 ns, a time which represents less than 3 % of the shortest time window generally accessible with the nanosecond diffuse reflectance detection system. At subsequent observable times the remaining transient will be difficult to discern due to its rapid decay and low residual concentration, particularly if the initial yield is small.³³⁸

Table 3-18. Correlation of the substituent parameter, σ^{c+} , with the decay of substituted cumyl cations in various environments.

Medium	ρ^{c+}
HFIP	2.2 ± 0.1
Na β	1.9 ± 0.1
LiY	1.3 ± 0.1

3.2.2.5 Bimolecular Addition Reactions of Cumyl Cations in Alkali Metal Cation Zeolites

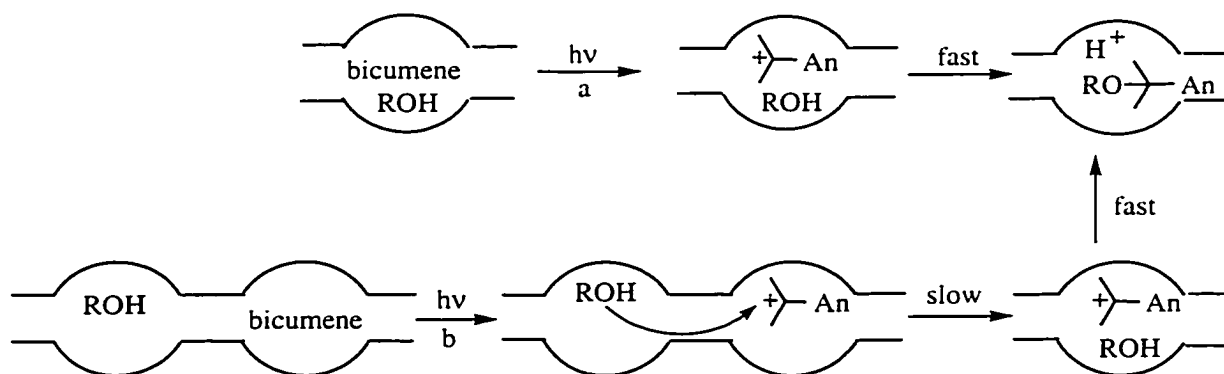
Studies of carbocation reactivity in dry alkali metal cation zeolites under conditions where other adsorbates are rigorously excluded have been used to probe direct zeolite-carbocation interactions and to establish the mechanisms for transformation of carbocation intermediates into reaction products. To obtain further insight into the influence of zeolite encapsulation on the chemistry of carbocations bimolecular reactions of these intermediates have been investigated. Nucleophilic addition reactions constitute an important class of reactions for carbocations in homogeneous solution and the heterogeneous, confined environment of zeolites should provide a versatile medium for modification of these reaction dynamics.

Intrazeolite Addition of Alcohols to the 4-Methoxycumyl Cation. In NaY, the 4-methoxycumyl cation reacts with coadsorbed methanol *via* two distinct types of quenching processes. Dynamic quenching is observed as the rate constant for decay of the 4-methoxycumyl cation increases linearly with increasing concentration of methanol. Rapid static quenching ($> 10^8 \text{ s}^{-1}$) is also observed such that the initial yield of carbocation detected immediately following the ca. 10 ns laser pulse decreases as the concentration of methanol increases.

The observation of static quenching is significant because it indicates that under certain conditions rapid addition of methanol to the 4-methoxycumyl cation takes place within the NaY matrix. A likely scenario where such a rapid reaction may be possible is presented in Scheme 3-7, path (a). In this scenario, a bicumene precursor is initially present in the same zeolite cavity as a molecule of methanol. Upon photolysis, a situation is created where the methanol is encapsulated in the same cavity as the carbocation when it is formed. Under these conditions, rapid intracavity addition of the nucleophilic methanol to the electrophilic carbocation center could take place, as exemplified by the observation of static quenching. Furthermore, the observation of dynamic quenching in addition to static quenching suggests that other conditions exist

where the addition of methanol to the 4-methoxycumyl cation is slow. Since the static quenching suggests rapid intracavity coupling, it is reasonable to assume that the dynamic process involves slow diffusion of the alcohol into the cavity containing the carbocation followed by the rapid intracavity addition reaction, Scheme 3-7, path (b). In combination, then, the observation of both static and dynamic quenching suggests that nucleophilic addition of methanol to the 4-methoxycumyl cation within NaY is *diffusion-controlled*.

Scheme 3-7



Bimolecular reactions of the 4-methoxycumyl cation with other small alcohols in NaY provide additional evidence that these intrazeolite reactions are diffusion controlled. The quenching plot shown in Figure 3-15, and the second-order rate constants for bimolecular addition presented in Table 3-7, provide clear evidence that the efficiency of dynamic quenching decreases dramatically with alcohol size. The magnitude of dynamic quenching is reduced by almost 50 % upon changing the quencher from methanol to ethanol. An even more drastic reduction in quenching efficiency is observed with *isopropanol*, and quenching becomes essentially negligible for the bulky *tert*-butanol. On the other hand, the magnitude of static quenching exhibits little dependence on alcohol size, Figure 3-16. This is significant as it indicates that the actual nucleophilic addition step within the cavity remains rapid even as the steric bulk of the alcohol is increased considerably. Thus the large decrease in dynamic quenching of the 4-methoxycumyl cation within NaY reflects the increasingly hindered diffusion of the larger alcohols through the framework to a cavity containing the carbocation. In combination, then, the variation in dynamic quenching efficiency with increasing alcohol size accompanied by

the invariant static quenching are completely consistent with the addition reaction being controlled by intrazeolite diffusion of the alcohol quencher.

The counterbalancing cation is expected to exert significant control over the mobility of nucleophiles within zeolite materials, particularly for small, polar molecules such as water and alcohols, where intrazeolite diffusion is often dominated by electrostatic interactions between the adsorbate and the zeolite counter cation and/or the anionic framework.²⁵ Therefore, further support for the importance of diffusion in the intrazeolite addition of small alcohols to the 4-methoxycumyl cation is obtained by considering these reactions in other alkali metal cation Y zeolites. Static quenching of the 4-methoxycumyl cation by methanol is observed with similar efficiency in each of the alkali metal cation Y zeolites, Figure 3-14. This is consistent with rapid intracavity coupling of the nucleophile and the carbocation when these reactants are tightly confined and nucleophile diffusion is unnecessary. Conversely, the rate constants for dynamic quenching increase as the counterion increases in size from Li^+ to Rb^+ , Figure 3-13, suggesting that the rate of methanol diffusion also increases with alkali cation size. This is not consistent with a simple model for alcohol diffusion within the microporous zeolite network which assumes that mobility is regulated by steric factors and should therefore decrease as the counterion size increases. Thus, if the interpretation of a diffusion controlled reaction is indeed valid, these results suggest that other factors are important in defining the intrazeolite mobility of alcohols.

Such a suggestion is, in fact, completely consistent with several recent studies.^{27,339-342} In particular, these studies suggest that binding of polar adsorbates will be pivotal to intrazeolite mobility, and reveal that the electrostatic interaction between hydroxyl-containing molecules and the zeolite cations decrease considerably as counterion size increases. For example, temperature-programmed desorption studies have established that water molecules in Li^+ -containing zeolites require up to 20 kJ/mol more energy for desorption than water molecules in zeolites containing larger cations such as Rb^+ .^{27,340} Consistent with this notion are very recent results^{341,342} based on combined theoretical and experimental investigations of the interaction of methanol with alkali metal cation zeolites. The results of this work demonstrate that adsorption of methanol within alkali metal cation zeolites is dominated by interactions between the methanol oxygen atom and the metal cation, while the interaction between the alcohol hydrogen and the framework oxygen is less significant. As a result, the Lewis acidity of the zeolite cation determines the adsorption site and energy of methanol adsorption, and the adsorption energy thus decreases with increasing alkali cation size. Such findings are

consistent with earlier conclusions that the interactions of methanol in Na^+ -exchanged zeolites are predominantly those between methanol and the Na^+ cations.^{339,343}

In combination, the available information indicates that inhibition of alcohol migration due to electrostatic interactions will become less significant as the counterion size is increased. This will lead to an increase in the diffusion of methanol molecules and correspondingly to the observed increase in the rate of dynamic quenching as the counterion is varied from Li^+ to Rb^+ . In the case of CsY, where little dynamic quenching is observed, unfavorable steric factors must dominate over electrostatic binding interactions, with the Cs^+ counterion being sufficiently large to severely inhibit the approach of methanol into the cavity containing the carbocation. Thus, diffusion of methanol around the large Cs^+ is simply too slow to compete with intracavity trapping of the carbocation by nucleophilic addition of the framework, a reaction which is faster in CsY than all other alkali metal cation Y zeolites.

Similar arguments can be used to rationalize the lack of both static and dynamic quenching of the 4-methoxycumyl cation by methanol in NaX. The activation energies for intrazeolite diffusion will be correlated with the charge, concentration and nature of these counterions.²⁵ The significantly higher concentration of cations in NaX (~ 86 per unit cell) compared to NaY (~ 56 per unit cell) will result in a higher activation barrier for diffusion of more tightly bound polar adsorbates in NaX than in NaY leading to corresponding smaller diffusivities in NaX. Consistent with this notion are recent results which show that methanol adsorption in alkali metal cation zeolites is dominated by the strong interaction with the Na^+ cations, and that methanol is more tightly bound in X type zeolites as compared to Y type zeolites.^{136,339,341,342} Furthermore, the inherent reactivity of the 4-methoxycumyl cation is higher in NaX due to rapid reaction with the more nucleophilic NaX framework. Thus, as described for CsY, the hindered mobility of methanol in NaX will render nucleophilic addition by methanol unable to compete with the framework addition.

Rather than steric factors as proposed for CsY, inhibited methanol mobility in NaX is largely attributed to the tight binding of methanol within the zeolite framework. Studies of methanol adsorption verify that the interactions of methanol within NaX are considerably different than within NaY.^{341,342} Methanol adsorbed in NaX is essentially locked within the zeolite micropore due not only to enhanced interactions of the methanol oxygen atom with the increased concentration of Na^+ cations, but also to hydrogen bonding between the methanol hydroxy group and the zeolite lattice oxygen, as well as hydrogen bonding between methanol molecules adsorbed on neighbouring cations within a supercage. Adsorbed methanol in NaX is therefore characterized by strong zeolite-

sorbate and sorbate-sorbate interactions which severely restrict freedom of motion. This picture of methanol in NaX explains why methanol is also an ineffective nucleophile towards static quenching. In addition to restricted intercavity mobility, the tight binding of methanol in the cavities of NaX must also render intracavity mobility very minimal. Furthermore, the extensive network of binding to the methanol oxygen by the metal cation and by hydroxyl hydrogens of other methanol molecules will also significantly reduce the nucleophilicity of the methanol oxygen. Thus, the combination of reduced intracavity motion and reduced nucleophilicity will decrease the reactivity of methanol towards carbocation addition in NaX even when the two are encapsulated within the same cavity.

Since the nucleophilic addition reactions are diffusion-controlled within alkali metal cation Y zeolites, the rate constants for dynamic quenching can be related to the diffusion coefficients of the alcohols. This is done using the modified version of the Smoluchowski equation,¹⁶⁸ eq. 3-32,

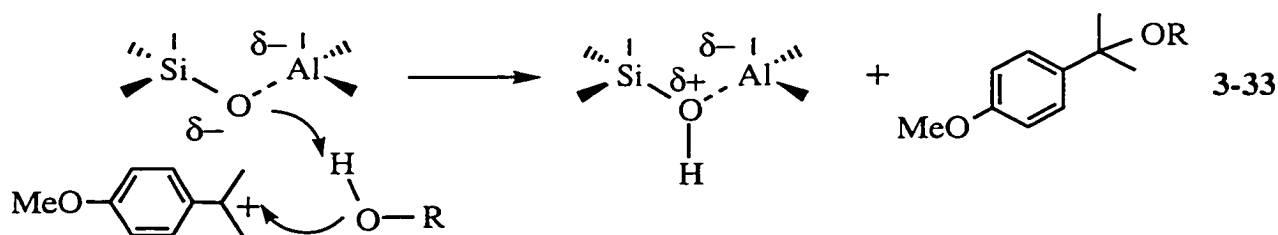
$$k_q = p\pi R_c^2 D_q N_{av} / 1000 R_q \quad 3-32$$

where k_q is the measured second-order rate constant for alcohol addition, $p = 1$, $R_c = 3.5 \times 10^{-8}$ cm, R_q is the radius of the quencher (estimated at 1.1×10^{-8} cm for methanol, 1.4×10^{-8} cm for ethanol, 2.0×10^{-8} cm for *isopropanol*, 2.4×10^{-8} cm for butanol, 2.8×10^{-8} cm for *isobutanol*, and 1.5×10^{-8} cm for TFE), D_q is the diffusion coefficient of the quencher, and N_{AV} is Avagadro's number. As shown in Table 3-19, the calculated diffusion coefficients are on the order of 10^{-9} cm² s⁻¹. These values are within the range expected for diffusion coefficients of small adsorbates in NaY¹³⁶ and therefore reinforce the conclusion that the observed dynamic quenching represents a diffusion controlled process. Furthermore, the diffusion coefficients are observed to decrease with quencher size as predicted for movement of these alcohols through the confined zeolite network. The relatively low diffusion coefficient of TFE may be a consequence of additional binding interactions between the fluoro substituents and the lattice atoms and interstitial cations.¹¹⁶

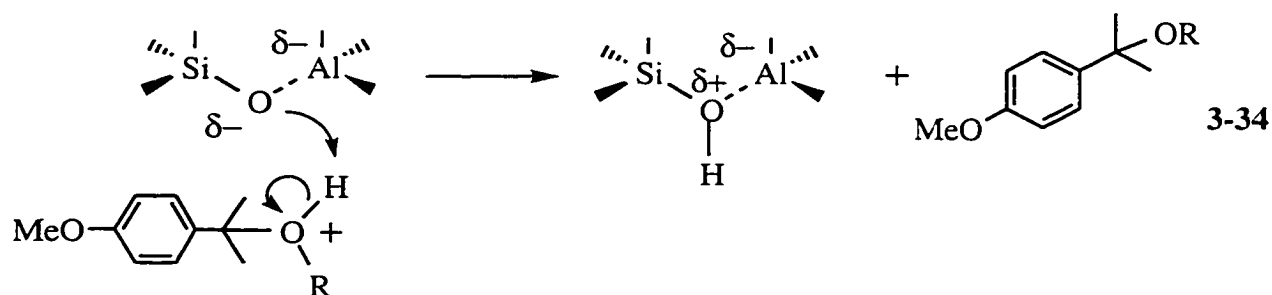
Table 3-19. Diffusion coefficients of various alcohols in alkali metal cation Y zeolites derived from second-order quenching rate constants for alcohol addition to the 4-methoxycumyl cation.

Zeolite	Alcohol	$D_q / 10^{-9} \text{ cm}^2 \text{ s}^{-1}$
NaY	methanol	1.2
	ethanol	0.91
	<i>isopropanol</i>	0.95
	butanol	0.93
	<i>isobutanol</i>	0.67
	trifluoroethanol	0.45
LiY	methanol	0.71
KY	methanol	1.7
RbY	methanol	2.6

Interesting comparisons can be made nucleophilic addition of alcohols to the 4-methoxycumyl cation in alkali metal cation zeolites to the same addition reaction in homogeneous solution. For instance, methanol addition to the 4-methoxycumyl cation in TFE is activation controlled, characterized by a bimolecular rate constant of ca. $9 \times 10^5 \text{ M}^{-1} \text{ s}^{-1}$,²³⁴ which is well below the diffusion limit. Modification of the dynamics of this reaction such that it becomes diffusion controlled within zeolites can be linked with two distinct influences of zeolite encapsulation. First, the zeolite *enhances* the reactivity of the nucleophile towards static quenching. Thus, in NaY, the encounter complex formed between the nucleophilic alcohol and the carbocation proceeds more rapidly to products than in solution. Here the role of the zeolite may be largely *passive*, whereby the enhanced reactivity can be associated with molecular confinement and favorable entropic effects. However the zeolite may also be an *active* participant. For instance, the electron-rich lattice oxygen atoms could assist nucleophilic attack by deprotonating the nucleophile during the addition reaction, eq. 3-33,



or by deprotonating the resultant oxonium ion adduct leading to product, eq. 3-34.



Second, the zeolite *attenuates* the reactivity of the nucleophile towards dynamic quenching. Thus, despite the rapid intracavity reaction of the alcohol and the carbocation, the second-order rate constants for nucleophilic addition are quite small. This effect is certainly associated with the structure and composition of the zeolite interior which inhibits quencher mobility through strong electrostatic binding and hindered diffusion within the restricted topology of channels and cavities. As such, it exemplifies the capacity of zeolites to modify bimolecular reactions of incorporated guests in a passive sense.

Evidence suggesting that alkali metal cation zeolites facilitate rapid intracavity quenching, as proposed in eqs. 3-33 and 3-34 for example, is also provided by considering the behaviour of the carbocation in the presence of less nucleophilic quenchers. For instance, the lifetime of the 4-methoxycumyl cation is approximately an order of magnitude longer in TFE than in NaY. This reactivity trend suggests that TFE is less nucleophilic than NaY. Based on relative nucleophilicity alone, then, addition of TFE to the carbocation within NaY is not expected to be very competitive with framework addition, and intrazeolite quenching by TFE would not be predicted. However, both static and dynamic quenching of the 4-methoxycumyl cation by coadsorbed TFE is observed in NaY. These observations suggest that the reactivity of TFE in addition reactions with the 4-methoxycumyl cation is enhanced through zeolite encapsulation.

Methanol quenching experiments in other zeolite types provide additional evidence for a mechanism involving framework-assisted nucleophilic attack of alcohols on encapsulated carbocations. In contrast to the situation in NaY where both dynamic and static quenching of the 4-methoxycumyl cation by methanol is observed, only dynamic quenching is observed in Na β . One possible explanation for the absence of static quenching of the carbocation in this zeolite is that the carbocation is generated at a

site within the framework that is remote from any site containing coadsorbed methanol. Due to the decreased Si/Al ratio of Na β such a situation could exist; however, it is unlikely, especially considering the relatively large amounts of methanol used in this study (up to 10 wt %). Alternatively, the lack of static quenching observed in Na β is consistent with the notion that the mechanism for intrazeolite quenching involves framework-assisted nucleophilic attack of the alcohols on encapsulated carbocations as suggested above. Thus, basic sites within the framework may facilitate the nucleophilic addition reaction. As the number of such sites and the basicity of each site is relatively low in Na β , the ability of Na β to assist the actual nucleophilic addition step is reduced considerably relative to NaY and rapid static quenching is not observed. Consistent with this proposal is the fact that the bimolecular rate constant for methanol addition to the 4-methoxycumyl cation in Na β is found to be $7.5 \times 10^4 \text{ mg mol}^{-1} \text{ s}^{-1}$. This is 130-fold smaller than the bimolecular quenching rate constant of $1 \times 10^7 \text{ mg mol}^{-1} \text{ s}^{-1}$ measured in NaY. Thus, since the encounter complex in Na β does not readily collapse to quench the carbocation, dynamic quenching is not diffusion limited, but instead becomes activation controlled.

Interestingly, in NaMor, which has an intermediate Si/Al ratio, static quenching continues to take place, suggesting that the NaMor framework can facilitate the addition reaction. Dynamic quenching, however, is not observed in NaMor, presumably due to the inhibited mobility of methanol in the more restrictive one-dimensional morphology of this zeolite. The results of the quenching reactions in NaY, NaX, Na β and NaMor thus clearly exemplify the unique ability of zeolites to alter the fundamental features controlling the reaction dynamics of coadsorbed reagents. Through simple modifications of zeolite structure and composition situations can be accessed where the carbocation is unreactive towards methanol attack (NaX), reacts more slowly with methanol than in solution (Na β), reacts more rapidly with methanol than in solution (NaMor), or reacts with methanol with a variety of rate constants both faster and slower than in solution (NaY).

Intrazeolite Addition of Water to the 4-Methoxycumyl Cation. The reactivity of coadsorbed water as a nucleophile in intrazeolite addition reactions with the 4-methoxycumyl cation is qualitatively similar to that of the alcohol nucleophiles previously discussed. The inclusion of water (2-12 %) in DMB/alkali metal cation Y zeolite composites prior to irradiation results in almost complete quenching of the 4-methoxycumyl cation within the ca. 10 ns laser pulse. As such, the lifetime of the 4-methoxycumyl cation in these hydrated zeolites can be estimated to be < 100 ns. The dramatic reduction in carbocation lifetime induced by the inclusion of water suggests that

the dominant mode of carbocation decay in the hydrated zeolites involves nucleophilic addition of water. The very short carbocation lifetimes under these conditions presumably reflect a significant degree of static quenching whereby carbocations are rapidly trapped by water molecules present in the cavity at the moment of carbocation generation. The dominance of static quenching is anticipated at the higher concentrations of water afforded by the experimental hydration procedure compared to the incremental incorporation of methanol.

The effects of water on the reactivity of the 4-methoxycumyl cation in NaX, Na β and NaMor parallel the effects described upon addition of methanol. Studies of the diffusion of water as a function of Si/Al with NaZSM-5 have demonstrated that the diffusivity of water increases as the Si/Al increases.^{25,139} Thus, in NaX the water molecules are rendered relatively immobile and less nucleophilic such that neither dynamic nor static quenching is observed.¹³⁶ In Na β , the lower concentration and basic strength of active sites reduce the ability of the framework to assist rapid intracavity quenching. As a result, only dynamic quenching of the 4-methoxycumyl cation by water is observed. In NaMor, the restrictive topology inhibits sufficient quencher mobility such that only carbocations formed within close proximity of a water molecule undergo the addition reaction and all observed quenching is *via* static processes.

Addition of Alkyl Enol Ethers to the 4-Methoxycumyl Cation in NaY. Bimolecular quenching reactions of the 4-methoxycumyl cation with a series of alkyl enol ethers exhibit characteristics analogous to those previously discussed for water and alcohols. Namely, both static and dynamic quenching of the 4-methoxycumyl cation is observed in NaY samples containing coadsorbed alkyl enol ethers. Static quenching involves rapid intracavity coupling of the alkyl enol ether and the carbocation, while dynamic quenching involves slow diffusion of the alkyl enol ether into a cavity containing the carbocation followed by the rapid intracavity addition. As discussed for the alcohol nucleophiles, these observations indicate that quenching of the 4-methoxycumyl cation by alkyl enol ethers is diffusion-controlled. The second-order rate constants for alkyl enol ether addition to the 4-methoxycumyl cation in NaY ($k \sim 10^5 \text{ M}^{-1} \text{ s}^{-1}$) are considerably smaller than the activation-controlled rate constants for addition of these nucleophiles to similar carbocations such as the 4,4'-dimethylphenylmethyl cation in solution ($k \sim 10^6\text{-}10^7 \text{ M}^{-1} \text{ s}^{-1}$).²³³ This is a direct consequence of the hindered diffusion of the alkyl enol ethers imposed by the zeolite microenvironment. The intrazeolite diffusion of these alkyl enol ethers can be quantified with the diffusion coefficients derived from the rate constants of these diffusion controlled bimolecular reactions as described in eq. 3-32. As shown in Table 3-20, the diffusion coefficients of

alkyl enol ethers in NaY are comparable to those of alcohols such as methanol and ethanol. These observations support the notion that addition reactions of both alcohol and ether nucleophiles are indeed diffusion controlled.

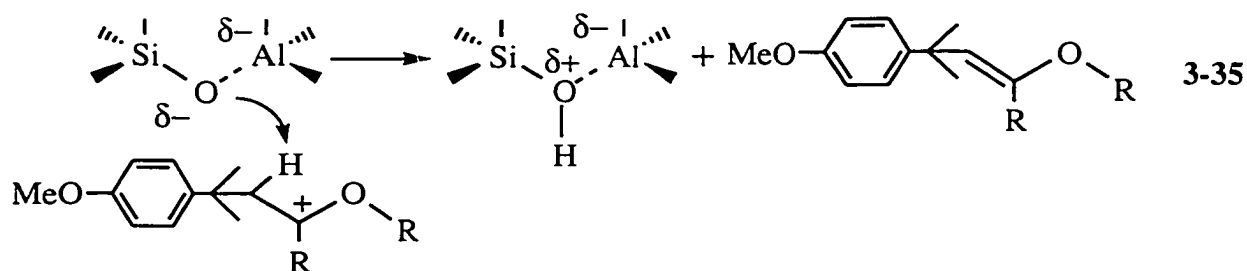
Table 3-20. Diffusion coefficients of various alkyl enol ethers in NaY derived from second-order quenching rate constants for addition to the 4-methoxycumyl cation.

Alkyl Enol Ether	Diffusion Coefficient / $10^{-9} \text{ cm}^2 \text{ s}^{-1}$
EVE	1.8
PVE	1.7
BVE	1.7
<i>t</i> BVE	0.9
IME	1.9
EPE	1.9

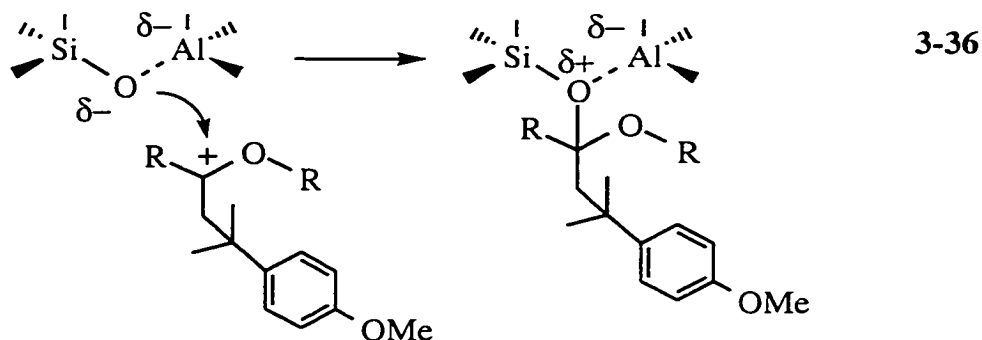
Interestingly, although the diffusion coefficients of both types of adsorbates are similar in magnitude, the values obtained for the alkyl enol ethers are consistently larger than the corresponding similarly sized alcohol. This suggests that the electrostatic interactions and binding between the NaY framework and the alkyl enol ethers is attenuated slightly relative to the alcohols. This is consistent with the expectation of stronger intrazeolite binding of the more polar alcohol hydroxy group than the ether moiety. Notably, however, the differences in diffusion coefficients between the alcohols and the ethers are relatively small. This is also consistent with expectations based on studies of alcohol binding in alkali metal cation zeolites.^{341,342} As previously discussed, these studies establish that the most significant interactions are *via* the alcohol oxygen and the framework cation, with binding of the alcohol hydrogen to the zeolite lattice oxygen atoms contributing significantly less to the overall interaction. A similarly strong interaction between the adsorbate oxygen and the intrazeolite cations is predicted for the ether moiety. Furthermore, the alkyl enol ether might also participate in binding *via* electrostatic or cation- π type interactions between the olefin unit and the zeolite cations. Overall, then, the observation of diffusion coefficients for alkyl enol ethers in NaY which are marginally larger than those of similarly sized alcohols suggests subtle differences in intrazeolite binding of these adsorbates. The structural differences between the alkyl enol ether and alcohol adsorbates along with the current information concerning zeolite binding to these organic moieties are consistent with this suggestion.

A very significant characteristic of the bimolecular addition of alkyl enol ethers to the 4-methoxycumyl cation in NaY is the fact that the reaction is diffusion-controlled for all nucleophiles. In solution, these reactions are activation-controlled with activation barriers and corresponding rate constants for addition that depend strongly on the nucleophilicity of the alkyl enol ether. This contrasts sharply with the reactivity observed in NaY. Thus, while the efficiency of dynamic quenching is dependent on nucleophile size, rapid intracavity addition ($> 10^8 \text{ s}^{-1}$) to the 4-methoxycumyl cation by each alkyl enol ether occurs with similar efficiency. The observation of such a rapid reaction that is independent of quencher nucleophilicity indicates that zeolite encapsulation significantly modifies the dynamics of the addition reaction relative to solution. These modifications result in an intracavity coupling reaction that is notably faster and less discriminating of quencher nucleophilicity than in homogeneous solution. Thus, the zeolite enhances the reactivity of all alkyl enol ethers towards static quenching such that diffusion of the nucleophile to the carbocation becomes rate limiting in all cases. These ideas are analogous to those describing the intrazeolite reactions of alcohols with the 4-methoxycumyl cation where zeolite encapsulation *decreases* the rate of nucleophile diffusion and *increases* the rate of nucleophile addition.

As mentioned above, the enhanced reactivity of alcohol nucleophiles towards static quenching may involve zeolite participation in a passive or active sense. Similar explanations can be applied to the role of the zeolite in intracavity additions of alkyl enol ethers to carbocations. Enhanced nucleophilic addition could arise from molecular confinement effects where the zeolite acts as rigid reaction vessel which enforces close interaction between the carbocation and the alkyl enol ether. In this respect, the role of the zeolite would be largely a passive one. Alternative to, or in addition to, this passive role, the zeolite may actively assist the nucleophilic addition reaction. As shown in eq. 3-19, addition of the olefin moiety to the carbocation yields the carboxonium ion, a secondary carbocation-like intermediate. Thus, active participation of the zeolite could involve a subsequent reaction with this secondary carbocation intermediate thereby moving the reaction towards completion. This reaction could involve deprotonation of the carbocation by the zeolite framework, eq. 3-35.



Alternatively, and more consistent with current studies of carbocation reactivity in alkali metal cation zeolites, the reaction could involve nucleophilic addition of the zeolite framework, eq. 3-36.

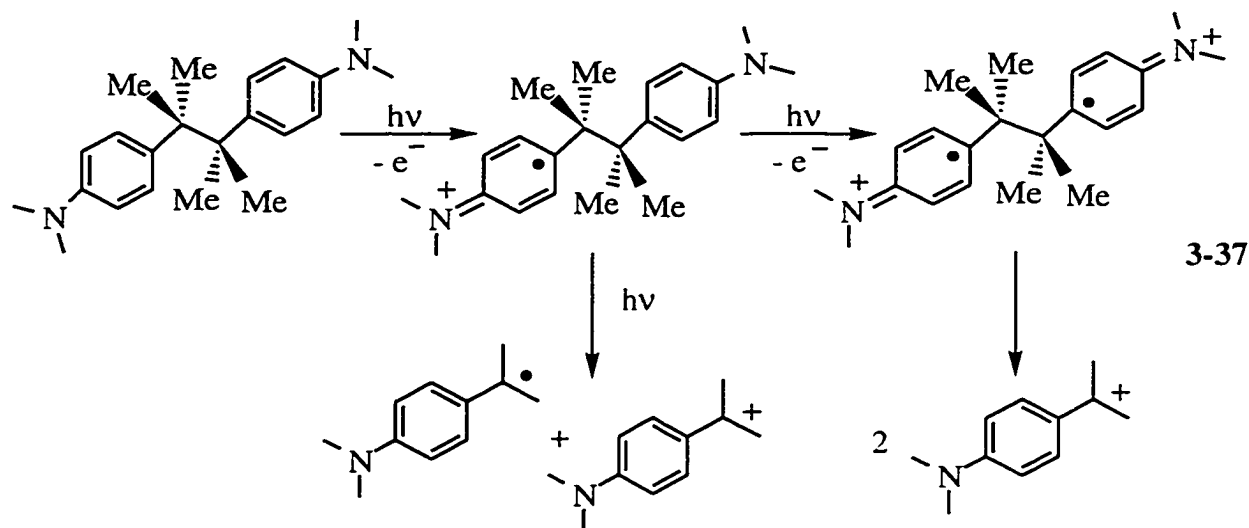


Regardless of the precise mechanism(s), the emerging picture from studies based on several different nucleophiles is one in which the zeolite environment plays a dominant role in facilitating rapid addition of nucleophiles to encapsulated carbocations.

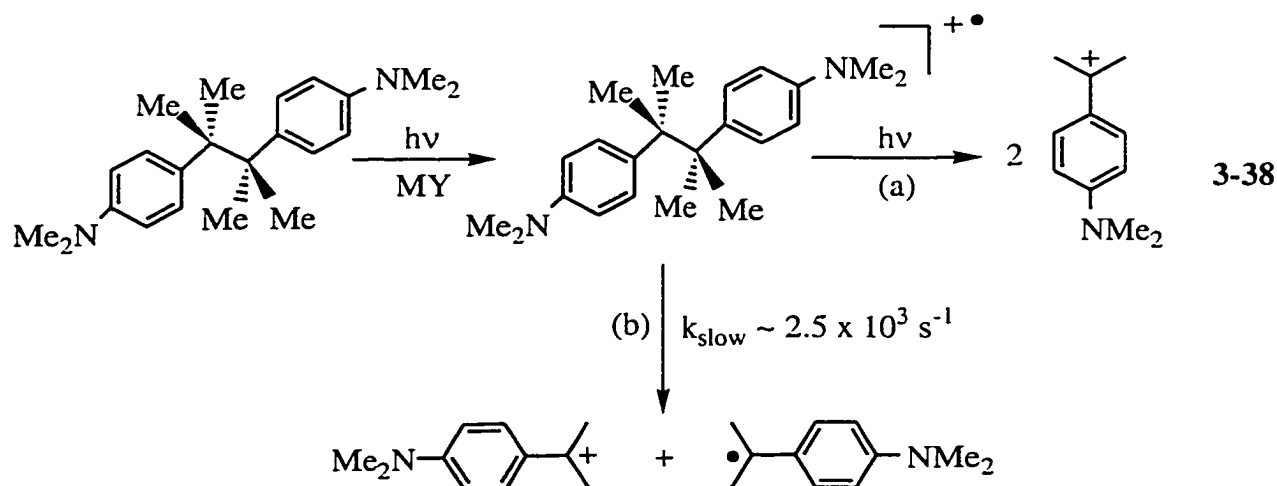
3.2.2.6 Preliminary Ideas Concerning the Formation of the 4-Dimethylaminocumyl Cation in Alkali Metal Cation Zeolites

Experimental studies of photoexcited DMAB in alkali metal cation zeolites were conducted in order to directly observe carbocation formation *via* C-C bond cleavage of photogenerated radical cations. This notion was based on experiments reported in solution, where nanosecond laser flash photolysis of DMAB generates the DMAB radical cation which cleaves on the μs time scale yielding the corresponding 4-dimethylaminocumyl cation.²³⁵ Although nanosecond laser flash photolysis of DMAB in alkali metal cation zeolites does indeed result in the observation of a time-resolved growth at 375 nm which can be attributed to formation of the 4-dimethylaminocumyl cation, the mechanistic details of carbocation formation cannot be completely accounted for by slow fragmentation of the DMAB radical cation as observed in solution. In particular, the experimental results are complicated by prompt carbocation formation. An interpretation of the mechanism(s) for carbocation formation is provided based on these preliminary investigations. However, more experimental results are necessary to accurately explain the dynamics observed upon photoexcitation of DMAB within alkali metal cation zeolites.

One rationale for the experimental observations is presented in eq. 3-37.



The DMAB radical cation formed upon absorption of a photon from a 308 nm laser pulse and ejection of an electron is sufficiently long-lived to absorb a second photon from the same laser pulse. Absorption of a second photon could induce direct cleavage of the radical cation. Alternatively, the second photon may cause a second electron to be ejected to generate a diradical dication which would then undergo bond cleavage to produce two 4-dimethylaminocumyl cations. All of these processes, including the absorption of both photons and the bond cleavage would be sufficiently rapid so that the carbocation would appear within the laser pulse. Therefore, these processes could account for the prompt carbocation formation, eq. 3-38, path (a). The subsequent growth of the 4-dimethylaminocumyl cation observed after the laser pulse is attributed to slow fragmentation of the DMAB radical cation as observed in solution,²³⁵ eq. 3-38 path (b).



Consistent with this second mechanism is the appearance of an isosbestic point at 430 nm in the transient spectrum recorded at relatively long times, Figure 3-41. This suggests that the observed growth of the carbocation at 375 nm originates from decay of the DMAB radical cation at 480 nm. This is also supported by the similarity between the decay kinetics of the radical cation and the growth kinetics of the carbocation.

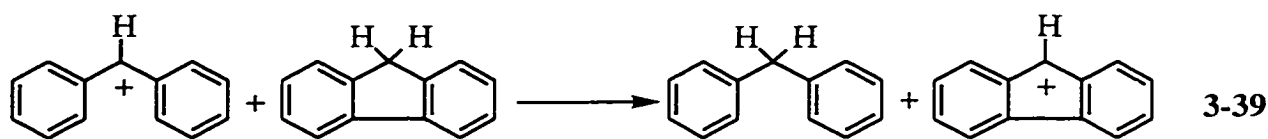
More experimental results are clearly necessary to understand the dynamics which take place upon photoexcitation of DMAB in alkali metal cation zeolites. However, the results obtained thus far definitely indicate that cleavage of the DMAB radical cation takes place within alkali metal cation zeolites and that this fragmentation reaction can be monitored using nanosecond laser flash photolysis. Interesting future work could thus examine the factors which determine the rate constants for C-C bond cleavage of bicumene radical cations in zeolites as compared to solution. Such studies could involve further investigation of DMAB using nanosecond laser photolysis, coupled with picosecond time-resolved diffuse reflectance to examine fast carbocation formation *via* fragmentation of this radical cation as well as the radical cations of other substituted bicumenes.

3.3 Generation and Reactivity of 9-Fluorenyl Cations in Non-Acidic Zeolites

The unusual reactivity of 9-fluorenyl cations has provoked considerable interest and controversy for nearly 40 years. Much of this interest originated from observations that ground state solvolysis reactions proceeding through 9-fluorenyl cation intermediates are several orders of magnitude slower than reactions of the corresponding diphenylmethyl derivatives.³⁴⁴⁻³⁴⁸ These results have initiated on-going investigations into the thermal generation and reactivity of 9-fluorenyl cations,³⁴⁹⁻³⁵⁴ including attempts to directly observe these carbocations under stable ion conditions.³⁵⁵ Although several substituted 9-fluorenyl cations, including those bearing destabilizing groups³⁵⁶ and cationic substituents (e.g., dications of fluorenylidenes and tetrabenzofulvalenes),³⁵⁷⁻³⁶⁰ have been generated in concentrated or super acid solution, the failure to detect the parent 9-fluorenyl cation³⁵⁵ remains one of the most significant aspects of this research and is in sharp contrast to the relative ease of generating diphenylmethyl and dibenzotropylium ions³⁶¹ under these conditions. Research in this area has therefore led to the conclusion that 9-fluorenyl cations are intrinsically unstable and significantly more reactive than diphenylmethyl cations and other structurally related dibenzylated analogs.

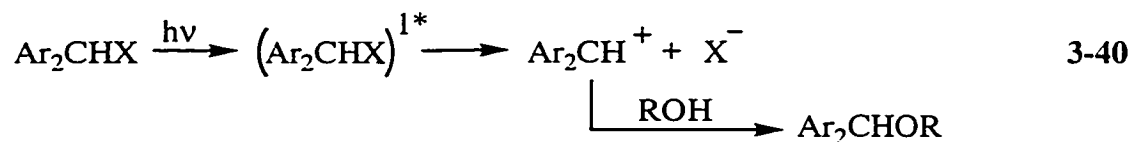
This notion is supported by various standard thermodynamic criteria. The pK_R values of -17.8 ³⁶² (-15.9)^{352,363} and -10.8 ^{364,365} for the 9-fluorenyl cation and the 9-

phenyl-9-fluorenyl cation, respectively, are several log units less than the pK_R values of -13.3^{366} and $-6.6^{366,367}$ for the diphenylmethyl cation and the triphenylmethyl cation, respectively. These differences in pK_R values indicate that the 9-fluorenyl cation is destabilized by 5.7 kcal/mol relative to the diphenylmethyl cation.³⁵² Hydride affinities also demonstrate the instability of 9-fluorenyl cations, with the free energy of hydride transfer to the 9-fluorenyl cation being 4 kcal/mol more exothermic than the diphenylmethyl cation.³⁶⁸ Theoretical investigations confirm that 9-fluorenyl cations should indeed be destabilized relative to diphenylmethyl cations. For instance, the enthalpy of isodesmic hydride transfer, eq. 3-39, has been estimated to be ~ 10 kcal/mol at various levels of theory.^{352,355,369,370}

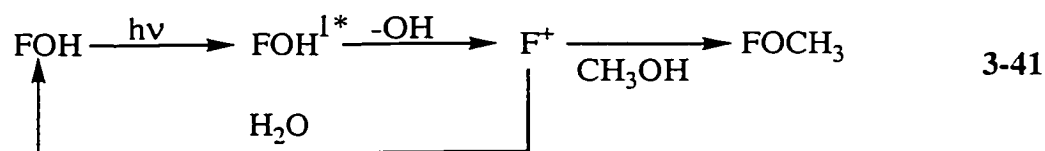


Traditionally, the suggestion that 9-fluorenyl cations are antiaromatic³⁷¹ has been the most pervasive explanation for the decreased stability of these carbocations. The notion of antiaromaticity is rooted in the cyclic conjugation of $4n$ π electrons in 9-fluorenyl cations and is consistent with the view of 9-fluorenyl cations as dibenzocyclopentadienyl cations, and the firmly established antiaromaticity of the cyclopentadienyl cation,^{370,372-374} as well as the indenyl cation.^{370,375,376} However, experimental and theoretical studies both indicate that antiaromaticity may not be the correct explanation for the unusually high reactivity of 9-fluorenyl cations. For example, the pK_R value of the 9-fluorenyl cation^{352,362} is only 4 log units less than that for the diphenylmethyl cation.^{352,366} In contrast, the pK_R value for the cyclopentadienyl cation, a prototypical antiaromatic system, is approximately 20 log units less than that for the allyl cation.³⁷⁷ Furthermore, proton NMR studies indicate that simple substituted 9-fluorenyl cations do not exhibit the paratropic chemical shifts expected as a result of antiaromatic ring currents,³⁶⁰ and recent theoretical work has shown that 9-fluorenyl cations do not fulfil various other magnetic requirements for antiaromaticity.³⁷⁰ As a result, it has been proposed that other factors, such as decreased π stabilization and enhanced van der Waals strain and ring strain, are more appropriate to account for the instability and unusual reactivity of the 9-fluorenyl cation.^{352,370}

In sharp contrast to the inefficient thermal solvolysis of 9-substituted fluorenes, many of these substrates are highly reactive towards photosolvolysis, a reaction which is characterized by photoinduced cleavage of a C-X bond to generate a carbocation intermediate which is subsequently trapped by solvent, eq. 3-40.



In particular, 9-fluorenols exhibit efficient photosolvolysis from the excited state in aqueous media, even though the hydroxide ion is a poor ground state leaving group. The studies of Wan and Krogh³⁷⁸⁻³⁸¹ established that photosolvolysis is initiated by C-O bond cleavage of the excited singlet 9-fluorenol generating the 9-fluorenyl cation intermediate. Steady-state photolysis of 9-fluorenol (FOH) in aqueous methanol results only in the production of 9-methoxyfluorene. In acetonitrile containing 20% ¹⁸O-labeled water, the only product observed after long photolysis times is ¹⁸O-exchanged 9-fluorenol. Similarly, irradiation of this photoproduct in aqueous acetonitrile leads to 100% conversion to the unlabeled alcohol. The mechanism most consistent with these observations involves generation of the 9-fluorenyl cation by photoheterolysis followed by trapping with the solvent, eq. 3-41.



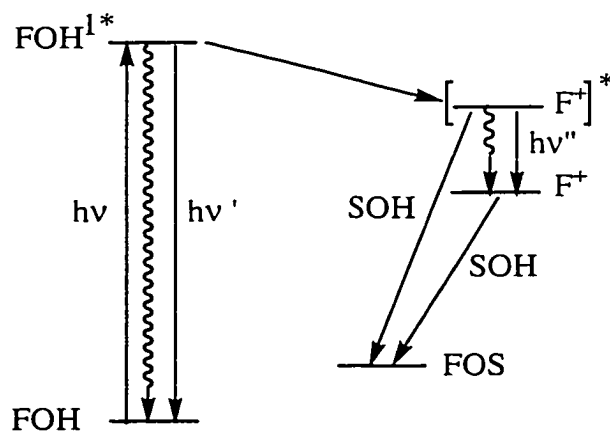
Additional experiments established that photoheterolysis is occurring through the singlet excited state. For instance, the fluorescence lifetime was found to be 300 ps in acetonitrile, but only 30 ps in 50% aqueous acetonitrile. This reduction in singlet lifetime suggests that water is assisting the cleavage of the hydroxide ion from the singlet excited state of the alcohol. Consistent with this interpretation is the fact that no photoreaction was observed using triplet sensitization.

In addition to identifying the 9-fluorenyl cation as an intermediate generated upon photolysis of 9-fluorenol, Wan *et al.* also found that photoheterolysis was surprisingly efficient. Although formation of the highly reactive 9-fluorenyl cation should be much less favorable than other available pathways, the reaction was found to have a quantum yield of 0.15 in aqueous methanol.³⁸⁰ These results indicate that photochemistry provides a mechanism for the efficient generation of fluorenyl cations. The enhanced reactivity of excited states leading to intermediates possessing $4n\pi$ electrons in a

conjugated cyclic array is a complete reversal of ground state reactivity and has been rationalized by proposing that such substrates are aromatic in the excited state.³⁸⁰ This is supported by the idea that singlet excited states of charged species with $4n\pi$ electrons in an internal cyclic array possess aromatic character.³⁸² This implies that the 9-fluorenyl cation has a low lying excited state which is easily accessible to photoexcited 9-fluorenyl, thereby creating a thermodynamically favorable pathway for adiabatic photoheterolysis leading to the formation of the excited state 9-fluorenyl cation, Scheme 3-8. This species can undergo solvolysis directly from the excited state, or decay to the ground state 9-fluorenyl cation which is subsequently trapped by solvent.

Further evidence that carbocation intermediates with $4n\pi$ electrons are readily formed in photosolvolysis reactions comes from experimental results which indicate that related compounds such as diphenylmethanol photosolvolyze with much lower efficiencies.³⁸⁰ Thus, substrates that lack an internal cyclic array, or that produce carbocations with $(4n + 2)\pi$ electrons in cyclic conjugation, do not undergo facile heterolysis upon photoexcitation. Although there is no direct evidence for the aromaticity of excited state 9-fluorenyl cations, ground state 9-fluorenyl cations are clearly attainable *via* a photochemical route that is not available to species lacking the conjugated system of $4n\pi$ electrons.

Scheme 3-8



The fact that photochemistry offers a facile route to reactive 9-fluorenyl cations has opened the door to a myriad of investigations employing laser flash photolysis to generate, directly observe, and examine the reactivity of short-lived 9-fluorenyl cations. 237,239,241,242,383-387 Hilinski and co-workers³⁸⁴ reported the first study of transient

intermediates generated by photolysis of 9-fluoreno1 in aqueous and neat methanol, conditions similar to those employed by Wan and Krogh. A transient absorption band at 515 nm and a weak broad absorption near 610 nm were observed within 30 ps of photolysis of 9-fluoreno1 in 9:1 water:methanol. These transients were extremely short-lived, with lifetimes less than 20 ps. In 1:1 water:methanol, both transients with the same lifetimes were again generated; however, the relative intensity of the 515 nm band was reduced, while the absorption at 610 nm was enhanced. In neat methanol the transient absorption at 515 nm was no longer observed, and the 610 nm transient was considerably more intense with a significantly longer lifetime of about 1 ns. Based on these observations, the transients at 610 nm and 515 nm were identified as the singlet excited state of 9-fluoreno1 and the 9-fluorenyl cation, respectively. These assignments are consistent with the suggestions of Wan and Krogh that water assists heterolysis of the C-O bond in the excited state alcohol. Analogous results were obtained using 9-methyl-9-fluoreno1. In this case the carbocation was assigned to a transient absorbing at 485 nm with a lifetime of 275 ps in aqueous methanol.

Following the studies of Hilinski and co-workers, the photochemistry of 9-fluoreno1 in HFIP was examined using nanosecond laser flash photolysis.²⁴¹ A transient displaying characteristic carbocation behaviour with an absorption spectrum very similar to that previously observed in aqueous methanol was identified as the 9-fluorenyl cation. In contrast to the extremely short lifetime of the 9-fluorenyl cation in aqueous methanol, the lifetime was found to be about 30 μ s in HFIP. The significant decrease in reactivity was attributed to the remarkably low nucleophilicity of HFIP compared to water. Numerous substituted 9-fluorenyl cations have subsequently been generated by photoheterolysis in non-nucleophilic solvents such as TFE and HFIP using laser flash photolysis,^{237,239,242,356,385-387} and the absorption spectra of these carbocations are well characterized. In addition, the absolute reactivity of these carbocations as a function of substituent and steric effects as well as their reactions with aromatic compounds and alkenes have been investigated through these studies.

The lifetime data which have been obtained by time-resolved observations of 9-fluorenyl cations provide direct evidence that these carbocations are significantly more reactive than structural analogs lacking the conjugated $4n\pi$ electron system. For instance, the solvent reactivities of the 9-fluorenyl cation and the 9-phenyl-9-fluorenyl cation are two to four orders of magnitude greater than diphenylmethyl^{229,388,389} and triphenylmethyl²²⁸ cations. In addition, 9-fluorenyl cations also exhibit enhanced reactivity towards nucleophiles, Table 3-21.

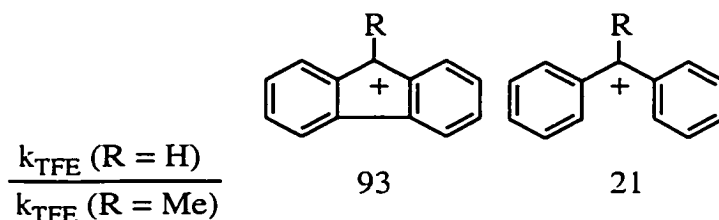
Table 3-21. First-order rate constants for reactions of 9-fluorenyl (F^+), 9-phenyl-9-fluorenyl (PhF^+), diphenylmethyl (Ph_2CH^+) and triphenylmethyl (Ph_3C^+) cations with solvent.

Carbocation	k_w/s^{-1}	k_{TFE}/s^{-1}	k_{HFIP}/s^{-1}
Ph_3C^+	1.5×10^{5a}		
PhF^+	1.5×10^{7b}	1.5×10^{4b}	
Ph_2CH^+	1.3×10^{9c}	3.2×10^{6d}	$\sim 1 \times 10^{1e}$
F^+	$> 4 \times 10^{10f}$	8×10^{8c}	$\sim 4 \times 10^{4g}$

^aRef. 228; ^bRef. 242; ^cRef. 388; ^dRefs. 229, 389; ^eRef. 226; ^fRef. 384; ^gRef. 241.

Further evidence supporting the decreased kinetic stability of 9-fluorenyl cations is the observation that substituents dramatically influence 9-fluorenyl cation chemistry. For example, the effect of methyl substitution on photosolvolysis rate constants of the reactive 9-fluorenyl cation is much more significant than for the diphenylmethyl cation, Scheme 3-9.²²⁶ The large substituent effect on the reactivity of the 9-fluorenyl cation is not associated with a localized positive charge at the C-9 position, as it is anticipated that the phenyl rings of the 9-fluorenyl moiety will be in an ideal position to disperse the positive charge of the C-9 center. This has been shown by ^{13}C NMR studies and semi-empirical calculations of the 9-methyl-9-fluorenyl cation that demonstrate delocalization of the positive charge to the *ortho*- and *para*-positions similar to that observed for the diphenylmethyl cation.³⁵⁵ Furthermore, the substituent effects are not associated with decreased reactivity of the 9-alkyl derivatives as a consequence of large steric effects. The most reasonable explanation for the large substituent effects, particularly upon going from the 9-fluorenyl cation to the 9-methyl-9-fluorenyl cation, is simply that the inherent reactivity of the 9-fluorenyl cation renders it more sensitive to the substituent effects than less reactive carbocation species.

Scheme 3-9



The inherent reactivity of many 9-fluorenyl cations, in particular the elusive 9-fluorenyl cation itself, renders these especially interesting and challenging intermediates to generate and study within the cavities of non-acidic zeolites. With nanosecond time resolution, the 9-fluorenyl cation has only been detected in the highly non-nucleophilic solvent HFIP.²⁴¹ Therefore, observation of the highly reactive and highly unstable 9-fluorenyl cation on the nanosecond time scale in alkali metal cation zeolites would be a remarkable testament to the extraordinary ability of non-protic zeolites to impart kinetic stabilization to electrophilic guests. The parent 9-fluorenyl cation and other reactive 9-substituted-9-fluorenyl cations therefore represent ideal probes for investigations of the ability of non-protic zeolites to host reactive carbocations and influence the chemistry of these intermediates.

Furthermore, the formation of reactive carbocations by photoheterolysis of 9-fluorenyls is also a useful probe reaction, particularly since considerable experimental evidence suggests that the photoheterolysis of the C-O bond of 9-fluorenyls in homogeneous solution is enhanced by ionizing, protic media.^{378-380,384} Therefore, generation of 9-fluorenyl cations within non-protic, cation-exchanged zeolites addresses questions concerning the ionizing ability of the zeolite environment as well as the existence and nature of acidic sites within these frameworks and the potential of such sites to assist heterolysis. Differences in the ability of the zeolite to support or even catalyze the heterolysis reaction as a function of counterion will also provide valuable information on the microenvironment of the zeolite cavity. In addition, the influence of the zeolite environment on alternate reaction pathways available to photoexcited 9-fluorenyls such as ionization and molecular rearrangement can also be explored. Since 9-fluorenyls are known²⁴¹ to undergo both heterolysis and ionization upon photoexcitation in solution, it should be possible to study the competition between carbocation and radical cation formation as a function of the local zeolite environment and interaction of the 9-fluorenyls with different types of acid sites present within the zeolite framework.

The results reported herein concern the generation of the parent 9-fluorenyl cation and a series of 9-substituted-9-fluorenyl cations *via* photoheterolysis of 9-fluorenyls within alkali metal cation zeolites, and the direct observation and investigation of these reactive carbocations on the nanosecond time scale. These investigations are directed towards understanding the ability of non-protic zeolites to mediate heterolysis and influence the reactivity of positive ion intermediates. Particular emphasis is placed on the influence of the alkali metal cation and coadsorbed reagents on the photoheterolytic generation and intrazeolite reactivity of 9-fluorenyl cations. The availability of several reaction pathways, other than heterolysis, to photoexcited 9-fluorenyls within the zeolite

cavities is also demonstrated and shown to be modified by coadsorbed protic reagents in a manner consistent with solvent-assisted dehydroxylation.

3.3.1 Results

The following sections present results concerning laser photolysis of 9-fluorenols in alkali metal cation zeolites. In all cases, the excitation source was 308 nm laser light with a pulse width of ca. 20 ns. The laser experiments were carried out under similar conditions as those described in the previous section. Preparation of the 9-fluorenol/zeolite composites and inclusion of coadsorbates within these composites was essentially identical to that previously described for bicumene/zeolite composites. The only deviation to note is that the 9-fluorenol precursor was typically introduced to the hexane/zeolite slurry as a small volume (100 – 500 μL) of a dichloromethane stock solution. The average loading level is typically about one 9-fluorenol molecule in every 10 cavities ($\langle S \rangle \sim 0.10$) in faujasite zeolites, or approximately 20 mg/g in the zeolites NaMor and Na β . Again, the utmost care was taken to prevent inclusion of water during the preparation of the 9-fluorenol/zeolite composites, and throughout the laser experiments.

3.3.1.1 Laser Photolysis of 9-Alkyl- and 9-Vinyl-9-Fluorenols in Alkali Metal Cation Zeolites

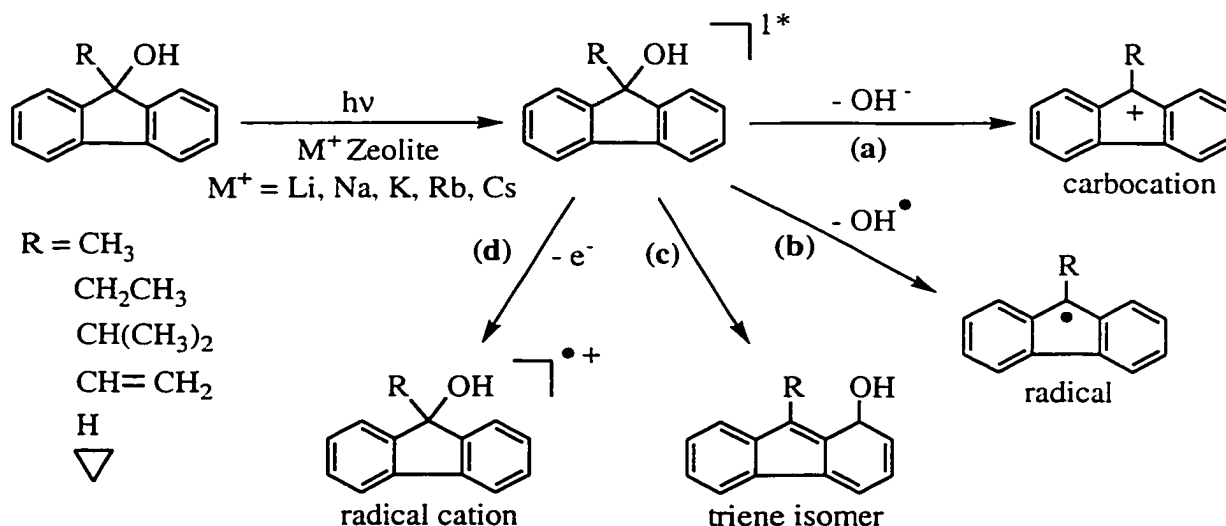
The transient diffuse reflectance spectrum obtained upon 308 nm laser irradiation of 9-methyl-9-fluorenol (MeFOH) in oxygen-saturated NaY possesses several distinct absorption bands, Figure 3-48 (The figures described in sections 3.3.1.1 to 3.3.1.7 are found on pages 179 to 214). An absorption band with a sharp maximum at 485 nm and a shoulder at 455 nm is clearly observed in the central region of the spectrum. This absorption band and accompanying shoulder closely match the absorption spectrum of the 9-methyl-9-fluorenyl cation previously observed by picosecond laser photolysis in aqueous methanol³⁸⁴ and under stable ion conditions in concentrated acid solution.³⁵⁵ The characteristic maxima and band shape strongly suggest that the transient species responsible for this absorption is the 9-methyl-9-fluorenyl cation. Consistent with this identification is the transient behaviour in NaY. The decay monitored at 485 nm is essentially complete in $\sim 2 \mu\text{s}$, Figure 3-48 inset, indicating that the transient species responsible for this absorption band is very reactive. This decay trace fits nicely to a first-order expression yielding a rate constant of $3.5 \times 10^6 \text{ s}^{-1}$, Table 3-22. Such a large

decay rate constant is anticipated on the basis of the high reactivity of the 9-methyl-9-fluorenyl cation in solutions such as 9:1 water:methanol ($k = 3.6 \times 10^9 \text{ s}^{-1}$)³⁸⁴ and TFE ($k = 3.6 \times 10^6 \text{ s}^{-1}$).³⁸⁶ The rapid decay of the 9-methyl-9-fluorenyl cation in NaY is also consistent with the high reactivity of the cumyl cations in alkali metal cation zeolites previously described. In addition, the rate constant for disappearance of the transient at 485 nm is unaffected by oxygen but increases strongly in the presence of coadsorbed nucleophiles such as water (*vide infra*) in a manner consistent with the behaviour of a carbocation species. Based on these considerations, the transient absorption at 485 nm can be confidently assigned to the 9-methyl-9-fluorenyl cation generated by photoheterolysis of 9-methyl-9-fluorenyl within the cavities of NaY, Scheme 3-10, path (a).

Table 3-22. First-order decay rate constants for 9-fluorenyl cations and the diphenylmethyl cation in alkali metal cation zeolites LiY, NaY and Na β .

Carbocation	$k_{\text{decay}} / 10^6 \text{ s}^{-1}$		
	LiY	NaY	Na β
Ph ₂ CH ⁺	0.55 ± 0.08	0.60 ± 0.08	-
9-Fluorenyl	2.9 ± 0.1	6.9 ± 0.1	not observed
9-Methyl-9-Fluorenyl	1.85 ± 0.1	3.45 ± 0.06	0.87 ± 0.02
9-Ethyl-9-Fluorenyl	1.38 ± 0.04	3.63 ± 0.12	0.83 ± 0.04
9- <i>iso</i> Propyl-9-Fluorenyl	1.44 ± 0.02	5.62 ± 0.08	0.81 ± 0.05
9-Vinyl-9-Fluorenyl	-	1.65 ± 0.06	-

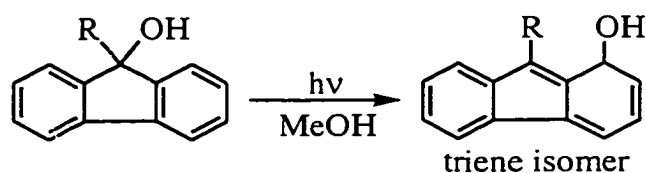
Scheme 3-10



Removal of oxygen from the NaY sample causes a slight increase in the intensity of the transient absorption at 485 nm, Figure 3-49, and reveals the presence of a new, slow decay at 485 nm, Figure 3-49 inset. These observations indicate that a second transient species, in addition to the 9-methyl-9-fluorenyl cation, is absorbing at 485 nm under vacuum conditions. A reasonable assignment for this second transient is the 9-methyl-9-fluorenyl radical generated by photohomolysis of MeFOH in NaY, Scheme 3-10, path (b). This radical has an absorption spectrum similar to the 9-methyl-9-fluorenyl cation, characterized by an absorption maximum at 485 nm,³⁹⁰ and is reactive towards oxygen. Furthermore, the 9-methyl-9-fluorenyl radical has been observed previously upon irradiation of MeFOH in solution.³⁸⁴

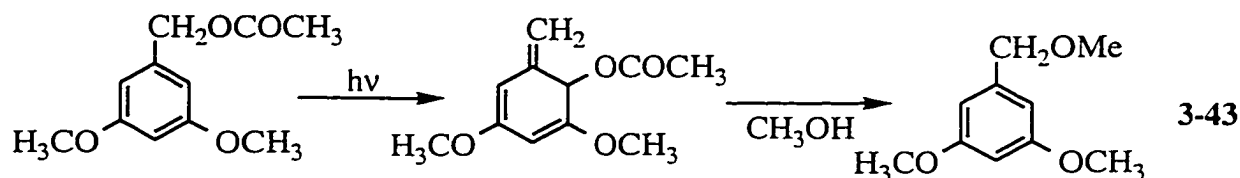
In addition to the absorption bands of the 9-methyl-9-fluorenyl cation and the 9-methyl-9-fluorenyl radical at 485 nm, the transient diffuse reflectance spectra observed upon photoexcitation of MeFOH in NaY under both vacuum and oxygen conditions are characterized by an intense, symmetrical absorption band with a maximum at 370 nm, Figures 3-48 and 3-49. Unlike the carbocation which decays rapidly in a few microseconds, or the radical which decays over tens to hundreds of microseconds and is reactive towards oxygen, the species responsible for the transient absorption at 370 nm shows no decay under vacuum or oxygen conditions, even over a time period as long as 1 ms, Figure 3-50, which is the longest time-scale accessible with the nanosecond laser system. In fact, this species is sufficiently long-lived to be detected by conventional diffuse reflectance spectroscopy. Over the long time-scales accessible with the conventional instrument, the species absorbing at 370 nm is observed to decay over several minutes with a rate constant of 0.0144 s^{-1} (*vide infra*).

The long lifetime of the transient absorbing at 370 nm is not characteristic of the reactivity of many transients commonly studied in non-protic zeolites such as triplets,^{52,54,145} radicals,^{122,123,155,391} radical ions^{66,71-73,75,89} or carbocations³⁹¹ which tend to show some decay over these times scales and/or react with oxygen. Thus, it is unlikely that any of these transients are responsible for the absorption at 370 nm. A long-lived transient with a similar absorption spectrum has been detected previously upon laser photolysis of 9-fluorenyl in methanol and was assigned as a metastable triene isomer generated by photoinduced rearrangement,³⁸³ eq. 3-42



3-42

Although this assignment was not rigorously established by the authors, the appearance of resonances assigned to vinylic protons in the ^1H NMR spectra during photolysis was used as evidence to support their proposal. In addition, there is literature precedent for similar rearrangements of related compounds³⁹² and it has been shown recently that 3,5-dimethoxybenzyl acetate undergoes photoinduced rearrangement to a triene isomer which decays with a half-life of 2.7 minutes in methanol,³⁹³ eq 3-43.



A similar half-life is observed for the 370 nm transient generated by photoexcitation of MeFOH and other 9-fluorenyl derivatives in methanol (*vide infra*). On the basis of these observations, the transient absorbing at 370 nm is identified as the triene isomer produced by photoinduced rearrangement of MeFOH, Scheme 3-10, path (c).

A long wavelength absorption band with a maximum at 640 nm and a distinctive shoulder at 600 nm is also evident in the transient diffuse reflectance spectra obtained upon 308 nm laser photolysis of MeFOH in evacuated or oxygen-saturated NaY. This absorption is not associated with any of the transients discussed thus far, but is highly characteristic of the radical cation of MeFOH in solution²⁴¹ and of radical cations of fluorene moieties in general.^{241,384,394} The absorption band at 640 nm is therefore attributed to the 9-methyl-9-fluorenyl radical cation produced by photoionization of MeFOH within NaY, Scheme 3-10, path (d). Several additional observations support this assignment. The transient absorbing at 640 nm is uninfluenced by the inclusion of oxygen within the zeolite sample, as expected for fluorene type radical cations.²⁴¹ The fluorene radical cation generated by photoionization of fluorene in alkali metal cation Y zeolites exhibits an identical absorption band centered at 640 nm with a 600 nm shoulder, Figure 3-51. The fluorene radical cation decays over a broad range of time scales from a few microseconds to several hundreds of μs and thus exhibits notable fast and slow components. Although the decay kinetics of the radical cation are somewhat complex, the decay rate constant of the fast component is comparable to the fast decay observed at 640 nm following laser photolysis of MeFOH in NaY, Table 3-23. In addition, identical long wavelength absorptions with similar lifetimes are observed upon irradiation of other 9-substituted-9-fluorenyls within alkali metal cation zeolites (*vide infra*). The substituent at the 9-position should have little influence on the absorption spectra,^{241,394} and

detection of this distinct long wavelength absorption provides evidence for the photoionization of 9-fluorenols within non-acidic zeolites. This is consistent with the well-documented ability of alkali metal cation zeolites to promote photoionization of organic guest molecules.^{66,69-73,75,89} Furthermore, a similar long wavelength absorption band observed upon incorporation of 9-fluorenol into the protic zeolites HMor and H β has previously been assigned to the 9-fluorenol radical cation generated by thermal oxidation within the strongly acidic and oxidizing environment of these zeolites.⁶³

In addition to the long wavelength absorption, the spectrum of the MeFOH radical cation in solution also exhibits a second band of similar intensity with a maximum at 380 nm.^{241,384,394} This absorption band can also be seen in the transient diffuse reflectance spectrum of fluorene radical cations in zeolites, Figure 3-51. In the diffuse reflectance spectrum produced by photoexcitation of MeFOH in NaY, the short wavelength band of the MeFOH radical cation is somewhat obscured by the intense absorption of the long-lived triene isomer at this wavelength. The existence of this band can nonetheless be detected as a fairly fast decay superimposed on the static absorption of the triene isomer at 370 nm, Figure 3-51. The rate constant for this fast decay, under vacuum and oxygen conditions, is the same as the decay at 640 nm, $k \sim 6 \times 10^5 \text{ s}^{-1}$, indicating that both bands due to the MeFOH radical cation can be observed in the zeolite. Furthermore, the transient diffuse reflectance spectrum monitored several hundred μs following the laser pulse represents the complete decay of the radical cation, while the triene isomer remains unchanged during this time, Figure 3-50. As can be seen in this spectrum, the short wavelength maximum exhibits a 10 nm shift from 380 nm to 370 nm during this time. This is consistent with the decay of the MeFOH radical cation leaving only the triene isomer absorbing at 370 nm.

Table 3-23. First-order rate constants for the decay of the 9-R-9-fluorenol radical cations and the fluorene radical cation observed at 640 nm in alkali metal cation zeolites.

Zeolite	Radical Cation $k_{\text{obs}} / 10^5 \text{ s}^{-1}$			
	R = Cyclopropyl	R = Methyl	R = H	Fluorene
LiY	6.7 ± 0.03	6.3 ± 0.05	1.1 ± 0.1	4.7 ± 0.2
NaY	8.7 ± 0.03	6.1 ± 0.03	1.3 ± 0.2	4.2 ± 0.2
KY	9.2 ± 0.05	5.8 ± 0.05	1.5 ± 0.1	4.2 ± 0.2
RbY	8.5 ± 0.05	6.5 ± 0.04	1.6 ± 0.1	4.6 ± 0.3
CsY	5.6 ± 0.02	7.3 ± 0.03	2.0 ± 0.1	6.2 ± 0.2

In summary, at least four distinct reaction pathways are available to MeFOH upon photochemical excitation within the cavities of dry NaY, Scheme 3-10. Photoheterolysis, path (a), takes place to generate the reactive 9-methyl-9-fluorenyl cation characterized by absorption maximum at 485 nm, and a rapid decay rate constant of $3.5 \times 10^6 \text{ s}^{-1}$. Photohomolysis, path (b), produces the 9-methyl-9-fluorenyl radical with an absorption maximum at 485 nm. It is significantly longer-lived than the carbocation under vacuum conditions, but is quenched by the inclusion of oxygen within the sample. Photoinduced rearrangement, path (c), leads to the triene isomer which has an intense absorption maximum at 370 nm and shows no decay over times as long as 1 ms. Photoionization, path (d), generates the 9-methyl-9-fluorenyl radical cation with a characteristic long-wavelength absorption at 640 nm, and an additional band near 380 nm. This transient is significantly longer-lived than the reactive carbocation, decays with a rate constant of $6 \times 10^5 \text{ s}^{-1}$ in NaY, and is unaffected by the addition of oxygen to the sample.

Laser photolysis of MeFOH in dry LiY gives results analogous to those observed in NaY and described by Scheme 3-10. As shown in Figure 3-52, 308 nm laser irradiation in oxygen-saturated LiY yields a short-lived transient with an absorption maximum at 485 nm which can be readily assigned to the 9-methyl-9-fluorenyl cation. Under vacuum conditions, the 9-methyl-9-fluorenyl radical also absorbs in this region, contributing additional, longer-lived absorption at this wavelength that is completely quenched by oxygen, Figure 3-52, inset. The long-lived absorption at 370 nm associated with the triene isomer is also observed. Again this transient shows no decay over times as long as 1 ms after the laser pulse and is sufficiently long-lived to be monitored using conventional diffuse reflectance (*vide infra*). Likewise, the characteristic long-wavelength absorption of the 9-methyl-9-fluorenyl radical cation is clearly detected as a maximum at 640 and a notable shoulder at 600 nm. Absorption due to the radical cation at 380 nm is evident from the observed decay superimposed on the static absorption of the triene isomer at 380 nm, Figure 3-52. The rate constant for the fast decay component at 380 nm matches the decay rate constant monitored at 640 nm, $k \sim 6 \times 10^5 \text{ s}^{-1}$, and is very similar to the rate constant for decay of the 9-methyl-9-fluorenyl radical cation in NaY.

The most significant difference between the results observed in LiY and those observed in NaY is the lifetime of the 9-methyl-9-fluorenyl cation. In LiY the carbocation decays with a rate constant of $1.9 \times 10^6 \text{ s}^{-1}$, Table 3-22, which is smaller by a factor of 1.8 than the rate constant observed in NaY. In larger alkali metal cation Y zeolites, KY, RbY and CsY, absorption at 485 nm due to the 9-methyl-9-fluorenyl cation is not detected at any time following the 10 ns laser pulse. In these zeolites, absorption

bands at 370 nm and 640 nm, previously associated with the triene isomer and 9-methyl-9-fluorenyl radical cation, dominate the transient diffuse reflectance spectra, Figures 3-53, 3-54 and 3-55. The inability to observe the 9-methyl-9-fluorenyl cation in KY, RbY and CsY may indicate that the reactive carbocation has a lifetime in these larger alkali metal cation zeolites that is too short to be measured with nanosecond diffuse reflectance. This idea is in agreement with the increased reactivity of the 9-methyl-9-fluorenyl cation observed upon increasing the alkali counterion size from Li^+ to Na^+ , and with previously described results concerning the reactivity of cumyl cations in alkali metal cation zeolites as a function of counterion size. Alternatively, it is possible that photoheterolysis of MeFOH to generate the 9-methyl-9-fluorenyl cation does not occur within these zeolites. For instance, decreased photoheterolysis efficiency may be a consequence of the decrease in Lewis acidity of alkali metal cation zeolites with counterion size.^{30,88,89} The efficiency of photoheterolysis as a function of alkali metal counterion can be probed by employing a 9-substituted-9-fluorenyl which would generate a less reactive carbocation (*vide infra*).

In addition to the inability to observe the 9-methyl-9-fluorenyl cation in KY, RbY and CsY, there are several other features of the dynamics of photoexcited MeFOH in these zeolites that are of interest. First, significant oxygen-induced quenching of the 370 nm absorption in the larger cation zeolites is clearly demonstrated by comparing the transient spectra observed in evacuated KY, RbY and CsY to those obtained in oxygen-saturated samples, Figures 3-53, 3-54, and 3-55. This indicates that there is an additional transient species absorbing at 370 nm in these zeolites which, in contrast to the triene isomer and the radical cation, reacts with oxygen. This additional transient species is likely the MeFOH triplet. Triplets of fluorene-type chromophores are known to have absorption maxima in this region, and are reactive towards oxygen.^{383,395} In addition, as can be seen in Figures 3-53, 3-54 and 3-55, the amount of oxygen quenching at 370 nm increases dramatically as the counterion is varied from K^+ to Cs^+ (and is even less in LiY and NaY). Thus, the yield of this additional transient increases with counterion size, consistent with enhanced intersystem crossing in the presence of larger metal cations as predicted by the heavy atom effect³⁹⁶ and as previously demonstrated for numerous organic guest molecules in zeolites.^{23,178,179,182-184} Second, the relative amount of transient decay observed at 370 nm under oxygen conditions increases as the counterion size increases, suggesting the yield of 9-methyl-9-fluorenyl radical cation increases at the expense of the triene isomer as the cation is varied from K^+ to Cs^+ , insets Figures 3-53, 3-54 and 3-55. In oxygen-saturated CsY, over all time scales, the transient decay at 370 nm closely matches that at 640 nm, which suggests that there is little, if any, long-lived

absorption associated with the triene isomer at 370 nm in CsY. In fact, the intensity of the 640 nm band is very similar to the 380 nm band, inset Figure 3-55, as observed for fluorene-type radical cations.

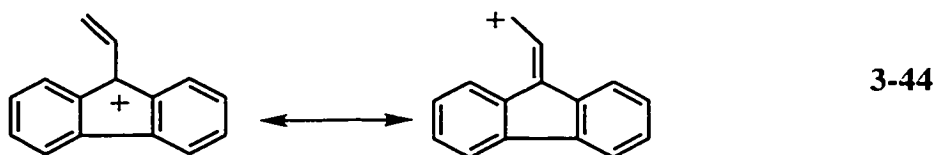
Certainly the influence of the alkali metal counterion on the overall dynamics of photoexcited MeFOH is difficult to predict due to the number of reaction pathways available. However, some trends can be clearly observed concerning the influence of alkali metal counterion on the individual yields of intersystem crossing to the triplet, photoinduced rearrangement to the triene isomer and photoionization to generate the radical cation. For instance, the triplet yield, determined from the amount of oxygen quenching of the 370 nm band, definitely increases with counterion size, Figure 3-56. On the other hand, the yield of the triene isomer (determined by the change in diffuse reflectance at 370 nm at 1 ms) first increases with alkali cation size from LiY to KY, but then decreases in the presence of the larger cations, Rb^+ and Cs^+ , Figure 3-57. Radical cation yield (determined by the initial change in diffuse reflectance at 640 nm) shows the opposite behaviour reaching a minimum in KY but then increasing in RbY and CsY.

The influence of other zeolites, such as NaX and Na β , on the photoheterolytic generation and reactivity of the 9-methyl-9-fluorenyl cation was also considered. The results obtained upon laser photolysis of MeFOH in NaX (Si/Al = 1.2) are similar to those described for larger alkali cation Y zeolites. In this zeolite, the transient spectrum is dominated by the intense absorption of the triene isomer at 370 nm, Figure 3-58. Absorption due to the 9-methyl-9-fluorenyl radical cation can be detected at 640 nm, and this transient is also responsible for the weak fast decay observed at 370 nm. As can be seen in the transient spectrum, decay of the radical cation at 640 nm and 380 nm is complete in a few hundred microseconds, while a significant absorption at 370 nm due to the triene isomer remains at these times. Of particular significance is the fact that no signal due to the 9-methyl-9-fluorenyl cation is detected at any time following laser photolysis of MeFOH in NaX, Figure 3-58 inset. This is analogous to the results observed in KY, RbY and CsY, where the inability to detect the 9-methyl-9-fluorenyl cation is attributed to either rapid decay of the carbocation within the laser pulse, or inefficient photoheterolysis of MeFOH in NaX.

In contrast to the results obtained in NaX, the 9-methyl-9-fluorenyl cation is readily generated and directly observed in the more dealuminated zeolite Na β (Si/Al = 18). In addition to the triene isomer at 370 nm and the 9-methyl-9-fluorenyl radical cation at 640 nm and 380 nm, the characteristic absorption bands of the 9-methyl-9-fluorenyl cation at 485 nm and 455 nm are observed distinctly following laser photolysis of MeFOH in oxygen-saturated Na β , Figure 3-59. In this zeolite, the carbocation remains

a fairly reactive intermediate, but is notably longer-lived than in NaY, Figure 3-59 inset. Again the carbocation decay can be fit to a first-order expression, yielding a rate constant of $0.87 \times 10^6 \text{ s}^{-1}$ which is four-fold smaller than that observed in NaY. In evacuated Na β the intensity of the transient absorption at 485 nm increases slightly and the decay kinetics exhibit a longer-lived component which can be attributed to the 9-methyl-9-fluorenyl radical as previously described.

Laser irradiation of 9-ethyl- and 9-isopropyl-9-fluorenyl in alkali metal cation zeolites yields results which are very similar to those described for MeFOH. In each case, the 9-alkyl-9-fluorenyl cation is generated and directly observed as a short-lived intermediate with an absorption maximum at 485 nm and shoulder at 455 nm. Representative examples are shown in Figures 3-60, 3-61, 3-62 and 3-63. Similarly, the 9-vinyl-9-fluorenyl cation³⁹⁷ is generated upon laser irradiation of 9-vinyl-9-fluorenyl, but its absorption maximum at 500 nm is somewhat broader, Figure 3-65. In solution, the 9-vinyl-9-fluorenyl cation has additional absorption bands at 400 nm and 360 nm. These bands are present in the Y zeolites, but are largely masked by the intense absorption of the triene isomer at 370 nm. The significant difference in the absorption spectrum of the 9-vinyl-9-fluorenyl cation as compared to the 9-alkyl-9-fluorenyl cations is due to the allylic nature of the 9-vinyl-9-fluorenyl cation as indicated by the resonance structures shown in eq. 3-44.³⁹⁷



Formation of the 9-alkyl-9-fluorenyl cations in LiY, NaY and Na β is accompanied by rearrangement to generate the triene isomer as a long-lived species at 370 nm, and photoionization to generate the radical cation at 370 nm and 640 nm. Under vacuum conditions, additional absorption at 485 nm is observed due to photolysis of these precursors to the 9-substituted-9-fluorenyl radical. The 9-alkyl- and 9-vinyl-9-fluorenyl cations each decay with rate constants similar to the methyl derivative. These decay rate constants are summarized in Table 3-22.

3.3.1.2. Laser Photolysis of 9-Fluoreno1 in Alkali Metal Cation Zeolites

The results described in the preceding section clearly indicate that LiY, NaY and Na β are sufficiently non-nucleophilic to support the detection of reactive 9-alkyl and 9-vinyl-9-fluorenyl cations. Although these carbocations are reactive, the alkyl or vinyl groups at the 9-position provide some stabilization and detection of these intermediates may not completely reflect the full potential of alkali metal cation zeolites to host very reactive carbocations. In order to more fully evaluate the ability of zeolites to support the generation and detection of reactive carbocations, laser photolysis experiments were conducted using 9-fluoreno1 (FOH), which upon photoheterolysis would produce the parent, unstabilized 9-fluorenyl cation.

The transient diffuse reflectance spectrum obtained upon 308 nm laser irradiation of 9-fluoreno1 in oxygen-saturated, dry LiY, Figure 3-65, exhibits features very similar to those observed upon laser irradiation of MeFOH in the same zeolite. A dominant spectral feature is the intense absorption band at 370 nm that is not influenced by oxygen and does not decay on the longest time-scale of the laser system, Figure 3-66. This absorption is assigned to the triene isomer generated by photoinduced rearrangement of FOH, Scheme 3-10, path (c), on the basis of the same reasoning discussed above for the triene isomer produced from MeFOH. A weaker, long wavelength absorption band with an absorption maximum at 640 nm is also evident in the transient diffuse reflectance spectra shown in Figures 3-65 and 3-66. The 640 nm band is attributed to absorption of the FOH radical cation generated by photoionization of FOH within the cavities of LiY, Scheme 3-10, path (d).

The most interesting aspect of the transient diffuse reflectance spectrum obtained upon 308 nm laser photolysis of FOH in oxygen-saturated LiY is the appearance of a distinct absorption band at 515 nm with a shoulder at 485 nm. This absorption is virtually identical to the absorption spectrum of the 9-fluorenyl cation in solution, Figure 3-65 inset, as established by picosecond laser photolysis in aqueous methanol³⁸⁴ and nanosecond laser photolysis in HFIP.²⁴¹ The characteristic absorption maxima and band shape strongly suggest that the transient species absorbing at 515 nm in LiY is the 9-fluorenyl cation. The reactivity of the transient in LiY is also consistent with this assignment. The transient species responsible for the absorption at 515 nm is very short-lived in LiY, decaying with a rate constant of $2.9 \times 10^6 \text{ s}^{-1}$, Table 3-22. In addition, the transient species is unreactive towards oxygen but reacts with nucleophiles such as water (*vide infra*) as anticipated for a carbocation. As a result, the transient absorption at 515

nm in LiY is identified as the 9-fluorenyl cation generated by photoheterolysis of FOH in LiY, Scheme 3-10, path (a).

Laser photolysis of FOH in evacuated LiY yields a transient diffuse reflectance spectrum which is very similar to that obtained under oxygen-saturated conditions, except in the 500 nm region, Figure 3-67. Under vacuum conditions (10^{-4} Torr), the absorption band at 515 nm due to the 9-fluorenyl cation is still visible, but the 485 nm shoulder is masked by an additional, significantly longer-lived transient with an absorption maximum at 500 nm. This additional transient can be observed more clearly in a direct comparison of the transient spectra obtained under evacuated and oxygen-saturated conditions, Figure 3-67 inset. In evacuated LiY two peaks are observed, one at 515 nm which corresponds to the 9-fluorenyl cation and another which corresponds to a second transient at 500 nm. Upon inclusion of oxygen, the 500 nm transient is quenched, which causes a slight decrease in the absorption intensity of the neighbouring 9-fluorenyl cation. Since the second transient absorbing at 500 nm is observed only in evacuated samples and is quenched by oxygen, it is assigned to the 9-fluorenyl radical produced by photohomolysis of FOH in LiY, Scheme 3-10, path (b). Consistent with this assignment is the well characterized maximum of the 9-fluorenyl radical at 500 nm in solution,³⁹⁸ and previously described results demonstrating that the 9-fluorenyl radical is produced upon irradiation of FOH in methanol.^{380,383,384}

Very similar results are obtained upon laser irradiation of FOH within the cavities of dry NaY. Photolysis in this alkali metal cation zeolite also generates the 9-fluorenyl cation, the 9-fluorenyl radical, the rearranged triene isomer, and the 9-fluorenyl radical cation, Figure 3-68. The 9-fluorenyl cation is readily detected in oxygen-saturated NaY as a short-lived species with a characteristic absorption maximum at 515 nm and shoulder at 485 nm. The 9-fluorenyl cation is even more reactive in NaY than in LiY. The very rapid disappearance of the 9-fluorenyl cation in NaY is essentially complete within about 800 ns after the laser pulse. In NaY, the carbocation decays in a first-order manner with a decay rate constant of $6.6 \times 10^6 \text{ s}^{-1}$. As has been observed in all experiments discussed thus far, the triene isomer is again very long-lived, exhibiting no decay over the times monitored by the nanosecond laser system, Figure 3-68 inset. Using conventional diffuse reflectance spectroscopy, the triene isomer derived from FOH is observed to decay very slowly over several minutes with a rate constant of 0.0037 s^{-1} (*vide infra*). Interestingly, this rate constant is approximately 3-4 times smaller than that observed for the triene isomer derived from MeFOH discussed earlier.

The 9-fluorenyl cation is not observed at any time following laser photolysis of FOH in KY, Figure 3-69, RbY, Figure 3-70, or CsY, Figure 3-71. This is not surprising

considering that the more stable 9-methyl-9-fluorenyl cation is not detected in these zeolites. In fact, observation of the 9-fluorenyl cation in these zeolites would be contrary to the expected increase in reactivity of the carbocation with zeolite counterion size, particularly since the decay rate constant of $6 \times 10^6 \text{ s}^{-1}$ for the 9-fluorenyl cation in NaY is already approaching the upper limit for measurement. The remaining features of the transient spectra derived from laser photolysis of FOH in KY, RbY and CsY are essentially identical to those previously described for MeFOH. Namely, decay at 370 nm becomes more significant as the counterion size is increased, Figures 3-70 to 3-72, and the degree of oxygen-induced quenching of this band increases in the same fashion, insets Figures 3-70 to 3-72. Again these observations indicate that the yield of triplet FOH increases with alkali counterion size, Figure 3-72, while the yield of the triene isomer and 9-fluorenol radical cation vary inversely, Figure 3-73. These trends are completely analogous to those observed for laser irradiation of MeFOH in alkali metal cation Y zeolites.

The transient diffuse reflectance spectrum observed following laser photolysis of FOH in NaX is dominated by the intense absorption of the triene isomer at 370 nm, Figure 3-74. Weak absorption due to the 9-fluorenol radical cation is visible at 640 nm, and this transient is also responsible for the slight fast decay seen at 370 nm. The decay of the radical cation at 640 nm and 380 nm is complete in a few hundred μs , while a significant absorption at 370 nm due to the triene isomer remains at these times. Not surprisingly, no signal due to the 9-fluorenyl cation is observed at any time following laser photolysis of FOH in NaX. This is analogous to the results observed in KY, RbY and CsY, and again the inability to detect the 9-fluorenyl cation may be due to either rapid decay of the carbocation within the laser pulse, or inefficient photolysis of FOH in NaX. As well, the absence of the 9-fluorenyl cation in NaX is consistent with the inability to detect the less reactive 9-methyl-9-fluorenyl cation in this zeolite.

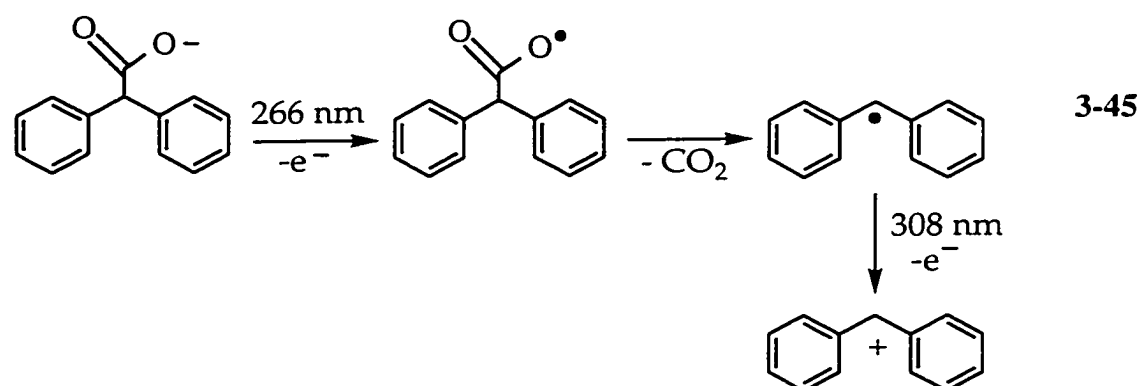
As described above, the reactivity of 9-alkyl-9-fluorenyl cations is found to be considerably lower in Na β than in NaY, Table 3-22. Based on these results it is expected that the 9-fluorenyl cation, which is sufficiently long-lived to be observed in NaY, should be readily detectable and even more long-lived if generated within Na β . The transient diffuse reflectance spectrum observed following laser photolysis of FOH in evacuated Na β does indeed possess a weak absorption band in the 500 nm region along with an intense band at 370 nm due to the triene isomer and absorption at 640 nm due to the FOH radical cation, Figure 3-75. However, inclusion of oxygen within the Na β sample results in significant quenching of the absorption in the 500 nm region, Figure 3-75 inset. Furthermore, the remaining absorption has a maximum centered at 500 nm, rather than

515 as required for the 9-fluorenyl cation. These observations suggest that the 9-fluorenyl radical is the source of the 500 nm absorption detected in evacuated Na β . In oxygen-saturated Na β , the very weak residual absorption at 500 nm may be due to incomplete oxygen quenching of the 9-fluorenyl radical. In any case, the intensity of the absorption at 500 nm in oxygen-saturated Na β is so low that it is difficult to assign the transient, and no kinetic information can be obtained, indicating that little or no carbocation is formed. Clearly, rearrangement to the triene isomer is the dominant reaction pathway of photoexcited FOH in Na β .

In an additional attempt to observe the reactive 9-fluorenyl cation in alkali metal cation zeolites, FOH was irradiated in NaMor. This zeolite has a relatively low concentration of framework aluminum (Si/Al = 6.5), and has been found to provide a relatively stabilizing environment for the 4-methoxycumyl cation (*vide supra*). As observed following laser photolysis of FOH in Na β , the transient diffuse reflectance spectrum obtained in NaMor is dominated by the intense absorption of the triene isomer at 370 nm, Figure 3-76. Notably, however, a weak, relatively short-lived absorption with a maximum at 515 nm persists under oxygen conditions, Figure 3-76 inset. Although weak, this absorption band can be identified with reasonable confidence as the 9-fluorenyl cation on the basis of the absorption maximum, band shape, and decay profile. The fast decay at 515 nm under oxygen conditions, Figure 3-76 inset, can be fit with a first-order expression to yield a rate constant of $1.1 \times 10^6 \text{ s}^{-1}$. This rate constant is consistent with the values obtained for the 9-fluorenyl cation in LiY and NaY, and the reactivity of the 4-methoxycumyl cation in NaMor as compared to the alkali metal cation Y zeolites.

3.3.1.3 Diphenylmethyl Cations in Alkali Metal Cation Zeolites

In order to compare the influence of the $4n\pi$ system of the 9-fluorenyl cation on intrazeolite reactivity of 9-fluorenyl cations, the decay kinetics of the diphenylmethyl cation were examined in the alkali metal cation Y zeolites. Unlike photoexcited fluorenols, heterolysis of photoexcited diphenylmethanol is very inefficient and an alternative technique for carbocation generation is required. The method of choice within alkali metal cation zeolites was found to be photoionization of the diphenylmethyl radical, eq. 3-45. This radical can be readily generated by photoionization of diphenylacetate anion to the diphenyl acetoxy radical which rapidly decarboxylates,³⁹⁹ eq. 3-45. Figure 3-77 shows the sharp maximum at 330 nm of the diphenylmethyl radical^{229,232} generated in this way upon 266 nm laser irradiation.



Subsequent irradiation of this radical with a second laser pulse, this time at 308 nm, causes photoionization, eq. 3-45, as demonstrated by the bleaching of the radical signal at 330 nm and the corresponding appearance of an absorption band with a maximum at 440 nm due to the diphenylmethyl cation,^{229,230,232} Figure 3-77.

Two photon excitation of diphenylacetic acid was conducted in each alkali metal cation Y zeolite in order to determine the rate constant for decay of the diphenylmethyl cation as a function of counterion. As shown in Figure 3-78, efficient photoionization of the diphenylmethyl radical leads to a significant yield of the diphenylmethyl cation in LiY and NaY. In KY, the photoionization is less efficient, but a reasonable yield of the diphenylmethyl cation is obtained by two photon excitation in this zeolite. Only a very weak signal attributed to the diphenylmethyl cation is observed in RbY, and no signal due to the diphenylmethyl cation is detected following photoexcitation of the diphenylmethyl radical in CsY.

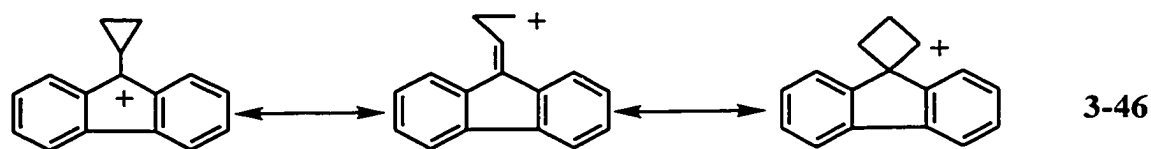
The rate constant for the disappearance of the diphenylmethyl cation is observed to increase as the counterion size increases from Li^+ to Rb^+ , Figure 3-79. In LiY to RbY, the carbocation decay fits well to a first-order expression, yielding rate constants in the 10^5 s^{-1} range, Table 3-22. Thus, the diphenylmethyl cation is one to two orders of magnitude less reactive than the 9-fluorenyl cation within alkali metal cation zeolites, consistent with the intrinsically higher reactivity of the 9-fluorenyl cation in solution, Table 3-21

3.3.1.4 Laser Photolysis of 9-Cyclopropyl-9-Fluorenol in Alkali Metal Cation Zeolites

The results described in the preceding sections demonstrate convincingly that alkali metal cation zeolites can support photoheterolysis of 9-fluorenol precursors leading

to the formation of these carbocations. These 9-fluorenyl cations are, however, very short-lived within alkali metal cation zeolites, and are not detected at all in larger cation zeolites, or NaX. As a result, it is useful to employ a 9-fluorenol precursor which will yield a less reactive carbocation upon photoheterolysis. In this way it should be possible to directly observe the 9-substituted-9-fluorenyl cation in a wider range of zeolites and therefore obtain a more complete picture of the influence of zeolite structure and composition on the reactivity of these carbocation intermediates. Furthermore, by employing a less reactive carbocation as a probe it will be possible to assess whether or not the inability to observe reactive 9-fluorenyl cations in larger alkali metal cation zeolites is a consequence of enhanced carbocation reactivity or decreased yield of photoheterolysis. Finally, the influence of zeolite parameters on the efficiency of photoheterolysis relative to other reaction pathways can be examined using a 9-substituted-9-fluorenyl cation that can be observed in a variety of zeolites. The most obvious candidate that might be used in order to address each of these issues is the 9-phenyl-9-fluorenyl cation. However, its precursor, 9-phenyl-9-fluorenol is too large to incorporate into X and Y zeolites. Instead, attention was focused on examining the dynamics of photoexcited 9-cyclopropyl-9-fluorenol (cPrFOH) in alkali metal cation zeolites. The presence of the cyclopropyl substituent at the 9-position affords a significant degree of stability to the 9-fluorenyl cation without introducing unwanted steric bulk, structural changes, or large increases in molecular size as would be a consequence of employing aryl substituents.

The transient diffuse reflectance spectrum obtained upon 308 nm laser irradiation of cPrFOH in evacuated, dry NaY has three distinct absorption maxima at 380 nm, 445 nm, and 640 nm, and a well defined shoulder at 330 nm, Figure 3-80. As described below, this spectrum is complicated by the presence of at least three species. Nonetheless, the absorption bands at 380 nm and 445 nm, and the shoulder at 330 nm bear a certain resemblance to the bands observed in the spectrum of the 9-cyclopropyl-9-fluorenyl cation generated previously in TFE,³⁹⁷ and reproduced in the inset of Figure 3-80. The difference in the absorption spectrum of the 9-cyclopropyl-9-fluorenyl cation as compared to unsubstituted or alkyl-substituted derivatives is attributed to the existence of additional resonance contributors to the structure of the former carbocations.³⁹⁷ The three resonance contributors of the 9-cyclopropyl-9-fluorenyl cation, eq. 3-46,



induce perturbations in the absorption spectra when compared with 9-fluorenyl cations lacking such resonance contributors. Similar reasoning has been used to explain why the absorption spectrum of the diphenylcyclopropylmethyl cation in $\text{FSO}_3\text{H-SbF}_5$ has three absorption bands at 435 nm, 358 nm, and 319 nm, whereas the diphenylethyl cation has two absorption bands at 440 nm and 310 nm.²¹⁸

The similarities between the diffuse reflectance spectrum in NaY and the absorption spectrum of the 9-cyclopropyl-9-fluorenyl cation observed in TFE strongly suggest that this carbocation contributes to the absorption bands at 330 nm, 380 nm and 445 nm observed in NaY. Furthermore, the transient species absorbing at these wavelengths decays in a first-order manner with a rate constant of $3.9 \times 10^5 \text{ s}^{-1}$, Table 3-24, that lies in the range expected for the 9-cyclopropyl-9-fluorenyl cation based on the reactivity of the cumyl cations and other 9-fluorenyl cations previously discussed. In addition, the rapidly decaying transient species observed at 380 nm and 445 nm is unreactive towards oxygen, Figure 3-81, but decays more rapidly in the presence of nucleophiles such as water and methanol, Figure 3-82. These observations are all consistent with the presence of the 9-cyclopropyl-9-fluorenyl cation generated by photolysis of cPrFOH within the cavities of NaY, Scheme 3-10, path (a).

Table 3-24. Decay rate constants for the 9-cyclopropyl-9-fluorenyl cation in dry and hydrated alkali metal cation Y zeolites, ratio of carbocation decay rate constant observed under hydrated and dry conditions, and increase in carbocation yield upon hydration.

Zeolite	$k_{\text{dry}} / 10^5 \text{ s}^{-1}$	$k_{\text{hyd}} / 10^5 \text{ s}^{-1}$	$k_{\text{hyd}}/k_{\text{dry}}$	Increase in Carbocation Yield Upon Hydration (%)
LiY	0.64 ± 0.01	2.5 ± 0.1	3.9	3
NaY	3.8 ± 0.1	7.2 ± 0.1	1.8	10
KY	8.0 ± 0.1	10.6 ± 0.3	1.4	32
RbY	10.4 ± 0.2	22.7 ± 0.2	1.6	54
CsY	not observed	not observed	-	-
NaX	7.9 ± 0.1	-	-	-

The absorption that remains at 380 nm after decay at 445 nm is complete, Figure 3-83, clearly indicates that an additional species that is significantly longer-lived than the 9-cyclopropyl-9-fluorenyl cation contributes to the absorption observed at 380 nm. The spectral appearance of this transient is identical to that previously observed upon laser

irradiation of other 9-fluorenols in alkali metal cation zeolites and identified as the triene isomer generated by photoinduced rearrangement. The reactivity of this species is also identical to that observed for the triene isomers of other 9-fluorenols in that it is insensitive to oxygen and shows no decay at times as long as 1 ms following the laser pulse, Figure 3-83 inset. These observations indicate that the long-lived transient at 370 nm is the triene isomer generated by photoinduced rearrangement of cPrFOH in NaY, Scheme 3-10, path (c).

The transient diffuse reflectance spectrum produced by laser photolysis of cPrFOH in NaY also possesses a long wavelength absorption with a maximum at 640 nm, Figure 3-80. As previously described for other 9-fluorenols, this absorption is attributed to the radical cation of cPrFOH generated by laser induced photoionization of cPrFOH with the NaY matrix, Scheme 3-10, path (d). The detection of the radical cation following laser photolysis of cPrFOH in NaY is expected based on the consistently observed photoionization of all fluorene chromophores considered in this study. Since the radical cations of 9-fluorenols have a second absorption band at 380 nm, part of the absorption observed at this wavelength contains a contribution from absorption by the cPrFOH radical cation.

Laser flash photolysis investigations of cPrFOH were conducted in alkali metal cation zeolites in order to examine the effect of the zeolite environment on the formation and reactivity of the 9-cyclopropyl-9-fluorenyl cation. The transient diffuse reflectance spectra obtained upon 308 nm laser photolysis of cPrFOH in alkali metal cation exchanged Y zeolites under vacuum conditions are shown in Figure 3-84. Each spectrum clearly exhibits distinct features, especially with regard to the signal of the 9-cyclopropyl-9-fluorenyl cation at 445 nm, which shows a dramatic dependence on the zeolite counterion both in terms of yield and absolute reactivity. For instance, as the size of the alkali metal counterion increases from Li^+ to Rb^+ , the observed rate constant for disappearance of the carbocations significantly increases, Table 3-24. In addition, the relative intensity due to carbocation absorption immediately following the laser pulse significantly decreases along the series, Figure 3-84 insets. Therefore, the alkali metal counterion exerts two distinct effects in that it modulates both the efficiency of the photolysis reaction and the reactivity of the resultant 9-cyclopropyl-9-fluorenyl cation.

The 9-cyclopropyl-9-fluorenyl cation is not observed in CsY, Figure 3-84(e). The absence of carbocation signal may indicate that the carbocation decays too rapidly in CsY to be detected. However, while the rate constant for carbocation decay increases dramatically upon going from Li^+ , $k = 0.64 \times 10^5 \text{ s}^{-1}$, to Rb^+ , $k = 14 \times 10^5 \text{ s}^{-1}$, the

increase is not sufficiently large to predict that the 9-cyclopropyl-9-fluorenyl cation would decay too rapidly to be observed in CsY.

A more likely explanation is that the efficiency of photoheterolysis decreases as the zeolite counterion size increases, and in CsY the efficiency is so low that the carbocation is not formed in detectable quantities. This decrease is clearly shown in Figure 3-85. The influence of alkali metal cation size on the other reaction pathways available to photoexcited cPrFOH is also significant. As shown in Figure 3-86, the yield of the triene isomer increases with alkali cation size to a maximum at KY. Subsequent increases in counterion size result in a decrease in the yield of the triene isomer. Correspondingly, the yield of radical cation decreases slightly upon going from Li^+ to K^+ and then increases in the larger alkali metal cation zeolites RbY and CsY. The variation in the yield of the radical cation and the triene isomer of cPrFOH as a function of counterion is analogous to that previously described for 9-fluorenols. As observed for both MeFOH and FOH, photoinduced rearrangement of cPrFOH dominates over photoionization in small cation zeolites, while photoionization dominates over photoinduced rearrangement in larger cation Y zeolites.

In contrast to the results obtained using MeFOH and FOH, where the carbocation is detected only in LiY and NaY, observation of the 9-cyclopropyl-9-fluorenyl cation in additional alkali metal cation zeolites provides further information concerning the absolute and relative yield of photoheterolysis as a function of counterion size. For instance, the absolute yield of the 9-cyclopropyl-9-fluorenyl cation can be determined by measuring the total change in diffuse reflectance at 445 nm (corrected for absorption due to the triene isomer at this wavelength) immediately following the laser pulse. As previously suggested, the absolute yield of the 9-cyclopropyl-9-fluorenyl cation decreases with alkali metal counterion size, Figure 3-85. Furthermore, the yield of photoheterolysis relative to the competing processes of photoionization and photoinduced rearrangement is found to decrease linearly with alkali metal cation size, Figure 3-87.

The transient diffuse reflectance spectrum generated upon laser photolysis of cPrFOH within the cavities of dry, evacuated NaX is characterized by three absorption maxima at 380 nm, 445 nm, and 640 nm, Figure 3-89, and closely resembles the spectrum observed in alkali metal cation Y zeolites, particularly KY. At short time scales ($< 20 \mu\text{s}$), the bands at 380 nm and 445 nm are readily identified as the 9-cyclopropyl-9-fluorenyl cation, while the long wavelength maximum at 640 nm is assigned as the cPrFOH radical cation. Significantly, the first-order decay rate constant for the carbocation in NaX, $k = 7.9 \times 10^5 \text{ s}^{-1}$, is twice as large as in NaY, Figure 3-89 inset. This indicates that the increase in framework aluminum content is associated with an increase

in the reactivity of the 9-cyclopropyl-9-fluorenyl cation as previously observed for the 4-methoxycumyl cation. At longer times scales after the carbocation has completely decayed ($> 20 \mu\text{s}$), and most of the radical cation has disappeared ($> 200 \mu\text{s}$), an intense absorption band at 370 nm due to the triene isomer is distinctly observed, Figure 3-90. As consistently noted for the all triene isomers observed in alkali metal cation Y zeolites, the triene isomer of cPrFOH exhibits no decay in NaX over times as long as 1 ms, Figure 3-90 inset. Again, the initial fast decay observed at 370 nm is attributed to the superimposed absorption of the rapidly decaying 9-cyclopropyl-9-fluorenyl cation at this wavelength.

3.3.1.5 Influence of Coadsorbed Protic Reagents on the Generation and Reactivity of 9-Fluorenyl Cations in Alkali Metal Cation Zeolites

The results described thus far unambiguously establish that 9-fluorenols undergo photoheterolysis in dry, non-protic zeolites to generate reactive 9-fluorenyl cations that are sufficiently stabilized in these environments to be observed directly. A greater understanding of both the photoheterolysis reaction and the intrazeolite reactivity of the corresponding carbocations can be achieved by examining the effects of coadsorbed additives. Of particular relevance with respect to the 9-fluorenyl system are protic reagents such as water or fluorinated alcohols. These substances exert a considerable influence on the photoheterolysis of 9-fluorenyl derivatives in solution and tend to increase the efficiency of photoheterolysis relative to non-protic solvents such as acetonitrile.^{380,381} Furthermore, coadsorbates may have a significant effect on the microenvironment of the zeolite cavity and it is of interest to examine how these effects are manifested in both the photochemistry of 9-fluorenols and reactivity of 9-fluorenyl cations. In addition, the coadsorbed reagents have a wide range of nucleophilicities depending on, for instance, the structure of the alcohol. Thus, the ability of these additives to modulate the intrazeolite lifetime of 9-fluorenyl cations can be assessed and compared to the influence of coadsorbed nucleophiles on the reactivity of the 4-methoxycumyl cation previously discussed. The following section describes the influence of both highly nucleophilic protic reagents, water and methanol, and a very non-nucleophilic protic reagent, HFIP, on the generation and reactivity of 9-fluorenyl cations in alkali metal cation zeolites.

The decay traces of the 9-cyclopropyl-9-fluorenyl cation observed at 445 nm in dry NaY and NaY containing coadsorbed water (6 wt %), or coadsorbed methanol (6 wt %) are shown in Figure 3-91. These decay traces indicate that the inclusion of either

water or methanol into the cavities of NaY has two distinct effects on the 9-cyclopropyl-9-fluorenyl cation. First, the intensity of absorption due to the carbocation immediately following the laser pulse is significantly higher in the samples containing coadsorbed protic reagents than in the dry zeolite. Second, the rate constant for disappearance of the 9-cyclopropyl-9-fluorenyl cation is significantly accelerated in the presence of either water or methanol.

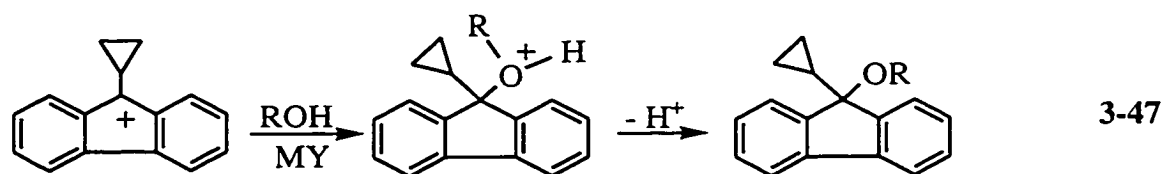
The higher absorption intensity at 445 nm indicates that the absolute yield of the 9-cyclopropyl-9-fluorenyl cation increases in the presence of water or methanol, and suggests that photoheterolysis of cPrFOH is more efficient in NaY containing these protic reagents. Thus, although photoheterolysis of cPrFOH is a major reaction pathway of cPrFOH in dry NaY, coadsorption of either methanol or water enhances this process. Furthermore, when the total change in diffuse reflectance observed at 445 nm immediately following photolysis of cPrFOH in NaY is monitored as a function of water or methanol content, a steady increase in the yield of carbocation with adsorbate concentration is revealed, Figure 3-92. This clearly demonstrates that C-O bond heterolysis of excited cPrFOH in NaY is progressively enhanced by coadsorption of increasingly higher concentrations of either water or methanol. The observation that both water and methanol enhance photoheterolysis efficiency is quite different from results observed in homogeneous solution which find inefficient photoheterolysis in neat methanol and generally require aqueous methanol to facilitate carbocation formation. Notably, however, the increase in photoheterolysis within NaY is more substantial using water as a protic additive as compared than methanol, Figure 3-92. This is certainly consistent with the higher efficacy of water as a reagent to promote photoheterolysis of 9-fluorenols in solution.^{378,380,381,384}

Further evidence indicating that coadsorbed water and methanol enhance intrazeolite photoheterolysis can be obtained by considering the influence of these additives on the reaction pathways competitive with carbocation formation. For instance, in dry alkali metal cation zeolites, photoexcited cPrFOH undergoes ionization and rearrangement in addition to heterolysis. The transient diffuse reflectance spectrum obtained upon laser photolysis of cPrFOH in hydrated NaY (6 wt %) is shown in Figure 3-93. Under these conditions the transient spectrum more closely resembles that observed upon photolysis of the same precursor in TFE where carbocation formation is the dominant reaction pathway, Figure 3-80 inset. In particular, long-lived absorption at 370 nm due to the triene isomer and long wavelength absorption due to the radical cation are significantly attenuated in the hydrated zeolite. The absence of these bands in hydrated NaY suggests that photoheterolysis of the C-O bond is the dominant reaction

pathway when the zeolite cavity is sufficiently hydrated, and that water coadsorbed within the zeolite framework strongly influences that behaviour of photoexcited cPrFOH. The fact that the triene isomer is a minor product from photoexcited cPrFOH under hydrated conditions is clearly visible in the decay kinetics monitored at 370 nm over long time scales, Figure 3-94. As can be seen in this figure, very little residual absorption due to the triene isomer is detected in hydrated NaY, in contrast to the dry zeolite where long-lived absorption of the triene isomer constitutes a significant portion of the signal intensity at 370 nm. This is consistent with earlier solution studies on the photolysis of 9-fluorenyl where the yield of triene isomer was greatly reduced upon changing from neat methanol to aqueous conditions.³⁸³ Overall the transient spectral features and decay kinetics observed in hydrated NaY consistently demonstrate that the absolute yield of photoheterolysis is increased by the inclusion of water, and that this increase is accompanied by decreased yields of the competing processes, photoionization and, particularly, photoinduced rearrangement.

Analogous trends are visible in the transient diffuse reflectance spectrum and decay kinetics obtained following laser photolysis of cPrFOH in NaY containing coadsorbed methanol (6 wt %), Figure 3-95. In the presence of methanol, the transient spectrum is very similar to the spectrum of the 9-cyclopropyl-9-fluorenyl cation in solution, with absorption due to the triene isomer and radical cation being considerably reduced. Thus, coadsorption of methanol increases the yield of photoheterolysis in a similar manner to that seen upon the addition of water to the zeolite composite indicating that methanol can likewise assist photoheterolysis of the C-O bond in the excited state. Notably, the influence of methanol is not as dramatic as the influence of water. The transient spectrum observed in NaY containing methanol continues to possess a visible absorption due to the triene at 370 nm, and the triene isomer contributes more residual absorption at long times than observed in the hydrated sample, Figure 3-95.

In addition to the enhanced yield of carbocation, the inclusion of water or methanol increases the rate constant for carbocation decay in NaY. The accelerated decay in the presence of these coadsorbates is evident in the decay traces shown in Figures 3-91. The enhanced reactivity of the carbocation is a consequence of nucleophilic attack of water or methanol at the positively charged center, eq. 3-47, consistent with the behaviour of these reagents towards reactive carbocations in solution and in zeolites (*vide supra*).



As can be seen in Figure 3-92, the decay of the carbocation is faster in the presence of coadsorbed methanol than in the presence of a similar amount of water. Likewise, fitting the decay traces to a first-order expression yields rate constants of $7.2 \times 10^5 \text{ s}^{-1}$ and $9.9 \times 10^5 \text{ s}^{-1}$ for the decay of the carbocation in NaY containing 6 wt % water and 6 wt % methanol, respectively. This relative reactivity is consistent with a mechanism involving nucleophilic attack on the carbocation and the greater nucleophilicity of methanol as compared to water. Furthermore, monitoring the first-order decay kinetics of the 9-cyclopropyl-9-fluorenyl cation at 445 nm as a function of water or methanol content indicates that the decay kinetics are highly dependent on the amount of nucleophile present within the zeolite cavities. Thus, in addition to the accelerated carbocation decay observed at relatively high water or methanol contents (*i.e.*, 6 wt %), the rate constant for decay of the carbocation increases with increasing coadsorbate concentration. Notably, however, the variation in decay rate constant with water or methanol content is not linear over the entire concentration range. For instance, as shown in Figure 3-96, the increase in the carbocation decay rate constant is linear at low methanol concentrations, but becomes much more dramatic at higher concentrations. As a result, the carbocation decay rate constant varies approximately quadratically with methanol concentration. This suggests that the quenching is not as efficient at low methanol concentrations as compared to high concentrations. The variation in the rate constant for carbocation decay with water content is similar, with the exception that the overall change is smaller and at low concentrations the rate constant decreases slightly before accelerating at higher concentrations, Figure 3-97. This again suggests that the first water molecules to be adsorbed are inefficient quenchers, and in this case may actually influence the mechanism of carbocation decay in the dry zeolite such that it is slowed slightly.

The accelerated carbocation decay observed in NaY containing coadsorbed water or methanol clearly demonstrates a dynamic quenching process. It is, however, much more difficult to determine whether or not static quenching of the 9-cyclopropyl-9-fluorenyl by water or methanol is taking place within the laser pulse because these protic reagents are responsible for an *increase* in carbocation generation by enhancing photoheterolysis in the excited state 9-fluorenyl. The only conditions where static quenching of the 9-cyclopropyl-9-fluorenyl cation can be observed are in the presence of sufficiently high concentrations of water or methanol. As shown in Figure 3-98, the yield of carbocation initially increases with increasing concentration of water or methanol, but eventually begins to decrease at high concentrations. Thus, only at high nucleophile concentrations does static quenching begin to dominate and overtake the effect of

enhanced carbocation generation.

The transient diffuse reflectance spectrum obtained upon 308 nm laser photolysis of cPrFOH in hydrated LiY strongly resembles the absorption spectrum of the 9-cyclopropyl-9-fluorenyl cation in solution, Figure 3-99. Absorption due to the cPrFOH radical cation at 640 nm persists under hydrated conditions, but no long-lived absorption is evident at 370 nm due to the triene isomer. These results contrast with those obtained in dry LiY where absorption due to the triene isomer is distinctly detected at 370 nm. Thus, as observed in NaY, inclusion of water within the cavities of LiY enhances carbocation generation *via* photoheterolysis and suppresses photoinduced rearrangement. Increased carbocation generation is also apparent from the transient diffuse reflectance spectra observed in hydrated KY, Figure 3-100, and hydrated RbY, Figure 3-101. Again, the transient spectra show a greater resemblance to the 9-cyclopropyl-9-fluorenyl cation than the spectra observed in the same zeolites in the absence of water, Figure 3-84(c) and (d). However, long-lived absorption due to the triene isomer continues to contribute to the absorption at 380 nm in hydrated KY, and particularly in hydrated RbY. Thus, when compared to the results in LiY, coincluded water is not as effective at suppressing photoinduced rearrangement. Interestingly, the transient diffuse reflectance spectrum observed in hydrated CsY bears no resemblance to the absorption spectrum of the 9-cyclopropyl-9-fluorenyl cation, Figure 3-102. In fact, the transient spectrum generated under hydrated conditions is quite similar to that observed in dry CsY, Figure 3-84(e), and again is quite similar to the radical cation of cPrFOH. Clearly neither heterolysis nor rearrangement are facile reaction pathways for photoexcited cPrFOH in CsY under either dry or hydrated conditions.

The experimental results obtained with the hydrated alkali metal cation Y zeolites indicate that the efficiency of photoheterolysis, both in terms of absolute carbocation yield and carbocation yield relative to other photogenerated transients, decreases with alkali counterion size. This is consistent with the conclusion made on the basis of results obtained with the dry Y zeolites that photoheterolysis becomes less efficient as the size of zeolite counterion is increased. However, the relative increase carbocation yield caused by the presence of water actually increases with counterion size. This trend is clearly visible when comparing the absorption intensity due to the carbocation monitored at 445 nm under dry and hydrated conditions in each alkali metal cation zeolite, insets Figures 3-99 to 3-102 (see Figure 3-91 for comparison in NaY). In LiY, where photoheterolysis is the most efficient under dry conditions, the increase in carbocation formation induced by hydration is the smallest. The increase in carbocation yield as a consequence of hydration becomes progressively more significant with subsequent increases in alkali

cation size from Na^+ to K^+ to Rb^+ , Table 3-24. The exception to this trend is CsY where coadsorbed water is not able to facilitate photoheterolysis to any observable extent.

In addition to the increase in carbocation yield observed upon laser photolysis of cPrFOH in hydrated alkali metal cation zeolites, the carbocation decays more rapidly due to nucleophilic attack by water as described for NaY, eq. 3-47. The effect of water is clearly visible in the decay traces observed under dry and hydrated conditions, insets Figures 3-99 to 3-102. In each zeolite the decay rate constant for carbocation disappearance increases upon hydration, Table 3-24. In LiY, where the carbocation is the longest lived under dry conditions, the increase in rate constant induced by hydration is the largest. Notably, the relative reactivity of the carbocation in hydrated alkali metal cation zeolites is the same as observed in the absence of water. Thus the 9-cyclopropyl-9-fluorenyl cation is longest lived in hydrated LiY and becomes progressively shorter-lived as the counterion size is increased.

In contrast to the increased yield of 9-cyclopropyl-9-fluorenyl cation observed in hydrated alkali metal cation zeolites, inclusion of water in LiY and NaY does not increase the yield of 9-alkyl-9-fluorenyl cations or the parent 9-fluorenyl cation detected immediately following the laser pulse. When MeFOH is photolyzed in NaY containing a relatively low concentration of water (< 3 wt %) the absorption intensity due to the 9-methyl-9-fluorenyl cation is decreased in intensity relative to dry conditions, Figure 3-103 inset. Upon further increases in water content, absorption at 485 nm due to the carbocation is no longer visible, Figure 3-103, indicating that the 9-methyl-9-fluorenyl cation is not present at any time following the laser pulse. Analogous results are observed upon laser photolysis of FOH in hydrated LiY and NaY, Figure 3-104. The inability to observe these 9-fluorenyl cations in hydrated zeolites can be attributed to rapid quenching within the laser pulse by nucleophilic addition of coadsorbed water. Complete quenching of the carbocation is consistent with the nucleophilic behaviour of water towards these reactive carbocations. In fact, on the basis of the short lifetime of 275 ps for the 9-methyl-9-fluorenyl cation and < 20 ps for the 9-fluorenyl cation in 9:1 water:methanol solutions,³⁸⁴ and the observation that less reactive carbocations such as the 4-methoxycumyl cation are completely quenched in hydrated zeolites, it would have been remarkable for these 9-fluorenyl cations to have survived sufficiently long to be observed in the hydrated zeolites.

The inclusion of water also affects that yield of triene isomer generated by laser photolysis of MeFOH and FOH in LiY and NaY. As can be seen in Figure 3-105, coincluded water reduces the intensity of absorption due to the triene isomer of MeFOH at 370 nm. In fact, the yield of triene isomer decreases significantly even at relatively

low concentrations of coadsorbed water. The triene isomer obtained from photoexcitation of FOH exhibits a similar decrease in yield as a function of water content in NaY. These results suggest that in addition to acting as a nucleophile towards reactive 9-fluorenyl cations, coadsorbed water also influences the reactivity of photoexcited MeFOH and FOH by altering the yields of photogenerated transients. This effect is similar to that observed with cPrFOH, where the yield of triene isomer in hydrated alkali metal cation zeolites is reduced as compared to dry conditions. Due to the complete quenching of the inherently more reactive 9-methyl-9-fluorenyl and 9-fluorenyl cations by water within the laser pulse, it is not possible to determine whether or not coincluded water enhances the yield of photoheterolysis as observed for cPrFOH. However, the fact that water decreases the yield of rearrangement suggests that water does alter the excited state dynamics of these 9-fluorenols in a manner analogous to that observed for photoexcited cPrFOH. This type of behaviour has been observed in solution studies in methanol where the efficiency of photoinduced rearrangement was found to be reduced with increasing water content.³⁸³ Thus, it is quite possible that water also enhances photoheterolysis of MeFOH and FOH in alkali metal cation zeolites, but the increased carbocation yield is not detected due to rapid nucleophilic quenching of these carbocations by water.

Direct evidence that water does indeed enhance photoheterolysis of MeFOH in alkali metal cation zeolites is obtained upon laser photolysis in hydrated Na β (3 wt %) where the resultant carbocation is sufficiently long lived to be observed. Under these conditions, the carbocation is shorter-lived, $k_{\text{hyd}} = 3 \times 10^6 \text{ s}^{-1}$ relative to dry conditions $k_{\text{Na}\beta} = 0.87 \times 10^6 \text{ s}^{-1}$ due to nucleophilic quenching by water, Figure 3-106, but its absorption intensity at 485 nm immediately following the laser pulse is significantly enhanced. In fact, the yield of the carbocation in hydrated Na β is approximately double that observed under dry conditions. Furthermore, a considerable reduction in the yield of triene isomer at 370 nm is observed in the presence of water, Figure 3-106 inset. It is therefore apparent that the coadsorbed water accelerates heterolysis from the excited state, and increases the efficiency of carbocation formation at the expense of the other photochemical reactions such as rearrangement to the triene isomer.

In order to obtain stronger evidence that the photoheterolysis of 9-fluorenols within alkali metal cation Y zeolites is enhanced by protic reagents, an alcohol with reduced nucleophilicity can be employed rather than water or methanol. It has previously been observed that photoheterolysis is the dominant reaction of photoexcited 9-fluorenols in HFIP, and that in this solvent even the highly reactive 9-fluorenyl cation is sufficiently long-lived to be easily observable on the nanosecond time scale.²⁴¹ Thus, HFIP should

be an ideal additive with which to probe the influence of protic reagents on the intrazeolite yield of photoheterolysis. Furthermore, it is also interesting to assess the influence of this relatively non-nucleophilic alcohol on the lifetimes of reactive 9-fluorenyl cations within alkali metal cation zeolites.

The inclusion of small amounts of HFIP within NaY influences both the yield and the lifetime of the 9-cyclopropyl-9-fluorenyl cation generated by laser photolysis of cPrFOH. A plot of the total change in reflectance monitored at 445 nm as a function of HFIP concentration demonstrates that coadsorption of HFIP increases carbocation formation, Figure 3-107. The magnitude by which HFIP enhances photoheterolysis is less than that achieved using water as a coadsorbate, but quite similar to the enhancement obtained with methanol. The rate constants for decay of the 9-cyclopropyl-9-fluorenyl cation are also affected by the inclusion of HFIP within NaY. Interestingly, coadsorption of HFIP actually *decreases* the rate constant for carbocation decay, Figure 3-108. This is in sharp contrast to the influence of water or methanol which increase the carbocation decay rate constant due to nucleophilic addition.

The amount of coadsorbed HFIP also has a dramatic impact on the absolute yield and decay rate constants of the 9-methyl-9-fluorenyl and 9-fluorenyl cations derived from laser photolysis of MeFOH and FOH in NaY. Inclusion of progressively higher concentrations of HFIP into NaY increases the yield of the both the 9-methyl-9-fluorenyl cation and the 9-fluorenyl cation, Figure 3-109, and decreases the rate constant for decay of these carbocations, Figure 3-110. The influence of coadsorbed HFIP on carbocation formation is more significant for photoexcited MeFOH than FOH, while the influence of coadsorbed HFIP on carbocation decay is more significant for the 9-fluorenyl cation than the 9-methyl-9-fluorenyl cation. These trends are clearly visible from the slopes of the plots in Figures 3-109 and 3-110, which are given in Table 3-25.

Table 3-25. Variation in k_{obs} and $\Delta J/J_0$ for 9-R-9-fluorenyl cations versus weight fraction of HFIP.

R	$\Delta (k_{\text{obs}} / 10^6 \text{ s}^{-1}) / \Delta (\text{wt. fr. HFIP})$		$\Delta (\Delta J/J_0) / \Delta (\text{wt. fr. HFIP})$	
	NaY	NaY	NaY	Na β
H	-35 ± 2	0.134 ± 0.004	-	-
Methyl	-22 ± 1	0.267 ± 0.006	0.090 ± 0.008	-

The influence of coadsorbed HFIP on the generation and reactivity of the 9-methyl-9-fluorenyl cation in Na β was also investigated. In this case, the relatively slow rate constant for carbocation decay in Na β exhibited little variation as a function of HFIP content. However, the yield of 9-methyl-9-fluorenyl cation again increased with increasing concentration of HFIP, with the efficiency doubling in the presence of 10 % HFIP by weight. Somewhat higher concentrations of HFIP are required to observe an increase in carbocation yield that is comparable to NaY. As well, at relatively low concentrations of HFIP, the change in reflectance density of the 9-methyl-9-fluorenyl cation in Na β is relatively gradual, while at higher concentrations the influence of added HFIP becomes increasingly significant. Thus, the relationship between carbocation yield and the weight fraction of HFIP appears to be quadratic over this range (*vide infra*).

The observation of enhanced carbocation generation *via* photoheterolysis within alkali metal cation zeolites containing coadsorbed HFIP does not prove that HFIP is actively assisting the C-OH bond cleavage of the excited state fluorenols. Although the results do support this notion, it is also possible that the inclusion of the HFIP is simply enhancing the internal ionizing ability of the zeolite microenvironment leading to more efficient photoheterolysis. In order to distinguish between these possibilities, the influence of 1,1,1,3,3,3-hexafluoroisopropanol-O-D (HFIP-OD) on the absolute yields of the 9-methyl-9-fluorenyl cation in NaY and Na β was considered relative to the undeuterated analog. The observed results demonstrate that HFIP-OD is a significantly less effective reagent than HFIP for enhancing photoheterolysis of 9-methyl-9-fluorenyl in both NaY and Na β . In NaY, Figure 3-111, the change in initial reflectance density of the 9-methyl-9-fluorenyl cation as function of HFIP is twice that produced by including the same amount of HFIP-OD into the sample, Table 3-26. In Na β , as mentioned above, the relationship between the initial reflectance and weight fraction is quadratic. However, the diminished effectiveness of HFIP-OD compared to HFIP is still readily apparent, Figure 3-112. When the reflectance change is plotted against the weight fraction of HFIP or HFIP-OD squared, a linear relationship is obtained, Figure 3-112 inset, and the slopes indicate that the non-deuterated HFIP is 1.6-fold more effective in enhancing carbocation formation than the deuterated HFIP-OD.

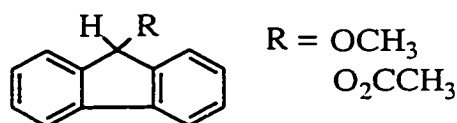
Table 3-26. Variation in $\Delta J/J_0$ for the 9-methyl-9-fluorenyl cation versus weight fraction (NaY) or weight fraction squared (Na β) of HFIP and HFIP-OD.

Zeolite	HFIP	HFIP-OD	Ratio HFIP/HFIP-OD
NaY	0.267 ± 0.006	0.133 ± 0.006	2.0
Na β	1.59 ± 0.04	0.98 ± 0.04	1.6

3.3.1.6 Other 9-Fluorenyl Precursors in Alkali Metal Cation Zeolites

Other attempts to generate the parent 9-fluorenyl cation in alkali metal cation Y zeolites were made using fluorene derivatives substituted with photolabile substituents other than the hydroxy group, Scheme 3-11.

Scheme 3-1



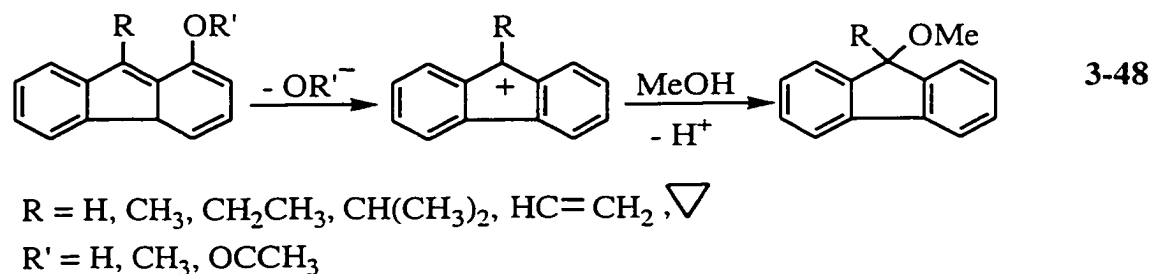
The transient diffuse reflectance spectrum obtained upon laser photolysis of 9-methoxyfluorene in NaY is dominated by an intense, long-lived absorption band with a maximum at 370 nm, Figure 3-113. This is identical to the triene isomer observed for all the 9-fluorenyls studied and indicates that rearrangement is facile for other photoexcited fluorenyl derivatives as well. No absorption due to the 9-fluorenyl cation is detected, with little absorption in the 500 nm region under either vacuum or oxygen. These observations are consistent with the reactivity of 9-fluorenyl ethers in homogeneous solution, in which efficient photolysis, rather than photolysis takes place.^{378,380,400} The absence of any significant absorption due to the 9-fluorenyl radical is also predicted from solution results which demonstrate rapid in cage disproportionation of the radical pair leading to the fluorene product.^{380,400}

When 9-acetoxyfluorene is photolyzed in NaY, a transient diffuse reflectance spectrum similar to that described for 9-methoxyfluorene is observed. Again, the spectrum is dominated by absorption due to the metastable triene isomer near 370 nm, Figure 3-114. Interestingly, in this case the triene isomer is much shorter lived, decaying over a 1 ms time scale with a rate constant of $3.5 \times 10^3 \text{ s}^{-1}$, Figure 3-114 inset (*vide infra*). Similar results are observed in LiY, where the triene isomer decays with a rate

constant of $2.4 \times 10^3 \text{ s}^{-1}$. A very weak, rapidly decaying transient is also observed near 515 nm, which may be tentatively attributed to the 9-fluorenyl cation. However, this absorption is very insignificant compared to the other spectral features and indicates that heterolysis is a very minor pathway for photoexcited 9-acetoxyfluorene in LiY and NaY. This is consistent with the reduced photoheterolysis efficiency of 9-acetoxyfluorene compared to 9-hydroxyfluorene observed in solution.³⁸⁰

3.3.1.7 Triene Isomers of 9-Fluorenols

Laser photolysis of all the 9-substituted fluorenes examined in this work produces a very unreactive transient with an absorption maximum at 370 nm which has been attributed to a triene isomer generated by photoinduced rearrangement, Scheme 3-10, path (c). Several pieces of evidence support this assignment including literature precedent for this type of rearrangement upon photolysis of 9-fluorenol³⁸³ and related compounds such as substituted benzyl acetates in solution.^{392,393} In addition, investigations of the behaviour of the long-lived transient in both zeolites and solution are consistent with this identification. The decay at 370 nm can be monitored over very long time regimes in solution and in zeolite environments using conventional UV-Vis transmission and diffuse reflectance spectroscopy. The decays of the absorption or diffuse reflectance at 370 nm upon photolysis of 9-fluorenols are first-order with decay rate constants in the range of 10^{-4} to 10^{-2} s^{-1} , Table 3-27. The observed trends in decay rate constants as a function of medium and leaving group are consistent with the expected behaviour of these triene isomers which presumably decay *via* thermal solvolysis/ionization through the carbocation intermediate, eq. 3-48.



The methyl substituted triene isomer of 9-fluorenol is significantly more reactive than the unsubstituted isomer in both methanol solution, Figure 3-115, and NaY, Figure 3-116. The decay rate constants for the triene isomers of 9-cyclopropyl-9-fluorenol and 9-phenyl-9-fluorenol in methanol are even larger, Table 3-27. Thus, consistent with a

reaction proceeding through a carbocation intermediate, as proposed in eq. 3-46, the reactivity increases with the ability of the substituent to stabilize the carbocation. In addition, the decay of the triene isomer of 9-acetoxyfluorene in NaY is considerably faster than the triene isomers of either 9-methoxyfluorene or 9-fluorenol. If the mechanism of triene isomer decay involves initial R-group heterolysis, it should be dependent on the nature of the leaving group. Since the acetoxy group is a considerably better leaving group than either methoxy or hydroxy, the triene isomer of 9-acetoxyfluorene should be the most reactive. Overall, the decay rate constants determined for the triene isomers parallel trends in leaving group efficiency and stability of the corresponding carbocation intermediate. Furthermore, both the unsubstituted and methyl substituted triene isomers are notably more reactive in NaY than in methanol, Table 3-27, which is consistent with the more ionizing environment within the cavities of NaY as compared to methanol.

Table 3-27. First-order rate constants for decay of the triene isomers of 9-R-9-fluorenols and 9-acetoxy-9-fluorene in methanol and NaY.

R	$k_{\text{decay}} / 10^{-4} \text{ s}^{-1}$	
	Methanol	NaY
H	2.49 ± 0.01	37.4 ± 0.3
Methyl	8.35 ± 0.01	144 ± 2
Cyclopropyl	146 ± 5	not measured
Phenyl	130 ± 5	not measured
9-Acetoxy-9-Fluorene	not measured	$(3.5 \pm 0.2) \times 10^7$

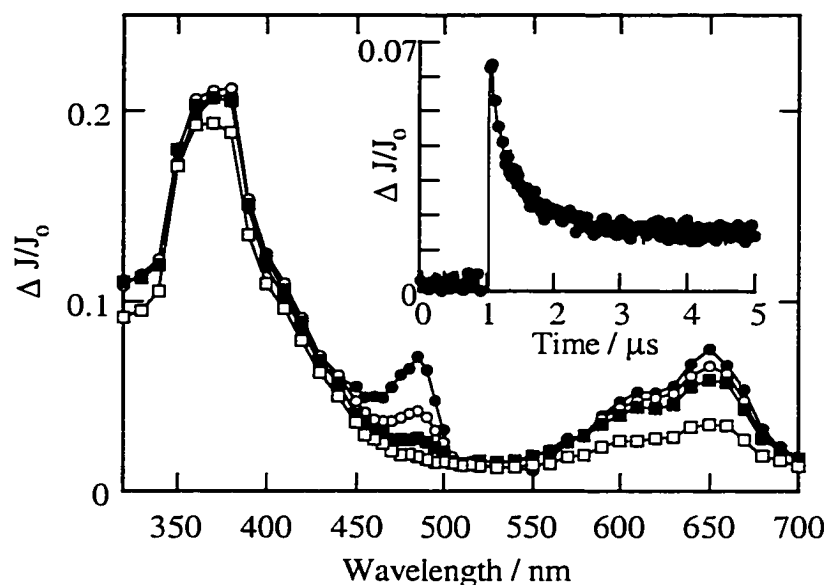


Figure 3-48. Transient diffuse reflectance spectrum generated 140 ns (closed circles), 360 ns (open circles), 760 ns (closed squares), and 7.00 μs (open squares) after 308 nm laser irradiation of MeFOH in oxygen-saturated NaY. Inset shows the decay trace monitored at 485 nm.

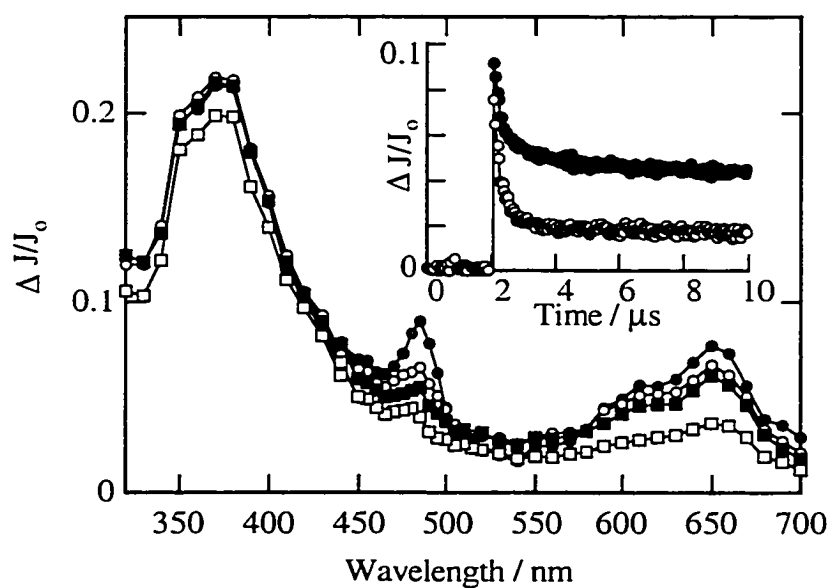


Figure 3-49. Transient diffuse reflectance spectrum generated 140 ns (closed circles), 360 ns (open circles), 760 ns (closed squares), and 7.00 μs (open squares) after 308 nm laser irradiation of MeFOH in evacuated NaY. Inset shows the decay trace monitored at 485 nm under vacuum (closed circles) and oxygen conditions (open circles).

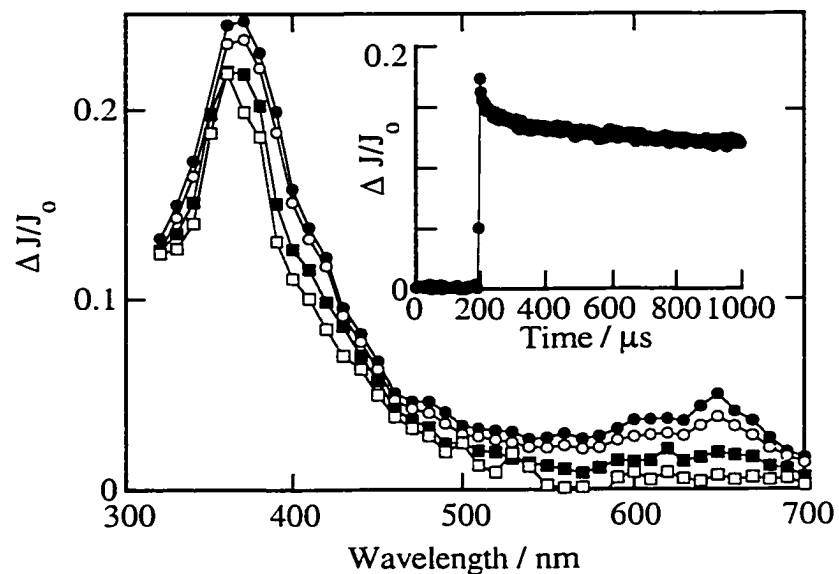


Figure 3-50. Transient diffuse reflectance spectrum generated 4.88 μs (closed circles), 14.8 μs (open circles), 106 μs (closed squares), and 744 μs (open squares) after 308 nm laser irradiation of MeFOH in oxygen-saturated NaY. Inset shows the decay trace monitored at 370 nm.

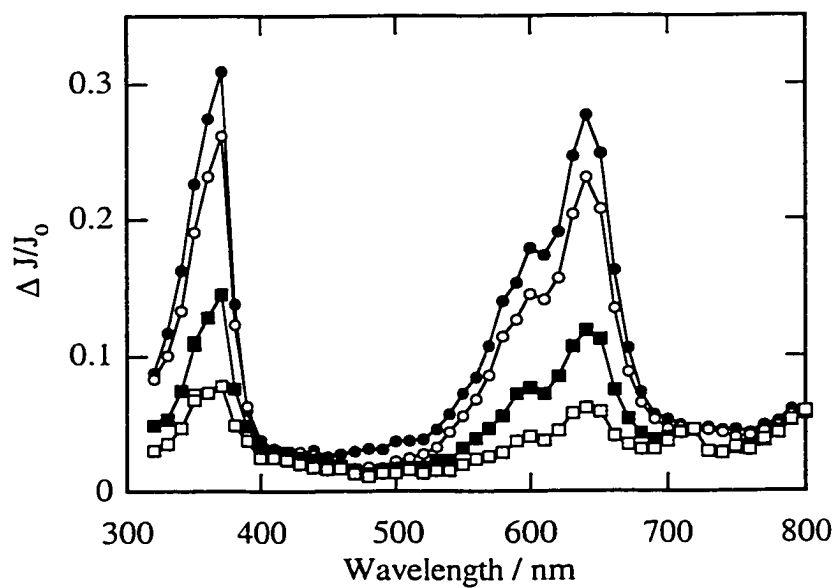


Figure 3-51. Transient diffuse reflectance spectrum generated 520 ns (closed circles), 7.80 μs (open circles), 98.0 μs (closed squares), and 314 μs (open squares) after 308 nm laser irradiation of fluorene in oxygen-saturated NaY.

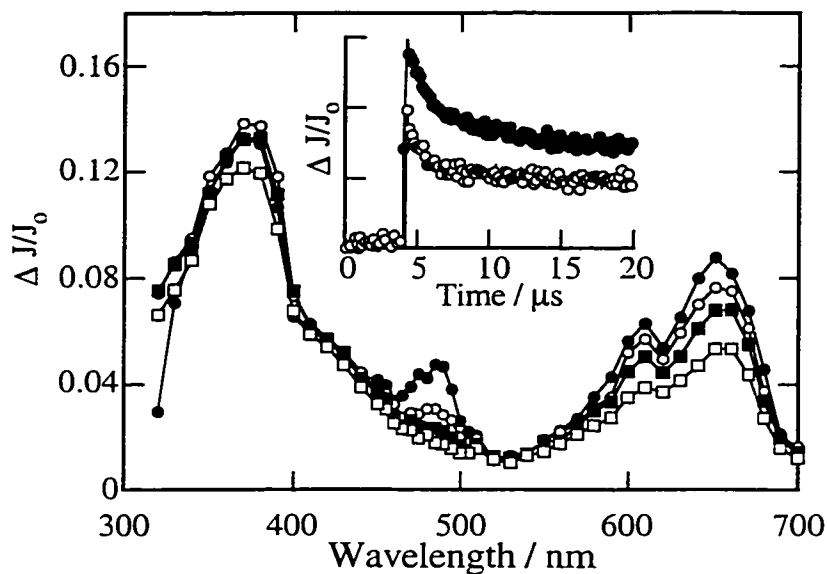


Figure 3-52. Transient diffuse reflectance spectrum generated 200 ns (closed circles), 800 ns (open circles), 2.00 μs (closed squares), and 7.40 μs (open squares) after 308 nm laser irradiation of MeFOH in oxygen-saturated LiY. Inset shows the decay trace monitored at 485 nm under vacuum (closed circles) and oxygen conditions (open circles).

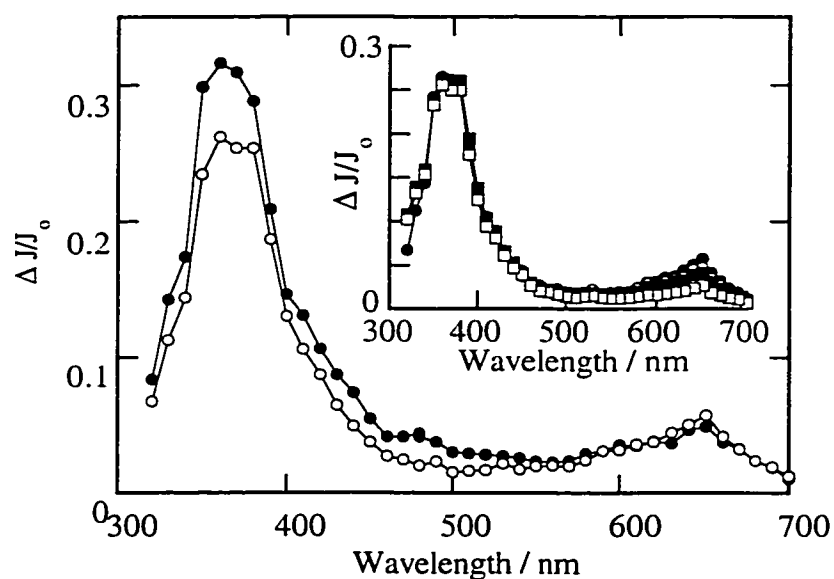


Figure 3-53. Transient diffuse reflectance spectrum generated 200 ns after laser photolysis of MeFOH in KY under vacuum (closed circles) and oxygen (open circles) conditions. Inset shows the transient spectrum observed 240 ns (closed circles), 640 ns (open circles), 1.56 μs (closed squares), and 14.8 μs (open squares) after 308 nm laser irradiation of MeFOH in oxygen-saturated KY.

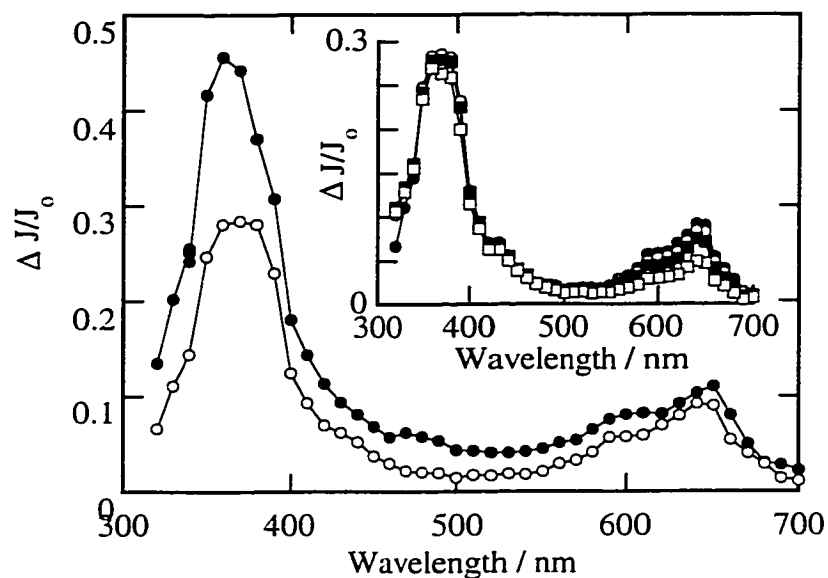


Figure 3-54. Transient diffuse reflectance spectrum generated 200 ns after laser photolysis of MeFOH in RbY under vacuum (closed circles) and oxygen (open circles) conditions. Inset shows the transient spectrum observed 240 ns (closed circles), 640 ns (open circles), 1.56 μ s (closed squares), and 14.8 μ s (open squares) after 308 nm laser irradiation of MeFOH in oxygen-saturated RbY.

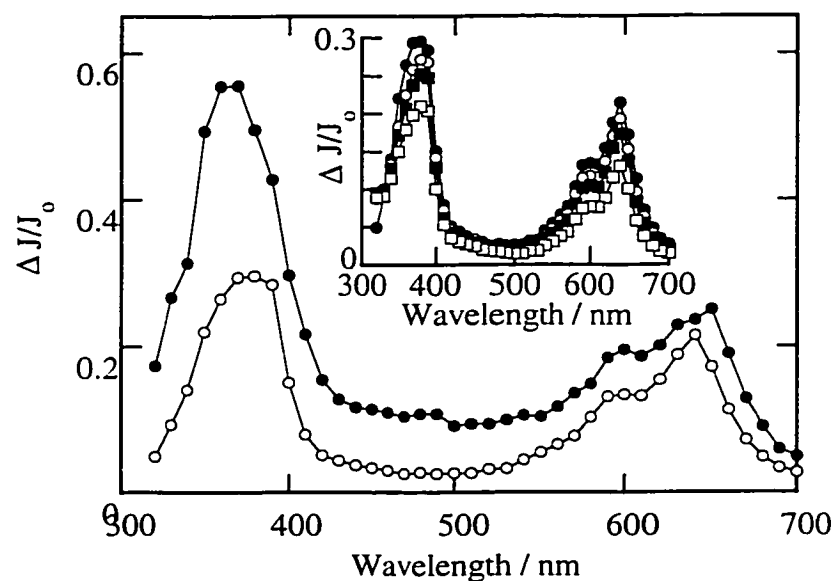


Figure 3-55. Transient diffuse reflectance spectrum generated 200 ns after laser photolysis of MeFOH in CsY under vacuum (closed circles) and oxygen (open circles) conditions. Inset shows the transient spectrum observed 240 ns (closed circles), 640 ns (open circles), 1.56 μ s (closed squares), and 14.8 μ s (open squares) after 308 nm laser irradiation of MeFOH in oxygen-saturated CsY.

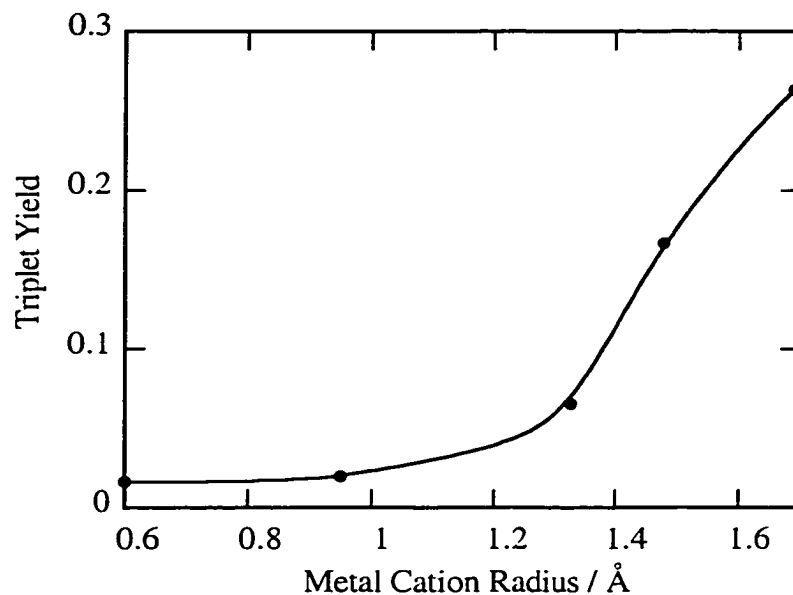


Figure 3-56. Yield of triplet MeFOH as a function of alkali metal cation radius observed following laser photolysis of MeFOH in evacuated alkali metal cation Y zeolites. The triplet yield is determined by the difference in the change in diffuse reflectance observed at 370 nm immediately following the laser pulse under vacuum and oxygen conditions.

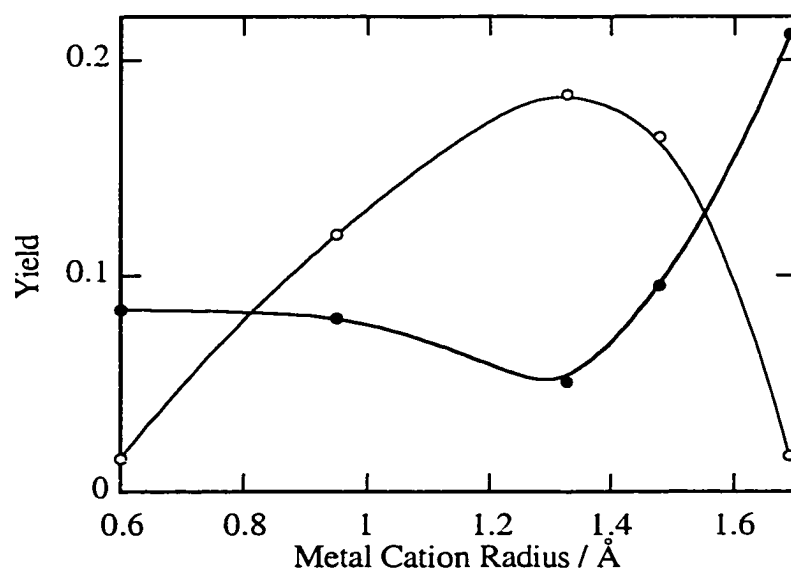


Figure 3-57. Yield of radical cation (closed circles) and triene isomer (open circles) of MeFOH as a function of alkali metal cation radius observed following laser photolysis of MeFOH in evacuated alkali metal cation Y zeolites. The yield of radical cation and triene isomer are determined by the change in diffuse reflectance at 640 nm immediately following the laser pulse, and at 370 nm 1 ms after the laser pulse, respectively.

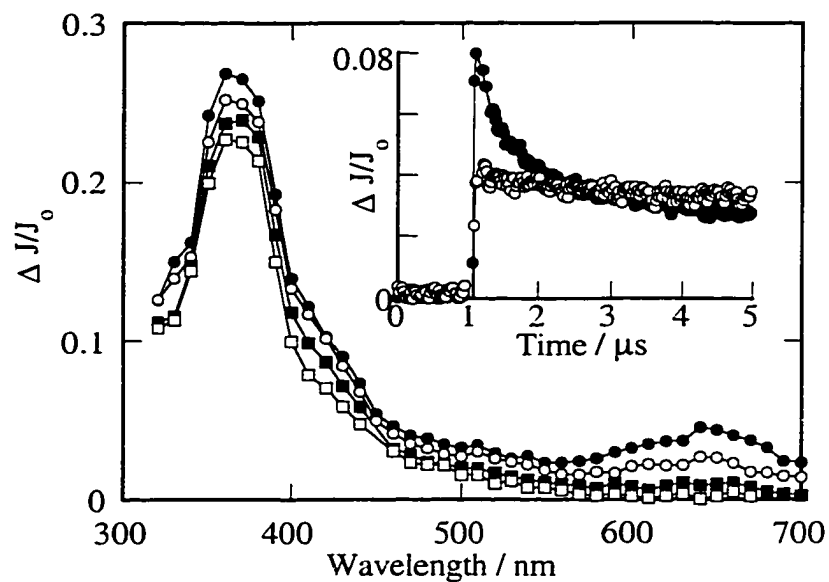


Figure 3-58. Transient diffuse reflectance spectrum generated 360 ns (closed circles), 4.88 μ s (open circles), 120 μ s (closed squares), and 680 μ s (open squares) after 308 nm laser irradiation of MeFOH in evacuated NaX. Inset compares the decay traces monitored at 485 nm following photolysis of MeFOH in NaY (closed circles) and NaX (open circles).

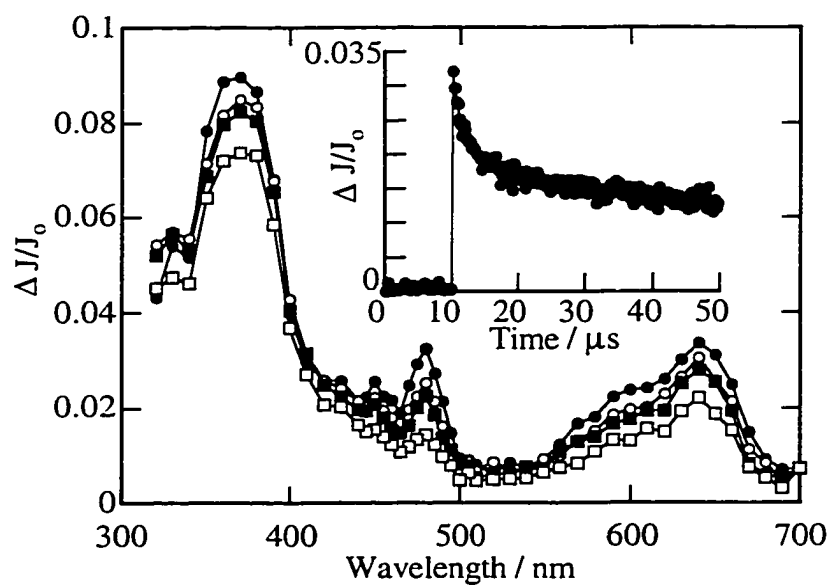


Figure 3-59. Transient diffuse reflectance spectrum generated 400 ns (closed circles), 1.90 μ s (open circles), 4.00 μ s (closed squares), and 37.0 μ s (open squares) after 308 nm laser irradiation of MeFOH in oxygen-saturated Na β . The decay trace monitored at 485 nm is shown in the inset.

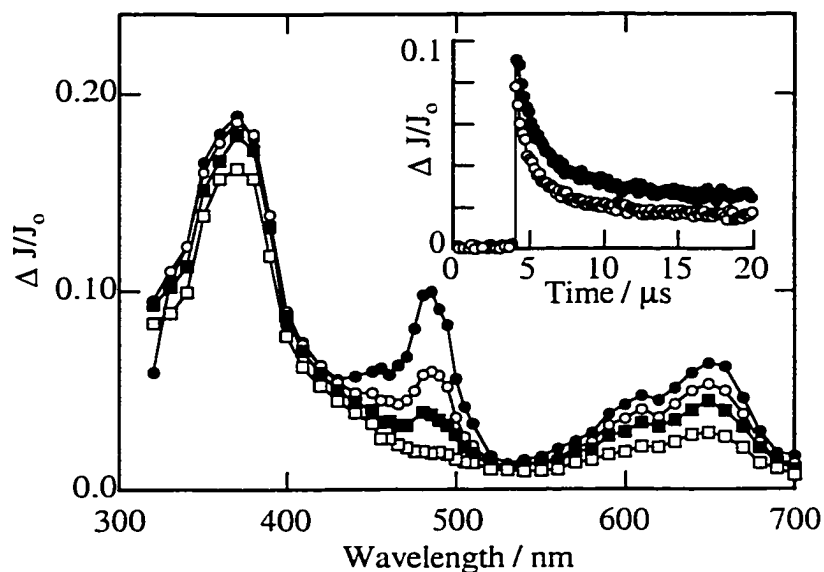


Figure 3-60. Transient diffuse reflectance spectrum generated 240 ns (closed circles), 800 ns (open circles), 2.00 μs (closed squares), and 7.40 μs (open squares) after 308 nm laser irradiation of EtFOH in oxygen-saturated LiY. Inset compares the decay traces monitored at 485 nm under vacuum (closed circles) and oxygen conditions (open circles).

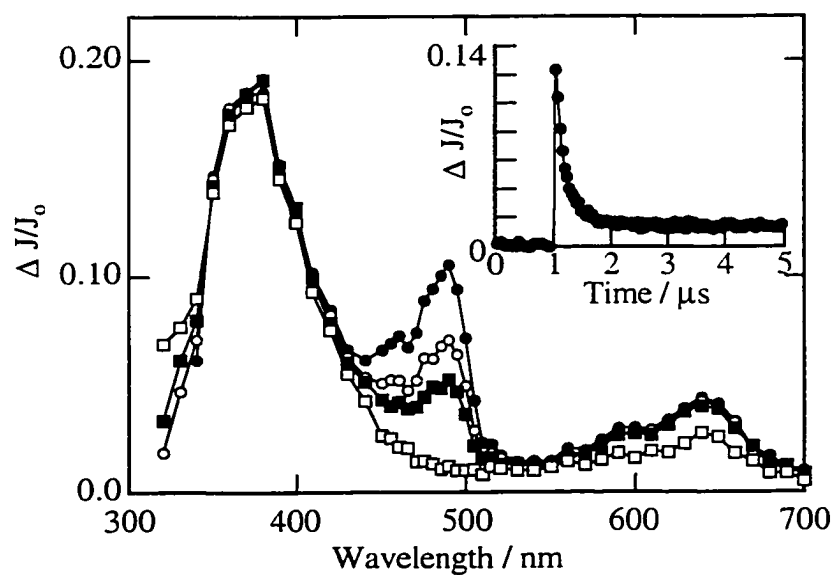


Figure 3-61. Transient diffuse reflectance spectrum generated 160 ns (closed circles), 240 ns (open circles), 320 ns (closed squares), and 6.08 μs (open squares) after 308 nm laser irradiation of iPrFOH in oxygen-saturated NaY. The decay trace monitored at 485 nm is shown in the inset.

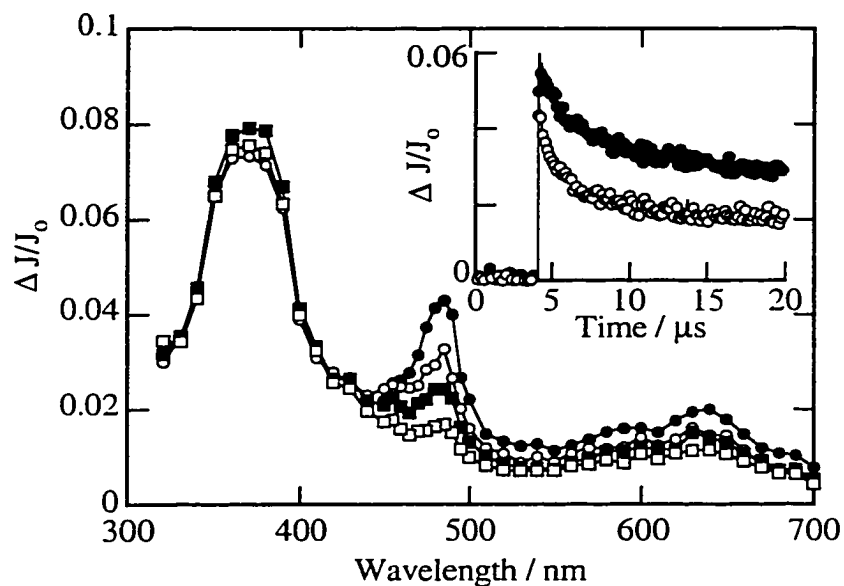


Figure 3-62. Transient diffuse reflectance spectrum generated 240 ns (closed circles), 880 ns (open circles), 2.08 μs (closed squares), and 14.8 μs (open squares) after 308 nm laser photolysis of EtFOH in oxygen-saturated Na β . Inset compares the decay traces at 485 nm under vacuum (closed circles) and oxygen (open circles) conditions.

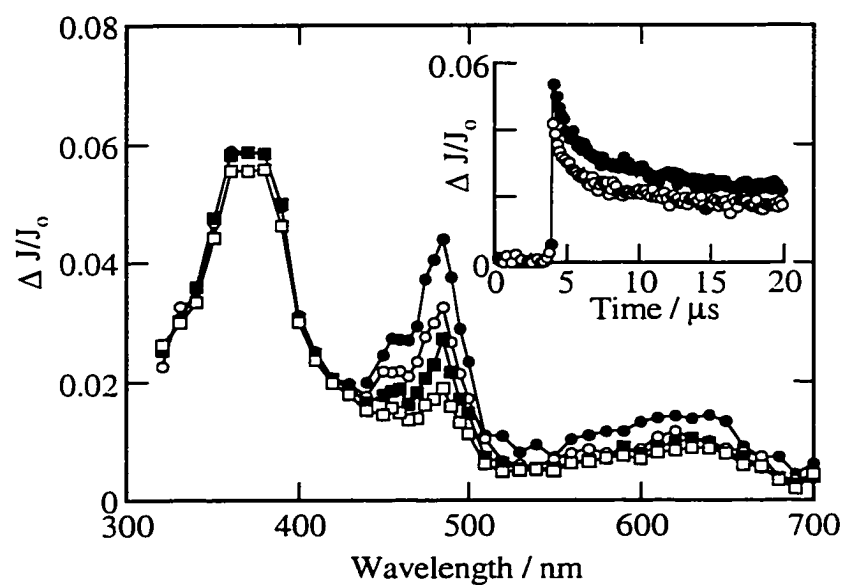


Figure 3-63. Transient diffuse reflectance spectrum generated 240 ns (closed circles), 880 ns (open circles), 2.08 μs (closed squares), and 14.8 μs (open squares) after 308 nm laser photolysis of iPrFOH in oxygen-saturated Na β . Inset compares the decay traces at 485 nm in evacuated (closed circles) and oxygen-saturated (open circles) Na β .

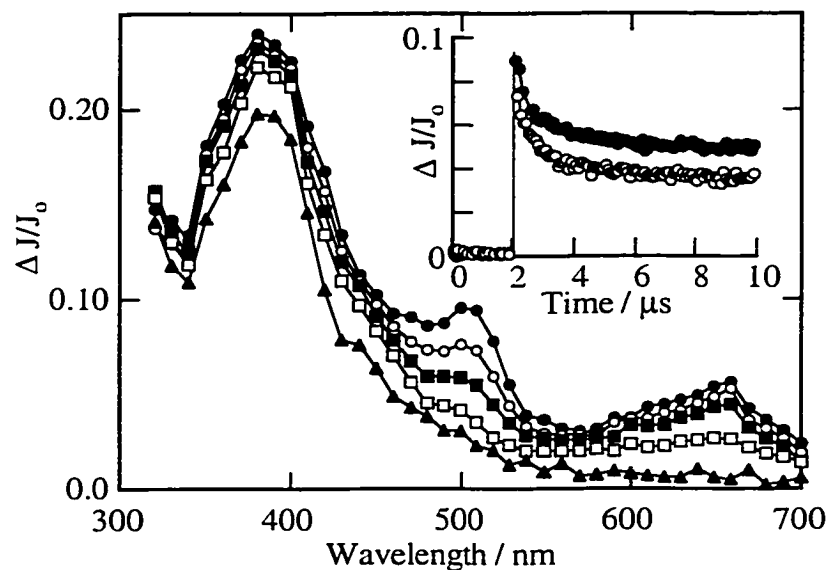


Figure 3-64. Transient diffuse reflectance spectrum generated 100 ns (closed squares), 6.88 μ s (open squares), and 704 μ s after 308 nm laser irradiation of vFOH in oxygen-saturated NaY. Inset compares the decay traces monitored at 485 nm under vacuum (closed circles) and oxygen conditions (open circles).

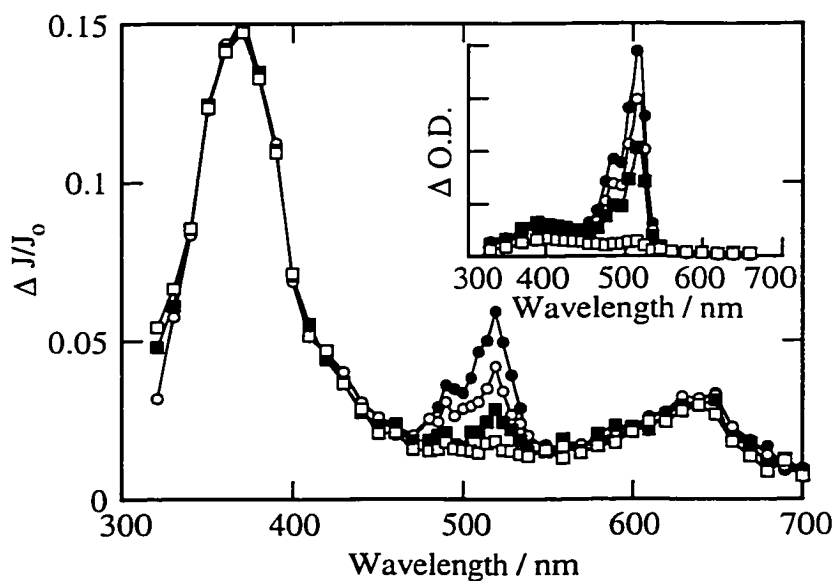


Figure 3-65. Transient diffuse reflectance spectrum generated 120 ns (closed circles), 480 ns (open circles), 1.18 μ s (closed squares), and 3.12 μ s (open squares) after 308 nm laser photolysis of FOH in oxygen-saturated LiY. Inset shows the transient absorption spectrum generated 200 ns (closed circles), 2.10 μ s (open circles), 5.10 μ s (closed squares), and 37.1 μ s (open squares) after 308 nm laser photolysis of FOH in HFIP.

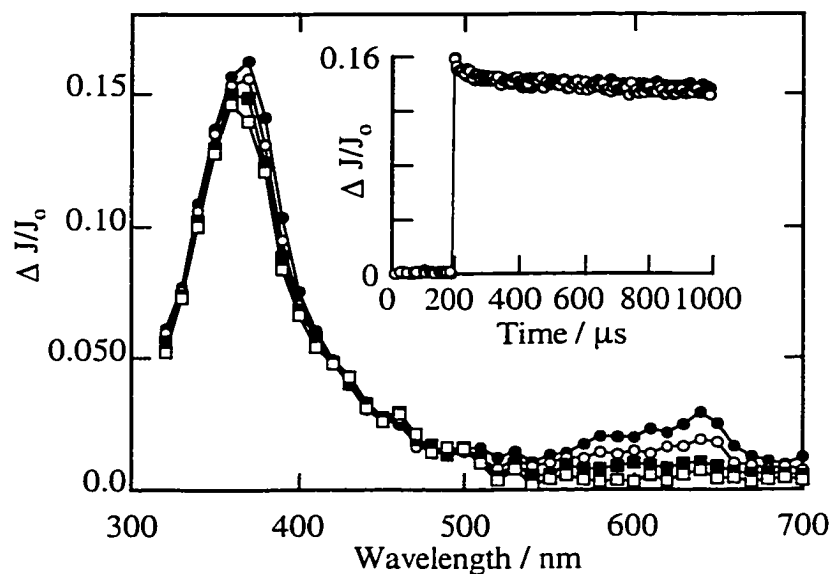


Figure 3-66. Transient diffuse reflectance spectrum generated 16.0 μs (closed circles), 74.0 μs (open circles), 278 μs (closed squares), and 748 μs (open squares) after 308 nm laser photolysis of FOH in oxygen-saturated LiY. A comparison of the decay kinetics monitored at 370 nm under vacuum (closed circles) and oxygen (open circles) conditions is shown in the inset.

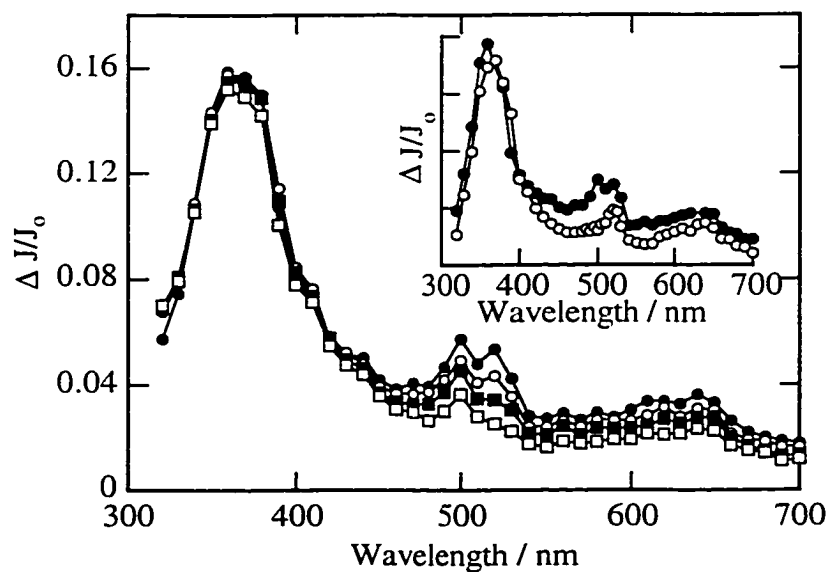


Figure 3-67. Transient diffuse reflectance spectrum generated 720 ns (closed circles), 1.36 μs (open circles), 2.88 μs (closed squares), and 15.2 μs (open squares) in LiY. Inset compares the decay traces monitored at 515 nm under vacuum (closed circles) and oxygen (open circles) conditions.

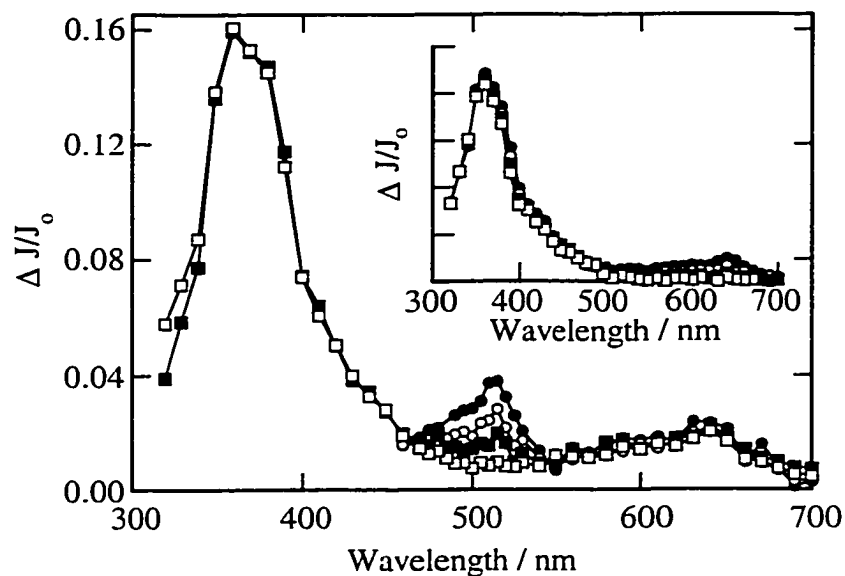


Figure 3-68. Transient diffuse reflectance spectrum generated 50 ns (closed circles), 120 ns (open circles), 320 ns (closed squares), and 3.70 μ s (open squares) after 308 nm laser photolysis of FOH in oxygen-saturated NaY. Inset shows the same transient spectrum observed 16.0 μ s (closed circles), 74.0 μ s (open circles), 278 μ s (closed squares), and 748 μ s (open squares) after photolysis.

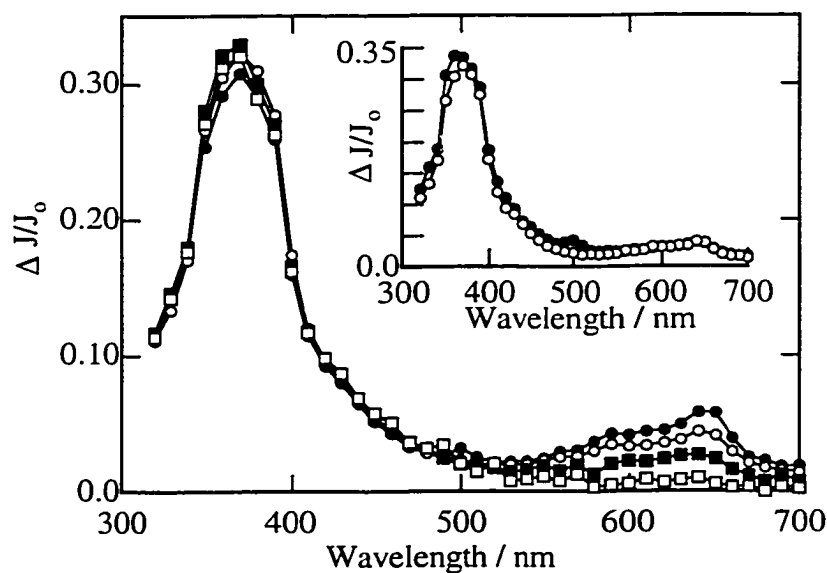


Figure 3-69. Transient diffuse reflectance spectrum generated 240 ns (closed circles), 8.40 μ s (open circles), 74.0 μ s (closed squares), and 748 μ s (open squares) after 308 nm laser irradiation of FOH in evacuated KY. Inset compares the transient spectrum generated 14.8 μ s after laser photolysis of FOH in KY under vacuum (closed circles) and oxygen conditions (open circles).

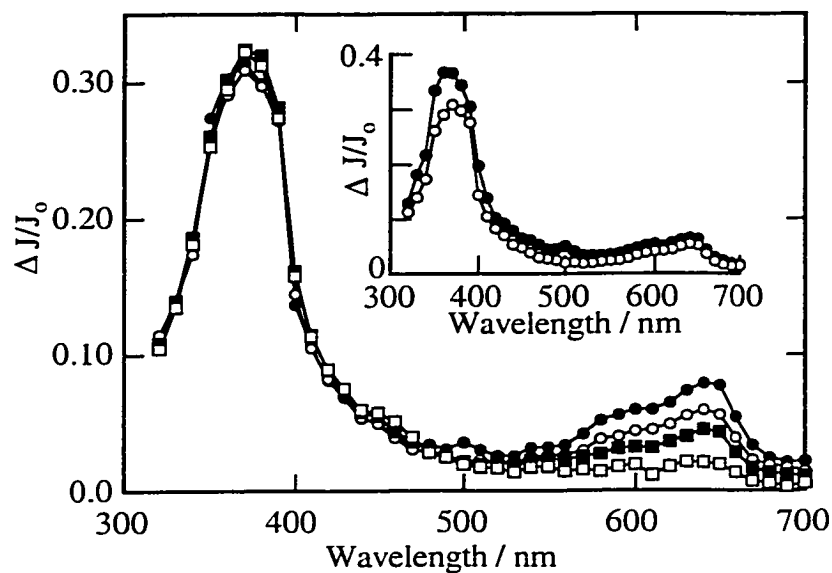


Figure 3-70. Transient diffuse reflectance spectrum generated 240 ns (closed circles), 8.40 μ s (open circles), 74.0 μ s (closed squares), and 748 μ s (open squares) after 308 nm laser irradiation of FOH in evacuated RbY. Inset compares the transient spectrum generated 14.8 μ s after laser photolysis of FOH in RbY under vacuum (closed circles) and oxygen conditions (open circles).

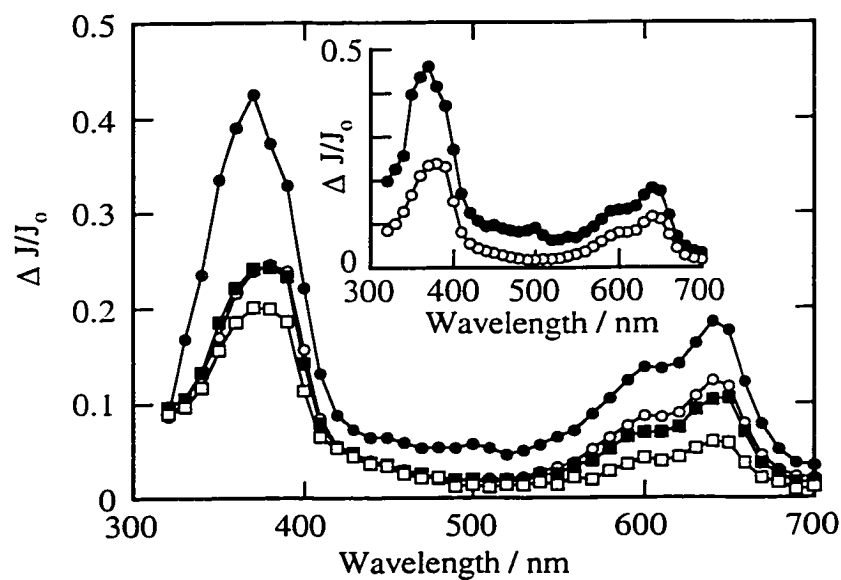


Figure 3-71. Transient diffuse reflectance spectrum generated 240 ns (closed circles), 8.40 μ s (open circles), 74.0 μ s (closed squares), and 748 μ s (open squares) after 308 nm laser irradiation of FOH in evacuated CsY. Inset compares the transient spectrum generated 14.8 μ s after laser photolysis of FOH in CsY under vacuum (closed circles) and oxygen conditions (open circles).

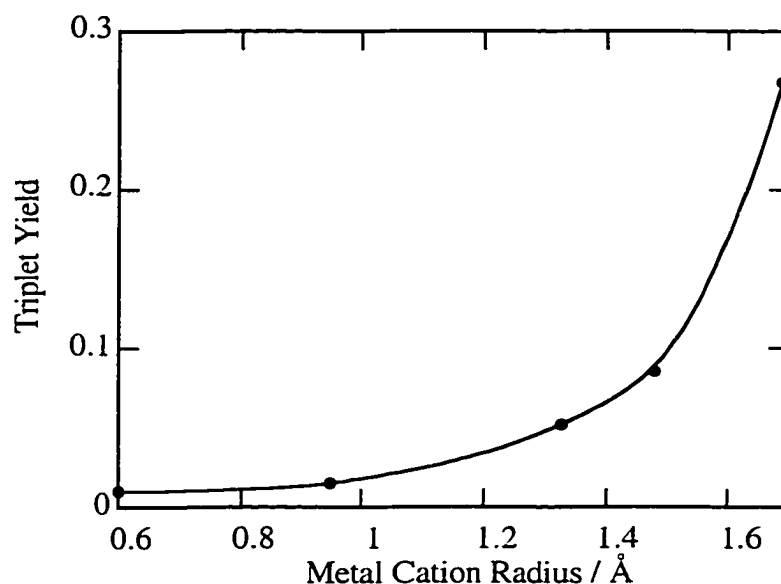


Figure 3-72. Yield of triplet FOH as a function of alkali metal cation radius observed following laser photolysis of FOH in evacuated alkali metal cation Y zeolites. The triplet yield is determined by the difference in the change in diffuse reflectance observed at 370 nm immediately following the laser pulse under vacuum and oxygen conditions.

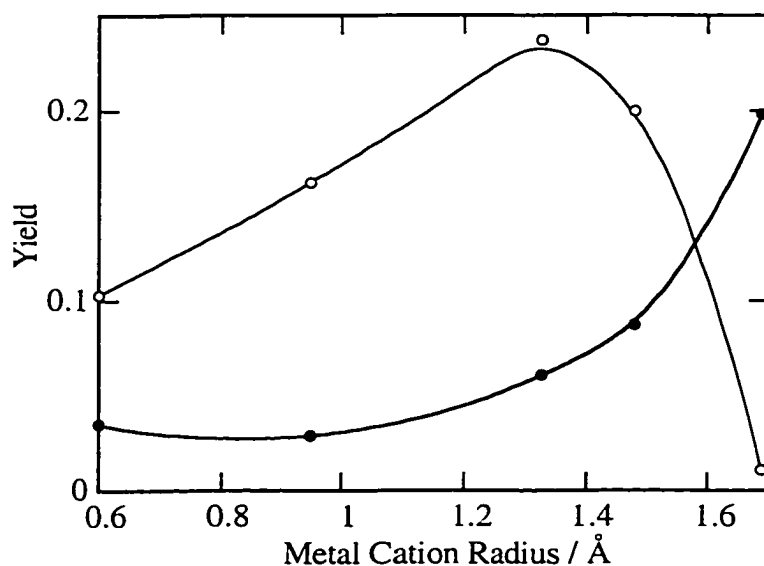


Figure 3-73. Yield of radical cation (closed circles) and triene isomer (open circles) of FOH as a function of alkali metal cation radius observed following laser photolysis of FOH in evacuated alkali metal cation Y zeolites. The yield of radical cation and triene isomer are determined by the change in diffuse reflectance at 640 nm immediately following the laser pulse, and at 370 nm 1 ms after the laser pulse, respectively.

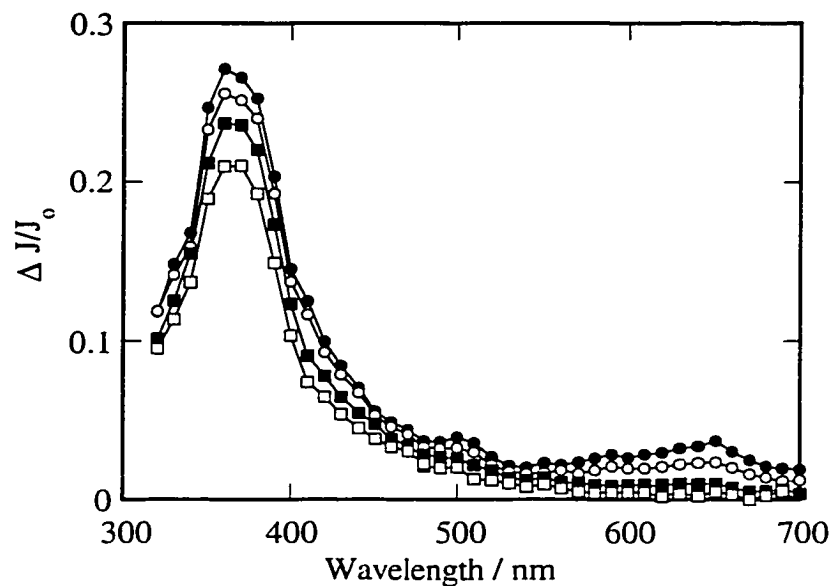


Figure 3-74. Transient diffuse reflectance spectrum generated 480 ns (closed circles), 7.36 μ s (open circles), 124 μ s (closed squares), and 684 μ s (open squares) after 308 nm laser irradiation of FOH in evacuated NaX.

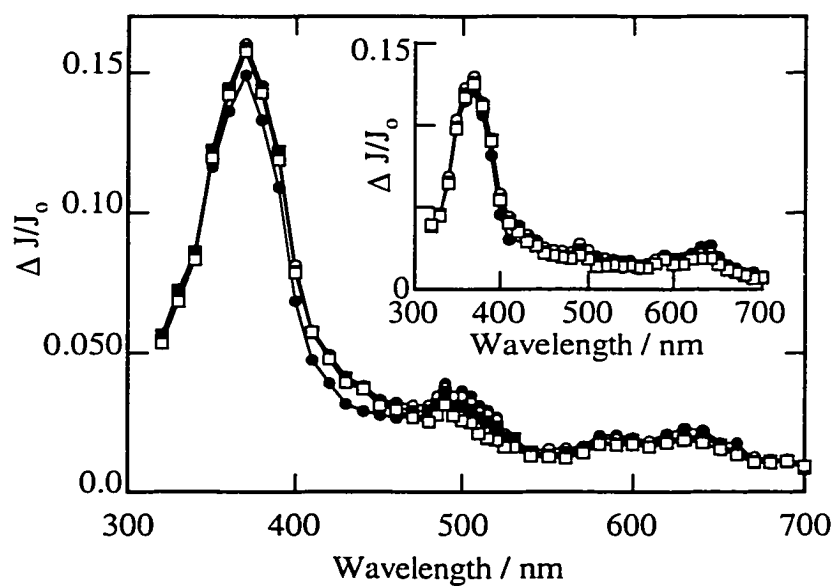


Figure 3-75. Transient diffuse reflectance spectrum generated 320 ns (closed circles), 2.24 μ s (open circles), 7.84 μ s (closed squares), and 14.8 μ s (open squares) after 308 nm laser irradiation of FOH in evacuated Na β . The transient diffuse reflectance spectrum observed at the same time delays in oxygen-saturated Na β is given in the inset.

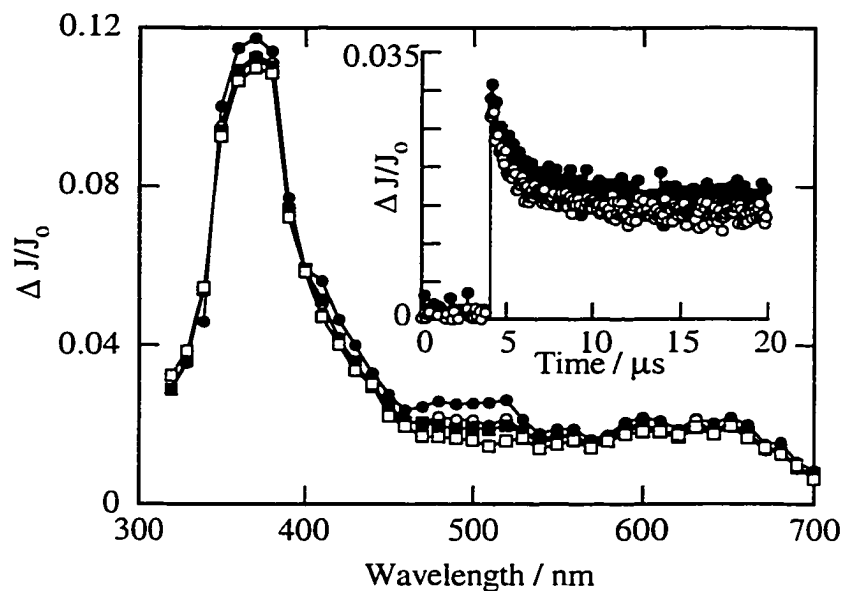


Figure 3-76. Transient diffuse reflectance spectrum generated 400 ns (closed circles), 1.44 μs (open circles), 2.08 μs (closed squares), and 14.0 μs (open squares) after 308 nm laser irradiation of FOH in evacuated NaMor. Inset shows the decay traces observed at 515 nm under vacuum (closed circles) and oxygen (open circles) conditions.

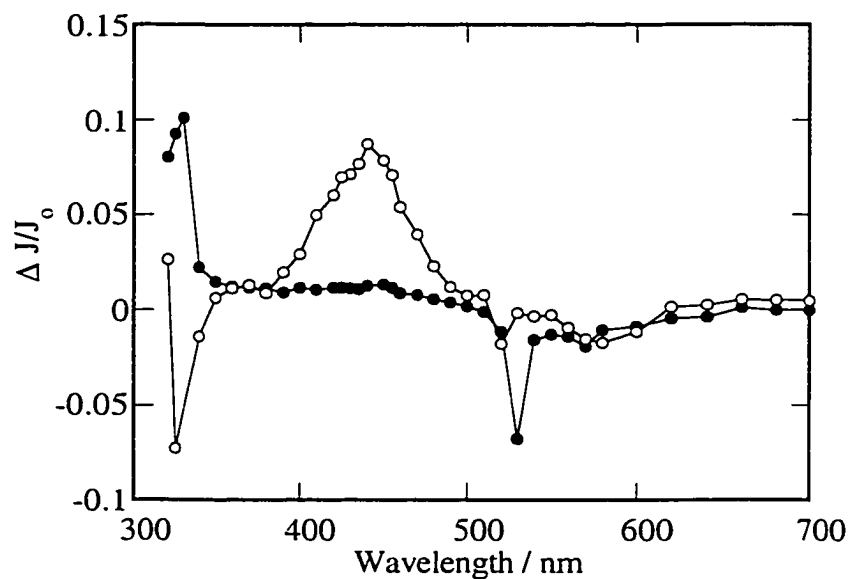


Figure 3-77. Transient diffuse reflectance spectrum generated by two laser excitation of diphenylacetic acid in evacuated NaY. Spectra are recorded immediately following 266 nm laser photolysis (closed circles) and immediately following 308 nm laser photolysis (open circles). The delay time between the two laser pulses is 1 μs .

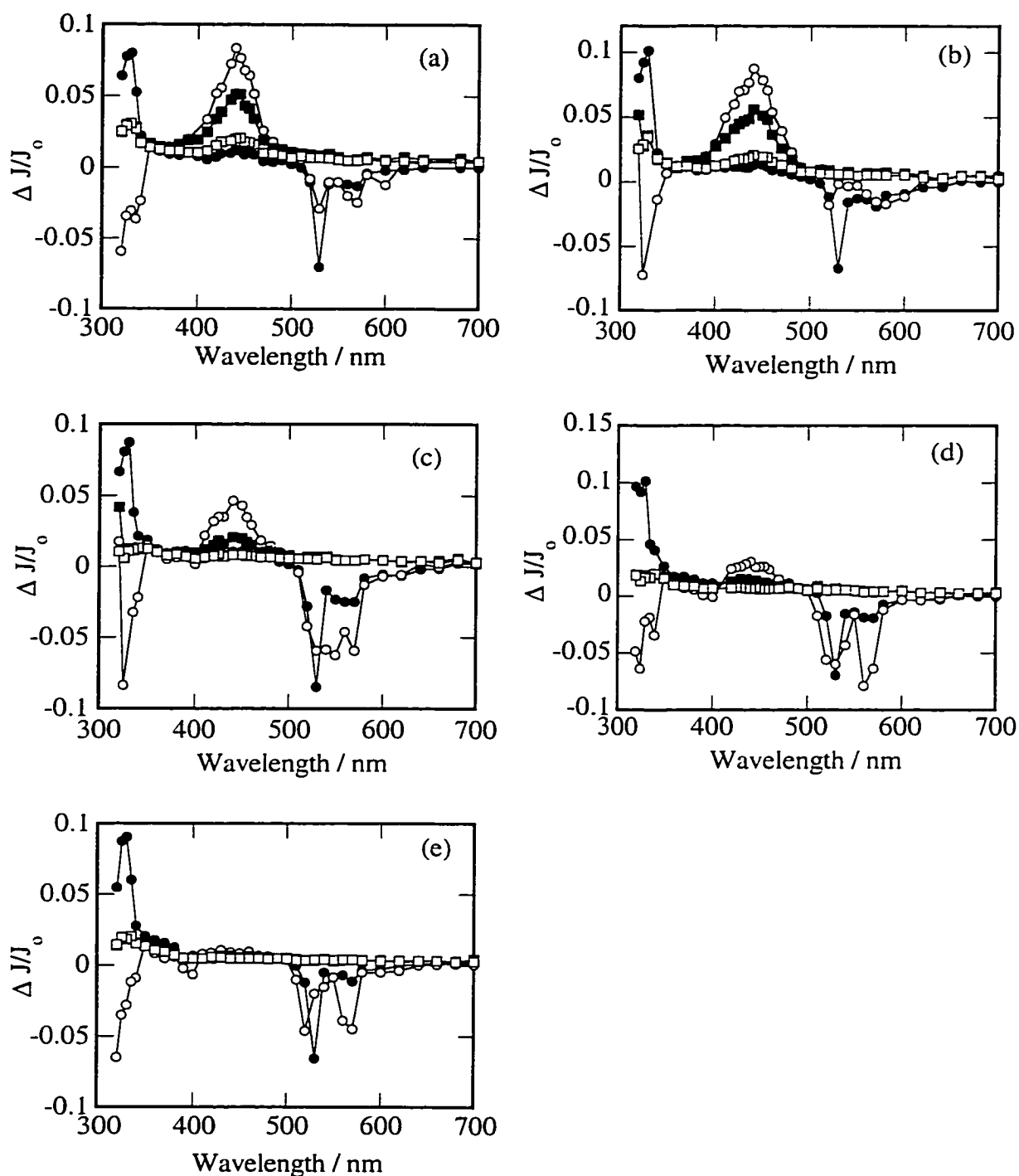


Figure 3-78. Transient diffuse reflectance spectra generated by two laser excitation of diphenylacetic acid in evacuated LiY (a), NaY (b), KY (c), RbY (d) and CsY (e). Spectra are recorded 320 ns (closed circles), 1.28 μ s (open circles), 3.24 μ s (closed squares), and 14.8 μ s (open squares) after the first (266 nm) laser pulse. The delay time between the two laser pulses is 1 μ s.

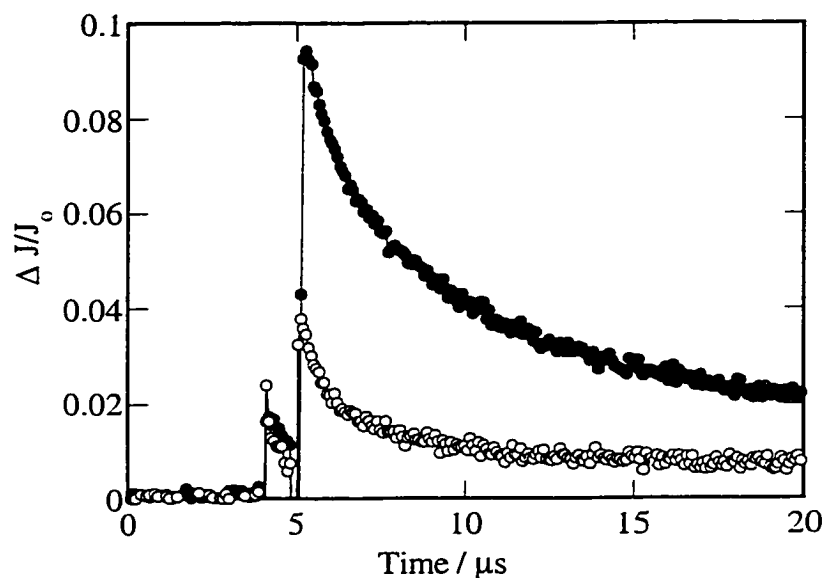


Figure 3-79. Decay traces monitored at 440 nm following two laser excitation of diphenylacetic acid in evacuated LiY (closed circles) and RbY (open circles).

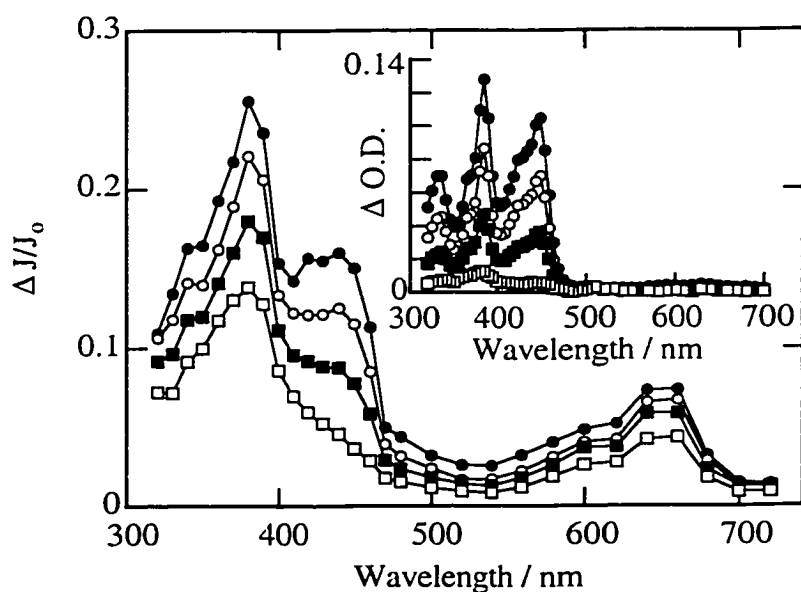


Figure 3-80. Transient diffuse reflectance spectrum generated 700 ns (closed circles), 2.40 μ s (open circles), 7.00 μ s (closed squares), and 34.0 μ s (open squares) after 308 nm laser irradiation of cPrFOH in evacuated NaY. Inset shows the transient absorption spectrum generated 4.00 μ s (closed circles), 35.0 μ s (open circles), 97.0 μ s (closed squares), and 352 μ s (open squares) after 308 nm laser photolysis of cPrFOH in TFE.

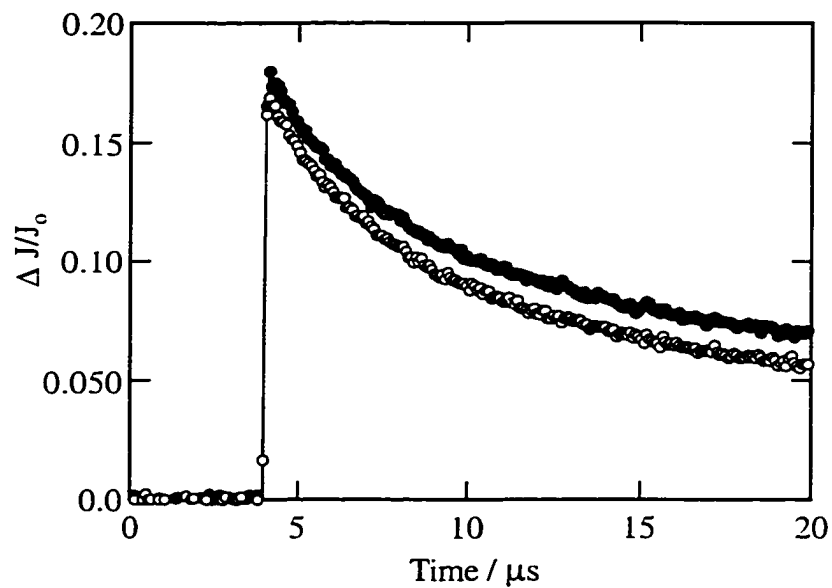


Figure 3-81. Decay traces monitored at 445 nm following 308 nm laser photolysis of cPrFOH in evacuated (closed circles) and oxygen-saturated (open circles) NaY.

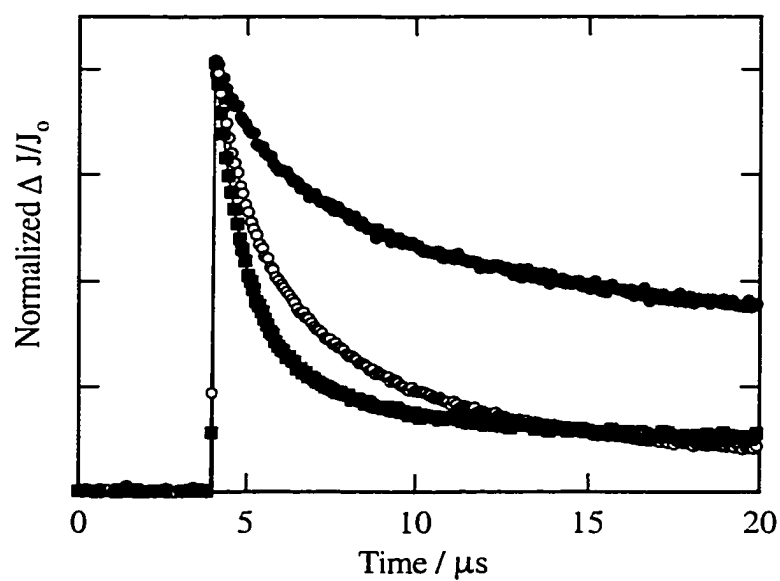


Figure 3-82. Normalized decay traces monitored at 445 nm following 308 nm laser photolysis of cPrFOH in dry NaY (closed circles), and in NaY containing 6 weight % water (open circles) or methanol (closed squares).

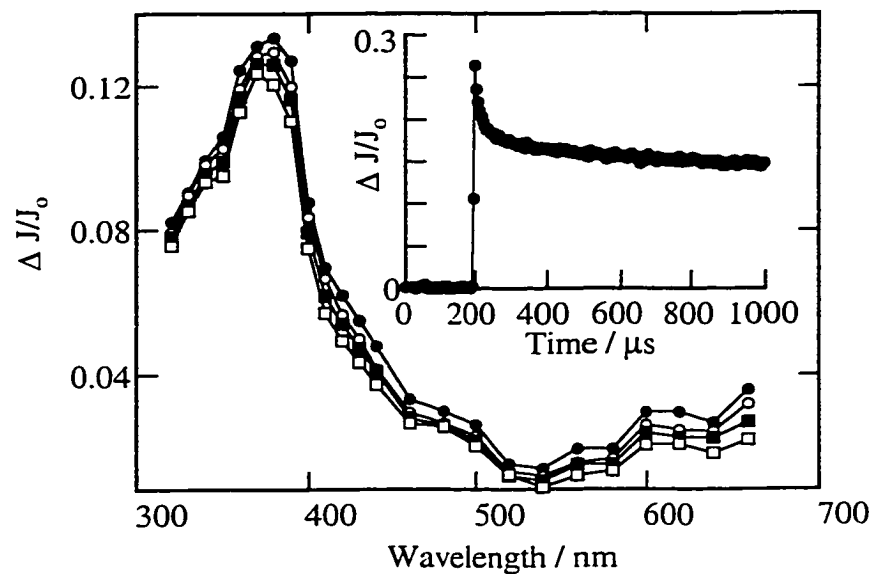


Figure 3-83. Transient diffuse reflectance spectrum generated 16.8 μ s (closed circles), 294 μ s (open circles), 440 μ s (closed squares), and 684 μ s (open squares) after 308 nm laser irradiation of cPrFOH in evacuated NaY. Inset shows the decay trace monitored at 370 nm.

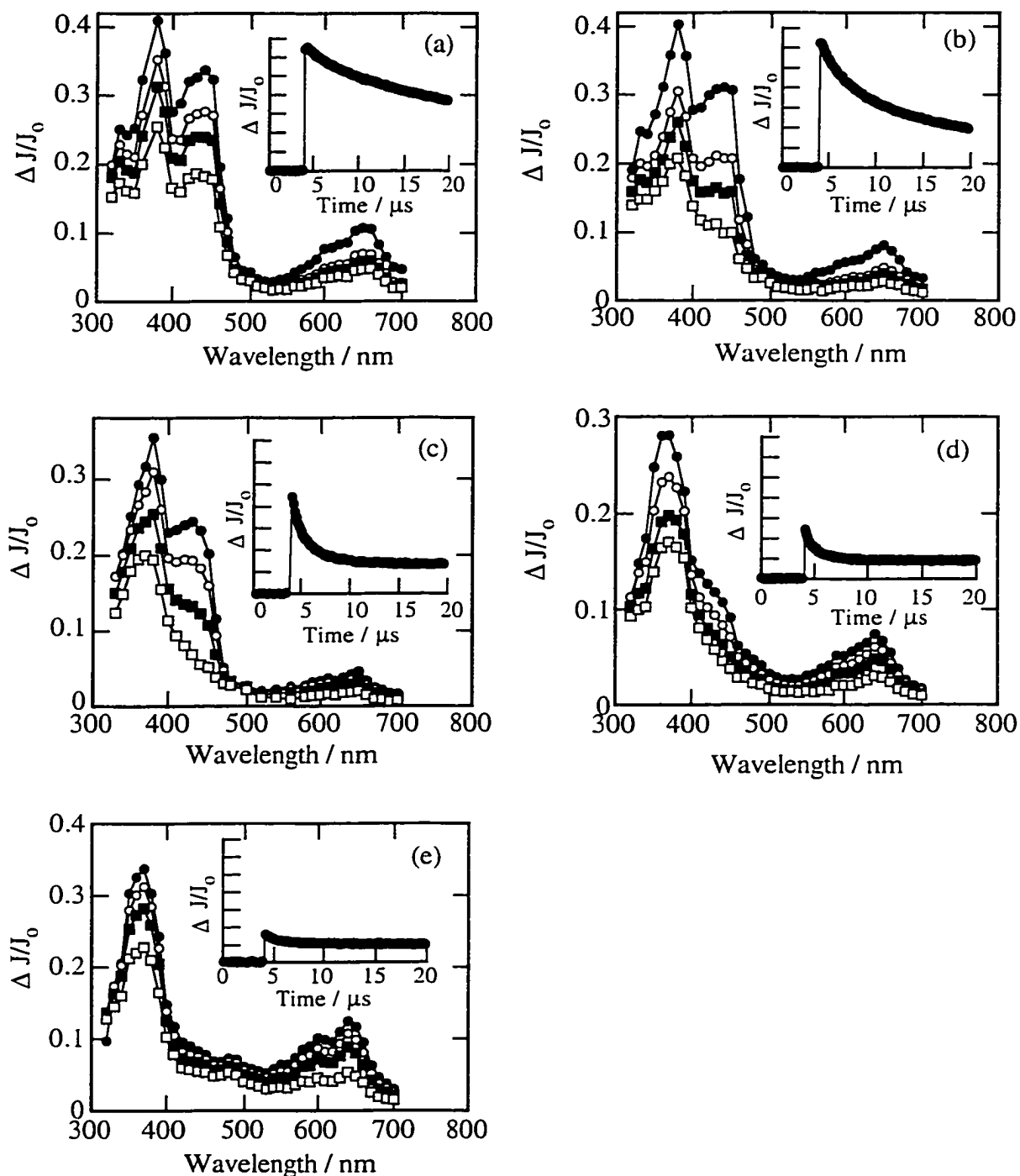


Figure 3-84. Transient diffuse reflectance spectrum generated 320 ns (closed circles), 2.96 μ s (open circles), 6.00 μ s (closed squares), and 14.8 μ s (closed squares) after photolysis in LiY (a) and NaY (b), and 320 ns (closed circles), 800 ns (open circles), 2.00 μ s (closed squares), and 14.0 μ s (open squares) after photolysis in KY (c), RbY (d) and CsY (e). Insets show decay traces monitored at 445 nm (top $\Delta J/J_0 = 0.35$ in each case).

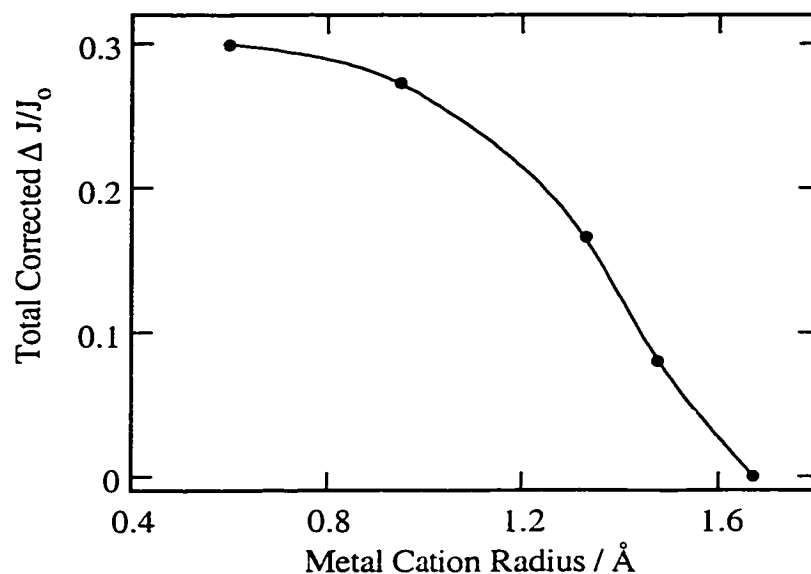


Figure 3-85. Yield of the 9-cyclopropyl-9-fluorenyl cation as a function of alkali metal cation radius observed following laser photolysis of cPrFOH in evacuated alkali metal cation Y zeolites. The yield of carbocation is determined from the change in diffuse reflectance at 445 nm immediately following the laser pulse, corrected for trailing absorption due to the triene isomer at 445 nm ($\lambda_{\text{max}} = 370$ nm).

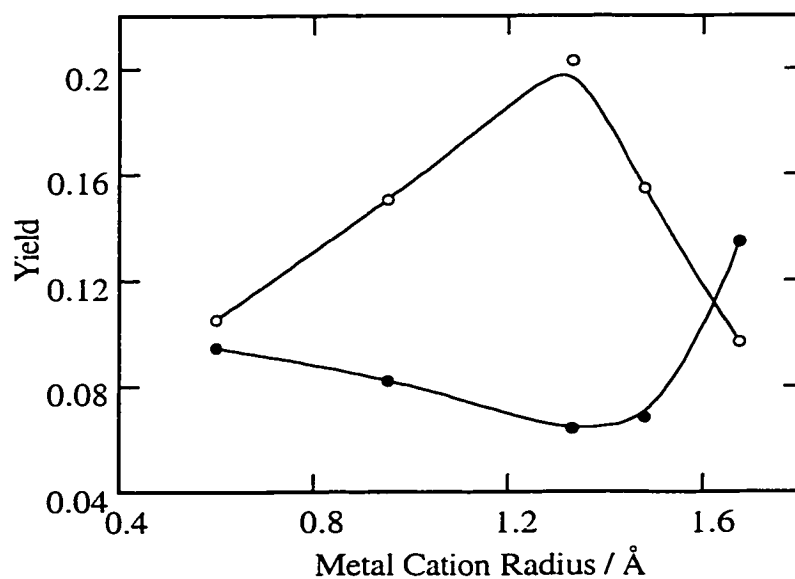


Figure 3-86. Yield of radical cation (closed circles) and triene isomer (open circles) of cPrFOH as a function of alkali metal cation radius observed following laser photolysis of cPrFOH in evacuated alkali metal cation Y zeolites. The yield of radical cation and triene isomer are determined by the change in diffuse reflectance at 640 nm immediately following the laser pulse, and at 370 nm 1 ms after the laser pulse.

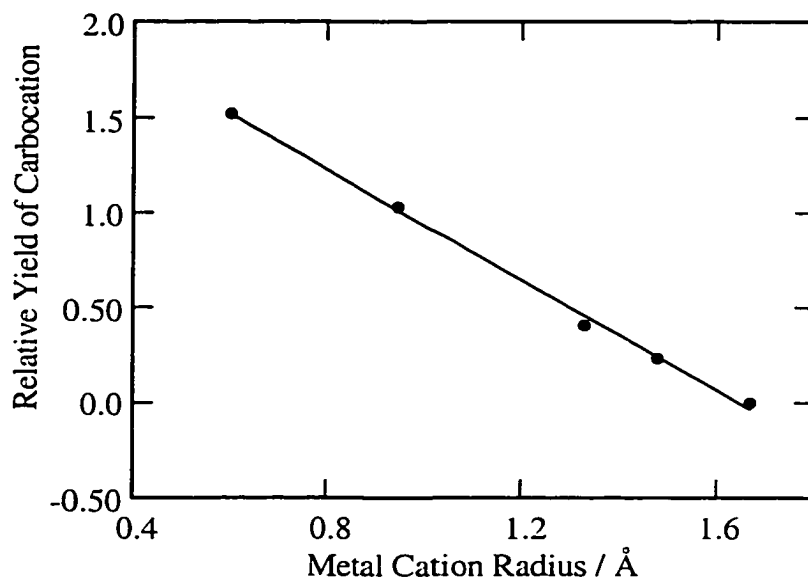


Figure 3-87. Yield of the 9-cyclopropyl-9-fluorenyl cation, relative to the cPrFOH radical cation and triene isomer, as a function of alkali metal cation radius observed following laser photolysis of cPrFOH in evacuated alkali metal cation Y zeolites. The relative carbocation yield is defined as the ratio of the carbocation yield to the sum of the yields of the radical cation and triene isomer.

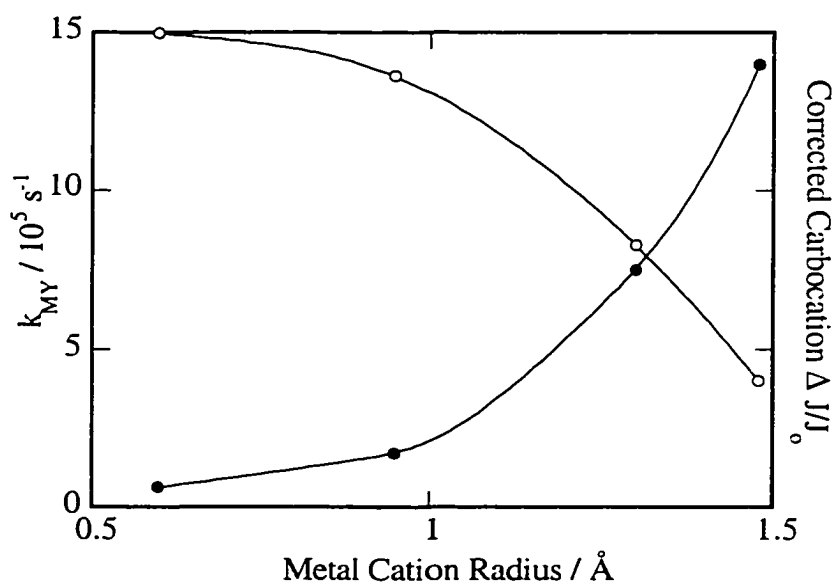


Figure 3-88. Variation in the first-order decay rate constant (closed circles) and yield (open circles) of the 9-cyclopropyl-9-fluorenyl cation as a function of alkali metal cation radius.

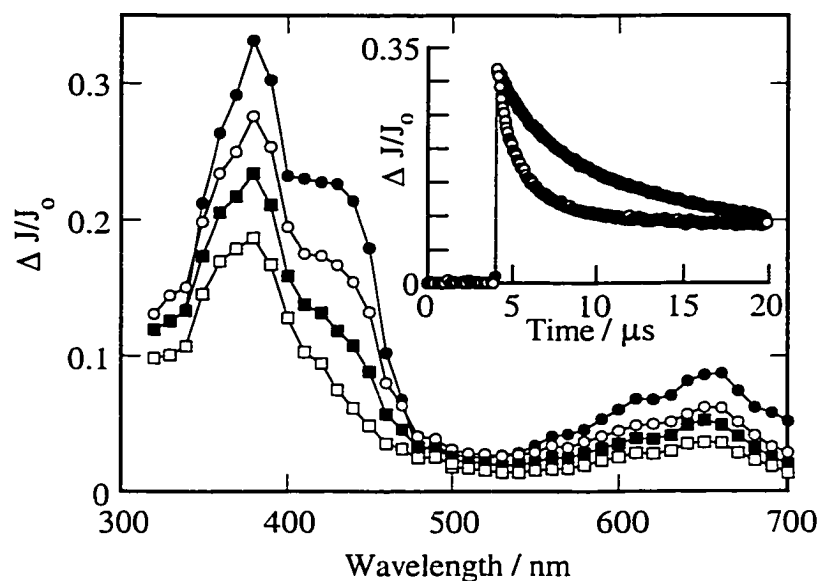


Figure 3-89. Transient diffuse reflectance spectrum generated 200 ns (closed circles), 800 ns (open circles), 1.96 μs (closed squares), and 13.7 μs (open squares) after 308 nm laser irradiation of cPrFOH in evacuated NaX. The inset compares the decay kinetics monitored at 445 nm following laser photolysis of cPrFOH in evacuated NaY (closed circles) and NaX (open circles).

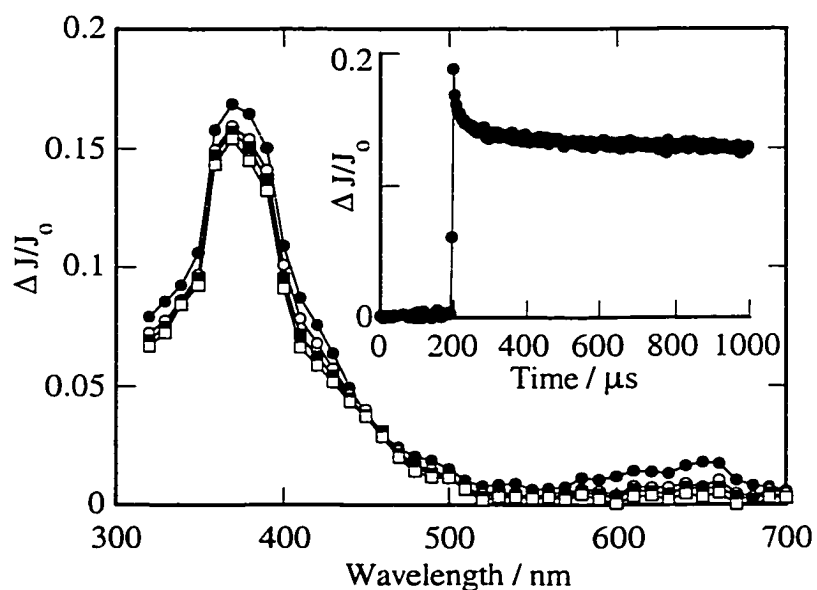


Figure 3-90. Transient diffuse reflectance spectrum generated 124 μs (closed circles), 336 μs (open circles), 474 μs (closed squares), and 684 μs (open squares) after 308 nm laser irradiation of cPrFOH in evacuated NaX. The decay trace monitored at 370 nm is shown in the inset.

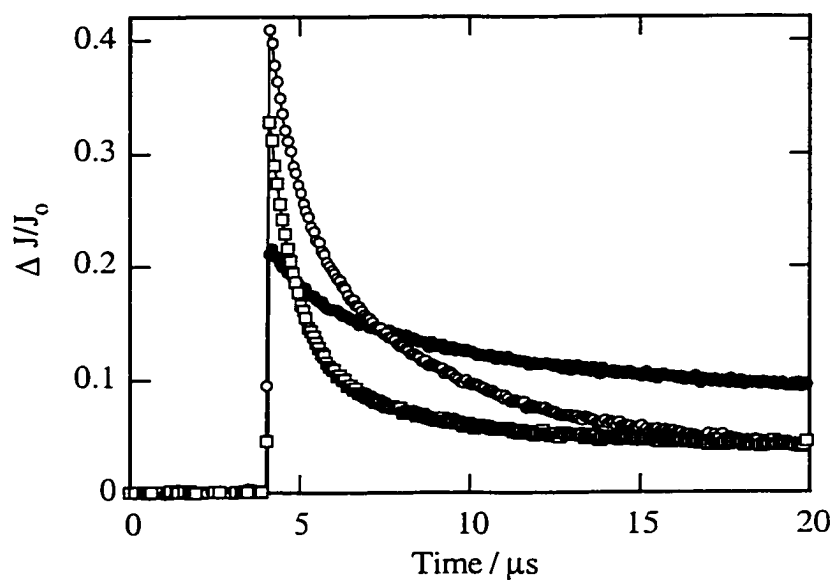


Figure 3-91. Decay traces observed at 445 nm following 308 nm laser photolysis of cPrFOH in dry NaY (closed circles), and NaY containing 6 weight % water (open circles) or methanol (open squares).

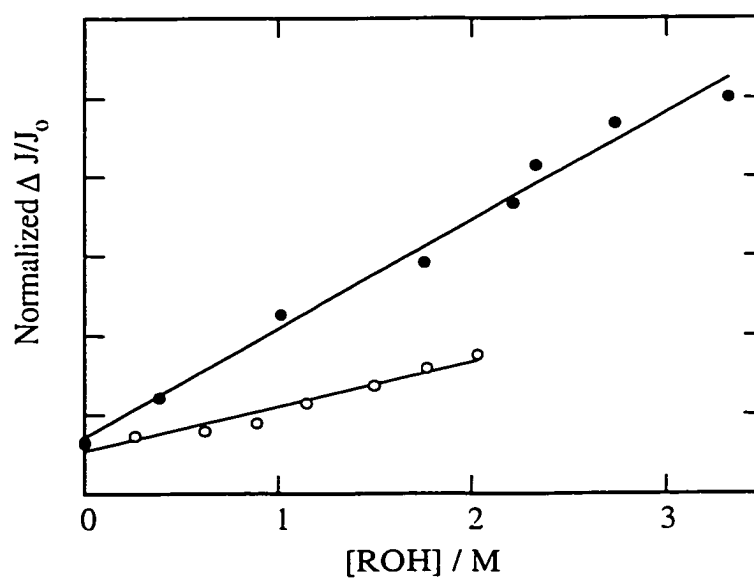


Figure 3-92. Normalized variation in the change in diffuse reflectance observed at 445 nm immediately following 308 nm laser photolysis of cPrFOH in NaY as a function of the concentration of water (closed circles) or methanol (open circles).

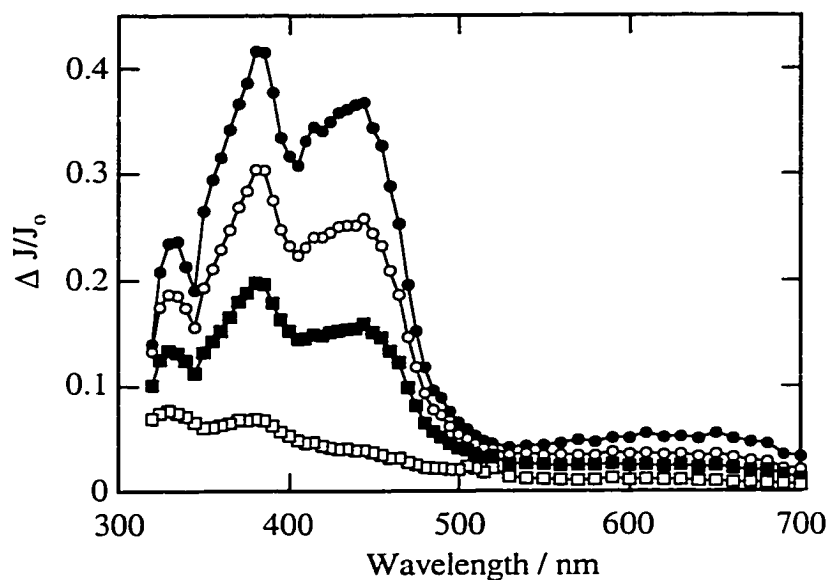


Figure 3-93. Transient diffuse reflectance spectrum generated 280 ns (closed circles), 1.00 μ s (open circles), 2.64 μ s (closed squares), and 14.9 μ s (open squares) after 308 nm laser irradiation of cPrFOH in NaY containing 6 weight % coadsorbed water.

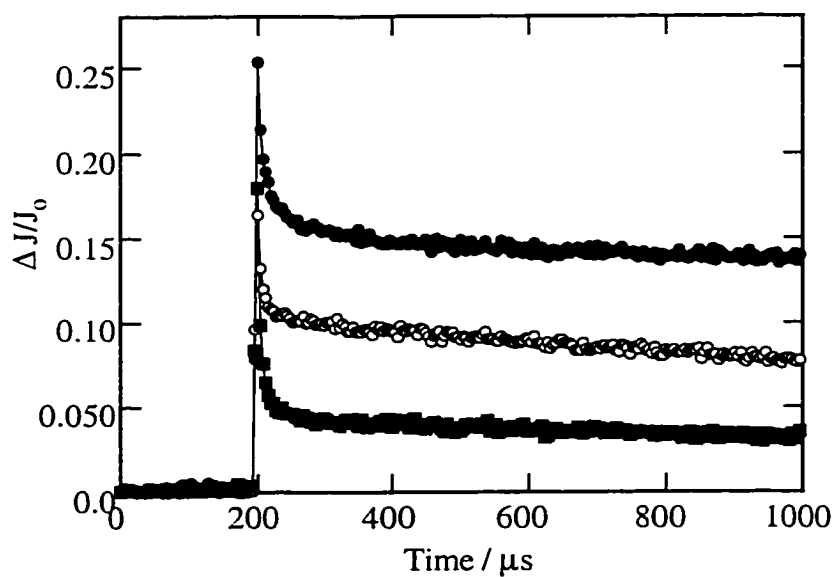


Figure 3-94. Decay traces monitored at 370 nm following laser photolysis of cPrFOH in dry NaY (closed circles) and NaY containing 6 weight % methanol (open circles) or water (closed squares).

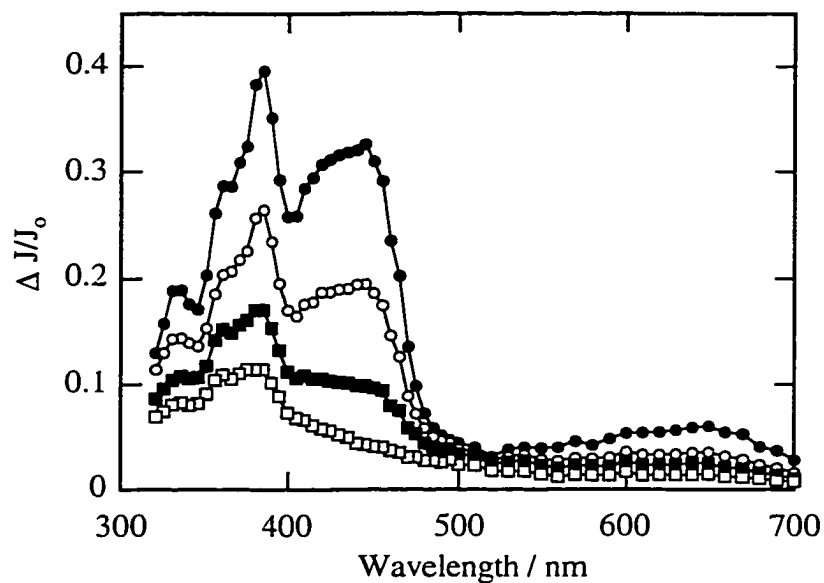


Figure 3-95. Transient diffuse reflectance spectrum generated 280 ns (closed circles), 1.00 μ s (open circles), 2.64 μ s (closed squares), and 14.9 μ s (open squares) after 308 nm laser irradiation of cPrFOH in NaY containing 6 weight % coadsorbed methanol.

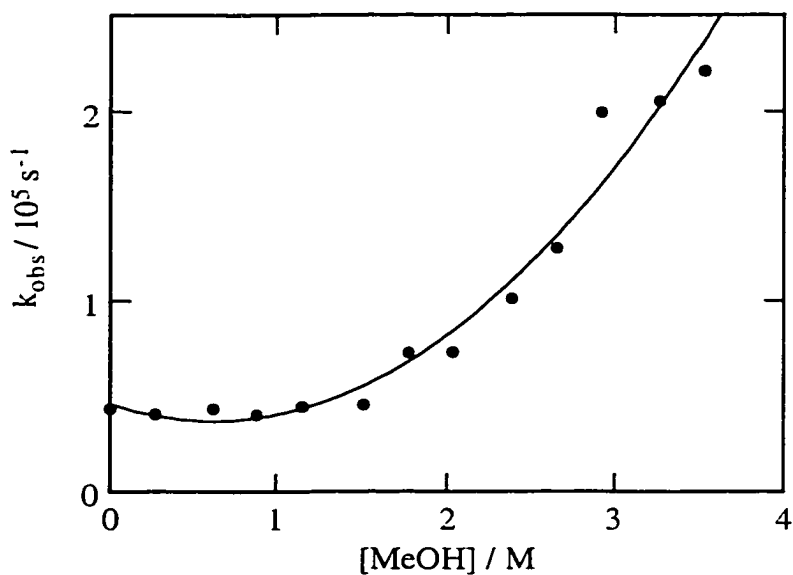


Figure 3-96. Variation in the first-order decay rate constant of the 9-cyclopropyl-9-fluorenyl cation monitored at 445 nm in NaY as a function of the concentration of methanol.

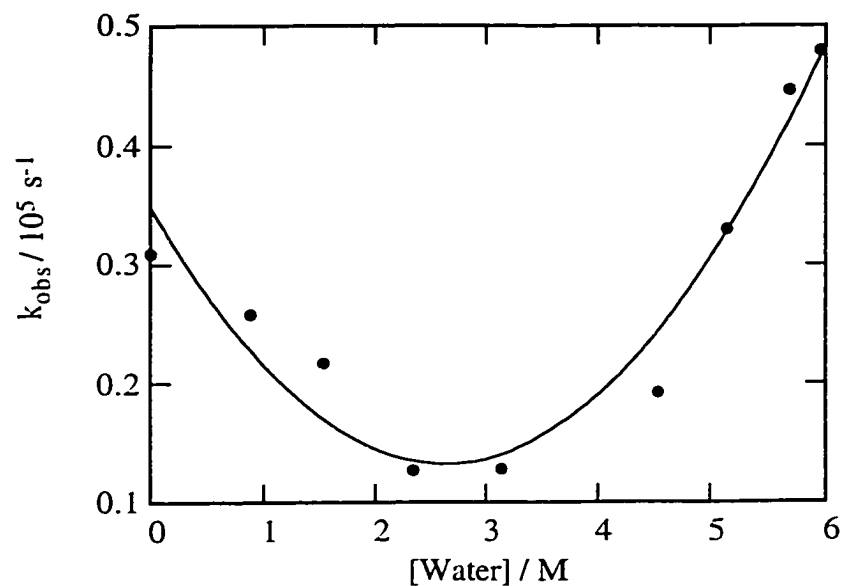


Figure 3-97. Variation in the first-order decay rate constant of the 9-cyclopropyl-9-fluorenyl cation monitored at 445 nm in NaY as a function of the concentration of water.

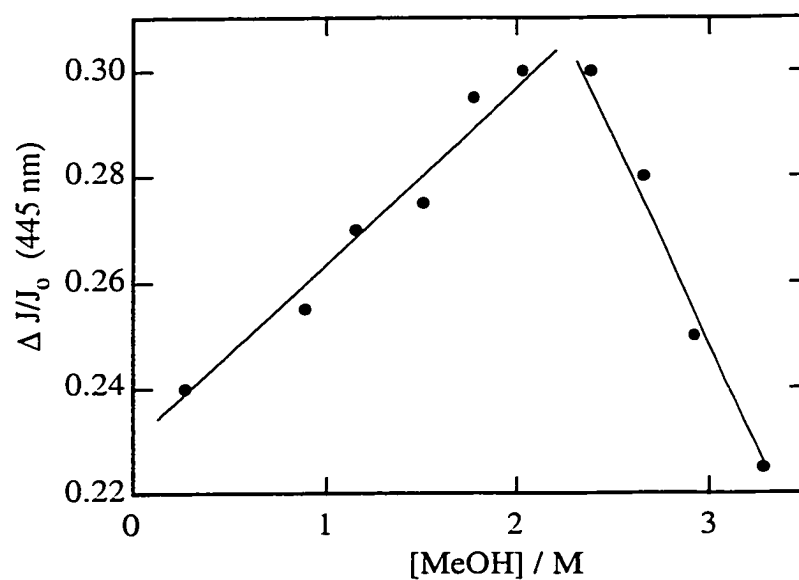


Figure 3-98. Variation in the change in diffuse reflectance ($\Delta J/J_0$) due to the 9-cyclopropyl-9-fluorenyl cation in NaY as a function of the concentration of methanol.

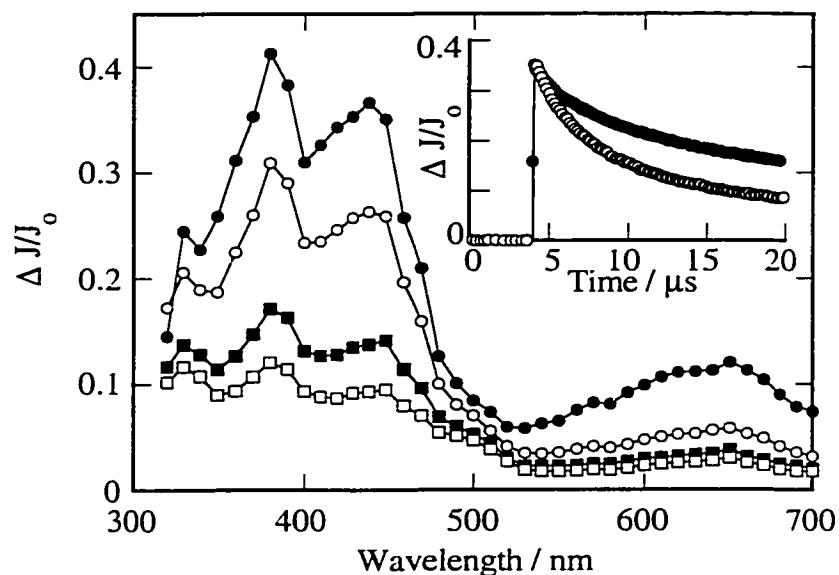


Figure 3-99. Transient diffuse reflectance spectrum generated 200 ns (closed circles), 1.76 μs (open circles), 7.40 μs (closed squares), and 14.0 μs (open squares) after 308 nm laser irradiation of cPrFOH in hydrated LiY (8 weight %). The inset compares the decay kinetics monitored at 445 nm under dry (closed circles) and hydrated (open circles) conditions.

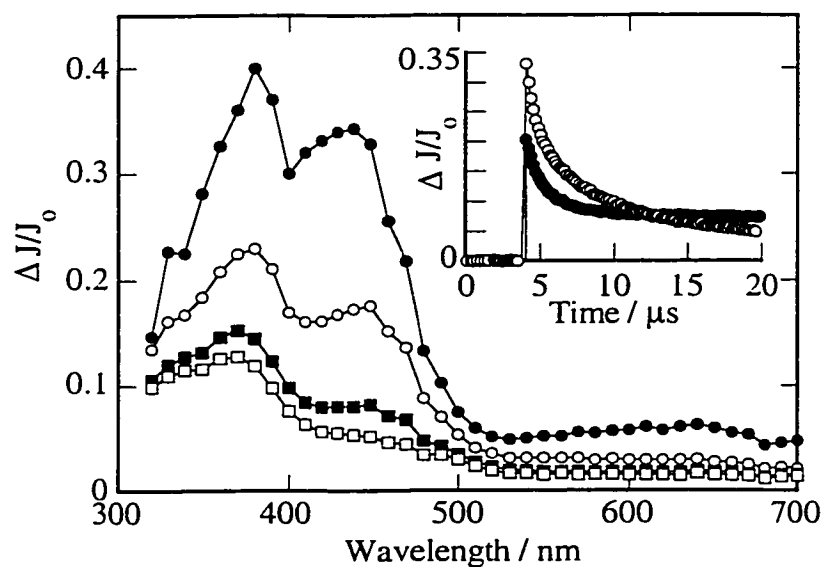


Figure 3-100. Transient diffuse reflectance spectrum generated 200 ns (closed circles), 1.76 μs (open circles), 7.40 μs (closed squares), and 14.0 μs (open squares) after 308 nm laser irradiation of cPrFOH in hydrated KY (5 weight %). The inset compares the decay kinetics monitored at 445 nm in dry (closed circles) and hydrated (open circles) KY.

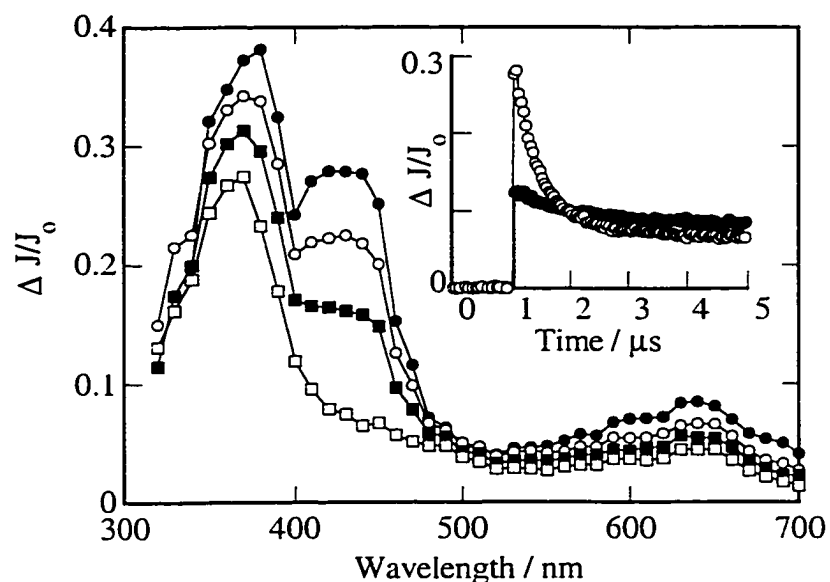


Figure 3-101. Transient diffuse reflectance spectrum generated 50 ns (closed circles), 180 ns (open circles), 380 ns (closed squares), and 3.46 μ s (open squares) after 308 nm laser irradiation of cPrFOH in hydrated RbY (4 weight %). The inset compares the decay kinetics monitored at 445 nm in dry (closed circles) and hydrated (open circles) RbY.

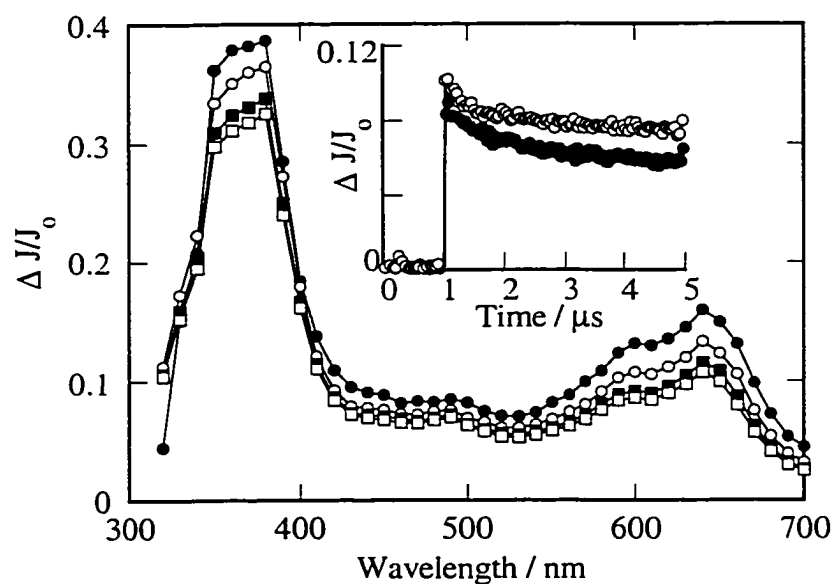


Figure 3-102. Transient diffuse reflectance spectrum generated 50 ns (closed circles), 180 ns (open circles), 380 ns (closed squares), and 3.46 μ s (open squares) after 308 nm laser irradiation of cPrFOH in hydrated CsY (3 weight %). The inset compares the decay kinetics monitored at 445 nm in dry (closed circles) and hydrated (open circles) CsY.

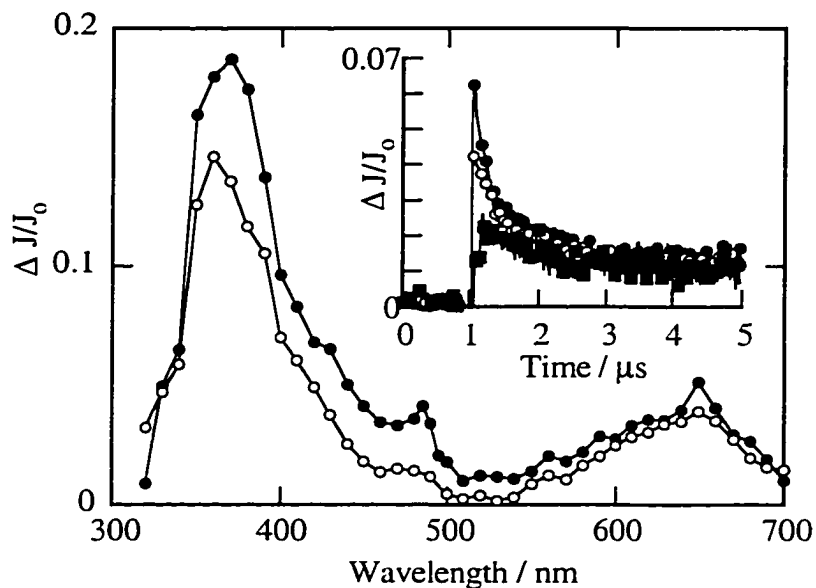


Figure 3-103. Transient diffuse reflectance spectrum generated 160 ns after 308 nm laser photolysis of MeFOH in dry NaY (closed circles), and NaY containing 3 weight % coadsorbed water (open circles). The inset compares the decay kinetics monitored at 445 nm in dry NaY (closed circles) and NaY containing 1 weight % (open circles) and 3 weight % (closed squares) coadsorbed water.

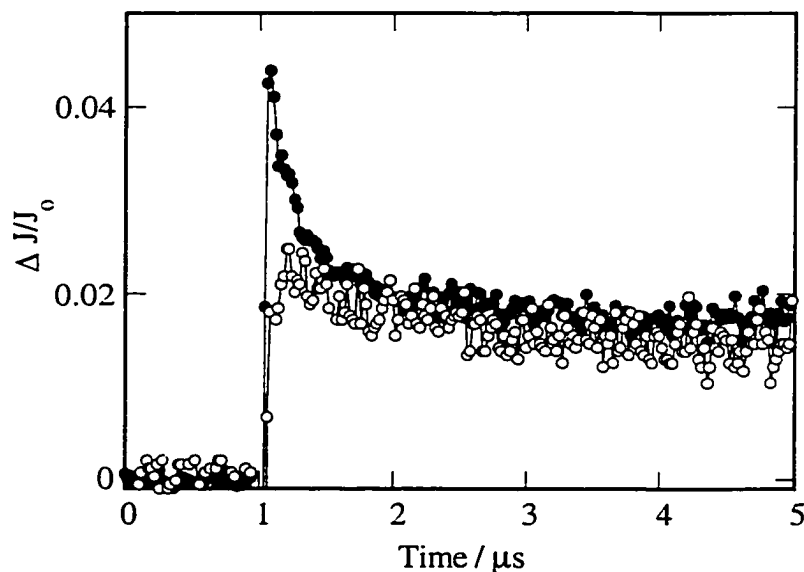


Figure 3-104. Decay traces monitored at 445 nm following 308 nm laser photolysis of FOH in dry NaY (closed circles) and NaY containing 5 weight % (open circles) coadsorbed water.

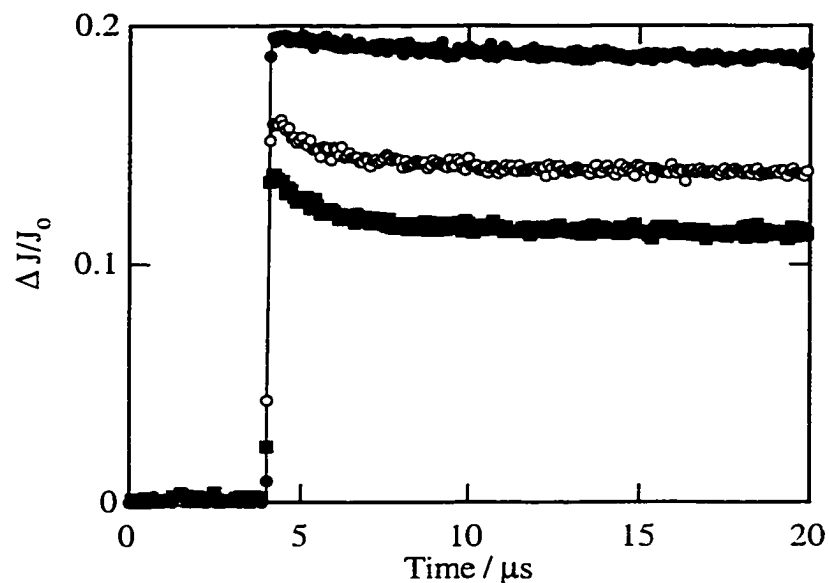


Figure 3-105. Decay traces monitored at 370 nm following 308 nm laser photolysis of MeFOH in dry NaY (closed circles) and NaY containing 1 weight % (open circles) and 3 weight % coadsorbed water (closed squares).

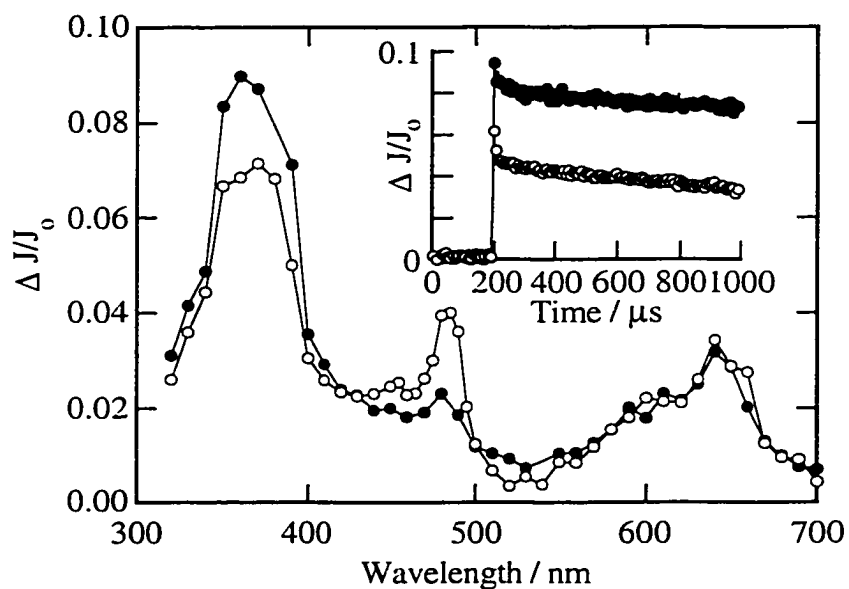


Figure 3-106. Transient diffuse reflectance spectrum generated 320 ns after 308 nm laser photolysis of MeFOH in dry Na β (closed circles), and 240 ns after 308 nm laser photolysis of MeFOH in Na β containing 3 weight % coadsorbed water (open circles). The inset compares the decay kinetics monitored at 370 nm in Na β under dry (closed circles) and hydrated conditions.

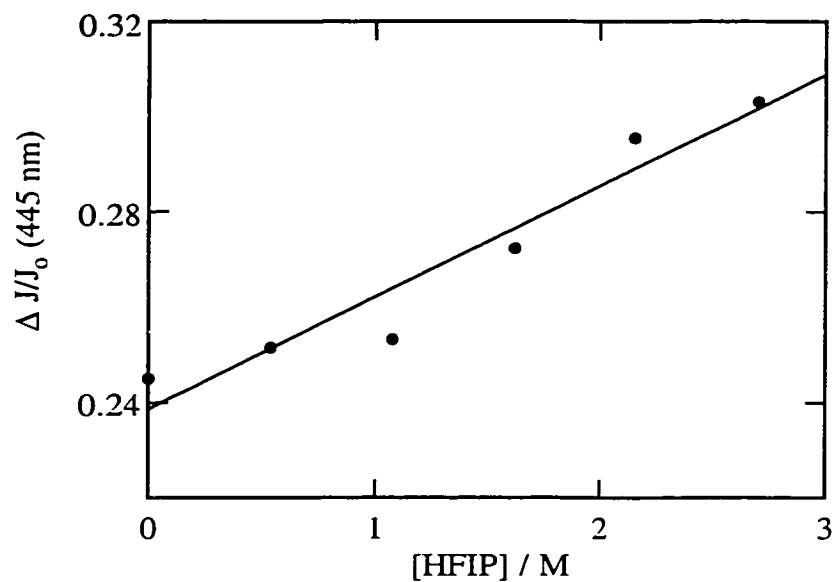


Figure 3-107. Variation in the change in diffuse reflectance at 445 nm due to the 9-cyclopropyl-9-fluorenyl cation following laser photolysis of cPrFOH in NaY as a function the concentration of coadsorbed HFIP.

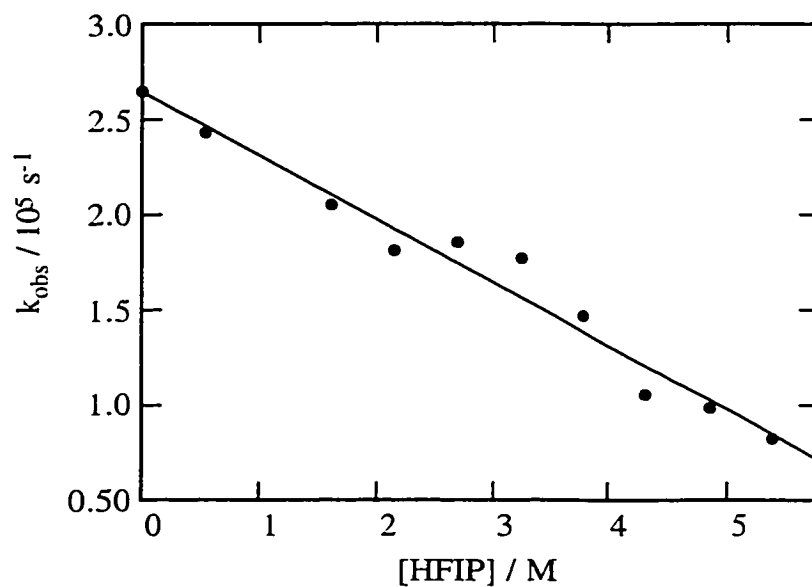


Figure 3-108. Variation in the first-order decay rate constant of the 9-cyclopropyl-9-fluorenyl cation monitored at 445 nm following laser photolysis of cPrFOH in NaY as a function the concentration of coadsorbed HFIP.

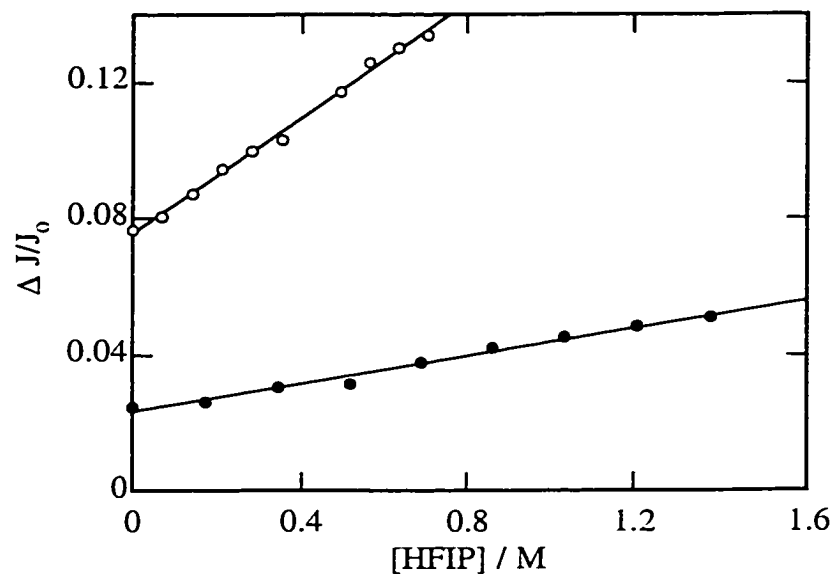


Figure 3-109. Variation in the change in diffuse reflectance at 485 nm due to the 9-methyl-9-fluorenyl cation (closed circles) and at 515 nm due to the 9-fluorenyl cation (open circles) following laser photolysis of MeFOH and FOH, respectively, in NaY as a function the concentration of coadsorbed HFIP.

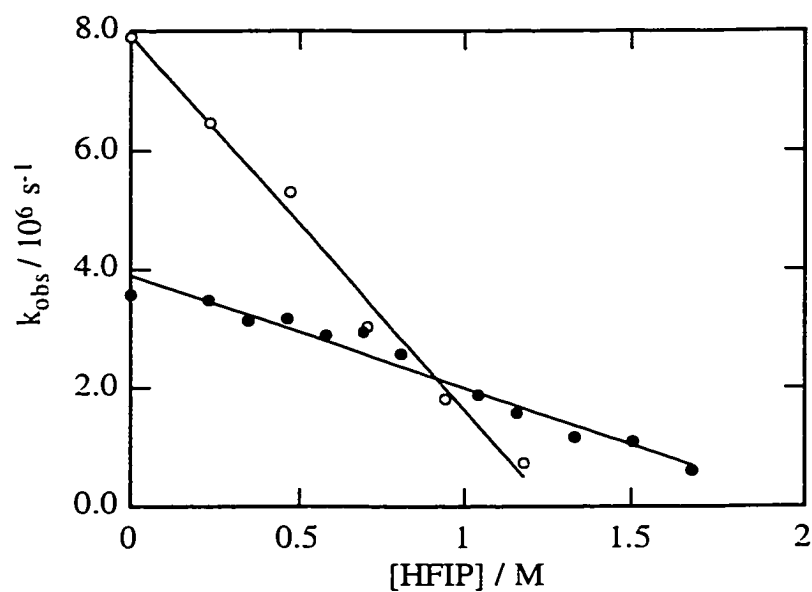


Figure 3-110. Variation in the first-order decay rate constant of the 9-methyl-9-fluorenyl cation monitored at 485 nm (closed circles) and the 9-fluorenyl cation monitored at 515 nm (open circles) following laser photolysis of MeFOH and FOH, respectively, in NaY as a function the concentration of coadsorbed HFIP.

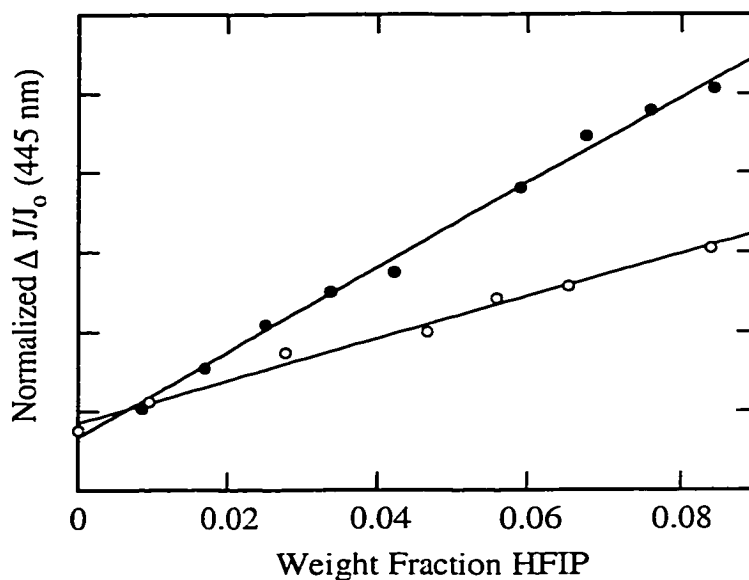


Figure 3-111. Normalized variation in the change in diffuse reflectance at 485 nm due to the 9-methyl-9-fluorenyl cation following laser photolysis of MeFOH in NaY as a function the concentration of coadsorbed HFIP (closed circles) and HFIP-OD (open circles).

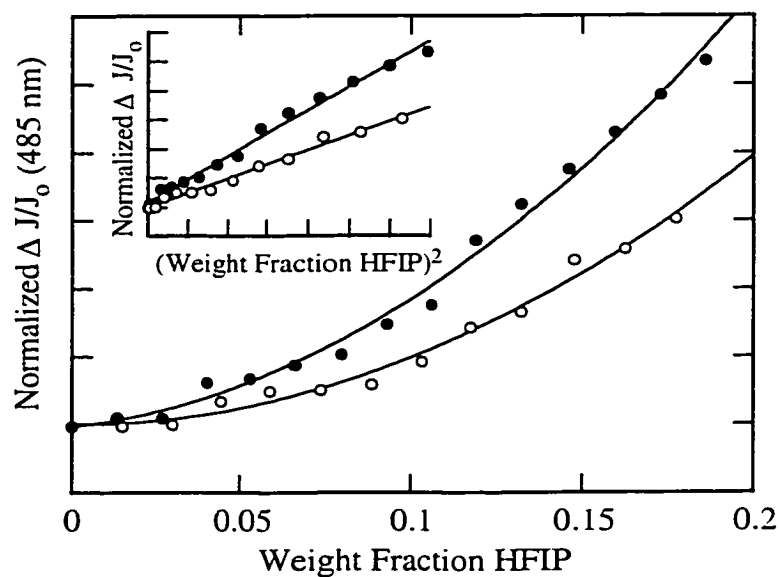


Figure 3-112. Normalized variation in the change in diffuse reflectance at 485 nm due to the 9-methyl-9-fluorenyl cation following laser photolysis of MeFOH in Na β as a function the coadsorbed HFIP content (closed circles) and HFIP-OD (open circles). Inset shows the same variation in the change in diffuse reflectance plotted against the HFIP content squared.

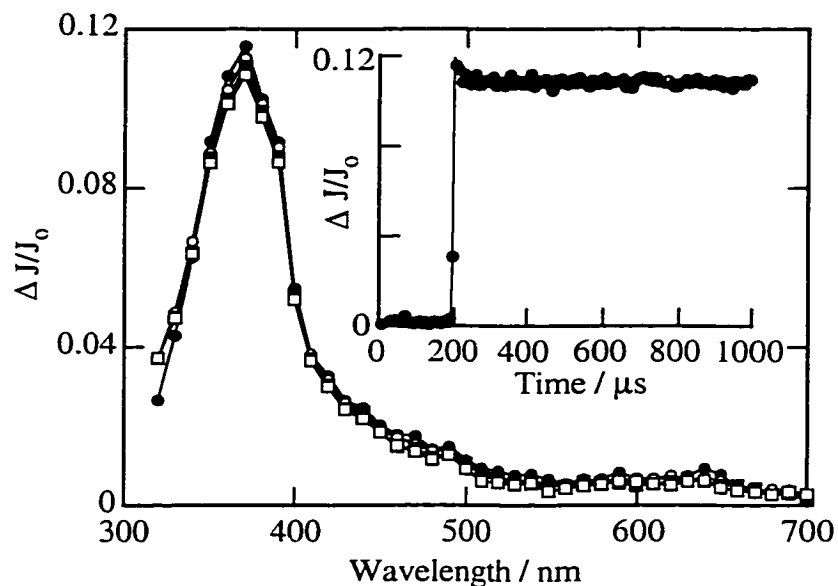


Figure 3-113. Transient diffuse reflectance spectrum generated 60 ns (closed circles), 2.40 μs (open circles), 5.52 μs (closed squares), and 14.8 μs (open squares) after 308 nm laser irradiation of 9-methoxyfluorene in evacuated NaY. The inset shows the decay trace monitored at 370 nm.

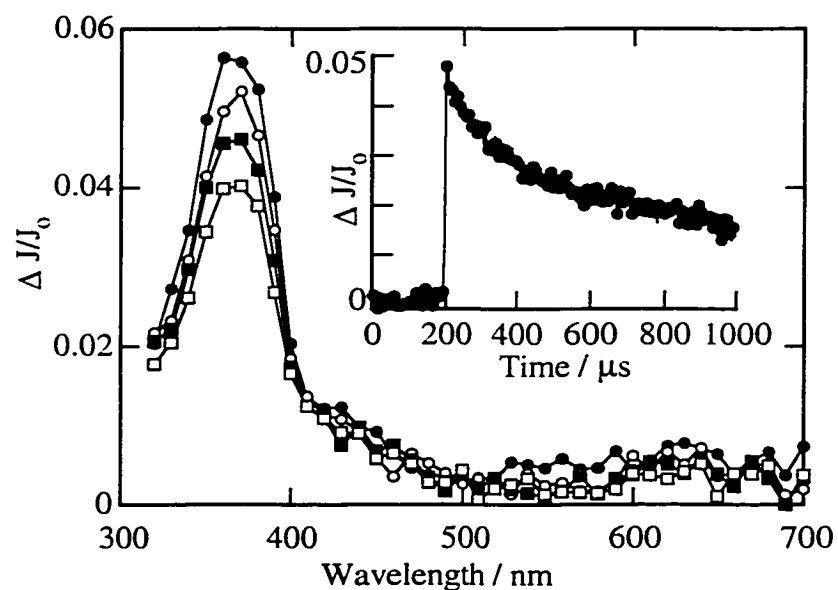


Figure 3-114. Transient diffuse reflectance spectrum generated 3.20 μs (closed circles), 30.0 μs (open circles), 69.6 μs (closed squares), and 141 μs (open squares) after 308 nm laser irradiation of 9-acetoxyfluorene in evacuated NaY. The inset shows the decay trace monitored at 370 nm.

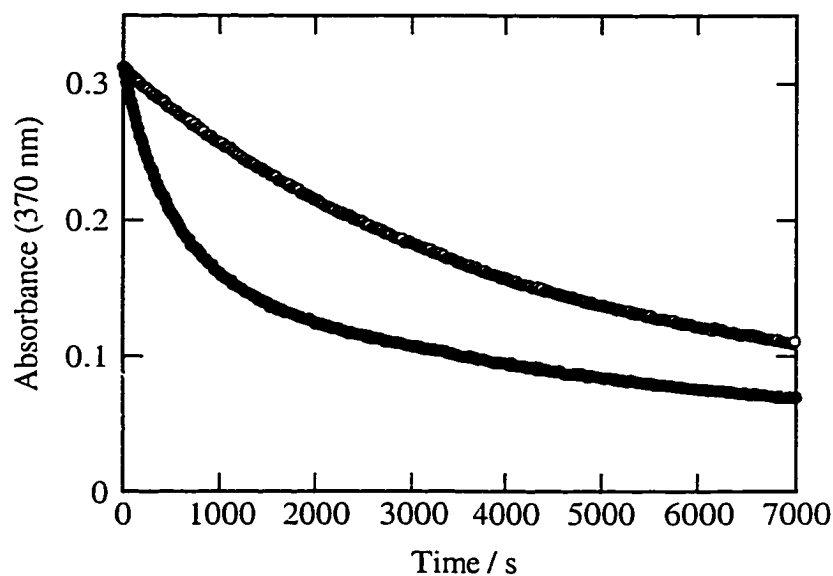


Figure 3-115. Decay traces of the triene isomers of MeFOH (closed circles) and FOH (open circles) in methanol. Triene isomers are rapidly generated with ca. 600 pulses (10 Hz repetition rate) of 308 nm laser light and the decay traces are obtained by monitoring the absorbance at 370 nm every 15 seconds using a conventional UV-vis spectrometer.

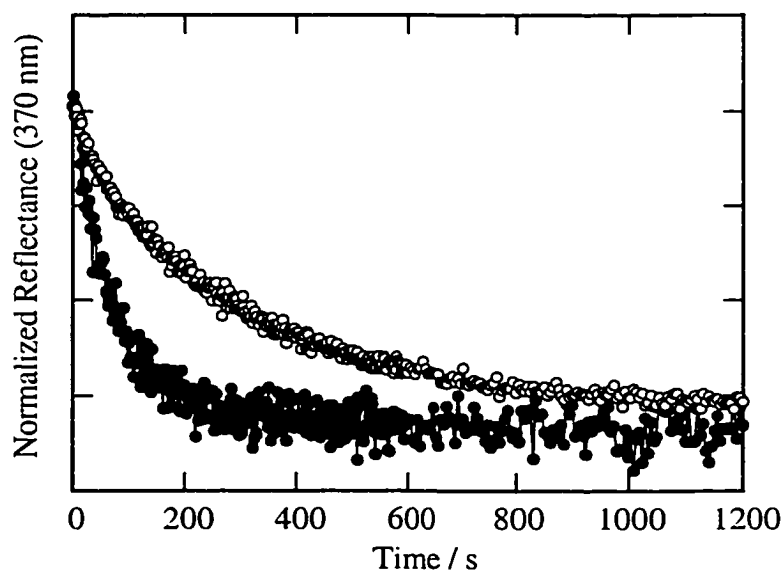


Figure 3-116. Decay traces of the triene isomers of MeFOH (closed circles) and FOH (open circles) in NaY. The triene isomers are rapidly generated with ca. 10 pulses (10 Hz repetition rate) of 308 nm laser light and the decay traces are obtained by monitoring the diffuse reflectance at 370 nm every 2 seconds using a conventional UV-vis spectrometer.

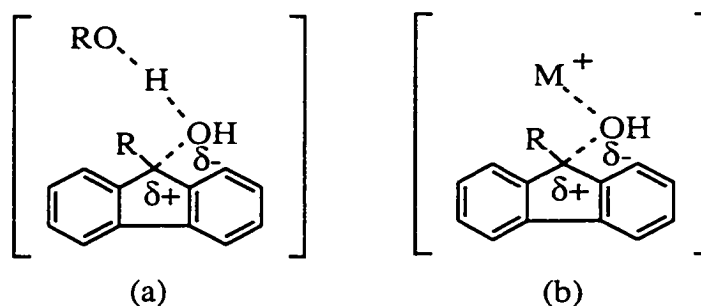
3.3.2 Discussion

The results described in the preceding section demonstrate unambiguously that photoexcited 9-fluorenyl and 9-substituted-9-fluorenyls heterolyze within dry alkali metal cation zeolites, and that the resultant 9-fluorenyl cations can be observed as reactive intermediates in the nanosecond time regime. Interpretation of the experimental observations is aimed at understanding two fundamental issues: (i) the ability of non-protic zeolites to mediate photoheterolysis, (ii) the factors which regulate the lifetime of reactive carbocations in non-protic zeolites.

3.3.2.1 Generation of 9-Fluorenyl Cations from Photoexcited 9-Fluorenyls in Alkali Metal Cation Zeolites

Photoexcitation of 9-fluorenyls encapsulated within alkali metal cation zeolites generates the corresponding 9-fluorenyl cations *via* heterolysis of the C-O bond as observed in ionizing, protic solvents. Several studies in solution have demonstrated that formation of 9-fluorenyl cations takes place by simple heterolysis of the C-O bond. It has been argued that this process is not acid catalyzed^{378,380} but the fact that protic solvents are required for carbocation formation to be efficient suggests that protons from the solvent may participate in the product determining step by interacting with the oxygen of the leaving hydroxide ion, Scheme 3-12 (a). Although the results observed in zeolites do not directly establish a mechanism for photoheterolysis in the absence of Brønsted acid sites or protic reagents, the experimental evidence indicates that the zeolite environment defines the efficiency of carbocation formation and suggests that the zeolite participates in photoheterolysis. In particular, generation of 9-fluorenyl cations in non-protic zeolites suggests that the zeolite framework plays a catalytic role in photodehydroxylation.

Scheme 3-12



Since no proton is available in dry alkali metal cation zeolites, stabilization of the leaving hydroxide ion by a hydrogen-bonding interaction is not possible. However, the metal cations could assist the excited state C-O cleavage *via* Lewis-acid type catalysis, Scheme 3-12 (b). In this case, interaction of the alkali metal cation stabilizes the hydroxide ion as the C-O bond cleaves in the excited state. An interaction between the alcohol functionality of the fluorenol and the zeolite cation is anticipated even in the ground state, based on the well known interactions between alkali metal cations and methanol in zeolites.^{339,341-343,401,402} Thus it is quite likely that the fluorenol is ideally oriented for Lewis-acid assisted heterolysis upon photoexcitation.

The notion that the zeolite counterions facilitate the hydroxyl group ionization from photoexcited 9-fluorenyls is also supported by the distinct variation in photoheterolysis efficiency as a function of zeolite counterion, Figure 3-84. For instance, the absolute and relative yield of the 9-cyclopropyl-9-fluorenyl cation decrease dramatically as the Y zeolite counterion is varied from Li^+ to Cs^+ . In fact, although carbocation formation is the dominant reaction pathway of photoexcited cPrFOH in LiY, no carbocation is detected in CsY. Based on the relative reactivity of the 9-cyclopropyl-9-fluorenyl cation in other alkali metal cation Y zeolites, the absence of observed carbocation signal in CsY cannot be attributed to rapid decay of this carbocation within the laser pulse. The large variation in carbocation signal as a function of alkali metal cation size is therefore most consistent with a reduction in the efficiency of photoheterolysis as the counterion size is increased. This is the anticipated trend in efficiency for a heterolysis mechanism involving Lewis-acid catalysis within the zeolite cavities, Scheme 3-12 (b), since the Lewis acidity of the counterion, and of the zeolite interior, decreases with increasing cation size.^{30,88}

In addition, experimental results within hydrated alkali metal cation zeolites are consistent with the notion that photoheterolysis becomes less efficient as the size of the zeolite counterion is increased. In fact, the dependence of carbocation yield on alkali metal cation size is maintained under hydrated conditions, whereby the yield is the highest in hydrated LiY and decreases dramatically with cation size such that no carbocation is observed in hydrated CsY. Thus, even under conditions where water is included within the zeolite cavities, the distinct influence of the zeolite microenvironment continues to regulate carbocation formation. This is remarkable considering the powerful ability of water to control the efficiency of photoheterolysis of 9-fluorenyls in homogeneous solution.^{378,380,384} This observation provides further evidence that the zeolite framework and, particularly the alkali metal counterions, play a direct and

defining role in intrazeolite photoheterolysis, and that carbocation formation is likely a consequence of Lewis-acid type interactions between the excited state 9-fluorenol and the alkali metal cation.

Regardless of the precise mechanism by which photoheterolysis occurs within alkali metal cation zeolites, the generation of reactive 9-fluorenyl cations clearly demonstrates that non-protic zeolites can facilitate a photochemical reaction characterized by heterolysis and a significant charge-separation in the rate determining step. In solution, photoheterolysis of 9-fluorenols is strongly dependent on the ionizing ability of the solvent.^{378,380} The fact that formation of reactive 9-fluorenyl cations occurs in alkali metal cation zeolites indicates that the environment within these zeolites, particularly LiY and NaY, is sufficiently ionizing to support these charge separation reactions. This is consistent with results demonstrating that the ionizing ability of LiY and NaY zeolites is comparable to that of neat HFIP.³⁷ The decreased efficiency of photoheterolysis in alkali metal cation Y zeolites as a function of counterion size is also expected based on the decrease in internal ionizing ability of these zeolites with counterion size.³⁷

In alkali metal cation zeolites, both the absolute yield of carbocation formation, and the yield relative to competing processes such as ionization and rearrangement, increase upon inclusion of protic reagents within the zeolite. The concentration of additive required to observe this effect is relatively small, often one molecule or less per zeolite cavity. Under these conditions, the surrounding environment observed by the photoexcited 9-fluorenol is not comparable to a solvent cage of these additives, as would be the case, for instance, at much higher additive concentrations, or in a slurry of the zeolite and the cosolvent. Instead, the intrazeolite environment is akin to that observed under dry conditions with the exception that additional guest molecules, the protic reagents, are present. Therefore, the ability of these protic guests to enhance photoheterolysis is likely a consequence of the combined influences of both the zeolite matrix and the additive.

The observation that carbocation generation *via* photoheterolysis is enhanced within alkali metal cation zeolites containing coincluded protic reagents such as water, methanol, or HFIP, is consistent with the protic additive actively participating in the C-OH bond cleavage of the excited state fluorenols. For instance, in a manner similar to that represented in Scheme 3-12 (a), the protic reagent incorporated within the zeolite cavity can interact with the oxygen of the excited fluorenol and stabilize the incipient charge on the developing hydroxide ion. It is also possible that the protic reagent is not directly assisting the heterolysis, but simply enhances the internal ionizing ability of the

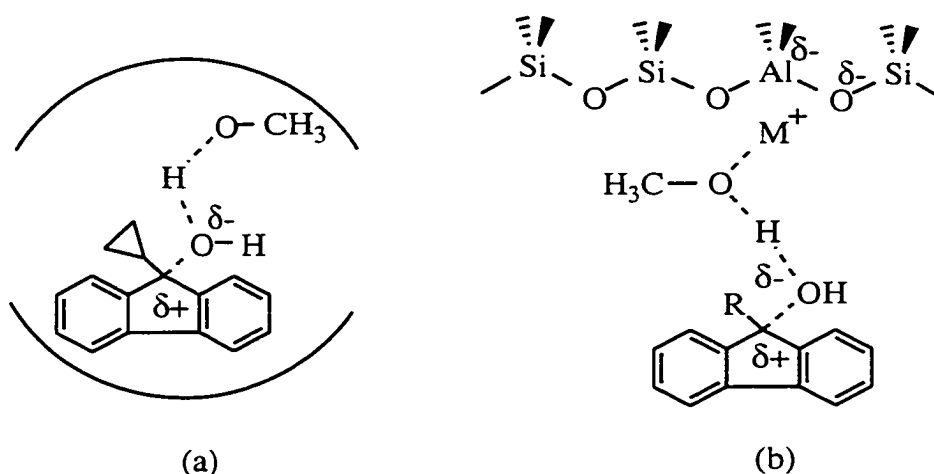
zeolite microenvironment. Thus, the additive may play a passive role making the zeolite cavity more hospitable for carbocation formation. Isotope effect studies employing HFIP and the deuterated analog HFIP-OD were conducted in order to distinguish between the two possible roles played by the added alcohol and presumably the other similar additives, methanol and water. The results obtained clearly demonstrate that the ability of HFIP-OD to enhance photoheterolysis of 9-fluorenols in alkali metal cation zeolites is significantly attenuated relative to HFIP, Figures 3-111 and 3-112. This is the isotope effect expected for a mechanism in which the alcohol shares its proton with the oxygen of the leaving hydroxide group as the product determining step progresses, Scheme 3-12 (a). Observing these isotope effects on the yield of carbocation formation provides evidence for the direct participation of the added alcohol in the intrazeolite photoheterolysis of 9-fluorenols.

The enhanced photoheterolytic generation of 9-fluorenyl cations observed in alkali metal cation zeolites upon inclusion of protic reagents is more significant for water than for methanol. The trend in relative efficiencies is not surprising considering the fact that water is superior in its ability to facilitate photoheterolysis of 9-fluorenols in homogeneous solution. However, the fact that inclusion of methanol increases the efficiency of intrazeolite photoheterolysis at all is somewhat contrary to results observed in homogeneous solution where carbocation formation is extremely inefficient in neat methanol. For instance, picosecond laser flash photolysis experiments directly established that the 9-methyl-9-fluorenyl cation is not generated upon excitation of MeFOH in neat methanol, but is readily formed in methanol-water mixtures, with the efficiency of photoheterolysis increasing at higher water content.³⁸⁴ Similarly, analysis of products derived from steady-state irradiation of FOH in solution have found that the efficiency of methyl ether formation increases dramatically in aqueous methanol as compared to the neat methanol.^{378,380} These observations, in combination with the results described herein, clearly indicate that photoheterolysis of 9-fluorenols is significantly more efficient in dry alkali metal cation zeolites, particularly those possessing small counterions such as Li^+ and Na^+ , than it is in methanol. It is therefore particularly surprising that inclusion of an additive which is less effective at facilitating heterolysis than the zeolite itself, actually *increases* the yield of carbocation formation. Thus the current observation that methanol can induce photoheterolysis of 9-fluorenols must be associated with the inclusion of methanol within the zeolite cavities.

It is possible that zeolite encapsulation enhances the ionizing catalysis of methanol due to close confinement of the methanol and the 9-fluorenol with the zeolite cavity, Scheme 3-13 (a). Alternatively, zeolite encapsulation may enhance the ability of

methanol to assist heterolysis as a result of binding between the alcohol oxygen and the alkali metal counterion, Scheme 3-13 (b). Such binding would increase the acidity of the alcohol proton and thereby elevate the ability of this proton to assist C-O bond cleavage. Intrazeolite binding of small alcohols such as methanol, dominated by the strong interaction between the alkali metal cations and the hydroxyl oxygen, is well documented in the literature.^{339,341-343,401,402}

Scheme 3-13



Obviously coadsorbed water will also be subject to interactions with the alkali metal cations^{28,340} which can accentuate the ability of the water to facilitate photoheterolysis in a manner similar to that described for adsorbed methanol. Consistent with this notion is the fact that water continues to be more effective than methanol at facilitating photoheterolysis of 9-fluorenols in zeolites.

In this regard it is interesting to consider the magnitude by which protic reagents influence the efficiency of photoheterolysis within different zeolite environments. For instance, the ability of coadsorbed water to modulate photoheterolysis of cPrFOH in alkali metal cation Y zeolite varies dramatically as a function of the zeolite counterion, Figures 3-99 to 3-102. In LiY, where heterolysis is the favored reaction path of photoexcited cPrFOH in the absence of protic reagents, the inclusion of water does little to further enhance the excited-state bond cleavage. Conversely, in RbY, where the yield of photoheterolysis is low compared to other reaction pathways, the inclusion of water dramatically increases the yield of photoheterolysis. The fact that water more successfully enhances photoheterolysis in larger cation zeolites suggests that photoheterolysis is less efficient in these zeolites and water can play a more significant

role in carbocation formation. This is consistent with the proposed mechanism of photoheterolysis involving alkali cation assisted C-O cleavage, Scheme 3-11 (b). In the strongest Lewis acid zeolite, LiY, Li⁺-assisted photoheterolysis dominates the chemistry of photoexcited 9-fluorenols, and coadsorbed water participates little in heterolysis. Conversely, in RbY, Rb⁺-assisted heterolysis is a relatively minor pathway for photoexcited cPrFOH, and water has a much greater opportunity to participate in photoheterolysis. In CsY, the ability of the zeolite to facilitate photoheterolysis of cPrFOH, even under hydrated conditions, is too small to compete with processes which are more favorable in CsY, particularly ionization to the radical cation. Significantly, the overall efficiency of photoheterolysis due to both metal cation assistance and assistance by water remains highest in the most acidic environment, LiY, and decreases with alkali cation size. The fact that the photoheterolysis efficiency remains counterion dependent in the presence of water suggests that the zeolite continues to directly influence the heterolysis and that the ability of water to modulate heterolysis is determined by combined effects of the coadsorbed water and the specific zeolite environment.

As discussed in the preceding section, dry alkali metal cation zeolites assist photoheterolysis of encapsulated 9-fluorenols yielding the 9-fluorenyl cations, most likely *via* Lewis-acid catalysis involving the metal cation. In addition, the efficiency of carbocation formation within these zeolites is increased by coincluded protic reagents in a manner that is consistent with direct participation of these reagents in the C-O bond cleavage. Furthermore, the observations that methanol can effectively increase the efficiency of photoheterolysis in zeolites, but not in solution, and that water is inefficient at effecting heterolysis in CsY but very efficient at inducing heterolysis in solution, suggest that the zeolite plays a defining role in the photoheterolysis even in cases where the cleavage is directly assisted by a coadsorbed reagent. This certainly must be a consequence of the unique interplay between the zeolite, the protic reagent and the 9-fluorenol substrate, and the influences of such interactions on heterolysis and other reaction pathways available to photoexcited 9-fluorenols in zeolites.

3.3.2.2 Absolute Reactivity of 9-Fluorenyl Cations in Alkali Metal Cation Zeolites

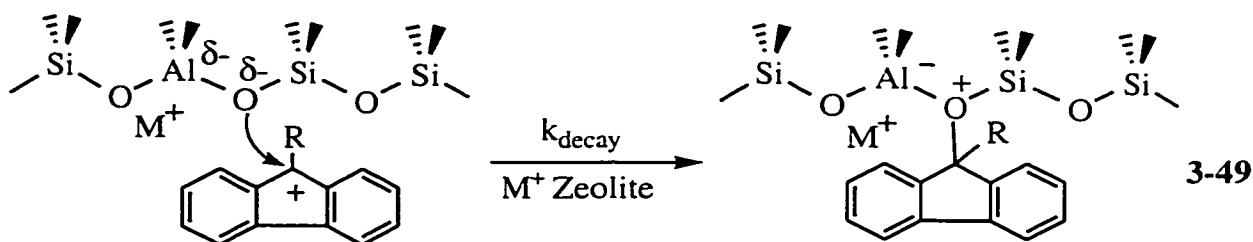
Regardless of the precise explanation, the fact that 9-fluorenyl cations are destabilized and consequently more reactive than diphenylmethyl analogs is undeniable. In particular, the parent 9-fluorenyl cation is a very elusive carbocation, characterized by unusually high reactivity which has frustrated many attempts aimed at observing this intermediate. The low thermodynamic stability of the 9-fluorenyl cation is clearly

illustrated by the lack of success in generating and observing the 9-fluorenyl cation under strong or superacid conditions.³⁵⁵ Likewise, the kinetic instability of the 9-fluorenyl cation is also well documented. For example, in purely aqueous solution, the rate constant for decay of the 9-fluorenyl cation is approximately 10^{11} s^{-1} .³⁸⁴ This is two orders of magnitude faster than the decay rate constant of $1 \times 10^9 \text{ s}^{-1}$ for decay of the diphenylmethyl cation in water.^{230,388} The difference in kinetic reactivity between the 9-fluorenyl cation and the diphenylmethyl cation is even more dramatic in less nucleophilic solvents such as TFE and HFIP, Table 3-21.

The 9-fluorenyl cation has been observed previously in solution using nanosecond laser photolysis, but only under a unique set of conditions where the carbocation is strongly kinetically stabilized by the weakly nucleophilic and highly polar solvent, HFIP.²⁴¹ The results described herein, where the 9-fluorenyl cation is directly observed in the zeolites LiY and NaY, therefore represent only the second set of experimental conditions whereby the 9-fluorenyl cation is sufficiently long-lived to be observed on the nanosecond time-scale. These results provide definitive evidence that the environment within alkali metal cation zeolites is exceptional in its ability to host extremely reactive positively charged intermediates, at least as transient species. The fact that the 9-fluorenyl cation, and other reactive 9-alkyl-9-fluorenyl cations could be detected in LiY and NaY is indeed quite remarkable upon recognition that these zeolites do not contain protons. Thus, the enhanced lifetime of these carbocations in alkali metal cation zeolites is not due to a thermodynamic effect, like that present in acid zeolites where the highly acidic environment shifts an otherwise unfavorable equilibrium to the side of the carbocation. Similarly, it is not due to a situation in which the strength of the nucleophilic sites of the zeolite framework is reduced by protonation. The ability to observe reactive 9-fluorenyl cations on the nanosecond time-scale in alkali metal cation zeolites must therefore be attributed to the unique intrazeolite environment, specifically the polar, anionic matrix and large electrostatic fields within the zeolite cages.

Even though it is possible to observe the 9-fluorenyl cation in LiY and NaY, the carbocation remains highly reactive compared to other similar species within alkali metal cation zeolites. For instance, the more stabilized 4-methoxycumyl cation decays with a rate constant of $4 \times 10^4 \text{ s}^{-1}$ in LiY that is 75-fold slower than the decay of the 9-fluorenyl cation in the same zeolite. In addition, the diphenylmethyl cation decays with a rate constant of in LiY that is 5-fold smaller than that of the 9-fluorenyl cation. This order of reactivity in LiY is the same as that observed in solution and indicates that the higher reactivity associated with 9-fluorenyl cations is maintained in zeolites.

Based on the results described in previous sections concerning the 4-methoxycumyl cation, it is reasonable to conclude that the decay of the 9-fluorenyl cations is dominated by addition of nucleophilic zeolite oxygen atoms leading to a framework bound intermediate, eq. 3-49.



Consistent with this conclusion is the observation that the carbocation lifetimes depend dramatically on the nature of the zeolite environment, specifically on the identity of the alkali metal counterion and the Si/Al ratio. In fact, the variation in lifetime of 9-fluorenyl cations with zeolite structure and composition is analogous to that previously observed for the 4-methoxycumyl cation, where carbocation decay has been shown to proceed through nucleophilic addition of the zeolite framework. For instance, the rate constant for decay of 9-alkyl-9-fluorenyl cations and 9-cyclopropyl-9-fluorenyl cations in alkali metal cation Y zeolites increases with counterion size, 9-alkyl-9-fluorenyl cations exhibit notably longer lifetimes in the dealuminated zeolite Na β (Si/Al = 18), and the 9-cyclopropyl-9-fluorenyl cation decays significantly faster in NaX (Si/Al = 1.2) than in NaY (Si/Al = 2.4). The alternative mechanism where the zeolite acts as a base to deprotonate the carbocation is not possible for the parent 9-fluorenyl cation. Furthermore, no elimination products are observed upon photolysis of 9-alkyl-9-fluorenols in TFE,³⁹⁷ and deprotonation has been described as unfeasible for the 9-fluorenyl cation in solution.³⁸¹

Further evidence that nucleophilic addition of the zeolite framework is responsible for the rapid disappearance of 9-fluorenyl cations within alkali metal cation zeolites can be obtained by correlating the lifetime of these carbocations with the nucleophilicity of the zeolite framework. As previously described, it is possible to discuss the nucleophilicity of the zeolite in terms of the electron density associated with the active nucleophilic sites, the zeolite lattice oxygen atoms bound to aluminum. One method for obtaining the average electron density at these sites is to calculate the partial negative charge on the framework oxygen atom using Sanderson electronegativity principles. This calculation has been carried out for each of the zeolites used in this study (*vide supra*), and the corresponding lattice oxygen charges are given in Table 3-17. A

plot of the log of the lifetime of the 9-cyclopropyl-9-fluorenyl cation in alkali metal cation Y zeolites versus the charge on the framework oxygen yields a linear relationship, Figure 3-117. The correlation between the lifetime of the carbocation and the charge on the framework oxygen, is consistent with a mechanism of carbocation decay involving addition of the zeolite framework. Furthermore, it is significant to note that the slope of the correlation is virtually identical to that obtained for the 4-methoxycumyl cation, Figure 3-117. The close match in lifetime variation as a function of the zeolite microenvironment strongly supports the notion that both carbocations decay *via* the same mechanism within alkali metal cation zeolites. Through detailed studies of the intrazeolite reactivity of 4-methoxycumyl cations, this mechanism has been established to be nucleophilic addition of the framework lattice oxygen atoms in $[\text{Si-O-Al}]^-$ sites.

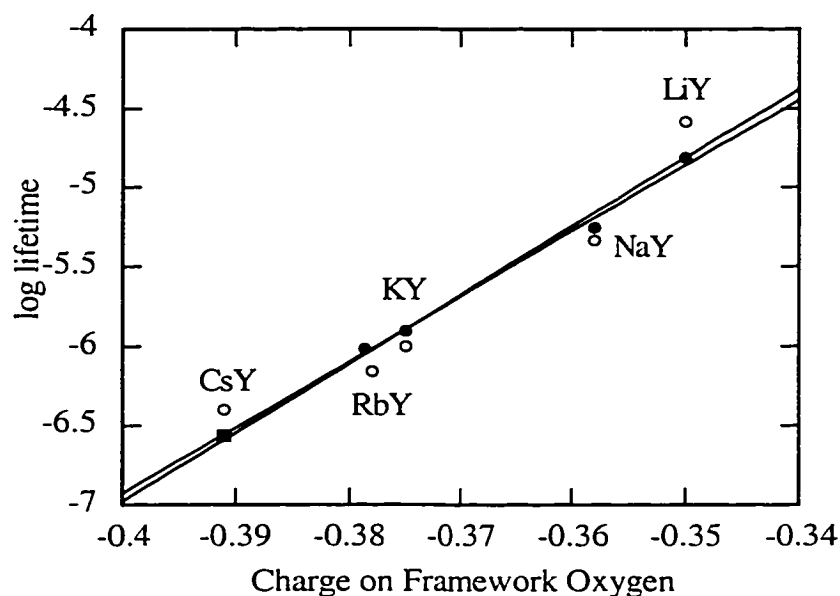


Figure 3-117. Variation in the log of the lifetime of the 9-cyclopropyl-9-fluorenyl cation (closed circles) and the 4-methoxycumyl cation (open circles) as a function of the charge on the framework oxygen atom. The 9-cyclopropyl-9-fluorenyl cation is not observed in CsY and the extrapolated lifetime is indicated by the closed square.

Beyond lending support to a decay mechanism characterized by nucleophilic addition, the observed variation in lifetime of the 9-cyclopropyl-9-fluorenyl cation with framework oxygen charge provides good evidence that this carbocation is not generated by photoheterolysis within CsY. As shown in Figure 3-117, the correlation between the

carbocation lifetime and the oxygen charge leads to a projected lifetime of approximately 280 ns for the 9-cyclopropyl-9-fluorenyl cation in CsY. This corresponds to a decay rate constant of $3.6 \times 10^6 \text{ s}^{-1}$, which is well within the practical time resolution of the diffuse reflectance system. Thus, the inability to detect the 9-cyclopropyl-9-fluorenyl cation in CsY is not due to rapid decay of this carbocation within the laser pulse, but instead it is more likely due to inefficient photolysis of cPrFOH within dry CsY.

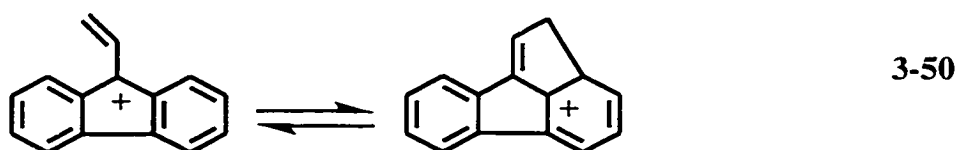
3.3.2.3 Substituent Effects on the Intrazeolite Reactivity of 9-Fluorenyl Cations

By examining a series of 9-R-9-fluorenyl cations, the current study facilitates an examination of the influence of substituents on the intrazeolite reactivity of these carbocations. Substituent effects on the reactivity of cumyl cations have been previously discussed. In particular, the influence of phenyl substituents on the reactivity of cumyl cations is found to be significantly attenuated in zeolites relative to organic solvents such as HFIP. It is likewise of interest to evaluate the effect of substituents on 9-fluorenyl cations in order to develop a better understanding of the general role substituents might play in the intrazeolite reactivity of carbocations and how this role may differ from the well-established roles of substituents in homogenous solution. In this regard, 9-fluorenyl cations are interesting intermediates as substituent effects have been shown to be particularly relevant in defining the lifetimes of these reactive carbocations in solution. As well, unlike the cumyl cations, where the substituent is somewhat distant from the carbocation center and mediates its influence through the phenyl ring, the substituent being varied on the 9-fluorenyl cations is directly attached to the carbocation center.

The variation in the reactivity of 9-fluorenyl cations in non-protic zeolites as a function of substituent shows trends similar to those observed in homogeneous solution.³⁹⁷ In alkali metal cation zeolites, the parent 9-fluorenyl cation is distinctly more reactive than the 9-alkyl-9-fluorenyl cations. Thus, the stabilizing influence of the alkyl groups observed in solution also plays an important role in defining the reactivity of the carbocations in zeolites. Interestingly, the reactivity of the 9-methyl-, 9-ethyl-, and 9-isopropyl-9-fluorenyl cations are approximately equal in both LiY and NaY. This contrasts with the reactivity of these carbocations in TFE where an increase in the steric bulk of the substituent at the 9-position is accompanied by a decrease in the rate constant for carbocation decay. In TFE, the effect is relatively small with the rate constant for decay of the 9-isopropyl-9-fluorenyl cation being approximately 2-fold smaller than the rate constant for decay of the 9-methyl-9-fluorenyl cation.³⁹⁷ The lack of any observable trend in the rate constants for intrazeolite decay of the 9-alkyl-9-fluorenyl cations

suggests that steric effects associated with the substituent at the 9 position exert even less influence over the reactivity of 9-fluorenyl cations in zeolites than in solution.

In NaY, as in solution,³⁹⁷ the rate constant for decay of the 9-vinyl-9-fluorenyl cation is slightly smaller than the rate constants for decay of 9-alkyl-9-fluorenyl cations, Table 3-22. In this case it is possible that the 9-vinyl-9-fluorenyl cation may decay *via* internal cyclization, eq. 3-50.



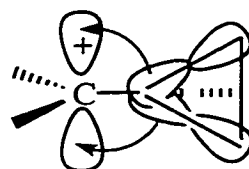
However, in order for this mode of decay to be operative, the rate constant for cyclization must be significantly greater than the rate constant for competing nucleophilic addition of the zeolite framework. Thus, if cyclization were indeed taking place, the lifetime of the 9-vinyl-9-fluorenyl cation would be notably shorter than the lifetime of the 9-alkyl-9-fluorenyl cations. The observation that the decay rate constant of the 9-vinyl-9-fluorenyl is comparable, and in fact slightly smaller, than the rate constant for decay of the 9-alkyl-9-fluorenyl cations indicates that cyclization is not the mechanism for decay of the 9-vinyl-9-fluorenyl cation in NaY.

The 9-cyclopropyl-9-fluorenyl cation is significantly less reactive within alkali metal cation zeolites than any of the other 9-fluorenyl cations investigated in this study. Again, this parallels the relative reactivity of these carbocations in solution, where the lifetime of the 9-cyclopropyl-9-fluorenyl cation is several orders of magnitude longer than the lifetimes of 9-alkyl-9-fluorenyl cations.⁴⁰³ This difference is attributed to the strong stabilization of the carbocation center provided by the cyclopropyl substituent.⁴⁰⁴ The stabilizing influence of the cyclopropyl group is associated with resonance delocalization of the positive charge into the p-orbitals of the cyclopropyl ring, Scheme 3-14. In this sense, the ability of a cyclopropyl ring to stabilize an adjacent carbocation is comparable to that of a phenyl ring, and indeed these two substituents often exert similar effects on the reactivity of carbocations.⁴⁰³

Overall, the order of 9-fluorenyl reactivity is due to the ability of the substituent to stabilize the carbocation center. This order is clearly maintained within the cavities of alkali metal cation zeolites, in a manner similar to that observed with phenyl-substituted cumyl cations. However, a significantly more interesting observation can be made when considering the reactivity range exhibited by these 9-fluorenyl cations in zeolites as

compared to solution, Table 3-28. This comparison exemplifies a remarkable influence of zeolite encapsulation on carbocation reactivity. In particular, it is observed that the most unstable 9-fluorenyl cation is significantly longer lived within the zeolites LiY and NaY as compared to water, or even the weakly nucleophilic solvent TFE. Conversely, the more stabilized 9-cyclopropyl-9-fluorenyl cation is one to two orders of magnitude more reactive in these alkali metal cation zeolites than in TFE. The net result is that the environment within the zeolite cavities provides a dramatic *leveling effect*, whereby the relative reactivity of carbocations is significantly less sensitive to the relative thermodynamic stability than observed in solution.

Scheme 3-14



3.3.2.4 Influence of Coadsorbed Protic Reagents on the Intrazeolite Reactivity of 9-Fluorenyl Cations

As observed in studies of intrazeolite addition of nucleophiles to cumyl cations, the inclusion of water and methanol within alkali metal cation zeolites enhances the rate constant for decay of 9-fluorenyl cations, and/or decreases the yield of carbocation observed immediately following the laser pulse. These processes are attributed to dynamic and static quenching, respectively, of the 9-fluorenyl cations by nucleophilic addition of water or methanol to the carbocation center within the zeolite cavities. The observation of static quenching by water or methanol is complicated by the fact that both reagents enhance photoheterolysis thereby increasing the yield of carbocation and also act as nucleophiles thereby facilitating rapid disappearance of the carbocation during the laser pulse. Ultimately, it appears that the influence of enhanced photoheterolysis is dominant at relatively low concentrations of water or methanol, and absorption due the 9-fluorenyl cations increases in the presence of these protic reagents, Figure 3-92. At sufficiently high concentrations of either water or methanol, however, static quenching must occur to a sufficiently large extent that the carbocation signal begins to decrease, Figure 3-98.

Table 3-28. Lifetimes of 9-R-9-fluorenyl cations in LiY, NaY, TFE, and water, and the reactivity range exhibited by these cations in each environment.

R	Lifetime / ns			
	LiY	NaY	Water	TFE
H	345	145	< 0.02 ^a	1.2 ^b
Methyl	540	290	1.0 ^a	110 ^c
Cyclopropyl	15600	2600	150 ^d	90 000 ^d
Reactivity Range:	45	18	> 7500	75 000

^aRef. 384; ^bRef. 234; ^cRef. 386; ^dRef. 397.

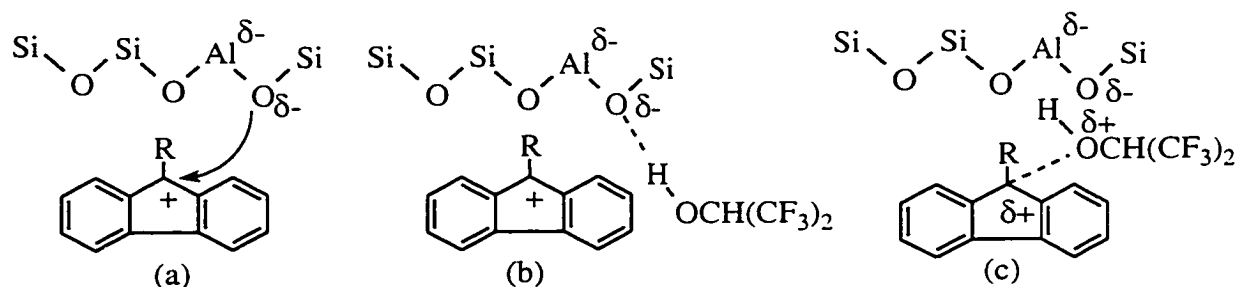
Dynamic quenching of the 9-cyclopropyl-9-fluorenyl cation by methanol is characterized by a quadratic dependence of the observed rate constant for carbocation decay on the concentration of methanol, Figure 3-96. This observation suggests that two molecules of methanol may be necessary to facilitate the intrazeolite nucleophilic addition. The decay rate constant of the 9-cyclopropyl-9-fluorenyl cation exhibits an interesting dependence on the concentration of coadsorbed water, Figure 3-97. The rate constant for carbocation decay actually *decreases* slightly when small concentrations of water are included within the zeolite matrix. Subsequent increases in water content eventually accelerate the rate constant for carbocation decay. Notably the overall variation in decay rate constant as a function of water content is relatively small, particularly when compared with the influence of methanol. Yet, the measured changes in decay rate constant at various levels of zeolite hydration are not within experimental error of each other. Considerable experimental evidence, including temperature-programmed desorption analysis and x-ray diffraction studies indicate that the first water molecules included within the zeolite matrix adsorb at the strongest binding sites.^{27,28,340} Thus, the energy required to remove water from the zeolite matrix decreases as the level of hydration increases. This binding behaviour of water could be responsible for the initial decrease in carbocation decay rate constant observed at low water content. At low concentrations, not only would the strong binding hinder the ability of the water to act as a nucleophile, but it is possible that the water initially binds to sites active in nucleophilic attack on the carbocation, thereby inhibiting this reaction. Consequently, the lifetime of the carbocation would increase relative to dry conditions. Interestingly, an increase in carbocation lifetime is also observed upon the inclusion of the much less nucleophilic, alcohol HFIP, and is likewise attributed to strong binding of the alcohol to zeolite sites involved in carbocation decay (*vide infra*). At higher concentrations of water, the

stronger binding sites will already be occupied and the included water molecules will be more free to act as nucleophiles and react directly with the carbocation.

Perhaps the most interesting observation concerning the influence of coadsorbed protic reagents on the intrazeolite lifetimes of 9-fluorenyl cations is the effect of HFIP. The lifetimes of 9-fluorenyl cations within alkali metal cation zeolites such as NaY and Na β are *enhanced* by the inclusion of relatively small amounts of the slightly acidic, weakly nucleophilic alcohol HFIP. This is analogous to the influence of HFIP on the lifetime of highly reactive cumyl cations such as the 4-fluorocumyl cation and the parent cumyl cation in alkali metal cation Y zeolites LiY and NaY. Such observations suggest that coadsorption of HFIP within the zeolite cavities reduces the nucleophilicity of the interior zeolite environment and thereby enhances the lifetimes of encapsulated carbocations.

As previously described, a likely mechanism for decay of the 9-fluorenyl cation within the dry zeolite involves nucleophilic addition of the oxygen atom within a [Si-O-Al]⁻ bridge to generate a framework bound species, Scheme 3-15 (a). A reasonable explanation for the observed decrease in carbocation decay within NaY upon adsorption of HFIP is that the HFIP interferes with nucleophilic addition by forming a hydrogen bond with the reactive framework oxygen as shown in Scheme 3-15 (b). Alternatively, the weakly nucleophilic oxygen of HFIP may interfere with the cationic center of the 9-fluorenyl cation, thus inhibiting an interaction between the carbocation center and the nucleophilic framework oxygen, Scheme 3-15 (c).

Scheme 3-15



3.4 Synopsis of Current Views of Carbocation Chemistry in Non-Acidic Zeolites and Direction of Future Studies

The results of the current work establish that non-acidic, alkali metal cation-exchanged zeolites can support the generation of reactive carbocations and stabilize these

intermediates such that they can be directly observed in the nanosecond to microsecond time regime, Table 3-29. This includes highly reactive carbocations, such as the unsubstituted 9-fluorenyl cation. Furthermore, the carbocations investigated in alkali metal cation zeolites exhibit a large range of lifetimes in homogeneous solution and therefore cannot all be examined in a single solvent using nanosecond laser flash photolysis. These observations are an unequivocal testament to the remarkable ability of non-acidic zeolites to stabilize carbocation intermediates as a consequence of the confined organized environment and electrostatic fields which are characteristic of the intrazeolite environment. As a result, many carbocation intermediates are significantly longer-lived in alkali metal cation zeolites than in relatively nucleophilic solvents such as, for instance, water, Table 3-29.

Table 3-29. First-order rate constants for the decay of carbocations in alkali metal cation-exchanged zeolites and solution.

Carbocation	$k / 10^6 \text{ s}^{-1}$				
	NaY	LiY	Na β	H ₂ O	TFE
4-MeOC ₆ H ₄ C ⁺ (CH ₃) ₂	0.22	0.038	0.003	~ 40 ^a	0.016 ^b
4-MeC ₆ H ₄ C ⁺ (CH ₃) ₂	3.2	2.2	0.33	-	10 ^b
4-FC ₆ H ₄ C ⁺ (CH ₃) ₂	not observed	5.0	1.0	-	-
C ₆ H ₅ C ⁺ (CH ₃) ₂	not observed	18*	2.0	-	> 50 ^c
3-MeOC ₆ H ₄ C ⁺ (CH ₃) ₂	not observed	23*	2.5	-	-
(C ₆ H ₅) ₂ CH ⁺	0.66	0.55	not measured	1300 ^d	3.2 ^b
9-Cyclopropyl-9-fluorenyl	0.38	0.064	not measured	-	0.007 ^c
9-Vinyl-9-fluorenyl	1.6	not measured	not measured	-	1.8 ^c
9-Methyl-9-fluorenyl	3.5	1.8	0.87	3600 ^f	8.6 ^e
9-Ethyl-9-fluorenyl	3.6	1.4	0.83	-	14 ^c
9-Isopropyl-9-fluorenyl	5.6	1.4	0.81	-	4.6 ^c
9-Fluorenyl	6.9	2.9	not observed	>50000 ^f	800 ^b
Reactivity Range	31	605	830	> 1250	114000

*Extrapolated values (see Section 3.2.2.); ^aRef. 226; ^bRef. 234; ^cRef. 397; ^dRef. 388; ^eRef. 386; ^fRef. 384.

However, although alkali metal cation zeolites are exceptional in their ability to stabilize many reactive carbocations such that they may be directly observable using nanosecond laser flash photolysis, these carbocations exist as *transient intermediates*

within non-acidic zeolites. Therefore, many reactive carbocations are significantly shorter lived in alkali metal cation zeolites, even relatively stabilizing zeolites such as LiY and Na β , than in TFE, Table 3-29. Consequently, the reactivity range exhibited by carbocation intermediates in alkali metal cation zeolites is dramatically smaller than observed in homogeneous solution. Thus, the approximately 30-fold difference in reactivity of the carbocations observed in NaY is significantly smaller than the greater than 10^5 -fold range of reactivity observed for these carbocations in TFE. In LiY and Na β , the reactivity range is extended somewhat but remains well below the reactivity range displayed by carbocations in TFE and even in water. These observations confirm that the role of the zeolites in carbocation chemistry is not simply that of an inert, non-nucleophilic reaction vessel which provides kinetic stabilization to all carbocations. *Zeolites are direct participants in the chemical transformations of carbocation intermediates.*

These interpretations are consistent with the current perspectives of carbocation-mediated reactions in acid zeolites where the role of the zeolite framework is now envisioned to be significantly more than a mere proton donor.²⁴⁹ Much of this thinking arises from the fact that many carbocations do not exist as persistent species in acid zeolites. In many such cases, framework-bound intermediates have been proposed as alternatives to long-lived free carbocations, even within the strongly acidic environment of protic zeolites. The investigations of carbocations in alkali metal cation zeolites described herein provide direct evidence for the transformation from a free reactive carbocation intermediate into framework-bound species *via* nucleophilic attack of the zeolite framework, and demonstrate that this process is highly dependent on the nature of the zeolite environment. The transformation from free carbocation to framework bound species likely represents a significant step in carbocation-mediated chemical transformation of organic reagents within zeolites.

Furthermore, the work presented in this thesis emphasizes that zeolite encapsulation also modulates the bimolecular reactions of carbocation intermediates leading to unique reactivity trends as compared to homogeneous solution. In particular, zeolites promote intracavity reaction between nucleophiles and reactive carbocations, as a consequence of both confinement effects and very likely direct participation of the zeolite framework in the nucleophilic addition reaction. However, zeolites also inhibit the bimolecular addition of nucleophiles to carbocations as a result of the molecular confinement of the carbocation within the micropore, and the hindered diffusion of nucleophiles thorough the zeolite topology. The interplay between the promotion of nucleophilic attack and the protection of carbocations from nucleophiles can be subtly or

dramatically varied by changing the zeolite environment in a rational manner.

The current work represents the first direct observation and investigation of carbocations in non-acidic zeolites. Although it has generated new insight into the intrazeolite reactions of carbocations, these investigations have also revealed a new aspect of research which warrants extensive future investigations. Possible directions for future studies of carbocations in non-acidic zeolites are listed below:

(i) Additional types of carbocation intermediates should be investigated in order to develop a more complete, quantitative picture describing the absolute reactivity of carbocation intermediates in non-acidic zeolites as has been developed in solution. In particular, it is of interest to establish structure-reactivity relationships and how they influence carbocation reactivity in zeolites as compared to solution.

(ii) The mechanism proposed for intrazeolite decay of the 4-methoxycumyl cation should be established rigorously *via* direct observation of the framework-bound alkoxy through, for instance, NMR. Furthermore, these investigations should be extended to other types of carbocation intermediates to assess the generality of this decay mechanism and to determine other possible modes of interaction between reactive carbocations and alkali metal cation zeolites.

(iii) Bimolecular addition reactions between carbocations and other types of nucleophiles may be considered. One interesting experiment could employ a bulky nucleophile which is immobilized or entrapped within the zeolite cavities. In this case, bimolecular reactions could be applied to probing the motion of carbocation intermediates within zeolite hosts.

(iv) The current work has focused largely on the intrazeolite reactivity of carbocations. However, to fully understand reactions mediated by carbocations, it is also necessary to examine the role of zeolites in carbocation formation. In this regard, it would be useful to employ diffuse-reflectance or fluorescence techniques in shorter time regimes (picoseconds to femtoseconds) in order to directly observe carbocation formation, for instance *via* carbon-carbon bond cleavage, photoheterolysis, or *via* additional photoinitiated methodologies. Evaluation of the influence of zeolite and carbocation structure on the rates and efficiencies of carbocation formation in non-acidic zeolites should provide a more complete picture of the role of zeolites in carbocation-mediated transformations from starting material to product.

Chapter 4. Photogeneration and Migration of Electrons and Holes in NaY

4.1 Introduction

The transfer of a single electron between two molecules is one of the most significant and ubiquitous reactions in the chemical and biological world, and electron transfer (ET) continues to be among the most actively pursued areas in contemporary chemistry.^{405,406} The fundamental natural process of converting light energy into the chemical energy in green plants relies on efficient photoinduced electron transfer (PET).⁴⁰⁷ Experimental attempts to emulate natural ET often employ organized, heterogeneous media^{408,409} to modify electron transfer dynamics and direct research at practical applications such as solar energy conversion,⁴¹⁰ photosynthetic mimicry,^{411,412} and molecular electronics.^{413,414} Such experiments probe ET reactions in novel environments, providing insight into the mechanisms of these reactions as well as the nature and influence of the media. Zeolites have been shown to be highly amenable hosts in many studies of heterogeneous ET. Yet, the role of zeolites in the observed ET chemistry, as well as the mechanisms of intrazeolite ET and charge migration, remain largely unexplained.

4.1.1 A Brief Introduction to Electron Transfer

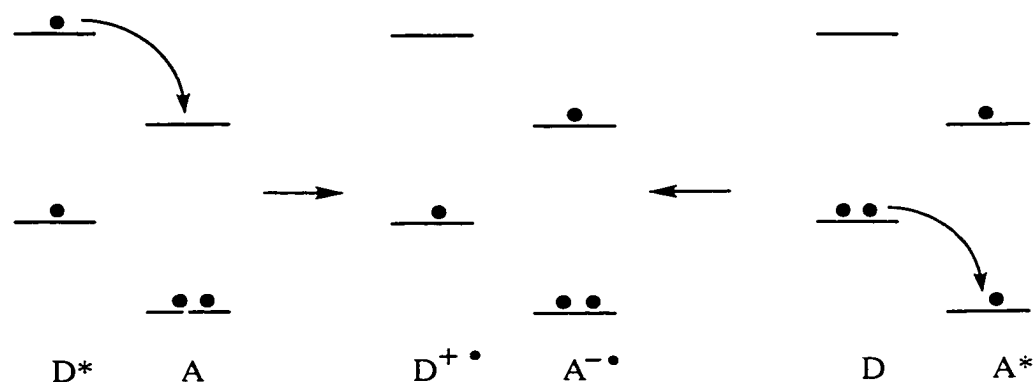
Electron transfer^{306,415,416} can be formally described as a one electron reaction in which an electron moves from an occupied orbital of one reagent to an unoccupied orbital of a second reagent. In a general sense, ET involves electron donation from an electron-rich donor, D, to an electron-deficient acceptor, A, which, for a neutral donor and acceptor, generates the donor radical cation and acceptor radical anion, respectively, eq. 4-1.



This inverts the normal electron demand of the reactants and hence their typical reactivity. In order to exploit this inverted electron demand it is necessary to drive the ion pair-reactant equilibrium towards the charge separated state. Here, the photon can be employed as a powerful tool. Photoinduced electron transfer (PET) provides a means of activating the donor-acceptor system such that the forward reaction yielding ion pairs is

more favorable. In PET, the electron is transferred between a photoexcited and a ground state species, thus distinguishing it from a redox reaction involving two unexcited compounds. The activation is based on the fact that certain species become powerful electron donors or acceptors in the excited state, Scheme 4-1. In this sense PET is regarded as a quenching pathway since the photoexcited state is quenched by a redox reaction between the donor and acceptor.

Scheme 4-1

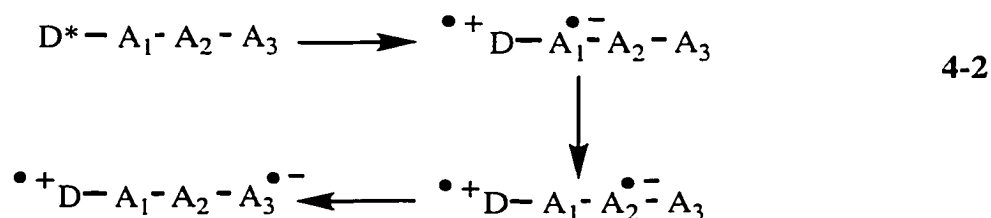


Experimental investigations of PET were initiated in the early 1960s, with, for example, the report of Leonhardt and Weller⁴¹⁷ of emission from complexes of perylene and dimethylaniline. These complexes, referred to as exciplexes, were postulated to form *via* ET between an excited and a ground state molecule. With the advent of laser flash spectroscopy and other time-resolved techniques in the 1970s, it became possible to observe directly the radical ions in reactions postulated to proceed *via* ET.^{418,419} Other types of investigations focused on the development of synthetic chemistry based on PET reactions.^{270,420,421} During this time, Gould and Farid began examining a number of chemical reactions initiated by PET.⁴²² Their seminal studies of return electron transfer, k_{-et} , within geminate radical ion pairs led to the remarkable experimental observation that k_{-et} decreased with increasing exothermicity,⁴²²⁻⁴²⁴ as predicted by Marcus nearly thirty years earlier.⁴²⁵ More recently, investigations of PET have evolved to include diverse studies involving biological systems^{407,426-428} and heterogeneous media,⁴²⁹⁻⁴³² and investigations of ET rates and the dynamics of radical ions with picosecond and femtosecond time resolution.^{295,433,434}

There are several possible pathways for ET quenching of excited states in fluid solution.³⁰⁶ For mobile, unrestrained reactants, ET quenching often involves the

formation of an encounter complex prior to actual ET. The encounter complex consists of the excited state and ground state reactants in close proximity, typically about 7 Å, surrounded by a solvent shell with the inner most solvent shell being referred to as the solvent cage. Within the encounter complex, reactants have sufficient time to undergo the structural and electronic changes necessary for ET to occur. Since the vibrational frequency required for such changes is on the order of 10^{12} s^{-1} , many such vibrations can take place within the lifetime of the encounter complexes which is approximately 10^{-9} to 10^{-10} s for small, uncharged molecules. After ET quenching within the encounter complex, a charge transfer species is initially formed which may dissociate somewhat to yield a solvent separated ion pair, or fully separate to generate completely independent free ions. In cases where there is a strong interaction between reactants, one of which is in the excited state, an encounter complex can form an intermediate which is sufficiently long-lived to emit light. These exciplexes are characterized by binding energies in the range of 5 to 20 kcal/mol, partial charge character, and large dipole moments. Exciplexes exhibit pronounced charge-transfer character and can separate into radical ion pairs, particularly in polar solvents. Therefore, another important quenching pathway, particularly for planar organic molecules, is *via* exciplex formation.

Quenching *via* ET is also possible in situations where the excited state and ground state reactants do not adopt a close approach as in an encounter complex or an exciplex. For instance, an electron can “hop” or migrate from a donor to an acceptor *via* a third molecule which serves as a relay. For example, intervening solvent molecules can serve as molecular relays in these “hopping” mechanisms. In addition, such a mechanism has been proposed for systems in which intramolecular ET in rigid molecules proceeds *via* a third functional group where ET can be envisioned as a consecutive cycle of electron accepting and donating processes, eq. 4-2.



Similar hopping mechanisms may also play a role in ET quenching in viscous or heterogeneous media where slow diffusion excludes the formation of an encounter complex during the excited state lifetime.

The feasibility of ET between a photoexcited and ground state reagent is governed by the overall free energy change associated with the reaction. As discussed in Chapter 3, the energetics of ET in solution are described by the Rehm-Weller equation,³⁰⁵ eq. 3-22, which can be used to calculate the free energy of ET quenching of an excited state.

$$\Delta G_{\text{PET}} = 23.06 \left[E_{\text{ox}}(\text{D} / \text{D}^{+\bullet}) - E_{\text{red}}(\text{A} / \text{A}^{-\bullet}) - e^2 / \alpha \epsilon \right] - E_{00} \quad 3-22$$

According to this equation, the energy required for ET to occur is given by the difference in redox potentials between the donor and the acceptor. The photon energy, corresponding to the energy of the excited state, E_{00} , provides the input energy necessary to overcome the energetic barrier which prohibits spontaneous reaction in the ground state. A term which accounts for the Coulombic interactions and solvation of the resultant radical ions also appears in the equation, $e^2/\alpha\epsilon$, but is often very minor compared to the other terms and therefore neglected. Exergonicity is generally required in order for ET to compete efficiently with other reactions pathways of the excited state.

Rate theories of PET have evolved from the original treatments of Marcus^{425,435,436} and Hush⁴³⁷ initially designed for ET between ground-state species in solution. All classical approaches, both qualitative and quantitative, view PET by separating nuclear and electronic motions, and an understanding of the factors affecting the rates of ET can be obtained by considering the time scales of these motions. According to the Franck-Condon principle, the interatomic distances and nuclear momenta are unchanged during the absorption and emission of light. In other words, the slower nuclear motion is negligible on the time scale of electronic motion associated with photon absorption and emission. A similar notion can be applied to ET reactions, whereby the transfer of an electron is essentially instantaneous compared to slower nuclear motions. However, since nuclear motions must take place in order to accommodate the new electronic configuration of the reactants and the surrounding shell of solvent molecules associated with ET, these slower motions can often limit rates of electron transfer. The elementary principle inherent in Marcus theory of ET is that, in accordance with the first law of thermodynamics, ET can only take place between two isoenergetic states. Therefore, nuclear changes, or *reorganization*, necessary to compensate for the electronic changes must take place *before* the electron is transferred. The nuclear geometry of the reactants as well as the surrounding molecules must achieve a high-energy, distorted conformation, typically possible through collisions with reactants and surrounding molecules. The transition state for ET then consists of two high energy species possessing equivalent nuclear geometry but different electronic configurations.

In the most general sense, the rate constant for ET can be described by an Arrhenius relationship which relates the rate constant, k_{ET} , to the free energy of activation, ΔG^\ddagger , for the reaction, eq. 4-3,

$$k_{ET} = k \exp \left[-\frac{\Delta G^\ddagger}{k_B T} \right] \quad 4-3$$

where T is the absolute temperature, and k_B is Boltzmann's constant. Here, k is a constant which reflects the electronic barrier associated with the reaction, while contributions from nuclear barriers are contained within ΔG^\ddagger , as will be described below. Overall, the rate constant for ET may be controlled largely by electronic factors, $k \ll 1$, $\Delta G^\ddagger \sim 0$, or largely by nuclear factors, $k \sim 1$, $\Delta G^\ddagger > 0$.

A convenient visualization of the electronic and nuclear factors associated with ET reactions can be made from potential energy surfaces which describe the potential energies of reactants and solvent molecules as a function of nuclear topology (e.g., variations in bond length, bond angle, molecular orientation, and position). For bimolecular ET reactions, the reactant surface describes the initial state consisting of an excited state and a ground state molecule (initial excitation of the sensitizer places the reacting system on an excited state surface), while the product surface describes the final state consisting of a radical ion pair, Scheme 4-2. The intersection between the excited-state reactant surface and product surface corresponds to the non-equilibrium, distorted nuclear geometry through which ET can proceed. Thus, as the electron moves from the donor to the acceptor, it switches from a point on the reactant surface to an isoenergetic point on the product surface.

The electronic barriers in ET are related to the movement of electrons between orbitals. The orbitals act as conductors of the electronic motion, and overlap between occupied and unoccupied orbitals of appropriate symmetry is highly significant to the occurrence of ET. The probability that ET will take place at the intersection is determined by the electronic interaction, or "mixing", between the reactant and product states, the magnitude of which is given by the electronic coupling matrix, H_{if} , eq. 4-4,

$$H_{if} = H_{if}^0 \exp[-\beta(d-d_0)/2] \quad 4-4$$

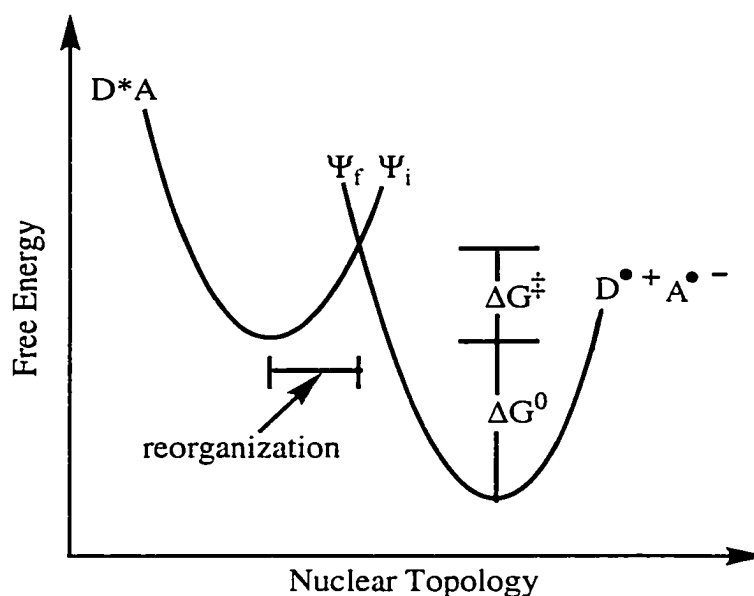
where d_0 is the electronic coupling distance, and $(d-d_0)$ refers to the electronic edge-to-edge distance which is inversely proportional to the magnitude of orbital overlap, and β is an orbital parameter which reflects the sensitivity of electronic coupling to distance. As

can be seen in eq. 4-4, the electronic interaction between two overlapping orbitals decreases exponentially with separation distance, from a maximum value, H_{if}^0 , when the donor and acceptor are in contact. Equation 4-4 can be written in terms of a rate constant for ET, eq. 4-5,

$$k = k^0 \exp[-\beta(d-d_0)] \quad 4-5$$

where k^0 is the maximum probability of electron passage between the reactant and product surfaces at the intersection point.

Scheme 4-2 (adapted from reference 306.)



As is evident in eq. 4-5, the rate constant for ET decreases exponentially with separation distance, with the precise nature of the distance variation specified by the parameter β . Values of β usually range from 0.9 to 2.0 \AA^{-1} . With β equal to 1.2 \AA^{-1} , as $(d-d_0)$ increases from 5 \AA to 10 \AA to 15 \AA , the rate constant for ET decreases from approximately 10^9 s^{-1} to 10^8 s^{-1} to 10^5 s^{-1} . Thus, for a typical singlet excited state with a lifetime of the order of 10 ns, ET quenching is only observed for reagents in close proximity, or when the donor and acceptor orbitals extend over large distances. In addition to separation distance, orientational and symmetry factors also play a role in determining the effective orbital overlap. Overall, when orbital electronic barriers

defined by distance, orientation, and symmetry inhibit electron motion between the donor and acceptor, ET is slow. Notably, PET in dilute or highly viscous solution, or other media where reactants are well separated, is consequently improbable.

In cases where reactant orbitals interact strongly (*i.e.* k approaching 1), electronic barriers are minimized and the rate-determining factors of ET are governed by nuclear reorganization. These nuclear changes consist of structural adjustments within the reactant molecules and surrounded media in the stages preceding ET which bring them into the high energy, distorted geometry of the transition state. The total energy associated with these perturbations is known as the reorganizational energy, λ , which is a combination of the free energy changes associated with nuclear motions of the reactants, the inner sphere reorganization, λ_i , and the free energy changes associated with nuclear motion of the solvent molecules, the outer-sphere reorganization, λ_o , eq. 4-6.

$$\lambda = \lambda_i + \lambda_o \quad 4-6$$

For the same nuclear coordinates, λ corresponds to the vertical separation difference between the reactant and product curves (see Scheme 4-4).

As mentioned above, the nuclear barriers to the ET reaction are contained within the free energy of activation, ΔG^\ddagger , shown in eq. 4-3. The free energy of activation depends on the total reorganizational energy, λ , and the reaction free energy, ΔG^0 , according to the famous Marcus relationship,⁴³⁶ eq 4-7. This is contrary to chemical intuition due to the quadratic dependence of the free energy of activation energy on the free energy of reaction.⁴³⁸

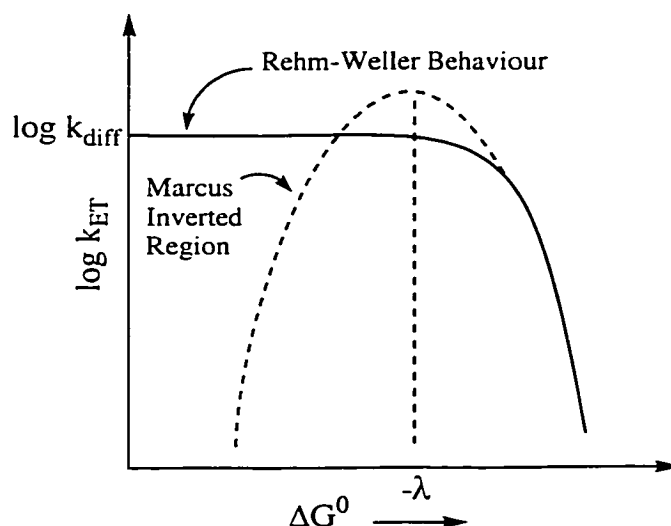
$$\Delta G^\ddagger = \frac{\lambda}{4} \left(\frac{\lambda + \Delta G^0}{\lambda} \right)^2 = \frac{(\Delta G^0 + \lambda)^2}{4\lambda} \quad 4-7$$

Combining eq. 4-3 and 4-7 gives an expression for the rate constant of ET in terms of the electronic barriers, k , the nuclear reorganizational energy, λ , and the overall free energy of the reaction, eq. 4-8.

$$k_{ET} = k \exp \left[-\frac{(\Delta G^0 + \lambda)^2}{4\lambda k_B T} \right] \quad 4-8$$

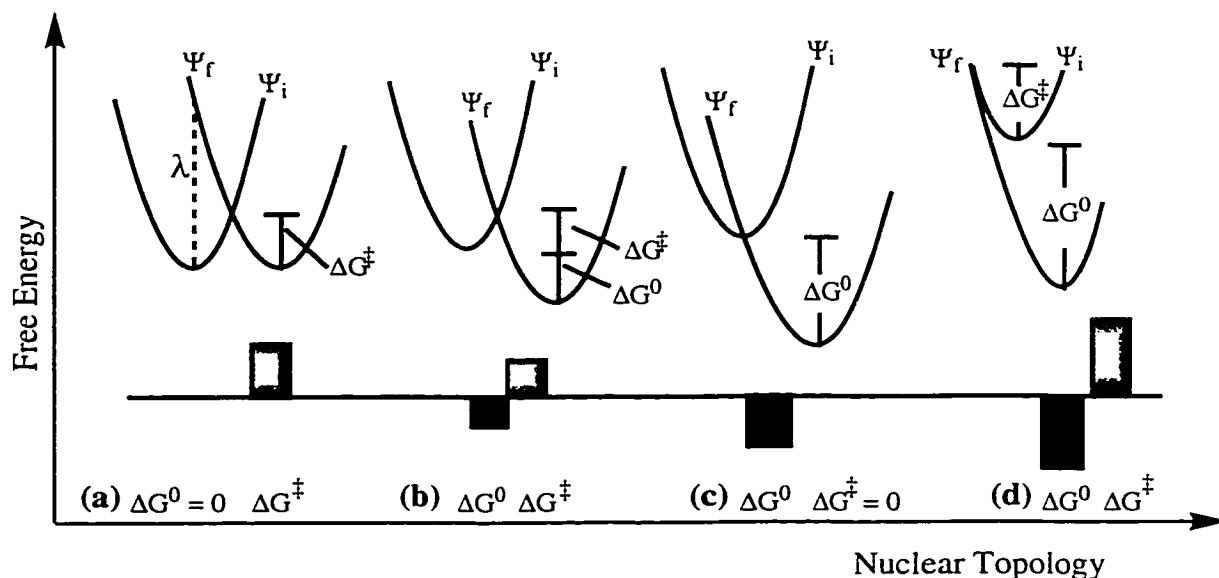
Certainly the most outstanding feature of Marcus theory is the prediction of a quadratic free energy relationship. According to eq. 4-8, the rate constant for ET should increase with increasing driving force, ΔG^0 , until a maximum is reached at $\Delta G^0 = -\lambda$. Subsequent increases in reaction free energy will lead to a decline in rate constant in what is known as the Marcus inverted region, Scheme 4-3.

Scheme 4-3



A simplified explanation for the quadratic relationship between free energy of activation and free energy of reaction can be obtained by considering the ET reaction as the intersection of two parabolic potential wells such as described previously, Scheme 4-4. Beginning with the disposition of reactant and product energy curves such that $\Delta G^0 = 0$, the free energy of reaction decreases as the product well drops in energy (a). This results in typical behaviour, the “normal region”, where the free energy of activation decreases as the free energy of reaction increases (b). As the product well drops further in energy, the free energy of activation continues to decrease until the reaction becomes activationless (c). At this point the rate constant for reaction corresponds to the diffusion controlled limit ($k_{ET} = k_{diff}$). However, for more negative reaction free energies, the product and reactant wells intersect only at relatively high free energies. This causes the activation barrier to rise with increasing exergonicity and leads to the inverted region (d).

Scheme 4-4



Experimental proof for the existence of a quadratic relationship between reaction rates and energetics was not definitively established until thirty years after being predicted by Marcus. From a practical standpoint, only photochemically or radiochemically induced energetic systems have sufficiently large exergonicities to exhibit Marcus inverted behaviour. However, contrary to the predictions of Marcus theory, Rehm and Weller's investigations of fluorescence quenching by ET firmly established that the rate constants for these reactions approach the diffusion limit (ca. 10^{10} s^{-1}) for reaction free energies in the range of -5 to -10 kcal/mol, and do not decrease at higher exergonicities, Scheme 4-3.^{305,439} The verification of Marcus theory came only in the 1980s when Closs and Miller demonstrated unambiguously that ET within rigid intramolecular systems displays Marcus inverted behaviour.^{440,441} Since then, the existence of the inverted region has been established for other intramolecular systems,⁴⁴² PET in organic glasses and melts,^{443,444} and intramolecular ET between inorganic ligands.⁴⁴⁵ These studies share the common feature that diffusion of the redox reagents has been eliminated due to either intramolecular tethering or media effects. Experimental manifestation of the inverted region at large thermodynamic driving forces is difficult to achieve due to the masking of fast ET by k_{diff} in solution. As a result, intermolecular ET reactions in solution typically exhibit Rehm-Weller behaviour. A notable exception is back electron transfer (BET) within contact ion pairs. The seminal studies of Farid and Gould in the late 1980s and early 1990s demonstrated the existence of the Marcus

inverted region for BET within geminate radical ion pairs generated by PET.^{307,423,424} Subsequently, the existence of the Marcus inverted region has been verified numerous times for charge recombination,⁴⁴⁵⁻⁴⁴⁷ including one recent example demonstrating the Marcus inverted region of BET in zeolites.¹⁶⁰ Analogous to intramolecular ET, diffusion is not necessary for ET to take place since the redox partners are held together within the initially formed contact ion pair.

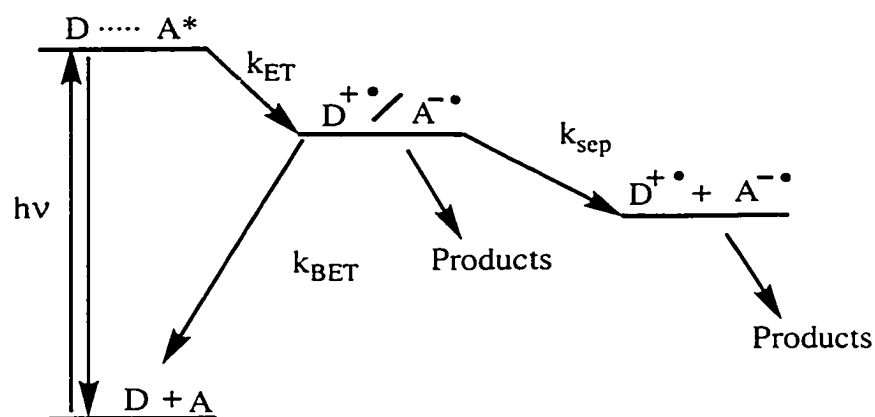
Marcus inverted behaviour has also been demonstrated for charge separation reactions. The investigations of Pincock and coworkers⁴⁴⁸⁻⁴⁵¹ have shown that the rate constants for forward ET within a geminate radical pair increase with increasing driving force at low exergonicities and eventually decrease with increasing driving force at high exergonicities, thereby displaying both normal and inverted behaviour as predicted by Marcus. Again, diffusion is eliminated in this system due to the close proximity of the geminate radical pair. Ishiguro *et al.* have reported the observation of the Marcus inverted region for the generation of carbocations and carbanions from benzyl-type radicals upon irradiation of donor/acceptor pairs containing substituted dibenzylketones as the radical precursors.⁴⁵² Observation of the Marcus inverted region for a charge separation reaction was reported for the photoinduced bimolecular reaction between ruthenium(II) diimines and cytochrome C.⁴⁵³ In this case, the Marcus curve was displaced below the diffusion limit allowing for its observation.

As previously discussed, the input of photon energy enhances the redox potentials of electron donors and acceptors and therefore accelerates the rates of ET reactions relative to that observed in the ground state. However, as a consequence of the added photon energy, the resultant radical ions are relatively reactive and are energetically inclined towards ion pair recombination, Scheme 4-5. For stable reactants there will be a significant driving force for thermal BET between the relatively high energy ions, due in part to the electrostatic interactions and the electron pairing of paramagnetic species. Often, the destabilization of the charge separated state is 1-4 eV or more. Thus, the photoinduced ion pair tends to relax rapidly back to the ground state, thereby destroying the chemical activation and energy stored in charge separation. Such BET often represents the fundamental obstacle to the generation of long-lived ion pair intermediates which are necessary for the productive application of PET.

Heterogeneous media are frequently used to achieve some control over PET, the chemistry of the resultant ions, and the thermodynamically favoured back reaction which severely hinders the production of free ions. Examples of such reaction control, including the suppression of BET, is widespread in natural systems. For instance, the highly efficient PET in photosynthetic reaction centers often generates charge separated

species in excess of 90% quantum yield, with photon energy yields near 30%. These successful light energy conversion processes rely on the electrostatic and steric effects of organized media to exert preferential kinetic control over complex photochemical and thermal reactions. Heterogeneous media, including micelles, vesicles, polymers, clays, and zeolites have been employed to study PET reactions, and/or incorporated into supramolecular electron transport systems.^{409,454} Such systems often introduce electrostatic and steric effects distinct from those found in solution while providing reactant organization which is not available in homogeneous media. Heterogeneous environments may also influence the relative stabilities of the donor and acceptor as well as the ion pair intermediates, hence altering the reaction driving forces and kinetics. These variables introduce new perspectives and challenges in the study of PET chemistry, and present a myriad of possible applications.

Scheme 4-5



4.1.2 Studies of Electron Transfer and Redox Processes in Zeolites

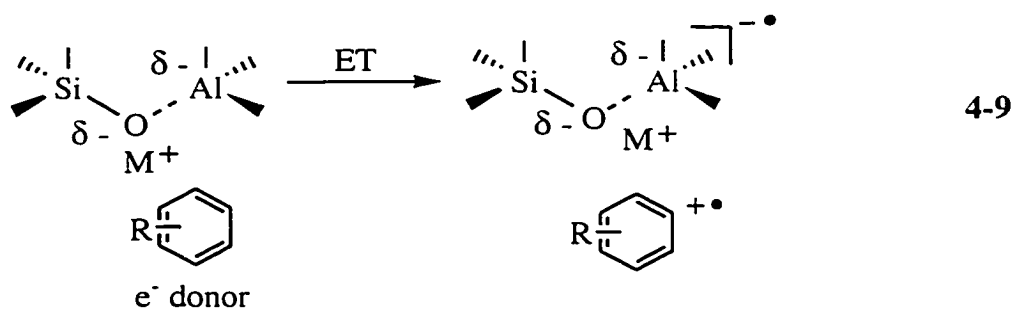
Physical and chemical variability coupled with unique microstructural organization render zeolites excellent host materials for the study and application of PET reactions.^{41,165,181,182} Within the three dimensional network of channels and cavities, guest molecules may be compartmentalized in specific arrangements. Reactant isolation is possible, as is direct chemical contact. The unique intrazeolite environment is different from many other microheterogeneous media in its ability to influence fundamental properties of incorporated species, including mobility, photochemistry, and thermal reactivity. Encapsulation within zeolite cavities has been shown to be critical to photoproduct stabilization, including enhancing the lifetime of transient species such as

radical ions. Furthermore, the zeolite environment can be readily modified to investigate the influence of specific parameters on the observed ET chemistry, or to implement desired reaction conditions.

Several roles have been demonstrated and/or can be envisioned for zeolites in ET processes. For instance, the zeolite host can offer a stabilizing environment, thus enhancing the yield of charge separation and the lifetimes of the radical ion intermediates, and inhibiting energy-wasting BET. The zeolite framework may participate as a redox partner in ET reactions with encapsulated electron donors and electron acceptors. In such cases the zeolite may be considered amphoteric, as it may take the role of either the electron donor or the electron acceptor. Furthermore, the zeolite may act as a medium, or bridge, to facilitate charge migration between co-encapsulated and spatially separated electron donors and acceptors.

The silicon and aluminum oxide frameworks of zeolites are more than passive vessels for reactions of included guests. In terms of ET chemistry, zeolites are active electron acceptors and electron donors in many important redox reactions of encapsulated guests. Lewis acid sites such as tricoordinate aluminum, extraframework aluminum, and charge balancing cations, as well as Lewis base sites such as the lone electron pairs on the bridging oxygen atoms, can participate in ET reactions and contribute to the amphoteric behaviour of zeolites in redox processes. These amphoteric properties vary dramatically with zeolite structure and composition.

The ability of protic and non-protic zeolites to act as electron acceptors in both thermal and photochemical oxidation reactions of guest molecules is well established, eq. 4-9.



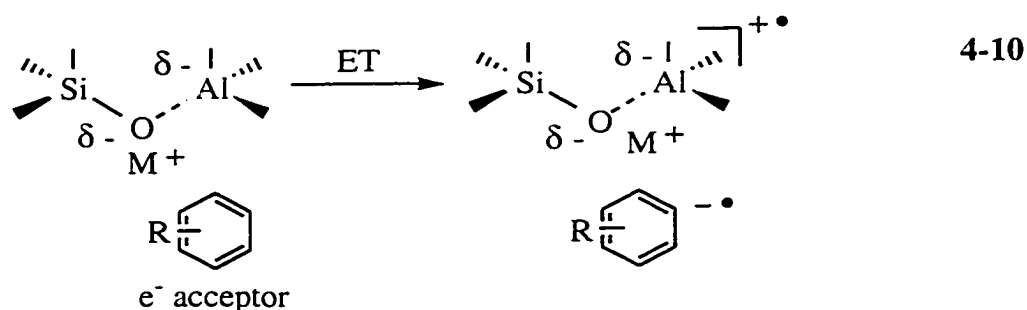
Many ground state organic molecules undergo spontaneous ET upon inclusion within zeolites, yielding long-lived radical cations. In 1964, Stamires and Turkevich were the first to demonstrate this phenomenon upon inclusion of several types of organic molecules, such as 1,1-diphenylethylene, triphenylamine, perylene and aniline within NH_4Y zeolites.⁵⁵ Subsequent to this initial report, the spontaneous generation of many

radical cations in a variety of different zeolites types has been extensively investigated, chiefly using ESR and diffuse reflectance spectroscopy.^{56-58,60-62,64,65,68,176,264-267} In general, these studies have shown that radical cations of organic species form spontaneously upon contact with X and Y zeolites possessing divalent cations, NH_4^+ , or H^+ as a counterbalancing cation. Alkali metal cation X and Y zeolites do not generally exhibit this property. In contrast, both acidic and Na^+ -exchanged ZSM-5 facilitate thermal formation of organic radical cations. After three decades of research, however, no clear mechanistic picture has emerged to explain the ET chemistry associated with radical cation formation, including definitive identification of the electron accepting sites. Aluminum is generally thought to be necessary, and that the intrazeolite impurities such as Fe^{3+} are not responsible for oxidation of the included organic species. Similarly, the role of molecular oxygen in these reactions is not clear. Although oxygen is not believed to be essential, the efficiency of oxidation has been shown to be enhanced in the presence of oxygen. Likewise, the strength of the accepting sites has not been fully characterized. Ramamurthy and coworkers have estimated that NaZSM-5 will oxidize molecules with oxidation potentials, E_{ox} , less than approximately 1.65 V,⁶⁸ while Frei *et al.* proposed that HY and HMor will oxidize species with ionization potentials less than approximately 8 eV.⁵⁹

The intrazeolite generation of radical cations from excited state molecular guests has been the subject of more recent investigations. Since many organic substrates undergo spontaneous thermal ionization in protic and divalent cation zeolites, studies of photoinduced ionization have focused on alkali metal cation zeolites, mostly Na^+ -exchanged X and Y zeolites. Thomas and Iu first demonstrated ionization of pyrene and anthracene upon photoexcitation in zeolites NaX and NaY in 1991.⁶⁹ Since then, photoionization of organic molecules including polycyclic aromatic hydrocarbons naphthalene,^{71,73} anthracene,⁷¹ and pyrene,^{70,89,156,455} stilbene,^{71-73,75} styrenes,⁶⁶ 1,1-diarylethylenes,¹⁵⁷ and biphenyl,^{73,74} have been investigated by many groups. The majority of these studies are based on unequivocal identification of the organic radical cation using transient diffuse reflectance spectroscopy. However, the zeolitic sites responsible for the photochemical oxidation are less well characterized. Capture of the photoejected electron by Na^+ cations has been well-established by spectroscopic identification of the sodium cluster Na_4^{3+} , but it is still not certain if the cations are the primary electron accepting sites within the zeolite. For instance, tricoordinate aluminum sites may play a role, or the electron may simply be ejected into the medium as a consequence of the high polarity of the zeolite interior, followed by subsequent cation trapping. In this regard it is interesting to note that Na_4^{3+} clusters have not been

identified in ground state processes where the zeolite acts as an electron acceptor. Also, although radical cations are observed in other alkali metal cation zeolites, the role of these cations in electron stabilization is unknown. Therefore, although alkali metal cation zeolites are generally considered to be efficient electron acceptors in reactions with photoexcited organic guests, the mechanistic details and loci of the electron within the zeolite matrix are unclear.

In contrast to the variety of examples demonstrating the ability of zeolites to accept electrons from ground state and excited state reactants, considerably less evidence exists concerning the ability of the zeolite matrix to act as an electron donor to reduce incorporated guests, eq. 4-10.



In early studies, powerful electron acceptors such as trinitrobenzene^{92,93} and tetracyanoethylene⁹³ were shown to be reduced upon incorporation into NaY, presumably by spontaneous electron transfer from the zeolite framework. More recent studies have considered electron donation from zeolite frameworks to photoexcited acceptors such as pyrene,⁸⁹ methyl viologen (MV²⁺),¹⁰² cyanosubstituted benzenes, and the xanthylum cation.¹⁰¹ In an investigation of single electron donation from NaY and CsY zeolites to a series of photoexcited cyanosubstituted aromatics and other electron acceptors, Hashimoto *et al.* tentatively suggested that the lower limit for the oxidation potential of NaY is between 1.7 and 2.2 V.¹⁰³ In addition, investigations using Cs⁺-exchanged zeolites impregnated with cesium acetate to enhance base catalysis have provided evidence for electron donation from these frameworks to tetrachloro-1,2-benzoquinone (o-chloranil).⁹⁴ Direct detection of both the o-chloranil radical anion and the hole in the zeolite framework was achieved using EPR spectroscopy. While this study is encouraging, little is currently known concerning the loci and strength of the electron donating sites in unmodified zeolites, as well as the nature and fate of the corresponding hole that is generated in the zeolite framework as a consequence of electron donation.

In addition to PET reactions in which the zeolite acts as an electron acceptor or an electron donor, the zeolite can be utilized as a host for PET reactions between redox pairs coincluded within the zeolite matrix, and/or at the zeolite interface. Studies of such intrazeolite PET have been the subject of considerable research within the past ten to fifteen years.^{41,87,105,158-170,172,187,205,206,456,457} To date, these investigations have revolved around three broad and somewhat interdependent themes: (i) decreasing the rate of BET through zeolite encapsulation; (ii) using zeolitic assemblies to achieve long-lived charge separation in PET reactions aimed at practical applications such as artificial photosynthesis; and (iii) employing the zeolite as a microscopic reactor to modify the dynamics of PET and the resultant products as compared to homogenous media.

Experimental methodology for the control of BET is limited. Zeolites have been examined rather extensively in terms of their ability to modulate rates of BET during photochemical activation of both charge transfer complexes and sensitizer acceptor or sensitizer donor systems. The common and significant phenomenon revealed through this research is that the rate of BET can be decreased dramatically within the zeolite environment as compared to homogeneous solution, and enhanced stabilization of charge separated states is achievable. The influence of zeolite encapsulation on BET is dramatically apparent from the seminal investigations of Kochi and Yoon concerning PET in charge transfer complexes between various cationic organic electrophiles and arene donors in NaY.^{158,159} Using picosecond and nanosecond diffuse reflectance spectroscopy, the resultant radical ion pairs were found to decay *via* BET with a range of lifetimes from tens of picoseconds to hundreds of microseconds. This contrasts sharply with the lifetime of these radical ion pairs in solution, which is less than 30 ps for all species examined. From these experiments, it was estimated that the charge transfer ion pairs are stabilized within NaY by approximately 8 kcal/mol over solution. The proposed explanations for these effects involve stabilization and maintained separation of the redox pair within the zeolite through intermolecular interactions with the zeolite walls, electrostatic stabilization, as well as physical influences such as molecular organization and compartmentalization. Notably the radical ion pairs exhibited a wide range, or distribution, of lifetimes. Thus while some decayed five to six orders of magnitude slower than in solution, others underwent rapid BET with rate constants comparable to solution.

Numerous studies involving diverse molecular systems have demonstrated the generality of decreased rates of BET in zeolitic systems. Three research groups have focused on exploiting the ability of zeolites to control BET within a redox system consisting of tris(2,2'-bipyridine) ruthenium(II) ($\text{Ru}(\text{bpy})_3^{2+}$) and methyl viologen

(MV^{2+}). Extensive investigations by Dutta *et al.*,¹⁶⁰⁻¹⁶⁵ have established that rapid ET transfer quenching of excited state $Ru(bpy)_3^{2+}$ (synthesized within the NaY cavities) by MV^{2+} and other diquat acceptors in neighbouring NaY cavities takes place as a result of molecular contact through the connecting pores. Decay of the resulting radical ion pairs occurs *via* BET in the μs time regime, or *via* hopping of the electron down successive molecules of closely packed MV^{2+} acceptors, leading to charge separated states with lifetimes of hours. Studies by Mallouk and coworkers¹⁶⁶⁻¹⁷⁰ have focused on PET between $Ru(bpy)_3^{2+}$ and MV^{2+} at the zeolite interface. In aqueous suspension, both the free reagents and those joined by intramolecular tethers display rates of BET which are several orders of magnitude slower than observed in solution. In addition, the research groups of both Dutta and Mallouk have investigated molecular triads based on $Ru(bpy)_3^{2+}$ and MV^{2+} which use a third redox reagent to establish a vectorial system of ET which further facilitates enhanced charge separation. Sykora and Kincaid^{171,172} have expanded on these trimolecular systems by preparing more elaborate and organized ensembles in which the zeolite entrapped reagents are strategically placed in adjacent cavities. An underlying theme of research within these groups is the application of zeolites in the construction of photocatalysts and spatially organized systems for artificial photosynthesis and energy storage.

In addition to investigations of long-lived charge separated states and their potential applications, studies of PET within zeolites have also focused on their unique ability to modify and control the photophysics and photochemistry of encapsulated guests. For instance, supramolecular photosensitizers have been assembled by ship-in-a-bottle synthesis of the 2,4,6-triphenylpyrylium cation and trityl cations within the cavities of HY zeolites.^{105,205,206,457} The imprisoned cations act as efficient photosensitizers for ET induced processes such as *cis-trans* isomerization of stilbene. Enhanced efficiency of the ET mediated reaction within the zeolite was attributed to a significant reduction in the rate of BET as compared to solution. A similar increase in the efficiency of PET from stilbene and 4,4'-dimethoxystilbene to organic cationic dyes within alkali metal cation Y zeolites has been reported by Ramamurthy and coworkers and proposed to be due to the localization and confinement of the sensitizer and the oxidant within the zeolite matrix.¹⁸⁷ Additional studies by Johnston *et al.* have demonstrated that arylalkene radical cations generated by PET to cyanosubstituted aromatic and pyridinium ion sensitizers react significantly differently in NaY than in homogeneous solution.⁸⁷ The lifetimes of the radical cations, measured directly using nanosecond diffuse reflectance spectroscopy, are in the μs time regime in NaY. Although the corresponding radical anions were not detected spectroscopically, the radical cation decay was assumed to be

via relatively slow BET. Cyclobutane dimers of the arylalkene radical cations, identified as the major products, also exhibited an isomeric distribution substantially different from that obtained in solution. The observed preferential formation of the *cis*-cyclobutane was proposed to be a consequence of the closer match of the spherical zeolite cavity to the shape of the *cis* isomer than the *trans* isomer.

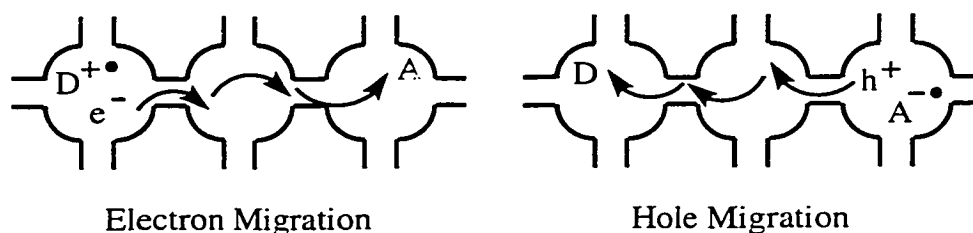
Experimental studies such as those described have generated considerable insight into the ability of zeolitic systems to modify PET reactions in useful ways. However, the mechanisms of ET reactions within zeolites have not yet been extensively explored. In particular, the fate of electrons and, especially, the holes generated by ET reactions involving the zeolite framework have not been determined. Likewise, the intrazeolite location and arrangement of co-included reagents involved in bimolecular ET, as well as the possible roles of the zeolite in mediating these redox reactions, has not been addressed. Furthermore, the possibility of long distance ET chemistry among molecules spatially separated within the zeolite matrix has received surprisingly limited attention. Thomas and coworkers reported ET quenching of singlet pyrene by Cu^{2+} and Tl^+ within zeolite X, and found the effective radii for ET quenching to be 13.6 Å and 11.2 Å for Cu^{2+} and Tl^+ , respectively.³⁵⁻³⁶ However, additional investigations concerning the intriguing possibility of long distance electron and hole migration and the mechanisms for these reactions do not currently exist.

4.1.3 Scope of Chapter Four

This chapter examines the generation and migration of electrons and holes within the channels and cavities of dehydrated NaY, Scheme 4-6. The electrons are generated by a photoinduced reaction between the zeolite and an encapsulated guest, wherein the zeolite acts as an electron acceptor. Likewise, the holes are generated by a photoinduced reaction between the zeolite and an encapsulated guest wherein the zeolite acts as an electron donor. The mobility of the resultant electrons and holes is probed by including a secondary electron acceptor or electron donor within the framework that scavenges the electron or hole thereby generating a spectroscopically visible intermediate. Each of these processes occurs within the nanosecond laser pulse. Therefore, no information concerning the rate constants for ET reactions or the speed of intrazeolite migration of electrons and hole is presented. However, the yields of electron and hole migrations are determined from the spectroscopic measurements and interpreted using two independent models in order to estimate the distance of electron and hole travel within the zeolite matrix. The results presented herein are based on experimental studies that have been

applied successfully to two donor-acceptor systems. In addition to presenting preliminary information concerning the distance dependence of intrazeolite charge migration, another goal of this work was to explore the feasibility of such experiments as well as the reliability and physical manifestation of necessary models in order to rationally design and implement future studies in this area.

Scheme 4-6



4.2 Results

The experimental results described in the following sections concern 308 nm laser photolysis (10 ns, < 100 mJ) of 1,2,4,5-tetrachlorobenzoquinone, chloranil (Chl), or *trans*-anethole (An) in NaY, either alone, or in the presence of coadsorbed 4,4'-dimethoxybicumene (DMB), or 1,4-dicyanobenzene (DCB). The preparation of samples containing coadsorbed donors and acceptors involved initially incorporating the photosensitizer, either Chl or An, into a batch of NaY (typically 1 – 2 g) using either dichloromethane or hexane as a carrier solvent (see experimental section). After removal of the carrier solvent by vacuum pumping (10^{-3} Torr) for at least 12 hours, the second reagent was added to a known mass of the sensitizer-zeolite composite using hexane. The hexane was then removed by further vacuum pumping, the composite was transferred to a laser cell and re-evacuated (10^{-4} Torr) for at least 8 hours prior to conducting experiments. As previously described, manipulation of the dried samples was carried out in an atmosphere of nitrogen, and every precaution was taken to avoid uptake of water during sample preparation. The concentration of each reagent within the NaY sample was determined by UV analysis of the decants and is reported as the loading level in molecules per cavity, or the average fractional occupancy, $\langle S \rangle$ (*vide supra*).

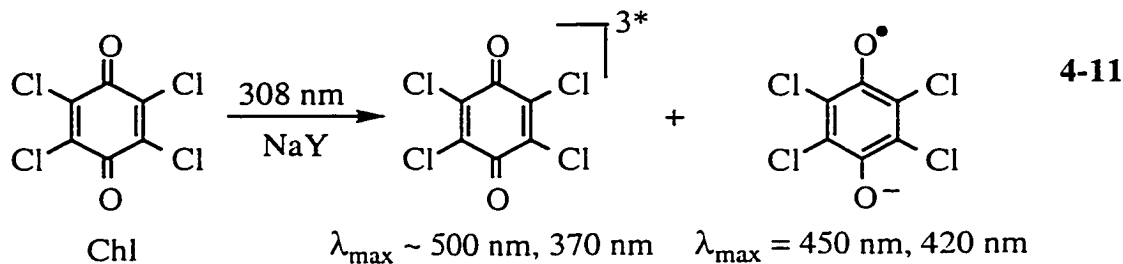
4.2.1 Nanosecond Laser Flash Photolysis of Chloranil in NaY

In order to investigate intrazeolite ET reactions in which the zeolite acts as an electron donor, it is necessary to employ a powerful electron accepting photosensitizer which generates a readily identifiable reduction product. This is particularly important since the second product of the ET reaction of interest, the hole in the zeolite framework, will not be observable with UV-vis spectroscopy. Based on such criteria, chloranil has emerged as a very appropriate candidate. Photoexcited Chl is a strong photo-oxidant. The reduction potential of both singlet ($E_{\text{red}}^0 = 2.77 \text{ V vs SCE}$)²⁹⁵ and triplet ($E_{\text{red}}^0 = 2.15 \text{ V vs SCE}$)²⁹⁵ Chl should be sufficient to ensure efficient abstraction of electrons from the zeolite framework. In addition, the photo- and ET-chemistry of Chl has been studied extensively in solution. The transient species generated upon photolysis of Chl, specifically the Chl triplet²⁹⁷⁻²⁹⁹ and Chl radical anion²⁹⁶⁻²⁹⁸ (and more recently the short-lived Chl singlet²⁹⁸) are very well characterized and quite distinctive spectroscopically. Of further convenience is the fact that the Chl radical anion, unlike many radical anions of less potent electron acceptors, is unreactive towards oxygen. This has proved useful from an experimental standpoint and has provided additional information concerning the ET dynamics between NaY and excited-state Chl.

The transient diffuse reflectance spectrum observed immediately following 308 nm laser excitation of chloranil included in evacuated NaY is shown in Figure 4-1 (The figures described in sections 4.2.1 to 4.2.4 are found on pages 268 to 287). Intense absorption extending between 320 nm and 550 nm dominates this transient spectrum. Absorption by at least two transient species is indicated clearly by the distinctly different decays observable within the spectrum. For instance, at wavelengths greater than about 480 nm, and less than about 400 nm, the transient decay is significantly more rapid than the transient decay in the central region of the spectrum. In particular, a longer lived transient with absorption maxima at 420 nm and 450 nm can be detected. Absorption due to this long-lived transient is even more evident in the diffuse reflectance spectrum obtained at longer delay times following the laser pulse, Figure 4-2. In these time regimes, the broad absorption which dominates both the short (< 400 nm) and long (> 480 nm) wavelength regions decays almost entirely, leaving the transient absorption bands at 420 nm and 450 nm clearly resolved. The time-resolved decay traces, Figure 4-3, also confirm that the decay at 500 nm is relatively rapid, resulting in complete disappearance of the transient in about 100 μs , while decay at 420 nm is notably slower and a significant amount of transient remains 100 μs after the laser pulse. In fact, the transient absorbing at 420 nm and 450 nm is very long-lived, as can be seen in the

transient diffuse reflectance spectrum recorded several hundred μs following laser photolysis, Figure 4-2, inset. Overall, these observations establish that two different transients with very distinct absorption spectra and decay kinetics are generated in less than 10 ns upon 308 nm laser photolysis of Chl in evacuated NaY.

Thorough studies of the photo- and ET-chemistry of Chl in solution make it possible to unambiguously identify the two transients observed upon laser photolysis of Chl in evacuated NaY as the Chl triplet and the Chl radical anion, eq 4-11.



First, the broad absorption between 350 and 550 nm, with a peak near 500 nm, is very characteristic of the Chl triplet,²⁹⁷⁻²⁹⁹ while the distinctive, sharp absorption maxima at 420 nm and 450 nm are identical to the known absorption spectrum of the Chl radical anion.²⁹⁸ Second, both the Chl triplet and the Chl radical anion are the expected transients based on the characteristically rapid and efficient intersystem crossing (ISC)²⁹⁵ and reduction of excited Chl in solution.^{297,298} Third, the relative lifetimes of the transients at 500 nm and 420 nm (or 450 nm) are consistent with the assignments of the Chl triplet and Chl radical anion, respectively. The complete decay of the Chl triplet within about 80 to 100 μs is in agreement with the reactivity of triplet states of other organic molecules such as xanthone¹⁴⁵ and 4-methoxy- β -propiophenone,⁵² previously observed in NaY. Similarly, the long lifetime of the Chl radical anion, and the persistence of considerable radical anion absorption at times longer than 1 ms are consistent with the reactivity of radical anions of pyrene⁸⁹ and 2,3,4,6-tetracyanobenzene¹⁰³ in NaY.

Quantitatively, the decay kinetics of both the Chl triplet and the Chl radical anion in NaY are somewhat complex, and are not first order over the entire decay range. Most of the decay of the Chl triplet fits reasonably well to a single first-order expression. However, an initial decay immediately following the pulse suggests the existence of a second, faster decay component. Combining this initial decay with longer times where the decay is complete, generates a decay trace that is nicely fit to a double first-order exponential expression. This fit yields a large rate constant, $8.2 \times 10^5 \text{ s}^{-1}$, which

comprises about 20 % of the total decay, and a slower rate constant, $2.71 \times 10^4 \text{ s}^{-1}$, which accounts for the majority, 80 %, of the total triplet decay in NaY. The decay kinetics of the Chl radical anion are even more disjointed over the observable region. For instance, although a significant fraction of the signal intensity due to the radical anion (monitored at either 420 nm or 450 nm) decays in the ten to hundred μs range, the remaining radical anion signal exhibits little decay over times as long as 1 ms, the longest time observable with the current laser system (see Figure 4-7 inset). This certainly indicates that the decay of the Chl radical anion in NaY is characterized by at least two very distinct rate constants, and more likely occurs *via* a distribution of rate constants about these central values. Although the slow decay is too long to measure, the fast decay component can be fit to a single first-order expression. This yields a rate constant of $(2.1 \pm 0.1) \times 10^5 \text{ s}^{-1}$ as an average value to describe these faster decay processes which comprise about 30 % of the total radical anion decay in NaY.

Further support for the identification of the Chl triplet and Chl radical anion is obtained from experiments conducted in oxygen-saturated NaY. In addition to being spectrally distinct from the Chl radical anion, the Chl triplet is very reactive towards oxygen, reacting at the diffusion limit in solution. The triplet generated by laser photolysis of Chl in NaY is completely quenched by coadsorbed oxygen in less than 500 ns following the laser pulse, Figure 4-4. Rather conveniently, the Chl radical anion is resistant to reactions with oxygen. Thus the transient diffuse reflectance spectrum observed following laser photolysis of Chl in oxygen-saturated NaY is characterized by the distinctive maxima of the Chl radical anion at 420 nm and 450 nm, Figure 4-5. The dramatic influence of oxygen can be seen in Figure 4-6 which compares the transient diffuse reflectance spectra obtained 1 μs after laser irradiation of Chl in NaY under vacuum and oxygen conditions. The absence of any absorption above 450 nm indicates that the triplet is completely quenched 1 μs after laser photolysis in oxygen-saturated NaY, leaving the Chl radical anion as the only observable transient.

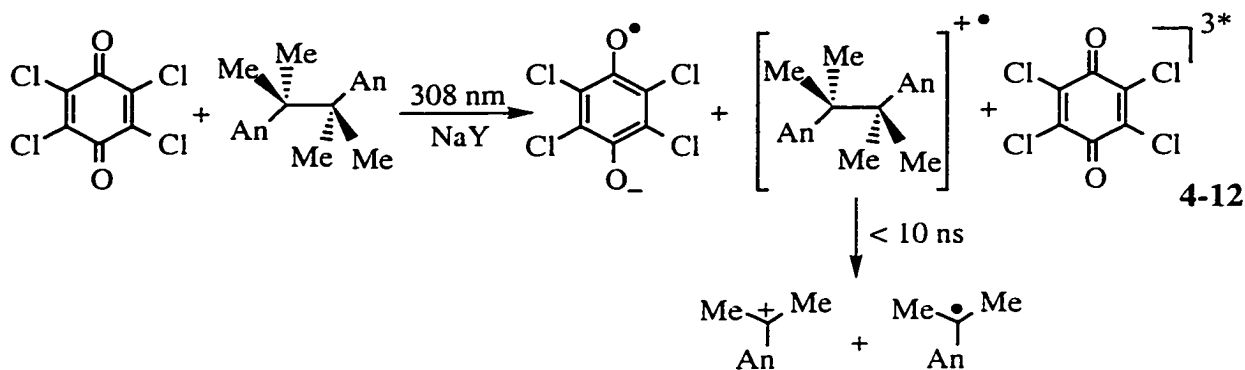
In addition to completely quenching the Chl triplet, oxygen also influences the yield of the Chl radical anion. This is evident from a comparison of the transient diffuse reflectance spectra observed in evacuated and oxygen-saturated NaY after the Chl triplet has completely decayed, Figure 4-7. Although the Chl radical anion does not react with oxygen, the yield of radical anion is significantly reduced by the inclusion of oxygen within the sample. The exact reduction in radical anion yield in oxygen-saturated NaY varies slightly as a function of the Chl loading level, with the absorption of the radical anion being between 40 % and 60 % lower than that under vacuum conditions. The decay traces monitored at 420 nm under vacuum and oxygen conditions also clearly

demonstrate the difference in radical anion yield, Figure 4-7 inset. Furthermore, these decay traces verify that the reduced yield of Chl radical anion is not due to more rapid decay of the radical anion under oxygen. Thus, the decreased yield of Chl radical anion observed in oxygen-saturated NaY, as compared to evacuated NaY, indicates that less radical anion is generated upon photolysis of NaY-encapsulated Chl when oxygen is present.

4.2.2 Photoexcitation of Chloranil in NaY containing a Secondary Electron Donor

The results described in the preceding section indicate that photoexcitation of Chl in NaY yields the Chl radical anion, under conditions where Chl is the only molecular guest within the NaY matrix. Therefore, reduction of Chl is not accompanied by oxidation of an added donor molecule, as would be observed for an ET reaction between a donor and an acceptor. Instead the surrounding media, in this case the zeolite, plays the role of the electron donor. It should, however, also be possible to reduce Chl to the radical anion in the presence of a neutral donor if Chl is photoexcited in NaY containing a co-included secondary electron donor. In fact, such ET has already been demonstrated for Chl and the electron donor, 4,4'-dimethoxybicumeme (DMB), within the cavities of NaY (*vide supra*). Perhaps fortuitously, DMB has also proved to be a very useful secondary electron donor in studies of intrazeolite ET reactions initiated by photoexciting the electron acceptor, Chl, in the presence of coincluded donors. The results of such investigations are the subject of the following section.

Figure 4-8 shows the transient diffuse reflectance spectrum observed upon 308 nm laser photolysis of Chl ($\langle S \rangle = 0.04$) in evacuated NaY containing coadsorbed DMB ($\langle S \rangle = 0.1$). As discussed in Chapter 3, this transient spectrum is a composite of the Chl triplet with broad absorption in the 500 nm region,²⁹⁷⁻²⁹⁹ the Chl radical anion with distinct sharp maxima at 420 nm and 450 nm,²⁹⁶⁻²⁹⁸ and the 4-methoxycumyl cation²³⁴ with an intense symmetrical maximum at 360 nm. The identification of the 4-methoxycumyl cation is confirmed by the close match of the 360 nm absorption band, Figure 4-9, and the decay kinetics monitored at 360 nm, Figure 4-9 inset, to the 4-methoxycumyl cation observed in NaY following direct excitation of DMB. As previously established, the 4-methoxycumyl cation ultimately arises from rapid fragmentation of the DMB radical cation, the initial transient generated by Chl-photosensitized ET, eq. 4-12. Control experiments in which NaY-encapsulated DMB is irradiated with 308 nm laser light yield no transients, confirming that the 4-methoxycumyl cation does not arise from direct 308 nm laser excitation of DMB.



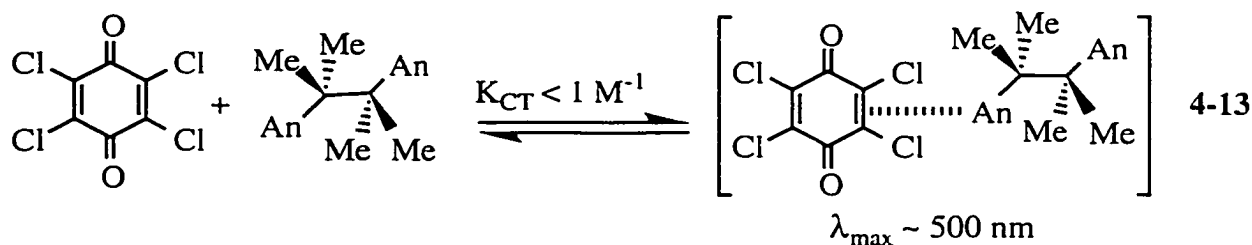
Selective excitation of Chl ($\langle S \rangle = 0.04$) in oxygen-saturated NaY containing coadsorbed DMB ($\langle S \rangle = 0.1$) likewise generates the Chl radical anion and the 4-methoxycumyl cation within the laser pulse, Figure 4-10. The Chl triplet is no longer observed due to rapid reaction with oxygen as observed upon excitation in oxygen-saturated NaY in the absence of DMB. Otherwise the transient diffuse reflectance spectrum and decay kinetics appear identical to those observed in evacuated NaY. In particular, no reduction in signal intensity due to the 4-methoxycumyl cation is observed upon the inclusion of oxygen. Similarly, the inclusion of an electron trap, nitrous oxide (*vide infra*), has no influence on the observed transient spectrum or decay kinetics. Unlike the results under oxygen where the Chl triplet is quenched, absorption due to the Chl radical anion, the 4-methoxycumyl cation, and the Chl triplet in nitrous oxide saturated NaY is identical to that observed under vacuum conditions, Figure 4-11.

The distribution of guest molecules within the zeolite matrix is highly significant to studies of intrazeolite reactivity. For the inclusion of a single adsorbate which is smaller than the zeolite pore dimensions and which lacks any notable propensity for molecular aggregation in solution, it can be initially assumed that the adsorbate will incorporate randomly within the framework, governed by maximizing favourable interactions with the zeolite matrix (see Chapter 1). This is particularly true at relatively low loadings (i.e. less than 1 molecule in every few cavities). Thus, although the intrazeolite environment is heterogeneous on a microscopic scale, the distribution of guest molecules through the entire zeolite sample can be homogeneous on a large, or global scale. However, if the molecular sizes are very similar to the zeolite dimensions and/or intermolecular interactions are favourable, then the included molecules may not disperse evenly throughout the zeolite matrix, and instead may form aggregates. In such cases the occupancy of zeolite cavities is skewed, with some cavities being more heavily occupied than others. This phenomenon has been demonstrated for several types of molecules, including polycyclic aromatics such as pyrene,^{126,127} anthracene,¹²⁸ and

naphthalene.¹²⁹ Incorporation of these molecules into alkali metal cation zeolites such as NaY results initially in dimer aggregates due to the slow diffusion of these species through the matrix, which is likely a consequence of the molecular size and rigidity as well as the strong cation π -type interaction between both monomeric and dimeric aromatic units and the alkali metal cations. Over time, varying from days to months depending on the sample and the conditions,¹²⁸ these aggregates are driven by the more favourable zeolite-guest interactions to disperse and eventually attain a more random distribution.

Based on such considerations, it is important to determine whether or not individual guest molecules are distributed statistically throughout the matrix, or if factors such as molecular size or intermolecular interactions, either zeolite-guest or guest-guest interactions, are defining the distribution in a non-random way. This will be particularly significant when studying bimolecular reactions between two guest molecules within the zeolite matrix where the relative arrangement of molecules will determine reaction dynamics and knowledge of this distribution will be pivotal to the interpretation of experimental results. In addition, when two different adsorbates are being coincluded within the zeolite matrix, intermolecular interactions may become more significant than for a single species.

An example of intermolecular interactions which may influence the distribution of molecules within zeolites are the ground-state charge-transfer complexes that may form between donor and acceptor molecules used in ET studies. These can be envisioned as an intermolecular complexation held together by partial transfer of charge due to the favorable redox potentials of the molecules involved. The resultant complex is usually characterized by a unique absorption spectrum which is considerably red-shifted relative to that of the individual components. Excitation into the charge-transfer band results in full ET from the donor to the acceptor, yielding the radical ion pair. Charge-transfer complexes are known to form between numerous electron donor-acceptor pairs in solution, and are often used to initiate ET chemistry. In fact, Chl and DMB are known to form a weak, 1:1 charge-transfer complex in the ground state, eq. 4-13.



The equilibrium constant for this charge-transfer complex in dichloromethane has been reported to be $K_{CT} = 0.3 \text{ M}^{-1}$ and $K_{CT} = 0.78 \text{ M}^{-1}$ by Sankararaman⁴⁵⁸ and Maslak,²⁸³ respectively. Charge-transfer complexation has been observed in zeolites, most notably between cation organic molecules and aromatic moieties,^{39,40,134} and recently for 1,2,4,5-tetracyanobenzene and arenes.⁴⁶ In such cases the complexation is generally accompanied by an observable coloration of the zeolite sample.

Two types of experiments were conducted in order to investigate the possibility that Chl and DMB aggregate within the NaY cavities and therefore do not attain a statistical distribution. The first experiment examines whether the fresh, as-prepared zeolite composites exhibit characteristics of intermolecular aggregation. As has been shown for other adsorbates, the time required to establish equilibrium distribution in a sample initially dominated by intermolecular aggregates may be several weeks or more. Thus, the influence of sample age on Chl photosensitized ET generation of the 4-methoxycumyl cation in NaY was considered. As shown in Figure 4-12, 308 nm laser photolysis of a 25 day old NaY sample containing coadsorbed Chl ($\langle S \rangle = 0.04$) and DMB ($\langle S \rangle = 0.07$) is essentially identical to that observed for a fresh sample. Absorption due to the radical anion at 420 nm and 450 nm, and the 4-methoxycumyl cation at 360 nm are clearly visible immediately after photolysis in oxygen-saturated NaY. Likewise the intensity due to carbocation absorption and the decay rate constant of the carbocation are unchanged by sample aging, Figure 4-12 inset.

The second experiment investigates the possibility that Chl and DMB form charge-transfer complexes in NaY given the method of sample preparation and adsorbate concentrations used in this study. Notably, the DMB is included after incorporation of Chl in NaY and vacuum drying the composite for at least 12 hours. In addition, no color change is observed upon addition of the DMB to the pale yellow Chl/NaY composites and no new bands are observed in the diffuse reflectance spectrum. However, the concentration of charge-transfer complexes may be too small to yield an observable color change, but is responsible for the observed ET chemistry. To test this possibility, the zeolite composites were irradiated with 532 nm light where the charge-transfer complex has a large absorption, and absorption by both Chl and DMB is negligible. As shown in Figure 4-13, irradiation into the charge-transfer band yields no observable transients. This contrasts sharply with the intense signals due to the 4-methoxycumyl cation and the Chl radical anion observed upon selective laser irradiation of Chl with 308 nm laser light.

Generation of the 4-methoxycumyl cation following selective irradiation of Chl in NaY containing coadsorbed DMB is a general phenomenon observed at a variety of different concentrations of both Chl and DMB. In particular, the distinctive absorption of

the 4-methoxycumyl cation is clearly visible even at remarkably low loadings of both reagents. For instance, Figure 4-14 presents the transient diffuse reflectance spectrum observed following 308 nm laser irradiation of Chl ($\langle S \rangle = 0.02$) and DMB ($\langle S \rangle = 0.01$) in oxygen-saturated NaY. These occupancies correspond to one molecule of Chl in every 50 NaY cavities and one molecule of DMB in every 100 NaY cavities. Even at these low concentrations, the characteristic maxima of the Chl radical anion are clearly present at 420 nm and 450 nm, as is absorption due to the 4-methoxycumyl cation at 360 nm. Although the relative intensity of the carbocation signal is somewhat smaller than observed in the higher loading samples, the 4-methoxycumyl cation is clearly present. This is particularly evident when the transient spectrum is compared to that obtained under oxygen conditions in the absence of DMB, Figure 4-15.

The results presented thus far indicate that photoinduced reduction of Chl accompanied by concomitant oxidation of coincluded DMB takes place readily within the cavities of NaY. This chemistry occurs even at surprisingly low adsorbate concentration, and in the absence of any detectable intermolecular aggregation between the donor and the acceptor. In addition, the redox products are consistently generated within the 10 ns laser pulse, with no growth due to either the Chl radical anion or the 4-methoxycumyl cation being detected at any time following the laser pulse, even at the lowest concentrations investigated ($\langle S \rangle = 0.01$ for both Chl and DMB; at lower concentrations the 4-methoxycumyl cation could not be definitely discerned in the transient spectra due to low signal intensity). This indicates that the observed redox reactions are rapid at all concentrations, being in each case instantaneous on the time-scale of the experiment. Although this inhibits the evaluation of any rate constants, the yield of photogenerated transients is expected to be influenced by the concentration of redox reagents within the zeolite matrix. Indeed, the results presented thus far suggest that the yield of 4-methoxycumyl cation is dependent on the loading level of both Chl and DMB.

In order to assess the relationship between adsorbate concentration and yield of redox products, laser photolysis experiments were conducted on samples containing a constant loading of Chl with varied concentrations of DMB. Maintaining a constant concentration of Chl ensures that the amount of light absorbed by each sample remains invariant. Such experiments involved a Chl loading, $\langle S \rangle$, of either 0.08, 0.04, or 0.02, for which the DMB concentrations were varied from $\langle S \rangle \sim 0.1 - 0.002$. Figure 4-16 presents the results of 308 nm laser photolysis of Chl ($\langle S \rangle = 0.08$) in oxygen saturated NaY containing increasing concentrations of DMB. The influence of DMB concentration on the yield of the 4-methoxycumyl cation is strikingly evident in this figure. As the concentration of DMB is increased from zero (a) to one molecule in every 10 cavities (f),

both the absolute intensity of the signal due to the 4-methoxycumyl cation and the intensity of this signal relative to the Chl radical anion increase markedly. This result is perhaps intuitive, given that the 4-methoxycumyl cation is derived directly from the DMB precursor. However, in this case the DMB is not photoexcited, so these results provide a convincing example of increased carbocation formation as a function of DMB concentration in the absence of direct photoionization. As such, the results demonstrate a progressive increase in the yield of photosensitized ET products as a function of ground-state donor concentration.

In order to quantify the yield of carbocation absorbing at 360 nm, the absorption at this wavelength must be corrected for absorption by the Chl radical anion, and under vacuum conditions, by the chloranil triplet. This correction can be accomplished using the extinction coefficients of each transient at 500 nm (Chl triplet only), 450 nm (Chl triplet and Chl radical anion), and 360 nm (Chl triplet, Chl radical anion and 4-methoxycumyl cation). The relevant extinction coefficients are provided in Table 4-1. When the corrected signal due to the 4-methoxycumyl cation (yield) is plotted against DMB loading, Figure 4-17, a clear trend emerges whereby the absolute yield of the carbocation increases with increasing concentration of the DMB precursor. However, the variation in carbocation yield with DMB concentration is not linear.

Table 4-1. Extinction coefficients of the chloranil triplet, chloranil radical anion and 4-methoxycumyl cation.

	$\epsilon / \text{L mol}^{-1} \text{cm}^{-1}$		
	ϵ_{500}	ϵ_{450}	ϵ_{360}
Chl Triplet	7200 ^a	3600 ^b	6840 ^b
Chl Radical Anion	~0	9700 ^c	3120 ^b
4-Methoxycumyl Cation	~0	~0	22000 ^d

^aRef. 459; ^bRef. 460; ^cRef. 296; ^dRef. 461.

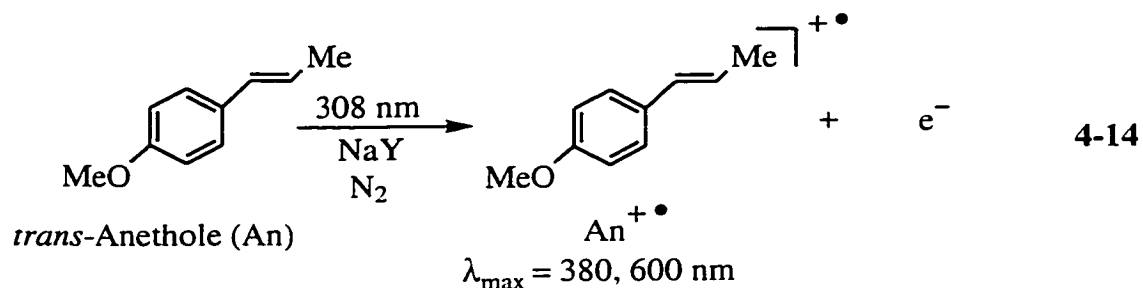
Notably, the yield of Chl triplet and Chl radical anion are also influenced by the concentration of DMB in NaY. As shown in Figure 4-18, the yield of triplet Chl observed immediately following laser photolysis in evacuated NaY decreases as the concentration of DMB increases. The yield of Chl radical anion observed at 450 nm under vacuum conditions (corrected for triplet absorption) also decreases with increasing DMB concentration. This is perhaps anti-intuitive, especially considering that the yield of the other redox product, the 4-methoxycumyl cation increases with DMB

concentration. Interestingly, the variation in yield of the Chl radical anion is different under vacuum and oxygen conditions.

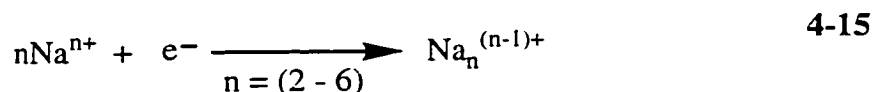
4.2.3 Photoexcitation of *t*-Anethole in NaY containing a Secondary Electron Acceptor

The ET reactions described above were initiated by photoexcitation of the electron acceptor, Chl. In the absence of a secondary electron donor, the acceptor is still observed to be reduced, presumably by accepting an electron from the surrounding zeolite matrix. In the presence of a secondary electron donor, Chl radical anion formation is accompanied by oxidation of the ground-state donor. The reverse process, whereby an electron donor can be photoexcited within the zeolite, resulting in radical cation formation, in the absence of a secondary electron acceptor, and concomitant radical anion formation in the presence of a secondary electron acceptor, is also of interest. The first step, photogeneration of a donor radical cation is a fairly well known reaction of many electron-rich organic molecules within alkali metal cation zeolites (*vide supra*). However, the corresponding reduction of a secondary ground-state electron acceptor coincided within the zeolite matrix has received considerably less attention and is of significant interest, particularly in relation to the results described in the preceding section. Therefore, the following results concern experiments employing *trans*-anethole (An) as a photoexcited electron donor, and 1,4-dicyanobenzene (DCB) as the secondary electron acceptor in zeolite NaY.

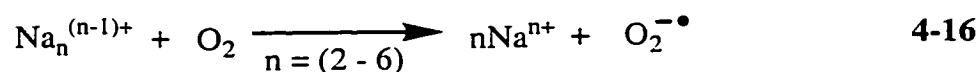
The transient diffuse reflectance spectrum obtained upon 308 nm laser excitation of An in evacuated NaY ($\langle S \rangle = 0.1$) is characterized by intense maxima at 380 nm and 600 nm, Figure 4-19. These absorption bands are assigned confidently to the An radical cation generated by photoionization of An within the cavities of NaY, eq. 4-14. Specifically, the transient spectrum is virtually identical to the absorption spectrum of the An radical cation in solution,^{304,462} and to that previously generated by 266 nm laser induced photoionization of An in NaY.⁶⁶ In addition, the decay kinetics monitored at 380 nm and 600 nm are virtually identical, Figure 4-20, suggesting that a single transient species is responsible for both absorption bands. Furthermore, the transient species absorbing at 380 and 600 nm is unreactive towards oxygen on these time scales, consistent with the well known reactivity of the An radical cation.



In contrast to the situations in the previous section, where the holes in the framework could not be observed, electrons generated by photoionization of suitable substrates within zeolite matrices are optically visible transient intermediates. Thus, photoionization of guest molecules in zeolites such as NaY is often accompanied by the formation of sodium complexes derived from the capture of an electron by intrazeolite sodium cations, eq. 4-15.

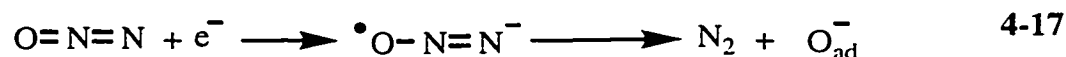


These sodium ion clusters are transient species which have been identified and characterized by a combination of ESR measurements and UV-Vis spectroscopic studies conducted at low temperatures and/or at fast time scales.⁸⁰ Electrons trapped by cation clusters in zeolites typically have absorption in the visible region, 400 nm to 800 nm, with the absorption bands being characteristically broad and unstructured. The specific absorption maximum of a sodium ion cluster depends both on the nature of the zeolite environment and the cluster size. Within a single zeolite type, such as NaY, the absorption maxima of sodium clusters increases with cluster size. The most commonly detected cluster in NaY, Na_4^{3+} , has an absorption maximum near 500 nm. The smaller cation clusters, Na_3^{2+} and Na_2^+ , have absorption maxima red-shifted to greater than 650 nm and 750 nm, respectively. In addition, these sodium ion clusters are reactive species, typically decaying in the μs time regime in evacuated NaY *via* a mechanism which likely involves electron return to the zeolite framework and ultimately the ionized donor molecule. Not surprisingly, the reactivity of the clusters increases notably with decreasing cluster size, and all clusters are highly reactive towards oxygen,⁸⁰ eq. 4-16.



The formation of sodium-cluster trapped electrons upon photoexcitation of An in NaY is clearly evident from both the decay kinetics and the transient diffuse reflectance spectrum. The decay traces monitored at 380 nm and 600 nm are not the same at short delay times following the laser pulse, Figure 4-21. Although the decay kinetics at these wavelengths closely match over longer times, Figure 4-20, the faster decay at 600 nm in the shorter time regime clearly indicates an additional species which is more reactive than the An radical cation, is also absorbing at the longer wavelengths. The long wavelength absorption and relatively short lifetime of this transient(s) is suggestive of a sodium-cluster trapped electron. Furthermore, the faster decay at 600 nm can also be detected in the transient spectrum generated in evacuated NaY, Figure 4-19. Broad absorption in the 400 nm to 700 nm region is observed which decays somewhat faster than the underlying radical cation at 600 nm and 380 nm. Again the spectral appearance and decay kinetics are typical of trapped electron species. Definitive evidence for additional, shorter-lived transient species is obtained from the decay kinetics at longer wavelengths where the An radical cation makes no contribution. For instance, a relatively intense short-lived transient which decays completely in approximately 2 μs ($k_{\text{decay}} \sim 6 \times 10^6 \text{ s}^{-1}$) is distinctly observed at 700 nm where the An radical cation has little absorption, Figure 4-22. The long wavelength and short lifetime of this absorption strongly suggest that it is due to a sodium-cluster trapped electron, most likely a smaller cluster such as Na_3^{2+} . Overall, the observation of broad absorption between 400 and 700 nm, and short-lived absorption at 700 nm, suggests that trapped electrons are generated upon 308 nm laser excitation of An in NaY, consistent with photoionization of An and the detection of the An radical cation.

The assignment of the transient(s) absorbing between 400 nm and 700 nm to sodium-cluster trapped electrons is supported by results obtained upon the inclusion of electron traps. For instance, if these absorption bands are associated with electrons trapped by sodium cations, it should be possible to extinguish these bands by incorporating an alternative reagent within the zeolite that will trap the electrons. Nitrous oxide is a well-known electron scavenger, and is expected to react with photoionized electrons within NaY, thereby preventing trapping by sodium cations. Electron trapping by nitrous oxide in the zeolite yields the nitrous oxide radical anion which cleaves to release nitrogen and an oxygen ion, O_{ad}^- , which is adsorbed within the framework,⁴⁶³ eq. 4-17.

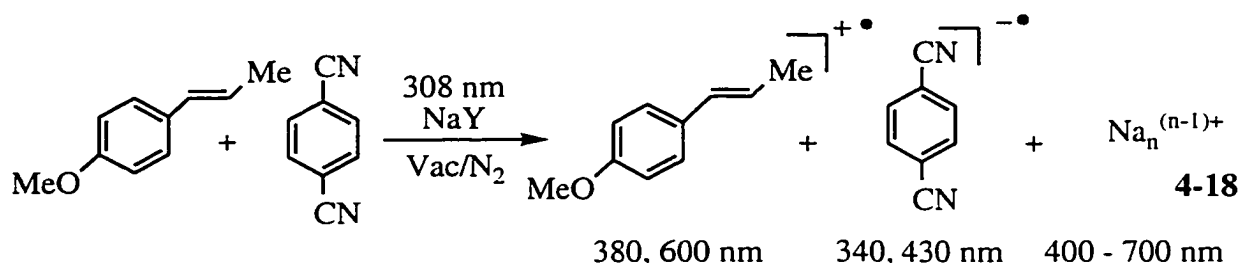


As shown in Figure 4-22, inclusion of nitrous oxide into the cavities of NaY completely eliminates absorption at 700 nm attributed to sodium-cluster trapped electrons. In fact, a comparison of the transient diffuse reflectance spectra observed under vacuum and nitrous oxide conditions indicates complete quenching of the broad absorption in the 400 nm to 700 nm region by nitrous oxide, Figure 4-23. Thus, the anticipated inhibition of cation trapping of electrons is observed upon the inclusion of an alternative electron trap in NaY. Furthermore, in nitrous oxide-saturated NaY, where the sodium complexes are not contributing to the long wavelength decay of the An radical cation, the decay kinetics monitored at 380 nm and 600 nm are virtually identical over all time regimes. The decay kinetics at each wavelength are therefore attributed to a single transient species, the An radical cation. The decay monitored at either 380 nm or 600 nm is best described as a composite of more than one first order processes. These decay traces fit well to a double first-order rate expression with a fast component of $3.3 \times 10^4 \text{ s}^{-1}$ that is very similar to previously reported values.^{66,87} Analogous results are obtained in oxygen-saturated NaY. Quenching of absorption due to the sodium-cluster trapped electrons by oxygen may be due to trapping of the photoionized electron by oxygen, or subsequent ET from the cluster to oxygen as described by eq. 4-15.

The results observed upon photoexcitation of An in NaY indicate that ionization takes place to yield the An radical cation and a corresponding electron that becomes trapped by the zeolite acting as an electron acceptor. These electrons can then be scavenged by small, mobile electron traps such as oxygen or nitrous oxide, although the corresponding trapping products are not observed. The redox chemistry initiated by photoexcitation of An in NaY containing a coadsorbed secondary electron acceptor is also of interest. The popular electron acceptor DCB is a viable candidate for such studies as it has little absorption at 308 nm, the wavelength used to photoionize the donor. Furthermore, the DCB radical anion has an absorption maximum at 340 nm which should be sufficiently distinct from the An radical cation to allow simultaneous observation of each transient.

A representative example of the transient diffuse reflectance spectrum generated by 308 nm laser irradiation of An ($\langle S \rangle = 0.1$) in evacuated NaY containing coadsorbed DCB ($\langle S \rangle = 0.2$) is shown in Figure 4-24. In addition to the An radical cation with characteristic absorption bands at 380 nm and 600 nm, there is an intense, sharp maximum at 340 nm and a weaker peak at 430 nm. The increase in intensity of absorption at 340 nm in samples containing DCB is clearly evident from the decay traces at this wavelength in the presence and absence of DCB, Figure 4-25. The transient responsible for these absorption bands is readily identified as the DCB radical anion,

based on the close resemblance of these absorption bands to the absorption spectrum of the DCB radical anion.^{419,462} In addition, the absorption bands at 340 nm and 430 nm are absent in oxygen-saturated NaY, consistent with the expected quenching of the DCB radical anion with oxygen. These observations establish that 308 nm excitation of An in NaY containing DCB as a secondary electron acceptor results in the formation of the An radical cation and the DCB radical anion within the 10 ns laser pulse, eq. 4-18.



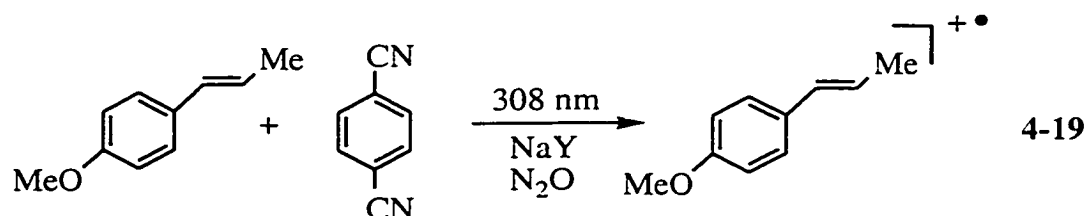
In addition, sodium-cluster trapped electrons are also observed following excitation of An encapsulated NaY in the presence of DCB. Notably, however, the yield of these complexes decreases dramatically with increasing DCB concentration (*vide infra*).

The laser experiments employ 308 nm excitation where the DCB chromophore has no detectable absorption in solution. Control experiments in which the DCB is irradiated in NaY in the absence of An do yield weak transients resembling the DCB radical anion if the concentration of the DCB is sufficiently high (> 1 molecule in 10 cavities). This is most likely due to relatively high power of the excimer laser (< 100 mJ/pulse). However, since the extinction coefficients of An at 308 nm is approximately 3000 times higher than DCB at this wavelength, absorption by DCB in samples containing An will be negligible, and generation of the DCB radical anion is not due to direct reduction of excited state DCB by the zeolite framework. Therefore radical anion generation must be attributed to intrazeolite electron transfer chemistry induced by photoexcitation of An.

Consistent with the notion that the DCB radical anion is generated by An-photosensitized ET reactions rather than direct excitation is the observation that absorption intensity due to sodium-cluster electron complexes is significantly reduced or eliminated when An is photoionized in NaY containing DCB. However, the intensity of the An radical cation does not show a corresponding decrease, indicating that the efficiency of photoionization and the yield of ejected electrons is not reduced by DCB. This suggests that the electron ejected from An upon radical cation generation is captured by a species other than the zeolite framework cations when DCB is present. The

concomitant observation of the DCB radical anion verifies that the DCB acts as the alternative electron acceptor in ET reactions initiated by selective excitation of An.

This interpretation is supported by laser photolysis of An in nitrous oxide saturated NaY containing coadsorbed DCB. As shown in Figure 4-26, the inclusion of this electron scavenger eliminates the absorption signals due to the DCB radical anion at 340 nm and 430 nm, eq. 4-19.



Since the radical anion will be unreactive towards nitrous oxide, the nitrous oxide must be quenching the formation of the DCB radical anion. As demonstrated above, nitrous oxide traps electrons within NaY preventing complexation of these electrons with sodium ion clusters. In the presence of DCB a similar effect is envisioned, whereby nitrous oxide trapping of the electron intercedes the ET chemistry between An and DCB.

The An radical cation and the DCB radical anion are both formed promptly within the 10 ns laser pulse when An is irradiated in the presence of DCB. The instantaneous generation of both radical ion products is observed for samples consisting of a variety of DCB and An concentrations. In each case the transient spectra are qualitatively similar, but exhibit distinct variations in the yield of DCB radical anion and trapped electrons, Figure 4-27. Specifically, the transient diffuse reflectance spectra indicate that the yield of DCB radical anion increases dramatically as the concentration of DCB is increased at a constant loading of An. In contrast to this increase in radical anion yield, the yield of trapped electrons decreases sharply with increasing DCB concentration. This is visible in the transient diffuse reflectance spectra which suggest a decrease in the more rapidly decaying absorption between 400 nm and 700 nm as the concentration of DCB increases. However the reduction in yield of trapped electrons becomes much more evident in the decay traces monitored at 700 nm, Figure 4-28. These decay traces nicely emphasize the significant, progressive reduction in the yield of sodium-cluster trapped electrons with increasing concentration of DCB. In combination, these results demonstrate a clear trend where the increase in yield of the DCB radical anion is accompanied by a corresponding decrease in the yield of sodium cation trapped electrons, Figure 4-29. Notably, the concentration of DCB has little influence on the yield of An radical cation. This remains

essentially the same as observed upon photoexcitation of anethole in NaY alone, with the exception that at very high concentrations of DCB, a slight decrease in the An radical cation yield is observed.

Significantly, both the An radical cation and the DCB radical anion, generated upon selective photoexcitation of An in NaY containing various concentrations of DCB, are consistently very long-lived. In all cases, the decay traces for both radical ions fit nicely to a double first-order expression yielding a fast ($k \sim 10^4 \text{ s}^{-1}$) and a slow ($k \sim 10^3 \text{ s}^{-1}$) decay rate constant. A summary of the decay rate constants of the An radical cation and the DCB radical anion observed at a constant An concentration and varied DCB concentrations is given in Table 4-2. While these rate constants should be regarded as an average representation of the decay kinetics of the radical ions within NaY, the rate constant of the An radical cation monitored at 380 nm and the DCB radical anion monitored at 340 nm are quite similar for all DCB concentrations. In particular, for samples containing the highest loadings of DCB, the decay of the DCB radical anion is virtually identical to the An radical cation, as is evident from the decay traces of the radical ions observed in this sample, Figure 4-30. At lower DCB loadings the decay kinetics remain quite similar, but the decay of the radical anion at 340 nm is slightly faster than the An radical cation at 380 nm, Figure 4-31.

Table 4-2. First-order decay rate constants of the An radical cation ($\langle \text{An} \rangle = 0.1$) and DCB radical anion monitored at 380 nm and 340 nm, respectively, in evacuated NaY.

$\langle \text{DCB} \rangle$	$k_{\text{fast}} / 10^4 \text{ s}^{-1}$		$k_{\text{slow}} / 10^3 \text{ s}^{-1}$	
	380 nm	340 nm	380 nm	340 nm
0.05	3.94 (64 %)	4.72 (67 %)	1.54 (36 %)	3.31 (33 %)
0.1	3.38 (50 %)	3.71 (67 %)	3.39 (50 %)	3.10 (33 %)
0.2	3.36 (49 %)	3.21 (67 %)	2.55 (51 %)	2.51 (33 %)
1	2.88 (27 %)	2.75 (39 %)	2.08 (62 %)	2.13 (61 %)

As previously mentioned, the inclusion of the electron scavenger, nitrous oxide, results in a complete disappearance of the absorption bands associated with the DCB radical anion. This effect is consistently observed for zeolite samples with various concentrations of DCB, as is evident from the absence of absorption bands at 340 nm and 430 nm in nitrous oxide-saturated NaY, Figure 4-32. However, when the loading level of DCB is very high ($\langle S \rangle = 1$), absorption due to the DCB radical anion is not completely quenched by the inclusion of nitrous oxide. Instead, a small shoulder remains at 340 nm

indicating incomplete quenching of radical anion formation at these high DCB concentrations. Notably, complete quenching of radical anion formation by nitrous oxide is observed in samples containing less than one DCB molecule in every cavity.

4.2.4 *Steady-State Fluorescence Measurements*

The experimental results described thus far have involved time-resolved investigations of the dynamics of photoexcited electron donors and acceptors in NaY, either alone, or in the presence of a coincluded redox partner. These investigations have provided considerable details concerning redox processes within NaY, although no information regarding the rates of radical ion formation is obtainable on the nanosecond time-scale. In addition to time-resolved methods, many studies of ET reactions in solution obtain useful information from steady-state techniques, in particular, steady-state fluorescence. For example, a photoexcited molecule, such as an electron donor, may fluoresce, thereby decaying to the ground-state by emission of light. In the presence of an electron acceptor, this photoexcited electron donor may also undergo ET rather than fluorescing down to the ground-state. This ET reaction would lead to a corresponding reduction in the intensity of fluorescence from the photoexcited donor which can be measured from steady-state experiments and quantified as a function of acceptor concentration. In solution such fluorescence measurements have been used extensively to investigate ET reactions. However, the observation of steady-state emission quenching provides no direct information about the reaction responsible for the quenching. Additional information is necessary to establish whether or not the reduction in fluorescence is due to ET.

The current experimental studies have employed Chl as a photoexcitable electron acceptor, and An as a photoexcitable electron donor. Redox reactions initiated by photoexcitation of Chl in NaY are not applicable to steady-state fluorescence measurements, due simply to the fact that photoexcited Chl does not fluoresce. However, it is possible to examine the fluorescence of An in NaY and examine the influence of coincluded electron donors on the steady-state emission intensity.

The steady-state fluorescence spectrum observed upon 308 nm excitation of An in NaY ($\langle S \rangle = 0.1$) is very similar to the fluorescence spectrum of An in hexane (ca. 10^{-4} M), Figure 4-33. In hexane, the emission maximum is at 328 nm, while in NaY the emission maximum is red-shifted slightly to 338 nm. The coinclusion of DCB within the zeolite cavities has a strong influence on the fluorescence of An in NaY, Figure 4-34. The variation in fluorescence intensity of An in NaY monitored at 338 nm as a function

of DCB concentration is shown in Figure 4-35. As can be clearly seen in both Figures 4-35, the intensity of fluorescence from photoexcited An decreases dramatically as the concentration of DCB increases.

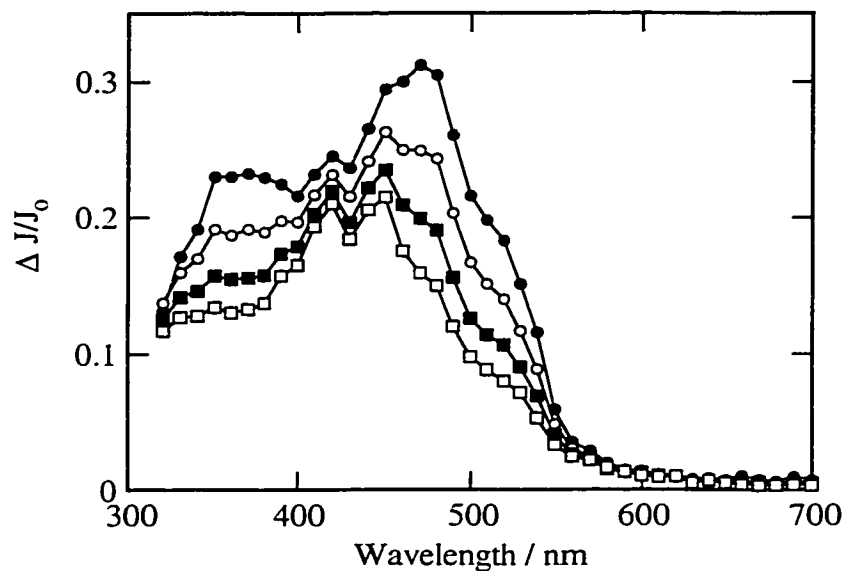


Figure 4-1. Transient diffuse reflectance spectrum obtained 480 ns (closed circles), 2.48 μ s (open circles), 7.20 μ s (closed squares), and 14.16 μ s (open squares) after 308 nm laser photolysis of Chl ($\langle S \rangle = 0.08$) in evacuated NaY.

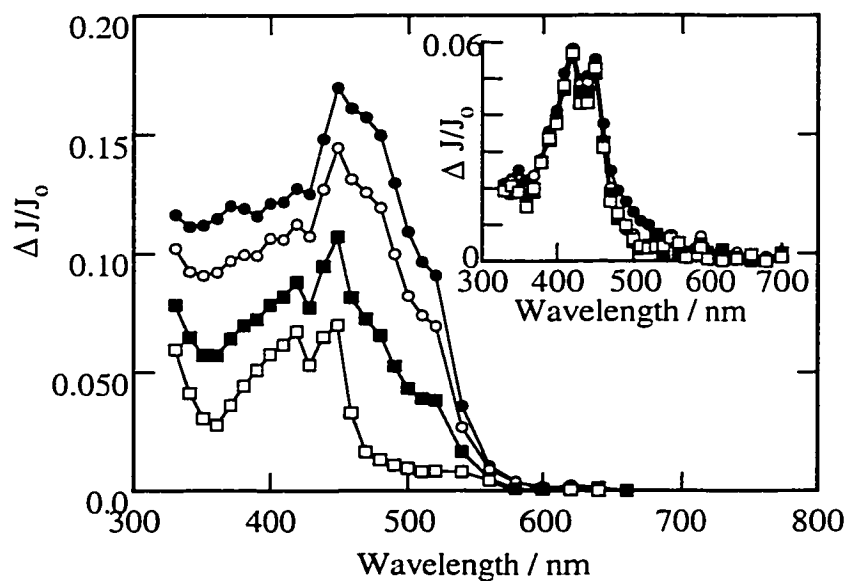


Figure 4-2. Transient diffuse reflectance spectrum obtained 1.00 μ s (closed circles), 2.80 μ s (open circles), 8.50 μ s (closed squares), and 32.0 μ s (open squares) after 308 nm laser photolysis of Chl ($\langle S \rangle = 0.02$) in evacuated NaY. Inset shows the transient diffuse reflectance spectrum observed 40 μ s (closed circles), 104 μ s (open circles), 232 μ s (closed squares), and 318 μ s (open squares) after laser irradiation.

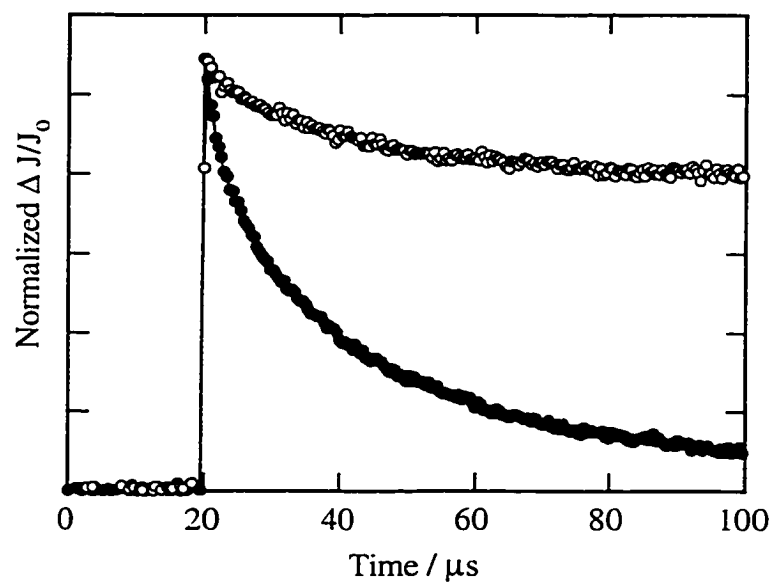


Figure 4-3. Normalized decay traces monitored at 500 nm (closed circles), and 420 nm (open circles) following 308 nm laser photolysis of Chl ($\langle S \rangle = 0.08$) in evacuated NaY.

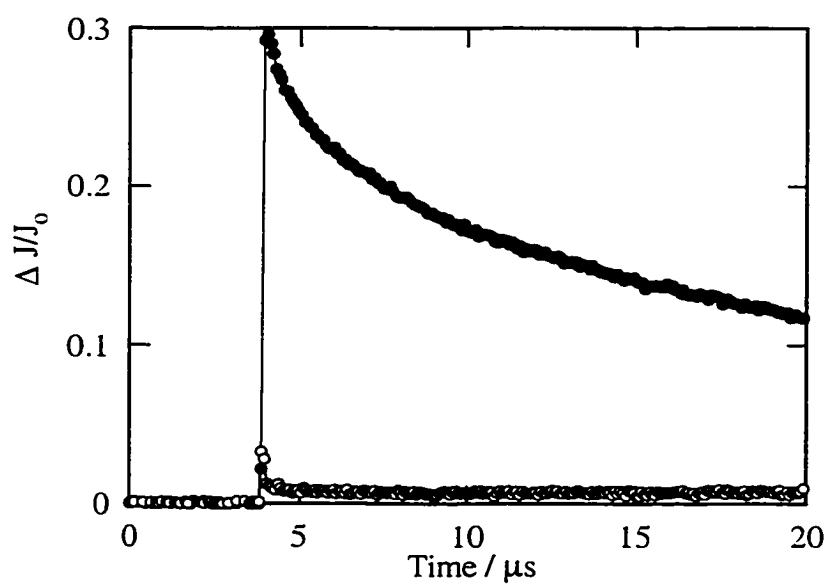


Figure 4-4. Normalized decay traces monitored at 500 nm following 308 nm laser photolysis of Chl ($\langle S \rangle = 0.08$) in evacuated (closed circles) and oxygen-saturated (open circles) NaY.

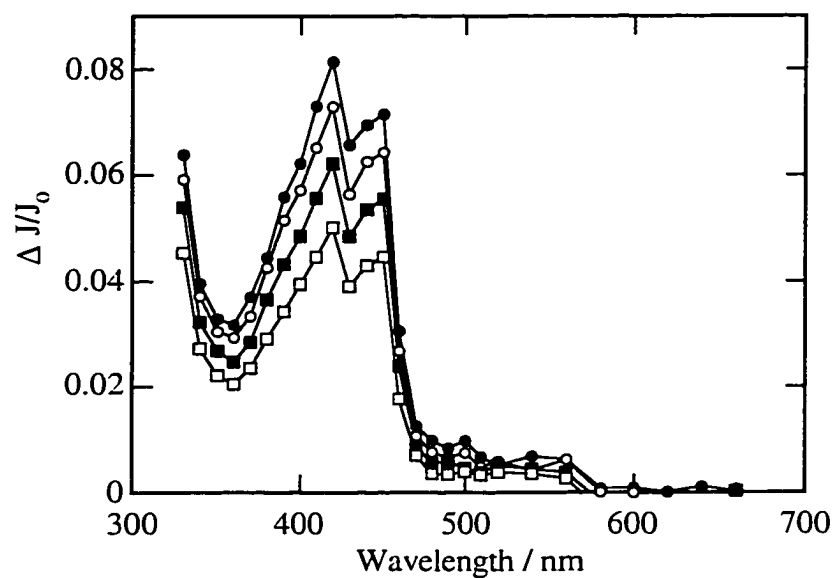


Figure 4-5. Transient diffuse reflectance spectrum obtained 1.00 μ s (closed circles), 2.80 μ s (open circles), 8.50 μ s (closed squares), and 32.0 μ s (open squares) after 308 nm laser photolysis of Chl ($\langle S \rangle = 0.02$) in oxygen-saturated NaY.

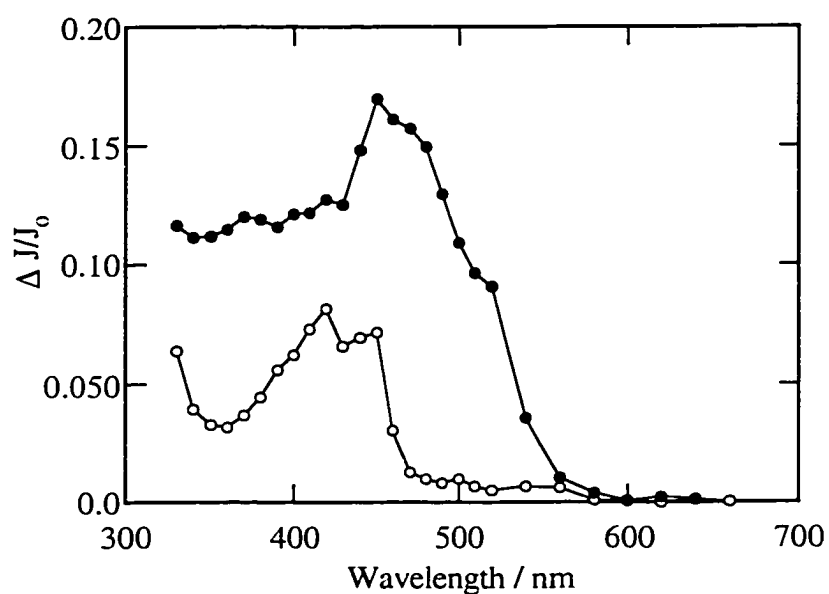


Figure 4-6. Transient diffuse reflectance spectrum observed 1.00 μ s after 308 nm laser photolysis of Chl ($\langle S \rangle = 0.02$) in evacuated (closed circles), and oxygen-saturated (open circles) NaY.

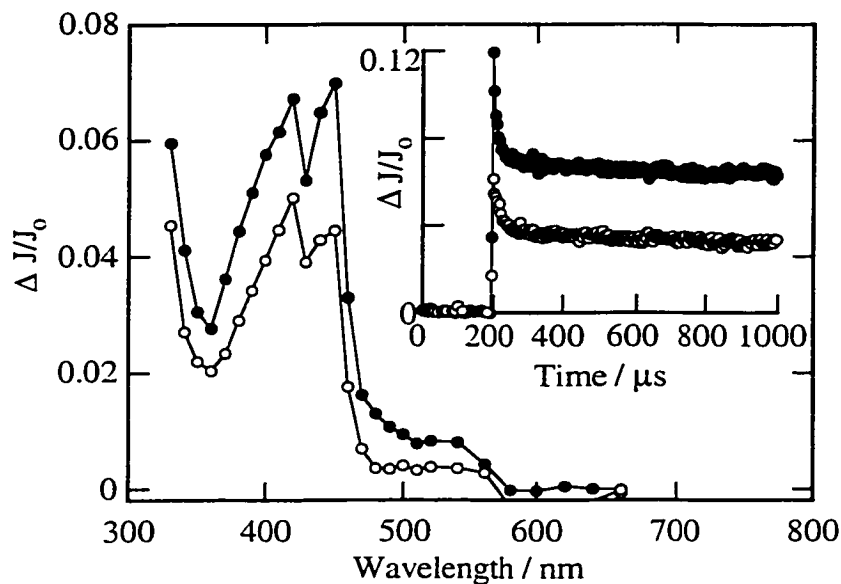


Figure 4-7. Transient diffuse reflectance spectrum observed 32.00 μs after 308 nm laser photolysis of Chl ($\langle S \rangle = 0.02$) in evacuated (closed circles), and oxygen-saturated (open circles) NaY. The inset shows the decay traces monitored at 420 nm following 308 nm laser photolysis of Chl in evacuated (closed circles) and oxygen-saturated (open circles) NaY.

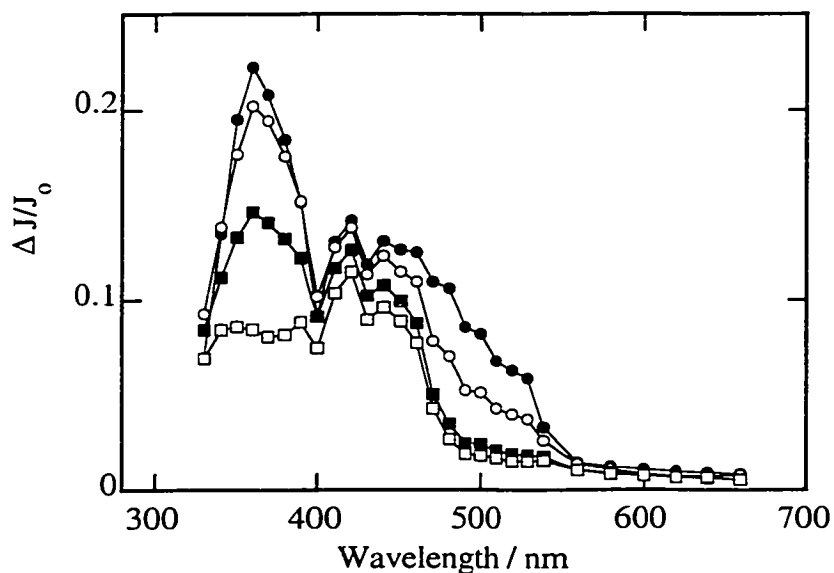


Figure 4-8. Transient diffuse reflectance spectrum obtained 400 ns (closed circles), 880 ns (open circles), 3.32 μs (closed squares), and 13.6 μs (open squares) after 308 nm laser photolysis of Chl ($\langle S \rangle = 0.04$) in evacuated NaY containing coadsorbed DMB ($\langle S \rangle = 0.1$).

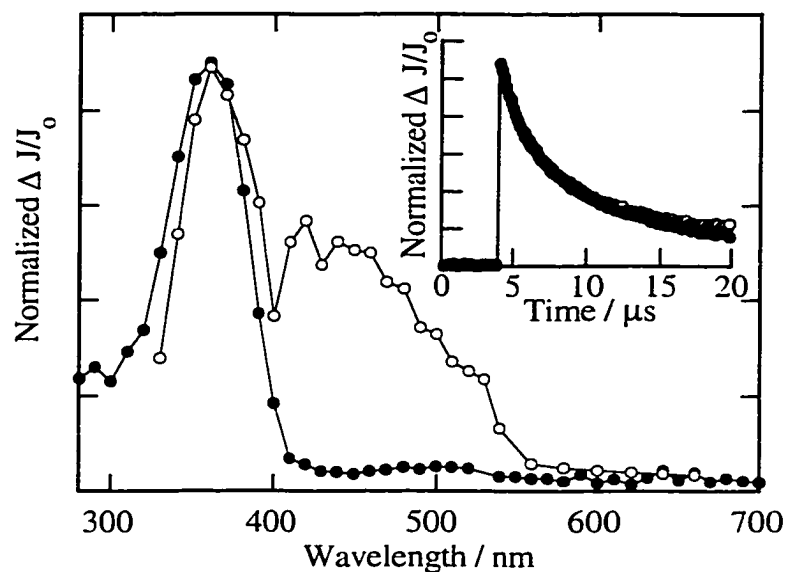


Figure 4-9. Transient diffuse reflectance spectrum obtained 400 ns after 308 nm laser photolysis of Chl ($\langle S \rangle = 0.04$) in evacuated NaY containing coadsorbed DMB ($\langle S \rangle = 0.1$) (open circles), and 400 ns after 266 nm laser photolysis of DMB ($\langle S \rangle = 0.1$) in evacuated NaY (closed circles). The decay traces monitored at 360 nm following 308 nm (open circles) and 266 nm (closed circles) laser photolysis are shown in the inset.

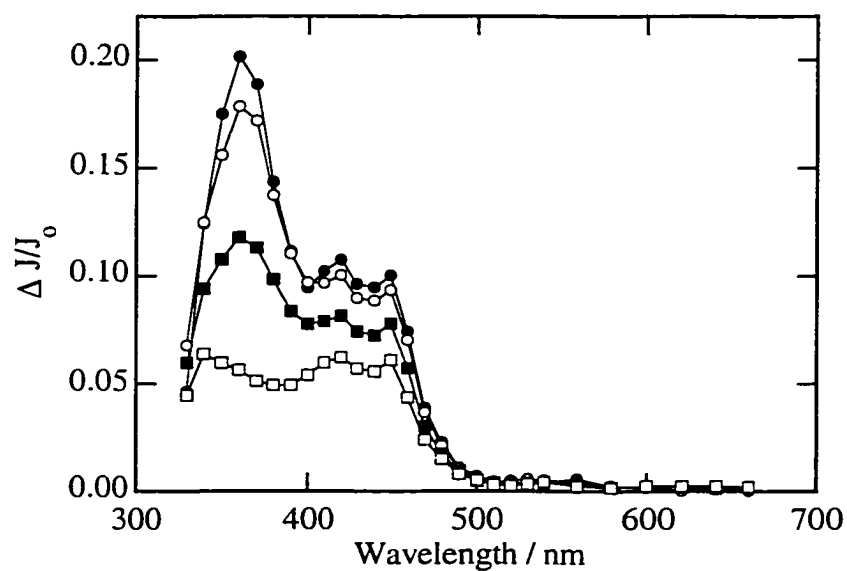


Figure 4-10. Transient diffuse reflectance spectrum obtained 400 ns (closed circles), 880 ns (open circles), 3.32 μ s (closed squares), and 13.6 μ s (open squares) after 308 nm laser photolysis of Chl ($\langle S \rangle = 0.04$) in oxygen-saturated NaY containing coadsorbed DMB ($\langle S \rangle = 0.1$).

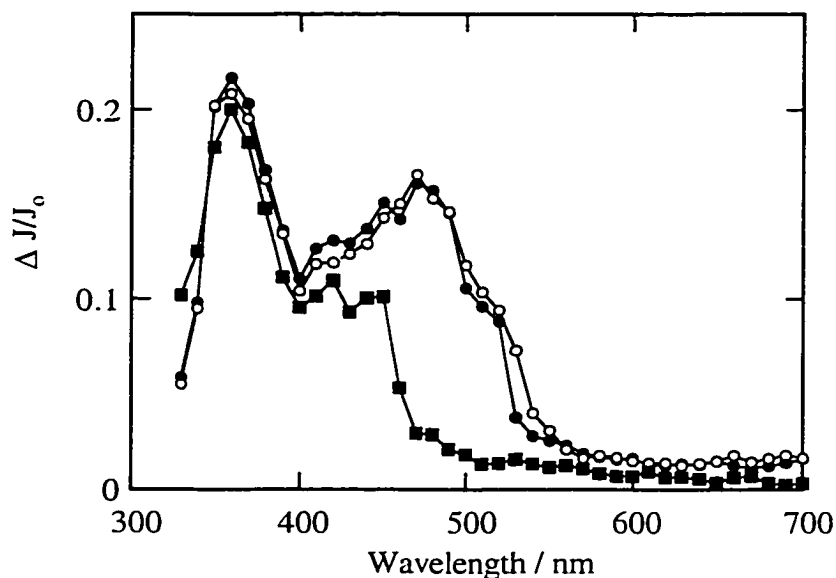


Figure 4-11. Transient diffuse reflectance spectrum generated 240 ns after 308 nm laser photolysis of Chl ($\langle S \rangle = 0.08$) in NaY containing DMB ($\langle S \rangle = 0.04$) under vacuum (closed circles), nitrous oxide (open circles), and oxygen (closed squares) conditions.

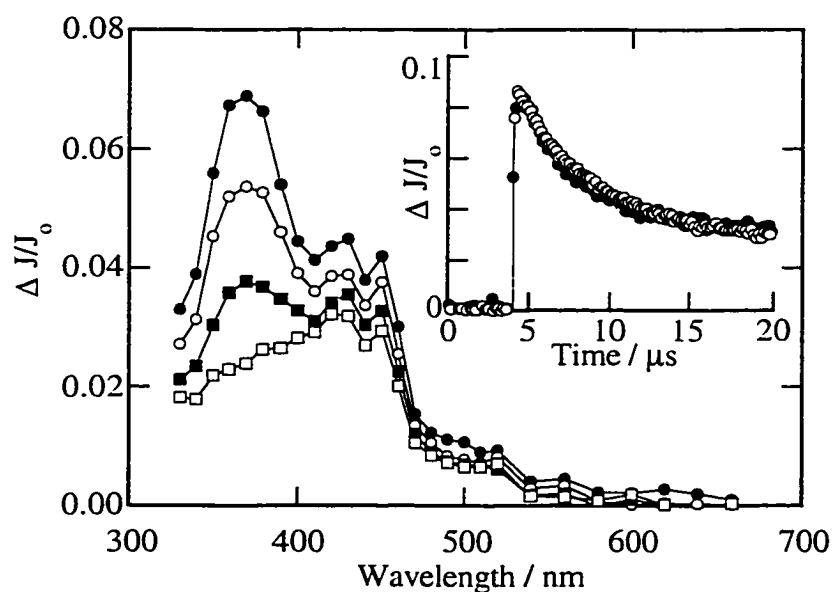


Figure 4-12. Transient diffuse reflectance spectrum obtained 800 ns (closed circles), 2.48 μs (open circles), 6.16 μs (closed squares), and 14 μs (open squares) after 308 nm laser photolysis of a 25 day old sample containing Chl ($\langle S \rangle = 0.04$) and DMB ($\langle S \rangle = 0.07$) in evacuated NaY. The inset compares the decay trace monitored at 360 nm in the fresh sample (closed circles), and the 25 day old sample (open circles).

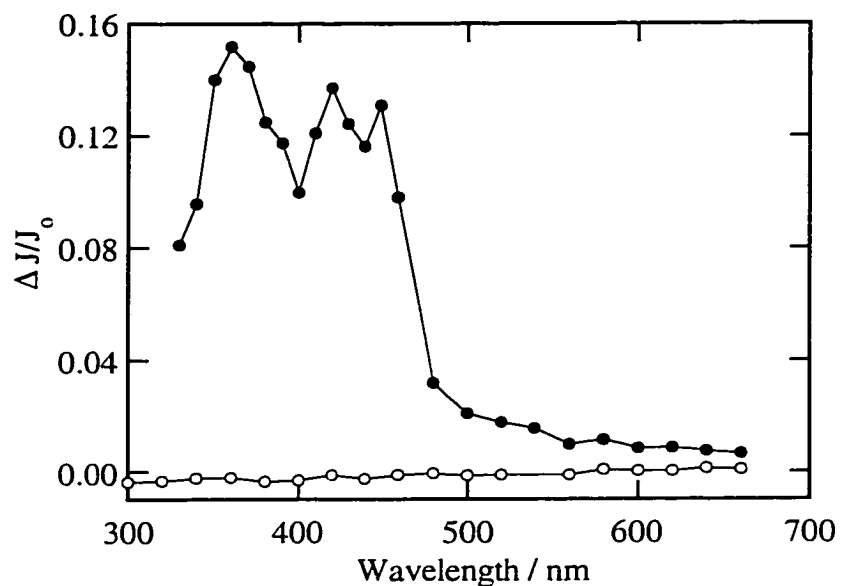


Figure 4-13. Transient diffuse reflectance spectrum observed immediately following 308 nm (closed circles) and 532 nm (open circles) laser photolysis of Chl ($\langle S \rangle = 0.02$) in evacuated NaY containing coadsorbed DMB ($\langle S \rangle = 0.1$).

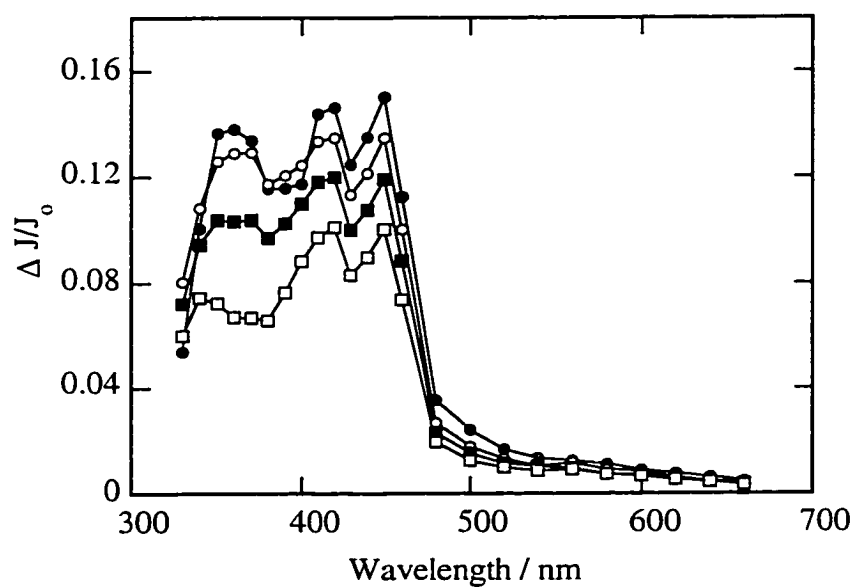


Figure 4-14. Transient diffuse reflectance spectrum obtained 360 ns (closed circles), 1.24 μ s (open circles), 3.92 μ s (closed squares), and 13.6 μ s (open squares) after 308 nm laser photolysis of Chl ($\langle S \rangle = 0.02$) and DMB ($\langle S \rangle = 0.01$) in oxygen-saturated NaY.

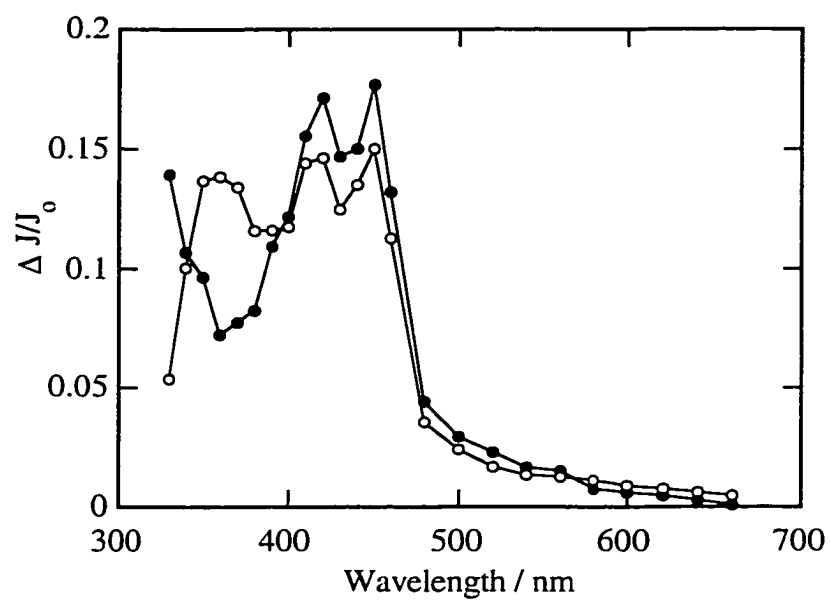


Figure 4-15. Transient diffuse reflectance spectrum obtained 360 ns after 308 nm laser photolysis of Chl ($\langle S \rangle = 0.02$) in oxygen-saturated NaY (closed circles) and Chl ($\langle S \rangle = 0.02$) and DMB ($\langle S \rangle = 0.01$) in oxygen-saturated NaY (open circles).

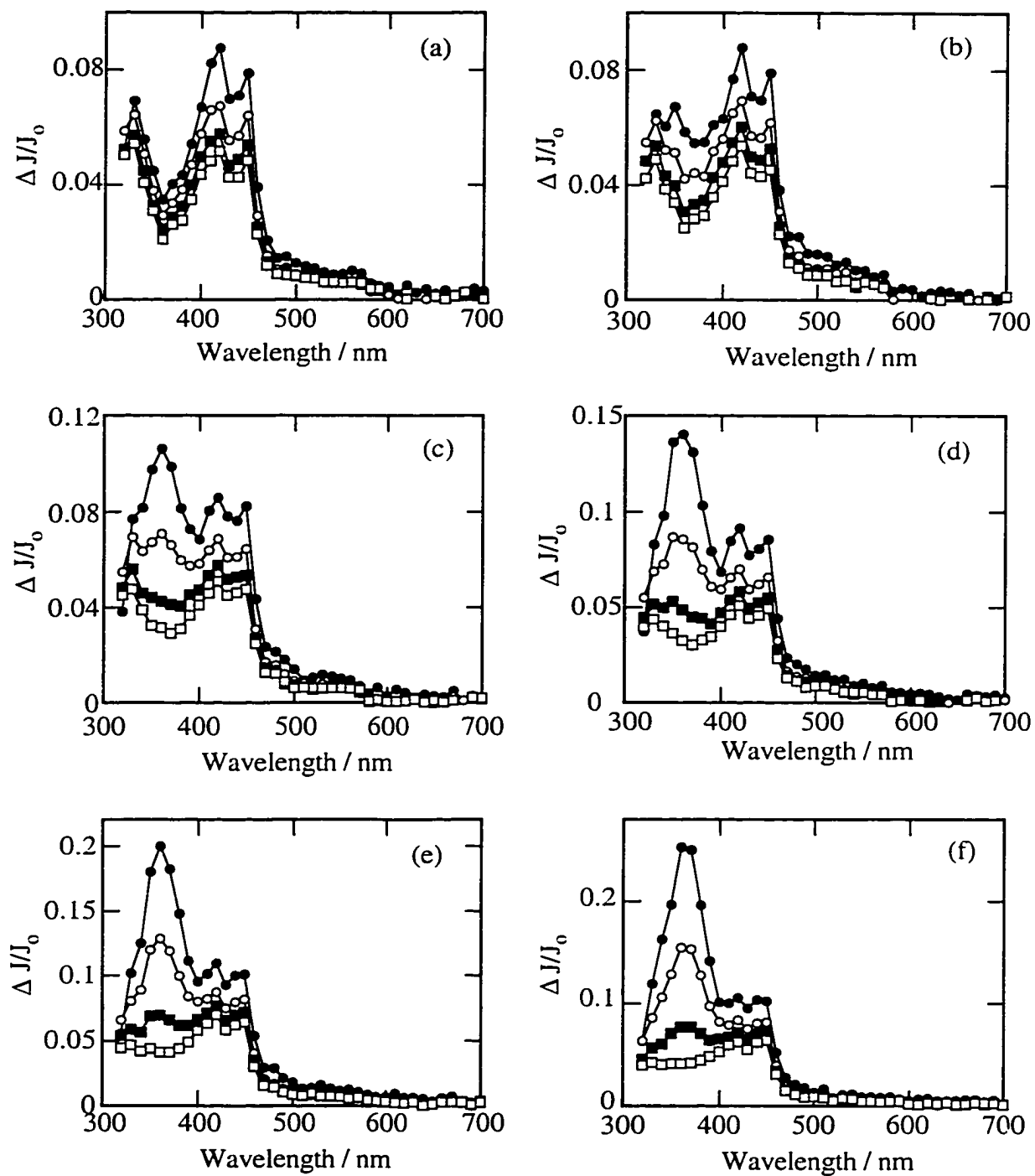


Figure 4-16. Transient diffuse reflectance spectra obtained 200 ns (closed circles), 1.96 μ s (open circles), 6.20 μ s (closed squares), and 14.0 μ s (open squares) after 308 nm laser photolysis of Chl ($\langle S \rangle = 0.02$) in oxygen-saturated NaY containing various concentrations of DMB: $\langle S \rangle = 0$ (a), $\langle S \rangle = 0.002$ (b), $\langle S \rangle = 0.01$ (c), $\langle S \rangle = 0.02$ (d), $\langle S \rangle = 0.04$ (e), $\langle S \rangle = 0.1$ (f).

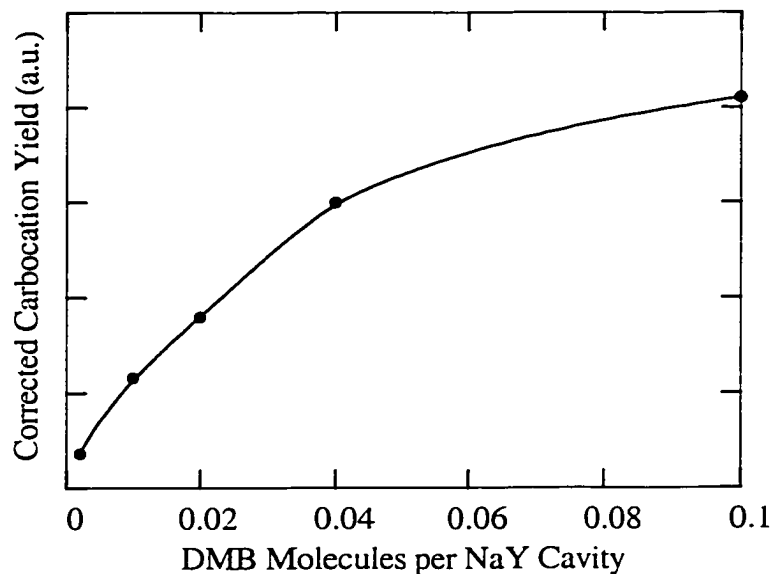


Figure 4-17. Yield of the 4-methoxycumyl cation generated by 308 nm laser photolysis of Chl in evacuated NaY as a function of concentration of coadsorbed DMB. The carbocation yield is determined from the total change in diffuse reflectance at 360 nm corrected for absorption at this wavelength due to the Chl triplet and Chl radical anion.

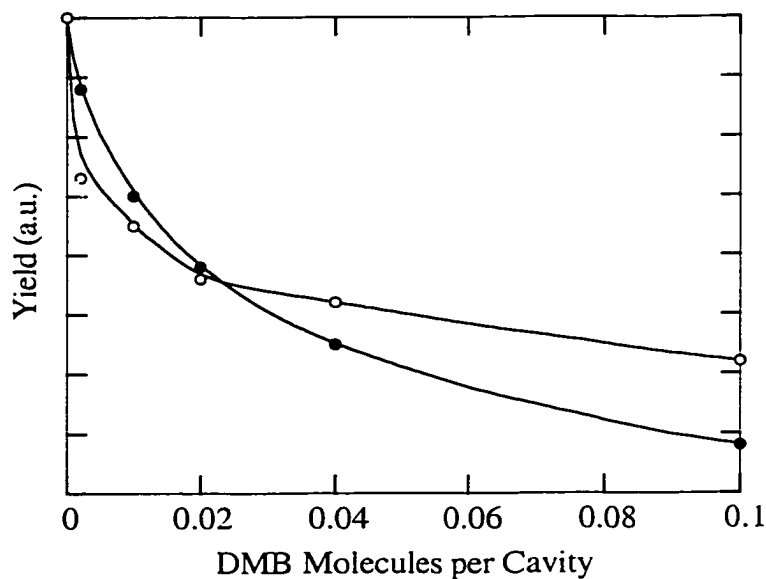


Figure 4-18. Yield of Chl triplet (closed circles) and Chl radical anion (open circles) generated by 308 nm laser photolysis of Chl in evacuated NaY as a function of concentration of coadsorbed DMB. The triplet yield is obtained from the change in diffuse reflectance monitored at 500 nm, and the radical anion yield is obtained from the change in diffuse reflectance at 450 nm corrected for triplet absorption.

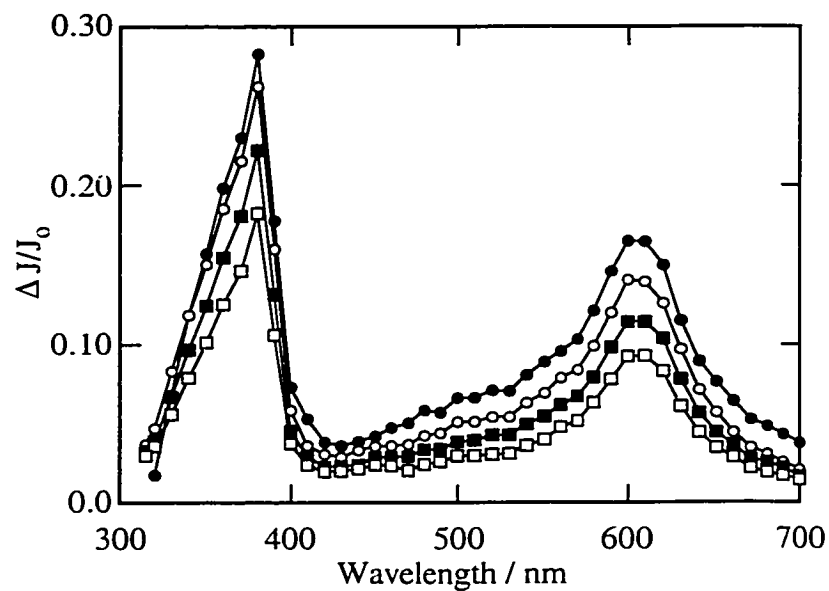


Figure 4-19. Transient diffuse reflectance spectrum obtained 360 ns (closed circles), 1.64 μs (open circles), 5.32 μs (closed squares), and 13.9 μs (open squares) after 308 nm laser photolysis of An ($\langle S \rangle = 0.1$) in evacuated NaY.

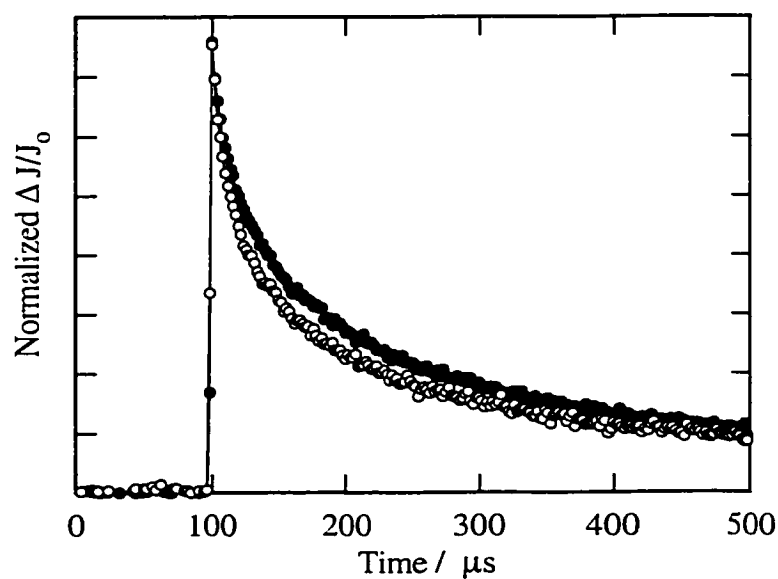


Figure 4-20. Normalized decay traces monitored at 380 nm (closed circles) and 600 nm (open circles) following 308 nm of An ($\langle S \rangle = 0.1$) in evacuated NaY (total time = 500 μs).

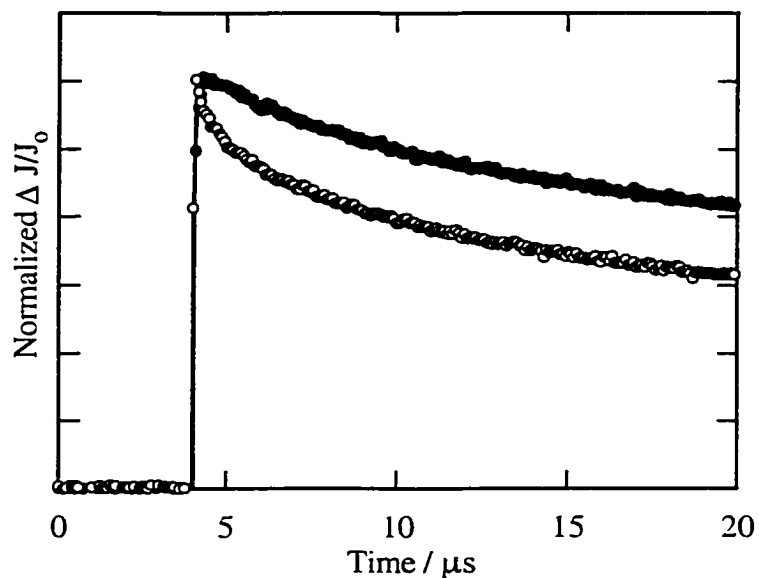


Figure 4-21. Normalized decay traces monitored at 380 nm (closed circles) and 600 nm (open circles) following 308 nm of An ($\langle S \rangle = 0.1$) in evacuated NaY (total time = 20 μs).

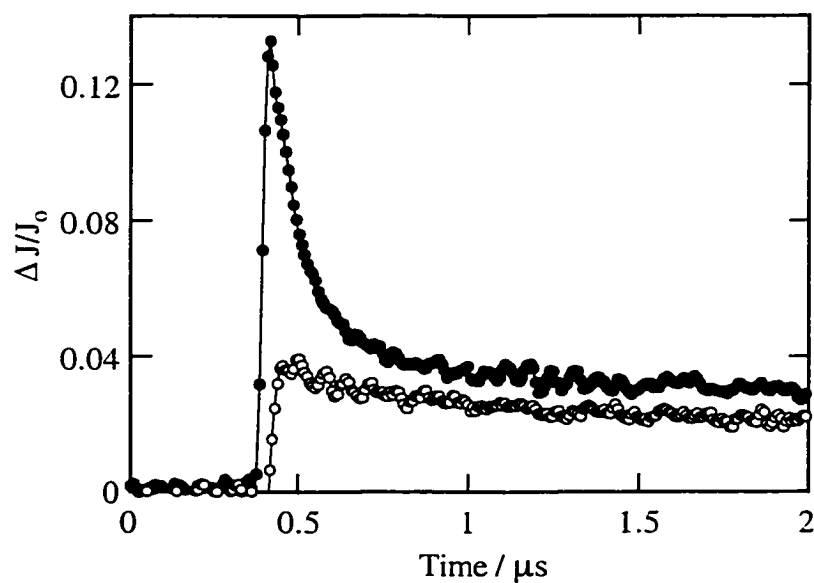


Figure 4-22. Decay traces monitored at 700 nm following 308 nm of An ($\langle S \rangle = 0.1$) in evacuated NaY (closed circles) and nitrous oxide-saturated NaY (open circles).

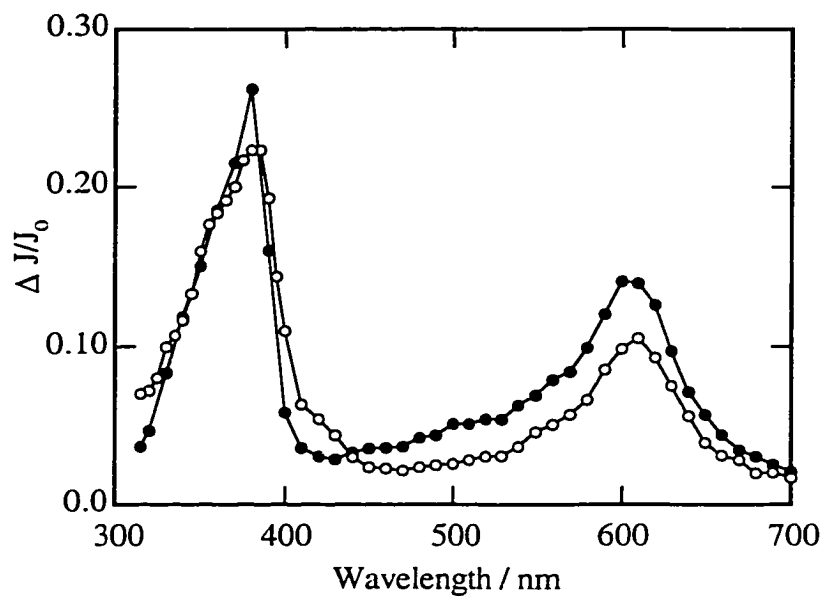


Figure 4-23. Transient diffuse reflectance spectrum obtained 1.64 μs after 308 nm laser photolysis of An ($\langle S \rangle = 0.1$) in evacuated NaY (closed circles) and nitrous oxide-saturated NaY (open circles).

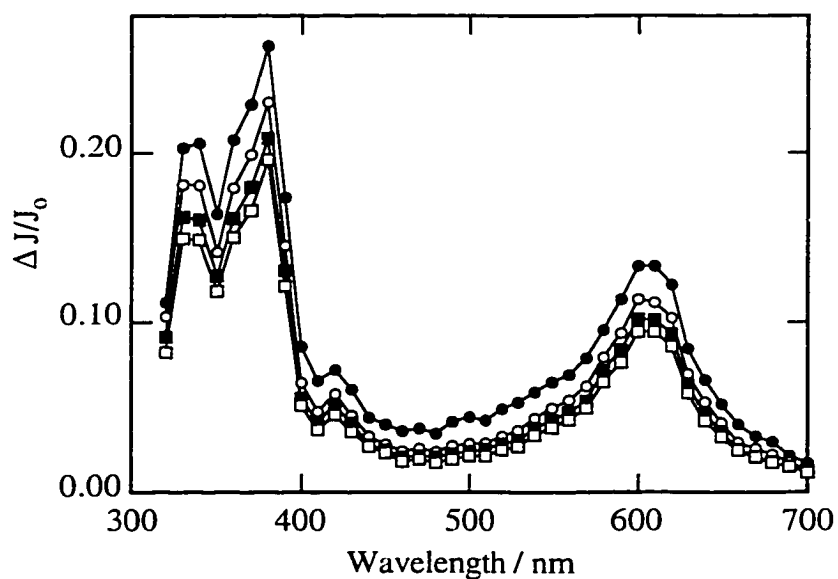


Figure 4-24. Transient diffuse reflectance spectrum obtained 640 ns (closed circles), 4.08 μs (open circles), 9.32 μs (closed squares), and 14.7 μs (open squares) after 308 nm laser photolysis of An ($\langle S \rangle = 0.1$) in evacuated NaY containing coadsorbed DCB ($\langle S \rangle = 0.2$).

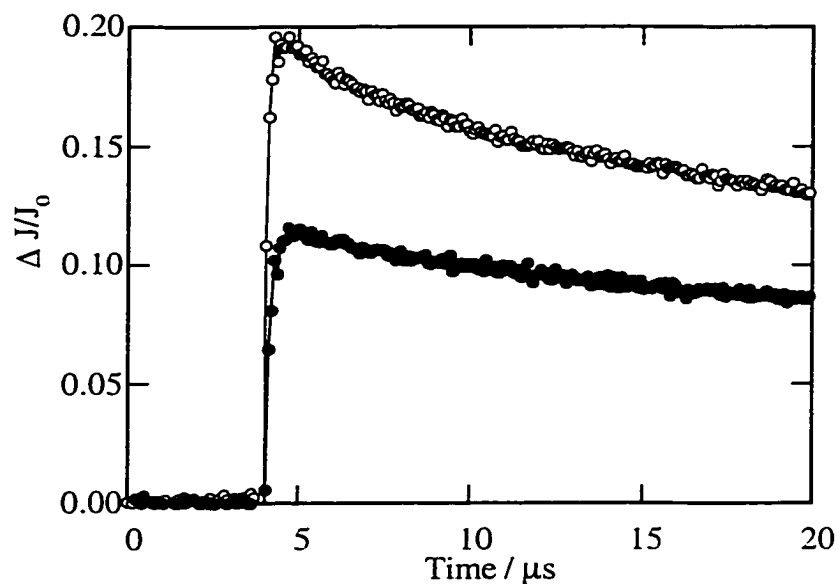


Figure 4-25. Decay traces monitored at 340 nm following 308 nm laser photolysis of An ($\langle S \rangle = 0.1$) in evacuated NaY (closed circles) and An ($\langle S \rangle = 0.1$) in NaY containing coadsorbed DCB ($\langle S \rangle = 0.2$) (open circles).

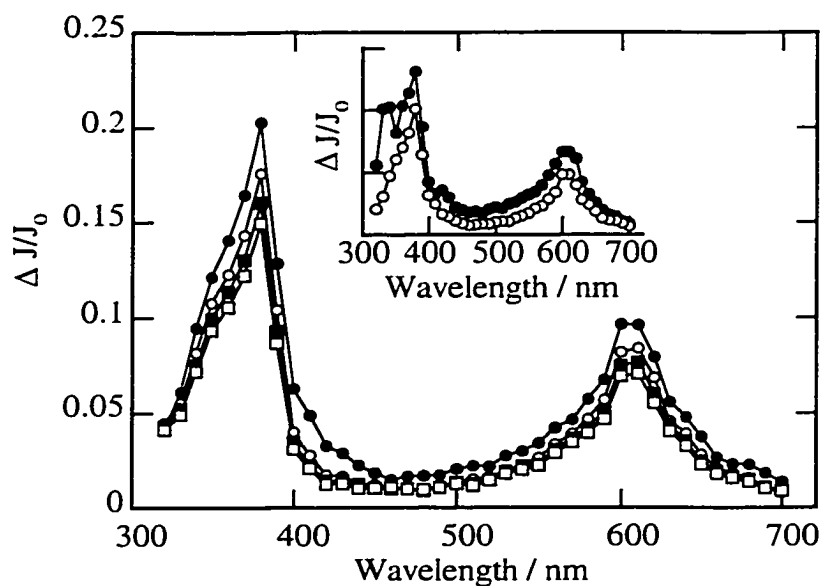


Figure 4-26. Transient diffuse reflectance spectrum obtained 640 ns (closed circles), 4.08 μ s (open circles), 9.32 μ s (closed squares), and 14.7 μ s (open squares) after 308 nm laser photolysis of An ($\langle S \rangle = 0.1$) in nitrous oxide-saturated NaY containing coadsorbed DCB ($\langle S \rangle = 0.2$). Inset compares the transient spectra observed after photolysis under vacuum (closed circles) and nitrous oxide conditions (open circles).

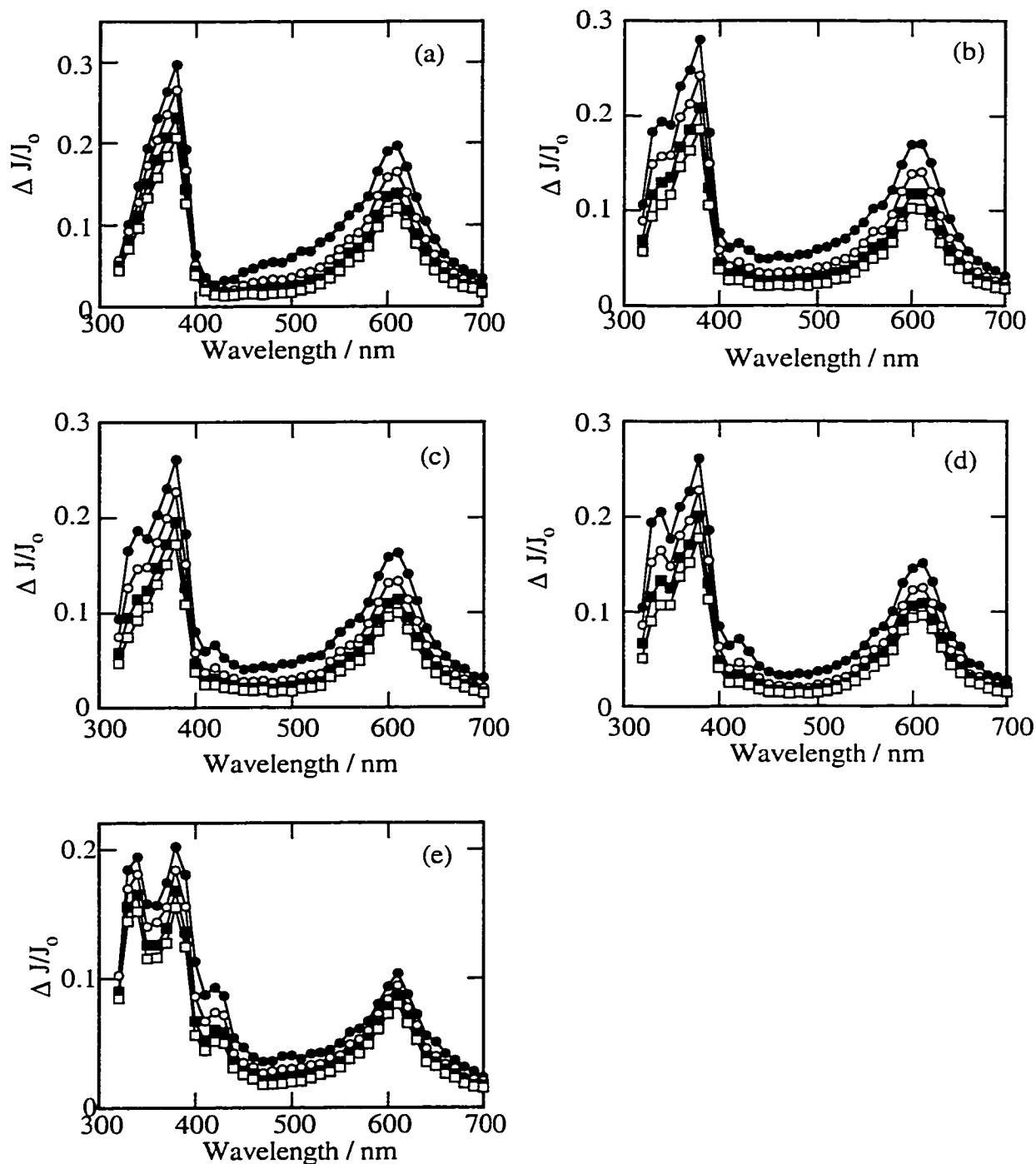


Figure 4-27. Transient diffuse reflectance spectra obtained 720 ns (closed circles), 3.32 μ s (open circles), 8.16 μ s (closed squares), and 14.8 μ s (open squares) after 308 nm laser photolysis of An ($\langle S \rangle = 0.1$) in nitrogen-saturated NaY containing various concentrations of DCB: $\langle S \rangle = 0$ (a), $\langle S \rangle = 0.05$ (b), $\langle S \rangle = 0.1$ (c), $\langle S \rangle = 0.2$ (d), $\langle S \rangle = 1$ (e).

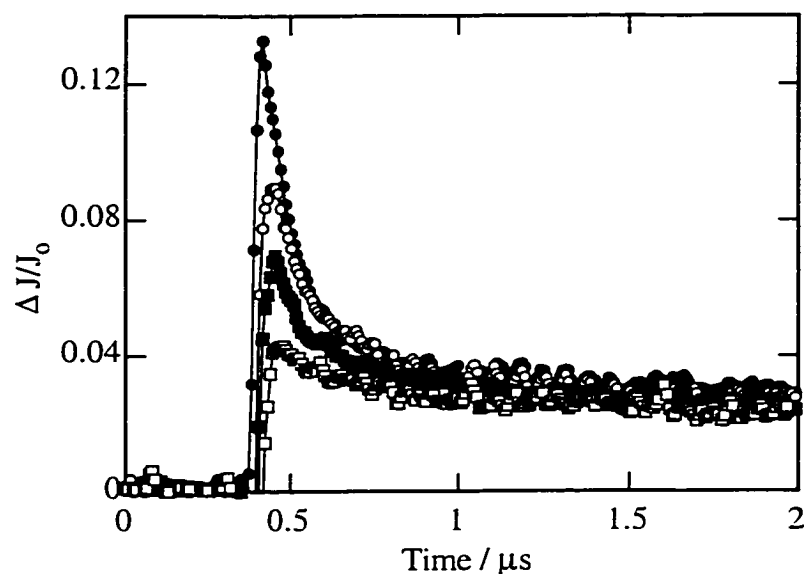


Figure 4-28. Decay traces monitored at 700 nm following 308 nm laser photolysis of An ($\langle S \rangle = 0.1$) in nitrogen-saturated NaY containing coadsorbed DCB: $\langle S \rangle = 0$ (closed circles), $\langle S \rangle = 0.05$ (open circles), $\langle S \rangle = 0.1$ (closed squares), $\langle S \rangle = 0.2$ (open squares).

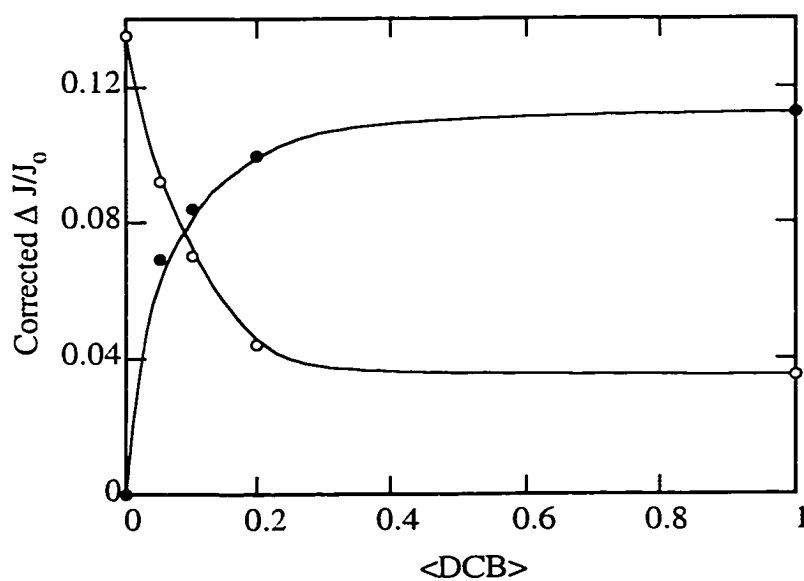


Figure 4-29. Yield of DCB radical anion (closed circles) and sodium-cluster trapped electrons (open circles) observed upon 308 nm laser photolysis of An ($\langle S \rangle = 0.1$) in nitrogen-saturated NaY as a function of DCB concentration. The radical anion and trapped electron yields are obtained from the change in diffuse reflectance at 340 nm and 700 nm respectively, corrected for absorption by the An radical cation at 340 nm.

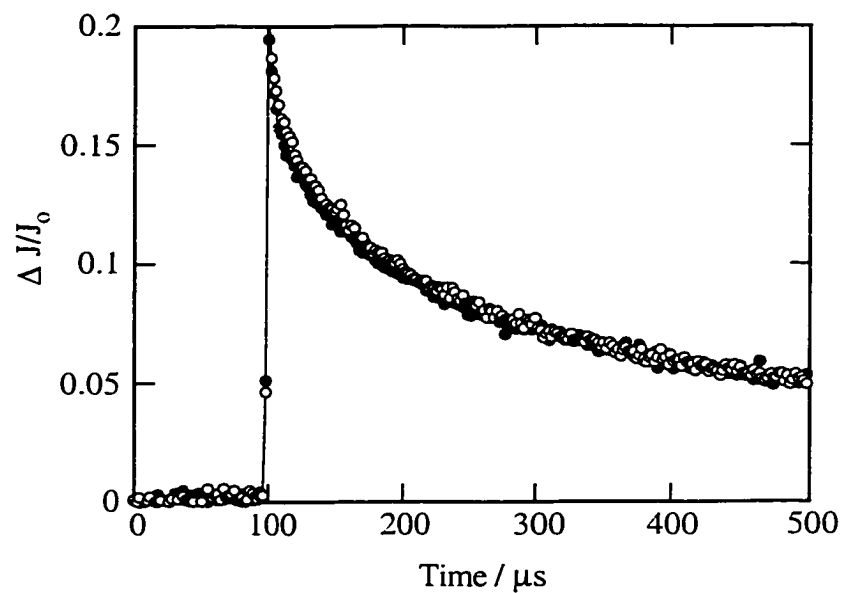


Figure 4-30. Decay traces monitored at 380 nm (closed circles) and 340 nm (open circles) following 308 nm laser photolysis of An ($\langle S \rangle = 0.1$) in nitrogen-saturated NaY containing coadsorbed DCB ($\langle S \rangle = 1$).

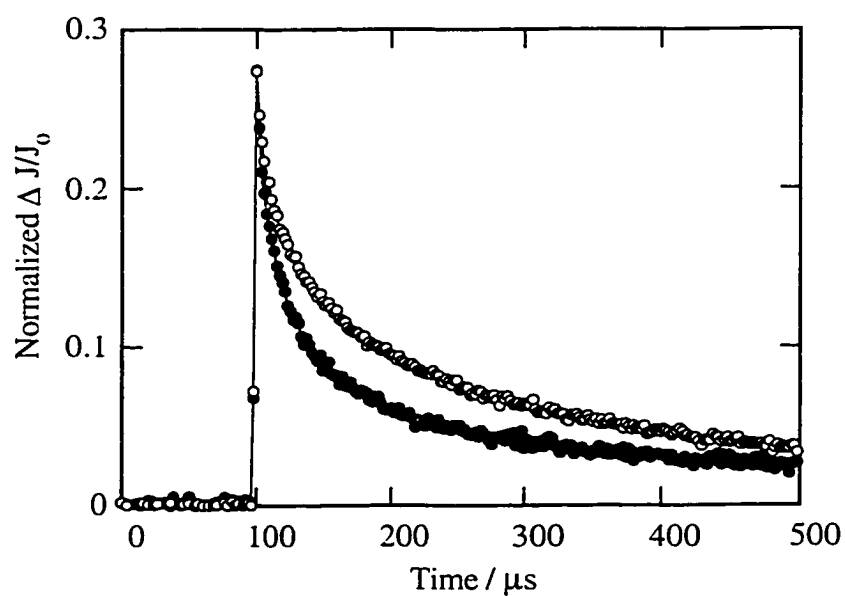


Figure 4-31. Decay traces monitored at 380 nm (closed circles) and 340 nm (open circles) following 308 nm laser photolysis of An ($\langle S \rangle = 0.1$) in nitrogen-saturated NaY containing coadsorbed DCB ($\langle S \rangle = 0.05$).

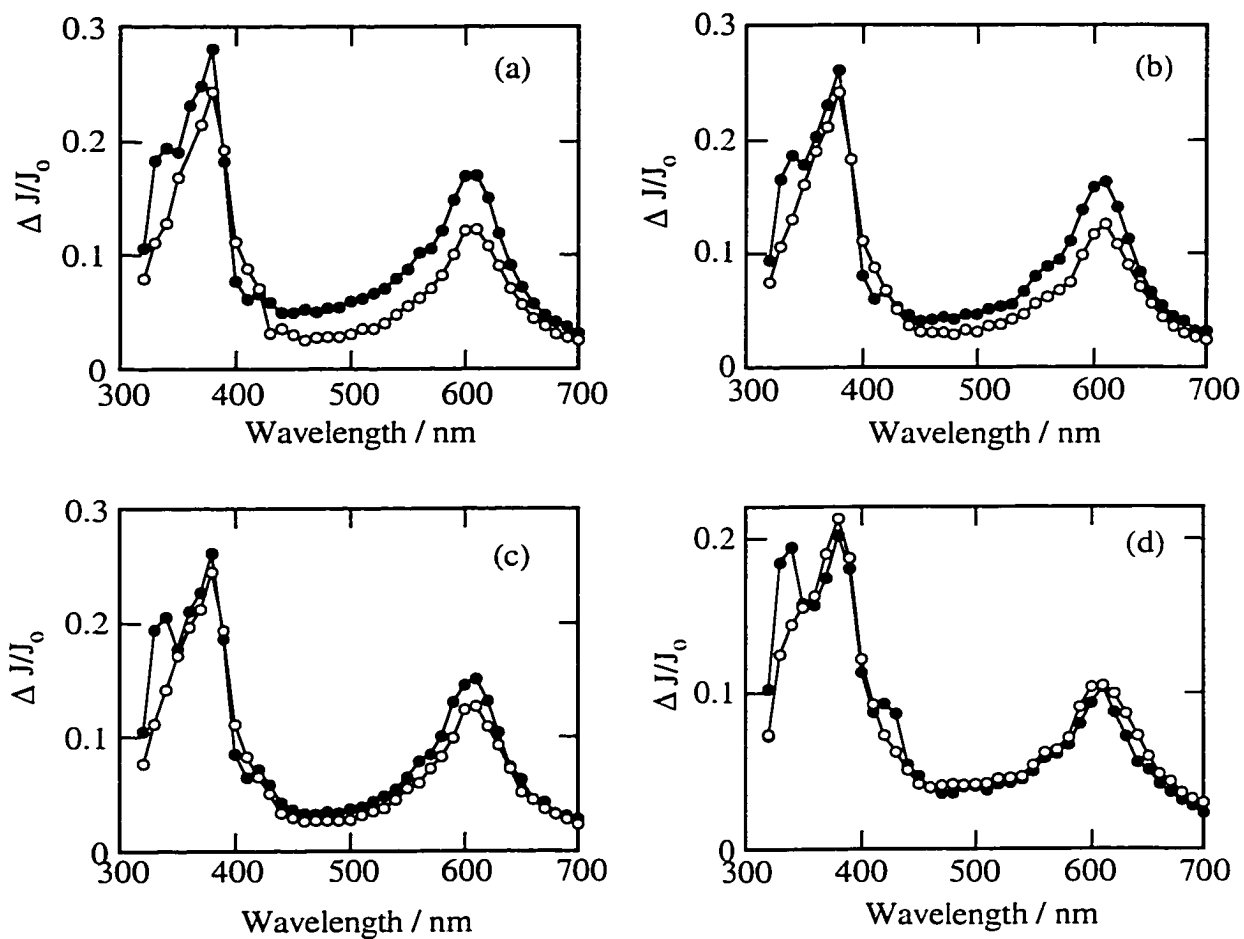


Figure 4-32. Transient diffuse reflectance spectra obtained 720 ns after 308 nm laser photolysis of An in nitrogen-saturated (closed circles), and nitrous oxide-saturated (open circles) NaY containing various concentrations of coadsorbed DCB: $\langle S \rangle = 0.05$ (a), $\langle S \rangle = 0.1$ (b), $\langle S \rangle = 0.2$ (c), $\langle S \rangle = 1$ (d).

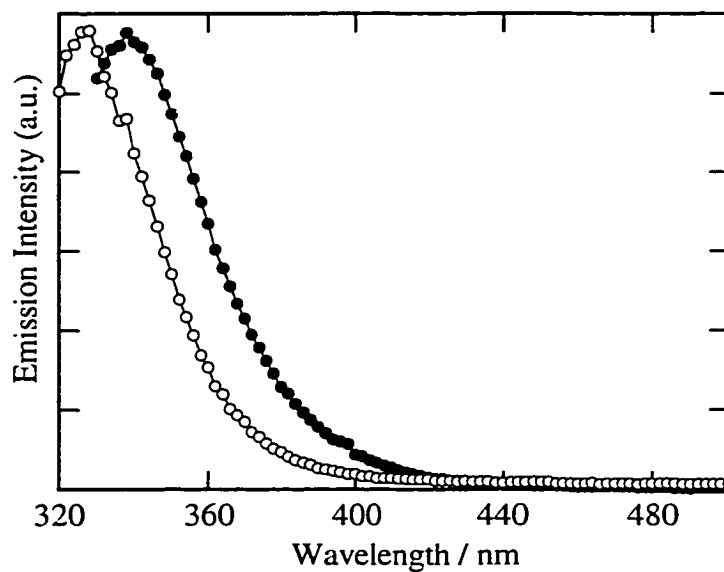


Figure 4-33. Steady-state fluorescence spectra observed following 308 nm excitation of An in NaY ($\langle S \rangle = 0.10$) (closed circles) and hexane (ca. 10^{-4} M) (open circles).

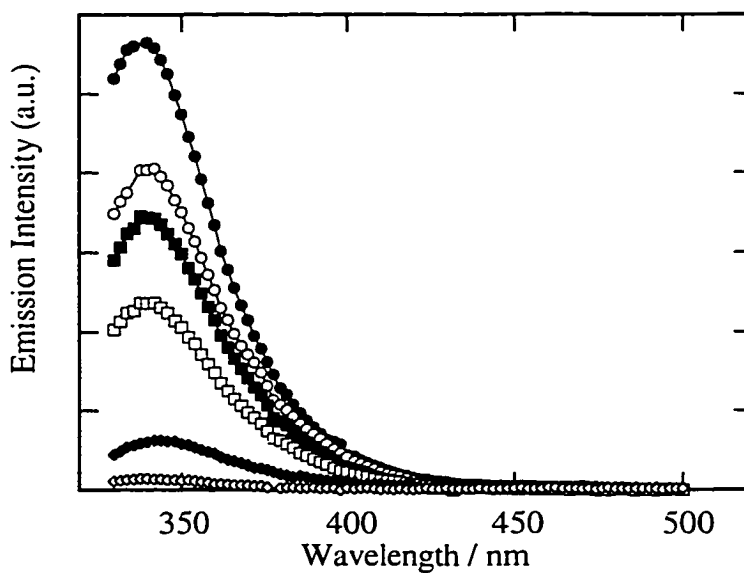


Figure 4-34. Steady-state fluorescence spectra observed following 308 nm excitation of An in NaY ($\langle S \rangle = 0.10$) containing various concentrations of coadsorbed DCB: $\langle S \rangle = 0$ (closed circles), $\langle S \rangle = 0.02$ (open circles), $\langle S \rangle = 0.04$ (closed squares), and $\langle S \rangle = 0.2$ (open squares), $\langle S \rangle = 0.3$ (closed diamonds), $\langle S \rangle = 1$ (open diamonds).

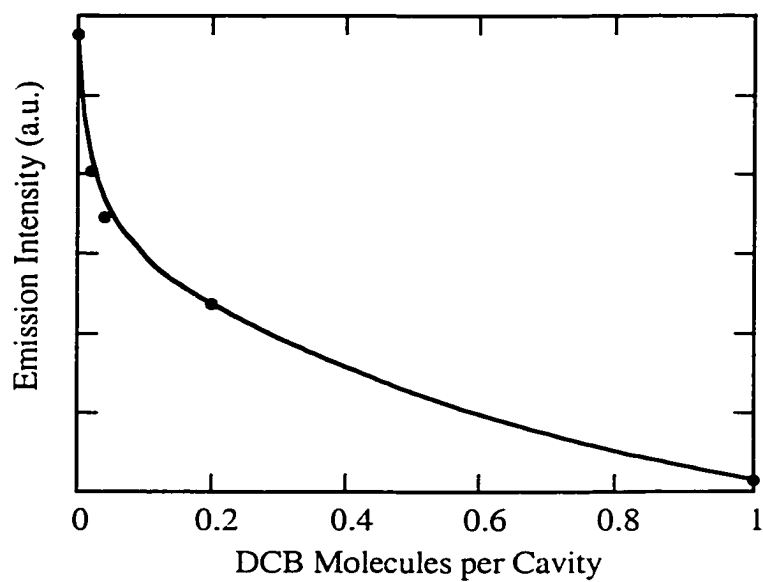


Figure 4-35. Variation in An steady-state fluorescence monitored at 338 nm following 308 nm excitation of An ($\langle S \rangle = 0.10$) in NaY as a function of DMB concentration.

4.3 Discussion

4.3.1 Generation of Holes in Zeolites: NaY as a Single Electron Donor

Photoexcitation of Chl in deoxygenated NaY generates both the Chl radical anion and the Chl triplet within the ca. 10 ns laser pulse, Figure 4-1. The Chl triplet exhibits a broad spectral absorption with maxima at 510 nm, 480 nm and 370 nm, while the Chl radical anion has two characteristic, sharp maxima at 450 nm and 420 nm. The first significant conclusion that can be drawn from these results is that photoexcited Chl is being reduced to its radical anion by ET from the NaY framework. The occurrence of this ET reaction is not surprising, considering recently reported results demonstrating ET from NaY to other powerful electron acceptors such as photoexcited methyl viologen ($E^*_{\text{red}} = 3.1 \text{ V}$)¹⁰² and photoexcited cyanosubstituted benzenes.¹⁰³ In addition, since the formation of the Chl radical anion is instantaneous on the time scales examined, a lower limit for the rate constant for ET from NaY to photoexcited Chl can be set at ca. $1 \times 10^8 \text{ s}^{-1}$. Therefore, these results demonstrate ultrafast ET from NaY to photoexcited Chl, and also confirm that the zeolite can participate as an electron donor.

A second significant observation that can be made concerning the photoexcitation of Chl in NaY is that both the Chl triplet and the Chl radical anion are present under deoxygenated conditions. As mentioned above, all Chl radical anion formation is static on the nanosecond time with no growth due to radical anion formation being observed after the laser pulse. However, in addition to the Chl radical anion, the Chl triplet is also observed following laser photolysis of Chl in evacuated NaY. These triplets decay on the μs time-scale with no concomitant growth due to the Chl radical anion. The absence of radical anion formation on these time scales indicates that the long-lived triplets do not react *via* slow reduction by the NaY framework. Thus, certain excited state Chl molecules abstract electrons from the zeolite framework in less than 10 ns, while other Chl molecules never abstract electrons, but instead deactivate from the triplet state *via* alternative reaction pathways. Therefore, ET from the framework to photoexcited Chl is either very rapid (i.e. $< 10 \text{ ns}$), or does not occur at all within the lifetime of the triplet state (i.e. $\sim 100 \mu\text{s}$).

At least two possible explanations can be envisioned to account for the simultaneous detection of both the Chl triplet and Chl radical anion in NaY. The first possibility is that the Chl radical anion does not originate from the Chl triplet. Photoexcitation of Chl initially generates the Chl singlet which intersystem crosses (ISC) very rapidly, with a rate constant of about $1.3 \times 10^{11} \text{ s}^{-1}$ in solution.²⁹⁵ Due to the correspondingly short lifetime of the Chl singlet ($\tau \sim 8 \text{ ps}$), the use of Chl as an ET

sensitizer is most often thought to involve triplet Chl. However, the Chl singlet rather than the Chl triplet may be responsible for Chl radical anion formation in NaY. In particular, observing both Chl radical anions as well as Chl triplets which do not undergo ET with the NaY framework might suggest that the radical anion is derived from the singlet and that the triplet is inert towards electron abstraction from NaY. Furthermore, recent studies using femtosecond laser flash photolysis have established that the Chl singlet can act as an electron acceptor within its short lifetime.²⁹⁵ Ultrafast electron transfer processes can effectively compete with intersystem crossing under certain conditions. In addition, the Chl singlet ($E_{\text{red}} = 2.77 \text{ V}$) is an even more powerful oxidant than the Chl triplet ($E_{\text{red}} = 2.15 \text{ V}$).²⁹⁵ On the basis of these considerations, it is not unreasonable to suspect that ET from NaY to singlet Chl accounts for Chl radical anion formation, while triplet Chl is not reduced by NaY and is therefore observed spectroscopically to decay *via* alternative pathways.

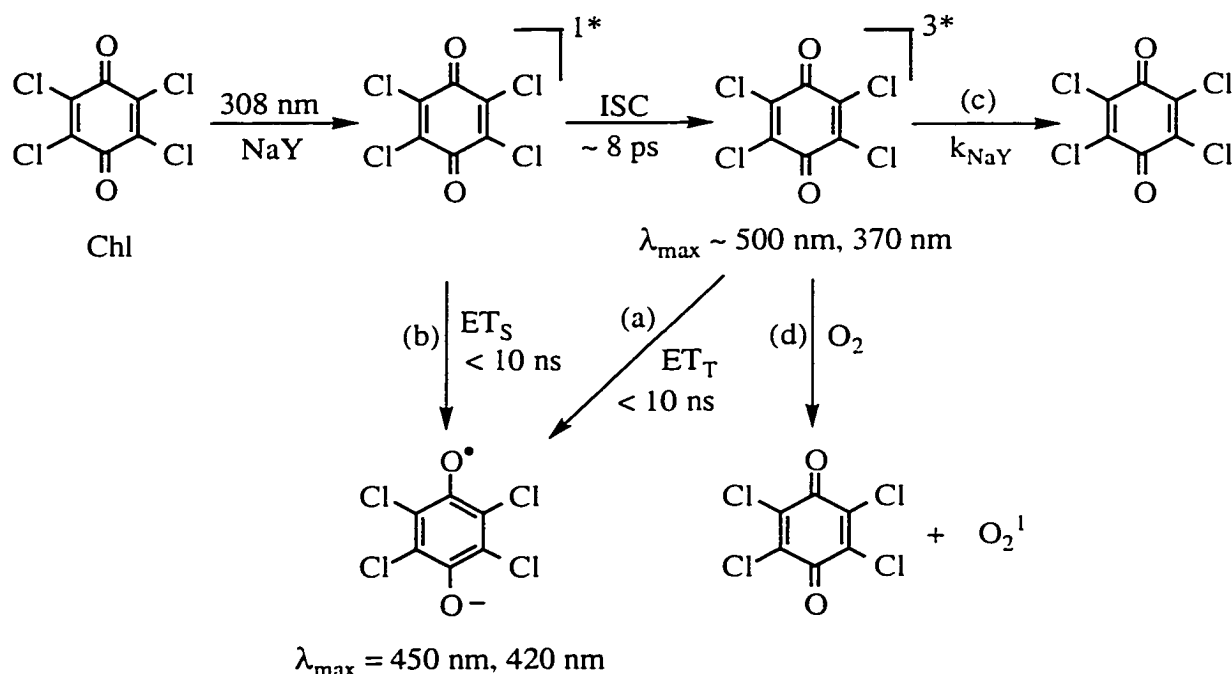
Upon closer consideration, however, generation of the entire radical anion population *via* singlet ET alone is unlikely. First, on the basis of previous observations of thermal electron donation from NaY zeolites to species with ground state redox potentials significantly smaller than triplet Chl,^{92,93} triplet Chl should be a sufficiently powerful oxidant to abstract an electron from the zeolite. Furthermore, the amount of radical anion observed under oxygen is significantly reduced such that the signal due to the radical anion in oxygen-saturated NaY is about half as intense as the signal due to the radical anion in evacuated NaY, Figure 4-5. As the Chl radical anion is not sensitive to oxygen, the reduction in the observed yield of radical anion must represent quenching of radical anion formation *via* oxygen trapping of the triplet state prior to electron abstraction.

A sensible explanation that accounts for these observations is that some, but not all, photoexcited Chl triplets accept electrons from the NaY framework. A reasonable rationale for this involves the heterogeneity of the zeolite interior, with the zeolite microenvironment possessing a distribution of oxidation sites of varied potential. Chl molecules in close proximity to strong donor sites are rapidly reduced upon photoexcitation, each generating a chloranil radical anion as well as a hole in the zeolite framework. Chl molecules not interacting with sites of sufficient oxidation potential, or too distant to diffuse to such sites to approach them within the μs triplet lifetime do not participate in ET reactions with the NaY framework. Instead, these molecules deactivate from the triplet state, most likely regenerating ground state chloranil, as the growth of photoproducts such as the semiquinone radical have never been observed. This is analogous to descriptions of photoexcited donors such as pyrene and anthracene within NaY,⁶⁹⁻⁷¹ whereby those photoexcited species in close proximity to a strong electron

accepting site undergo ionization, while those species distant from such a site undergo different reactions such as ISC to the triplet or absorbing a second photon to induce ionization.

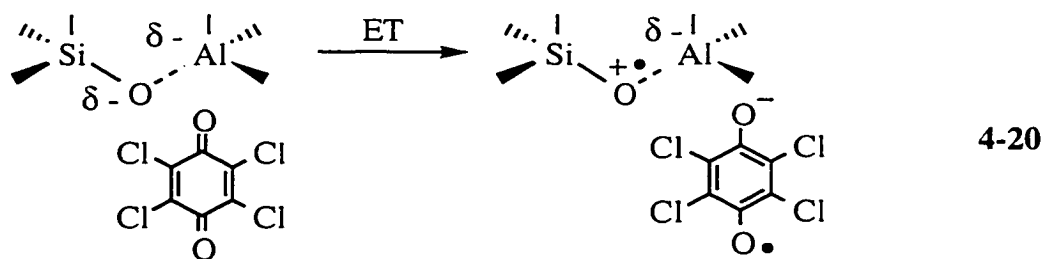
A summary of the processes discussed above for the behaviour of photoexcited Chl in NaY is shown in Scheme 4-7. The initial transient generated upon 308 nm laser excitation of Chl within NaY is the Chl singlet, which is not detected due to rapid ISC to the Chl triplet.²⁹⁵ The Chl radical anion is generated by ET from the zeolite framework to the Chl triplet, Scheme 4-7 path (a), and perhaps also to the Chl singlet, path (b), in less than 10 ns. The Chl triplets observed following the laser pulse do not decay *via* ET, but instead decay in the μs time regime under vacuum, most likely through deactivation to the ground state, path (c). In oxygen-saturated NaY, the Chl triplet is rapidly quenched, path (d), resulting in a concomitant reduction in the yield of Chl radical anion, path (a). Because paths (a) and (b) leading to the radical anion are so rapid, only partial quenching of the Chl radical anion is observed.

Scheme 4-7



The generation of the Chl radical anion upon photoexcitation of Chl within the cavities of NaY indicates that an electron is transferred from the zeolite framework to the Chl molecule. Correspondingly, this results in the zeolite radical cation, or a hole in the

framework. An intuitively obvious source of electron density for donation to a photoexcited acceptor is the lone pair electrons on the bridging lattice oxygen atoms, particularly those in $[\text{Si-O-Al}]^-$ sites. Studies of electron donation from NaY to included organic acceptors are consistent with this notion. For instance, photoreduction of pyrene within the cavities of alkali metal cation X and Y zeolites has been proposed to involve donation from oxygen atoms within $[\text{Si-O-Al}]^-$ sites.⁸⁹ This proposal is supported by the observation that increasing the electron density at this site by increasing the alkali cation size or decreasing the Si/Al ratio results in an increase in the relative yield of radical anion formation. In fact, the yield of pyrene radical anion was found to correlate nicely with the charge on the zeolite framework oxygen atom as determined by Sanderson electronegativity. Similarly, electron donation from alkali metal cation Y zeolites to photoexcited methyl viologen has been rationalized by suggesting $[\text{Si-O-Al}]^-$ bridges as the electron-donating sites.¹⁰² In this case the lifetime of the resulting methyl viologen radical cation was found to increase with alkali counterion size, and therefore charge density on the framework oxygen. Decay of the methyl viologen radical cation was attributed to BET with the electron donation sites which should become slower as the charge density, and hence electron donating strength, of the framework oxygen atom increases. Furthermore, recent EPR investigations of thermal ionization of *o*-chloranil (tetrachloro-1,2-benzoquinone) in cesium acetate impregnated CsX and CsY zeolites suggest that the hole generated upon electron donation is localized on the oxygen atoms adjacent to the aluminum centers.⁹⁴ On the basis of these results, the dominant electron donating sites responsible for reduction of photoexcited Chl in NaY are proposed to be the lattice oxygen atoms within $[\text{Si-O-Al}]^-$ bridges, eq. 4-20.



In light of this discussion, the time-resolved decays of the chloranil radical anion are of interest. Under oxygen, in the absence of any triplet absorption, the radical anion decay exhibits at least two distinct components. Along with a very long-lived component, a considerably faster decay is also visible, Figure 4-7 inset. These distinctly

different rate constants for radical anion decay may be related to the heterogeneity of the zeolite interior and its redox sites. For instance, if the framework contains sites of various oxidation potentials, some might be more susceptible to BET than others. Radical anions generated by weaker donor sites might undergo BET on observable time scales, while those associated with more oxidative sites might resist BET long enough for either the radical anion or hole to escape. This type of behaviour would be consistent with the two distinct decays observed for the radical anion. The existence of both singlet and triplet radical ion pairs could possibly be playing a role in the highly significant variations in the radical anion lifetime. Thus more experimental results are required to understand the nature of the electron acceptor and corresponding donor site(s) in NaY.

Regardless of the precise nature of the electron donor and acceptor, the substantial lifetime of the resulting radical anion is undeniable and represents an important aspect of these experiments. A significant fraction of the transients show no decay over more than 800 μs . This lack of observable decay suggests that the radical anion/zeolite hole is quite resistant to BET which is traditionally a significant barrier to deriving useful chemistry from photoinduced electron transfer. Studies of photoinduced electron transfer between intercalated species have demonstrated a substantial reduction in BET efficiencies within zeolite supercages, but the singlet ion pairs typically decay in the picosecond to μs time regime under most circumstances.¹⁵⁸⁻¹⁶¹ Experiments involving framework donation to zeolite-incorporated methyl viologen¹⁰² or 1,2,4,5-tetracyanobenzene,¹⁰³ however, have observed significant lifetimes for the electron transfer products. For instance, in Y zeolites such as HNaY, LiNaY and NaY, the methyl viologen radical cation was found to decay over a hundred to several hundred μs . This decay is attributed to BET, based on the corresponding appearance of ground state methyl viologen. Furthermore, similar experiments in more basic zeolites such as RbY and CsY found the radical cation to persist for several hundred minutes. Some decay observed over these time scales was again attributed to BET, but the coincident growth of the ground state was not shown. Thus the long lifetime of the Chl radical anion is consistent with the available information. The explanation for this behaviour might be related to some type of ion-pair escape such that the generation of long-lived charge separated states due to both favorable electrostatic stabilization and spatial separation within the zeolite matrix is possible.

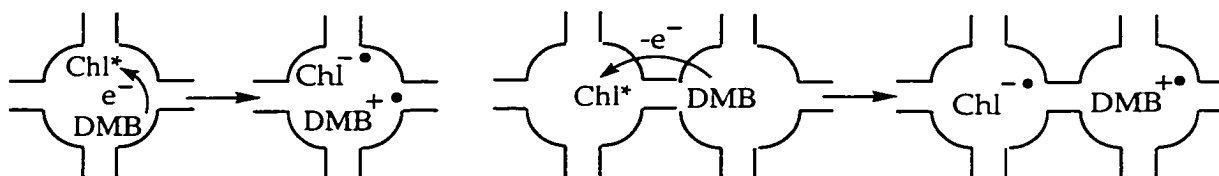
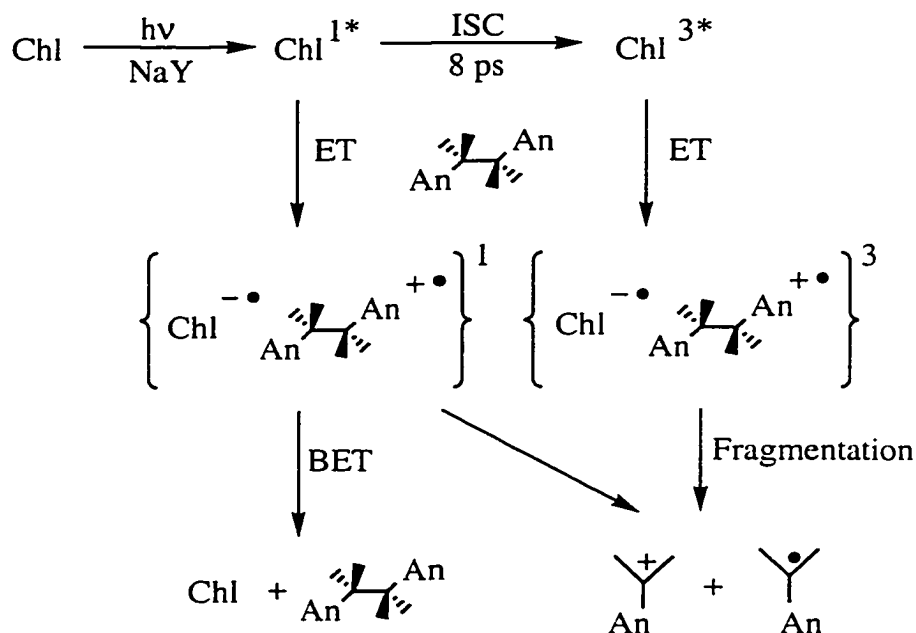
4.3.2 Mechanism(s) for Intrazeolite Electron Transfer Following Selective Excitation of an Electron Acceptor in NaY

Every molecule of Chl that abstracts an electron from NaY generates a corresponding hole in the framework. Little is currently known about the loci, reactivity, mobility and ultimate fate of these holes. One means of probing zeolite holes is to generate them in the presence of secondary electron donors with which they might react. The secondary donor considered in this study is DMB. Selective photoexcitation of Chl in NaY containing coadsorbed DMB leads to the observation of the Chl triplet, the Chl radical anion, and the 4-methoxycumyl cation, immediately following the 308 nm laser pulse. As previously discussed, the Chl triplet and the Chl radical anion are generated upon laser photolysis of Chl in NaY in the absence of a secondary electron donor, where the Chl radical anion is produced by electron donation from the zeolite framework, while the simultaneous observation of the triplet indicates that not all photoexcited Chl molecules undergo ET with the framework. Therefore, the fact that the Chl triplet and Chl radical anion are detected when Chl is photoexcited in NaY containing DMB is not surprising. The generation of the 4-methoxycumyl cation, however, clearly indicates that additional reactions occur when DMB is present within the zeolite matrix. Specifically, since the 4-methoxycumyl cation originates from fragmentation of the DMB radical cation within the laser pulse (*vide supra*), the observation of the carbocation indicates that the DMB radical cation is generated upon 308 nm excitation of Chl in NaY containing coadsorbed DMB. Since DMB does not absorb at 308 nm, and control experiments establish that no transients are generated upon 308 nm laser photolysis of NaY containing only DMB, direct 308 nm photoexcitation of DMB is not responsible for the formation of the DMB radical cation. Instead, the DMB radical cation must be generated due to reactions initiated by photoexcited Chl in NaY.

Two distinct mechanistic schemes can be applied to rationalize the formation of the DMB radical cation upon photoexcitation of Chl in NaY containing coadsorbed DMB. Perhaps the most immediately obvious mechanism involves ET from ground state DMB to photoexcited Chl, in a manner analogous to solution, Scheme 4-8 (a). Depending on the rate constant for ET in NaY, this process could involve either singlet or triplet Chl, generating the corresponding singlet and triplet radical ion pairs. The resultant radical ion pairs could decay back to the ground state *via* BET, or if BET is sufficiently slow, the DMB radical cation may have ample time to undergo fragmentation to the 4-methoxycumyl cation as observed experimentally. This ET mechanism, as presented in Scheme 4-8 (b), would most likely involve a direct interaction between

photoexcited Chl and a DMB molecule in close proximity, either within the same cage or in one of the neighbouring cages.

Scheme 4-8



Alternatively, the formation of the Chl radical anion upon photoexcitation of Chl in NaY containing no DMB suggests another mechanism may exist for the formation of the DMB radical cation. In this case, the initial photochemical step, ET from the NaY to photoexcited Chl to generate the radical anion and a hole in the framework, Scheme 4-9 (a), continues to take place in the presence of DMB. Migration of this hole to a cavity containing DMB followed by ET from the DMB to the zeolite hole then generates the

zeolite matrix and it is very unlikely that direct PET cannot completely account for the generation of the ET products.

Other evidence for radical cation, and carbocation, formation by hole migration lies in the effect of DMB content on the yields of the radical anion and carbocation. In particular, if the only mechanism for ET were direct transfer of the electron from DMB to Chl, then every carbocation observed should be accompanied by a radical anion. Thus, if adding DMB increased carbocation formation, a concomitant increase in radical anion formation should be observed. This is especially true since both the carbocations and the radical anions are long-lived under the experimental conditions.

The fact that the two transients resulting from ET do not show the same dependence on DMB concentration therefore is strong evidence for the presence of a redox partner other than DMB. The redox partner is proposed to be the zeolite framework. In this case, the ratio of initially formed holes and radical anions must be the same. However, since radical anion formation is in principle independent of DMB concentration, while the fraction of holes trapped by DMB to generate the carbocation is concentration dependent, the yield of carbocations should increase as the concentration of DMB increases, while the radical anion yield will remain unchanged.

The results described earlier show that increasing DMB content does in fact increase the yield of the carbocation, but instead of remaining constant, radical anion yield decreases. At the same time, the relative yield of the triplet also decreases. A reasonable explanation for the decrease in the radical anion and triplet yield is that singlet intersystem crossing to the triplet is intercepted at sufficiently high concentrations of DMB. The singlet radical ion pairs formed in this way will then rapidly collapse by BET to ground state Chl and neutral DMB. As a result, triplet yield would be reduced, as would any radical anions that might be produced by redox reactions of the singlets. On the other hand, oxidation of the framework by singlet Chl is likely to be too rapid to be affected by DMB; thus, the number of holes generated remains unchanged. Therefore, increasing DMB content introduces a DMB dependent pathway that depletes the triplet and the radical anion, while the reaction pathway that provides increasing carbocation formation as DMB content increases remains unchanged.

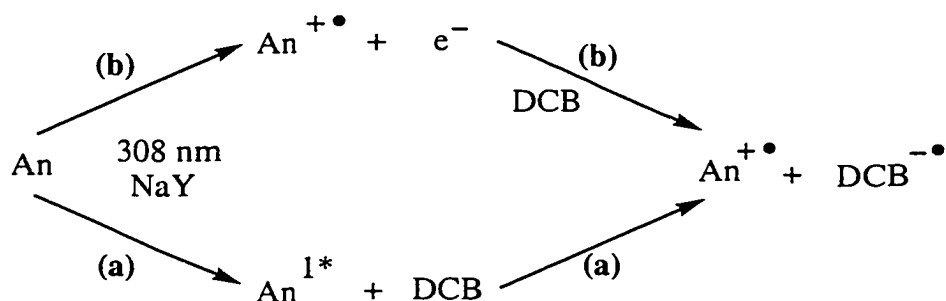
Of course, the behaviour of the remaining triplets will be DMB dependent. In particular, triplet Chl can undergo direct ET with DMB to give the carbocation and the radical anion. Thus, some triplets that are unproductive in the absence of DMB now produce electron transfer products. Also, since triplet Chl has a longer inherent lifetime than the singlet, direct ET might intercept oxidation of the framework by Chl generating triplet radical ion pairs that would separate and give detectable radical anions and

carbocations. This process, however, would give products that are ultimately the same as those that would otherwise have been observed upon triplet Chl induced oxidation of the framework. Thus, the overall effect of increasing DMB content on the products from the triplet is to increase the yield of the radical anion and the carbocation. However, since the results show that overall radical anion yield decreases as a function of DMB, we can conclude that any increases in radical ion formation from the triplet in the presence of DMB are more than compensated for by the decrease in initial triplet formation.

4.3.3 Mechanism(s) for Intrazeolite Electron Transfer Following Selective Excitation of an Electron Donor in NaY

The experimental results described earlier clearly demonstrate that photoexcitation of An in NaY embedded with DCB molecules leads to the generation of An radical cations and DCB radical anions within the 10 ns laser pulse. As was the case upon photoexcitation of Chl in the presence of a secondary electron donor, two mechanistically distinct methods can be envisioned for radical anion formation following photoexcitation of anethole. The first involves a PET reaction whereby an electron is transferred from a DCB acceptor in close contact with an excited state An donor, Scheme 4-10 path (a). The second involves photoionization of the An donor as observed in the absence of DCB, followed by subsequent trapping of the electron by a DCB molecule elsewhere within the zeolite matrix, Scheme 3 path (b). In this latter scenario the DCB plays the role of a secondary electron trap (the first being the zeolite) rather than a redox partner in a direct PET reaction.

Scheme 4-10



Certainly direct PET is expected to play a role in radical ion generation, particularly at high loadings where the probability of double cage occupancy and

occupancy of adjacent cages is quite high (see section 4.3.4). Furthermore, the observed quenching of An fluorescence by DCB clearly demonstrates that direct interactions between photoexcited An and DCB do take place within the cavities of NaY. Although the steady-state fluorescence experiments do not explicitly establish the mechanism of interaction, the detection of the An radical cation and the DCB radical anion following nanosecond laser photolysis of these precursors in NaY suggests a mechanism for fluorescence quenching involving ET from ground state DCB to photoexcited An. Furthermore, quenching by energy transfer is unlikely due to the high singlet energy of DCB, 98.6 kcal/mol,⁴⁶⁴ as compared to the singlet energy of 93.1 kcal/mol for An.⁴⁶⁵ Therefore, observed quenching of An fluorescence by DCB is most likely due to ET from DCB to An molecules in close proximity.

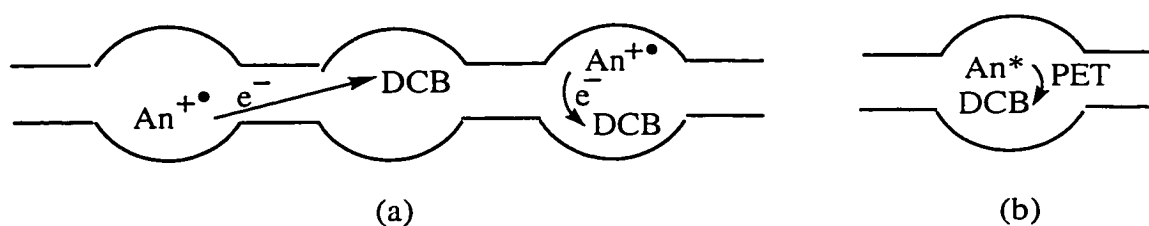
It is important to recognize, however, that only those An molecules that do not undergo photoionization are able to fluoresce. Photolysis of An in NaY is expected to generate some excited state species which photoionize, and others which do not, depending on the location of the An molecules and the interaction of these molecules with the zeolite framework. Consistent with this notion are previously reported studies of laser photolysis of pyrene and anthracene in NaY which propose that molecules associated with so-called "active sites" undergo ionization upon the absorption of a single photon, while other species not associated with these sites do not photoionize, but instead undergo alternative reactions,⁶⁹⁻⁷¹ such as emission. Therefore, the singlet species being observed in steady-state fluorescence studies in the absence of DCB are different from those responsible for the formation of the radical cations being observed in time-resolved experiments. Furthermore, varying the light source from the steady-state lamp to the laser pulse is likely to favor the relative proportions of molecules which undergo photoionization. Therefore, although the steady-state measurements indicate that ET quenching of photoexcited An by DCB is possible, and that contact interactions between these species exist in NaY, they do not by any means indicate that direct PET is the major pathway for the radical ions detected in nanosecond time-resolved experiments.

In fact, the notion that photoionization, rather than direct PET, continues to be the dominant mechanism for radical cation generation in the presence of DCB, is suggested by the observation that the yield of An radical cation remains approximately constant for a single An concentration regardless of DCB concentration. This indicates that enhanced generation of An radical cations by PET with DCB, Scheme 4-10, path (a), as may have been predicted from steady-state measurements, does not occur upon laser excitation of An in NaY with coadsorbed DCB, or that those additional radical ions generated by direct PET quenching are not observed due to rapid BET. A slight decrease in the yield

of An radical cation is evident at the extremely high loading of one DCB molecule per cavity. Under these circumstances, direct PET quenching and rapid BET is probably competitive with photoionization and reduces radical cation formation by photoionization. Overall, it appears that direct PET can take place between photoexcited An and DCB within the cavities of NaY, particularly at higher loadings, but this reaction does not exert a significant influence on the radical ions observed in laser photolysis studies, where the dominant mechanism of ion formation is *via* photoionization followed by electron migration and trapping, Scheme 4-10, path (b).

More convincing evidence that photoionization followed by electron migration and trapping is the significant mechanism for radical anion generation is obtained from experiments employing nitrous oxide. In the presence of nitrous oxide, a well known electron scavenger, no DCB radical anion is detected after laser photolysis of An in NaY containing DCB, Figure 4-27. This observation is consistent with a mechanism whereby nitrous oxide scavenges the photoionized electron before it can be captured by DCB, therefore inhibiting radical anion formation. An obvious interpretation of this result is that the electron must travel a finite distance between the photoexcited An and the DCB in order to be intercepted by nitrous oxide, Scheme 4-11 (a). The fact that DCB radical anion formation is not completely quenched by N₂O at high loading levels, Figure 4-32 (d), where some detectable radical ion pairs are likely formed by PET indicates that direct PET is not affected by N₂O, Scheme 4-11 (b). This reinforces the conclusion that N₂O quenching involves capture of the electron.

Scheme 4-11



The experimental investigations of hole migration described earlier employed an electron donor, DMB, whose radical cation undergoes rapid fragmentation. The rapid reaction of the radical cation prohibits BET reactions that are slower than C-C bond cleavage, and therefore eliminates the possibility of monitoring slow BET using nanosecond diffuse reflectance spectroscopy. However, a different situation exists for studies of electron migration employing the An/DCB redox pair. In this case, the primary

redox products are spectroscopically observable and decay traces of the radical ions, for example, Figures 4-30 and 4-31, can be monitored following laser photolysis, yielding the corresponding decay rate constants, Table 4-2. The appearance of the decay traces and the calculated rate constants for decay of the DCB radical anion and the An radical cation are generally quite similar. This suggests that the decay mechanism of the radical ions most likely involves mutual annihilation *via* BET to regenerate ground state An and DCB. Notably, the greatest similarity in the rate constants for the decay of the two radical ions is found at the highest concentration of DCB where some detectable radical ions are formed by direct PET. At lower concentrations of DCB the decay of the radical anion is somewhat faster than the decay of the radical cation, indicating that direct BET may not be the only mechanism for decay of these widely separated radical ion species.

It is also significant to note that the ions are very long-lived, decaying over hundreds of μs and longer, with decay rate constants on the order of 10^4 and 10^3 s^{-1} for both the An radical cation and DCB radical ion. The long lifetimes of these radical ions indicate that the zeolite environment provides a significant degree of stabilization to the charge separated state. Although similarly long-lived charge separated states have previously been reported, in these cases, either the electron acceptor,^{158,159} or both the electron donor and the electron acceptor^{160,161} were positively charged species. Strong Coulombic interactions are expected to exert distinct influences on the starting reagents, as well as the radical cation pair generated by PET in these systems, as compared to the radical cation-radical anion pair generated by PET between two neutral species. In fact, Hashimoto recently reported rate constants of ca. 10^7 to 10^9 s^{-1} for BET between contact radical ion pairs generated by PET in charge-transfer complexes consisting of neutral species.⁴⁶ Although the BET was slowed by approximately an order of magnitude compared to solution, the results indicate that BET between contact ion pairs within zeolites can be rapid. In light of these observations, the long lifetime of the An radical cation-DCB radical anion pair further supports the notion that these species achieve enhanced stabilization due to their spatial separation within the zeolite.

4.3.4 *Estimating the Distance of Electron and Hole Migration in Zeolite NaY*

The previously described experimental results suggest that both electron and hole migration can occur between electron donors and acceptors spatially separated within the NaY matrix. In order to confirm this possibility and to estimate the intrazeolite distances for electron and hole migration, consideration of the data in more detail is necessary. Although no information concerning the rate constants of these redox processes is

available, models of the radical ion yield as a function of adsorbate concentration can generate useful insight. In particular it is necessary to establish, based on the concentration of adsorbates and their distribution within the zeolite matrix, that the observed redox products cannot be accounted for strictly by contact interactions, and therefore determine over what distances charge migration is feasible.

Experimental data concerning the yields of redox products as a function of the concentration of redox reagents are examined herein using two independent models. Each model explicitly assumes that the distribution of molecules within the zeolite framework is determined by the concentration of adsorbed species. In other words, the molecular guests distribute in a statistically random manner. As previously mentioned, this assumption is usually valid provided the molecules are smaller than the zeolite dimensions, the loading levels are not extremely high (i.e. > 1 molecule per cavity), and there is no significant intermolecular interactions between the adsorbates which would influence the random adsorption process of individual species. These criteria are fulfilled by the reagents employed in the current study, and each species is expected to distribute in a random fashion within the matrix. Furthermore, no evidence could be obtained to indicate the contrary, and evidence against non-statistical aggregation was noted. For instance, experiments carried out on composites of Chl and DMB in NaY found no obvious change in transient yields or kinetics after several weeks of sample aging during which time aggregates of guest molecules would have equilibrated through the framework. As well, the formation of charge transfer complexes, which is predicted for aggregates for Chl and DMB, was not detected. Based on such considerations, a statistically determined distribution of redox molecules is assumed within the samples under investigation.

The Perrin model^{396,466,467} is often used to describe quenching of an excited state species in situations where no motion is possible within the excited state lifetime. In this approach, the excited state is imagined to be surrounded by an “active-sphere” of volume, V , and radius, r . According to the Perrin formulation, if a quencher is present within the sphere, then quenching will take place instantaneously with unit efficiency. However, if the quencher is outside the active sphere, quenching will not take place, and the excited species decays as it would in the absence of quencher. As a result, the Perrin treatment is a static model, and has often been applied to studies of the quenching of photoexcited emitters by energy transfer and ET. In its most general form it predicts a logarithmic decline in emitter intensity with increasing quencher concentration, eq. 4-21,

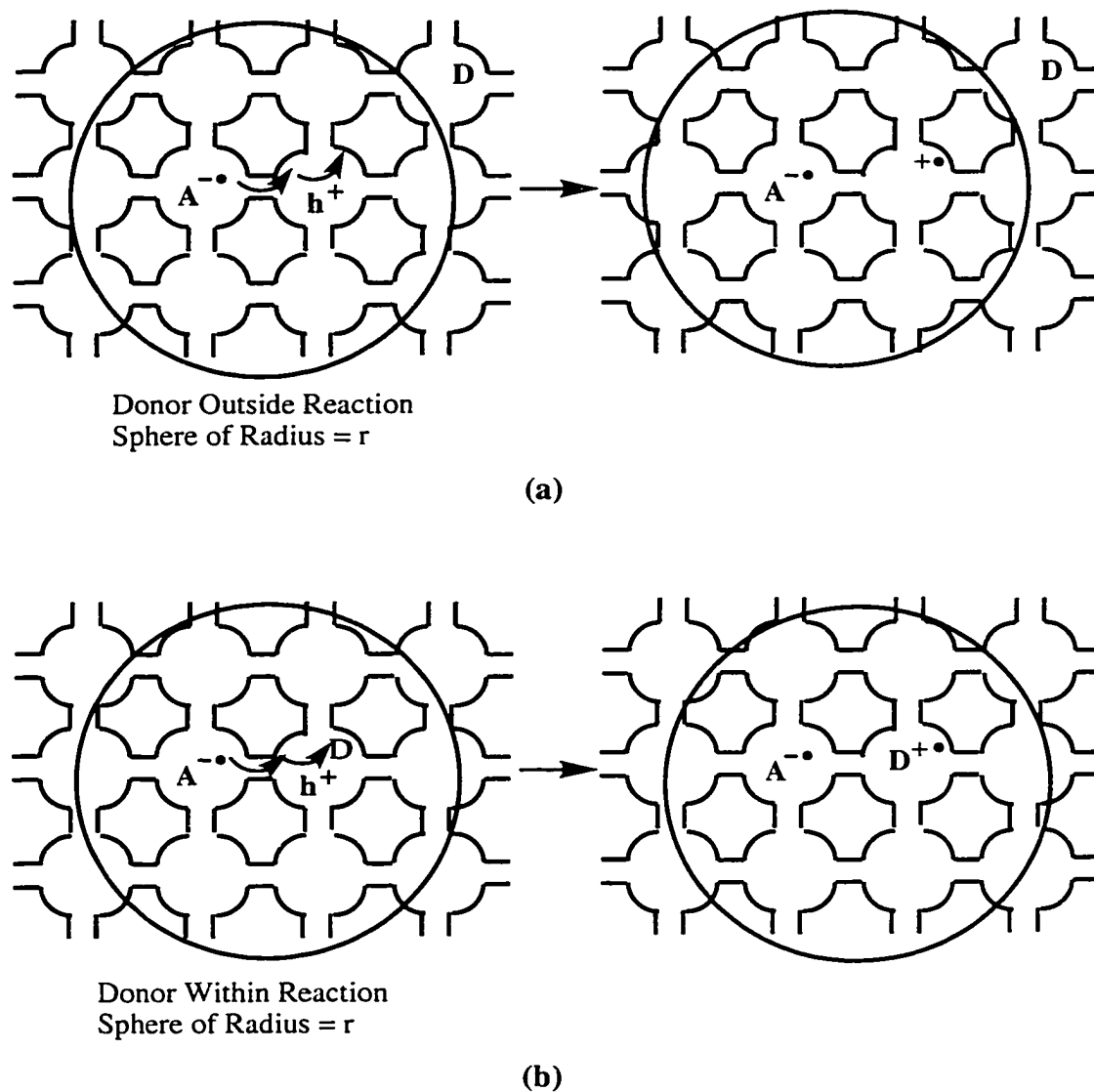
$$\ln(\Phi_0/\Phi) = VN[Q] \quad 4-21$$

where Φ_0 and Φ are the quantum yields of emission in the absence and the presence of quencher respectively, V is the volume of the active quenching sphere, equal to $4/3\pi r^3$, and N is Avagadro's constant. In accordance with the Perrin model, a plot of the natural logarithm of emission intensity as a function of quencher concentration should be linear, and the radius of the active quencher sphere, r , can be extracted from the slope. As a result, the Perrin model can be applied to estimate the distances over which quenching reactions may occur in situations where the possibility of diffusion is eliminated.

The Perrin model has been applied by Dutta *et al.* to the quenching of photoexcited $\text{Ru}(\text{bpy})_3^{2+}$ by MV^{2+} in zeolitic systems.⁴⁶⁸ In this case a Perrin radius of approximately 13 Å was determined for the quenching reaction. As this value is very close to the sum of the molecular radii of the molecules involved, the quenching was proposed to proceed *via* molecular contact mediated through the zeolite pores. Similarly, Thomas and coworkers used the Perrin model to predict the distance over which ET quenching of excited state pyrene by metal ions, Cu^{2+} ³⁵ and Tl^+ ,³⁶ can take place in zeolite X. In addition, the Perrin model has been extended to include reactions in zeolites which do not involve excited state species, using it to estimate the migration distance of the hydrated electron within NaY zeolites to a MV^{2+} trap.⁸² The electron was generated radiolytically, and analysis of the yield of methyl viologen radical cation according to Perrin model found that the hydrated electron can travel up to 30 Å.

Based on the nature of the model and the successful application to intrazeolite reactions, including one considering electron motion directly, the Perrin model represents a reasonable method for examining the current data and obtaining estimates for the distance of electron and hole migration. With regards to the migration of electrons and holes within NaY, the Perrin formulation can be envisioned as shown in Scheme 4-12. This scheme depicts hole migration, but an analogous picture exists for electron migration. As described by the Perrin model, the hole, initially generated by ET from the NaY framework to the photoexcited acceptor, is considered to be surrounded by an imaginary reaction sphere of radius, r , the magnitude of which determines the distance over which the hole can migrate. If the donor is outside this sphere, Scheme 4-12 (a), trapping of the hole by this donor will not take place, and the donor radical cation will not be observed. In this case the hole remains on the zeolite framework. Conversely, if the donor is within this sphere, Scheme 4-12 (b), trapping will take place and the donor radical cation will be detected.

Scheme 4-12



First consider hole migration as studied between photoexcited Chl and DMB. In this case, as the yield of DMB is increased at a constant concentration of Chl, the yield of the redox product, the 4-methoxycumyl cation, is found to increase, as shown in Figure 4-17. The general Perrin formulation, given by eq. 4-21, cannot be applied directly to these data, since the quantity being considered is formed by the reaction of interest, rather than being quenched. However, the exponential decrease in yield as a function of quencher concentration predicted by the Perrin model, can be rewritten according to eq. 4-22,

$$Y/Y_{\infty} = 1 - \exp(-VN[Q])$$

4-22

where Y and Y_{∞} represent the observed yield of product formed in the reaction, and the maximum possible yield of product in the reaction, respectively. An accurate value of Y_{∞} may be obtained from the experimental data if sufficiently high concentrations of quencher are used. However, it can also be determined by extrapolating the data according to the model. Thus a plot of $((Y/Y_{\infty}) - 1)$ versus $[Q]$ should be exponential with a coefficient of 1. The value of Y_{∞} can be adjusted in order to fulfil the requirements of the model. Manipulation of eq. 4-22 gives an equation analogous to the general Perrin formula, eq. 4-23.

$$-\ln(1 - Y/Y_{\infty}) = VN[Q] \quad 4-23$$

Plotting the data according to eq. 4-23, where Y represents the yield of the 4-methoxycumyl cation obtained from the transient diffuse reflectance experiments, and $[Q]$ represents the concentration of DMB in NaY in moles per liter, yields a nicely linear correlation as predicted by the Perrin model, Figure 4-36. Similar plots are observed for other data sets in which the Chl loadings have been varied from $\langle S \rangle = 0.02$ and $\langle S \rangle = 0.08$. In each case the slopes of the plots match reasonably well, and the average radius for the reaction sphere is determined to be $(27 \pm 2) \text{ \AA}$. This is significantly larger than the sum of the molecular radii of the molecules. In fact, as shown by the shaded region in Figure 4-36, the slopes of the Perrin plots would have been dramatically more shallow if the reaction was restricted to contact interactions between these molecules.

A similar analysis was carried out for the An/DCB system. In this case, examination of both the yield of the product formed in the redox reaction, the DCB radical anion, according to eq. 4-23, as well as the yield of the electron "quenched" by the reaction, according to eq. 4-21, where quantum yield is replaced by transient yield, Y_s is possible. The yields of both the DCB radical anion and zeolite trapped electron exhibit variations predicted by the Perrin model, and very similar reaction sphere radii are obtained from a the both sets of data, Figure 4-37. The average reaction radius obtained from considering the radical anion and electron yields in two independent trials is $(18 \pm 2) \text{ \AA}$. Again this reaction radius is considerably larger than the sum of the molecular radii, and the slope of the Perrin plot predicted for ET due to contact interaction (shaded region Figure 4-37) is notably more shallow than the experimental slopes.

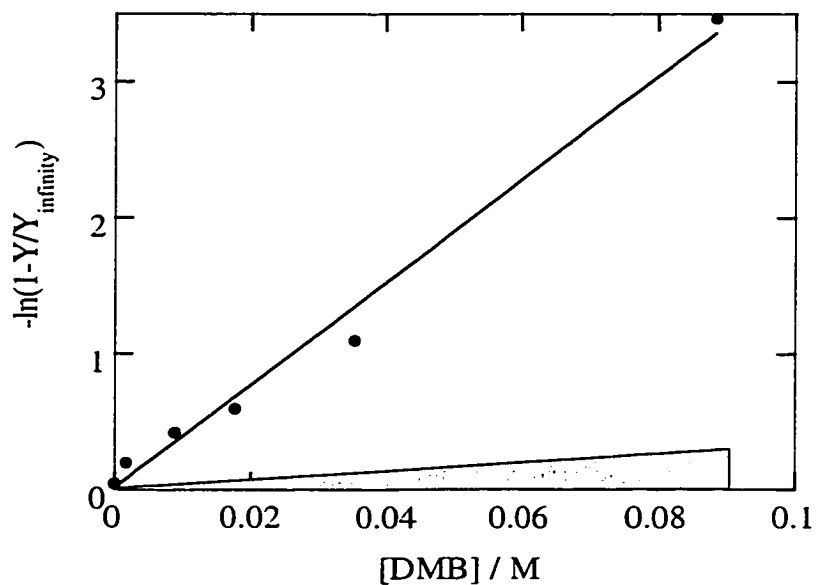


Figure 4-36. Perrin plot of $-\ln(1-Y/Y_{\infty})$ against DMB concentration, where Y represents the yield of the 4-methoxycumyl cation in NaY. The shaded region indicates the behaviour expected for DMB and Chl molecules in direct contact.

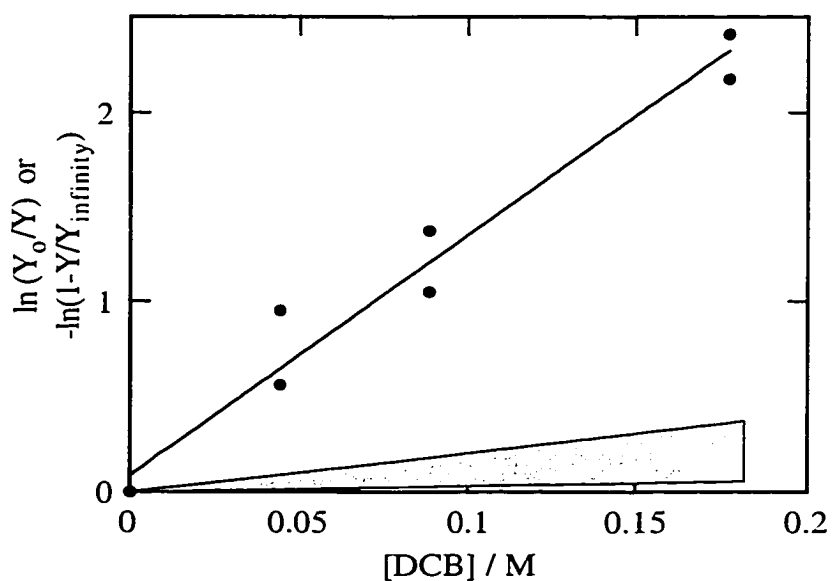
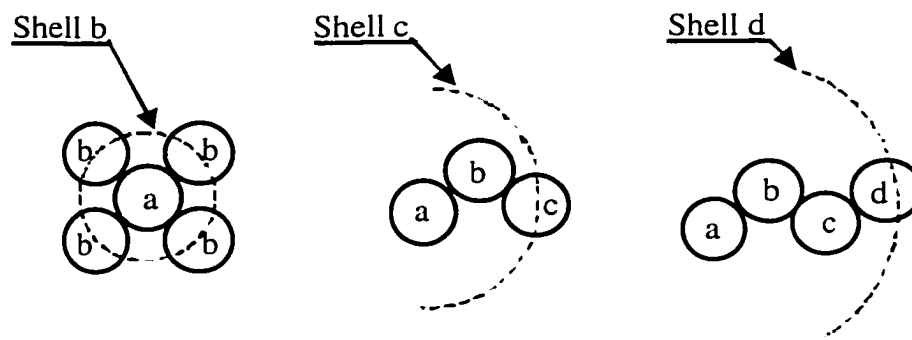


Figure 4-37. Perrin plot of $-\ln(1-Y/Y_{\infty})$ or $\ln(Y_0/Y)$ against DCB concentration, where Y represents the yield of the DCB radical anion and trapped electron, respectively in NaY. The shaded region indicates the behaviour expected for DCB and An molecules in direct contact.

In solution and many types of heterogeneous media, a continuum of intermolecular distances between reagents is possible. In contrast, the regular structure of zeolites restricts possible intermolecular distances to discrete values defined by the number of unfilled cages between molecules. In addition, relatively large organic molecules cannot move within the cage and channel structure of the zeolite on the time scales of chemical reactions such as PET. Due to the specific, well-defined structural arrangement of adsorbates, formulation of a simple model of the molecular distribution is possible, and hence intermolecular interactions between adsorbates in zeolites. Specifically, from the structure of Y zeolites, the allowable intermolecular distances between adsorbates can be determined, and knowing the loading of adsorbate molecules, the fraction of reagents separated by 0, 1, 2, and higher numbers of empty supercages. Such an approach to mapping the distribution of adsorbates within zeolites has been adopted by Dutta and coworkers to understand intermolecular reactions between NaY-encapsulated $\text{Ru}(\text{bpy})_3^{2+}$.⁴⁶⁹ The application of this model to the distribution of electron donors and acceptors in NaY and the interpretation of the ET chemistry within this model is now described.

Scheme 4-13



The first step in applying the model is to consider an arbitrary supercage, **a**, Scheme 4-13. Due to the tetrahedral arrangement of supercages within the Y zeolite, supercage **a** will be surrounded by four neighbouring supercages, denoted **b**. As the diameter of each supercage is approximately 13 Å, the distance from the center of supercage **a**, to the center of any **b** supercage is about 13 Å. Therefore, the centers of the 4 **b** supercages are equidistant from the center of supercage **a**, and form a “shell”, shell **b** with a radius of 13 Å. Correspondingly, each of the 4 supercages in shell **b** has 3 additional neighbours which are also equidistant from supercage **a**. These 12 supercages

generate a third shell, shell **c**, which can be determined from geometric considerations to be about 21 Å from the center of shell **a**. A series of successive shells and the distance of these shells from the central supercage **a** can likewise be constructed, Table 4-3.

Table 4-3. Intracavity distances in NaY obtained from the "shell model", and intermolecular distances between Chl and DMB, and An and DCB within the cavities.

Shell	Cages / Shell	Shell Radius / Å	Estimated Chl-DMB Distance / Å	Estimated An-DCB Distance / Å
a	1	-		
b	4	13.0	2.3	4
c	12	21.2	11	12
d	12	24.9	14	16
e	6	30.0	19	21
f	12	32.7	22	24
g	24	36.8	26	28
h	12	39.0	28	30

From the radius of each shell and the size of adsorbed molecules the intermolecular distances between a reagent in supercage **a** and a reagent in any of the supercages comprising the surrounding shells can be estimated. For instance, the periphery-periphery distance between a molecule of Chl occupying supercage **a**, and a molecule of DMB occupying a supercage in a surrounding shell can be determined by subtracting the molecular radii of Chl and DMB from the shell radius. These intermolecular distances are also reported in Table 4-3, along with the analogous interatomic distances between An and DCB. In each case, the molecular "radii" correspond to half the longest interatomic distance determined from a molecular model constructed with standard bond lengths and bond angles. The longest interatomic distances thus determined are 6.3 Å, 15 Å, 10 Å and 8.1 Å, for Chl, DMB, An, and DCB, respectively.

In order to map the distribution of molecules within the NaY matrix, the probability for occupancy of cavities within each shell as a function of sample concentration must be determined. Consider, for example, NaY samples containing a constant concentration of Chl and varied concentrations of DMB. Starting with a single supercage **a**, that is occupied by a Chl molecule, the probability that a DMB molecule will be within the cavities of adjacent shells can be determined using the occupancy

levels of DMB, assuming that the distribution of DMB is not influenced by the presence of Chl (this is a reasonable assumption considering the relatively low loading levels of each species and the fact that both can fit within the same cavity if necessary).

As an example, consider a DMB occupancy of one molecule in every 10 cavities ($\langle S \rangle = 0.1$). Within the first shell surrounding the central Chl-containing supercage, shell **b**, the probability that any single cavity is occupied is 0.1. Likewise, the probability that a single cavity within this shell is empty is 0.9. The probability that all four cavities of shell **b** are empty is $(0.9)^4$ or 0.656, and therefore, the probability that one or more of the cavities in shell **b** is occupied by a DMB molecule is 0.344. For subsequent shells it is necessary to consider the total number of cavities in all shells surrounding the central cavity. So, for shell **c**, the total number of cavities surrounding cavity **a** are the 16 cavities in shell **b** and shell **c**. The probability that all 16 cavities are empty is $(0.9)^{16}$, or, 0.185. Therefore, the probability that at least one is occupied is 0.815. The probability that this occupancy is in shell **c** can be obtained by subtracting the probability of shell **b** occupancy, 0.344, from the total probability of occupancy, 0.815, to give 0.471 as the occupancy probability of shell **c** at a DMB occupancy level of 0.1. Similarly, the probability that each successful shell is occupied can be determined until the majority of molecules are accounted for. Table 4-4 presents the calculated occupancy probabilities for successive shells at various concentrations of DMB within NaY, and Table 4-5 presents similar results for various concentrations of DCB within NaY.

Table 4-4. Distribution of DMB in various shells surrounding a central NaY cavity as a function of DMB occupancy level.

Shell	Chl-DMB distance / Å	DMB Distributions at Various DMB Occupancies				
		$\langle S \rangle = 0.1$	$\langle S \rangle = 0.04$	$\langle S \rangle = 0.02$	$\langle S \rangle = 0.01$	$\langle S \rangle = 0.002$
b	2.3	0.34	0.15	0.078	0.039	0.0080
c	11	0.47	0.33	0.20	0.11	0.023
d	14	0.13	0.20	0.16	0.097	0.023
e	19	0.024	0.069	0.065	0.044	0.011
f	22	0.020	0.097	0.11	0.081	0.022
g	26	0.0073	0.096	0.15	0.13	0.043
h	28	0	0.022	0.052	0.056	0.02
Total		0.99	0.96	0.81	0.56	0.15

Table 4-5. Distribution of DCB in various shells surrounding a central NaY cavity as a function of DCB occupancy level.

Shell	An-DCB distance / Å	DCB Distributions at Various DMB Occupancies			
		$\langle S \rangle = 0.05$	$\langle S \rangle = 0.1$	$\langle S \rangle = 0.2$	$\langle S \rangle = 1$
b	4	0.19	0.34	0.59	1
c	12	0.37	0.47	0.38	
d	16	0.21	0.13	0.028	
e	21	0.06	0.024	0	
f	24	0.08	0.02	0	
g	28	0.07	0.007	0	
h	30	0.005	0	0	
Total		0.99	0.99	1	1

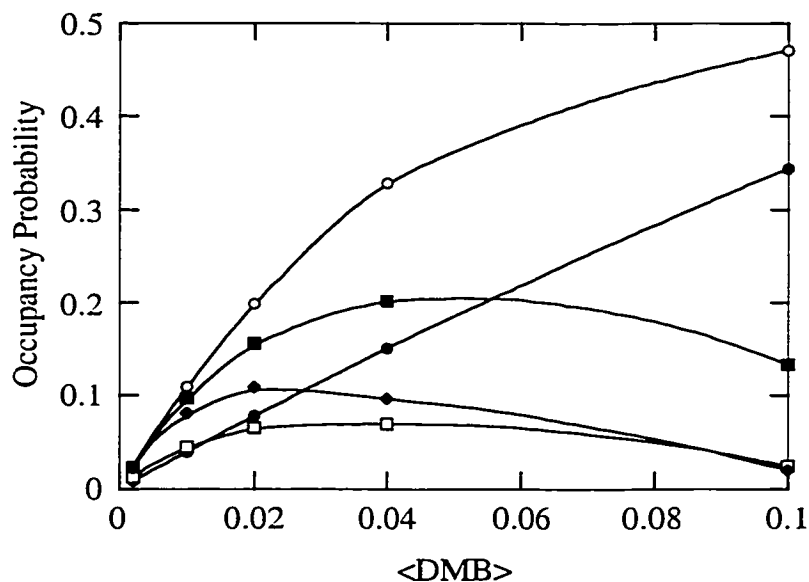


Figure 4-38. Calculated occupancy probabilities for molecules in shells **b** (closed circles), **c** (open circles), **d** (closed squares), **e** (open squares), and **f** (closed diamonds) surrounding a central shell, **a**, as a function of the fractional occupancy of DMB in NaY.

Figure 4-38 shows the variation in occupancy probability of individual shells **b** through **g** as a function of the loading level of DMB. For the innermost shell **b**, the occupancy probability increases with DMB loading over the examined range. Occupancy probability in shell **c** also increases with DMB loading, but begins to level off at high

loadings. For more distant shells the occupancy probability plateaus earlier and actually decreases at higher loadings. Therefore, with increasing loading of DMB, the occupancy of outer shells becomes less probable, and correspondingly the occupancy of inner shells becomes more probable. In other words, as the DMB concentration is increased, fewer shells need to be considered to map the total DMB distribution. This notion becomes more apparent when the total occupancy of successive shells from the initial supercage **a** is considered. For instance, Figure 4-39 presents the summed occupancy probability of successive shells as a function of DMB loading level. In this case a clear, intuitive trend is observed whereby the total distribution is approached more rapidly the greater number of summed shells included.

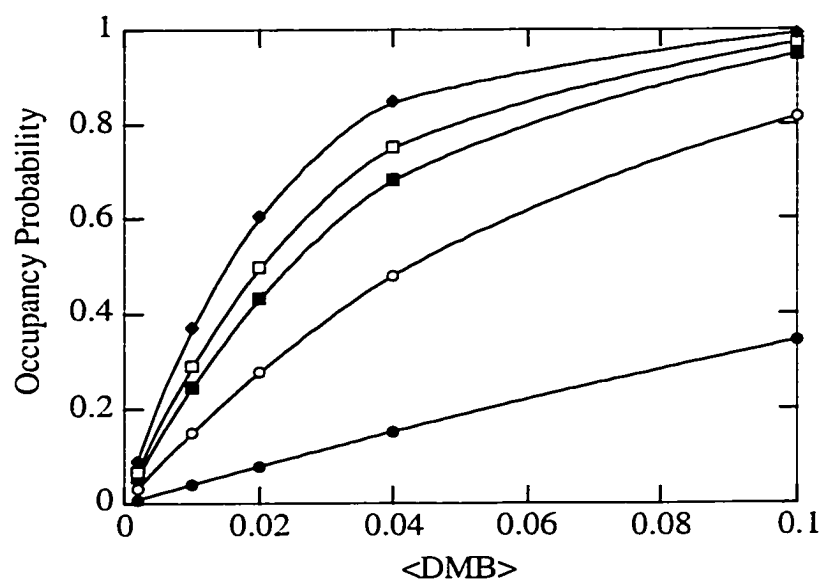


Figure 4-39. Calculated sum of occupancy probabilities for molecules in shells **b** (closed circles), **b + c** (open circles), **b + c + d** (closed squares), **b + c + d + e** (open squares), and **b + c + d + e + f** (closed diamonds) as a function of DMB fractional occupancy in NaY.

The distribution of reagents obtained from this model can be used to rationalize interactions between adsorbates and bimolecular chemical reactions within the zeolite. For instance, the distribution of reagents can be applied to the current results in order to obtain estimates for the distance of electron or a hole travel within the cavities of NaY. Consider first hole migration between photoexcited Chl and DMB within the NaY matrix. Comparing the yield of hole migration (i.e. the yield of 4-methoxycumyl cation) with the DMB occupancy as a function of DMB concentration relates the efficiency of hole migration to separation distance. Such a comparison is shown in Figure 4-40, which

plots the observed yield of carbocation and the curves generated by the sum of successively more shells. Notably, the data do not fit perfectly to any of the summed shells distributions, suggesting that this model may not be an ideal representation of the data for this system. However, these plots demonstrate unambiguously that hole migration is not limited to adjacent cavities, shell **b**. Likewise, the hole can clearly travel farther than shell **c** since the data normalized to the sum of shells **b** and **c** is very poor (sum of the square of residuals is 0.048), Figure 4-40a. The best correlation between the observed data and the summed occupancy of shells is obtained for shells **b** through **d** (sum of the square of residuals is 0.022), Figure 4-40b, and for shells **b** through **e** (sum of the square of residuals is 0.024), Figure 4-40c. Including the occupancy of shell **f** worsens the correlation (sum of the square of residuals is 0.058), Figure 4-40d. The direct, through-space distance between the central supercage **a** and shells **d** and **e** corresponds to 24 Å and 30 Å respectively. However, when the molecular sizes of Chl and DMB are considered, by using half the largest molecular dimension in each case, the vacant, through-space distance for hole migration is estimated to be between 14 Å and 19 Å.

Analogous comparisons can be made for electron migration between photoexcited An and DCB. Thus, comparing the yield of electron migration (i.e. the yield of the DCB radical anion) as a function of DCB concentration with the DCB occupancy probability as a function of loading gives an indication of the efficiency of electron migration as a function of intermolecular separation. Once again the experimental data do not fit perfectly to the modeled distribution in the summed shells. However, the comparison again confirms that the interactions leading to the observed ET chemistry are not solely contact interactions and do not correlate to electron motion only to neighbour cages, shell **b**, Figure 4-41. For this system, the observed data fits best to the summed occupancy probability of shells **b** and **c**, suggesting that the electron can traverse at least one unoccupied NaY cavity. The direct through space separation from the center of supercage **a** to the center of a cavity in shell **c** corresponds to 21 Å. Subtracting half the longest interatomic distances of An and DCB from this values yields 12 Å as an estimate for the vacant, through-space distance for electron migration between An and DCB in NaY.

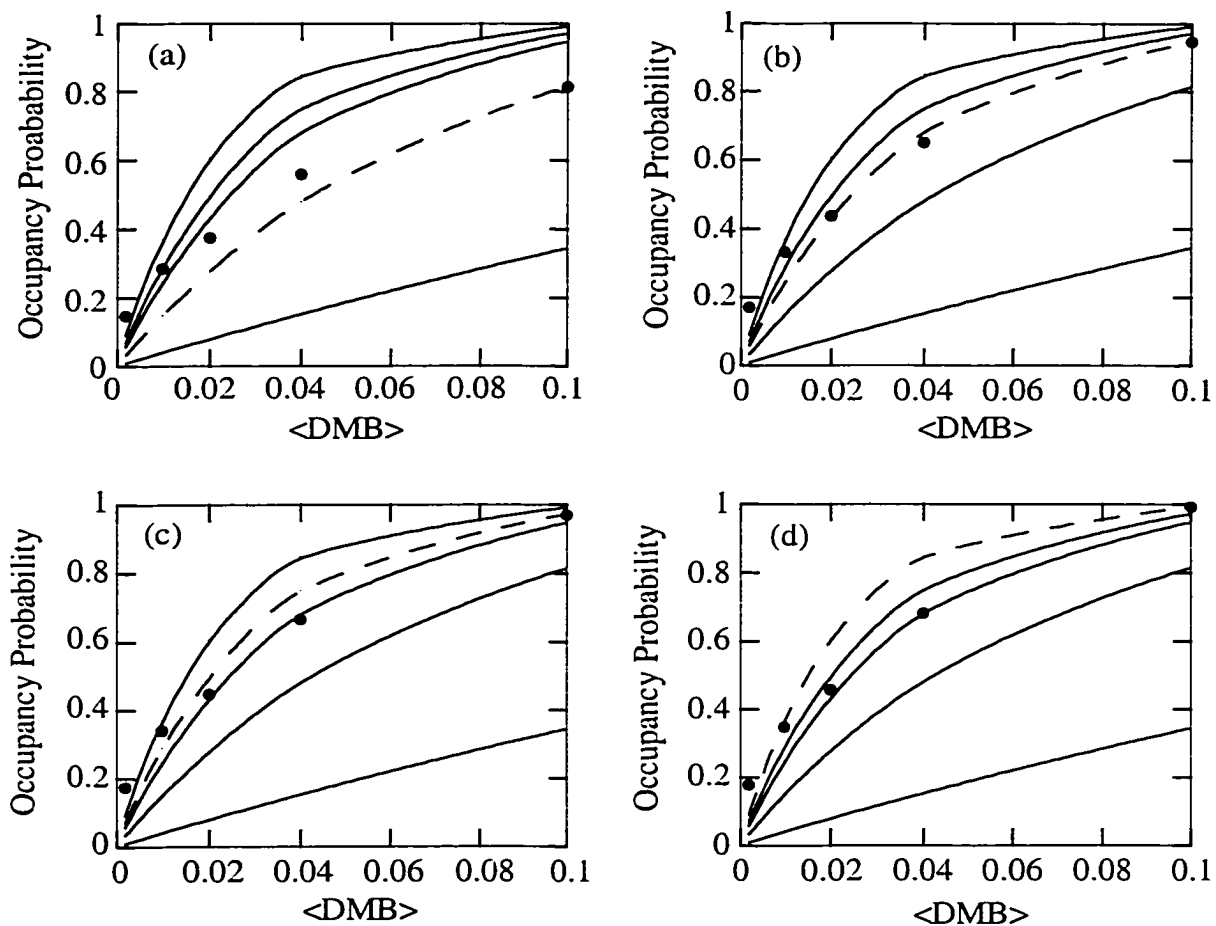


Figure 4-40. Experimental variation in the yield of the 4-methoxycumyl cation (closed circles) as a function of the fractional occupancy of DMB in NaY compared to the variation predicted by the shells model (dotted lines) incorporating shells **b + c** (a), **b + c + d** (b), **b + c + d + e** (c), and **b + c + d + e + f** (d). The experimental data have been normalized, in each individual case using the data point for $\langle \text{DMB} \rangle = 0.1$ (see text).

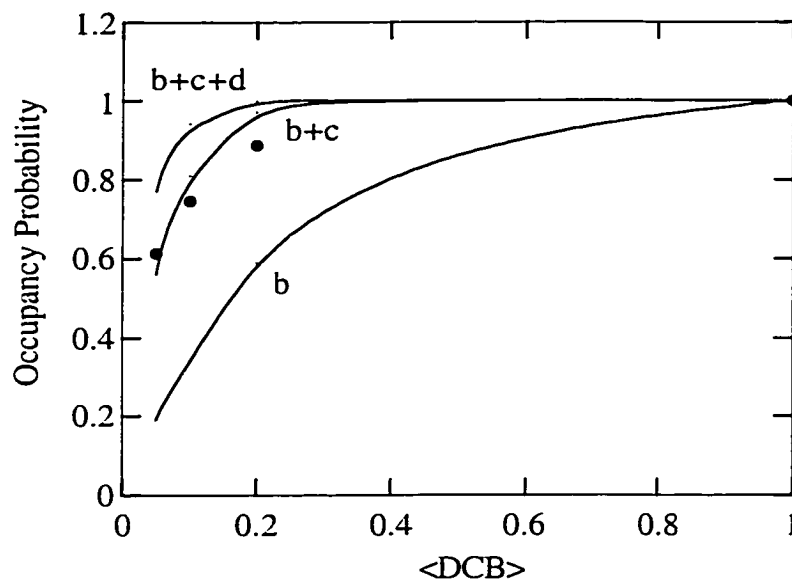
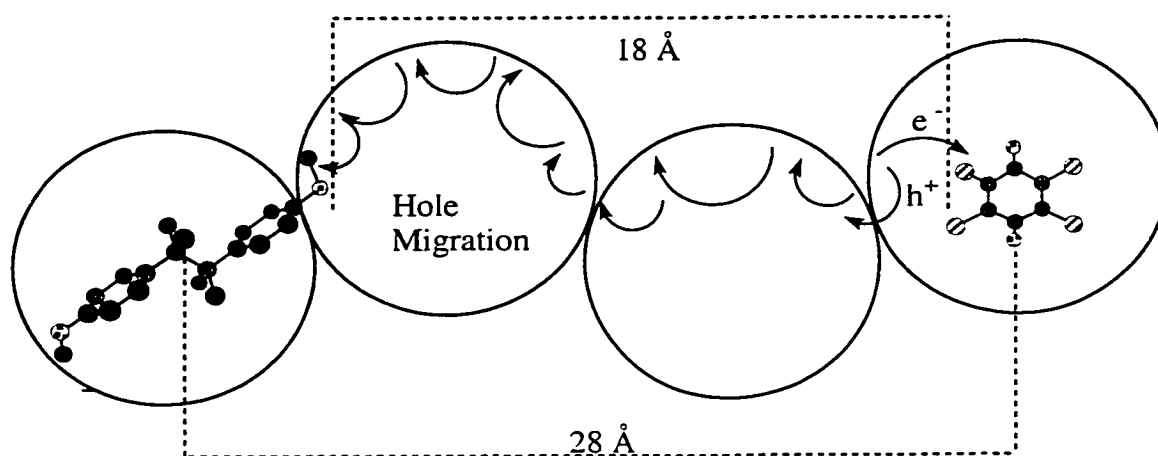


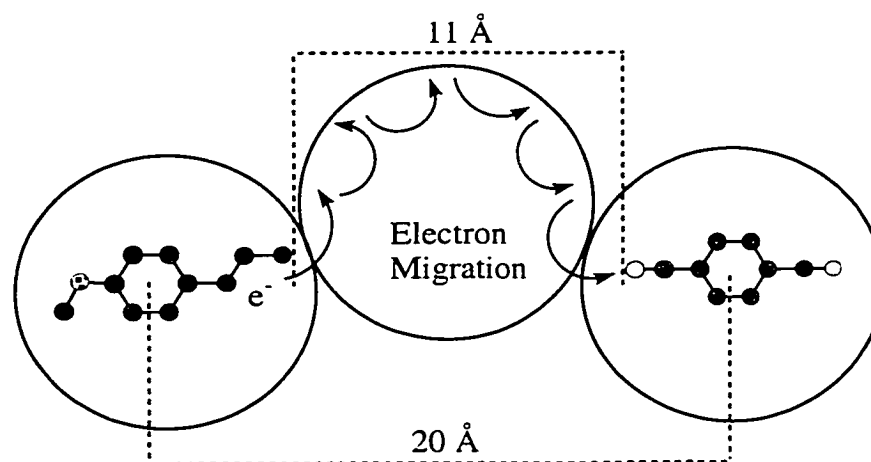
Figure 4-41. Experimental variation in the yield of the DCB radical anion (closed circles) as a function of the fractional occupancy of DCB in NaY compared to the predicted variation (lines). The experimental data have been normalized using the $\langle \text{DCB} \rangle = 1$ data point (see text).

The above discussion indicates that a model based on the distribution of reagents within zeolites can provide useful information concerning the interactions of adsorbates within these systems. In this case a mapping of the intrazeolite distribution has been used to estimate the distances over which redox processes, specifically electron and hole migration, can occur. Notably, the data do not fit exactly to the model, indicating that methods for determination of intrazeolite concentration of reagents as well as the model and/or assumptions used to obtain the distribution for the mixed adsorbate systems may be improved. Overall, however, data determined for the two unique systems employed to study electron and hole migration are fit reasonably well by the distribution model. Furthermore, the similarity of the predictions derived from this model to those obtained from the Perrin treatment lends support to the validity of both models. Thus, both models predict that the total distance traveled by the hole and the electron are in the range of 25 Å to 30 Å and 18 Å to 21 Å, respectively. Average distances obtained by considering both models distance are 28 Å for hole migration, Scheme 4-14 (a), and 20 Å for electron migration, Scheme 4-14 (b).

Scheme 4-14



(a)



(b)

Significantly, the charge migration distances reported above make no account of molecular size and therefore do not realistically represent the distance that the hole and electron are traveling through intrazeolite space devoid of the molecular reagents. Incorporation of the molecular dimensions of the specific reagents within the distribution model allows the extraction of explicitly periphery-periphery distances and therefore the empty space within the zeolite cavity through which the hole and electron travel. The resultant prediction for the specific systems are 14 – 19 Å for hole migration and 12 Å for electron migration. In the application of the Perrin model, no account of the specific

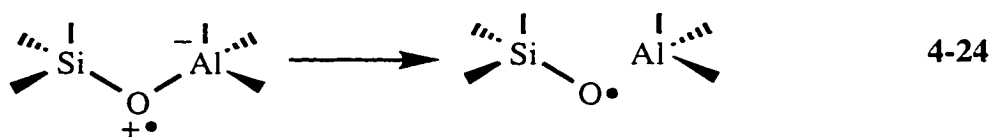
molecular sizes is made. However, if it is assumed that at least half of the quencher molecule must be contained within the reaction sphere in order for reaction to take place, the sum of half the largest molecular dimensions for each reagent must be subtracted from the total reaction radius in order to obtain the vacant space distance between the reactants. This leads to estimates of 18 Å for hole migration and 9 Å for electron migration, which are again quite similar to the predictions of the distribution model. The average vacant space distance for hole and electron migration predicted from both models is therefore 17 Å and 11 Å. Notably, considerable insight into the investigation of electron and hole migration between spatially separated reagents could be obtained by using other types of molecules, particularly since these molecules, especially DMB, are not spherical, in order to see how molecular size and shape influences the estimated migration distances.

Regardless of the exact estimates of the distance traveled by electrons and holes, the experimental results definitively demonstrate that the observed redox reactions cannot be accounted for through contact interactions alone. This does not imply that species in molecular contact do not exist, nor that such contact interactions do not participate in ET reactions leading to the observed products. However, in addition to these interactions, chemistry over longer distances must be taking place, at a variety of distances up to the maximum values predicted by the models. As such the zeolite must mediate these more distant processes, actively participating in the migration of charge between the donor and acceptor. In this regard, an aspect of both models which must also be recognized is that the distances predicted refer to direct through-space distances. This likely does not accurately represent the mechanism by which the charge migrates within the zeolite. More likely the hole and the electron migrate, or hop, along the zeolite framework from the site of origin to the secondary redox partner, as depicted in Scheme 4-14. For instance, the hole may move along electron rich framework sites such as oxygen atoms within [Si-O-Al]⁻ bridges, while the electron may move along electron deficient sites such as cations, cation clusters or aluminum centers. For charge migration proceeding along the framework, the total distance traveled is likely significantly longer than the direct, through-space distance. A distinction between hole and electron migration should be made, however, as a consequence of the method for initial generation of the hole and electron. The hole is generated by electron donation from the zeolite framework to the photoexcited acceptor, and is necessarily associated with a framework site upon formation. The electron is generated by ejection from a photoexcited molecule. The photoionization may involve a direct interaction with framework sites, in which case association of the electron with the framework will be instantaneous. However, it is also

possible that the electron may travel through space a finite distance before making contact with the framework, thereby introducing a distinction between the electron and the hole. Still, it is unlikely that the electron will travel the entire 11 Å without the participation of framework interactions.

Upon considering the proposed migration of electrons and holes between spatially isolated reagents in the absence of contact interactions, two obvious questions emerge, namely, what causes the electron or hole to move, and, what causes the motion to stop and thereby limits the migration distance? In order for migration to occur, a hole or electron that is pre-associated with a framework site must jump to an adjacent site. Thermodynamically a driving force exists for the hole or electron to reach the secondary donor or acceptor. However, since direct contact with this reagent is not always ensured, the zeolite must mediate the intermolecular interaction and hence the migration.

One general rationale for how this may be possible would be for the zeolite framework with its associated molecular orbital system to act as a bridge facilitating charge migration. This is somewhat analogous to ET in intramolecular systems where the donor and acceptor are physically separated by a rigid molecular spacer and ET is mediated through the σ -bonded network of the bridging spacer. In such a scenario, the distance for charge migration may be limited if charge migration disrupts the ability of the bridge to continue to mediate intermolecular interaction. For instance, the presence of excess positive or negative charge at a certain site may reduce the integrity of the bridge by inducing a reaction at that site such as framework bond cleavage, eq. 4-24,



thereby stopping migration at that point. A second interpretation would be to assume that the included donor or acceptor modulates the redox potentials of neighbour zeolitic sites. For instance, an included electron donor may increase the electron density near adjacent electron donating sites, thereby rendering these sites more easily oxidized. Similarly, an included electron acceptor may decrease the electron density near adjacent electron accepting sites, thereby rendering these sites more easily reduced. Such an effect is predicted to be most significant at zeolitic sites in close contact with the adsorbed molecule, and progressively decrease with distance from the adsorbate. Thus a vectorial arrangement can be envisioned wherein migration becomes increasingly more favorable

as the electron or hole moves closer to the secondary acceptor or donor, until it reaches these reagents which act as the ultimate sinks for the charge. In this case the limit on the distance of charge migration would be imposed by the range over which such vectorial effects can extend. In light of this discussion, an interesting experiment would involve varying the redox potentials to determine if a greater migration distance can be achieved with more powerful reagents.

One additional point of interest is the difference between the distances estimated for hole and electron migration. Although these distances are preliminary predictions, the current results indicate that intrazeolite hole migration can take place over longer distances than intrazeolite electron migration. This may be associated with the mechanistic differences for electron and hole generation mentioned previously, where photoionization was employed for electron generation and framework participation may have not been initially ensured. However, the greater migration distance of a hole as compared to an electron in the zeolite framework is perhaps consistent with intuition. This is based on the perceived notion that zeolites are better oxidizing agents than reducing agents and therefore provide a more stabilizing environment for electrons than for holes. Certainly interesting future work can be aimed at evaluating the differences in electron and hole migration among other donor-acceptor pairs. It will be particularly significant to determine if the current observation is indeed representative of the general mobility of electrons and holes in NaY.

4.3.5 Direction for Ongoing Studies of Charge Migration in Zeolites

The work presented herein concerning electron and hole migration within NaY represents the first stages of a potentially large, multifaceted and exciting research project. Significantly, the results gathered thus far have established that redox reactions can occur between spatially separated species in NaY zeolites. The ET reactions observed in the absence of intermolecular contact are mediated by the intervening zeolite framework and can more accurately be represented as electron or hole migration as opposed to direct ET quenching of excited states as in traditional PET reactions. In addition the current results have been successfully interpreted using two independent models in order to rationally access the distances of intrazeolite charge migration. However, in spite of these encouraging results, many more questions have been raised than have been answered. In particular experiments employing other molecular systems will be required in order to establish the generality of the phenomenon as well as the validity of the interpretation and the reliability of the experimental models. This too will

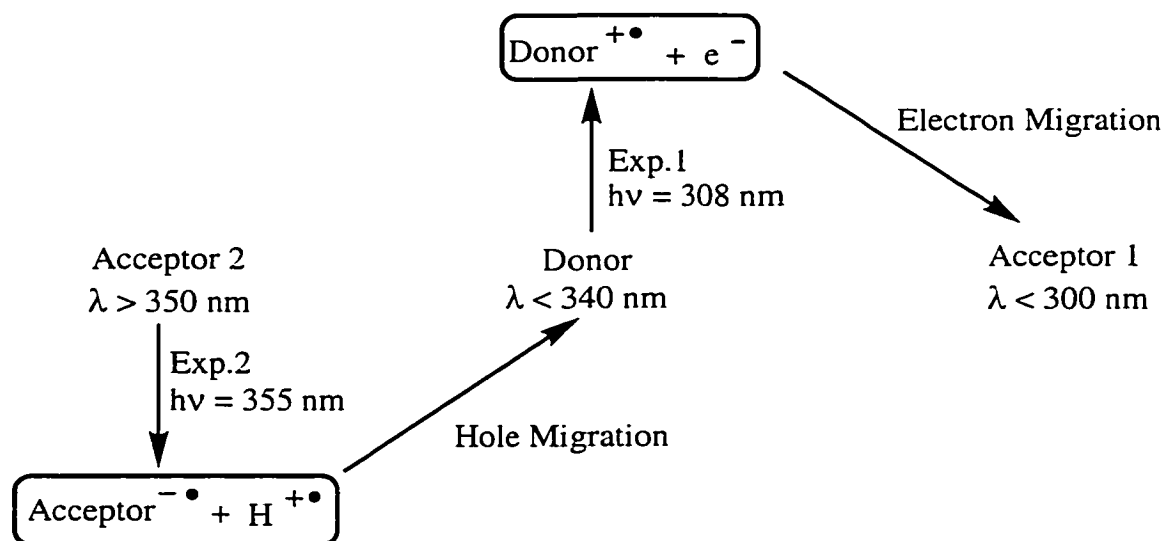
hopefully shed some light on the mechanisms of these charge migration reactions and the factors which influence the migration distance. In this regard, investigations of the migration reactions within other types of zeolites, for instance different alkali cation Y zeolites, could be useful in assessing the influence of counterion on charge mobility within these materials.

The next logical step in this project is a more systematic investigation of the charge migration reactions. At this stage, an appropriate system must be designed which employs a series of molecules to examine both electron and hole migration such that the two can be rationally compared. For instance, a concern of the current study is that the differences between the molecules employed for electron and hole migration studies renders direct comparisons somewhat ambiguous. A more cohesive study of electron and hole migration can be proposed. The proposal is based on a unified, single system for the study of both types of charge migration, as outlined in Scheme 4-15. This system involves using a common donor to study both electron and hole migration, in combination with two structurally similar acceptors. With the appropriate three molecules, both electron and hole migration reactions would be accessible. For instance, electron migration could be initiated by selectively exciting the donor at a wavelength where acceptor 1 does not absorb (308 nm is the experimentally available laser wavelength). This will induce photoionization of the donor and ejection of an electron into the zeolite matrix. Electron migration followed by transfer to acceptor 1 will generate the corresponding radical anion as an observable reactive intermediate. Similarly, hole migration can be initiated by selectively exciting acceptor 2 at a wavelength where the donor does not absorb (355 nm is the experimentally available laser wavelength). Initially this will generate the radical anion of acceptor 1 and a hole in the zeolite framework. Hole migration followed by electron donation from the donor to the zeolite matrix will produce the donor radical cation as an observable reactive intermediate.

One of the most difficult features of the proposed experimental scheme is finding the appropriate donor and acceptor molecules. Several criteria must be satisfied, including appropriate ground state absorption spectra to ensure selective excitation, sufficient oxidation and reduction potentials to ensure the redox chemistry takes place, and, ideally, the generation of radical cations and radical anions with absorption spectra that are reasonably well resolved for decisive identification and quantification. However, implementation of this unified investigation of electron and hole migration should be possible using nanosecond laser photolysis to examine the transients generated and the yields of these transients as a function of concentration. Furthermore, since the processes

are static on the nanosecond time-scale, further insight may be obtained by combining the nanosecond study with picosecond fluorescence measurements, to determine, for instance, if it is possible to resolve the initial PET from the zeolite framework to acceptor 2. This would introduce an additional molecular criteria that acceptor 2 should have a reasonable quantum yield for fluorescence.

Scheme 4-15



Chapter 5. Experimental

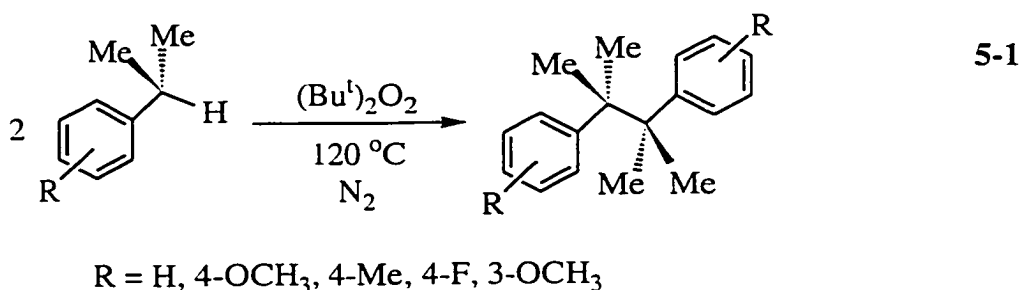
5.1 General

NMR spectra (^1H and ^{13}C) were recorded on a Bruker AC-250 spectrometer. All chemical shifts are reported in ppm with respect to TMS at 0.0 ppm. Gas chromatography was carried out on a Perkin Elmer Autosystem Gas Chromatograph with a DB5 15 meter column, or a Perkin Elmer Autosystem XL GC coupled with a TurboMass Spectrometer. High pressure liquid chromatography (HPLC) was conducted on a Waters instrument equipped with a reverse phase column. UV-vis absorption and diffuse reflectance spectra were recorded on either a Hewlett Packard 8452A Diode Array Spectrometer, or a Cary UV-Vis spectrophotometer. A PTI Fluorimeter was used in steady-state fluorescence studies.

5.2 Materials

5.2.1 Bicumenes

The bicumenes employed in this study were prepared by radical-initiated dimerization of the appropriately substituted cumene, eq. 5-1.⁴⁷⁰



This reaction involved thermal decomposition of *tert*-butyl peroxide, yielding the corresponding *tert*-butyl radical, which subsequently generated the cumyl radical *via* hydrogen abstraction. Coupling of the cumyl radicals afforded the bicumene product. Synthesis of a wide variety of bicumenes and other bibenzylic substrates using this methodology has previously been described by both Röchardt^{471,472} and Maslak.^{281,282,287,288}

Preparation of the Starting Cumenes. Both cumene and 4-methylcumene (*p*-cymene) were obtained from Aldrich and distilled prior to use. All other cumenes used in

this work are known compounds prepared according to literature procedures. 4-Methoxycumene and 3-methoxycumene were prepared by methylation of 4-*isopropyl* phenol or 3-*isopropyl* phenol, respectively, with dimethyl sulfate in greater than 95 % yield.^{281,473} To prepare 4-fluorocumene, 4-aminocumene (distilled) was first converted to the tetrafluoroborate diazonium salt by treatment with sodium nitrate and sodium tetrafluoroborate.⁴⁷³ Decomposition of the diazonium salt, accomplished by heating the pinkish tetrafluoroborate salt with a Bunsen flame, yielded crude 4-fluorocumene as a reddish liquid (40 %). All 4-substituted cumenes (transparent liquids) were distilled to greater than 98 % purity (GC) before proceeding to the dimerization step.

The deuterated precursor, 4-methoxycumene-*d*₆ was prepared by Grignard addition of acetone-*d*₆ to 4-bromoanisole followed by subsequent reduction of the corresponding alcohol. This involved dripping 4-bromoanisole (0.08-0.14 mol) into anhydrous ether containing magnesium (1-1.5 eq.) with stirring over 1-3 hours, followed by addition of acetone-*d*₆ (1 eq.) to the resulting Grignard reagent. Treatment with 5 % aqueous HCl yielded crude 4-methoxycumyl alcohol-*d*₆ as a yellow liquid (ca. 80 %) which was purified by distillation under reduced pressure (ca. 75%). Reduction of the alcohol was accomplished using the procedure of Nutaitis and Bernardo for the preparation of 4-*n*-pentylanisole.⁴⁷⁴ Specifically, 4-methoxycumyl alcohol-*d*₆ (ca. 0.08 mol) was combined with sodium borohydride in tetrahydrofuran to which was added trifluoroacetic acid (ca. 1 mol) dropwise over a period of two hours, while maintaining the flask at room temperature. The reaction mixture was poured into approximately 150 mL of 25 % aqueous NaOH and extracted into ether to yield a yellowish liquid. Flash chromatography (hexanes, and hexanes-ethyl acetate mixtures) followed by distillation under reduced pressure yielded pure 4-methoxycumene-*d*₆ as a transparent liquid.

4-Methoxycumyl Alcohol-*d*₆: transparent liquid; ¹H NMR (CDCl₃, 250 MHz): δ 2.4 (broad s, 1 H), 3.7 (s, 3 H), 6.8 (d, 2 H), 7.3 (d, 2 H); ¹³C NMR (CDCl₃, 62.9 MHz): δ 31.2 (multiplet), 55.7, 72.3, 113.9, 126.1, 141.9, 158.6.

4-Methoxycumene-*d*₆: transparent liquid; ¹H NMR (CDCl₃, 250 MHz): δ 2.8 (s, 1 H), 3.8 (s, 3 H), 6.8 (d, 2 H), 7.1 (d, 2 H) ¹³C NMR (CDCl₃, 62.9 MHz): δ 23.3 (multiplet), 32.8, 55.3, 113.6, 127.3, 141.1, 157.7.

Dimerization of Cumenes. The general procedure for the synthesis of the bicumenes is very similar to that described by Maslak *et al.*²⁸¹ This typically involved combining 1 equivalent of the cumene (from <1 g to 10 g depending of the amount of cumene available) with 1 equivalent of *tert*-butyl peroxide and refluxing the mixture at

110-120 °C under a constant stream of nitrogen for a period of 48-72 hours. During the reflux, the progress of the reaction was monitored by GC and additional equivalents of peroxide were added as necessary until 40-60 % of the starting material had been consumed. This typically required 3 to 4 equivalents of peroxide. The crude crystalline bicumene could often be isolated upon cooling the mixture to room temperature or lower, although in some cases it was necessary to distill off the starting material and any volatile products under reduced pressure (ca. 0.01 Torr). Purification of the crude bicumene products was accomplished using column chromatography and/or recrystallization or sublimation depending on the specific compound as listed below. Typical yields of purified bicumene varied from 10-50 % depending on the substituent and the quantity of cumene precursor used.

4,4'-Dimethoxybicumene (2,3-dimethyl-2,3-bis(4-methoxyphenyl)butane): white solid; sublimed; > 99 % pure by GC; mp: 174-176 °C; ¹H NMR (CDCl₃, 250 MHz): δ 1.3 (s, 12 H), 3.8 (s, 6 H), 6.8 (dd, 8 H); ¹³C NMR (CDCl₃, 62.9 MHz): δ 25.3, 43.1, 55.2, 111.9, 129.6, 139.1, 157.3. Melting point, ¹H and ¹³C NMR are identical to those previously reported.²⁸¹

4,4'-Dimethylbicumene (2,3-dimethyl-2,3-bis(4-methylphenyl)butane): white solid; recrystallized twice from 95 % ethanol; > 99 % pure by GC; mp: 149-151 °C; ¹H NMR (CDCl₃, 250 MHz): δ 1.3 (s, 12 H), 2.3 (s, 6 H), 7.0 (dd, 8 H); ¹³C NMR (CDCl₃, 62.9 MHz): δ 20.8, 25.3, 43.2, 127.3, 128.6, 134.0, 143.9.

4,4'-Difluorobicumene (2,3-dimethyl-2,3-bis(4-fluorophenyl)butane): white solid; recrystallized twice from 95 % ethanol; > 99 % pure by GC; ¹H NMR (CDCl₃, 250 MHz): δ 1.25 (s, 12 H), 6.9 (m, 8 H); ¹³C NMR (CDCl₃, 62.9 MHz): δ 25.4, 43.6, 113.3, 113.6, 142.4, 142.5, 159.3, 163.2.

3,3'-Dimethoxybicumene (2,3-dimethyl-2,3-bis(3-methoxyphenyl)butane): white solid; recrystallized twice from 95 % ethanol; > 99 % pure by GC; mp: 105-109 °C; ¹H NMR (CDCl₃, 250 MHz): δ 1.3 (s, 12 H), 3.7 (s, 6 H), 6.6-7.1 (m, 8 H); ¹³C NMR (CDCl₃, 62.9 MHz): δ 25.3, 43.8, 55.1, 110.6, 115.3, 121.3, 127.4, 148.6, 158.2.

Bicumene (2,3-dimethyl-2,3-diphenylbutane): white solid; recrystallized twice from 95 % ethanol; > 99 % pure by GC; ¹H NMR (CDCl₃, 250 MHz): δ 1.3 (s, 12 H), 7.1 (m, 8 H); ¹³C NMR (CDCl₃, 62.9 MHz): δ 25.2, 43.7, 125.5, 126.7, 128.7, 146.8. ¹H and ¹³C NMR are identical to those previously reported.⁴⁷²

4,4'-Dimethoxybicumene-*d*₁₂: white solid; purified by column chromatography (hexanes-ethyl acetate) and recrystallization from hexanes-dichloromethane mixtures; >

98 % pure by GC; mp: 174-176 °C; ¹H NMR (CDCl₃, 250 MHz): δ 3.8 (s, 6 H), 6.8 (dd, 8 H); ¹³C NMR (CDCl₃, 62.9 MHz): δ 42.6, 55.2, 111.9, 129.6, 139.1, 157.3.

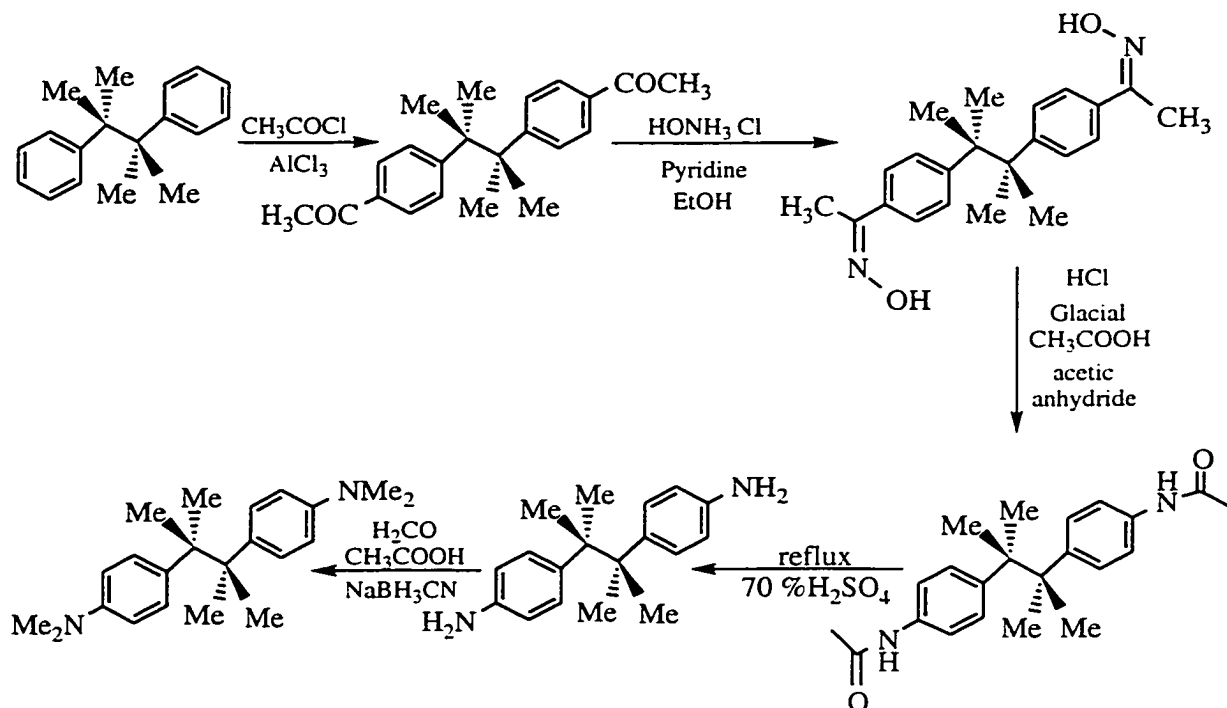
4,4'-(*N,N*-Dimethylamino)bicumene. (2,3-dimethyl-2,3-bis(4-*N,N*-dimethylamino-phenyl)butane): This compound was prepared in a slightly different manner than the other bicumenes. Specifically, dimerization of cumene to yield bicumene as described above was initially carried out, followed by derivatization as shown in Scheme 5-1. The procedure employed is analogous to that previously described for the conversion of 1-methylnaphthalene to 1-amino-4-methylnaphthalene.⁴⁷⁵ Acylation^{473,476} was accomplished by the dropwise addition of acetyl chloride (4 eq.) to a chilled (-5 °C) solution of bicumene (ca. 0.05 mol) and AlCl₃ (4 eq. ca. 13 g) in nitrobenzene. The mixture was stirred for several hours under vacuum in order to remove the HCl gas, poured over ice, washed with 5 % HCl and saturated Na₂CO₃ before distilling off the nitrobenzene to yield the crude acylated products. The mono- and di-acylated products were separated by treating the crude mixture with hot glacial acetic acid, and filtering off the diacylbicumene (**2**) which was insoluble (ca. 50 %).

Diacylbicumene (**2**) (ca. 0.03 mol) was converted into the oxime (**3**) using hydroxylamine hydrochloride (ca. 12 g) and pyridine (ca. 12 mL) in refluxing ethanol for 4 hours.⁴⁷³ After removing the ethanol by distillation, water was added to the residue, and the white-yellow oxime solid precipitated out. The crude product (ca. 100 %) was rinsed with distilled water, dried overnight in a vacuum oven (45 °C) to remove residual pyridine, and used without further purification.

Acid catalyzed Beckmann rearrangement was accomplished by bubbling HCl gas through a chilled solution of the oxime (**3**) (0.02 mol) in glacial acetic acid (30 mL) and acetic anhydride (30 mL) for approximately 1 hour. After an additional 3 hours of stirring at room temperature, the solution was added to ice water and dichloromethane and washed with sodium bicarbonate, yielding the crude amide (**4**) as an oily yellow solid (66 %). The amide (2 mmol) was hydrolyzed to the amine (**5**), by refluxing in 70 % H₂SO₄ (ca. 50 %). Methylation of (**5**) was carried out by treating the amine (1 mmol) in acetonitrile (30 mL) with formaldehyde (1.5 mL), sodium cyanoborohydride (5 mmol), and acetic acid (500 μL).²⁸⁸ After stirring for 4 hours, a second portion of acetic acid (500 μL) was added to the reaction. The solution was diluted with ether (ca. 60 mL), washed with 1 M KOH, brine, and then rinsed with HCl (aq). The aqueous layer was treated with solid KOH until basic and extracted with ether to yield a crude yellow powder. The purified 4,4'-(*N,N*-dimethylamino)bicumene (**6**) was obtained after extensive washing of the crude yellow solid with boiling ethanol (10 %). ¹H NMR

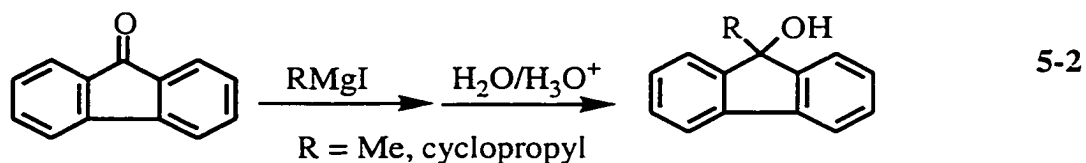
(CDCl₃, 250 MHz): δ 1.2 (s, 12 H), 2.8 (s, 12 H), 6.7 (d, 4 H) 7.1 (d, 4 H); ¹³C NMR (CDCl₃, 62.9 MHz): δ 24.1, 33.1, 41.0, 113.1, 127.0, 137.3, 149.1. The ¹H and ¹³C spectra are similar to those previously reported by Maslak for the unsymmetrical, 4-(*N,N*-dimethylamino)bicumene.

Scheme 5-1



5.2.2 9-Fluorenols and 9-Substituted Fluorenes

9-Fluorenol is commercially available (Aldrich) and was used as received. 9-Ethyl- and 9-*isopropyl*-9-fluorenol were provided by Dr. N. Mathivanan. 9-Methyl- and 9-cyclopropyl-9-fluorenol were synthesized by addition of the appropriate alkyl Grignard to 9-fluorenone, eq. 5-2, as previously described.^{380,381}



The Grignard reagent was prepared by combining equimolar (e.g. 0.03 mol) quantities of methyl iodide or cyclopropyl bromide and magnesium in anhydrous ether under reflux. After most of the magnesium had been consumed, a solution of fluorenone (0.03 mol) in ether was slowly added and the mixture was stirred for a few hours until GC analysis indicated that no further reaction was taking place. After treatment with aqueous acid, a bright yellow crystalline solid was obtained (ca. 75 %). The crude 9-fluorenol derivative was recrystallized repeatedly from 95 % ethanol until the product appeared colorless and no fluorenone could be detected by GC or NMR.

9-Methyl-9-Fluorenol: white solid; recrystallized three times from 95 % ethanol; > 99 % pure by GC; ^1H NMR (CDCl_3 , 250 MHz): δ 1.72 (s, 3 H), 2.01 (s, 1 H), 7.45 (m, 8 H); ^{13}C NMR (CDCl_3 , 62.9 MHz): δ 26.1, 79.6, 120.1, 123.3, 128.1, 129.0, 138.8, 149.8, 157.7.

9-Cyclopropyl-9-Fluorenol: pale yellow solid; purified by column chromatography (ether-hexanes) and three recrystallizations from 95 % ethanol; > 99 % pure by GC; ^1H NMR (CDCl_3 , 250 MHz): δ 0.45 (m, 2 H), 0.70 (m, 2 H), 1.2 (m, 2 H), 1.9 (s, 1 H), 7.45 (m, 8 H); ^{13}C NMR (CDCl_3 , 62.9 MHz): δ 0.5, 19.4, 80.2, 120.0, 123.0, 127.9, 128.9, 139.2, 149.4.

9-Methoxyfluorene was prepared by 9-bromofluorene in methanol for approximately 50 hours. 9-Acetoxyfluorene was a gift from Dr. Dayal DeCosta.

9-Methoxyfluorene: whitish beige solid; > 99 % pure by GC; ^1H NMR (CDCl_3 , 250 MHz): δ 3.02 (s, 3 H), 5.55 (s, 1 H), 7.5 (m, 8 H); ^{13}C NMR (CDCl_3 , 62.9 MHz): δ 26.1, 79.6, 120.1, 123.3, 128.1, 129.0, 138.8, 149.8, 157.7. The ^1H NMR signals are identical to those previously reported by Wan *et al.*³⁸⁰

5.2.3 Other Materials

The remaining compounds (chloranil, *trans*-anethole, 1,4-dicyanobenzene, diphenylacetic acid) were commercially available (Aldrich) and were generally used as received. 1,4-Dicyanobenzene was recrystallized from 95 % ethanol. Spectroscopic grade solvents used in laser experiments and zeolite sample preparation were commercially available (OmniSolv, BDH) and were used without additional purification. The spectroscopic grade alcohols, methanol, ethanol, 2-propanol, butanol, 2-methyl-1-propanol, 2-methyl-2-propanol, 2,2,2,-trifluoroethanol, 1,1,1,3,3,3-

hexafluoroisopropanol, and 1,1,1,3,3,3,-hexafluoro-isopropanol-OD and the alkyl enol ethers, ethyl vinyl ether, propyl vinyl ether, butyl vinyl ether, *tert*-butyl vinyl ether, isopropenyl methyl ether (2-methoxypropene), ethyl 1-propenyl ether, were all commercially available (Aldrich) and used as received.

5.2.4 Zeolites

Zeolites NaY, Si/Al = 2.4 (Aldrich), and NaX, Si/Al = 1.2 (Aldrich), were obtained from Aldrich. NaMordenite, Si/Al = 6.5 (PQ Corporation), was commercially available from the PQ corporation. Na β , Si/Al = 18, was a gift from Prof. H. García. All Na⁺-exchanged zeolites were used without additional purification. The alkali metal cation-exchanged Y zeolites were prepared by stirring NaY with 1 M aqueous solutions of the corresponding chlorides (LiCl, KC, RbCl, CsCl) at 80 °C for 1 h. The zeolites were then washed until no chlorides appeared in the washing water (tested using a saturated silver nitrate solution) and dried under vacuum. This procedure was repeated three times and the zeolite was calcinated between washings. NaY has three types of exchangeable cations. The numbers of cations per unit cell of zeolite Y are 16 site I cations, 32 site II cations, and 8 site III cations. It is well established that only site II and III cations are accessible to guest molecules.²³ The percent exchange, as determined from atomic absorption, is typically 47 % for LiY, 97 % for KY, 44 % for RbY and 47 % for CsY. It is known that for the larger cations such as Rb⁺ and Cs⁺ only the accessible Na⁺ which occupy type II and type III sites can be readily exchanged.⁶ Thus, the maximum cation exchange is ~70 %. Values of ~50 % exchange indicate that a small percentage of type II cations are not completely exchanged. The low percent exchange for the LiY sample used in this study is because hydrated Li⁺ also does not readily exchange the type III cations.

5.3 Transient Generation

A computer-controlled nanosecond laser flash photolysis system was employed to study the reactive intermediates. A schematic of the apparatus used in nanosecond diffuse reflectance experiments is shown in Figure 5-1 (the transmission apparatus is analogous with the exception that the monitoring beam is aligned at 90° relative to the excitation beam). The laser system consists of two pulsed excitation sources, a Lambda-Physik excimer laser containing a Xe/HCl/He gas mixture (308 nm, \leq 100 mJ/pulse, < 10 ns pulse) or the fourth harmonic of a Continuum Nd:YAG laser (266 nm, \leq 10 mJ/pulse, < 10 ns/pulse) which generate the transient species of interest. Time resolved

optical spectroscopy is used to monitor the photogenerated transients. The detection system consists of a pulsed xenon-arc lamp, a monochromator and a photomultiplier tube which is used to monitor changes in either transmission or diffuse reflectance. In transmission experiments the fraction of transmitted light absorbed by the transient, expressed as the change in optical density, $\Delta O.D.$, is measured. Diffuse reflectance experiments involve measuring the fraction of reflected light absorbed by the transient, denoted as the reflectance change, $\Delta J/J_0$, where J_0 is the reflectance intensity before laser excitation and ΔJ is the change in reflectance intensity after excitation due to absorption by photogenerated transients. The transmitted or reflected light is focused through a grating monochromator into a photomultiplier system before being captured with a Tektronix 620A digitizing oscilloscope. This provides a time-dependent recording of the transient behaviour which is transferred into a computer for analysis and storage. Interfacing the entire system with a Macintosh PowerPC computer, operated using the LabView programming language, allows precise control of every aspect of the laser experiment and subsequent analysis of the kinetic and spectroscopic behaviour of the transient species. The resulting apparatus couples relatively short laser pulse widths with a rapid and efficient detection system so that reactive intermediates with lifetimes ≥ 20 ns can be studied. Reported rate constants were obtained by fitting the experimental decay traces with a single or multiple first-order exponential function using KaleidagraphTM. The reported errors are 2σ , where σ is the standard deviation of the fit from the experimental data. Lifetime distributions were obtained by fitting stretched decay traces to 100 lifetimes between $0.1 \mu s$ and $1000 \mu s$ using the ESM method as described in Chapter 2.

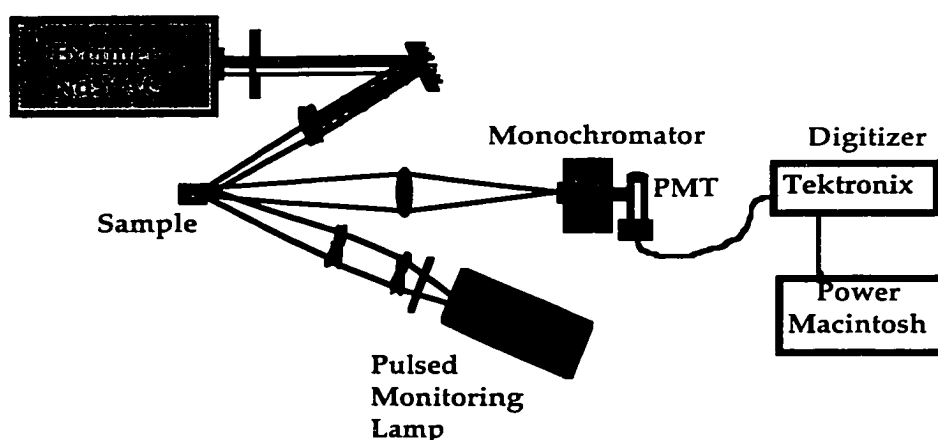


Figure 5-1. Schematic representation of laser system used in ns diffuse reflectance studies.

Zeolite samples used in nanosecond diffuse reflectance experiments were contained in quartz cells constructed of 3 x 7 mm² tubing and were either sealed under vacuum, or purged with dry nitrogen, oxygen, or nitrous oxide for 30-60 minutes prior to laser photolysis. The sample cell was moved and/or shaken throughout the laser experiment to ensure that a fresh region of the zeolite surface is examined with each laser shot. Samples for transmission experiments were prepared by adjusting the concentration of substrate in solution such that the absorbance at the excitation wavelength (266 nm or 308 nm) was between 0.2 and 0.3. In most cases the solutions to be photolyzed were flowed through the sample cell to ensure that fresh solution is continually in the path of the laser beam and secondary photolysis is avoided. This typically required about 100 mL of solution which was purged with N₂ or O₂ for approximately one hour before irradiation, and continually purged during the course of the experiment. Solutions for static samples were placed in 7 x 7 mm² quartz sample cells, sealed with a rubber septum and bubbled with either N₂ or O₂ for 30 minutes prior to photolysis. The static sample was shaken every couple of laser shots to minimize secondary photolysis.

5.4 Experimental Procedures

5.4.1 Preparation of Zeolite Samples

The general steps employed in the preparation of zeolite samples containing organic adsorbates were: (i) heating, or activating, the hydrated zeolite to remove coadsorbed water; (ii) incorporating the substrate of interest using an anhydrous organic solvent as a carrier; (iii) removal of the organic solvent under reduced pressure; and (iv) transferring the dried zeolite-adsorbate composites to the cells or vessels required for the experiment of interest. Throughout the entire procedure the utmost care was taken to minimize contact with water and to keep the zeolite sample dry. This is particularly important for dried zeolite-adsorbate composites obtained after removal of the organic carrier solvent. As these composites were no longer immersed in the anhydrous, hydrophobic solvent, they are much more vulnerable to adsorbing water from the surrounding environment. Therefore, the dried composites were never exposed to the ambient atmosphere. This was accomplished by conducting the necessary handling of the dried composites in a glove bag under an atmosphere of dry nitrogen, and by storing the composites and conducting the experiments of interest in sealed vessels.

The first step in the preparation of all zeolite samples, activation to eliminate the adsorbed water, involved heating the hydrated zeolite in porcelain crucibles samples for

at least 12 hours in an ambient atmosphere at 450 °C. Following activation, the hot, dehydrated zeolite was removed from the oven, rapidly poured into a dry vessel (either a tube, or Erlenmeyer flask depending on the sample size) containing anhydrous hexane (OmniSol, < 0.02 % water) and immediately sealed with a rubber septum. This minimizes the possibility that the zeolite will have an opportunity to adsorb water from the air, as might occur if the sample was allowed to cool in the ambient atmosphere before combining with the carrier. The substrate of interest must not be dissolved in the carrier at this time as adsorption onto or within the hot zeolite can cause thermal decomposition. It is also important to note that although the methodology of rapidly combining the hot zeolite with the carrier works well for hexane, it is not always feasible for other common carrier solvents such as, for instance, dichloromethane. Contact of the hot zeolite powders with dichloromethane often leads to rapid thermal reactions as is evident from the immediate discoloration of the zeolite powders. With the exception of some experiments involving NaY-chloranil composites, all results reported in this thesis were obtained on zeolite samples prepared with using hexane as a carrier solvent. In the cases where dichloromethane was used, the zeolite sample was first allowed to cool, either in a desiccator or under vacuum before contact with the dichloromethane. In general, hexane is the preferred choice as it is more inert to thermally initiated reactions, tends to induce greater adsorption of the substrate molecule within the zeolite, and is easier to remove from the zeolite framework (see Appendix) than dichloromethane. Introduction of the organic substrate to the zeolite-hexane slurry was accomplished using a small volume of a relatively concentrated stock solution. When possible, the stock solution was prepared in hexane. However, one drawback associated with hexane is that it is often less successful at dissolving organic molecules than dichloromethane. Thus, in some cases it was necessary to prepare stock solutions in dichloromethane. The same solvents and relative proportions were used for all samples within a series in which direct comparison of the results have been made.

Zeolite Composites Containing a Single Adsorbate. A general procedure for the preparation of single adsorbate zeolite samples is as follows. Zeolites (typically 300 mg - 400 mg) were activated for at least 12 hours at 450 °C to remove the co-absorbed water. The dehydrated zeolite was removed from the oven and immediately placed in approximately 20 mL of anhydrous hexane in a sample tube. A small quantity of a relatively concentrated (typically 10^{-1} to 10^{-2} M) hexane or dichloromethane solution containing the compound of interest (typically < 250 μ L) was then added to the zeolite-hexane slurry with stirring. The resulting slurry was allowed to stir for 1-2 hours and the carrier solvent was then separated from the zeolite solid by centrifuge. The sample was

sealed from the atmosphere during the periods of stirring and centrifuging, and care was taken to avoid hydration. An additional 20 mL of hexane was then added to the material and the mixture was stirred for approximately 30 minutes to remove surface adsorbates, centrifuged and the zeolite sample was separated from the supernatant liquid. To remove the remaining hexane the zeolite-substrate complex was placed in a desiccator which was evacuated with a vacuum pump for several hours (typically 8 - 12 hours). After vacuum drying the sealed desiccator containing the zeolite powder was placed in a glove bag under an atmosphere of dry nitrogen. The sample was then transferred to a 3 x 7 mm² quartz laser cell and attached to a vacuum line equipped with a diffusion pump (10⁻⁴ Torr) for an additional 12 hours to remove any oxygen and any residual hexane which may have been present.

Zeolite Composites Containing Two Adsorbates. Zeolite samples containing two adsorbates were prepared by incorporating the two molecules separately. In most cases a series of samples were prepared containing a constant concentration of one adsorbate and a variable concentration of the other. The fixed concentration adsorbate was first included within a large batch of activated zeolite. This procedure was analogous to the description given above, aside from the fact that it was conducted on a larger scale (ca. 5-6 fold increase). In this case, 1 to 3 g of hot, activated zeolite was added to approximately 120 mL of anhydrous hexane contained within an Erlenmeyer flask and immediately sealed. Again the substrate was introduced using a small volume (typically < 1 mL) of stock solution. After stirring these larger samples for 3 to 4 hours, the zeolite was separated from the solvent, and a second aliquot of hexane was added. This slurry was stirred for approximately 30 minutes to 1 hour to rinse the zeolite surface. The hexane was removed by decanting and then by vacuum pumping (10⁻³ Torr) in a desiccator for approximately 12 hours. Under an atmosphere of dry nitrogen, the initial zeolite-adsorbate composite was divided into pre-weighed sample tubes sealed with septa. The septa-sealed tubes were removed from the glove bag and massed. The septa were removed from each momentarily in order to quickly add ca. 20 mL of hexane and then immediately re-sealed. The requisite volume of stock solution of the second adsorbate was then added to the zeolite-composite in hexane and incorporation of the second adsorbate was carried out as described above.

The amount of adsorbate included within all zeolite samples was determined by UV spectroscopic analysis of the decanted organic carrier solvent. For all substrates discussed in this thesis, essentially 100 % incorporation of the organic precursor within NaY could be achieved using hexane as a carrier. A reduction in the percent incorporation was observed for some species in NaY at extremely high loading levels

(i.e. > 1 molecule in 2 cavities). In other alkali metal cation zeolites, 100 % incorporation of the substrates was not always possible. In these cases, the original amount of substrate added to the zeolite was adjusted to compensate for the reduced percent incorporation, such that the final concentration in each alkali metal cation zeolite was approximately equal.

The thermal stability of each substrate in the alkali metal cation zeolites was established by experiments in which the compounds were incorporated into the zeolite and subsequently removed by continuous extraction with dichloromethane. In all cases, the only material obtained following this procedure was the starting material as determined by GC, NMR and/or UV-vis spectroscopy.

5.4.2 Inclusion of Alcohols, Alkyl Enol Ethers, and Water into Zeolite-Adsorbate Composites

Co-absorbed alcohols and vinyl ethers were introduced after substrate incorporation and evacuation. In this case the laser cells to contain the zeolite composites were preweighed before putting the samples into the cells in the glove bag. In this manner the mass of the zeolite samples within the cells could be determined. The typical zeolite mass used in studies with coadsorbed reagents is ca. 100 – 200 mg. In order to inject the coadsorbate, the laser cells were sealed with a rubber septum. A small quantity of the neat alcohol or vinyl ether (typically 1 μ l) was then injected into the top of the cell using a syringe. Care was taken to ensure that the zeolite powder did not come into contact with the liquid alcohol. The sample was then gently heated with hot air to vaporize the alcohol, during which time the cell was rotated to ensure even distribution. The sample was then allowed to cool and thoroughly shaken before laser experiments were conducted.

Hydration experiments were carried out by exposing a known quantity of the vacuum dried substrate/zeolite composite to the atmosphere. The sample was spread into a thin layer in a petri dish to allow efficient, complete hydration. The changes in sample mass due to water uptake were monitored until the sample was fully hydrated and no further change in mass was observed. The final concentration of water in the fully hydrated zeolite was dependent on the charge balancing cation, Si/Al ratio and framework morphology. Typical values of water uptake (expressed as weight percent) by the 4,4'-dimethoxybicumene/zeolite composites are ca. 12 %, 10 %, 6 %, 3 % and 2 % for the alkali metal cation zeolites LiY through CsY, respectively, and ca. 5 %, 4 % and 3 % for NaX, NaMor and Na β , respectively.

5.4.3 *Steady-State Photolysis*

Steady-state photolysis experiments were conducted by irradiating the dry substrate-NaY composite (typically 1-2 g) contained within a sealed quartz cell under a continuous flow of either dry nitrogen or argon. The light source was a medium-pressure 450 W mercury lamp passed through a quartz or pyrex filter as required. The duration of the photolysis and the subsequent sample treatment varied depending on the substrate and reaction of interest. Steady-state irradiation of DMB in NaY generally required long photolysis periods of 72-96 hours. Following photolysis small amounts of methanol (typically 100 – 200 μL) were injected into the irradiation cell and heat vaporized. The resultant products were separated from the zeolite by continuous extraction with dichloromethane for 24-48 hours. The photochemical conversion was consistently about 10 %, while the mass balance varied between 40 and 60 %. The extracts were analyzed by a combination of GC, GC/MS and HPLC, and the products were identified and quantified by comparisons to known standards. Dark experiments in which the substrates were included within NaY and subsequently removed by continuous extraction were conducted in order to confirm the thermal stability of each substrate in NaY.

Appendix 1. Examination of the Water and Residual Organic Solvent Content in Zeolite Samples

The research presented in this thesis considers the reaction dynamics of organic intermediates in zeolites. In order to accurately evaluate the role of the zeolite in the reaction dynamics it is necessary to confirm that it is indeed the zeolite, and not an extraneous adsorbate, that is responsible for experimentally observed effects. At minimum, it is necessary to be aware of the contents within the zeolite cavities when interpreting experimental results. In particular, due to the hydrophilicity of most zeolites employed in the current work, it is necessary to determine the water content in the prepared samples. The results of such a determination, presented in this Appendix, establish that the water content present in the samples following standard incorporation procedures is minimal, certainly less than 1 % by weight. This is consistent with many results reported in Chapter 3 wherein dramatic differences in the reactivity of carbocation intermediates were observed in post-hydrated as compared to as-prepared dry samples. However, in the course of investigations aimed at establishing the water content, it was discovered that the samples may contain residual hexane. Also described in this Appendix are modifications made to sample preparation procedures to reduce the quantity of residual hexane. An examination of the reactivity of the 4-methoxycumyl cation in these modified zeolite samples suggests that the residual hexane has little influence on the decay of this intermediate.

The technique employed to determine the amount of volatile adsorbates present in zeolite samples is as follows. The zeolite sample (250 - 350 mg) was added to a preweighed, oven dried Erlenmeyer flask fitted with a ground-glass stopper. Except for fully hydrated samples this was carried out under a nitrogen atmosphere in a glove bag. The stoppered flask was taken from the glove bag and immediately weighed. The stopper was then removed and the open flask was placed in a vacuum oven, carefully evacuated and heated to 180 °C over a 60 minute period. The sample was maintained at this temperature for about 30 minutes at which point it was slowly cooled to approximately 90 °C over a period of about 90 minutes. The vacuum was then released with a slow stream of dry nitrogen and the flask was immediately stoppered upon release of the vacuum seal. The flask was allowed to cool to room temperature before being weighed. The result is a determination of the mass loss incurred upon heating which corresponds to the mass of volatile adsorbates within the sample (varied from

approximately 2 - 100 mg for samples under investigation). When an empty flask was subjected to the same heating regiment, the observed change in mass is minimal (< 1 %).

Table A-1 presents the determined percent mass loss due to volatile adsorbates for a series of zeolite samples. Three types of samples are represented in this table. Type 1 samples are hydrated zeolites, such as those obtained directly from the bottle, 1a and 1b. The percent mass loss from these samples corresponds well with the water content in fully hydrated NaY and NaX zeolites, as can be predicted from the molecular formula. Sample 1c is the same as 1a, except that it was placed in a vacuum desiccator and evacuated (ca. 10^{-3} Torr) continuously for 14 hours prior to the heating regiment described above. Sample 1d was first activated, then hydrated by addition of water and evacuated (ca. 10^{-3} Torr) continuously in a vacuum desiccator overnight. The mass loss from samples 1c and 1d is significantly less than from samples 1a and 1b, indicating that vacuum pumping at ambient temperatures can remove a large fraction of water adsorbed within NaY.

Table A-1. Observed mass loss upon heating zeolite samples prepared under several different conditions.

#	Sample Conditions ^a	% Mass Loss
1a	NaY from bottle	27.2/28.8 ^b
1b	NaX from bottle	24.0
1c	NaY from bottle/pumped desiccator 14 hrs	9.6
1d	Activated NaY/water/pumped desiccator overnight	8.4
2a	Activated NaY/hexane/pumped desiccator overnight	9.9/11.5/10.7
2b	Activated NaY/dried hexane/pumped desiccator overnight	11.4
2c	Activated NaY/hexane/pumped desiccator 4-5 hrs	11.7
2d	Activated NaY/hexane/pumped on line overnight	10.3
3a	Activated NaY/hexane/immediate evacuation/pumped on line 2 hrs	12.5
3b	Activated NaY/hexane/immediate evacuation/pumped on line 5 hrs	13.7
3c	Activated NaY/68 mg hexane/immediate evacuation/pumped on line 15 hrs	7.5

^aAll vacuum pumping is conducted at room temperature. ^bThe slash separates mass loss values determined in different trials.

Type 2 samples correspond to activated zeolites which have been treated with hexane according to the standard incorporation procedures used throughout this work. This involved adding the hot zeolites to ca. 20 mL of anhydrous hexane, stirring for ca. 1 hour, centrifuging, adding a second aliquot of hexane, stirring for an additional 30 minutes and then evacuating using various pumping procedures. Attaching the sample directly to the vacuum line equipped with a diffusion pump gives a better vacuum (10^{-4} Torr), than placing the sample within the desiccator (10^{-3} Torr). Sample 2b was prepared using anhydrous hexane which first was stored over NaX for 24 hours. Sample 2d was evacuated in a small vessel directly attached to the vacuum line, rather than in the desiccator. The data presented in Table A-1 clearly show that a significant amount of volatile material, ca. 10 % by weight, remained in the zeolite, even for sample 2d which was evacuated overnight on-line.

It was initially thought that the significant mass loss may be due to water that had been adsorbed during sample preparation. However, the rate at which water is absorbed by dehydrated alkali metal cation zeolites completely exposed to the atmosphere is relatively slow. For example, as shown in Figure A-1, a sample of dry NaX requires approximately 5 minutes of atmosphere exposure to adsorb about 1 % by mass water. Under the sample preparation conditions, where the activated zeolites are immediately immersed in hexane, and the dried composites are handled under an atmosphere of nitrogen, large water contents, such as the ca. 10–11 mass % loss observed in these studies are not reasonably attributed to water. To further rule out the possibility that water is responsible for the observed mass loss, hot, activated samples were treated with anhydrous hexane, immediately sealed, and placed under vacuum, without being subject to the incorporation procedure (type 3 samples). Under these conditions, no atmospheric moisture could have entered the samples. However, as can be seen in Table A-1, the percent mass loss from each of the type 3 samples is comparable to that observed for type 2 samples, even when only a very small amount of hexane (68 mg ~ 100 μ L) is introduced into the sample. The most obvious conclusion is that the observed mass loss is due to residual hexane which is not removed from the zeolite by vacuum pumping at room temperature.

In order to further investigate the possibility that residual hexane is responsible for the mass lost upon heating the zeolite sample, a second method of sample characterization was employed. Zeolite samples were first subjected to the standard incorporation procedure using hexane, with the final evacuation method being varied slightly as indicated in Table A-2. A known quantity of the zeolite sample was then extracted with a measured amount, 4 or 5 mL, of CDCl_3 by stirring in a nitrogen glove

bag. Stirring for 2 to 3 hours gave the same results as overnight stirring. After centrifugation, 1 mL of the CDCl_3 extract was placed into a NMR tube, along with a known mass (10-20 mg) of benzene as an internal standard. This technique permits determination of the mass of hexane in the NMR sample and thus the original extract. The results, presented in Table A-2, clearly indicate that the mass lost due to volatile adsorbates from samples prepared according to the standard protocol, type 4 samples, can be completely accounted for by residual hexane. This is true for both NaY, samples 4a, and NaX, samples 4b-d, and for vacuum pumping of samples contained within a desiccator or directly on the vacuum line.

Table A-2. Observed % total mass loss upon heating, and % mass of residual solvent in zeolite samples prepared under several different conditions.

#	Sample Conditions	% Mass Loss	% Mass Solvent
4a	Activated NaY/hexane/pumped desiccator 4-5 hrs	11.7/9.5	11.4/13.5
4b	Activated NaX/hexane/pumped desiccator 4-5 hrs	11.4	13.5
4c	Activated NaX/hexane/pumped on line 5 hrs	12	11.5
4d	Activated NaX/hexane/pumped desiccator 5 hrs then on line 16 hrs	11.7/9.3	12.8/10.8
5a	Activated NaY/DCM/pumped on line 5 hr	20.5	n/a
5b	Activated NaY/DCM/pumped on line overnight	16	n/a
5c	Activated NaY/isooctane/pumped desiccator overnight	15.8	16.7

Analogous results were obtained using isooctane as a carrier solvent, Sample 5c, where the even higher mass loss due to volatile adsorbates can be attributed to residual carrier solvent. This is not surprising considering the larger size and higher boiling point of isooctane as compared to hexane. Using dichloromethane as a carrier solvent also results in a higher mass of volatile adsorbates after sample preparation. However no dichloromethane could be extracted from the zeolite samples using CDCl_3 . Neither of these observations are surprising based on the higher affinity of dichloromethane for the zeolite than the other carrier solvents.

The results described thus far strongly suggest that the zeolite composites obtained from the standard preparations contain a little, if any coadsorbed water, but do contain a non-negligible amount of residual hexane. *Notably, the concentrations of*

residual hexane predicted by these results likely represent a maximum value which may be significantly reduced in samples containing an adsorbed substrate molecule. Thus the inclusion of a larger organic substrate with a higher affinity for the zeolite is likely to force much of the hexane out of the zeolite and to occupy many adsorption sites. The mass of volatile species in zeolite-composites containing typical non-volatile organic substrates is not readily determined due to thermal decomposition of the substrate molecules. However, although the concentration of hexane in the zeolite-substrate composites may be reduced somewhat, these results suggest that residual hexane is difficult to remove by vacuum pumping at room temperature.

To determine if residual hexane affects the dynamics of reactive carbocations in the zeolite samples, experiments were carried out in which the zeolites were evacuated at slightly elevated temperatures after incorporation of the carbocation precursor. To ensure that this additional treatment did not lead to complete decomposition of the precursor, the zeolites were evacuated at 45 °C for 22 hours. These conditions are effective for removing hexane from NaY samples, as shown from results using zeolite samples prepared in the absence of a precursor, Table A-3.

Table A-3. Observed mass loss due to volatile adsorbates, and mass due to residual hexane in zeolite samples prepared under various conditions.

#	Sample Condition	% Mass Loss	% Mass Hexane
6a	Activated NaY/Hexane/pumped on line ca. 100 °C 1 hr	6.7	-
6b	Activated NaY/Hexane/pumped on line 80 - 90 °C 5 hrs	5.5	-
6c	Activated NaY/Hexane/pumped in vacuum oven 80 - 100 °C 5 hrs	1	-
6d	Activated NaY/Hexane/pumped in vacuum oven 65 °C 14 hrs	3.4	2.3
6e	Activated NaY/Hexane/pumped in vacuum oven 45 °C 22 hrs	2.7	1.2

The mild vacuum heating procedure was less effective for other alkali metal Y zeolites and NaX, Table A-4. However, even in these samples, considerably less hexane remains in the zeolite as compared to those samples prepared without the additional heating.

Table A-4. Observed mass loss due to volatile adsorbates, and mass due to residual hexane in zeolite samples prepared by heating under reduced pressure.

Zeolite	Standard Protocol		Heat at 45 °C under vacuum	
	% Mass Lost	% Mass Hexane	% Mass Lost	% Mass Hexane
NaY	11.7	10.0	2.7	1.2
NaX	9.3	10.8	4.4	4.6
LiY	10.6	n/a ^a	3.7	3.7
KY	14	13	8.4	8.7
RbY	10	9.9	8.6	8.7
CsY	11.7	n/a ^a	6.3	-

^aNMR data were not obtained on these samples.

The influence of residual hexane on the behaviour of encapsulated carbocation intermediates was investigated using the reactivity of the 4-methoxycumyl cation as a probe. This was accomplished by comparing experimental results obtained upon laser photolysis of DMB in zeolite samples prepared according the standard protocol, and in zeolite samples prepared by heating in a vacuum oven at 45 °C for 22 hours.

In each alkali metal cation Y zeolite and NaX, the decay kinetics of the 4-methoxycumyl cation observed in the vacuum heated samples are virtually identical to those observed in samples prepared by the standard methods, Figure A-2. In all cases, the calculated rate constants match extremely well and the trend in decay rate constants as a function of zeolite composition is identical for both types of samples. Furthermore, in all cases, the shape of the absorption bands in the transient diffuse reflectance spectra of the 4-methoxycumyl cation observed in the vacuum heated samples and those samples prepared without heating are closely similar, Figures A-3 and A-4. The intensity of the signal in the heated sample is somewhat weaker, presumably due to decomposition or evaporation/sublimation of the precursor. These observations suggest that any residual hexane which may be present in the zeolite-substrate composites does not significantly influence the intrazeolite reactivity of the 4-methoxycumyl cation in any of the alkali metal cation Y zeolites, or NaX.

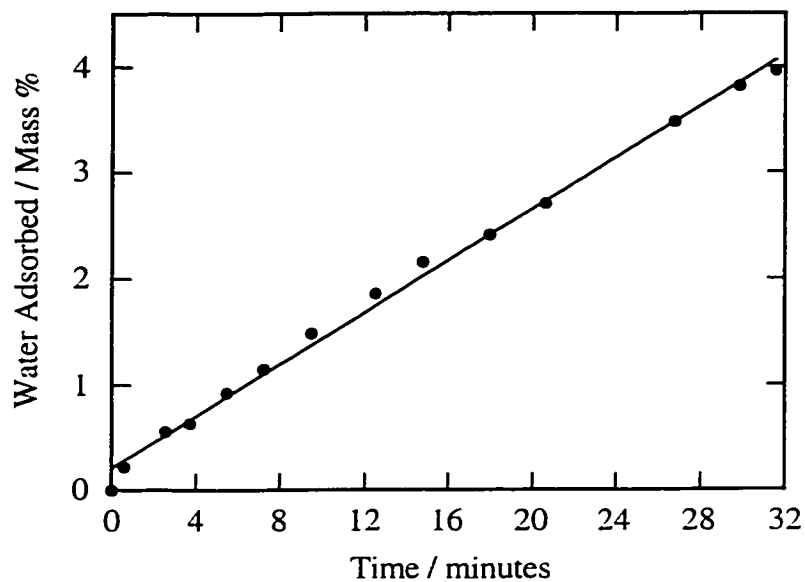


Figure A-1. Amount of water adsorbed (mass %) as a function of time by a dehydrated sample of NaX. The sample was activated at 450 °C for in excess of 12 hours and allowed to room temperature under vacuum before recording mass changes as a function of time sitting open in the ambient atmosphere.

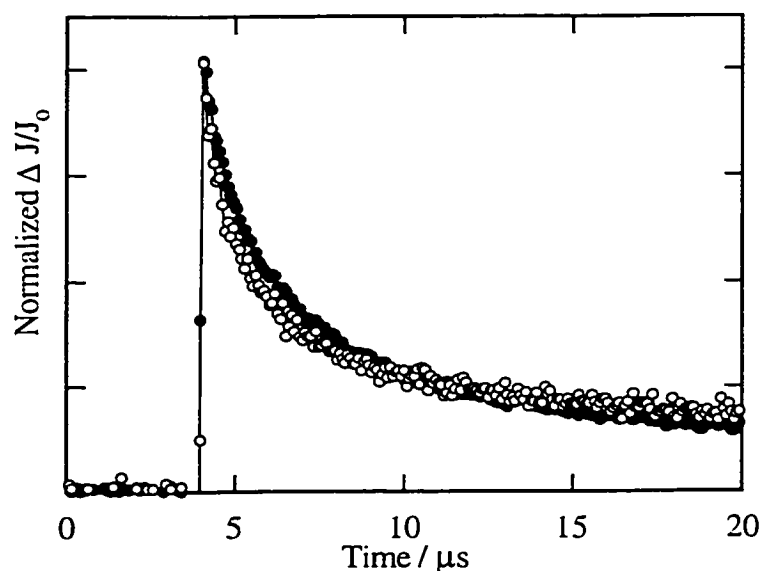


Figure A-2. Decay traces monitored at 360 nm following 266 nm laser photolysis of DMB in NaY containing 11 % (closed circles) and 2 % (open circles) residual hexane by mass. Hexane was removed from the sample by vacuum pumping in a desiccator for 5 hours and on the vacuum line for 16 hours (closed circles) or by heating in a vacuum oven at 45 °C for 22 hours. (open circles).

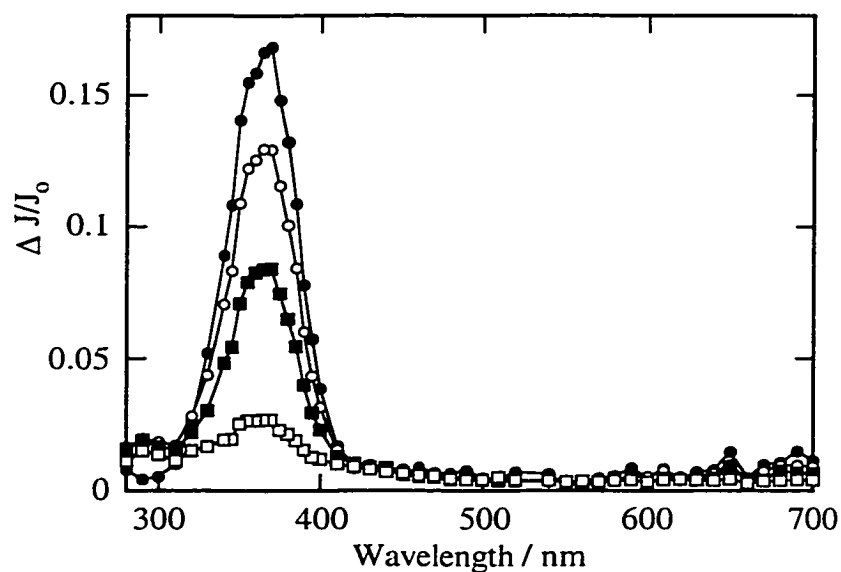


Figure A-3. Transient diffuse reflectance spectrum obtained 240 ns (closed circles), 760 ns (open circles), 2.24 μ s (closed squares), and 14.8 μ s (open squares) after 266 nm laser photolysis of DMB in NaY containing 11 % residual hexane by mass. Hexane was removed from the sample by vacuum pumping in a desiccator for 5 hours and on the vacuum line for 16 hours.

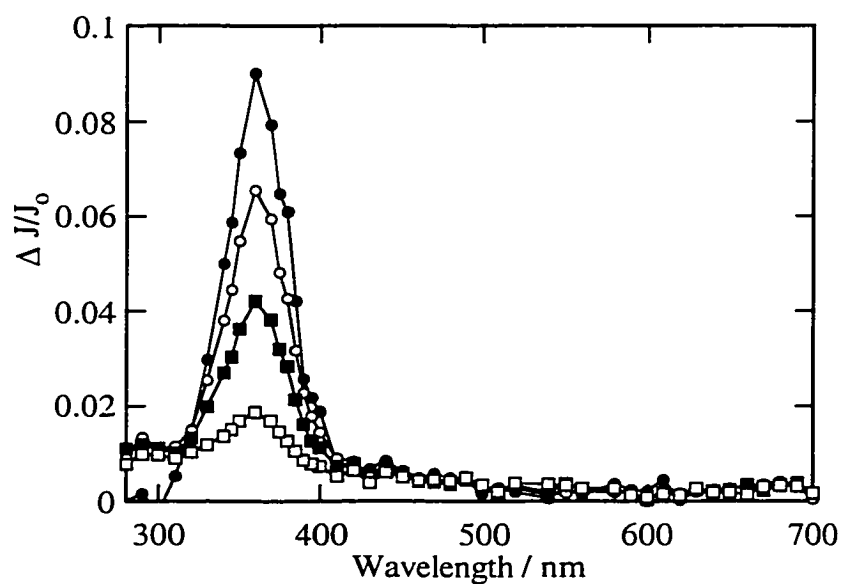


Figure A-4. Transient diffuse reflectance spectrum obtained 240 ns (closed circles), 760 ns (open circles), 2.24 μ s (closed squares), and 14.8 μ s (open squares) after 266 nm laser photolysis of DMB in NaY containing 2 % residual hexane by mass. Hexane was removed from the sample by pumping in a vacuum oven at 45 °C for 22 hours.

References

1. Breck, D. W. *J. Chem. Educ.* **1964**, *41*, 678-689.
2. Breck, D. W. *Zeolite Molecular Sieves: Structure, Chemistry and Use*; John Wiley and Sons: New York, 1974.
3. Rabo, J. A. *Zeolite Chemistry and Catalysis, ACS Monograph No. 171*; ACS: Washington, 1976.
4. Mortier, W. J.; Schoonheydt, R. A. *Prog. Solid State Chem.* **1985**, *16*, 1-125.
5. Dyer, A. *An Introduction to Zeolite Molecular Sieves*; John Wiley and Sons: Bath, 1988.
6. van Bekkum, H.; Flanigen, E. M.; Jansen, J. C. *Introduction to Zeolite Science and Practice*; Elsevier Science Ltd.: Amsterdam, 1991.
7. Davis, M. E. *Acc. Chem. Res.* **1993**, *26*, 111-115.
8. Corma, A.; García, H. *J. Chem. Soc., Dalton Trans.* **2000**, 1381-1394.
9. Mumpton, F. A. *Proc. Natl. Acad. Sci. USA* **1999**, *96*, 3463-3470.
10. Sherman, J. D. *Proc. Natl. Acad. Sci. USA* **1999**, *96*, 3471-3478.
11. Hölderich, W.; Hesse, M.; Näumann, F. *Angew. Chem. Int. Ed. Engl.* **1988**, *27*, 226-246.
12. Meier, W. M.; Olson, D. H. *Atlas of Zeolite Structure Types*; Elsevier: London, 1996.
13. Mortier, W. *Compilation of Extra-framework sites in Zeolites*; Butterworth Scientific Limited: Guildford, England, 1982.
14. Eulenberger, G. R.; Shoemaker, D. P.; Keill, J. G. *J. Phys. Chem.* **1967**, *71*, 1812-1819.
15. Olson, D. H. *J. Phys. Chem.* **1970**, *74*, 2758-2764.
16. Zhu, L.; Seff, K. *J. Phys. Chem. B* **2000**, *104*, 8946-8951.
17. Fyfe, C. A.; Mueller, K. T.; Kokotailo, G. T. *NMR Techniques in Catalysis*; Bell, A. T. and Pines, A., Ed.; Marcel Dekker Inc.: New York, 1994, pp 11-67.
18. Hriljac, J. J.; Eddy, M. M.; Cheetham, A. K.; Donohue, J. A.; Ray, G. J. *J. Solid State Chem.* **1993**, *106*, 66-72.
19. Morris, R. E.; Weigel, S. J.; Henson, N. J.; Bull, L. M.; Janicke, M. T.; Chmelka, B. F.; Cheetham, A. K. *J. Am. Chem. Soc.* **1994**, *116*, 11849-11855.
20. Kvick, A.; Smith, J. V. *J. Chem. Phys.* **1983**, *79*, 2356-2362.
21. Loewenstein, W. *Am. Mineral.* **1954**, *39*, 92-96.
22. Norby, P.; Poshni, F. I.; Gualtieri, A. F.; Hanson, J. C.; Grey, C. P. *J. Phys. Chem. B* **1998**, *102*, 839-856.

23. Ramamurthy, V.; Turro, N. J. *J. Inclusion Phenom. Mol. Recognit. Chem.* **1995**, *21*, 239-282.
24. Turro, N. J. *Acc. Chem. Res.* **2000**, *33*, 637-646.
25. Karger, J.; Ruthven, D. M. *Diffusion in Zeolites and Other Microporous Solids*; John Wiley and Sons: New York, 1992.
26. Trif, E.; Strugaru, D.; Ivan, I.; Gheorghe, G.; Nicula, A. *J. Therm. Anal.* **1994**, *41*, 871-880.
27. Hunger, B.; Klepel, O.; Kirschhock, C.; Heuchel, M.; Toufar, H.; Fuess, H. *Langmuir* **1999**, *15*, 5937-5941.
28. Kirschhock, C. E. A.; Hunger, B.; Martens, J.; Jacobs, P. A. *J. Phys. Chem. B* **2000**, *104*, 439-448.
29. Ramamurthy, V.; Sanderson, D. R.; Eaton, D. F. *Photochem. Photobiol.* **1992**, *56*, 297-303.
30. Ward, J. W. *J. Catal.* **1968**, *10*, 34-46.
31. Rabo, J. A.; Angell, C. L.; Kasai, P. H.; Schomaker, V. *Discuss. Faraday Soc.* **1966**, *41*, 328-349.
32. Rabo, J. A. *Catal. Rev. Sci. Eng.* **1981**, *23*, 293-313.
33. Preuss, E.; Linden, G.; Peuckert, M. *J. Phys. Chem.* **1985**, *89*, 2955-2961.
34. Yoon, K. B.; Kochi, J. K. *J. Am. Chem. Soc.* **1988**, *110*, 6586-6588.
35. Liu, X.; Iu, K.-K.; Thomas, J. K. *J. Phys. Chem.* **1989**, *93*, 4120-4128.
36. Iu, K.-K.; Thomas, J. K. *Langmuir* **1990**, *6*, 471-478.
37. Ortiz, W.; Cozens, F. L.; Schepp, N. P. *Org. Lett.* **1999**, *1*, 531-534.
38. Uppili, S.; Thomas, K. J.; Crompton, E. M.; Ramamurthy, V. *Langmuir* **2000**, *16*, 265-274.
39. Yoon, K. B.; Kochi, J. K. *J. Am. Chem. Soc.* **1989**, *111*, 1128-1130.
40. Yoon, K. B.; Kochi, J. K. *J. Phys. Chem.* **1991**, *95*, 3780-3790.
41. Yoon, K. B. *Chem. Rev.* **1993**, *93*, 321-339.
42. Blatter, F.; Frei, H. *J. Am. Chem. Soc.* **1993**, *115*, 7501-7502.
43. Blatter, F.; Frei, H. *J. Am. Chem. Soc.* **1994**, *116*, 1812-1820.
44. Sun, H.; Blatter, F.; Frei, H. *J. Am. Chem. Soc.* **1996**, *118*, 6873-6879.
45. Takeya, H.; Kuriyama, Y.; Kojima, M. *Tetrahedron Lett.* **1998**, *39*, 5967-5970.
46. Hashimoto, S.; Hagiwara, N.; Asahi, T.; Masuhara, H. *Langmuir* **1999**, *15*, 3123-3133.
47. Corma, A. *Chem. Rev.* **1995**, *95*, 559-614.
48. Farneth, W. E.; Gorte, R. J. *Chem. Rev.* **1995**, *95*, 615-635.
49. van Santen, R. A.; Kramer, G. J. *Chem. Rev.* **1995**, *95*, 637-660.

50. Rao, V. J.; Perlstein, D. L.; Robbins, R. J.; Lakshminarasimhan, P. H.; Kao, H.; Grey, C. P.; Ramamurthy, V. *Chem. Commun.* **1998**, 269-270.
51. Thomas, K. J.; Ramamurthy, V. *Langmuir* **1998**, *14*, 6687-6692.
52. Scaiano, J. C.; Kaila, M.; Corrent, S. *J. Phys. Chem. B* **1997**, *101*, 8564-8568.
53. Corrent, S.; Hahn, P.; Pohlens, G.; Connolly, T.; Scaiano, J. C.; Fornés, V.; García, H. *J. Phys. Chem. B* **1998**, *102*, 5852-5858.
54. Corrent, S.; Martinez, L. J.; Scaiano, J. C.; García, H.; Fornés, V. *J. Phys. Chem. B* **1999**, *103*, 8097-8102.
55. Stamiros, D. N.; Turkevich, J. *J. Am. Chem. Soc.* **1964**, *86*, 749-757.
56. Dollish, F. R.; Hall, W. K. *J. Phys. Chem.* **1967**, *71*, 1005-1013.
57. Rhodes, C. J.; Standing, M. *J. Chem. Soc., Perkin Trans. 2* **1992**, 1455-1460.
58. Rhodes, C. J. *Colloids Surf., A* **1993**, *72*, 111-118.
59. Chen, F. R.; Fripiat, J. J. *J. Phys. Chem.* **1992**, *96*, 819-823.
60. Roduner, E.; Crockett, R.; Wu, L.-M. *J. Chem. Soc., Faraday Trans.* **1993**, *89*, 2101-2105.
61. Crockett, R.; Roduner, E. *J. Chem. Soc., Perkin Trans. 2* **1993**, 1503-1509.
62. Liu, X. L.; Iu, K.; Thomas, J. K.; He, H.; Klinowski, J. *J. Am. Chem. Soc.* **1994**, *116*, 11811-11818.
63. Cano, M. L.; Corma, A.; Fornes, V.; García, H. *J. Phys. Chem.* **1995**, *99*, 4241-4246.
64. Corma, A.; Fornes, V.; García, H.; Marti, V.; Miranda, M. A. *Chem. Mater.* **1995**, *7*, 2136-2143.
65. Corma, A.; García, H. *Top. Catal.* **1998**, *6*, 127-140.
66. Cozens, F. L.; Bogdanov, R.; Regimbald, M.; García, H.; Marti, V.; Scaiano, J. C. *J. Phys. Chem. B* **1997**, *101*, 6821-6829.
67. Gener, I.; Moissette, A.; Brémard, C. *Chem. Commun.* **2000**, 1563-1564.
68. Ramamurthy, V.; Caspar, J. V.; Corbin, D. R. *J. Am. Chem. Soc.* **1991**, *113*, 594-600.
69. Iu, K.; Thomas, J. K. *J. Phys. Chem.* **1991**, *95*, 506-509.
70. Iu, K.-K.; Thomas, J. K. *Colloids Surf.* **1992**, *63*, 39-48.
71. Iu, K.; Liu, X.; Thomas, J. K. *J. Photochem. Photobiol., A* **1994**, *79*, 103-107.
72. Lednev, I. K.; Mathivanan, N.; Johnston, L. J. *J. Phys. Chem.* **1994**, *98*, 11444-11451.
73. Hashimoto, S.; Mutoh, T.; Fukumura, H.; Masuhara, H. *J. Chem. Soc., Faraday Trans.* **1996**, *92*, 3653-3660.
74. Gener, I.; Buntinx, G.; Brémard, C. *Angew. Chem. Int. Ed.* **1999**, *38*, 1819-1822.
75. Gessner, F.; Scaiano, J. C. *J. Photochem. Photobiol., A* **1992**, *67*, 91-100.
76. Ward, J. W. *J. Catal.* **1967**, *9*, 225-236.

77. Kasai, P. H.; Bishop, J. R. *J. Phys. Chem.* **1973**, *77*, 2308-2312.
78. Edwards, P. P.; Harrison, M. R.; Klinowski, J.; Ramdas, S.; Thomas, J. M.; Johnson, D. C.; Page, C. J. *J. Chem. Soc., Chem. Commun.* **1984**, 982-94.
79. Anderson, P. A.; Barr, D.; Edwards, P. P. *Angew. Chem. Int. Ed. Engl.* **1991**, *30*, 1501-1502.
80. Zhang, G.; Liu, X.; Thomas, J. K. *Radiat. Phys. Chem.* **1998**, *51*, 135-152.
81. Liu, X.; Zhang, G.; Thomas, J. K. *J. Phys. Chem. B* **1997**, *101*, 2182-2194.
82. Liu, X.; Zhang, G.; Thomas, J. K. *J. Phys. Chem.* **1995**, *99*, 10024-10034.
83. Iu, K.-K.; Liu, X.; Thomas, J. K. *J. Phys. Chem.* **1993**, *97*, 8165-8170.
84. Thomas, J. K. *Chem. Rev.* **1993**, *93*, 301-320.
85. Liu, X.; Thomas, J. K. *Langmuir* **1992**, *8*, 1750-1756.
86. Takatani, S.; Fukumura, H.; Masuhara, H.; Hashimoto, S. *J. Phys. Chem. B* **1997**, *101*, 3365-3369.
87. Bracaleon, L.; Brousmiche, D.; Rao, V. J.; Johnston, L. J.; Ramamurthy, V. *J. Am. Chem. Soc.* **1998**, *120*, 4926-4933.
88. Barthomeuf, D. *J. Phys. Chem.* **1984**, *88*, 42-45.
89. Liu, X.; Iu, K.; Thomas, J. K. *J. Phys. Chem.* **1994**, *98*, 7877-7884.
90. Barthomeuf, D. *Acidity and Basicity of Solids*; Fraissard, J. and Petrakis, L., Ed.; Kluwer Academic Publishers: Netherlands, 1994, pp 181-197.
91. Hattori, H. *Chem. Rev.* **1995**, *95*, 537-558.
92. Turkevich, J.; Ono, Y. *Adv. Catal.* **1969**, *20*, 135-152.
93. Flockhart, B. D.; McLoughlin, L.; Pink, R. C. *J. Catal.* **1972**, *25*, 305-313.
94. Samoilova, R. I.; Shublin, A. A.; Bowman, M. K.; Hüttermann, J.; Dikanov, S. A. *Chem. Phys. Lett.* **2000**, *316*, 404-410.
95. Lavalley, J.; Lamotte, J.; Travert, A.; Czyniewska, J.; Ziolek, M. *J. Chem. Soc., Faraday Trans.* **1998**, *94*, 331-335.
96. Okamoto, Y.; Ogawa, M.; Maezawa, A.; Imanaka, T. *J. Catal.* **1988**, *112*, 427-436.
97. Huang, M.; Adnot, A.; Kaliaguine, S. *J. Catal.* **1992**, *137*, 322-332.
98. Abou-Kais, A.; Vedrine, J. C.; Massardier, J.; Dalmai-Imelik, G. *J. Chem. Soc., Faraday Trans. I* **1974**, *70*, 1039-1045.
99. Vedrine, J. C.; Naccache, C. *J. Phys. Chem.* **1973**, *77*, 1606-1610.
100. Iton, L. E.; Turkevich, J. *J. Phys. Chem.* **1978**, *82*, 200-214.
101. Cozens, F. L.; García, H.; Scaiano, J. C. *Langmuir* **1994**, *10*, 2246-2249.
102. Alvaro, M.; García, H.; García, S.; Marquez, F.; Scaiano, J. C. *J. Phys. Chem. B* **1997**, *101*, 3043-3051.
103. Hashimoto, S. *J. Chem. Soc., Faraday Trans.* **1997**, *93*, 4401-4408.

104. Millini, R. *Catal. Today* **1998**, *41*, 41-51.
105. Corma, A.; Fornés, V.; García, H.; Miranda, M.; Primo, J.; Sabater, M. *J. Am. Chem. Soc.* **1994**, *116*, 2276-2280.
106. Cano, M. L.; Cozens, F. L.; Fomes, V.; García, H.; Scaiano, J. C. *J. Phys. Chem.* **1996**, *100*, 18145-18151.
107. Alvaro, M.; García, H.; García, S.; Fernández, L. *Tetrahedron Lett.* **1996**, *37*, 2873-2876.
108. Smith, L.; Cheetham, A. K.; Morris, R. E.; Marchese, L.; Thomas, J. M.; Wright, P. A.; Chen, J. *Science* **1996**, *271*, 799-802.
109. Klein, H.; Kirschhock, C.; Fuess, H. *J. Phys. Chem.* **1994**, *98*, 12345-12360.
110. Cano, M. L.; Corma, A.; Fornes, V.; García, H.; Miranda, M. A.; Baerlocher, C.; Lengauer, C. *J. Am. Chem. Soc.* **1996**, *118*, 11006-11013.
111. Förster, H.; Fuess, H.; Geidel, E.; Hunger, B.; Jobic, H.; Kirschhock, C.; Klepel, O.; Krause, K. *Phys. Chem. Chem. Phys.* **1999**, *1*, 593-603.
112. Primet, M.; Garbowski, E.; Mathieu, M. V.; Imelik, B. *J. Chem. Soc., Faraday Trans. I* **1980**, *76*, 1942-1952.
113. Förster, H.; Kiricsi, I.; Hannus, I. *J. Mol. Struct.* **1993**, *296*, 61-67.
114. Bertsch, L.; Habgood, H. W. *J. Phys. Chem* **1963**, *67*, 1621-1628.
115. Ward, J. W. *J. Catal.* **1968**, *11*, 238-250.
116. Bosch, E.; Huber, S.; Weitkamp, J.; Knözinger, H. *Phys. Chem. Chem. Phys.* **1999**, *1*, 579-584.
117. Su, B.-L.; Norberg, V. *Langmuir* **2000**, *16*, 6020-6028.
118. Hepp, M. A.; Ramamurthy, V.; Corbin, D. R.; Dybowski, C. *J. Phys. Chem.* **1992**, *96*, 2629-2632.
119. Liu, S.-B.; Ma, L.-J.; Lin, M.-W.; Wu, J.-F.; Chen, T.-L. *J. Phys. Chem.* **1992**, *96*, 8120-8125.
120. Grey, C. P.; Poshni, F. I.; Gualtieri, A. F.; Norby, P.; Hanson, J. C.; Corbin, D. R. *J. Am. Chem. Soc.* **1997**, *119*, 1981-1989.
121. Casal, H. L.; Scaiano, J. C. *Can. J. Chem.* **1985**, *63*, 1308-1314.
122. Kelly, G.; Willsher, C. J.; Wilkinson, F.; Netto-Ferreira, J. C.; Olea, A.; Weir, D.; Johnston, L. J.; Scaiano, J. C. *Can. J. Chem.* **1990**, *68*, 812-819.
123. Johnston, L. J.; Scaiano, J. C.; Shi, J.; Siebrand, W.; Zerbetto, F. *J. Phys. Chem.* **1991**, *95*, 10018-10024.
124. Garcia-Garibay, M. A.; Lei, X. G.; Turro, N. J. *J. Am. Chem. Soc.* **1992**, *114*, 2749-2751.
125. Ramamurthy, V. *J. Am. Chem. Soc.* **1994**, *116*, 1345-1351.

126. Ramamurthy, V.; Sanderson, D. R.; Eaton, D. F. *J. Phys. Chem.* **1993**, *97*, 13380-13386.
127. Cozens, F. L.; Regimbald, M.; García, H.; Scaiano, J. C. *J. Phys. Chem.* **1996**, *100*, 18165-18172.
128. Hashimoto, S.; Ikuta, S.; Asahi, T.; Masuhara, H. *Langmuir* **1998**, *14*, 4284-4291.
129. Thomas, K. J.; Sunoj, R. B.; Chandrasekhar, J.; Ramamurthy, V. *Langmuir* **2000**, *16*, 4912-4921.
130. Pearson, J. G.; Chmelka, B. F.; Shykind, D. N.; Pines, A. *J. Phys. Chem.* **1992**, *96*, 8517-8522.
131. Hong, S. B.; Cho, H. M.; Davis, M. E. *J. Phys. Chem.* **1993**, *97*, 1622-1628.
132. Ramamurthy, V.; Sanderson, D. R.; Eaton, D. F. *J. Am. Chem. Soc.* **1993**, *115*, 10438-10439.
133. Park, Y. S.; Lee, K.; Lee, C.; Yoon, K. B. *Langmuir* **2000**, *16*, 4470-4477.
134. Yoon, K. B.; Huh, T. J.; Kochi, J. K. *J. Phys. Chem.* **1995**, *99*, 7042-7053.
135. Scaiano, J. C.; García, S.; García, H. *Tetrahedron Lett.* **1997**, *38*, 5929-5932.
136. Karger, J.; Pfeifer, H. *NMR Techniques in Catalysis*; Bell, A. T. and Pines, A., Ed.; Marcel Dekker, Inc.: New York, 1994, pp 69-138.
137. Reyes, S. C.; Sinfelt, J. H.; DeMartin, G. J. *J. Phys. Chem. B* **2000**, *104*, 5750-5761.
138. Kaiser, L. G.; Meersmann, T.; Logan, J. W.; Pines, A. *Proc. Natl. Acad. Sci. USA* **2000**, *97*, 2414-2418.
139. Cavo, J.; Bülow, M.; Schirmer, W. J.; Karger, J.; Heink, W.; Pfeifer, H.; Zdanov, S. *P. Chem. Soc., Faraday Trans. I* **1985**, *81*, 2541-2550.
140. Jobic, H.; Bée, M.; Pouget, S. *J. Phys. Chem. B* **2000**, *104*, 7130-7133.
141. Weiss, R. G.; Ramamurthy, V.; Hammond, G. S. *Acc. Chem. Res.* **1993**, *26*, 530-536.
142. Zicovich-Wilson, C. M.; Corma, A.; Viruela, P. *J. Phys. Chem.* **1994**, *98*, 10863-10870.
143. Corma, A.; García, H.; Sastre, G.; Viruela, P. M. *J. Phys. Chem. B* **1997**, *101*, 4575-4582.
144. Márquez, F.; García, H.; Palomares, E.; Fernández, L.; Corma, A. *J. Am. Chem. Soc.* **2000**, *122*, 6520-6521.
145. Scaiano, J. C.; de Lucas, N. C.; Andraos, J.; García, H. *Chem. Phys. Lett.* **1995**, *223*, 5-9.
146. Scaiano, J. C.; García, H. *Acc. Chem. Res.* **1999**, *32*, 783-793.
147. Turro, N. J. *Pure Appl. Chem.* **1986**, *58*, 1219-1228.
148. Turro, N. J.; Zhang, Z. *Tetrahedron Lett.* **1987**, *28*, 5637-5640.

149. Garcia-Garibay, M.; Zhang, Z.; Turro, N. J. *J. Am. Chem. Soc.* **1991**, *113*, 6212-6218.
150. Turro, N. J.; Lei, X.; Li, W.; McDermott, A.; Abrams, L.; Ottaviani, M. F.; Beard, H. S. *Chem. Commun.* **1998**, 695-696.
151. Turro, N. J.; McDermott, A.; Lei, X.; Li, W.; Abrams, L.; Ottaviani, M. F.; Beard, H. S.; Houk, K. N.; Beno, B. R.; Lee, P. S. *Chem. Commun.* **1998**, 697-698.
152. Hirano, T.; Li, W.; Abrams, L.; Krusic, P. J.; Ottaviani, M. F.; Turro, N. J. *J. Am. Chem. Soc.* **1999**, *121*, 7170-7171.
153. Hirano, T.; Li, W.; Abrams, L.; Krusic, P. J.; Ottaviani, M. F.; Turro, N. J. *J. Org. Chem.* **2000**, *65*, 1319-1330.
154. Jockusch, S.; Hirano, T.; Liu, Z.; Turro, N. J. *J. Phys. Chem. B* **2000**, *104*, 1212-1216.
155. Cozens, F. L.; Ortiz, W.; Schepp, N. P. *J. Am. Chem. Soc.* **1998**, *120*, 13543-13544.
156. Liu, X.; Iu, K.-K.; Thomas, J. K. *Chem. Phys. Lett.* **1993**, *204*, 163-167.
157. Lakshminarasimhan, P.; Thomas, K. J.; Brancalion, L.; Wood, P. D.; Johnston, L. J.; Ramamurthy, V. *J. Phys. Chem. B* **1999**, *103*, 9247-9254.
158. Sankararaman, S.; Yoon, K. B.; Yabe, T.; Kochi, J. K. *J. Am. Chem. Soc.* **1991**, *113*, 1419-1421.
159. Yoon, K. B.; Hubig, S. M.; Kochi, J. K. *J. Phys. Chem.* **1994**, *98*, 3865-3871.
160. Vitale, M.; Castagnola, N. B.; Ortins, N. J.; Brooke, J. A.; Vaidyalingam, A.; Dutta, P. K. *J. Phys. Chem. B* **1999**, *103*, 2408-2416.
161. Dutta, P. K.; Turberville, W. *J. Phys. Chem.* **1992**, *96*, 9410-9416.
162. Dutta, P. K.; Incavo, J. A. *J. Phys. Chem.* **1987**, *91*, 4443-4446.
163. Borja, M.; Dutta, P. K. *Nature* **1993**, *362*, 43-45.
164. Ledney, M.; Dutta, P. K. *J. Am. Chem. Soc.* **1995**, *117*, 7687-7695.
165. Dutta, P. K.; Ledney, M. *Prog. Inorg. Chem.* **1996**, *44*, 209-271.
166. Yonemoto, E. H.; Kim, Y.; Schmehl, R. H.; Wallin, J. O.; Shoulders, B. A.; Richardson, B. R.; Haw, J. F.; Mallouk, T. E. *J. Am. Chem. Soc.* **1994**, *116*, 10557-10563.
167. Brigham, E. S.; Snowden, P. T.; Kim, Y.; Mallouk, T. E. *J. Phys. Chem.* **1993**, *97*, 8650-8655.
168. Kim, Y. L.; Mallouk, T. E. *J. Phys. Chem.* **1992**, *96*, 2879-2885.
169. Krueger, J. S.; Mayer, J. E.; Mallouk, T. E. *J. Am. Chem. Soc.* **1988**, *110*, 8232-8234.
170. Persaud, L.; Bard, A. J.; Campion, A.; Fox, M. A.; Mallouk, T. E.; Webber, S. E.; White, J. M. *J. Am. Chem. Soc.* **1987**, *109*, 7309-7314.

171. Sykora, M.; Mareszewski, K.; Treffert-Ziemelis, S. M.; Kincaid, J. R. *J. Am. Chem. Soc.* **1998**, *120*, 3490-3498.
172. Sykora, M.; Kincaid, J. R. *Nature* **1997**, *387*, 162-164.
173. Cano, M. L.; Cozens, F. L.; Esteves, M. A.; Márquez, F.; García, H. *J. Org. Chem.* **1997**, *62*, 7121-7127.
174. Cano, M. L.; Fornes, V.; García, H.; Miranda, M. A.; Perez-Prieto, J. *J. Chem. Soc., Chem. Commun.* **1995**, 2477-2478.
175. García, H.; García, S.; Perez-Prieto, J.; Scaiano, J. C. *J. Phys. Chem.* **1996**, *100*, 18158-18164.
176. Adam, W.; Casades, I.; Fornés, V.; García, H.; Weichold, O. *J. Org. Chem.* **2000**, *65*, 3947-3951.
177. Cano, M. L.; Cozens, F. L.; García, H.; Vicente, M.; Scaiano, J. C. *J. Phys. Chem.* **1996**, *100*, 18152-18157.
178. Ramamurthy, V. *Photoprocesses of Organic Molecules Included in Zeolites*; Ramamurthy, V., Ed.; VCH: New York, 1991, pp 429-493.
179. Ramamurthy, V.; Eaton, D. F.; Caspar, J. V. *Acc. Chem. Res.* **1992**, *25*, 299-307.
180. Ramamurthy, V.; Eaton, D. F. *Chem. Mater.* **1994**, *6*, 1128-1136.
181. Ramamurthy, V.; Lakshminarasimhan, P.; Grey, C. P.; Johnston, L. J. *Chem. Commun.* **1998**, 2411-2424.
182. Ramamurthy, V.; Robbins, R. J.; Thomas, K. J.; Lakshminarasimhan, P. H. *Organized Molecular Assemblies in the Solid State*; Whitesell, J. K., Ed.; John Wiley & Sons Ltd.: New York, 1999, pp 63-140.
183. Ramamurthy, V.; Caspar, J. V.; Corbin, D. R.; Eaton, D. F. *J. Photochem. Photobiol., A* **1989**, *50*, 157-161.
184. Ramamurthy, V.; Caspar, J. V.; Corbin, D. R.; Schlyer, B. B.; Maki, A. H. *J. Phys. Chem.* **1990**, *94*, 3391-3393.
185. Ramamurthy, V.; Corbin, D. R.; Johnston, L. J. *J. Am. Chem. Soc.* **1992**, *114*, 3870-3882.
186. Pitchumani, K.; Gamlin, J. N.; Ramamurthy, V.; Scheffer, J. R. *Chem. Commun.* **1996**, 2049-2050.
187. Li, X.; Ramamurthy, V. *Tetrahedron Lett.* **1996**, *37*, 5235-5238.
188. Ramamurthy, V.; Corbin, D. R.; Turro, N. J.; Sato, Y. *Tetrahedron Lett.* **1989**, *30*, 5829-5832.
189. Ramamurthy, V.; Lei, X. G.; Turro, N. J.; Lewis, T. R.; Scheffer, J. R. *Tetrahedron Lett.* **1991**, *32*, 7675-7678.

190. Ramamurthy, V.; Caspar, J. V.; Corbin, D. R.; Eaton, D. E.; Kaufmann, J. S.; Dybowski, C. *J. Photochem. Photobiol., A* **1990**, *51*, 259-263.
191. Ramamurthy, V.; Corbin, D. R.; Kumar, C. V.; Turro, N. J. *Tetrahedron Lett.* **1990**, *31*, 47-50.
192. Lem, G.; Kaprinidis, N. A.; Schuster, D. I.; Ghatlia, D.; Turro, N. J. *J. Am. Chem. Soc.* **1993**, *115*, 7009-7010.
193. Pitchumani, K.; Warriar, M.; Cui, C.; Weiss, R. G.; Ramamurthy, V. *Tetrahedron Lett.* **1996**, *37*, 6251-6254.
194. Gu, W.; Warriar, M.; Ramamurthy, V.; Weiss, R. G. *J. Am. Chem. Soc.* **1999**, *121*, 9467-9468.
195. Pitchumani, K.; Warriar, M.; Ramamurthy, V. *J. Am. Chem. Soc.* **1996**, *118*, 9428-9429.
196. Li, X.; Ramamurthy, V. *J. Am. Chem. Soc.* **1996**, *118*, 10666-10667.
197. Robbins, R. J.; Ramamurthy, V. *Chem. Commun.* **1997**, 1071-1072.
198. Rao, V. J.; Uppili, S. R.; Corbin, D. R.; Schwarz, S.; Lustig, S. R.; Ramamurthy, V. *J. Am. Chem. Soc.* **1998**, *120*, 2480-2481.
199. Xiang, Y.; Larsen, S. C.; Grassian, V. H. *J. Am. Chem. Soc.* **1999**, *121*, 5063-5072.
200. Panov, A. G.; Larsen, R. G.; Totah, N. I.; Larsen, S. C.; Grassian, V. H. *J. Phys. Chem. B* **2000**, *104*, 5706-5714.
201. Zhou, W.; Clennan, E. L. *J. Am. Chem. Soc.* **1999**, *121*, 2915-2916.
202. Zhou, W.; Clennan, E. L. *Org. Lett.* **2000**, *2*, 437-440.
203. Stratakis, M.; Froudakis, G. *Org. Lett.* **2000**, *2*, 1369-1372.
204. Baldovi, M. V.; Cozens, F. L.; Fornes, V.; García, H.; Scaiano, J. C. *Chem. Mater.* **1996**, *8*, 152-160.
205. Fornés, V.; García, H.; Miranda, M. A.; Mojarrad, F.; Sabater, M.; Suliman, N. N. E. *Tetrahedron* **1996**, *57*, 7750-7760.
206. Sanjuan, A.; Mercedes, A.; Aguirre, G.; García, H.; Scaiano, J. C. *J. Am. Chem. Soc.* **1998**, *120*, 7351-7352.
207. Hadel, L. M. *Handbook of Organic Photochemistry*; Scaiano, J. C., Ed.; CRC Press: Boca Raton, 1989; Vol. I, pp 279-292.
208. Bohne, C.; Redmond, R. W.; Scaiano, J. C. *Photochemistry in Organized and Constrained Media*; Ramamurthy, V., Ed.; VCH: New York, 1991, pp 79-132.
209. Oelkrug, D.; Honnen, W.; Wilkinson, F.; Willsher, C. J. *J. Chem. Soc., Faraday Trans. 2* **1987**, *83*, 2081-2095.
210. Wilkinson, F.; Kelly, G. *Handbook of Organic Photochemistry*; Scaiano, J. C., Ed.; CRC Press: Boca Raton, 1989; Vol. I, pp 293-313.

211. Ware, W. *Photochemistry in Organized and Constrained Media*; Ramamurthy, V., Ed.; VCH: New York, 1991, pp 563-602.
212. Wagner, B. D.; Ware, W. R. *J. Phys. Chem.* **1990**, *94*, 3489-3494.
213. Olah, G. A.; Schleyer, P. v. R. *Carbonium Ions*; John Wiley and Sons: New York, 1968-1976; Vol. 1-5.
214. Bethell, D.; Gold, V. *Carbonium Ions. An Introduction*; Academic Press: London, 1967.
215. Olah, G. A. *Angew. Chem. Int. Ed. Engl.* **1973**, *12*, 173-212.
216. Olah, G. A. *Angew. Chem. Int. Ed. Engl.* **1995**, *34*, 1393-1405.
217. Deno, N. C. *Prog. Phys. Org. Chem.* **1964**, *2*, 129-193.
218. Olah, G. A.; Pittman, J. C. U.; Waack, R.; Doran, M. *J. Am. Chem. Soc.* **1966**, *88*, 1488-1495.
219. Fraenkel, G.; Farnum, D. G. *Carbonium Ions*; Olah, G. A. and Schleyer, P. v. R., Ed.; Wiley: New York, 1968; Vol. 1, Chapter 7.
220. Olah, G. A.; Comisarow, M. B.; Cupas, C. A.; Pittman, J. C. P. *J. Am. Chem. Soc.* **1965**, *87*, 2997-2998.
221. Olah, G. A.; Porter, R. D.; Kelly, D. P. *J. Am. Chem. Soc.* **1971**, *93*, 464-466.
222. Ritchie, C. D. *Acc. Chem. Res.* **1972**, *5*, 348-354.
223. Ritchie, C. D. *Can. J. Chem.* **1986**, *64*, 2239-2250.
224. Richard, J. P.; Jencks, W. P. *J. Am. Chem. Soc.* **1984**, *106*, 1373-1383.
225. Richard, J. P.; Rothenberg, M. E.; Jencks, W. P. *J. Am. Chem. Soc.* **1984**, *106*, 1361-1372.
226. McClelland, R. A. *Tetrahedron* **1996**, *52*, 6823-6858.
227. Das, P. K. *Chem. Rev.* **1993**, *93*, 119-144.
228. McClelland, R. A.; Banait, N.; Steenken, S. *J. Am. Chem. Soc.* **1986**, *108*, 7023-7027.
229. McClelland, R. A.; Kanagasabapathy, V. M.; Steenken, S. *J. Am. Chem. Soc.* **1988**, *110*, 6913-6914.
230. McClelland, R. A.; Kanagasabapathy, V. M.; Banait, N. S.; Steenken, S. *J. Am. Chem. Soc.* **1989**, *111*, 3966-3972.
231. McClelland, R. A.; Kanagasabapathy, V. M.; Banait, N. S.; Steenken, S. *J. Am. Chem. Soc.* **1991**, *113*, 1009-1014.
232. Bartl, J.; Steenken, S.; Mayr, H.; McClelland, R. A. *J. Am. Chem. Soc.* **1990**, *112*, 6918-6928.
233. Bartl, J.; Steenken, S.; Mayr, H. *J. Am. Chem. Soc.* **1991**, *113*, 7710-7716.

234. McClelland, R. A.; Chan, R. A.; Cozens, F. L.; Modro, A.; Steenken, S. *Angew. Chem. Int. Ed. Engl.* **1991**, *30*, 1337-1339.
235. Cozens, F. L.; Kanagasabapathy, V. M.; McClelland, R. A.; Steenken, S. *Can. J. Chem.* **1999**, *77*, 2069-2082.
236. Steenken, S.; McClelland, R. A. *J. Am. Chem. Soc.* **1990**, *112*, 9648-9649.
237. Cozens, F. L.; Li, J.; McClelland, R. A.; Steenken, S. *Angew. Chem. Int. Ed. Engl.* **1992**, *31*, 743-745.
238. Cozens, F. L.; McClelland, R. A.; Steenken, S. *J. Am. Chem. Soc.* **1993**, *115*, 5050-5055.
239. McClelland, R. A.; Cozens, F. L.; Li, J.; Steenken, S. *J. Chem. Soc., Perkin Trans. 2* **1996**, 1531-1542.
240. Steenken, S.; Ashokkumar, M.; Maruthamuthu, P.; McClelland, R. A. *J. Am. Chem. Soc.* **1998**, *120*, 11925-11931.
241. McClelland, R. A.; Mathivanan, N.; Steenken, S. *J. Am. Chem. Soc.* **1990**, *112*, 4857-4861.
242. Cozens, F. L.; Mathivan, N.; McClelland, R. A.; Steenken, S. *J. Chem. Soc., Perkin Trans. 2* **1992**, 2083-2090.
243. Thomas, J. M. *Sci. Am.* **1992**, 112-118.
244. Fernández, L.; Marti, V.; García, H. *Phys. Chem. Chem. Phys.* **1999**, *1*, 3689-3695.
245. Cozens, F. L.; García, H.; Scaiano, J. C. *J. Am. Chem. Soc.* **1993**, *115*, 11134-11140.
246. Haw, J. F.; Nicholas, J. B.; Song, W.; Deng, F.; Wang, Z.; Xu, T.; Heneghan, C. S. *J. Am. Chem. Soc.* **2000**, *122*, 4763-4775.
247. Nicholas, J. B.; Haw, J. F. *J. Am. Chem. Soc.* **1998**, *120*, 11804-11805.
248. Xu, T.; Barich, D. H.; Goguen, P. W.; Song, W.; Wang, Z.; Nicholas, J. B.; Haw, J. F. *J. Am. Chem. Soc.* **1998**, *120*, 4025-4026.
249. Haw, J. F.; Nicholas, J. B.; Xu, T.; Beck, L. W.; Ferguson, D. B. *Acc. Chem. Res.* **1996**, *29*, 259-267.
250. Haw, J. F. *NMR Techniques in Catalysis*; Bell, A. T. and Pines, A., Ed.; Marcel Dekker Inc.: New York, 1994, pp 139-194.
251. Xu, T.; Haw, J. F. *J. Am. Chem. Soc.* **1994**, *116*, 10188-10195.
252. Xu, T.; Haw, J. F. *J. Am. Chem. Soc.* **1994**, *116*, 7753-7759.
253. Oliver, F. G.; Munson, E. J.; Haw, J. F. *J. Am. Chem. Soc.* **1992**, *96*, 8106-8111.
254. Lazo, N. D.; Richardson, B. R.; Schettler, P. D.; White, J. L.; Munson, E. J.; Haw, J. F. *J. Phys. Chem.* **1991**, *95*, 9420-9425.

255. Lazo, N. D.; White, J. L.; Munson, E. J.; Lambregts, M.; Haw, J. F. *J. Am. Chem. Soc.* **1990**, *112*, 4050-4052.
256. Haw, J. F.; Richardson, B. R.; Oshiro, I. S.; Lazo, N. D.; Speed, J. A. *J. Am. Chem. Soc.* **1989**, *111*, 2052-2058.
257. Tao, T.; Maciel, G. E. *Langmuir* **1999**, *15*, 1236-1246.
258. Tao, T.; Maciel, G. E. *J. Am. Chem. Soc.* **1995**, *117*, 12889-12890.
259. Bronnimann, C. E.; Maciel, G. E. *J. Am. Chem. Soc.* **1986**, *108*, 7154-7159.
260. Kiricsi, I.; Förster, H.; Tasi, G.; Nagy, J. B. *Chem. Rev.* **1999**, *99*, 2085-2114.
261. Kiricsi, I.; Tasi, G.; Fejes, P.; Förster, H. *J. Chem. Soc., Faraday Trans.* **1993**, *89*, 4221-4224.
262. Kramer, G. J.; van Santen, R. A.; Emels, C. A.; Nowak, A. K. *Nature* **1993**, *363*, 529-231.
263. Kazansky, V. B. *Acc. Chem. Res.* **1991**, *24*, 379-383.
264. Kao, H.; Grey, C. P.; Pitchumani, K.; Lakshminarasimhan, P. H.; Ramamurthy, V. *J. Phys. Chem. A* **1998**, *102*, 5627-5639.
265. Pitchumani, K.; Joy, A.; Prevost, N.; Ramamurthy, V. *Chem. Commun.* **1997**, 127-128.
266. Pitchumani, K.; Lakshminarasimhan, P. H.; Prevost, N.; Corbin, D. R.; Ramamurthy, V. *Chem. Commun.* **1997**, 181-182.
267. Pitchumani, K.; Lakshminarasimhan, P. H.; Turner, G.; Bakker, M. G.; Ramamurthy, V. *Tetrahedron Lett.* **1997**, *38*, 371-374.
268. Pitchumani, K.; Ramamurthy, V. *Chem. Commun.* **1996**, 2763-2764.
269. Maslak, P. *Top. Curr. Chem.* **1993**, *168*, 1-65.
270. Arnold, D. R.; Maroulis, A. J. *J. Am. Chem. Soc.* **1976**, *98*, 5931-5936.
271. Okamoto, A.; Snow, M. S.; Arnold, D. R. *Tetrahedron* **1986**, *42*, 6175-6178.
272. Popielarz, R.; Arnold, D. R. *J. Am. Chem. Soc.* **1990**, *112*, 3068-3082.
273. Arnold, D. R.; Du, X.; Chen, J. *Can. J. Chem.* **1995**, *73*, 307-318.
274. Reichel, L. W.; Griffin, G. W.; Muller, A. J.; Das, P. K.; Ege, S. *Can. J. Chem.* **1984**, *62*, 424-436.
275. Davis, H. F.; Das, P. K.; Reichel, L. W.; Griffin, G. W. *J. Am. Chem. Soc.* **1984**, *106*, 6968-6973.
276. Albini, A.; Fasani, E.; Mella, M. *J. Am. Chem. Soc.* **1986**, *108*, 4119-4125.
277. Albini, A.; Mella, M. *Tetrahedron* **1986**, *42*, 6219-6224.
278. Maslak, P.; Asel, S. L. *J. Am. Chem. Soc.* **1988**, *110*, 8260-8261.
279. Maslak, P.; Chapman, W. H., Jr. *J. Chem. Soc., Chem. Commun.* **1989**, 1809-1811.
280. Maslak, P.; Chapman, W. H., Jr. *Tetrahedron* **1990**, *46*, 2715-2724.

281. Maslak, P.; Chapman, W. H., Jr. *J. Org. Chem.* **1990**, *55*, 6334-6347.
282. Maslak, P.; Chapman, W. H., Jr.; Vallombroso, T. M., Jr.; Watson, B. A. *J. Am. Chem. Soc.* **1995**, *117*, 12380-12390.
283. Maslak, P.; Chapman, W. H., Jr. *J. Org. Chem.* **1996**, *61*, 2647-2656.
284. Maslak, P.; Narvaez, J. N. *J. Chem. Soc., Chem. Commun.* **1989**, 138-139.
285. Maslak, P.; Kula, J.; Narvaez, J. N. *J. Org. Chem.* **1990**, *55*, 2277-2279.
286. Maslak, P.; Kula, J.; Chateaneuf, J. E. *J. Am. Chem. Soc.* **1991**, *113*, 2304-2306.
287. Maslak, P.; Narvaez, J. N.; Vallombroso, T. M., Jr. *J. Am. Chem. Soc.* **1995**, *117*, 12373-12379.
288. Maslak, P.; Narvaez, J. N.; Kula, J.; Malinski, D. S. *J. Org. Chem.* **1990**, *55*, 4550-4559.
289. Maslak, P.; Vallombroso, T. M., Jr.; Chapman, W. H., Jr.; Narvaez, J. N. *Angew. Chem. Int. Ed. Engl.* **1994**, *33*, 73-75.
290. Maslak, P.; Narvaez, J. N. *Angew. Chem. Int. Ed. Engl.* **1990**, *29*, 283-285.
291. Liu, A.; Saucer, M. C.; Loffredo, D. M.; Trifunac, A. D. *J. Photochem. Photobiol., A* **1992**, *67*, 197-208.
292. Baciocchi, E.; Del Giacco, T.; Elisei, F. *J. Am. Chem. Soc.* **1993**, *115*, 12290-12295.
293. Tokumura, K.; Ozaki, T.; Nosaka, H.; Saigusa, Y.; Itoh, M. *J. Am. Chem. Soc.* **1991**, *113*, 4974-4980.
294. Mann, C. K.; Barnes, K. K. *Electrochemical Reactions in Non-Aqueous Systems*; Dekker: New York, 1970.
295. Hubig, S. M.; Bockman, T. M.; Kochi, J. K. *J. Am. Chem. Soc.* **1997**, *119*, 2926-2955.
296. Andre, J. J.; Weill, G. *Mol. Phys.* **1968**, *15*, 97-99.
297. Kawai, K.; Shirota, Y.; Tsubomura, H.; Mikawa, H. *Bull. Chem. Soc. Jpn.* **1972**, *45*, 77-81.
298. Gschwind, R.; Haselbach, E. *Helv. Chim. Acta* **1979**, *62*, 941-955.
299. Kemp, D. R.; Porter, G. *Chem. Commun.* **1969**, 1029-1030.
300. Banks, J. T.; Scaiano, J. C. *J. Am. Chem. Soc.* **1993**, *115*, 6409-6413.
301. Mayr, H.; Schneider, R.; Schade, C.; Bartl, J.; Bederke, R. *J. Am. Chem. Soc.* **1990**, *112*, 4446-4454.
302. Mayr, H.; Patz, M. *Angew. Chem. Int. Ed. Engl.* **1994**, *33*, 938-957.
303. Burfeindt, J.; Patz, M.; Müller, M.; Mayr, H. *J. Am. Chem. Soc.* **1998**, *120*, 3629-3634.
304. Schepp, N. P.; Johnston, L. J. *J. Am. Chem. Soc.* **1996**, *118*, 2872-2881.

305. Rehm, D.; Weller, A. *Isr. J. Chem.* **1970**, *8*, 259-271.
306. Kavarnos, G. J.; Turro, N. J. *Chem. Rev.* **1986**, *86*, 401-449.
307. Gould, I. R.; Ege, D.; Moser, J.; Farid, S. *J. Am. Chem. Soc.* **1990**, *112*, 4290-4301.
308. Hamill, W. H. *Radical Ions*; Kaiser, E. T. and Kevan, L., Ed.; Wiley Interscience, 1968; New York, pp 399.
309. Carey, F. A.; Sundburg, R. J. *Advanced Organic Chemistry Part A: Structure and Mechanisms*; 3rd ed.; Plenum Press: New York, 1990; pp. 216-220.
310. Thibblin, A. J. *J. Phys. Org. Chem* **1989**, *2*, 15-25.
311. Thibblin, A. *Chem. Soc. Rev.* **1993**, *22*, 427-433.
312. Forester, T. R.; Howe, R. F. *J. Am. Chem. Soc.* **1987**, *109*, 5076-5082.
313. Ono, Y.; Mori, T. *J. Chem. Soc., Faraday Trans. I* **1981**, *77*, 2209-2221.
314. Kondo, J. N.; Ishikawa, H.; Yoda, E.; Wakabayashi, F.; Domen, K. *J. Phys. Chem. B* **1999**, *103*, 8538-8543.
315. Ishikawa, H.; Yoda, E.; Kondo, J. N.; Wakabayashi, F.; Domen, K. *J. Phys. Chem. B* **1999**, *103*, 5681-5686.
316. Aronson, M. T.; Gorte, R. J.; Farneth, W. E.; White, D. *J. Am. Chem. Soc.* **1989**, *111*, 840-846.
317. Stepanov, A. G.; Zamaraev, K. I.; Thomas, J. M. *Catal. Lett.* **1992**, *13*, 407-422.
318. Tsiao, C.; Corbin, D. R.; Dybowski, C. *J. Am. Chem. Soc.* **1990**, *112*, 7140-7144.
319. Murray, D. K.; Chang, J.; Haw, J. F. *J. Am. Chem. Soc.* **1993**, *115*, 4732-4741.
320. Murray, D. K.; Howard, T.; Goguen, P. W.; Krawietz, T. R.; Haw, J. F. *J. Am. Chem. Soc.* **1994**, *116*, 6354-6360.
321. Bosáček, V. *J. Phys. Chem.* **1993**, *97*, 10732-10737.
322. Bosáček, V. *Z. Phys. Chem.* **1995**, *189*, 241-250.
323. Viruela-Martín, P.; Zicovich-Wilson, C. M.; Corma, A. *J. Phys. Chem.* **1993**, *97*, 13713-13719.
324. Mota, C. J. A.; Esteves, P. M.; de Amorim, M. B. *J. Phys. Chem.* **1996**, *100*, 12418-12423.
325. Choi, S. Y.; Park, Y. S.; Hong, S. B.; Yoon, K. B. *J. Am. Chem. Soc.* **1996**, *118*, 9377-9386.
326. Kramer, G. J.; van Santen, R. A. *J. Am. Chem. Soc.* **1993**, *115*, 2887-2897.
327. Sanderson, R. T. *Chemical Bonds and Bond Energy*; 2nd ed.; Academic Press: New York, 1976.
328. Sanderson, R. T. *J. Am. Chem. Soc.* **1983**, *105*, 2259-2261.
329. Sanderson, R. T. *J. Chem. Educ.* **1988**, *65*, 112-118.
330. Sanderson, R. T. *J. Chem. Educ.* **1988**, *65*, 227-231.

331. Mortier, W. J. *Catal.* **1978**, *55*, 138-145.
332. Jacobs, P. A.; Mortier, W. J.; Uytterhoeven, J. B. *J. Inorg. Nucl. Chem.* **1978**, *40*, 1919-1923.
333. Barnabas, M. V.; Trifunac, A. D. *Chem. Phys. Lett.* **1992**, *193*, 298-304.
334. Werst, D. W.; Tartakovsky, E. E.; Pioscos, E. A.; Trifunac, A. D. *J. Phys. Chem.* **1994**, *98*, 10249-10257.
335. Werst, D. W.; Han, P.; Trifunac, A. D. *Radiat. Phys. Chem.* **1998**, *51*, 255-262.
336. Stock, L. M.; Brown, H. C. *Adv. Phys. Org. Chem.* **1963**, *1*, 35-154.
337. Brown, H. C.; Kelly, D. P.; Periasamy, M. *Proc. Natl. Acad. Sci. USA* **1980**, *77*, 6956-6960.
338. The initial detection of the parent cumyl cation reported in 1997 may represent a small fraction of those carbocations with a longer lifetime component rendered observable under conditions of high laser intensity where a greater yield of carbocation was initially generated.
339. Mirth, G.; Lercher, J. A.; Anderson, M. W.; Klinowski, J. *J. Chem. Soc., Faraday Trans.* **1990**, *86*, 3039-3044.
340. Kirmse, A.; Karger, J.; Stallmach, F.; Hunger, B. *Appl. Catal. A* **1999**, *188*, 241-246.
341. Rep, M.; Palomares, A. E.; Eder-Mirth, G.; van Ommen, J. G.; Rösch, N.; Lercher, J. A. *J. Phys. Chem. B* **2000**, *104*, 8624-8630.
342. Vayssilov, G. N.; Lercher, J. A.; Rösch, N. *J. Phys. Chem. B* **2000**, *104*, 8614-8623.
343. Hunger, B.; Matysik, S.; Heuchel, M.; Einicke, W. *Langmuir* **1997**, *13*, 6249-6254.
344. Lovins, R. E.; Andrews, L. J.; Keefer, R. M. *J. Am. Chem. Soc.* **1962**, *84*, 3959-3962.
345. Bolton, R.; Chapman, N. B.; Shorter, J. *J. Chem. Soc.* **1964**, 1895-1906.
346. Ledwith, A.; Morris, D. G. *J. Chem. Soc.* **1964**, 508-509.
347. Cowell, G. W.; George, T. D.; Ledwith, A.; Morris, D. G. *J. Chem. Soc. (B)* **1966**, 1169-1172.
348. Cowell, G. W.; Ledwith, A. *J. Chem. Soc. (B)* **1967**, 695-697.
349. Friedrich, E. C.; Taggart, D. B. *J. Org. Chem.* **1978**, *43*, 805-808.
350. Bethell, D.; Hare, G. J.; Kearney, P. A. *J. Chem. Soc., Perkin Trans. 2* **1981**, 684-691.
351. Bethell, D.; Clare, P. N.; Hare, G. *J. Chem. Soc., Perkin Trans. 2* **1983**, 1889-1893.
352. Amyes, T. L.; Richard, J. P.; Novak, M. *J. Am. Chem. Soc.* **1992**, *114*, 8032-8041.
353. Allen, A. D.; Colomvakos, J. D.; Tee, O. S.; Tidwell, T. T. *J. Org. Chem.* **1994**, *59*, 7185-7187.

354. Liu, K.; Lin, Y. *Tetrahedron Lett.* **1997**, *38*, 1419-1422.
355. Olah, G. A.; Surya Prakash, G. K.; Liang, G.; Westerman, P. W.; Kunde, K.; Chandrasekhar, J.; Schleyer, P. v. R. *J. Am. Chem. Soc.* **1980**, *102*, 4485-4492.
356. Johnston, L. J.; Kwong, P.; Shelemay, A.; Lee-Ruff, E. *J. Am. Chem. Soc.* **1993**, *115*, 1664-1669.
357. Malandra, J. L.; Mills, N. S.; Kadlecsek, D. E.; Lowery, J. A. *J. Am. Chem. Soc.* **1994**, *116*, 11622-11623.
358. Mills, N. S.; Malandra, J. L.; Burns, E. E.; Green, A.; Unruh, K. E.; Kadlecsek, D. E.; Lowery, J. A. *J. Org. Chem.* **1997**, *62*, 9318-9322.
359. Mills, N. S.; Burns, E. E.; Hodges, J.; Gibbs, J.; Esparza, E.; Malandra, J. L.; Koch, J. *J. Org. Chem.* **1998**, *63*, 3017-3022.
360. Mills, N. S.; Malinky, T.; Malandra, J. L.; Burns, E. E.; Crossno, P. *J. Org. Chem.* **1999**, *64*, 511-517.
361. Olah, G. A.; Liang, G. *J. Org. Chem.* **1975**, *40*, 2108-2116.
362. Wayner, D. D. M.; McPhee, D. J.; Griller, D. *J. Am. Chem. Soc.* **1988**, *110*, 132-137.
363. Since the 9-fluorenyl cation has never been generated under stable ion conditions, the pK_R value cannot be obtained directly from acidity functions and has been estimated to be -17.3 from thermodynamic cycles and -15.9 from kinetic methods.
364. Breslow, R.; Chang, H. W. *J. Am. Chem. Soc.* **1961**, *83*, 3727-3728.
365. Toone, T. W.; Lee-Ruff, E.; Hopkinson, A. C. *Can. J. Chem.* **1975**, *53*, 1635-1641.
366. Deno, N. C.; Jaruzelski, J. J.; Schriesheim, A. *J. Am. Chem. Soc.* **1955**, *77*, 3044-3051.
367. Mathivanan, N.; McClelland, R. A.; Steenken, S. *J. Am. Chem. Soc.* **1990**, *112*, 8454-8457.
368. Cheng, J.; Handoo, K. L.; Parker, V. D. *J. Am. Chem. Soc.* **1993**, *115*, 2655-2660.
369. Rodriguez, C. F.; Vuckovic, D. L.; Hopkinson, A. C. *J. Mol. Struct.* **1996**, *363*, 131-138.
370. Jiao, H.; Schleyer, P. v. R.; Mo, Y.; McAllister, M. A.; Tidwell, T. T. *J. Am. Chem. Soc.* **1997**, *119*, 7075-7083.
371. Breslow, R. *Acc. Chem. Res.* **1973**, *6*, 393-398.
372. Breslow, R.; Hoffman, J. M., Jr. *J. Am. Chem. Soc.* **1972**, *94*, 2110-2111.
373. Saunders, M.; Berger, R.; Jaffe, A.; McBride, J. M.; O'Neill, J.; Breslow, R.; Hoffman, J. M., Jr.; Perchonock, C.; Wasserman, E.; Hutton, R. S.; Kuck, V. J. *J. Am. Chem. Soc.* **1973**, *95*, 3017-3018.
374. Allen, A.; Sumonja, M.; Tidwell, T. T. *J. Am. Chem. Soc.* **1997**, *119*, 2371-2375.

375. Friedrich, E. C.; Tam, T. M. *J. Org. Chem.* **1982**, *47*, 315-319.
376. Allen, A. D.; Fujio, M.; Mohammed, N.; Tidwell, T. T.; Tsuji, Y. *J. Org. Chem.* **1997**, *62*, 246-252.
377. Breslow, R.; Mazur, S. *J. Am. Chem. Soc.* **1973**, *95*, 584-585.
378. Wan, P.; Krogh, E. *J. Chem. Soc., Chem. Commun.* **1985**, 1207-1208.
379. Krogh, E.; Wan, P. *Tetrahedron Lett.* **1986**, *27*, 823-826.
380. Wan, P.; Krogh, E. *J. Am. Chem. Soc.* **1989**, *111*, 4887-4895.
381. Blazek, A.; Pungente, M.; Krogh, E.; Wan, P. *J. Photochem. Photobiol., A* **1992**, *64*, 315-327.
382. Malar, E. J. P.; Jug, K. *Tetrahedron* **1986**, *42*, 417-426.
383. Gaillard, E.; Fox, M. A.; Wan, P. *J. Am. Chem. Soc.* **1989**, *111*, 2180-2186.
384. Mecklenburg, S. L.; Hilinski, E. F. *J. Am. Chem. Soc.* **1989**, *111*, 5471-5472.
385. Lew, C. S. Q.; Wong, D. F.; Johnston, L. J.; Bertone, M.; Hopkinson, A. C.; Lee-Ruff, E. *J. Org. Chem.* **1996**, *61*, 6805-6808.
386. Lew, C. S. Q.; McClelland, R. A.; Johnston, L. J.; Schepp, N. P. *J. Chem. Soc., Perkin Trans. 2* **1994**, 395-397.
387. Lew, C. S. Q.; Wagner, B. D.; Angelini, M. P.; Lee-Ruff, E.; Lusztyk, J.; Johnston, L. J. *J. Am. Chem. Soc.* **1996**, *118*, 12066-12073.
388. Chateauneuf, J. E. *J. Chem. Soc., Chem. Commun.* **1991**, 1437-1438.
389. Kirmse, W.; Kilian, J. *J. Am. Chem. Soc.* **1990**, *112*, 6399-6400.
390. Falvey, D. E.; Schuster, G. B. *J. Am. Chem. Soc.* **1986**, *108*, 7419-7420.
391. Cozens, F. L.; Cano, M. L.; García, H.; Schepp, N. P. *J. Am. Chem. Soc.* **1998**, *120*, 5667-5673.
392. Jaeger, D. A. *J. Am. Chem. Soc.* **1974**, *96*, 6216-6217.
393. Cozens, F. L.; Pincock, A.; Pincock, J. A.; Smith, R. *J. Org. Chem.* **1998**, *63*, 434-435.
394. Delcourt, M. O.; Rossi, M. J. *J. Phys. Chem.* **1982**, *86*, 3233-3239.
395. Hug, G. L.; Carmichael, I. *J. Phys. Chem. Ref. Data* **1986**, *15*, 1-240.
396. Turro, N. J. *Modern Molecular Photochemistry*; Benjamin-Cummings: Menlo Park, CA, 1978.
397. Cozens, F. L. *Ph. D. Thesis*; University of Toronto, 1992.
398. Wong, P. C.; Griller, D.; Scaiano, J. C. *J. Am. Chem. Soc.* **1981**, *103*, 5934-5935.
399. Faria, J. L.; Steenken, S. *J. Am. Chem. Soc.* **1990**, *112*, 1277-1279.
400. Tomioka, H.; Nakamura, H.; Izawa, Y. *J. Chem. Soc., Chem. Commun.* **1983**, 1070-1071.

401. Kiselev, A. V.; Kubelkova, L.; Lygin, V. I. *Russ. J. Phys. Chem.* **1964**, *38*, 1480-1484.
402. Geodakyan, K. T.; Kiselev, A. V.; Lygin, V. I. *Russ. J. Phys. Chem.* **1967**, *41*, 227-232.
403. Kirmse, W.; Krzoss, B.; Steenken, S. *J. Am. Chem. Soc.* **1996**, *118*, 7473-7477.
404. Carey, F. A.; Sundburg, R. J. *Advanced Organic Chemistry Part A: Structure and Mechanisms*; 3rd ed.; Plenum Press: New York, 1990; p. 278.
405. Sunström, V. *Femtochemistry and Femtobiology*; Imperial College Press: London, 1996.
406. Mariano, P. S. *Advances in Electron Transfer Chemistry*; Jai Press: Greenwich, CT, 1991-1994; Vol. 1-4.
407. Moser, C. C.; Keske, J. M.; Warncke, K.; Farid, R. S.; Dutton, P. L. *Nature* **1992**, *355*, 796-802.
408. Kalyanasundaram, K. *Photochemistry in Microheterogeneous Systems*; Academic Press: New York, 1987.
409. Fox, M. A. *Top. Curr. Chem.* **1991**, *159*, 68-101.
410. Whitten, D. G. *Acc. Chem. Res.* **1980**, *13*, 83-90.
411. Gust, D.; Moore, T. A.; Moore, A. L. *Z. Phys. Chem.* **1999**, *213*, 149-155.
412. Kuciauskas, D.; Liddell, P. A.; Lin, S.; Stone, S. G.; Moore, A. L.; Moore, T. A.; Gust, D. *J. Phys. Chem. B* **2000**, *104*, 4307-4321.
413. Joachim, C.; Roth, S. *Atomic and Molecular Wires*, ACS Monograph No. 341; Kluwer: Dordrecht, 1997.
414. Leatherman, G.; Durantini, E. N.; Gust, D.; Moore, T. A.; Moore, A. L.; Stone, S.; Zhou, Z.; Rez, P.; Liu, Y. Z.; Lindsay, S. M. *J. Phys. Chem. B* **1999**, *103*, 4006-4010.
415. Fox, M. A.; Chanon, M. *Photoinduced Electron Transfer*; Elsevier: New York, 1988.
416. Kavarnos, G. J. *Top. Curr. Chem.* **1990**, *156*, 21-57.
417. Leonhardt, H.; Weller, A. *Ber. Bunsen-Ges. Phys. Chem.* **1963**, *67*, 791-795.
418. Mataga, N.; Mitiga, M.; Nishimura, T. *J. Mol. Struct.* **1978**, *47*, 199-219.
419. Masuhara, H.; Saito, T.; Maeda, Y.; Mataga, N. *J. Mol. Struct.* **1978**, *47*, 243-259.
420. Neunteufel, R. A.; Arnold, D. R. *J. Am. Chem. Soc.* **1973**, *95*, 4080-4081.
421. Borg, R. M.; Arnold, D. R.; Cameron, T. S. *Can. J. Chem.* **1984**, *62*, 1785-1802.
422. Gould, I. R.; Farid, S. *Acc. Chem. Res.* **1996**, *29*, 522-528.
423. Gould, I. R.; Ege, D.; Mattes, S.; Farid, S. *J. Am. Chem. Soc.* **1987**, *109*, 3794-3796.
424. Gould, I. R.; Moody, R.; Farid, S. *J. Am. Chem. Soc.* **1988**, *110*, 7242-7244.
425. Marcus, R. A. *J. Chem. Phys.* **1956**, *24*, 966-978.

426. Netzel, T. L. *J. Chem. Educ.* **1997**, *74*, 646-651.
427. Kelley, S. O.; Barton, J. K. *Science* **1999**, *285*, 375-381.
428. Núñez, M. E.; Barton, J. K. *Curr. Opin. Chem. Biol.* **2000**, *4*, 199-206.
429. Gopidas, K. R.; Leheny, A. R.; Caminati, G.; Tomalia, D. A.; Turro, N. J. *J. Am. Chem. Soc.* **1991**, *113*, 7335-7342.
430. Tavernier, H. L.; Barzykin, A. V.; Tachiya, M.; Fayer, M. D. *J. Phys. Chem. B* **1998**, *102*, 6078-6088.
431. Worrall, D. R.; Williams, S. L.; Wilkinson, F. J. *J. Phys. Chem. A* **1998**, *102*, 5484-5490.
432. Zhang, G.; Thomas, J. K.; Eremenko, A.; Kikteva, T.; Wilkinson, F. J. *J. Phys. Chem. B* **1997**, *101*, 8569-8577.
433. Wan, C.; Fiebig, T.; Kelley, S. O.; Treadway, C. R.; Barton, J. K.; Zewail, A. H. *Proc. Natl. Acad. Sci. USA* **1999**, *96*, 6014-6019.
434. Castleman, J. A. W.; Zhong, Q.; Hurley, S. M. *Proc. Natl. Acad. Sci. USA* **1999**, *96*, 4219-4220.
435. Marcus, R. A. *Annu. Rev. Phys. Chem.* **1964**, *15*, 155.
436. Marcus, R. A. *Angew. Chem. Int. Ed. Engl.* **1993**, *32*, 1111-1121.
437. Hush, N. S. *Mechanistic Aspects of Inorganic Reactions*; Rorabacker, D. B. and Endicott, J. F., Ed.; ACS: Washington, D.C., 1982; Vol. 198, Chapter 13.
438. Grampp, G. *Angew. Chem. Int. Ed. Engl.* **1993**, *32*, 691-693.
439. Rehm, D.; Weller, A. *Ber. Bunsen-Ges. Phys. Chem.* **1969**, *73*, 834-839.
440. Miller, J. R.; Calcaterra, L. T.; Closs, G. L. *J. Am. Chem. Soc.* **1984**, *106*, 3047-3049.
441. Closs, G. L.; Miller, J. R. *Science* **1988**, *240*, 440-447.
442. Wasielewski, M. R.; Niewczyk, M. P.; Svec, W. A.; Pewitt, E. B. *J. Am. Chem. Soc.* **1985**, *107*, 1080-1082.
443. Miller, J. R.; Beitz, J. V.; Huddleston, R. K. *J. Am. Chem. Soc.* **1984**, *106*, 5057-5068.
444. Kemnitz, K. *Chem. Phys. Lett.* **1988**, *152*, 305-310.
445. Chen, P.; Duesing, R.; Graff, D. K.; Meyer, T. J. *J. Am. Chem. Soc.* **1991**, *95*, 5850-5858.
446. Weng, Y.-X.; Chan, K.-C.; Tzeng, B.-C.; Che, C.-M. *J. Chem. Phys.* **1998**, *109*, 5948-5956.
447. Guldi, D. M.; Luo, C.; Prato, M.; Dietel, E.; Hirsch, A. *Chem. Commun.* **2000**, 373-374.
448. DeCosta, D. P.; Pincock, J. A. *J. Am. Chem. Soc.* **1989**, *111*, 8948-8950.

449. DeCosta, D. P.; Pincock, J. A. *J. Am. Chem. Soc.* **1993**, *115*, 2180-2190.
450. Hilborn, J. W.; MacKnight, E.; Pincock, J. A.; Wedge, P. J. *J. Am. Chem. Soc.* **1994**, *116*, 3337-3346.
451. Pincock, J. A.; Wedge, P. J. *J. Org. Chem.* **1994**, *59*, 5587-5595.
452. Ishiguro, K.; Nakano, T.; Shibata, H.; Sawaki, Y. *J. Am. Chem. Soc.* **1996**, *118*, 7255-7264.
453. Turró, C.; Zaleski, J. M.; Karabatsos, Y. M.; Nocera, D. G. *J. Am. Chem. Soc.* **1996**, *118*, 6060-6067.
454. Grätzel, M.; Kalyanasundaram, K. *Kinetics and Catalysis in Microheterogeneous Systems*; Marcel Dekker: New York, 1991.
455. Hashimoto, S. *Chem. Phys. Lett.* **1996**, *252*, 236-242.
456. Yoon, K. B.; Park, Y. S.; Kochi, J. K. *J. Am. Chem. Soc.* **1996**, *116*, 12710-12718.
457. Corma, A.; Fornés, V.; García, H.; Miranda, M.; Sabater, M. *J. Am. Chem. Soc.* **1994**, *116*, 9767-9768.
458. Sankararaman, S.; Perrier, S.; Kochi, J. K. *J. Am. Chem. Soc.* **1989**, *111*, 6448-6449.
459. Kobashi, H.; Gyoda, H.; Morita, T. *Bull. Chem. Soc. Jpn.* **1977**, *50*, 1731-1738.
460. Calculated from transient absorption spectra and molar absorptivity at another wavelength.
461. Determined from the absorption spectrum of the 4-methoxycumyl cation. The carbocation was generated from a solution of α -methyl-4-methoxystyrene in dichloromethane and concentrated sulfuric acid.
462. Shida, T. *Electronic Absorption Spectra of Radical Ions*; Elsevier: Amsterdam, 1988.
463. Nakazato, C.; Masuda, T. *Bull. Chem. Soc. Jpn.* **1986**, *59*, 2237-2239.
464. Murov, S. L.; Carmichael, I.; Hug, G. L. *Handbook of Photochemistry*; 2nd ed.; Marcel Dekker: New York, 1993.
465. Kojima, M.; Sakuragi, H.; Tokumaru, K. *Bull. Chem. Soc. Jpn.* **1989**, *62*, 3863-3868.
466. Perrin, M. J. *Comptes Rendus Acad. Sci.* **1923**, *177*, 469-475.
467. Perrin, M. F. *Comptes Rendus Acad. Sci.* **1924**, *178*, 1978-1980.
468. Turberville, W.; Robins, D. S.; Dutta, P. K. *J. Phys. Chem.* **1992**, *96*, 5024-5029.
469. Sykora, M.; Kincaid, J. R.; Dutta, P. K.; Castagnola, N. B. *J. Phys. Chem. B* **1999**, *103*, 309-320.
470. Johnston, K. M.; Williams, G. H. *J. Chem. Soc.* **1960**, *82*, 1168-1170.

471. Kratt, G.; Beckhaus, H. D.; Bernlöhr, W.; Rüchardt, C. *Thermochim. Acta.* **1983**, *62*, 279-294.
472. Kratt, G.; Beckhaus, H.-D.; Linder, H. J.; Rüchardt, C. *Chem. Ber.* **1983**, *116*, 3235-3263.
473. Vogel, A. I. *Vogel's Textbook of Physical Organic Chemistry*; 4th ed.; Longman: New York, 1978.
474. Nutaitis, C. F.; Joseph, E. B. *Synth. Commun.* **1990**, *20*, 487-493.
475. Foster, B. E. *M. Sc. Thesis*; Dalhousie University, 1987.
476. Sauer, J.; Huisga, R.; Hauser, A. *Chem. Ber.* **1958**, *91*, 1461-1473.